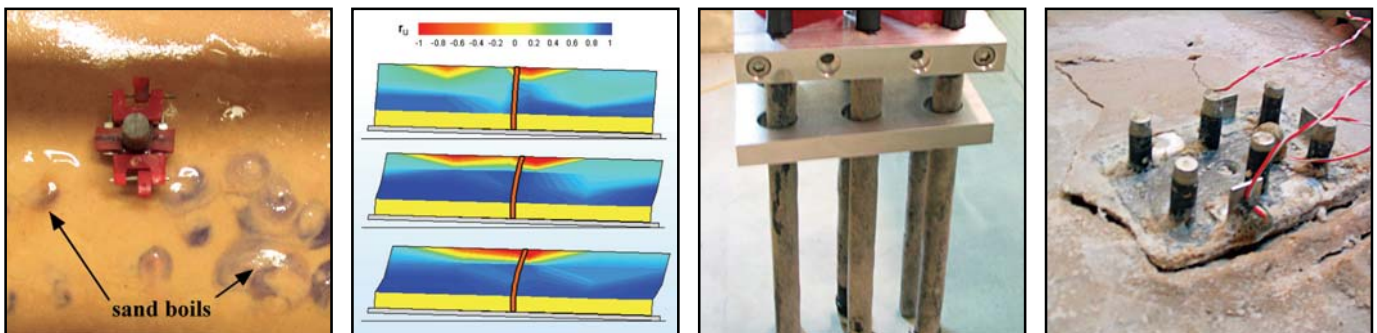


Centrifuge Modeling of Permeability and Pinning Reinforcement Effects on Pile Response to Lateral Spreading

by
Lenart Luis Gonzalez Lagos, Tarek Abdoun and Ricardo Dobry



Technical Report MCEER-07-0020


December 10, 2007

NOTICE

This report was prepared by Rensselaer Polytechnic Institute as a result of research sponsored by MCEER through a contract from the Federal Highway Administration. Neither MCEER, associates of MCEER, its sponsors, Rensselaer Polytechnic Institute, nor any person acting on their behalf:

- a. makes any warranty, express or implied, with respect to the use of any information, apparatus, method, or process disclosed in this report or that such use may not infringe upon privately owned rights; or
- b. assumes any liabilities of whatsoever kind with respect to the use of, or the damage resulting from the use of, any information, apparatus, method, or process disclosed in this report.

Any opinions, findings, and conclusions or recommendations expressed in this publication are those of the author(s) and do not necessarily reflect the views of MCEER or the Federal Highway Administration.

Report Documentation Page 50272-101	1. Report No. MCEER-07-0020	2.	
4. Title and Subtitle Centrifuge Modeling of Permeability and Pinning Reinforcement Effects on Pile Response to Lateral Spreading		5. Report Date 12/10/2007	
7. Authors L.L. Gonzalez-Lagos, T. Abdoun and R. Dobry		8. Performing Organization Report No.	
9. Performing Organization Name and Address		10. Project / Task / Work Unit No. 094	
12. Sponsoring Organization Name and Address Multidisciplinary Center for Earthquake Engineering Research State University of New York at Buffalo Red Jacket Quadrangle Buffalo, NY 14261		11. Contract (C) or Grant (G) No. (C) DTH61-98-C-00094 (G)	
15. Supplementary Notes This research was conducted at Rensselaer Polytechnic Institute and was supported by the Federal Highway Administration.		13. Type of Report / Period Covered Technical Report	
16. Abstract (limit 200 Words) The vulnerability of highway bridges to earthquake-induced ground failures arising from liquefaction has been clearly demonstrated by the extensive damage observed in the past earthquakes, particularly when a nonliquefied soil layer rides on top of the liquefied soil. Liquefaction induced lateral spreading may be reduced by the restraining forces provided by pile group foundations. This reduction in lateral displacement reduces the loads and displacement demands that are imposed on the piles. The first part of this work presents experimental results and analyses of six centrifuge tests that were conducted at the 150 g-ton RPI centrifuge to investigate the effect of soil permeability in the response of single piles and pile groups to lateral spreading. In the models that simulate a liquefiable coarse sand layer (saturated with water), the piles bounced back after a couple of cycles of shaking; however in the models that simulate a liquefiable fine sand layer (saturated with viscous fluid), the piles never bounced back, reaching maximum displacements and bending moments as large as 6 times the one measured in the models saturated with water. In the models with lower soil permeability (saturated with viscous fluid) the results and analyses indicate that negative excess pore pressures developed close to the foundations stiffened the soil, increasing the effective area subjected to the liquefied soil pressure, explaining hence the large bending moments. The second part presents experimental results and analyses of four centrifuge tests that were conducted at the RPI centrifuge. The project was to study the reinforcing or pinning effect the pile groups have on the lateral spreading. An analysis approach developed in this study proved to be very useful in understanding the reinforcement effect pile groups have in liquefaction induced lateral spreading and to give a good estimation, at least in centrifuge modeling, of the expected pile group deformations.		14.	
17. Document Analysis a. Descriptors Earthquake Engineering. Centrifuge modeling. Seismic vulnerability assessments. Highway infrastructure. Bridges. Ground failure. Liquefaction. Lateral spreading. Pile group foundations. Soil permeability. Reinforcing effects. Pinning effects.			
b. Identifiers/Open-Ended Terms			
c. COSATI Field/Group			
18. Availability Statement Release Unlimited.		19. Security Class (This Report) Unclassified	21. No. of Pages 354
		20. Security Class (This Page) Unclassified	22. Price

NTIS DISCLAIMER



This document has been reproduced from the best copy furnished by the sponsoring agency.

Centrifuge Modeling of Permeability and Pinning Reinforcement Effects on Pile Response to Lateral Spreading

by

Lenart Luis Gonzalez Lagos,¹ Tarek Abdoun² and Ricardo Dobry³

Publication Date: December 10, 2007

Submittal Date: October 16, 2007

Technical Report MCEER-07-0020

Task Number 094-C-2.4

FHWA Contract Number DTFH61-98-C-00094

- 1 Ph.D. Candidate, Department of Civil and Environmental Engineering, Rensselaer Polytechnic Institute
- 2 Associate Professor and Associate Director, NEES-NSF Geotechnical Centrifuge Research Center, Department of Civil and Environmental Engineering, Rensselaer Polytechnic Institute
- 3 Professor and Director, NEES-NSF Geotechnical Centrifuge Research Center, Department of Civil and Environmental Engineering, Rensselaer Polytechnic Institute

MCEER

University at Buffalo, The State University of New York

Red Jacket Quadrangle, Buffalo, NY 14261

Phone: (716) 645-3391; Fax (716) 645-3399

E-mail: mceer@buffalo.edu; WWW Site: <http://mceer.buffalo.edu>

Preface

The Multidisciplinary Center for Earthquake Engineering Research (MCEER) is a national center of excellence in advanced technology applications that is dedicated to the reduction of earthquake losses nationwide. Headquartered at the University at Buffalo, State University of New York, the Center was originally established by the National Science Foundation in 1986, as the National Center for Earthquake Engineering Research (NCEER).

Comprising a consortium of researchers from numerous disciplines and institutions throughout the United States, the Center's mission is to reduce earthquake losses through research and the application of advanced technologies that improve engineering, pre-earthquake planning and post-earthquake recovery strategies. Toward this end, the Center coordinates a nationwide program of multidisciplinary team research, education and outreach activities.

MCEER's research is conducted under the sponsorship of two major federal agencies, the National Science Foundation (NSF) and the Federal Highway Administration (FHWA), and the State of New York. Significant support is also derived from the Federal Emergency Management Agency (FEMA), other state governments, academic institutions, foreign governments and private industry.

The Center's Highway Project develops improved seismic design, evaluation, and retrofit methodologies and strategies for new and existing bridges and other highway structures, and for assessing the seismic performance of highway systems. The FHWA has sponsored three major contracts with MCEER under the Highway Project, two of which were initiated in 1992 and the third in 1998.

Of the two 1992 studies, one performed a series of tasks intended to improve seismic design practices for new highway bridges, tunnels, and retaining structures (MCEER Project 112). The other study focused on methodologies and approaches for assessing and improving the seismic performance of existing "typical" highway bridges and other highway system components including tunnels, retaining structures, slopes, culverts, and pavements (MCEER Project 106). These studies were conducted to:

- assess the seismic vulnerability of highway systems, structures, and components;
- develop concepts for retrofitting vulnerable highway structures and components;
- develop improved design and analysis methodologies for bridges, tunnels, and retaining structures, which include consideration of soil-structure interaction mechanisms and their influence on structural response; and
- develop, update, and recommend improved seismic design and performance criteria for new highway systems and structures.

The 1998 study, “Seismic Vulnerability of the Highway System” (FHWA Contract DTFH61-98-C-00094; known as MCEER Project 094), was initiated with the objective of performing studies to improve the seismic performance of bridge types not covered under Projects 106 or 112, and to provide extensions to system performance assessments for highway systems. Specific subjects covered under Project 094 include:

- development of formal loss estimation technologies and methodologies for highway systems;
- analysis, design, detailing, and retrofitting technologies for special bridges, including those with flexible superstructures (e.g., trusses), those supported by steel tower substructures, and cable-supported bridges (e.g., suspension and cable-stayed bridges);
- seismic response modification device technologies (e.g., hysteretic dampers, isolation bearings); and
- soil behavior, foundation behavior, and ground motion studies for large bridges.

In addition, Project 094 includes a series of special studies, addressing topics that range from non-destructive assessment of retrofitted bridge components to supporting studies intended to assist in educating the bridge engineering profession on the implementation of new seismic design and retrofitting strategies.

The report presents the results of an experimental and analytical study of the soil-structure response of pile groups subjected to liquefaction induced lateral spreading. The first section of the report presents the experimental results and analyses of six centrifuge tests that were conducted to investigate the effects of soil permeability on the response of pile foundations subjected to lateral spreading. In the centrifuge models simulating liquefiable coarse sand layer, the piles bounced back after a couple of cycles of shaking; however in models that simulate a liquefiable fine sand layer, the piles never bounced back, reaching maximum displacements and bending moments as large as six times those measured in the models simulating liquefiable coarse sand layer. In the models with lower soil permeability, the results and analyses indicate that negative excess pore pressures developed close to the foundations stiffened the soil, increasing the effective area subjected to the liquefied soil pressure, hence explaining the large bending moments measured. The second part of the report presents experimental results and analyses of four centrifuge tests that were conducted to study the reinforcing or pinning effect pile groups have on reducing lateral spreading. An analysis approach developed in this study proved to be very useful in understanding the reinforcement effect pile groups have on liquefaction induced lateral spreading.

ABSTRACT

Earthquake-induced lateral spreading of sloping ground and near waterfronts continues to be a major cause of damage to deep foundations. Currently there is a huge uncertainty associated with the maximum lateral pressures and forces applied by the liquefied soil to deep foundations. Furthermore, recent centrifuge and 1g shaking table tests of pile foundations indicate that the permeability of the liquefied sand is an extremely important and poorly understood factor. The first part of this work presents experimental results and analyses of six centrifuge tests that were conducted at the 150 g-ton RPI centrifuge to investigate the effect of soil permeability in the response of single piles and pile groups to lateral spreading. In the models that simulate a liquefiable coarse sand layer (saturated with water), the piles bounced back after a couple of cycles of shaking; however in the models that simulate a liquefiable fine sand layer (saturated with viscous fluid), the piles never bounced back, reaching maximum displacements and bending moments as large as 6 times the ones measured in the models saturated with water. In the models with lower soil permeability (saturated with viscous fluid) the results and analyses indicate that negative excess pore pressures developed close to the foundations stiffened the soil, increasing the effective area subjected to the liquefied soil pressure, explaining hence the large bending moments.

The vulnerability of highway bridges to earthquake-induced ground failures arising from liquefaction has been clearly demonstrated by the extensive damage observed in past earthquakes, particularly when a nonliquefied soil layer rides on top of the liquefied soil. Liquefaction induced lateral spreading may be reduced by the restraining forces provided by pile group foundations. This reduction in lateral displacement in fact reduces the loads and displacement demands that are imposed on the piles. The second part of this work presents experimental results and analyses of four centrifuge tests that were conducted also at the RPI centrifuge to study the reinforcing or pinning effect the pile groups have on the lateral spreading. An analysis approach developed in this study proved to be very useful to understand the reinforcement effect pile groups have in liquefaction induced lateral spreading and to give a good estimation, at least in centrifuge modeling, of the expected pile group deformations.

ACKNOWLEDGMENT

Having studied at RPI has been a great experience in my life, both professionally and personally. What I have achieved during this period has been possible thanks to the support and help from many people and institutions. I would like to start expressing my sincere gratitude to Professor Tarek Abdoun for his support, guidance and friendship throughout this work. Working with Professor Abdoun has been a rich educational experience.

Special thanks are also extended to Professors Ricardo Dobry, Mourad Zeghal, Thomas Zimmie, and Ramón Verdugo for the valuable discussions, suggestions and for serving as members of the thesis committee. Professor Ricardo Dobry has been a source of support and encouragement, not only in the academic aspect but also in the personal one. Professor Ramon Verdugo has been like a mentor in my geotechnical studies and I really appreciate his friendship. I would also like to thank Professor José Holguín-Veras from the Civil Engineering Department for his friendship and support.

I would like to extend my appreciation to the staff of the Geotechnical Centrifuge Center: lab technician Alex Sankovich and previous Lab technician Ralph Bourne for their friendship and hard work to ensure successful centrifuge tests; systems programmer Hassan Radwan for his help debugging computational problems; URP students for their valuable help building the centrifuge models; secretaries Norina Dowd, Marcia Hartnett, Janet Pertierra, and Kimberly Robitaille for their patience and help; and current and former colleagues graduate students: Claudia Medina, Javier Ubilla, Da Ha, Ahmed Elmekati, Matt Sausville, Victoria Bennett, Usama El Shamy, Ahmet Pamuk, Salvador Peña, Caglar Oskay, Vivian Kallou, Yingjuan Wang, and Pickett Simpson, with whom I have shared a lot of experiences at RPI.

I would like to express my sincere gratitude to my friends Diana, Chris and Adriana Delker for their care and friendship through all this years in the United States. Special thanks to my parents who have always supported me; what I have accomplished here is in great part thanks to them.

The work reported herein was jointly supported by the National Science Foundation (NSF) and the Federal Highway Administration (FHWA) of the United States; this support is gratefully appreciated.

I would like to finish by expressing my utmost gratitude and appreciation to my wife Daniela and daughter Camila for their patience and support during all these years of study. I could not have achieved what I did without their love and sacrifices.

TABLE OF CONTENTS

CHAPTER	TITLE	PAGE
1.	INTRODUCTION	1
1.1	Earthquakes and Soil Liquefaction	1
1.1.1	Evaluation of Liquefaction Potential	1
1.1.2	Ground Failure Resulting from Soil Liquefaction	2
1.2	Pile Foundations Subjected to Lateral Spreading	3
1.2.1	Background	3
1.2.2	Representative Case Histories	4
1.2.3	Current Practice in Foundation Analysis under Lateral Spreading	12
1.2.4	Engineering and Scientific Uncertainties	12
1.3	Evidence on Pore Pressure Decrease and Soil Stiffening near Piles Subjected to Lateral Spreading	13
1.3.1	Centrifuge Tests	13
1.3.2	Full-Scale Shaking Table Tests	16
1.3.3	1-g Small-Scale Tests	21
1.3.4	Field Test	24
1.4	Pile Pinning Effect on Liquefaction Induced Lateral Spreading	24
1.4.1	Background	24
1.4.2	Pile Pinning Approach	26
1.4.3	Previous Centrifuge Modeling of Pile Pinning Effect	28
1.5	Scope of Research	30
1.5.1	Effect of permeability on pile response to lateral spreading	30
1.5.2	Effect of pile pinning on lateral spreading	31
1.6	Report Organization	32
2.	RPI CENTRIFUGE FACILITY	35
2.1	Concept of Centrifuge Modeling	35
2.2	RPI Geotechnical Centrifuge	36
2.3	In-Flight 1-D Large Shaker	40
2.4	1-D Large Laminar Box	41
2.4.1	Design Philosophy	41
2.4.2	1-D Large Laminar Box Description	43
2.5	Data Acquisition System	46
2.6	Sensors used in Centrifuge Models	48
2.6.1	Accelerometers	48
2.6.2	LVDTs	50
2.6.3	Pore Pressure Transducers	50
2.6.4	Strain Gages	51
2.7	Construction Process and Calibration of Model Piles	51
2.7.1	Construction Process of Model Piles	51
2.7.2	Calibration of Model Piles Type U1	52
2.7.3	Calibration of Model Piles Type U2	58
2.7.4	Calibration of Model Piles Type A	58

TABLE OF CONTENTS (CONT'D)

CHAPTER	TITLE	PAGE
2.8	Soil Properties	66
2.8.1	Nevada Sand	66
2.8.2	Slightly Cemented Sand	66
3.	EFFECT OF SOIL PERMEABILITY ON SINGLE PILE RESPONSE TO LATERAL SPREADING	73
3.1	Introduction	73
3.2	Model Preparation	74
3.3	Model Description	79
3.4	Model 1x1-w	80
3.4.1	Recorded Accelerations	80
3.4.2	Recorded Excess Pore Pressures	80
3.4.3	Recorded Lateral Displacements	83
3.4.4	Pattern of Soil Displacement around the Single Pile	83
3.4.5	Recorded Bending Moments	88
3.4.6	P-y Curve Analysis	88
3.4.7	Limit Equilibrium Analysis	92
3.5	Model 1x1-v	95
3.5.1	Recorded Accelerations	95
3.5.2	Recorded Excess Pore Pressures	95
3.5.3	Visualization of Pore Pressure Build-up and Dissipation	96
3.5.4	Recorded Lateral Displacements	104
3.5.5	Pattern of Soil Displacement around the Single Pile	104
3.5.6	Recorded Bending Moments	104
3.5.7	P-y Curve Analysis	108
3.5.8	Limit Equilibrium Analysis	110
3.6	Comparison of Free Field Results between Model 1x1-w and 1x1-v	111
3.6.1	Comparison of Free Field Soil Accelerations	113
3.6.2	Comparison of Excess Pore Pressures	113
3.6.3	Comparison of Free Field Lateral Displacements	115
4.	EFFECT OF SOIL PERMEABILITY ON 3x1 PILE GROUP + SINGLE PILE RESPONSE TO LATERAL SPREADING	117
4.1	Introduction	117
4.2	Model Preparation	120
4.3	Model Description	120
4.4	Model 3x1-w	124
4.4.1	Recorded Accelerations	124
4.4.2	Recorded Excess Pore Pressures	127
4.4.3	Recorded Lateral Displacements	127
4.4.4	Pattern of Soil Displacement around Piles	130
4.4.5	Recorded Bending Moments	132
4.4.6	Limit Equilibrium Analysis	135

TABLE OF CONTENTS (CONT'D)

CHAPTER	TITLE	PAGE
4.5	Model 3x1-v	137
4.5.1	Recorded Accelerations	137
4.5.2	Recorded Excess Pore Pressures	137
4.5.3	Recorded Lateral Displacements	143
4.5.4	Pattern of Soil Displacement around Piles	144
4.5.5	Recorded Bending Moments	144
4.5.6	Limit Equilibrium Analysis	148
4.6	Comparison of Free Field Results between Model 3x1-w and 3x1-v	150
4.6.1	Comparison of Free Field Soil Accelerations	151
4.6.2	Comparison of Excess Pore Pressures	152
4.6.3	Comparison of Free Field Lateral Displacements	153
5.	EFFECT OF SOIL PERMEABILITY ON 2X2 PILE GROUP RESPONSE TO LATERAL SPREADING	155
5.1	Introduction	155
5.2	Model Preparation	155
5.3	Models Description	157
5.4	Model 2x2-w	159
5.4.1	Recorded Accelerations	159
5.4.2	Recorded Excess Pore Pressures	162
5.4.3	Recorded Lateral Displacements	166
5.4.4	Pattern of Soil Displacement around Piles	167
5.4.5	Recorded Bending Moments	168
5.4.6	Recorded Axial Forces	170
5.4.7	Limit equilibrium analysis	172
5.5	Model 2x2-v	173
5.5.1	Recorded Accelerations	173
5.5.2	Recorded Excess Pore Pressures	177
5.5.3	Recorded Lateral Displacements	178
5.5.4	Pattern of Soil Displacement around Piles	178
5.5.5	Recorded Bending Moments	180
5.5.6	Recorded Axial Forces	183
5.5.7	Limit equilibrium analysis	184
5.6	Comparison of Free Field Results between Model 2x2-w and 2x2-v	184
5.6.1	Comparison of Free Field Soil Accelerations	185
5.6.2	Comparison of Excess Pore Pressures	187
5.6.3	Comparison of Free Field Lateral Displacements	189
6.	SUMMARY AND DISCUSSIONS ON SOIL PERMEABILITY EFFECT ON PILE RESPONSE TO LATERAL SPREADING	191
6.1	Introduction	191
6.2	Summary of Soil Acceleration in the Free Field	191
6.3	Summary of Excess Pore Pressure Development	192

TABLE OF CONTENTS (CONT'D)

CHAPTER	TITLE	PAGE
6.3.1	Short-Term in the Free Field	194
6.3.2	Short-Term in the Near Field	194
6.3.3	Long-Term (Dissipation Process)	195
6.4	Summary of Soil Lateral Displacement	195
6.5	Summary of Piles Lateral Displacement	196
6.6	Summary of Soil Pattern Displacement around Piles	198
6.7	Summary of Bending Moment Profiles	200
6.8	Summary of the Relationship between Bending Moment and Pile Displacement	202
6.9	Summary of Limit Equilibrium Analysis	203
6.10	Summary of p-y Curve Analysis on the Single Pile	205
7.	PILE PINNING EFFECT ON LIQUEFACTION INDUCED LATERAL SPREADING	209
7.1	Introduction	209
7.2	Model Preparation	210
7.3	Model p-0 (free field)	214
7.3.1	Model Description	214
7.3.2	Recorded Accelerations	214
7.3.3	Recorded Excess Pore Pressures	217
7.3.4	Recorded Lateral Displacements	219
7.4	Model p-3x2	224
7.4.1	Model Description	224
7.4.2	Recorded Accelerations	229
7.4.3	Recorded Excess Pore Pressures	232
7.4.4	Recorded and Back-calculated Lateral Displacements	233
7.4.5	Soil Condition around Pile Cap	238
7.4.6	Recorded Bending Moments	240
7.4.7	Recorded Axial Forces	243
7.4.8	Lateral Force against Piles	245
7.5	Model p-6x2	247
7.5.1	Model Description	247
7.5.2	Recorded Accelerations	248
7.5.3	Recorded Excess Pore Pressures	256
7.5.4	Recorded and Back-calculated Lateral Displacements	257
7.5.5	Soil Condition around Pile Cap	261
7.5.6	Pattern of Soil Displacement around Piles	262
7.5.7	Recorded Bending Moments	264
7.5.8	Recorded Axial Forces	268
7.5.9	Lateral Force against Piles	268
7.6	Model p-3x1	271
7.6.1	Model Description	271
7.6.2	Recorded Accelerations	274
7.6.3	Recorded Excess Pore Pressures	278

TABLE OF CONTENTS (CONT'D)

CHAPTER	TITLE	PAGE
7.6.4	Recorded and Back-calculated Lateral Displacements	278
7.6.5	Soil Condition around Pile Cap	285
7.6.6	Pattern of Soil Displacement around Piles	287
7.6.7	Recorded Bending Moments	287
7.6.8	Recorded Axial Forces	292
7.6.9	Lateral Force against Piles	292
8.	SUMMARY, ANALYSES AND DISCUSSIONS ON PILE PINNING EFFECT ON LATERAL SPREADING	297
8.1	Introduction	297
8.2	Summary of Soil Accelerations	298
8.3	Summary of Excess Pore Pressure Development	298
8.4	Summary of Soil Lateral Displacement and Ground Settlement	298
8.5	Summary of Soil Condition around Pile Groups	301
8.6	Summary of the Rotational Stiffness Provided by the Bottom Cemented Layer	303
8.7	Summary of Bending Moments	304
8.8	Summary of Lateral Resistance against Pile Groups	304
8.9	Summary and Analyses of Lateral Forces against Pile Groups	307
8.10	Analysis of Pile Pinning Effect	309
9.	CONCLUSIONS AND RECOMMENDATIONS	317
9.1	Soil Permeability Effect on Pile Response to Lateral Spreading	317
9.1.1	Conclusions	317
9.1.2	Recommendations	318
9.2	Pile Pinning Effect on Lateral Spreading	319
9.2.1	Conclusions	319
9.2.2	Recommendations	321
10	REFERENCES	323

LIST OF FIGURES

FIGURE	TITLE	PAGE
1.1	Schematic examples of liquefaction-induced global site instability and/or “large” displacement lateral spreading (Seed et al., 2003).....	5
1.2	Schematic of a liquefaction induced lateral spread (Rauch, 1997).....	6
1.3	Schematic of the damage to Yachiyo Bridge in the 1964 Niigata earthquake (Hamada et al., 1986).....	7
1.4	Collapse of Showa Bridge during the 1964 Niigata earthquake (Iwasaki, 1973).....	7
1.5	Schematic of a deformed steel pile extracted from Showa Bridge, after the 1964 Niigata earthquake (after Fukuoka, 1966)	8
1.6	Typical damage pattern on pile foundations subjected to lateral spreading in the 1995 Kobe earthquake (Tokimatsu, 1999).....	8
1.7	Damage to floating and end-bearing piles and standard penetration test, NFCH building, 1964 Niigata earthquake (Hamada et al., 1986)	9
1.8	Photographs of damage piles shown in Fig. 1.7, (a) upper part of Pile No. 2, (b) lower part of Pile No. 2, and (c) upper part of Pile No. 1, (Hamada, 1992)	10
1.9	The Landing Road Bridge, after the 1987 Edgecumbe earthquake, New Zealand (Berrill et al., 2002).....	11
1.10	Schematic of the raked-pile foundation at the Landing Road Bridge (Berrill et al., 2002).....	11
1.11	Proposed limit equilibrium design method of bridge pile foundations against lateral spreading in Japan (Japan Road Association, 1996; Yokoyama, et al., 1997)	13
1.12	Typical partial model layout of centrifuge models Csp2 and Csp3 (Wilson et al., 2000).....	14
1.13	P-y curve behavior during shaking, model Csp3 (Wilson et al., 2002)	15
1.14	Setup and instrumentation used in centrifuge test SKH-14 (Haigh and Madabhushi, 2002).....	16
1.15	Excess pore pressure time histories measured near pile at 3m depth (Haigh and Madabhushi, 2002).....	17
1.16	Setup and instrumentation of 6 m full-scale Test No.1 of single pile and 2x2 pile group subjected to lateral spreading using inclined laminar box, NIED, Japan (Sato et al., 2004, unpublished)	17
1.17	Final free field deformation profile of 6 m inclined laminar box after Test No.1, NIED, Japan (Sato et al., 2004, unpublished)	19
1.18	Maximum bending moment profiles measured in single pile in 1g full-scale Test No.1 at NIED (water) and centrifuge tests at RPI (water and viscous pore fluid), (Ubilla, 2004, unpublished)	19
1.19	Setup and instrumentation of full-scale shaking table test on level ground at NIED, Japan (Suzuki and Tokimatsu, 2004)	20
1.20	Reduction in pore water pressure near piles in pile group during full-scale shaking table tests at NIED, Japan (Suzuki and Tokimatsu, 2004)	20
1.21	Schematic of model container to study the liquefied soil lateral resistance against the lateral displacement of a cylinder (Dungca et al., 2004)	22
1.22	Liquefied soil lateral resistance against lateral displacement of cylinder (Dungca et al., 2004).....	22

LIST OF FIGURES (CONT'D)

FIGURE	TITLE	PAGE
1.23	Schematic of experimental apparatus to pull a sphere through a liquefied sand (De Alba and Ballestero, 2004)	23
1.24	Sphere velocity versus apparent drag force in a liquefied sand, test 19 (De Alba and Ballestero, 2004)	23
1.25	Plan view of test site layout during load test at 3x3 pile group location, Treasure Island Test (Rollins et al.,2005)	25
1.26	Time histories of total load and excess pore pressure ratios near the ground surface adjacent to the pile group, Treasure Island Test (Rollins et al.,2005)	25
1.27	Pseudo-static stability analysis, Newmark approach (Martin et al., 2002).....	27
1.28	Setup of centrifuge model with two facing abutments, prototype dimensions in meters (Boulanger et al., 2005).....	29
1.29	Critical slip surfaces with and without pile restraining force (Boulanger et al., 2005)	29
2.1	Centrifuge physical modeling concept (after Pamuk, 2004)	36
2.2	RPI geotechnical facility's layout.....	38
2.3	RPI geotechnical centrifuge, (a) picture, (b) schematic.....	39
2.4	RPI 1-D large shaker, (a) schematic, (b) frequency response (Van Laak, 1996)	42
2.5	RPI 1-D large laminar box, (a) picture, (b) schematic.....	44
2.6	RPI 1-D large laminar box, (a) plan view, (b) cross section (after Pamuk, 2004)	45
2.7	Signal conditioning system.....	47
2.8	Control and teleparticipation room	47
2.9	Sensors used in centrifuge models.....	49
2.10	Construction process for model piles, (a) strain gages attachment and wiring, (b) phone cables connection, (c) wax application, (d) a shrink tube with glued sand covers the pile.....	54
2.11	Diagram of model pile type U1 configuration, used in Model 2x2-w and 2x2-v, and in Model 3x1-w and 3x1-v (3x1 pile group).....	55
2.12	Model pile calibration under bending, pile #2 type U1 (in model units).....	56
2.13	Modulus of elasticity (in bending) of model pile #1 and #2, type U1	57
2.14	Modulus of elasticity (in axial) of model pile #1 and #2, type U1	59
2.15	Diagram of model pile type U2 configuration, used in Model 1x1-w and 1x1-v, and in Model 3x1-w and 3x1-v (single pile).....	60
2.16	Model pile calibration under bending, pile #1 type U2 (in model units).....	61
2.17	Modulus of elasticity (in bending) of model pile #1 and #2, type U2	62
2.18	Modulus of elasticity (in axial) of model pile #1 and #2, type U2	63
2.19	Diagram of model pile type A configuration, used in Model p-0, p-3x2, p-6x2 and p-3x1	64
2.20	Model pile calibration under bending, pile #3, type A (in model units).....	65
2.21	Modulus of elasticity (in bending) of model pile #1 and #2 (type A)	67
2.22	Modulus of elasticity (in bending) of model pile #3 and #4, type A.....	68
2.23	Grain size distribution for Nevada sand (after Arulmoli et al., 1992)	69

LIST OF FIGURES (CONT'D)

FIGURE	TITLE	PAGE
2.24	Hydraulic conductivity versus relative density for Nevada sand (after Arulmoli et al., 1992)	70
2.25	Stress-strain curves for cemented sand (Abdoun, 1997)	71
2.26	Triaxial test results for cemented sand plotted on p-q diagram (Abdoun, 1997)	72
3.1	(a) Setup and instrumentation used in Models 1x1-w and 1x1-v, (in prototype units) (b) Transversal and (c) horizontal sections of Models 1x1-w and 1x1-v	75
3.2	(a) Preparation of slightly cemented sand later, (b) saturation of the cemented sand layer: (c) Pluviation of Nevada sand, (d) saturation of the model.....	77
3.3	Model during preparation, Models 1x1-w and 1x1-v	81
3.4	Colored sand placed at an intermediate depth, Models 1x1-w and 1x1-v	81
3.5	Soil acceleration time histories in the free field, Model 1x1-w	84
3.6	Accelerations recorded on the laminar rings, Model 1x1-w	85
3.7	Excess pore pressure time histories in the free field, the dashed lines correspond to initial liquefaction, Model 1x1-w.....	85
3.8	Excess pore pressure time histories close to the pile, upslope and downslope, Model 1x1-w	86
3.9	Excess pore pressure time histories close and next to the pile, Model 1x1-w	86
3.10	Lateral displacement time histories, Model 1x1-w	87
3.11	Profiles of soil lateral displacement in the free field, Model 1x1-w	87
3.12	Pattern of soil displacement around the pile, (a) z = 1 m, (b) z = 3 m, Model 1x1-w	89
3.13	Bending moment time histories, Model 1x1-w	90
3.14	Profiles of bending moment, Model 1x1-w	90
3.15	Bending moment at the base of the liquefiable layer versus pile head lateral displacement, Model 1x1-w	91
3.16	Back-calculated rotational stiffness of the cemented sand around the pile versus bending moment at the base of the liquefiable layer, Model 1x1-w	92
3.17	Back-calculated pile head lateral displacement, Model 1x1-w	93
3.18	Back-calculated p-y curves, Model 1x1-w	93
3.19	(a) Effective area subjected to liquefied soil pressure and (b) lateral view of the model used for limit equilibrium analyses, Model 1x1-w	94
3.20	Soil acceleration time histories in the free field, Model 1x1-v	97
3.21	Accelerations recorded on the laminar rings, Model 1x1-v	98
3.22	Excess pore pressure time histories in the free field, the dashed lines correspond to initial liquefaction, Model 1x1-v	98
3.23	Excess pore pressure time histories close to the pile, upslope and downslope, Model 1x1-v	99
3.24	Excess pore pressure time histories close and next to the pile, Model 1x1-v	99
3.25	Long term excess pore pressure time histories, (a) free field and (b) next to the pile, Model 1x1-v	100
3.26	Short term excess pore pressure ratios and lateral displacements for selected time instants, Model 1x1-v	101

LIST OF FIGURES (CONT'D)

FIGURE	TITLE	PAGE
3.27	Long term excess pore pressure ratios and lateral displacements for selected time instants, Model 1x1-v	102
3.28	Sand boils on the downslope side of the pile, (a) far view, (b) close view, Model 1x1-v.....	103
3.29	Lateral displacement time histories, Model 1x1-v.....	105
3.30	Profiles of soil lateral displacement in the free field, Model 1x1-v.....	105
3.31	Pattern of soil displacement around the pile, (a) z = 1 m, (b) z = 3 m, Model 1x1-v..	106
3.32	Bending moment time histories, Model 1x1-v	107
3.33	Profiles of bending moment, Model 1x1-v	107
3.34	Bending moment at the base of the liquefiable layer versus pile head lateral displacement, Model 1x1-v.....	108
3.35	Back-calculated rotational stiffness of the cemented sand around the pile versus bending moment at the base of the liquefiable layer, Model 1x1-v.....	109
3.36	Back-calculated pile head lateral displacement, Model 1x1-v	110
3.37	Back-calculated p-y curves, Model 1x1-v	110
3.38	(a) Effective area subjected to liquefied soil pressure, (b) lateral view of model used for limit equilibrium analyses, (c) snapshot of excess pore pressures during shaking taking from visualization in transversal direction, Model 1x1-v	112
3.39	Comparison of soil acceleration in the free field between Model 1x1-w and 1x1-v ...	114
3.40	Comparison of excess pore pressure in the free field between Model 1x1-w and 1x1-v	114
3.41	Comparison of excess pore pressure next to the pile between Model 1x1-w and 1x1-v	115
3.42	Comparison of free field lateral displacement profiles between Model 1x1-w and 1x1-v	116
4.1	(a) Setup and instrumentation used in Models 3x1-w and 3x1-v, (in prototype units) (b) Transversal sections of Models 3x1-w and 3x1-v.....	118
4.2	Pile-cap-structure, (a) schematic, (b) picture, Models 3x1-w and 3x1-v.....	121
4.3	Model during preparation, Models 3x1-w and 3x1-v	122
4.4	Colored sand placed at an intermediate depth, Models 3x1-w and 3x1-v	122
4.5	Soil acceleration time histories in the free field, Model 3x1-w.....	125
4.6	Soil acceleration time histories in the near field, Model 3x1-w	126
4.7	Accelerations recorded on the pile cap, Model 3x1-w	126
4.8	Accelerations recorded on the laminar rings, Model 3x1-w.....	127
4.9	Excess pore pressure time histories in the free field, the dashed lines correspond to initial liquefaction, Model 3x1-w	128
4.10	Excess pore pressure time histories next to pile group, Model 3x1-w	128
4.11	Excess pore pressure time histories downslope and upslope from pile group, Model 3x1-w	129
4.12	Lateral displacement time histories, Model 3x1-w.....	129
4.13	Profiles of soil lateral displacement in the free field, Model 3x1-w.....	130

LIST OF FIGURES (CONT'D)

FIGURE	TITLE	PAGE
4.14	Pattern of soil displacement around piles at a depth of 3 m, (a) pile group, (b) single pile, Model 3x1-w.....	131
4.15	Bending moment time histories, external pile (IP 1), Model 3x1-w	132
4.16	Bending moment time histories, center pile (IP 2), Model 3x1-w.....	133
4.17	Bending moment time histories, single pile (IP 3), Model 3x1-w.....	133
4.18	Profiles of bending moment, center pile (IP 2), Model 3x1-w	134
4.19	Profiles of bending moment, single pile (IP 3), Model 3x1-w	134
4.20	Bending moment at the base of the liquefiable layer versus pile cap lateral displacement, pile group, Model 3x1-w	135
4.21	(a) Effective area subjected to liquefied soil pressure and (b) lateral view of the model used for limit equilibrium analyses, Model 3x1-w	136
4.22	Soil acceleration time histories in the free field, Model 3x1-v.....	138
4.23	Soil acceleration time histories in the near field, Model 3x1-v	138
4.24	Accelerations recorded on the pile cap, Model 3x1-v	139
4.25	Accelerations recorded on the laminar rings, Model 3x1-v.....	139
4.26	Excess pore pressure time histories in the free field, the dashed lines correspond to initial liquefaction, Model 3x1-v	140
4.27	Excess pore pressure time histories next to pile group, Model 3x1-v	140
4.28	Excess pore pressure time histories downslope and upslope from pile group, Model 3x1-v.....	141
4.29	Filtered excess pore pressure time histories at 2 m depth, (a) short term and (b) long term, Model 3x1-v.....	141
4.30	Long term excess pore pressure time histories in the free field, Model 3x1-v.....	142
4.31	Lateral displacement time histories, Model 3x1-v.....	143
4.32	Profiles of soil lateral displacement in the free field, Model 3x1-v.....	144
4.33	Pattern of soil displacement around piles at a depth of 3 m, (a) pile group, (b) single pile, Model 3x1-v.....	145
4.34	Bending moment time histories, external pile (IP 1), Model 3x1-v	146
4.35	Bending moment time histories, center pile (IP 2), Model 3x1-v	146
4.36	Bending moment time histories, single pile (IP 3), Model 3x1-v.....	147
4.37	Profiles of bending moment, center pile (IP 2), Model 3x1-v	147
4.38	Profiles of bending moment, single pile (IP 3), Model 3x1-v	149
4.39	Bending moment at the base of the liquefiable layer versus pile cap lateral displacement, pile group, Model 3x1-v	149
4.40	(a) Effective area subjected to liquefied soil pressure and (b) lateral view of the model used for limit equilibrium analyses, Model 3x1-v	150
4.41	Comparison of soil acceleration in the free field between Model 3x1-w and 3x1-v ...	151
4.42	Comparison of excess pore pressure in the free field between Model 3x1-w and 3x1-v	152
4.43	Comparison of excess pore pressure next to the external pile in the pile group, between Model 3x1-w and 3x1-v	153
4.44	Comparison of free field lateral displacement profiles, between Model 3x1-w and 3x1-v	154

LIST OF FIGURES (CONT'D)

FIGURE	TITLE	PAGE
5.1	(a) Setup and instrumentation used in Models 2x2-w and 2x2-v, (in prototype units); (b) Transversal section of Models 2x2-w and 2x2-v	156
5.2	Pile-cap-structure, (a) schematic, (b) picture, Models 2x2-w and 2x2-v.....	158
5.3	Model during preparation, Models 2x2-w and 2x2-v	159
5.4	Colored sand placed at an intermediate depth, (a) Model 2x2-w, (b) Model 2x2-v....	160
5.5	Soil accelerations time histories in the free field, Model 2x2-w	163
5.6	Soil acceleration time histories between piles, Model 2x2-w.....	163
5.7	Accelerations recorded on the pile cap, Model 2x2-w	164
5.8	Accelerations recorded on the laminar rings, Model 2x2-w.....	164
5.9	Excess pore pressure time histories in the free field, the dashed lines correspond to initial liquefaction, Model 2x2-w	165
5.10	Excess pore pressure time histories between piles, the dashed lines correspond to initial liquefaction, Model 2x2-w	165
5.11	Lateral displacement time histories, Model 2x2-w.....	166
5.12	Profiles of soil lateral displacement in the free field, Model 2x2-w.....	167
5.13	Pattern of soil displacement around pile group at a depth of 4 m, Model 2x2-w.....	168
5.14	Bending moment time histories, upslope pile (IP 1), Model 2x2-w.....	169
5.15	Bending moment time histories, downslope pile (IP 2), Model 2x2-w	169
5.16	Profiles of bending moment, upslope (IP 1) and downslope (IP 2) piles, Model 2x2-w	170
5.17	Bending moment at the base of the liquefiable layer versus pile cap lateral displacement, Model 2x2-w.....	171
5.18	Axial force time histories, upslope pile (IP 1), Model 2x2-w	171
5.19	Axial force time histories, downslope pile (IP 2), Model 2x2-w.....	172
5.20	(a) Effective area subjected to liquefied soil pressure and (b) lateral view of the model used for limit equilibrium analyses, Model 2x2-w	173
5.21	Soil acceleration time histories in the free field, Model 2x2-v.....	174
5.22	Soil acceleration time histories between piles, Model 2x2-v	175
5.23	Accelerations recorded on the pile cap, Model 2x2-v	175
5.24	Accelerations recorded on the laminar rings, Model 2x2-v.....	176
5.25	Excess pore pressure time histories in the free field, the dashed lines correspond to initial liquefaction, Model 2x2-v	176
5.26	Excess pore pressure time histories between piles, the dashed lines correspond to initial liquefaction, Model 2x2-v	177
5.27	Long term excess pore pressure time histories in the free field, Model 2x2-v.....	178
5.28	Lateral displacement time histories, Model 2x2-v.....	179
5.29	Profiles of lateral displacement in free field, Model 2x2-v	179
5.30	Pattern of soil displacement around pile group at a depth of 4 m, Model 2x2-v.....	180
5.31	Bending moment time histories, upslope pile (IP 1), Model 2x2-v.....	181
5.32	Bending moment time histories, downslope pile (IP 2), Model 2x2-v.....	181
5.33	Profiles of bending moment, upslope (IP 1) and downslope (IP 2) piles, Model 2x2-v.....	182

LIST OF FIGURES (CONT'D)

FIGURE	TITLE	PAGE
5.34	Bending moment at the base of the liquefiable layer versus pile cap lateral displacement, Model 2x2-v.....	182
5.35	Axial force time histories, upslope pile (IP 1), Model 2x2-v	183
5.36	Axial force time histories, downslope pile (IP 2), Model 2x2-v	183
5.37	(a) Effective area subjected to liquefied soil pressure and (b) lateral view of the model used for limit equilibrium analyses, Model 2x2-v.....	185
5.38	Comparison of soil acceleration in the free field between Model 2x2-w and 2x2-v	187
5.39	Comparison of excess pore pressure in the free field between Model 2x2-w and 2x2-v	188
5.40	Comparison of excess pore pressure between piles, between Model 2x2-w and 2x2-v	189
5.41	Comparison of free field lateral displacement profiles between Model 2x2-w and 2x2-v	190
6.1	Comparison of excess pore pressure dissipation in the models saturated with viscous fluid.....	194
6.2	Summary of free field lateral displacement profiles.....	197
6.3	Summary of ground surface and pile head lateral displacements (the lateral displacements in figures (c) correspond to the 3x1 pile group).....	198
6.4	Summary of soil pattern displacement around piles (the arrows indicate the direction of lateral spreading; the dashed lines show the area of influence around the piles)....	199
6.5	Summary of bending moment profiles (the bending moment profiles in figures (c) and (d) correspond to the 3x1 pile group).....	201
6.6	Summary of measured pile bending moment versus measured pile head lateral displacement ((b) corresponds to the 3x1 pile group)	202
6.7	Summary of the effective areas used in the limit equilibrium analyses (not perfectly on scale), e_a : effective area corresponding to shadow zone, h_f : distance to the resultant force, p_l : liquefied soil pressure	204
6.8	Back-calculated rotational stiffnesses (with the p-y approach) provided by the cemented sand in Models 1x1-w and 1x1-v	205
6.9	Summary of single pile response	206
7.1	(a) Preparation of slightly cemented sand later, (b) saturation of the cemented sand layer (c) Pluviation of Nevada sand, (d) saturation of the model.....	211
7.2	Setup and instrumentation used in Model p-0, (in prototype units)	215
7.3	Soil acceleration time histories in the free field, Model p-0.....	217
7.4	Acceleration time histories on the laminar rings, Model p-0.....	218
7.5	Short and long term excess pore pressure time histories in the free field, the dashed lines correspond to initial liquefaction, Model p-0.....	218
7.6	Soil lateral displacement time histories in the free field, Model p-0.....	219

LIST OF FIGURES (CONT'D)

FIGURE	TITLE	PAGE
7.7	Relative displacement time histories between the rings attached to the LVDTs, the dashed lines represent the allowable relative displacement between these rings in prototype units, Model p-0.....	220
7.8	Soil lateral displacement time histories in the free field, considering the first 30 cycles of shaking, Model p-0.....	221
7.9	Profiles of soil lateral displacement in the free field, Model p-0.....	221
7.10	Ground surface settlement time history, (a) short term, (b) long term, Model p-0	222
7.11	Longitudinal crack and sand boils developed on the surface, (a) picture, (b) schematic, Model p-0.....	223
7.12	(a) Setup and instrumentation used in Model p-3x2, (in prototype units): (b) Transversal section of Model p-3x2.....	225
7.13	Pile-cap-structure, (a) schematic, (b) picture, Model p-3x2.....	226
7.14	Model during preparation, the dashed line represents the pile cap, Model p-3x2.....	228
7.15	Soil acceleration time histories far from the pile group, Model p-3x2.....	229
7.16	Soil acceleration time histories between piles, Model p-3x2.....	230
7.17	Acceleration time histories on the pile cap, Model p-3x2.....	231
7.18	Acceleration time histories on the laminar rings, Model p-3x2.....	231
7.19	Short term excess pore pressure time histories in the free field and between piles, the dashed lines correspond to initial liquefaction, Model p-3x2.....	232
7.20	Long term excess pore pressure time histories in the free field and between piles, the dashed lines correspond to initial liquefaction, Model p-3x2.....	233
7.21	Soil and pile cap lateral displacement time histories, Model p-3x2.....	234
7.22	Profiles of soil lateral displacement, Model p-3x2.....	234
7.23	Back-calculated rotational stiffness provided by the bottom cemented layer versus bending moment at the base of the liquefiable layer, Model p-3x2.....	236
7.24	Lateral displacement time histories of the pile cap and top cemented layer, (*) after subtracting the increment in displacement above the pile cap, Model p-3x2.....	237
7.25	Profiles of soil and pile group lateral displacement, Model p-3x2.....	237
7.26	Ground surface settlement time history close to the pile group, (a) short term, (b) long term, Model p-3x2.....	238
7.27	Ground surface condition around pile cap after the test, (a) upslope, (b) downslope, Model p-3x2.....	239
7.28	Bending moment time histories, upslope pile (IP 1), Model p-3x2.....	241
7.29	Bending moment time histories, downslope pile (IP 2), Model p-3x2.....	242
7.30	Profiles of bending moment, upslope (IP 1) and downslope (IP 2) piles, Model p-3x2.....	243
7.31	Axial force time histories, upslope pile (IP 1), Model p-3x2.....	244
7.32	Axial force time histories, downslope pile (IP 2), Model p-3x2.....	244
7.33	Profiles of axial force, upslope (IP 1) and downslope (IP 2) piles, Model p-3x2.....	245
7.34	Profiles of back-calculated soil lateral resistance, Model p-3x2.....	246
7.35	Back-calculated lateral force time histories against the piles, Model p-3x2.....	247
7.36	(a) Setup and instrumentation used in Model p-6x2, (in prototype units) (b) Transversal section of Model p-6x2.....	249

LIST OF FIGURES (CONT'D)

FIGURE	TITLE	PAGE
7.37	Pile-cap-structure, (a) schematic, (b) picture, Model p-6x2	250
7.38	Model during preparation, the dashed line represents the pile cap, Model p-6x2	251
7.39	Colored sand placed at an intermediate depth, Model p-6x2.....	251
7.40	Soil acceleration time histories far from the pile group, Model p-6x2.....	254
7.41	Soil acceleration time histories between piles, Model p-6x2	254
7.42	Accelerations time histories on the pile cap, Model p-6x2.....	255
7.43	Accelerations time histories on the laminar rings, Model p-6x2	255
7.44	Short term excess pore pressure time histories in the free field and between piles, the dashed lines correspond to initial liquefaction, Model p-6x2.....	256
7.45	Long term excess pore pressure time histories in the free field and between piles, the dashed lines correspond to initial liquefaction, Model p-6x2.....	256
7.46	Soil and pile cap lateral displacement time histories, Model p-6x2	257
7.47	Profiles of soil lateral displacement, Model p-6x2	258
7.48	Back-calculated rotational stiffness provided by the bottom cemented layer versus bending moment at the base of the liquefiable layer, Model p-6x2	258
7.49	Lateral displacement time histories of the pile cap and top cemented layer, (*) after subtracting the increment in displacement above the pile cap, Model p-6x2.....	259
7.50	Profiles of soil and pile group lateral displacement, Model p-6x2.....	260
7.51	Ground surface settlement time histories far and close from the pile group, (a) short term, (b) long term, Model p-6x2.....	261
7.52	Ground surface condition around pile cap after the test, Model p-6x2	262
7.53	Soil condition in the top cemented layer after the test, Model p-6x2.....	263
7.54	Pattern of soil displacement around pile group, Model p-6x2.....	264
7.55	Bending moment time histories, upslope pile (IP 1), Model p-6x2.....	265
7.56	Bending moment time histories, downslope pile (IP 2), Model p-6x2.....	266
7.57	Bending moment time histories, downslope pile (IP 3), Model p-6x2.....	267
7.58	Profiles of bending moment, upslope (IP 1) and downslope (IP 3) piles, Model p-6x2.....	268
7.59	Axial force time histories, upslope pile (IP 1), Model p-6x2	269
7.60	Profiles of axial force, upslope pile (IP 1), Model p-6x2	269
7.61	Profiles of back-calculated soil lateral resistance, Model p-6x2	270
7.62	Back-calculated lateral force time histories against the piles, Model p-6x2	271
7.63	(a) Setup and instrumentation used in Model p-3x1, (in prototype units) (b) Transversal section of Model p-3x1	272
7.64	Pile-cap-structure, (a) schematic, (b) picture, Model p-3x1	275
7.65	Model during preparation, the dashed line represents the pile cap, Model p-3x1	276
7.66	Colored sand placed at an intermediate depth, Model p-3x1.....	276
7.67	Soil acceleration time histories far from the pile group, Model p-3x1	277
7.68	Soil acceleration time histories close to the external pile, Model p-3x1	277
7.69	Acceleration time histories on the pile cap, Model p-3x1	279
7.70	Acceleration time histories on the laminar rings, Model p-3x1.....	279
7.71	Short term excess pore pressure time histories in the free field and between piles, the dashed lines correspond to initial liquefaction, Model p-3x1	280

LIST OF FIGURES (CONT'D)

FIGURE	TITLE	PAGE
7.72	Long term excess pore pressure time histories in the free field and between piles, the dashed lines correspond to initial liquefaction, Model p-3x1	280
7.73	Soil and pile cap lateral displacement time histories, Model p-3x1	281
7.74	Profiles of soil lateral displacement, Model p-3x1	281
7.75	Back-calculated rotational stiffness provided by the bottom cemented layer versus bending moment at the base of the liquefiable layer, Model p-3x1	282
7.76	Lateral displacement time histories of the pile cap and top cemented layer, (*) after subtracting the increment in displacement above the pile cap, Model p-3x1.....	282
7.77	Profiles of soil and pile group lateral displacement, Model p-3x1	283
7.78	Ground surface settlement time histories far from the pile group and on the passive wedge, (a) short term, (b) long term, Model p-3x1	284
7.79	Ground surface condition around pile cap after the test, (a) top view, Model p-3x1 Ground surface condition around pile cap after the test, (b) inclined view, (c) lateral view, Model p-3x1.....	285
7.80	Soil condition in the top cemented layer after the test, Model p-3x1	288
7.81	Pattern of soil displacement around pile group, Model p-3x1	289
7.82	Bending moment time histories, center pile (IP 1), Model p-3x1	290
7.83	Bending moment time histories, external pile (IP 2), Model p-3x1	291
7.84	Profiles of bending moment, center (IP 1) and external (IP 2) piles, Model p-3x1.....	292
7.85	Axial force time histories, center pile (IP 1), Model p-3x1	293
7.86	Axial force time histories, external pile (IP 2), Model p-3x1	294
7.87	Profiles of back-calculated soil lateral resistance, Model p-3x1	294
7.88	Back-calculated lateral force time histories against the piles, Model p-3x1	295
8.1	Summary of ground surface lateral displacements	299
8.2	Summary of soil lateral displacement profiles.....	300
8.3	Summary of ground surface settlement	301
8.4	Summary of ground surface condition around pile caps	302
8.5	Back-calculated rotational stiffness provided by the bottom cemented layer versus bending moment at the base of the liquefiable layer	304
8.6	Summary of bending moment profiles	305
8.7	Summary of back-calculated lateral resistance profiles.....	306
8.8	Summary of back-calculated lateral force time histories.....	307
8.9	Back-calculated lateral force versus pile cap lateral displacement.....	308
8.10	Normalized lateral force versus pile cap lateral displacement.....	308
8.11	Relative displacement between the pile cap and ground surface time histories	310
8.12	Lateral force versus relative displacement between pile cap and ground surface	310
8.13	Reduction of lateral spreading time histories.....	311
8.14	Relative displacement between the pile cap and the ground surface in the free field condition (Model p-0) time histories	311
8.15	Integrated force (over time) time histories.....	312
8.16	Integrated force (Fig. 8.15) versus relative displacement between the pile cap and the ground surface in the free field condition (Fig. 8.14)	312

LIST OF FIGURES (CONT'D)

FIGURE	TITLE	PAGE
8.17	Normalized pile cap lateral displacement time histories	313
8.18	Steps to estimate the pile cap displacement, (Δp_g corresponds to the relative displacement between the pile cap and the ground surface in the free field)	315
8.19	Iteration curve to estimate the 3x1 pile group lateral displacement	316

LIST OF TABLES

TABLE	TITLE	PAGE
1.1	Classification of soil liquefaction consequences (after Castro, 1987).....	3
1.2	Testing properties of first series of centrifuge models (permeability effect).....	30
1.3	Testing properties of second series of centrifuge models (pinning effect).....	31
2.1	Scaling relations for centrifuge modeling (Taylor, 1995)	37
2.2	RPI centrifuge specifications	40
2.3	RPI 1-D large shaker technical specifications (Van Laak, 1996).....	43
2.4	Accelerometer specifications (after Pamuk, 2004).....	50
2.5	Strain gage specifications (after Pamuk, 2004)	52
2.6	Summary of model pile properties.....	53
2.7	General test results for Nevada sand (Arulmoli et al., 1992).....	69
2.8	Sieve analysis for Nevada sand (Arulmoli et al., 1992)	70
2.9	Constant-head permeability tests results for Nevada sand (Arulmoli et al., 1992)	70
3.1	Testing properties of centrifuge Models 1x1-w and 1x1-v.....	76
3.2	Location of instruments in Models 1x1-w and 1x1-v (in model units)	82
3.3	Parameters used in the limit equilibrium analysis, as well as measured and calculated values, Models 1x1-w and 1x1-v	95
4.1	Testing properties of centrifuge Models 3x1-w and 3x1-v.....	117
4.2	Location of instruments in Models 3x1-w and 3x1-v (in model units)	123
4.3	Parameters used in the limit equilibrium analysis, as well as measured and calculated values, Models 3x1-w and 3x1-v	136
5.1	Testing properties of centrifuge Models 2x2-w and 2x2-v.....	157
5.2	Location of instruments in Models 2x2-w and 2x2-v (in model units)	161
5.3	Parameters used in the limit equilibrium analysis, as well as measured and calculated values, Models 2x2-w and 2x2-v	186
6.1	Summary of properties and measurements from centrifuge tests.....	192
6.2	Summary of parameters used in the limit equilibrium analyses, as well as measured and calculated values	193
7.1	Testing properties of centrifuge models	210
7.2	Location of instruments in Model p-0 (in model units).....	216
7.3	Location of instruments in Model p-3x2 (in model units).....	227
7.4	Location of instruments in Model p-6x2 (in model units).....	252
7.5	Location of instruments in Model p-3x1 (in model units).....	273
8.1	Summary of properties and measurements from centrifuge tests.....	297

CHAPTER 1

INTRODUCTION

1.1 Earthquakes and Soil Liquefaction

Earthquakes have occurred for millions of years and will continue in the future. Some will occur in remote areas with negligible damage, while others will occur near densely populated areas. It does not seem possible to prevent earthquakes from occurring, but it is possible and necessary to mitigate their effects (Kramer, 1996).

A very important seismic hazard is liquefaction, a phenomenon in which the strength and stiffness of a saturated cohesionless soil is reduced by earthquake shaking or other rapid loading. During an earthquake, the cyclic shear waves that propagate upward from the bedrock induce a tendency for a loose to medium-dense sand layer to decrease in volume. If undrained conditions during an earthquake are assumed, an increase in pore water pressure and resulting decrease in the effective confining stress is required to keep the sand at constant volume.

Liquefaction and related phenomena have been responsible for large amounts of damage in historical earthquakes around the world. Some of them are the 1964 Niigata earthquake (Japan), the 1964 Anchorage earthquake (USA), the 1985 Loma Prieta earthquake (USA), the 1994 Northridge earthquake (USA), the 1995 Kobe earthquake (Japan), the 1999 Kocaeli earthquake (Turkey), and the 1999 Chi-Chi earthquake (Taiwan). Since liquefaction occurs in saturated soils, its effects are most commonly observed near rivers, lakes, bays, and oceans. Ports, bridges, buried pipes, and buildings near the shore are usually affected by this phenomenon.

1.1.1 Evaluation of Liquefaction Potential

The current state of practice for the evaluation of liquefaction potential depends on empirical correlations of in-situ measurements of soil density, strength or stiffness (SPT, CPT, V_s), versus field experience of liquefaction at shallow depth, supplemented by laboratory data of the behavior of saturated sand elements under undrained cyclic loading (Steedman et al., 2000). This approach, known as the simplified procedure (Seed et al., 1985; Youd et al., 2001), has been a standard of engineering practice for evaluating soil liquefaction over the past 25 years. This method is part of a more general approach known as the “cyclic stress approach”. Seed and Lee (1966) defined initial liquefaction as the time of the cyclic loading at which the increase in pore pressure becomes equal to the initial effective confining pressure ($r_u = 100\%$), and hence the effective stress is zero.

The basic concept behind this approach was born in the 1960's from cyclic undrained laboratory tests. However, by the 1980's the simplified procedure had become mainly an empirical correlation between field observations of liquefaction and soil standard penetration resistance

(SPT) measured in the field, supplemented by laboratory tests (Seed et al., 1985). The field evidence of liquefaction generally consisted of superficial observations of sand boils, ground fissures or lateral spreads. Data were collected mostly from sites on level or mildly sloping terrains at shallow depths (<15 m). Currently, the simplified procedure has evolved in two different directions (Youd et al., 2001): (i) it allows the use of other field tests in addition to SPT (CPT, BPT and Vs), and (ii) it relies exclusively or almost exclusively on empirical correlations, with laboratory tests playing a very small role.

In order to estimate the liquefaction potential, the earthquake-induced loading, expressed in terms of cyclic shear stress, is compared with the liquefaction resistance of the soil, also expressed in terms of cyclic shear stress. If the loading exceeds the resistance, liquefaction is expected to occur.

1.1.2 Ground Failure Resulting from Soil Liquefaction

If liquefaction potential is identified, an assessment must focus on the mode and magnitude of the ground failures that may result. The National Research Council (1985) lists eight types of failure commonly associated with soil liquefaction in earthquakes:

- Sand boils, which usually result in subsidence and relative minor damage.
- Flow failures of slopes involving very large downslope movements of a soil mass.
- Lateral spreads resulting from the lateral displacement of gently sloping ground.
- Ground oscillation where liquefaction of a soil deposit beneath a level site leads to back and forth movements of intact blocks of surface soil.
- Loss of bearing capacity causing foundation failure.
- Buoyant rise of buried structures such as tanks.
- Ground settlement, often associated with some other failure mechanism.
- Failure of retaining walls due to increase lateral loads from liquefaction backfill soil or loss of support from liquefied foundation soils.

The nature and severity of liquefaction damage is a function of the reduced shear strength and the magnitude of the static shear loads supported by the soil deposit (Ishihara et al., 1991). Castro (1987) classifies the possible consequences of liquefaction, as shown in Table 1.1, based on the relative magnitude of static driving shear stresses that may be present due to a surface slope or a foundation bearing load.

Table 1.1: Classification of soil liquefaction consequences (after Castro, 1987)

In situ stress condition	Soil behavior	Typical field observation
No driving shear stress	Volume decrease	Ground settlement
	Pore pressure increase	Sand boils from surface fissures
Driving shear greater than residual strength	Loss of stability	Flow slides
	Liquefaction	Sinking of heavy buildings
		Floating of light structures
Driving shear less than residual strength	Limited shear distortion	Slumping of slopes
	Soil mass remains stable	Settlement of buildings
		Lateral spreading

For situations in which the post-liquefaction strengths are judged to be less than the static driving shear stresses, deformations and displacements can be expected to be “large”, generally greater than 1 m. Figure 1.1 shows examples of global site instability corresponding to situations wherein post-liquefaction strengths are less than gravity-induced driving shear stresses (Seed et al., 2003). However, if the driving shear stress is less than the shear strength of the liquefied soil, only limited shear deformations are likely to occur. As illustrated in Fig. 1.2, liquefaction-induced lateral spreading are generally observed close to open faces, or in gently sloping ground. These deformations are usually driven by a combination of transient and static shear stresses and attributed to the loss of shear strength of underlying saturated soils. According to the National Research Council (1985): “Damage caused by lateral spreads, though seldom catastrophic, is severely disruptive and often pervasive... Cumulatively, more damage has been caused by lateral spreads than by any other form of liquefaction-induced ground failure.”

1.2 Pile Foundations Subjected to Lateral Spreading

1.2.1 Background

Liquefaction-induced lateral spreading of sloping ground and near waterfronts continues to be a major cause of damage to deep foundations. In the US, Japan, and other countries, buildings, bridges, and other structures supported by deep foundations have been damaged in many earthquakes. Permanent lateral ground deformations induce cracking and rupture of piles at both shallow and deep elevations, rupture of pile connections, and permanent lateral and vertical movements and rotations of pile heads with corresponding effects on the superstructure (McCulloch and Bonilla, 1970; Hamada et al., 1986; Mizuno, 1987; Hamada and O’Rourke,

1992; O'Rourke and Hamada, 1992; Youd, 1993; Swan et al., 1996; Ishihara et al., 1996; Tokimatsu et al., 1996; Yokoyama et al., 1997; Tokimatsu, 1999; Dobry and Abdoun, 2001).

Examination and analysis of case histories have revealed important aspects of pile foundations response to lateral spreading. While in some cases the top of the foundation displaces laterally a distance similar to that in the free field, in others it moves much less due to the lateral stiffness of the foundation and/or constraining effect of the superstructure. The foundation may be exposed to large lateral soil pressures, including passive pressures from nonliquefied shallow soil layers riding on top of the liquefied soil. In some cases the soil has failed before the foundation, with negligible bending distress and very small deformation of the piles and superstructure; while in others the foundation has failed first, experiencing large permanent deformation and rotation. The observed damage and cracking to piles is often concentrated at the upper and lower boundaries of the liquefied soil layer where there is a sudden change in soil properties, or at the connection with the pile cap. More damage tends to occur to piles when the lateral movement is forced by a strong nonliquefied shallow soil layer than when the forces acting on them are limited by the strength of the liquefied soil (Abdoun and Dobry, 2002).

1.2.2 Representative Case Histories

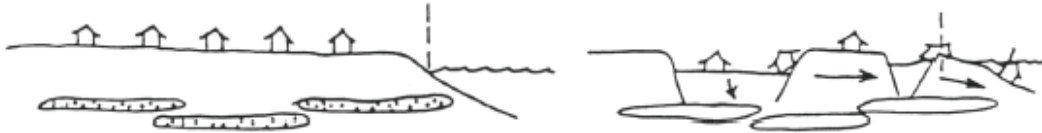
Hamada (1992) summarized the destructive effect of lateral spreading on two bridges during the 1964 Niigata earthquake in Japan, event that caused extensive damage due to soil liquefaction. Figure 1.3 illustrates the damage to the abutment and piers of the Yachiyo Bridge. The foundations of the abutments and piers were reinforced concrete piles, 30 cm in diameter and about 10 m in length. Pier No. 2 broke at the ground surface level, displaying a permanent deformation of 1.1 m between top and bottom. Once extracted, the piles showed severe damage at the bottom of the liquefied layer, damage that was clearly caused by the 2–5 m free field lateral spreading toward the river.

Figure 1.4 shows the collapse of the Showa Bridge during the same earthquake. The lateral spreading pushed the piers toward the river, causing five simple supported spans to fall. The bridge was founded on 60 cm diameter steel piles driven through a 10 m layer of loose to medium sand and 6 m into an underlying layer of dense fine sand. The 10 m layer is believed to have liquefied from the level of the riverbed down through its full depth (Berrill and Yasuda, 2002). Figure 1.5 illustrates a pile that was extracted after the earthquake, evidencing a permanent lateral displacement of approximately 1 m and a maximum curvature close to the transition from loose to medium dense sand.

☐ - Liquefied zone with low residual undrained strength



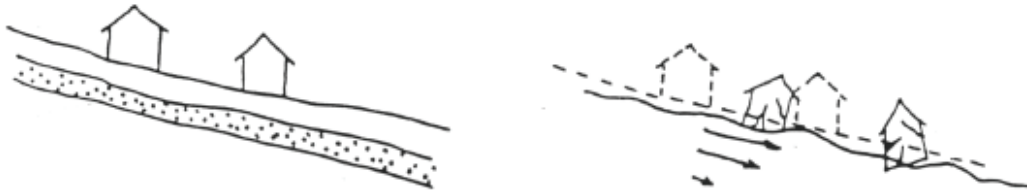
(a) Edge Failure/Lateral Spreading by Flow



(b) Edge Failure/Lateral Spreading by Translation



(c) Flow Failure



(d) Translational Displacement



(e) Rotational and/or Translational Sliding

Figure 1.1: Schematic examples of liquefaction-induced global site instability and/or “large” displacement lateral spreading (Seed et al., 2003)

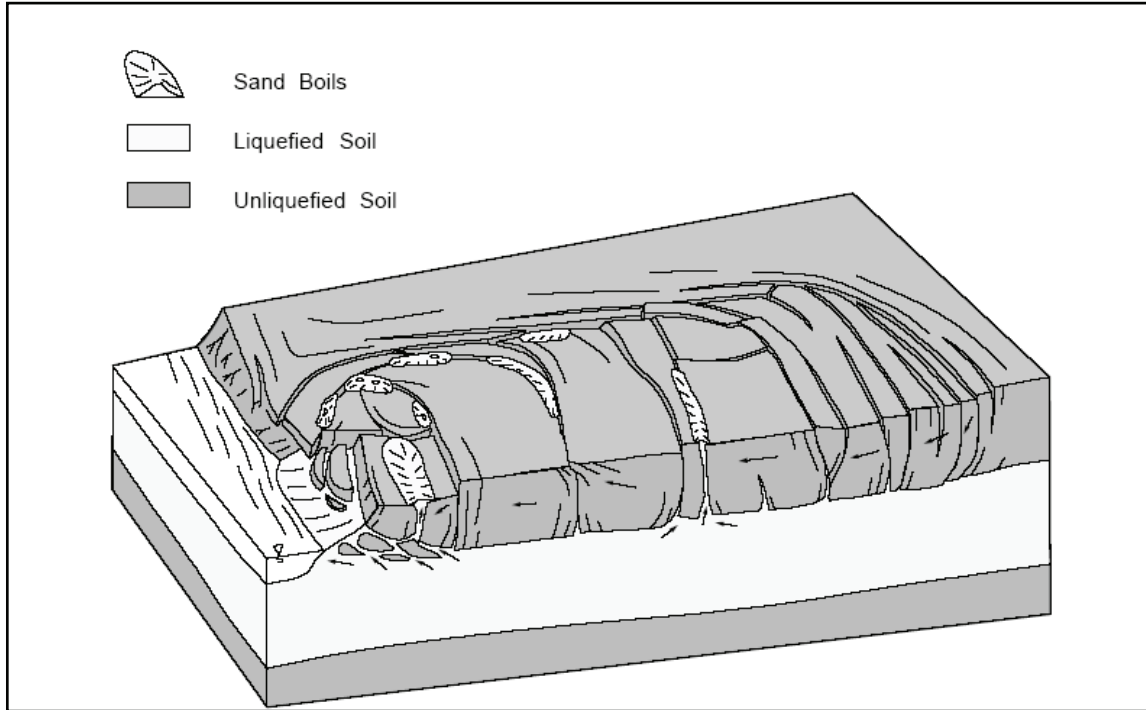


Figure 1.2: Schematic of a liquefaction induced lateral spread (Rauch, 1997)

The previous examples from the Niigata earthquakes clearly show that critical locations in the shear and bending response of deep foundations to lateral spreading are the head of the foundation and close to the bottom of the liquefied layer. Other examples indicate that when a nonliquefiable layer overlies the liquefied layer, a third critical point is the top of the liquefied layer. This is illustrated by the sketches in Fig. 1.6 (a)-(e), which summarize the damage on pile foundations near the waterfront from a number of field investigations after the 1995 Kobe earthquake (Tokimatsu, 1999).

The importance of the upper and lower boundaries of the liquefied layers is clearly illustrated in another example of pile damage during the Niigata earthquake. An investigation of piles beneath the Niigata Family Court House (NFCH) building provided evidence of the damage and regions of high bending moment in the piles (Yoshida and Hamada, 1991; Hamada et al., 1986; Hamada, 1992). During the earthquake the building slightly tilted due to differential settlements. After minor repairs, the building was in operation for the next 25 years, until it was reconstructed. At that time, two piles were excavated for inspection. Pile No. 1 was a floating pile about 6 m long that terminated within the upper loose sand layer, with SPT N-values in the range of 5 to 8. Pile No. 2 extended a further 2 m into a denser layer, with N-values of around 20. Horizontal ground displacements at the site were about 1 m. Figure 1.7 shows sketches of the deformed piles and soil profile, as well as the SPT profile. The floating pile was damaged a depth of about 2 m, near the groundwater level which is also the upper boundary of the liquefiable soil. The end-bearing

pile on the other hand, was damaged at both its top and towards the bottom, close to the boundary between the loose and dense sand, at about 8 m, presumably marking the bottom of the liquefied zone (Berrill and Yasuda, 2002). Figure 1.8 shows photographs of the damaged regions. Clearly, large bending moments developed in the pile near both boundaries between liquefied and non-liquefied soil.

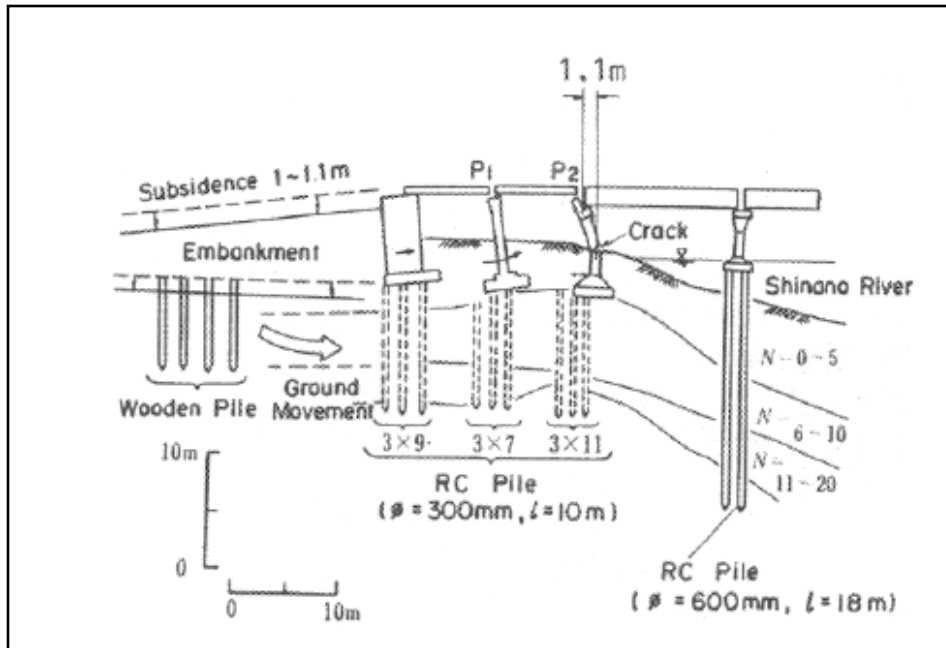


Figure 1.3: Schematic of the damage to Yachiyo Bridge in the 1964 Niigata earthquake (Hamada et al., 1986)



Figure 1.4: Collapse of Showa Bridge during the 1964 Niigata earthquake (after Iwasaki, 1973)

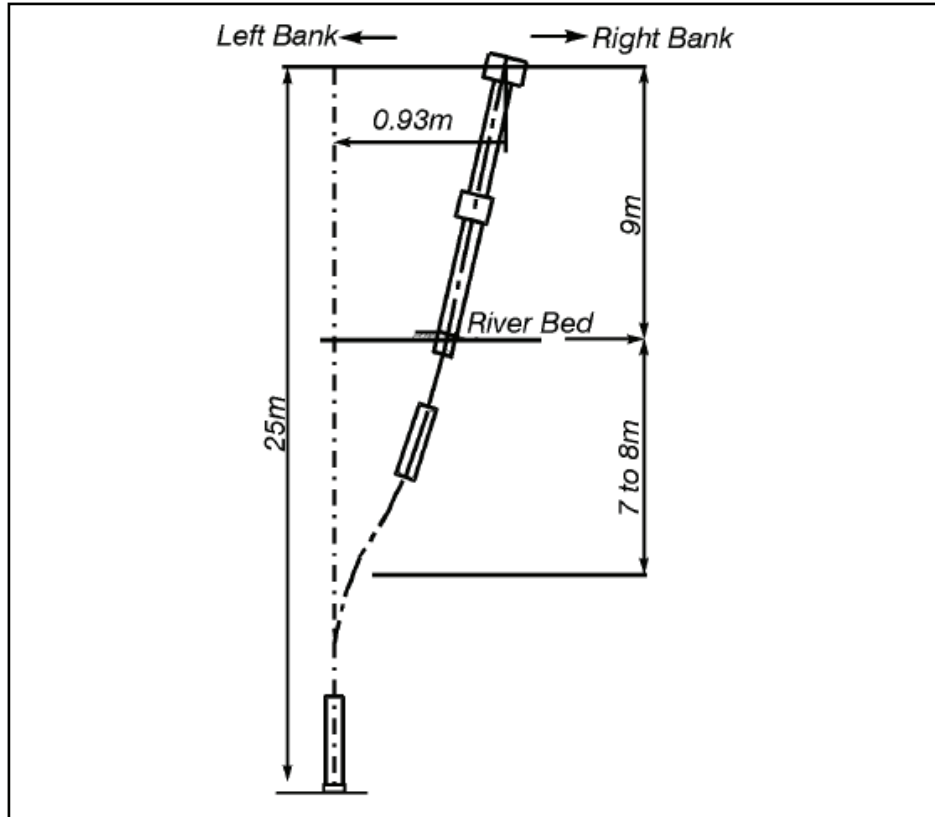


Figure 1.5: Schematic of a deformed steel pile extracted from Showa Bridge, after the 1964 Niigata earthquake (after Fukuoka, 1966)

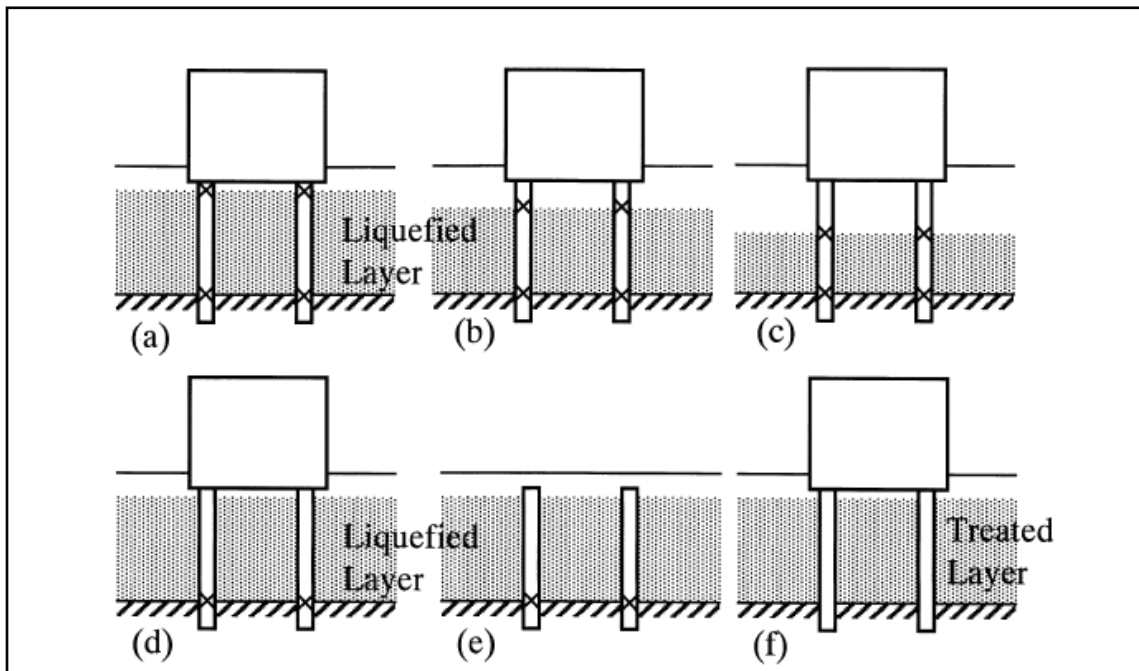


Figure 1.6: Typical damage pattern on pile foundations subjected to lateral spreading in the 1995 Kobe earthquake (Tokimatsu, 1999)

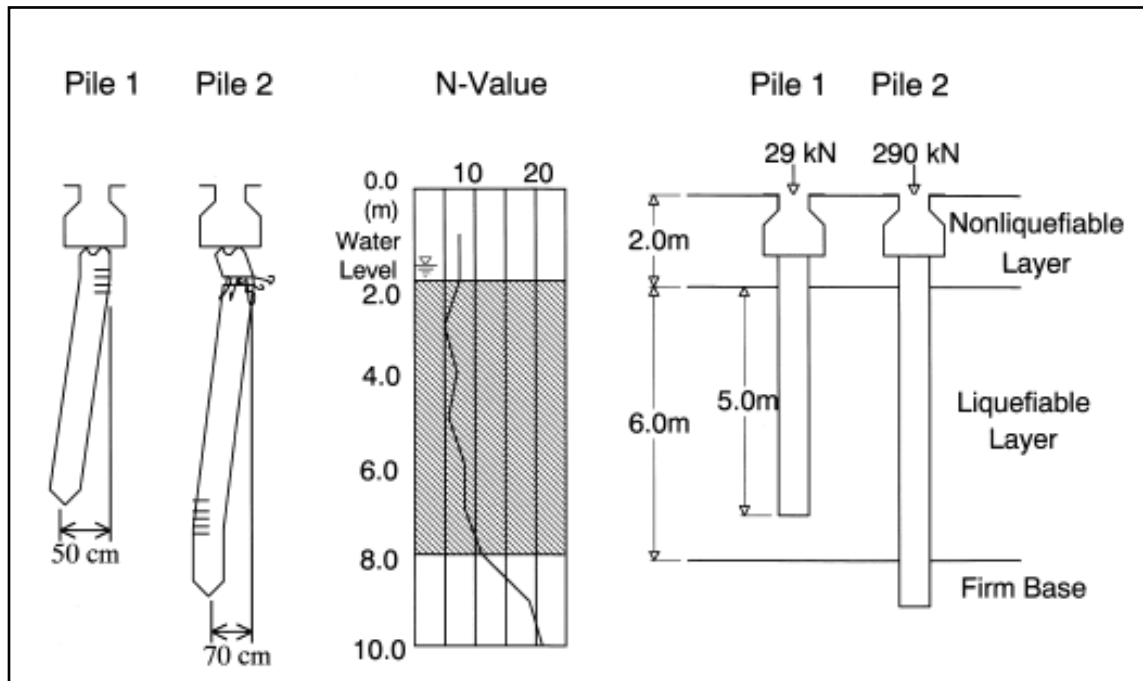
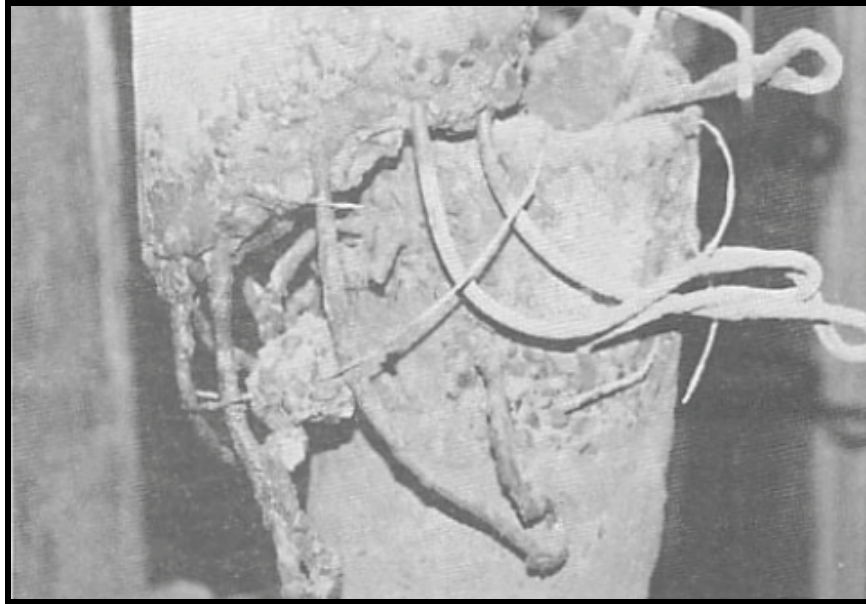
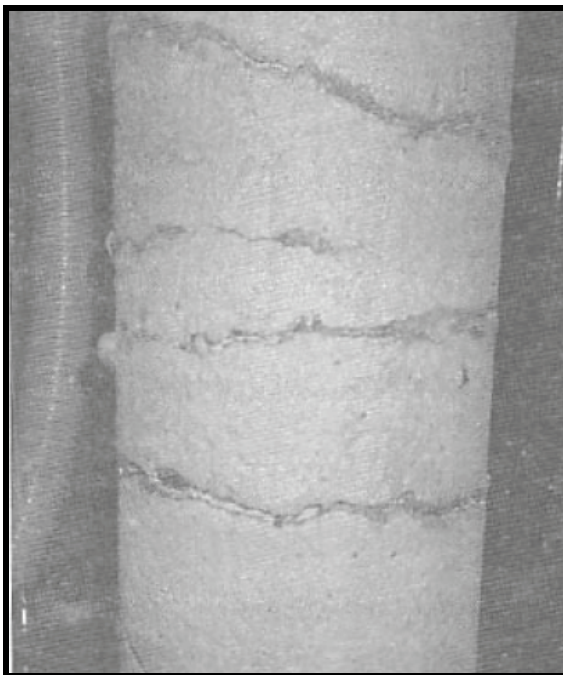


Figure 1.7: Damage to floating and end-bearing piles and standard penetration test, NFCH building, 1964 Niigata earthquake (Hamada et al., 1986)

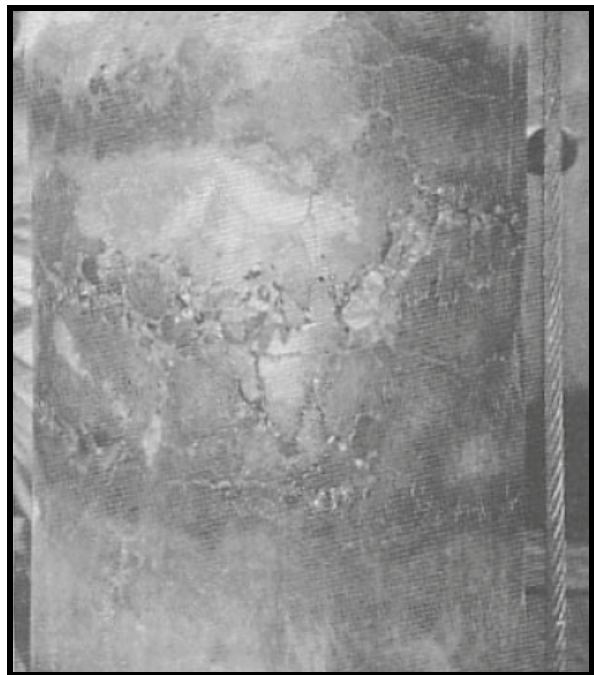
Another important lesson of shallow nonliquefied layers riding on top of liquefied soils is provided by the lateral spreading that occurred at the site of the Landing Road Bridge (Fig. 1.9) during the 1987 M6.3 Edgecumbe Earthquake. A liquefied 4 m thick loose sand layer moved about 1.5 to 2 m toward the river, carrying on top a nonliquefied 1.5 m thick clayey silt layer. That movement was resisted by the five piers of the on-land spans of the bridge, which consisted on eight 400 mm square raked pre-stressed concrete piles connected by a pile cap and slab pier, as shown in Fig. 1.10. During the earthquake, soil was mounded up behind the piers in what was apparently a passive failure. Subsequent trenching (Berrill et al., 1997, 2001) found failure surfaces and disturbed failure masses of soil confirming the occurrence of passive failure in the nonliquefied crust as it was driven against the buried piers and pile cap. The passive forces were estimated from in situ direct shear measurements and found to be very large, about 1.0 MN per pier. This was of the order of 10 times the estimated drag force exerted on the pile group by the liquefied sand. Berrill and Yasuda, (2002) concluded that nonliquefied layers can exert very large forces on piers and piles passing through them. The forces should be estimated from passive earth-pressure theory, and they may be the dominant lateral forces on the foundation under lateral spreading. The fact that the Landing Road Bridge did not collapse indicate the very good performance of the raked pile groups.



(a)



(b)



(c)

Figure 1.8: Photographs of damage piles shown in Fig. 1.7, (a) upper part of Pile No. 2, (b) lower part of Pile No. 2, and (c) upper part of Pile No. 1, (Hamada, 1992)



Figure 1.9: The Landing Road Bridge, after the 1987 Edgecumbe earthquake, New Zealand (Berrill et al., 2002)

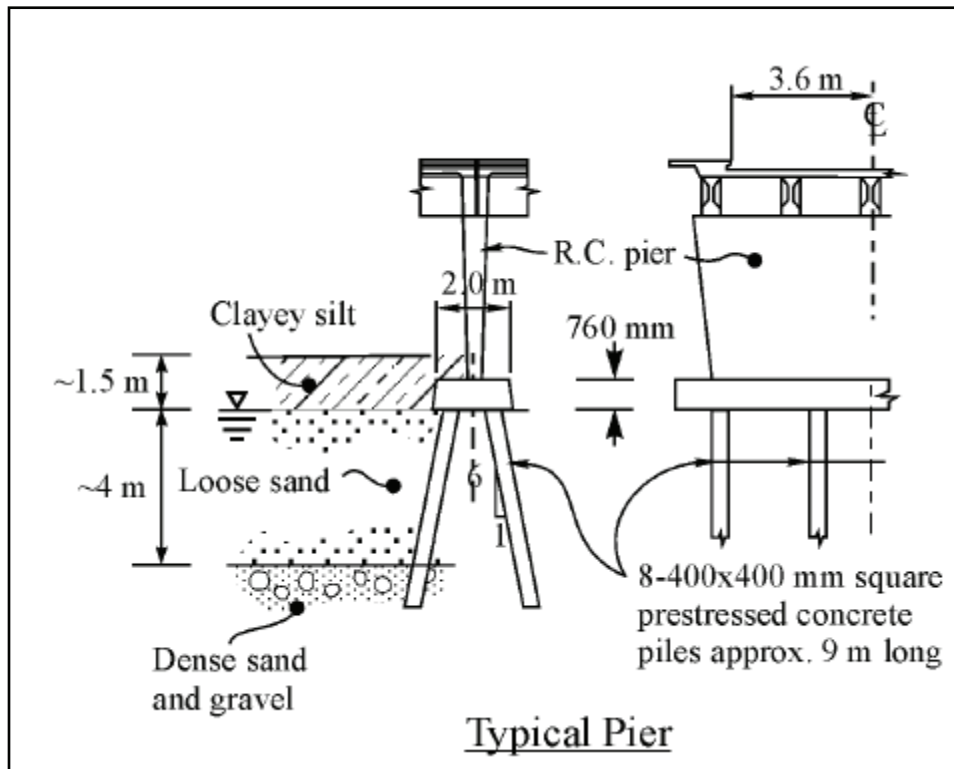


Figure 1.10: Schematic of the raked-pile foundation at the Landing Road Bridge (Berrill et al., 2002)

1.2.3 Current Practice in Foundation Analysis under Lateral Spreading

Case histories, as well as 1g shaking table and centrifuge model tests, indicate that the effect of lateral spreading on piles can be characterized in first approximation as a pseudostatic, kinematic soil-structure interaction phenomenon, driven by the permanent lateral movement of the ground in the free field (Dobry, 2004). Various foundation analysis and design methods have been proposed, where the soil applies static lateral forces to the pile foundation, either (i) as a function of the relative displacement between the foundation and the free field (p-y approach); or (ii) depending on the soil strength, taking the maximum possible values of the lateral soil forces (limit equilibrium method). A third approach (iii) suggested by several Japanese researchers assumes that the liquefied soil is a viscous fluid and hence the lateral soil static forces are a function of the relative velocity, rather than the relative displacement between foundation and free field (Hamada, 1998; Higuchi and Matsuda, 2002).

1.2.4 Engineering and Scientific Uncertainties

Although reasonable methods have been developed to define the shape of p-y curves for nonliquefied sand, considerable uncertainty remains regarding the appropriate shape and magnitude of p-y curves in liquefied sand (Rollins et al., 2005). While in some cases, liquefied sand is assumed to have no lateral resistance, others have recommended to multiply the p value for the nonliquefied sand by a reduction factor usually between 0.1 and 0.3 (Liu and Dobry 1995; Wilson 1998). Still others have suggested that the p-y curve for liquefied sand be based on the curve shape for soft clay (e.g., Matlock, 1970) with the residual shear strength for liquefied sand being used as the undrained shear strength (Wang and Reese, 1998). Finally, Ashour and Norris (2003) use an effective stress approach that account for the generation of pore pressure to generate p-y curves.

Therefore, even though the methods discussed in the previous section have been used frequently in the engineering practice and extensive research has been conducted, there are still significant uncertainties associated with the maximum lateral pressures and forces applied by the liquefied soil, which translates into a similar huge uncertainty in the calculated maximum pile bending moments. For example, in the Japan Road Association (JRA) method the lateral pressure is specified as 30% of the total overburden pressure (Fig. 1.11), while Abdoun et al. (2003) have recommended a constant lateral pressure with depth of 10 kPa. For a range of field conditions involving single piles (but not necessarily pile groups), the JRA and Abdoun method give similar results. However, a main source of uncertainty is the area over which this pressure is applied in the case of pile groups. Yokoyama et al. (1997) suggests that the value of the lateral pressure must be multiplied for the whole area of the pile group including the soil between the piles, which for a pile separation of $3d$ (d = pile diameter) may give a lateral force as much as three times greater than if the lateral pressure is applied only to the piles.

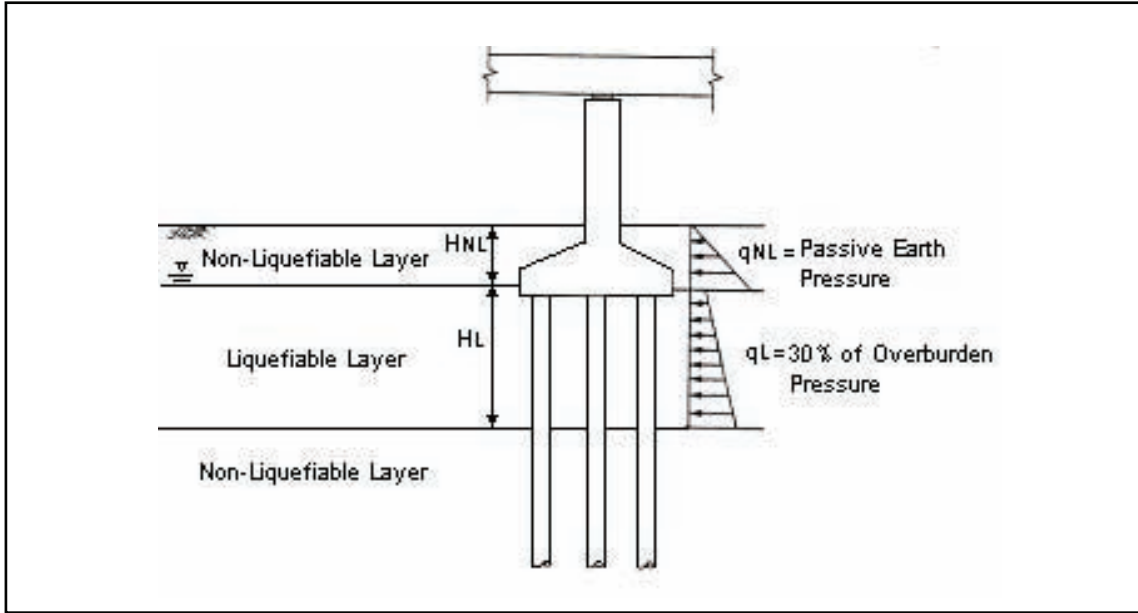


Figure 1.11: Proposed limit equilibrium design method of bridge pile foundations against lateral spreading in Japan (Japan Road Association, 1996; Yokoyama, et al., 1997)

Furthermore, recent centrifuge and full-scale 1g shaking table tests of single piles and pile groups indicate that the permeability of the liquefied sand is an extremely important and poorly understood factor, with a suggestion that the pile bending moments in silty sands may also be much greater than in clean sands.

1.3 Evidence on Pore Pressure Decrease and Soil Stiffening near Piles Subjected to Lateral Spreading

This section examines existing evidence on pore pressure decrease and stiffening of liquefied soil near piles and other buried objects during centrifuge tests, full-scale shaking table tests, small-scale tests, and field test.

1.3.1 Centrifuge Tests

Evidence on pore pressure decrease and stiffening of liquefied soil near piles at large relative displacements has been observed by other researchers in centrifuge tests. However, in the experiments discussed below, the decrease in pore pressure and soil stiffening have been a transient rather than a sustained phenomenon.

A series of centrifuge tests were carried out at the University of California in Davis to study the dynamic response of pile foundations in liquefying sand during seismic loading (Wilson et al., 2000). The models simulated a single-pile-supported structure, as shown in Fig. 1.12. The level soil profile consisted of a 9.1 m thick liquefiable layer on top of a 11.4 m thick dense sand layer.

The relative density of the top layer was 35% in model Csp2 and 55% in model Csp3. Both models were saturated with a pore fluid having 10 times the viscosity of water, in order to improve the simultaneous scaling of consolidation and dynamic processes. The models were spun up to a centrifugal acceleration of 30g and excited each by two different excitations.

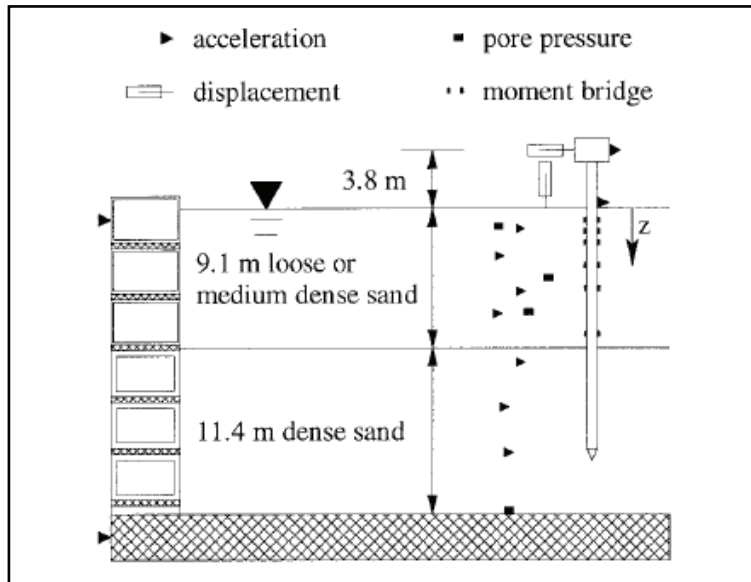


Figure 1.12: Typical partial model layout of centrifuge models Csp2 and Csp3 (Wilson et al., 2000)

The records exhibited a transient decrease in pore pressure close to the piles, with this tendency being more pronounced in model Csp3 than in model Csp2. The back-calculated p-y curves indicated that the soil resistance in the loose sand was much smaller than in the medium dense sand (Csp3). In model Csp3 the p-y behavior stiffened with increasing displacement when relative displacements approached or exceeded past values, especially near the surface (Fig. 1.13). Wilson and collaborators attributed this behavior to nearly undrained loading conditions and the tendency for the soil to dilate under these loading conditions (i.e., large enough strains to move the sand through a phase transformation). In medium dense sand, the p-y relationship progressively softened during shaking as excess pore pressures, strains, and number of load cycles increased.

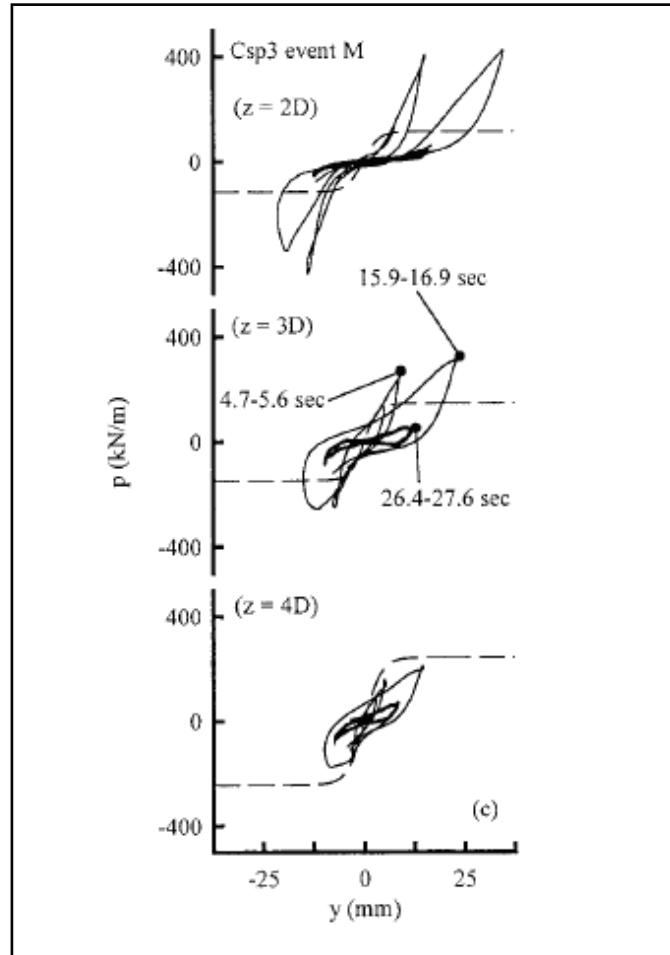


Figure 1.13: P-y curve behavior during shaking, model Csp3 (Wilson et al., 2002)

At the University of Cambridge in the UK, another series of centrifuge tests were carried out by Haigh and Madabhushi (2002) to study the single pile response to lateral spreading. The model corresponding to test SKH-14 simulated a single pile embedded on an inclined liquefiable soil layer on top of a nonliquefiable layer, as shown in Fig. 1.14. Pore pressure transducers were placed next to the upslope and downslope sides of the pile, as well as in the free-field. Once the model was saturated with viscous fluid (silicone oil) and spun up to a centrifugal acceleration of 50g, it was excited by a sinusoidal acceleration at the base. The records showed that the 5 m thick loose sand layer liquefied after about one cycle of excitation. The pile did not bounce back, reaching a maximum bending moment at the base of the liquefied layer of approximately 200 kN-m. Since the moment distribution was almost linear with depth, Haigh and Madabhushi suggested that the predominant lateral loading was coming from a non-liquefied surface layer generated by the g-field curvature.

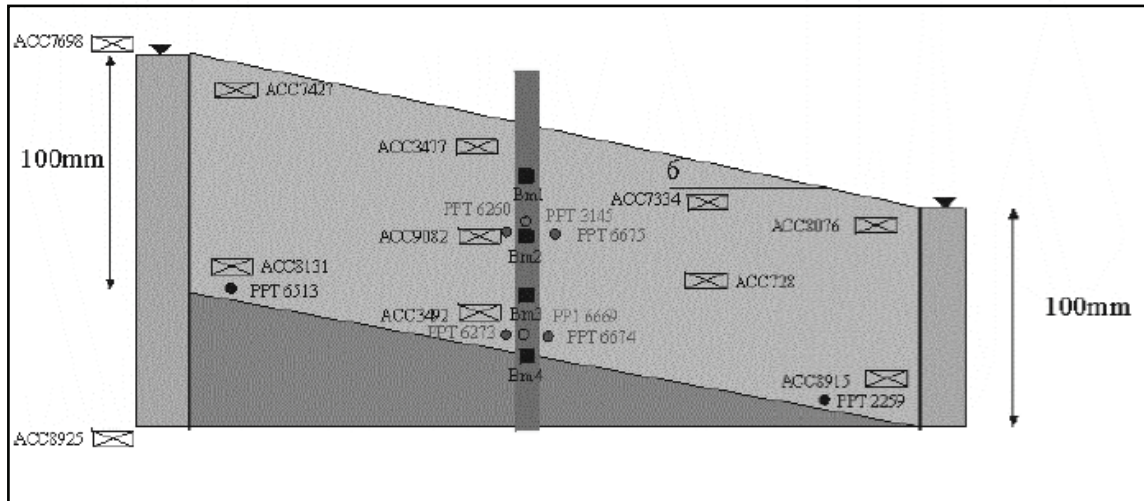


Figure 1.14: Setup and instrumentation used in centrifuge test SKH-14 (Haigh and Madabhushi, 2002)

Figure 1.15 shows the excess pore pressures measured at a depth of 3 m on the upslope and downslope side of the pile, as well as in the free field. The records exhibit large negative spikes next to the pile, with these spikes being larger on the downslope side of the pile. Haigh and Madabhushi indicated that this difference caused a net downslope hydrodynamic force acting on the pile. They concluded that while much of the load on the pile was coming by a non-liquefied crust, significant loading was also applied by the net hydrodynamic force.

1.3.2 Full-Scale Shaking Table Tests

Decrease in pore pressure near piles has also been observed by other researchers in full-scale shaking table tests during shaking, in single pile and pile group tests. Following the same trend observed in some of the centrifuge tests discussed above, the decrease in pore pressure has tended to be a transient rather than a sustained phenomenon.

A full-scale 1g shaking table test (Test No.1) was conducted in 2003 at the NIED shaking table in Tsukuba, Japan (Sato et al., 2004, unpublished). The NIED shaking table was at that time the largest shaking table (and largest soil laminar box container: 12 m in length, 3.5 m in width, and 6 m in height) in the world. The setup consisted in a water-saturated coarse sand, including a 6 m long single pile and a 2x2 pile group, as illustrated in Fig. 1.16. The slightly inclined laminar box was subjected to base excitation to induce lateral spreading. This test was part of a US-Japan project funded by NSF, involving cooperation from RPI to conduct parallel centrifuge tests using the same Japanese sand.

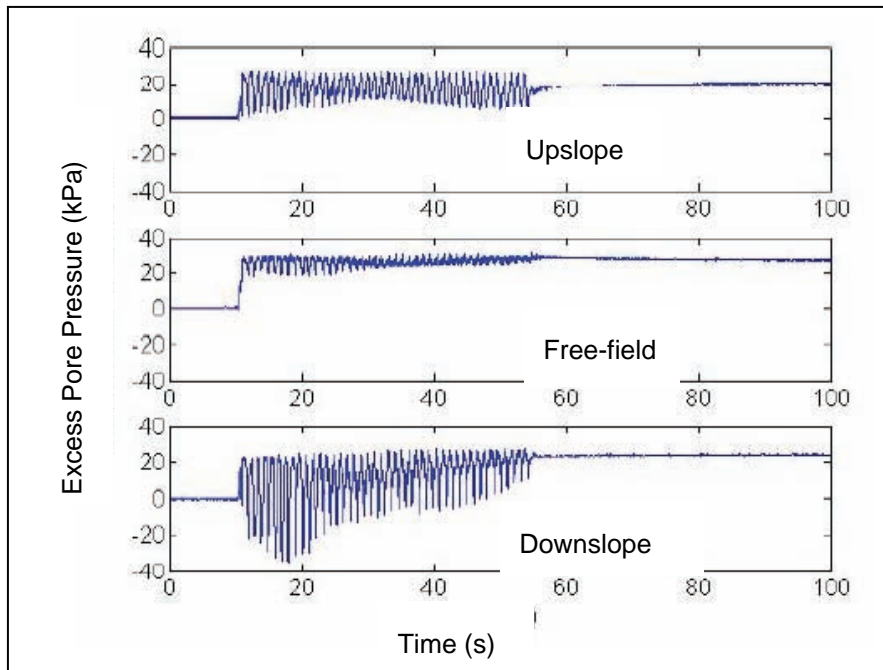


Figure 1.15: Excess pore pressure time histories measured near pile at 3m depth (Haigh and Madabhushi, 2002)

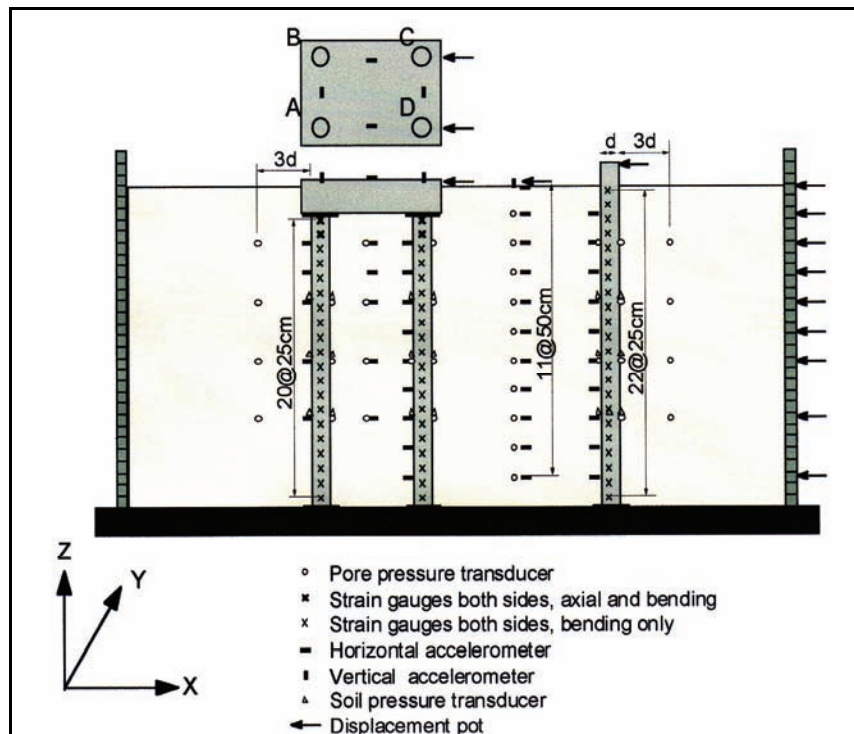


Figure 1.16: Setup and instrumentation of 6 m full-scale Test No.1 of single pile and 2x2 pile group subjected to lateral spreading using inclined laminar box, NIED, Japan (Sato et al., 2004, unpublished)

The soil displaced gradually during the excitation, reaching a maximum deformation on the ground surface of 27 cm. Figure 1.17 shows the free field deformation profile of the upstream side of the laminar box after the test. The single pile reached a maximum head displacement of 10 cm and a maximum bending moment at the base of 125 kN-m during the excitation, bouncing back afterwards. Pore pressure transducers were placed very close to the piles, as shown in Fig. 1.16. Negative excess pore pressure developed close to the single pile near the surface; however, it was smaller and dissipated during shaking, explaining the pile bouncing back.

On the other hand, one of the centrifuge models conducted at RPI as part of this US-Japan project was saturated with viscous fluid, trying to simulate as close as possible Test No.1 at NIED. Since the model was spun up to a centrifugal acceleration of 35g, the viscosity of the pore fluid was 35 times the viscosity of water, in order to satisfy strictly the permeability scaling relationship. The pile displaced gradually reaching a maximum displacement of 35 cm and bending moment of 350 kN-m at the end of the excitation, without ever bouncing back. Using the same Japanese coarse sand, the centrifuge model was repeated using water as pore fluid. In this case the pile bounced back during shaking, reaching a maximum bending moment of approximately 50 kN-m. Figure 1.18 compares the maximum bending moment profiles measured in Test No.1 and in the two centrifuge tests (Ubilla, 2004, unpublished). The results evidence the important effect of soil permeability in pile foundation response subjected to lateral spreading, exposing a “gap” in earthquake engineering knowledge.

In a different study, Suzuki and Tokimatsu (2004) investigated the effect of pore water pressure reduction around a pile on the p-y behavior during liquefaction. Three large 1g-shaking table tests were conducted in the NIED shaking table using different soil densities. The level soil profile included a top 0.5 m thick dry sand layer, a 3 m thick liquefiable sand layer and an underlying 1.5 m thick dense gravelly layer, as shown in Fig. 1.19. The 2x2 pile group consisted of hollow steel piles fixed to the base of the container, including a mass on top in two of the tests. Figure 1.20 summarizes the measurements of transient pore pressure reductions near one of the piles in the pile group. The results show a considerably decrease in pore water pressure around a pile in dense sand with increasing relative displacement between soil and pile. This caused an increase in subgrade reaction, making the p-y behavior stress to hardener. The reduction in pore water pressure was greater on the extension side than on the compression side of the soil around the pile. The pore water pressure on the extension side decreased due to the combined effects of extension stress and dilatancy characteristics of the soil induced by the shear stress developed around the pile, while that on the compression side did not decrease due to the opposite effects of compression stress and dilatancy characteristics (Suzuki and Tokimatsu, 2004).



Figure 1.17: Final free field deformation profile of 6 m inclined laminar box after Test No.1, NIED, Japan (Sato et al., 2004, unpublished)

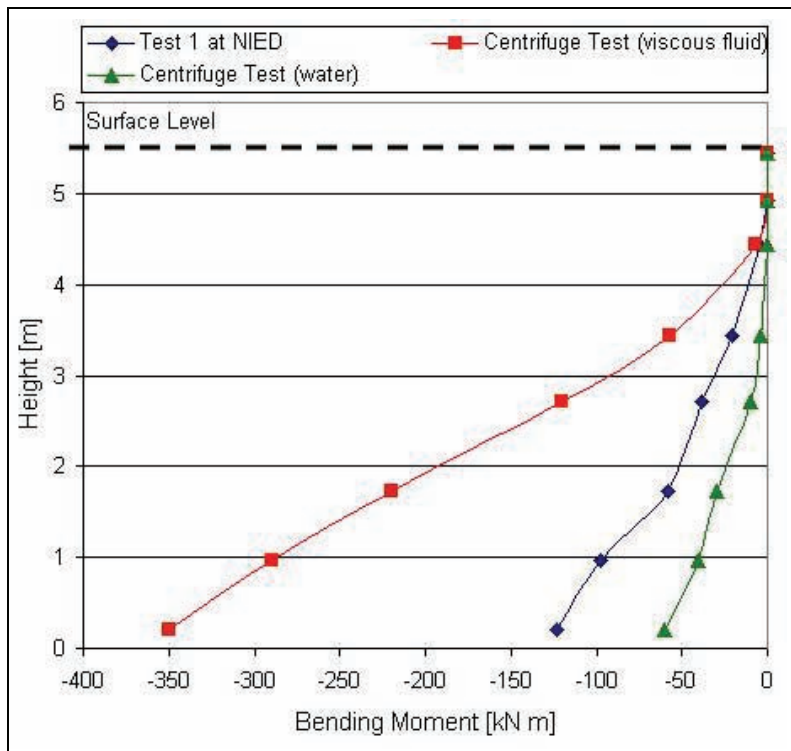


Figure 1.18: Maximum bending moment profiles measured in single pile in 1g full-scale Test No.1 at NIED (water) and centrifuge tests at RPI (water and viscous pore fluid), (Ubilla, 2004, unpublished)

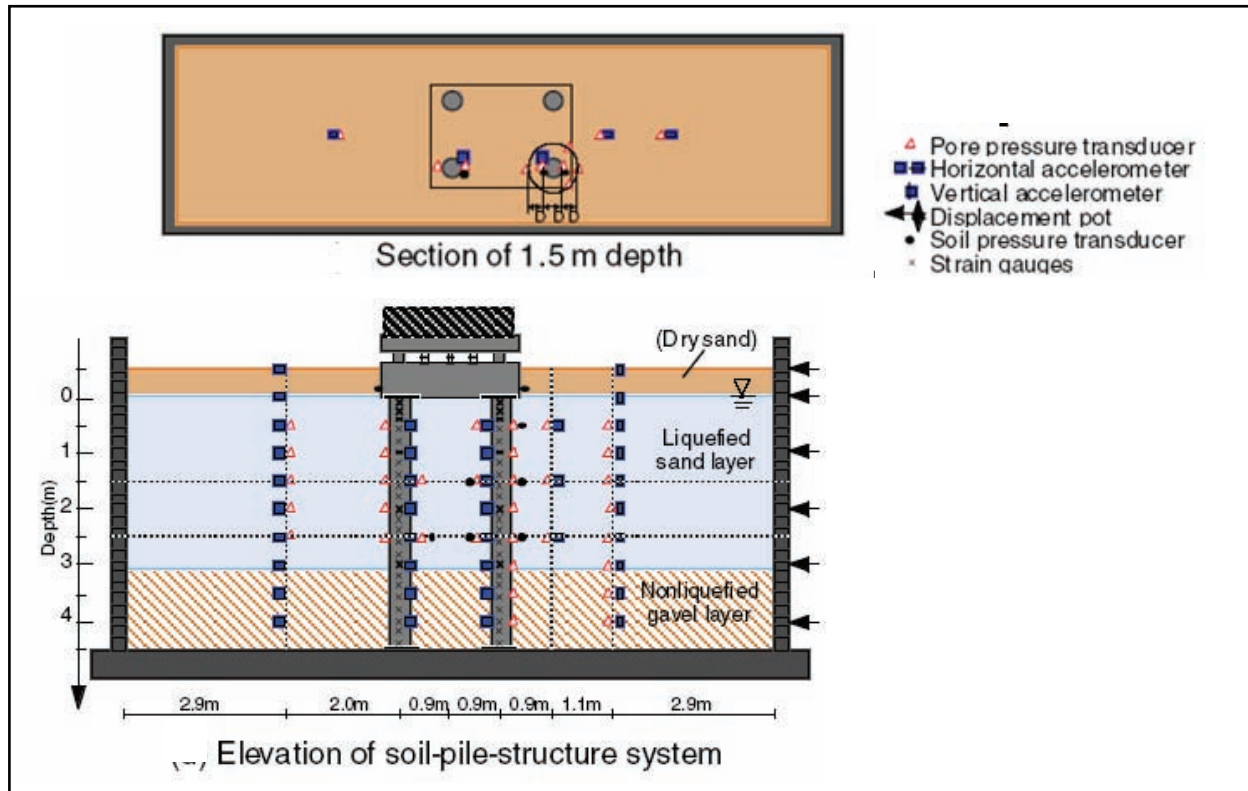


Figure 1.19: Setup and instrumentation of full-scale shaking table test on level ground at NIED, Japan (Suzuki and Tokimatsu, 2004)

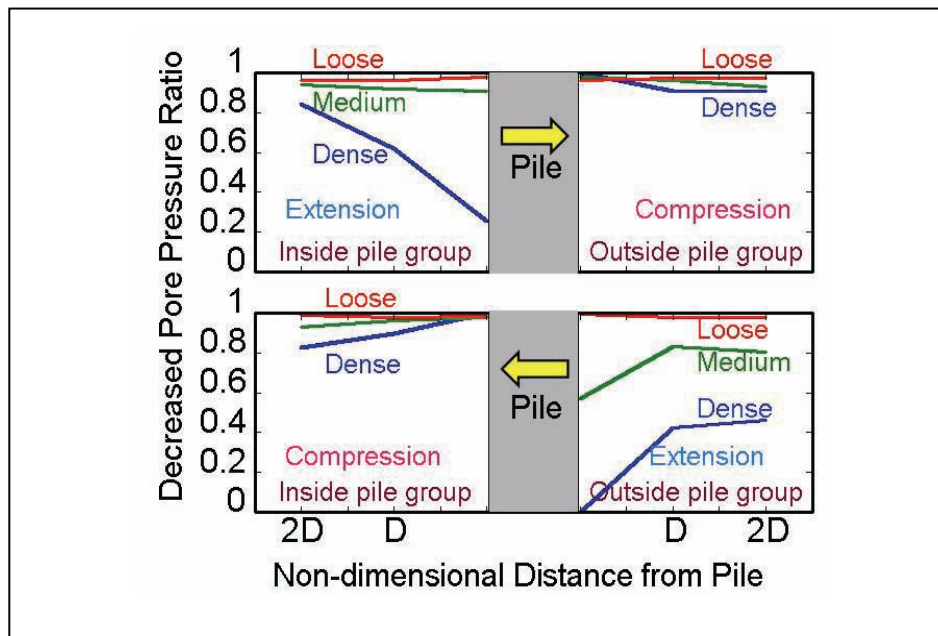


Figure 1.20: Reduction in pore water pressure near piles in pile group during full-scale shaking table tests at NIED, Japan (Suzuki and Tokimatsu, 2004)

1.3.3 1-g Small-Scale Tests

Several researchers have found out recently that the resistance of the liquefied soil to the movement of an object (pile, cylinder, or sphere) increases as the relative velocity of the object and the soil increases. These results support the theory that the liquefied soil can be modeled as a viscous fluid (e.g. Dungca et al., 2004; De Alba and Ballesterro, 2004; Hwang et al., 2004).

Dungca et al. (2004) conducted small-scaled shaking table tests to study the lateral resistance of a pile subjected to liquefaction-induced lateral flow, where the pile was modeled as a buried cylinder. The model setup used in the study is illustrated in Fig. 1.21. An aluminum model container was used with inner sizes of 450 mm in width, 150 mm in width, and 250 mm in height. A rubber pressure bag was attached underneath the top cover of the container to apply an overburden pressure on the surface of the soil. A fluid tank was connected at the bottom of the box to supply and drain out fluid and to apply a back pressure to the pore fluid of the soil. Once the model was ready, an horizontal shaking was applied to the container by a mechanical shaker. During the tests, acceleration of the container, horizontal load and displacement of the cylinder, and earth pressure and pore fluid pressure around the cylinder were measured. The results support that the pore fluid migration rate, i.e. the hydraulic conductivity of the soil with respect to the loading rate, is the crucial factor for mobilization of the lateral resistance of a buried cylinder in liquefied soil, because there is less time for the pore fluid to come rushing from the free field to dissipate the negative pore pressures near the object. Figure 1.22 shows the first loops of the relationship between normalized lateral resistance and normalized displacement of the cylinder for loading rates of 1 mm/sec, 10 mm/sec and 100 mm/sec. The initial lateral resistance was negligibly small; however it increased significantly as the loading rate became higher.

De Alba and Ballesterro (2004) carried out a series of tests to prove or disprove if sand behaves as a Newtonian fluid by observing how spheres move through a liquefied sand of low relative density. Long triaxial specimens were prepared around a 12.7 mm-diameter sphere loaded by a wire/deadweight system, as illustrated in Fig. 1.23. Sphere velocities and drag forces were measured over a large range of shear strains and strain rates, and plotted in Fig. 1.24. The resistance to motion, which they called “apparent drag,” raised with velocity up to a value of about 60 cm/sec, then tended to level off and oscillate around a mean value. De Alba and Ballesterro suggest that the residual strength of sand after liquefaction is indeed rate-dependent.

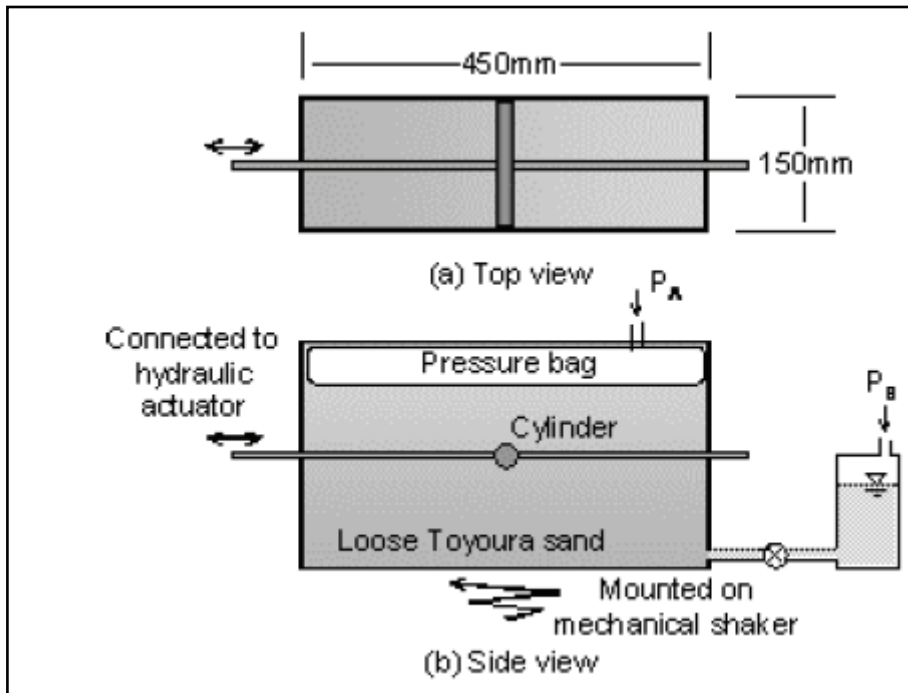


Figure 1.21: Schematic of model container to study the liquefied soil lateral resistance against the lateral displacement of a cylinder (Dungca et al., 2004)

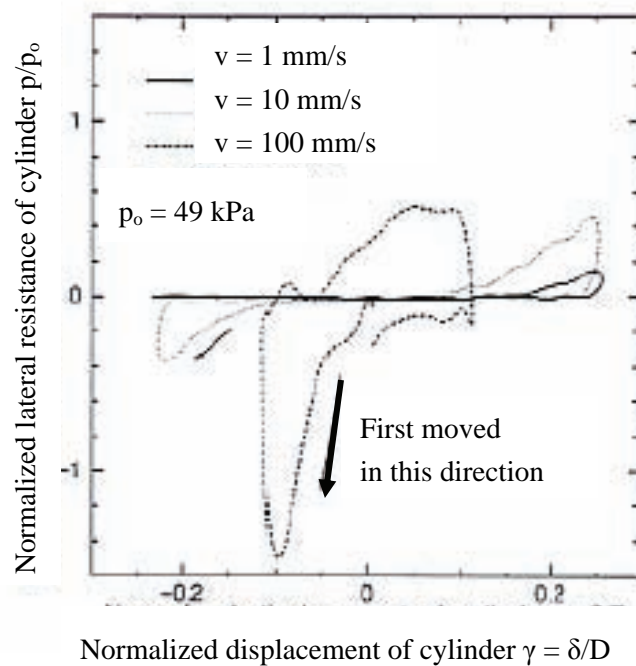


Figure 1.22: Liquefied soil lateral resistance against lateral displacement of cylinder (Dungca et al., 2004)

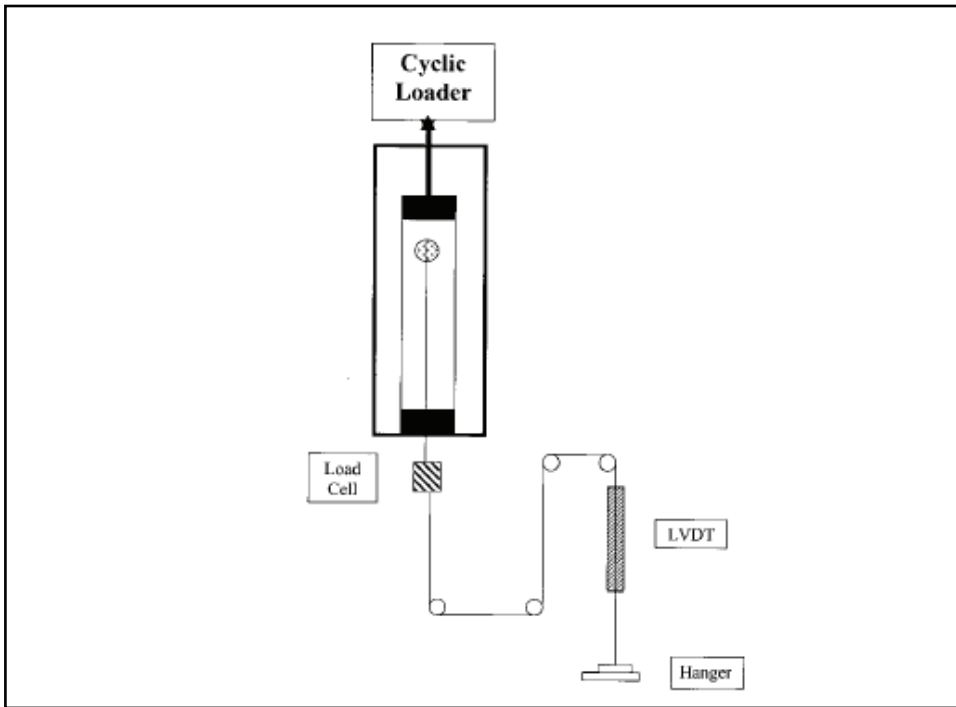


Figure 1.23: Schematic of experimental apparatus to pull a sphere through a liquefied sand (De Alba and Ballestero, 2004)

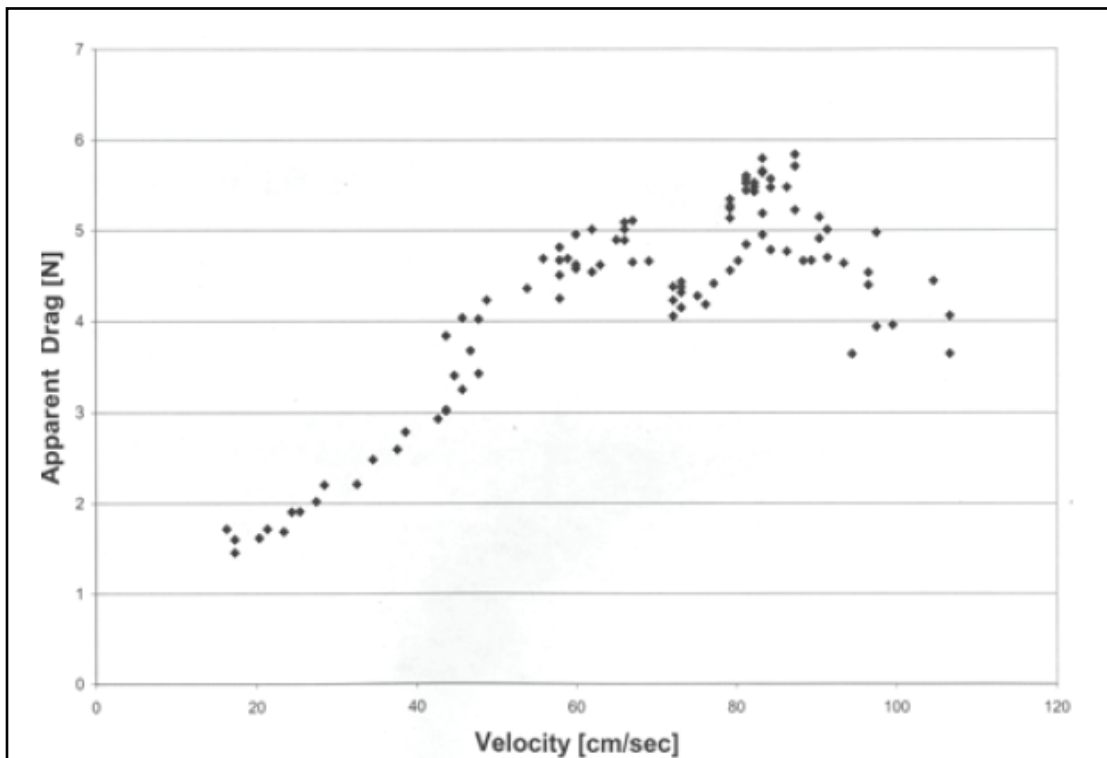


Figure 1.24: Sphere velocity versus apparent drag force in a liquefied sand, test 19 (De Alba and Ballestero, 2004)

1.3.4 Field Test

Based on the lack of full-scale field tests, Rollins et al. (2005) carried out a full-scale foundation testing program to develop p-y curves for deep foundations in liquefied sand. This testing program, known as the Treasure Island liquefaction test (TILT), was located in Treasure Island, a 160 ha manmade island immediately northwest of the rock outcrop on Yerba Buena Island in San Francisco Bay, California. The lateral load test was performed on a 3x3 full-scale pile group following a blast-induced liquefaction. The soil profile consists of a 6 m thick layer of loose fine sand or silty sand, on top of a silty sand and Young Bay Mud. A plan view of the test site during the pile group testing is shown in Fig. 1.25. Pore pressure transducers were installed around the pile group to measure the pore pressure response with load and deflection.

Figure 1.26 shows that the pore pressure ratios decreased significantly at shallow depths near the pile group as the lateral load increased, decrease that was attributed in part to a phase transformation induced by large shear strains. The records also evidenced that the reduction of pore pressure decreased with depth and distance from the pile group. The p-y curves in liquefied sand were characterized by a concave-up shape with the slope of the curve increasing with displacement. Rollins et al. (2005) concluded that this characteristic concave-up shape appears to be related to a dilative behavior during shearing.

1.4 Pile Pinning Effect on Liquefaction Induced Lateral Spreading

1.4.1 Background

Of all the components of the surface transportation system, bridges have been shown to be among the most vulnerable to earthquake damage. About 70 percent of the approximately 600,000 highway bridges in the U.S. were constructed prior to 1971, with little or no consideration given to seismic resistance (MCEER Highway Project 094, 2000). In fact, the vulnerability of highway bridges to earthquake induced liquefaction related ground failures has been clearly demonstrated by the extensive damage observed in past earthquakes.

If liquefaction induced lateral spreading is identified as a potential problem in a highway bridge site, two mitigation methods are normally considered: (i) soil-structure interaction analyses to determine if the deformation and load capacity of the existing foundation-bridge structure is able to accommodate the ground deformation demands, and (ii) the use of site remediation techniques to prevent liquefaction and/or minimize ground displacement demands.

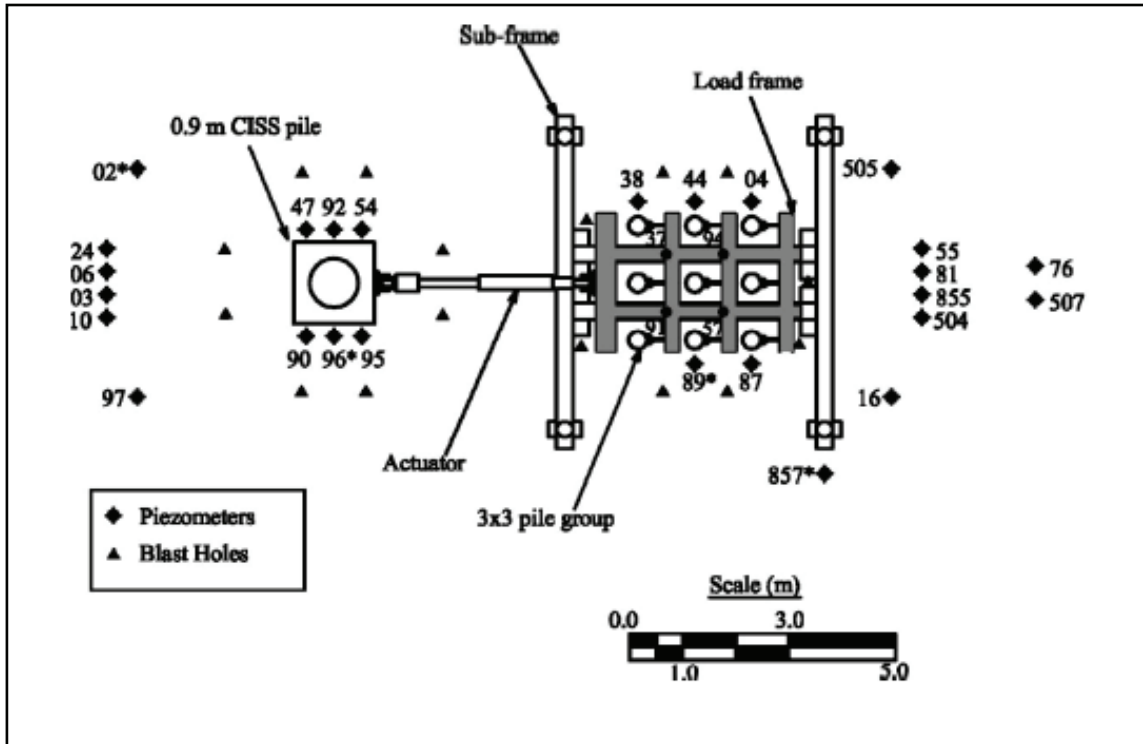


Figure 1.25: Plan view of test site layout during load test at 3x3 pile group location, Treasure Island Test (Rollins et al.,2005)

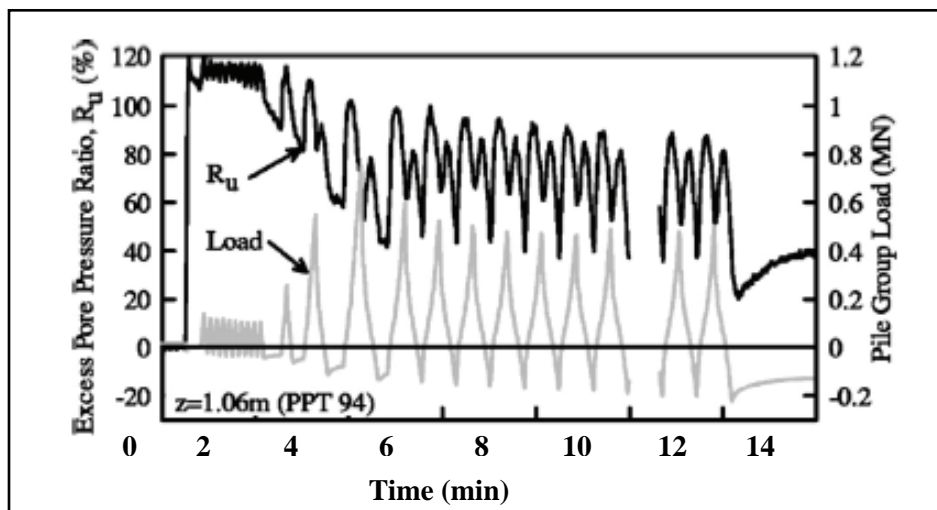


Figure 1.26: Time histories of total load and excess pore pressure ratios near the ground surface adjacent to the pile group, Treasure Island Test (Rollins et al.,2005)

Although ground remediation techniques are often used at bridge sites to mitigate lateral spreads, further research is needed on mitigation options related to foundation design or retrofit, as methods of soil improvement are often costly and time-consuming to implement. A number of case histories and a limited number of analyses have indicated that, with appropriate design, foundations can accommodate relatively large ground deformation demands from lateral spreads (Martin, 2000).

Damage modes associated with lateral ground deformation demands on bridges include: (i) lateral deformation of abutments and piers arising from liquefaction induced flow failures or lateral spreads, leading to substructure pile damage and potential span collapse, and (ii) liquefaction induced differential settlement causing potential span collapse.

Whereas the evaluation of the mode and magnitude of liquefaction induced lateral ground deformations involves considerable uncertainty, the current state of practice utilizes the Newmark sliding block approach on an assumed dominant failure plane within the liquefied zone. The approach requires initial pseudo-static stability analyses to determine the critical surface of failure and associated yield acceleration (Fig. 1.27), and a design earthquake time history representative of ground motions at the base of the sliding mass usually assumed at the base of the liquefied layers (Martin, 2000).

The Newmark method has been used to study earthquake induced slope displacements in dams and natural slopes. However, the approach for lateral spreading involves a number of assumptions like: (i) the time during the earthquake at which liquefaction is triggered, (ii) the magnitude of the shear strength of the liquefied soil, and (iii) the influence of the thickness of liquefied soil on displacement.

Once the geometry of the failure and magnitude of the liquefaction induced lateral deformation are estimated, an assessment should be made to see if the foundation is able to withstand the displacement demands and the superstructure can accommodate those deformations. The magnitude of moments and shear induced in the piles may be computed with a p-y curve approach, using the estimated displacement field.

1.4.2 Pile Pinning Approach

A refinement of the above approach is to consider the reinforcing or pinning effects the piles or pile group have on the lateral stability, by representing the pile shear forces at the location of the failure plane as an equivalent shear strength in the calculation of yield accelerations used in the Newmark analyses. This becomes an iterative approach as shear forces are a function of displacements which in turn are reduced as shear forces increase. Analysis methods that account for this "pile pinning" interaction effect can reduce the expected foundation loads to values significantly smaller than those estimated without consideration of this pile pinning effect

(Boulanger et al., 2005). Design methods that account for this compatibility in displacement between the pile foundation and the abutment soils have been used in practice (Perez-Cobo and Abghari, 1996; Law, 2000; Zha, 2004) and incorporated in the NCHRP 472 recommended specifications for seismic design of bridges (Transportation Research Board, 2002; Martin et al., 2002).

These design methods, as summarized by Boulanger et al. (2005), consist of the following three primary steps.

1. Estimate the abutment displacement for a range of restraining forces from the piles and bridge superstructure. This step involves performing a slope stability analysis to estimate the yield acceleration, followed by a Newmark sliding block analysis to estimate the abutment displacement.
2. Estimate the expected restraining force exerted on the abutment by the piles and bridge superstructure for a range of imposed abutment displacements. This step involves either a pseudo-static pile pushover analysis or some simpler approximation to determine the pile restraining forces or pushover curve.
3. Determine the compatible displacement and interaction force between the abutment and the piles/bridge based on the intersection of the relations established in steps 1 and 2 above.

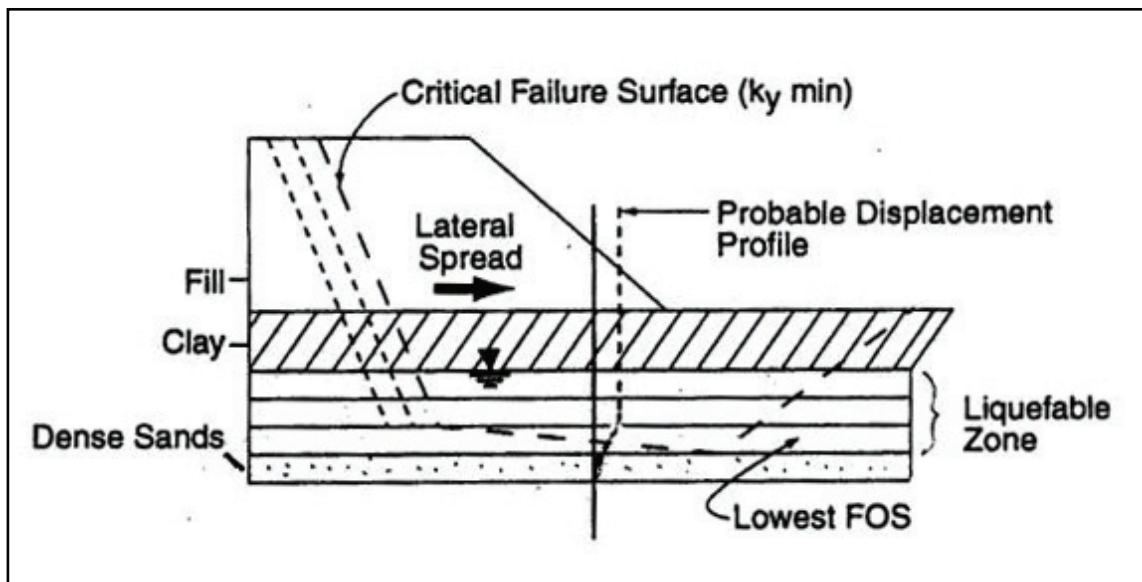


Figure 1.27: Pseudo-static stability analysis, Newmark approach (Martin et al., 2002)

If the forces and displacements on the foundation and superstructure are acceptable, the design is complete. If not, additional piles can be included in the analysis, not necessarily connected to the foundation (passive piles) or the cap.

1.4.3 Previous Centrifuge Modeling of Pile Pinning Effect

Since the design methods for pile pinning effects had not previously been evaluated or validated against physical data, Boulanger et al. (2005) conducted a centrifuge test at UC Davis to evaluate this analysis method. Figure 1.28 illustrates the setup of the centrifuge model. The prototype soil profile consisted of a 4.8 m thick loose Nevada sand layer on top of a dense Nevada sand layer, including thin layers of non-plastic silt located above and below the loose sand layer. The two abutments were constructed of coarse Monterey sand, with the crest sloping slightly toward the channels. The water table was at the top of the upper silt layer. The foundation consisted of a row of six 0.72 m diameter piles, driven along the head of one abutment. At a centrifugal acceleration of 60g, the model was excited by a single earthquake motion. The lateral displacement at the head of the abutment slopes was approximately 1.6 m for the abutment without piles and approximately 1.2 m for the abutment with piles.

First, a slope stability analyses was carried out to determine the yield acceleration for the abutment. The critical failure surface, as shown in Fig. 1.29, was found to shift when the pile restraining force exceeded a certain level. The results indicated that the yield acceleration, for a given level of pile restraining force, was much smaller when the failure surface was allowed to change. The abutment displacements were then computed using Newmark sliding block analysis with different amount of pile restraining force, with this force assumed to be constant through the excitation, as is assumed in existing design methods (e.g., Zha, 2004; Martin et al., 2002). On the other side, a pseudo-static pushover analysis of the piles was done using p-y curves based on the American Petroleum Institute recommendations.

Unfortunately, the solution from the compatibility of displacements between the abutment and piles predicted a much smaller pile displacement than the measured one. The following modifications to these pile pinning analysis methods were introduced and subsequently shown to result in reasonable agreement between computed and observed pile displacements.

- Take into account the increase in critical slide mass with increasing pile pinning force.
- Consider the equivalent constant restraining force from the piles as the average restraining force that would develop as the displacement increases from zero to its final value.
- The tributary mass of the abutment should include a portion of the side slope masses, and not just the mass of the soils behind the crest width.

- Consider the reduction in pile fixity above or below the liquefied layer that can occur due to internal abutment deformations or shear strains in the underlying strata.

The dynamic interactions between pile foundations and laterally spreading ground are only crudely approximated by the combination of a Newmark analysis for the abutment and a static (pushover) analysis for the piles. Nonetheless, these simplified analyses do provide a first-order approximation of the pile pinning effect, and can be useful for design purposes provided that the uncertainties in the input parameters and analysis method are reasonably accounted for (Boulanger et al., 2005).

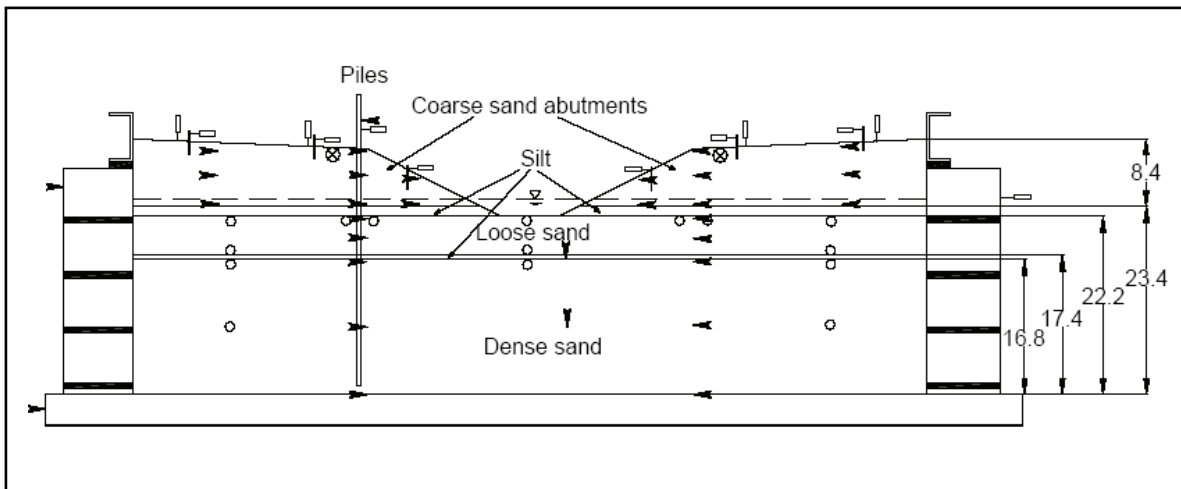


Figure 1.28: Setup of centrifuge model with two facing abutments, prototype dimensions in meters (Boulanger et al., 2005)

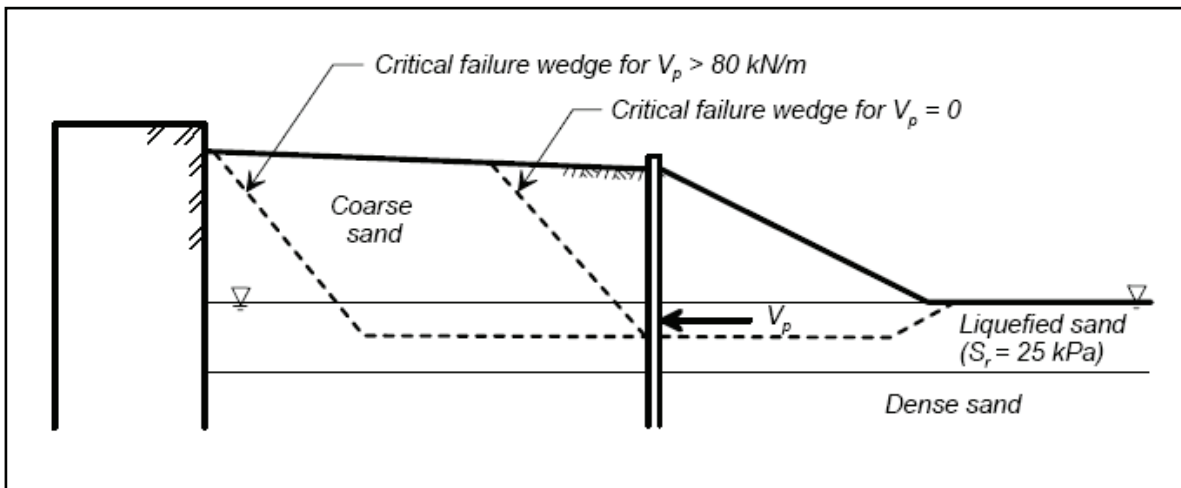


Figure 1.29: Critical slip surfaces with and without pile restraining force (Boulanger et al., 2005)

1.5 Scope of Research

1.5.1 Effect of permeability on pile response to lateral spreading

The first part of this work focus on the effect of soil permeability on the response of pile foundations subjected to lateral spreading. Six centrifuge tests were conducted at the 150g-ton RPI centrifuge described in chapter 2. The corresponding six models, tested in a large laminar box, simulate a mild infinite slope with a 6 m thick loose sand layer on top of a 2 m thick cemented sand layer. Three models consisting of a single pile, a 3x1 pile group, and a 2x2 pile group were tested using water as pore fluid. Since in centrifuge modeling of liquefaction there is a conflict with the consolidation and dynamic processes, these models consolidated much faster than desired, hence simulating a loose layer of coarse sand. These models were then repeated, using the same fine Nevada sand, but saturated this time with a viscous fluid (metulose), hence simulating a loose layer of fine sand. As a result, these models simulate deposits of wide different permeability in the field.

Table 1.2: Testing properties of first series of centrifuge models (permeability effect)

Model	Pile configuration	# of piles	# of instrument. piles	Pile cap	# of layers	Fluid viscosity (μ_w)
1x1-w	single pile	1	1	no	2	1
1x1-v	single pile	1	1	no	2	42
3x1-w	(3 x 1) + 1	4	3	in 3 x 1	2	1
3x1-v	(3 x 1) + 1	4	3	in 3 x 1	2	40
2x2-w	2 x 2	4	2	yes	2	1
2x2-v	2 x 2	4	2	yes	2	38

The specific objectives of this study to be accomplished through centrifuge modeling, corresponding data interpretation and comparisons, and analytical analyses are:

1. Study the soil-pile interaction in a two-layer soil profile during liquefaction induced lateral spreading, for single pile and pile groups, in particular pile displacement and bending moments.
2. Study the effect of soil permeability in the development of negative excess pore pressures close to the foundations during lateral spreading.

3. Study the effect of soil permeability in the pattern of soil deformation around the foundations to find out if the lateral pressure acts only on the foundation or also in the soil in between in the case of pile groups.
4. Conduct a limit equilibrium analysis to estimate the liquefied soil pressure acting on the single piles and pile groups, as well as the fixation provided by the bottom cemented layer.
5. Conduct p-y curves analyses on the single pile to back-calculate the profiles of liquefied soil pressure at different times.

1.5.2 Effect of pile pinning on lateral spreading

The second part of this work focus on the effect of passive piles or pin piles in restricting the amount of lateral spreading. Four centrifuge tests were conducted at the 150g-ton RPI centrifuge. The centrifuge models, conducted on a slightly inclined laminar box subjected to in-flight base shaking, simulate the case when a nonliquefied crust rides on top of a liquefied sand layer. The prototype profiles consist of a 3 m thick layer of liquefiable Nevada sand on top and below a 3 m thick slightly cemented sand layer. The first centrifuge test (Model p-0) did not include piles and was the benchmark experiment to simulate lateral spreading in the free field. Using a similar setup, the other centrifuge tests simulated the response of a 3x2, 6x2, and 3x1 pile group respectively. The pile groups were connected by a cap and embedded in the three layer soil profile. In this type of soil profiles, the load applied to the foundations is essentially controlled by the top nonliquefiable layer, with the pressure of the liquefied soil being negligible. Therefore, the models were saturated with water instead of viscous pore fluid.

Table 1.3: Testing properties of second series of centrifuge models (pinning effect)

Model	Pile configuration	# of piles	# of instrument. piles	Pile cap	# of layers	Fluid viscosity (μ_w)
p-0	No foundation	0	0	–	3	1
p-3x2	3 x 2	6	2	yes	3	1
p-6x2	6 x 2	12	3	yes	3	1
p-3x1	3 x 1	3	2	yes	3	1

The specific objectives of this study to be accomplished through centrifuge modeling, corresponding data interpretation and comparisons, and analytical analyses are:

1. Study the soil-pile interaction in a three-layer soil profile during liquefaction induced lateral spreading, for single pile and pile groups, in particular pile displacement and bending moments profiles.
2. Study the reinforcing effect that pile foundations have on liquefaction induced lateral spreading.
3. Help establish general guidelines of use of pile pinning as ground remediation technique.
4. Try to modify the current Newmark approach, by including pin pile shear forces at the location of the failure plane as equivalent shear strength; or develop a simple method to estimate the pinning effect on the reduction of lateral deformation.

1.6 Report Organization

This report contains 9 chapters plus a list of references. A review of relevant previous research and a brief overview of the research conducted in this study as well as the objectives have already been presented in this chapter.

Chapter 2 describes the geotechnical centrifuge facility at RPI, with emphasis on the equipment used in this research, like the in-flight 1-D large shaker and the 1-D large laminar box. Descriptions of the upgraded data acquisition system and sensors, as well as the construction process and calibration of the instrumented piles used in the centrifuge tests are also presented. This chapter also presents properties of the sand (Nevada sand) and slightly cemented sand used in the centrifuge experiments.

Chapters 3, 4 and 5 present experimental results and data interpretation of the six centrifuge tests of Table 1.2, conducted to investigate the effect of soil permeability in the response of single piles and pile groups subjected to liquefaction induced lateral spreading. Three models consisting of different pile configurations were tested using water as the pore fluid, simulating a loose layer of coarse sand. These models were then repeated, using the same fine sand, but saturated with a viscous fluid (metulose), hence simulating a loose layer of fine sand. Consequently, these centrifuge tests simulated deposits of wide different permeability in the field.

Chapter 3 presents the results of Models 1x1-w and 1x1-v, corresponding to a single pile, saturated with water and viscous fluid respectively. This chapter also describes in detail the preparation steps to build these and the rest of the centrifuge models. A p-y curve and limit equilibrium analysis, as well as comparison of results obtained in both tests are presented as well in this chapter. Chapter 4 presents the results of Models 3x1-w and 3x1-v, corresponding to a 3x1 pile group plus a single pile, saturated with water and viscous fluid respectively. A limit equilibrium analysis and comparison of results obtained in both tests are also included in this

chapter. Chapter 5 presents the results of Models 2x2-w and 2x2-v, corresponding to a 2x2 pile group, saturated with water and viscous fluid respectively. A limit equilibrium analyses and comparison of results obtained in both tests are also included in this chapter.

Chapter 6 summarizes and compares the results of all six centrifuge tests of Table 1.2, discussing the trends and highlighting the huge effect of soil permeability in pile foundation response to lateral spreading.

Chapter 7 presents experimental results and data interpretation of the four centrifuge tests listed in Table 1.3, conducted to study the reinforcing or pinning effect the pile groups have on the lateral spreading, analyzing the case when a nonliquefied crust rides on top of a liquefied sand layer. The first centrifuge test (Model p-0) did not include piles and was the benchmark experiment to simulate lateral spreading in the free field. Using a similar setup, Models p-3x2, p-6x2, and p-3x1 simulated the response of a 3x2, 6x2, and 3x1 pile group respectively.

Chapter 8 summarizes and compares the results of all four centrifuge tests of Table 1.3, including a practical analysis approach to estimate the pinning effect on the amount of lateral deformation.

Chapter 9 presents conclusions obtained in this study, engineering recommendations and suggestions for future research.

CHAPTER 2 RPI CENTRIFUGE FACILITY

2.1 Concept of Centrifuge Modeling

Geotechnical centrifuge modeling of earthquake problems was introduced in the U.S. in the early 1970s. Since about 1980 there has been a rapid development of interest worldwide in centrifuge modeling of earthquake problems. A number of centrifuge centers in different countries around the world have acquired the capability of earthquake centrifuge modeling, as the geotechnical centrifuge offers the ability to create fairly realistic full-scale stress states with uniform and measurable soil properties. Centrifuge modeling is considered a cost-effective method for modeling and predicting the properties and behavior of soil deposits.

Centrifuge modeling is useful for studying phenomena in which the earth's gravity has a dominant influence in the material properties. In general the properties of earth materials are dependent on the gravitational stresses, and hence centrifuge modeling is especially useful for systems including soils.

The main principle in centrifuge modeling is that a $1/N$ model subjected to a centrifugal acceleration of Ng will be subjected to the same stresses at comparable points in the model and in the prototype, where N is the scaling factor and g is the acceleration of gravity (Fig. 2.1). Arulandan et al. (1988) stated that using the same soil in the prototype and in the model will preserve the stress-strain relation at equivalent points. A list of centrifuge scaling relations is given in Table 2.1 (Taylor, 1995). More scaling relationships governing different geotechnical problems can be developed by dimensional analysis.

In centrifuge modeling of liquefaction, which involves relative particle-fluid motion, the time scaling relations present a problem. The dynamic time to generate liquefaction is scaled by $1/N$, while the diffusion time of pore pressure dissipation is scaled by $1/N^2$. A unique time scale for dynamic shaking and pore pressure dissipation can be achieved either by increasing the viscosity of the pore fluid, or by reducing the soil particle size (Steedman and Ledbetter, 1994). Increasing the viscosity of the pore fluid is typically achieved by using silicon oil, a glycerin/water mix, metulose, or another viscous fluid.

It is always desirable to verify the centrifuge scaling laws by comparison with full scale systems. Since monitoring full scale structures is difficult and/or expensive, the “modeling-of-models” concept has evolved as an alternative to verify centrifuge modeling procedures. A series of models of the same prototype can be tested at different centrifuge accelerations and compare directly the results at the same prototype units.

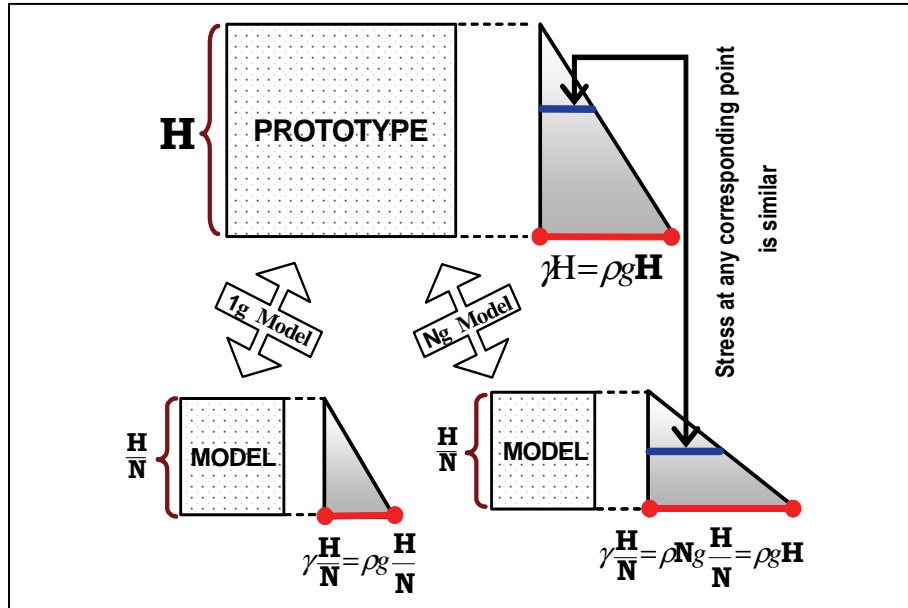


Figure 2.1: Centrifuge physical modeling concept (after Pamuk, 2004)

2.2 RPI Geotechnical Centrifuge

The RPI centrifuge was manufactured in 1989 by Acutronic, in France, and was the first of its type (Model 665-1). It belongs to a line of Acutronic Machines (about a dozen exist) all of which have the same basic mechanical structure. The extremely simplified structure of these machines was a noteworthy safety feature.

In year 2000 the centrifuge at RPI was selected as one of the experimental sites of the Network for Earthquake Engineering Simulation (NEES). In the first phase, which ended in September 2004, the RPI centrifuge was upgraded and networked to the rest of the NEES network. After the upgrade, the geotechnical facility consists of: a) centrifuge room, b) two model preparation rooms, c) storage area, d) computer servers area, e) control & teleparticipation room, f) robot area, g) electronics development area, h) computer laboratory, and i) teleconference room. Figure 2.2 shows the geotechnical facility's layout.

Table 2.1: Scaling relations for centrifuge modeling (Taylor, 1995)

Parameter	Centrifuge (model units)	Full scale (prototype units)
Length	$1/N$	1
Area	$1/N^2$	1
Moment of inertia	$1/N^4$	1
Stress	1	1
Strain	1	1
Displacement	$1/N$	1
Area	$1/N^2$	1
Volume	$1/N^3$	1
Density	1	1
Mass	$1/N^3$	1
Force	$1/N^2$	1
Time (dynamic event)	$1/N$	1
Time (diffusion event)	$1/N^2$	1
Acceleration	N	1
Frequency	N	1
Energy	$1/N^3$	1
Velocity	N	1
Elastic modulus, E	1	1
Flexural rigidity, EI	$1/N^4$	1

The upgraded 150 g-ton centrifuge consist of: a) swinging basket, b) centrifuge boom, c) balancing counter weight, d) hydraulic rotary joint and electronic slip-ring assembly, e) drive system, f) aerodynamic enclosure, and g) in-flight balancing system. Figure 2.3 shows a picture and schematic of RPI geotechnical centrifuge. The performance envelope of a centrifuge indicates the allowable levels of acceleration as a function of payload mass. For the RPI centrifuge, the limits are 160 g, 1.5 Ton, and 150 g-ton. Table 2.2 summarizes some of the characteristics, like in-flight radius of 3.0 m and usable payload dimensions of 100 cm in depth, length and width. The centrifuge is equipped with a fiber optic rotary joint, 28 slip rings and wireless network, which are available to the user for data transmission. A hydraulic rotary joint is also installed with a total of 6 joint passages, two of which can hold 3,000 psi hydraulic oil.

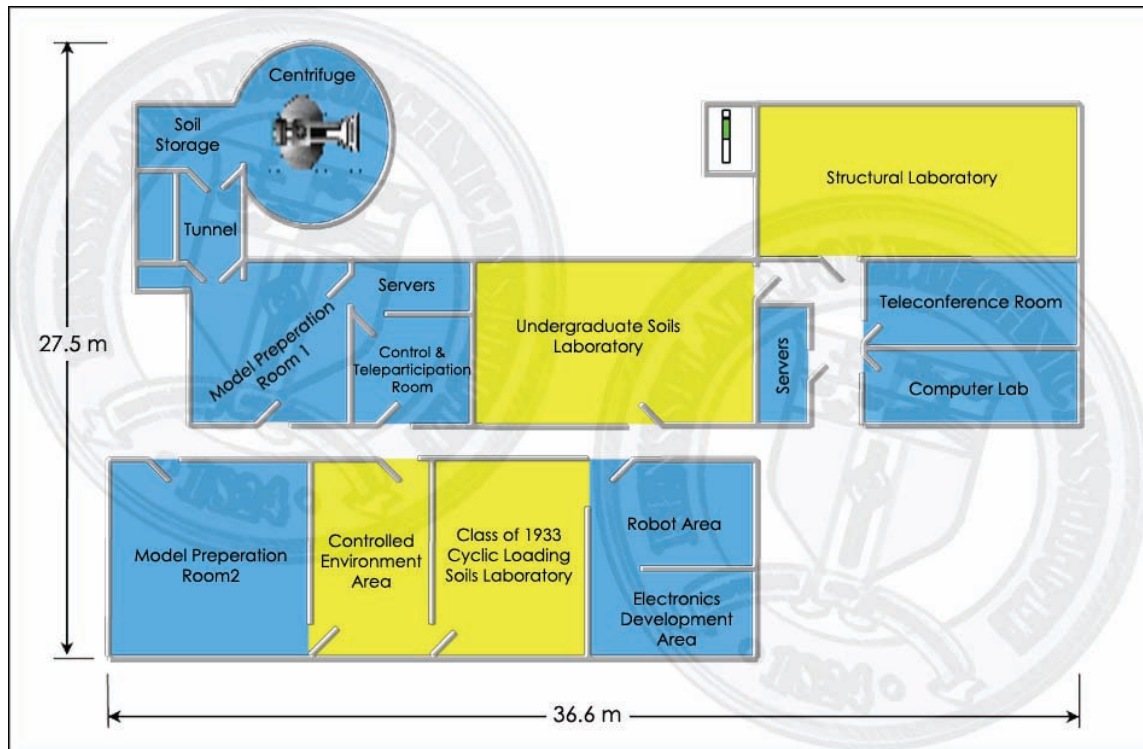
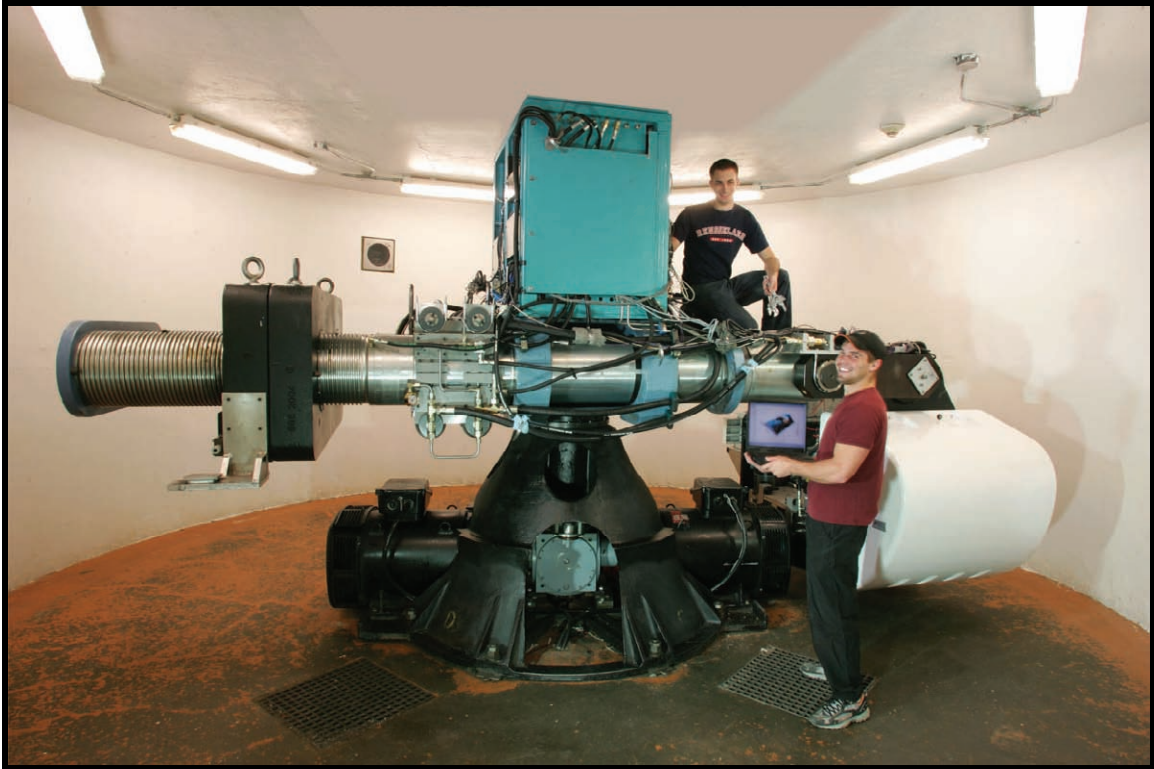


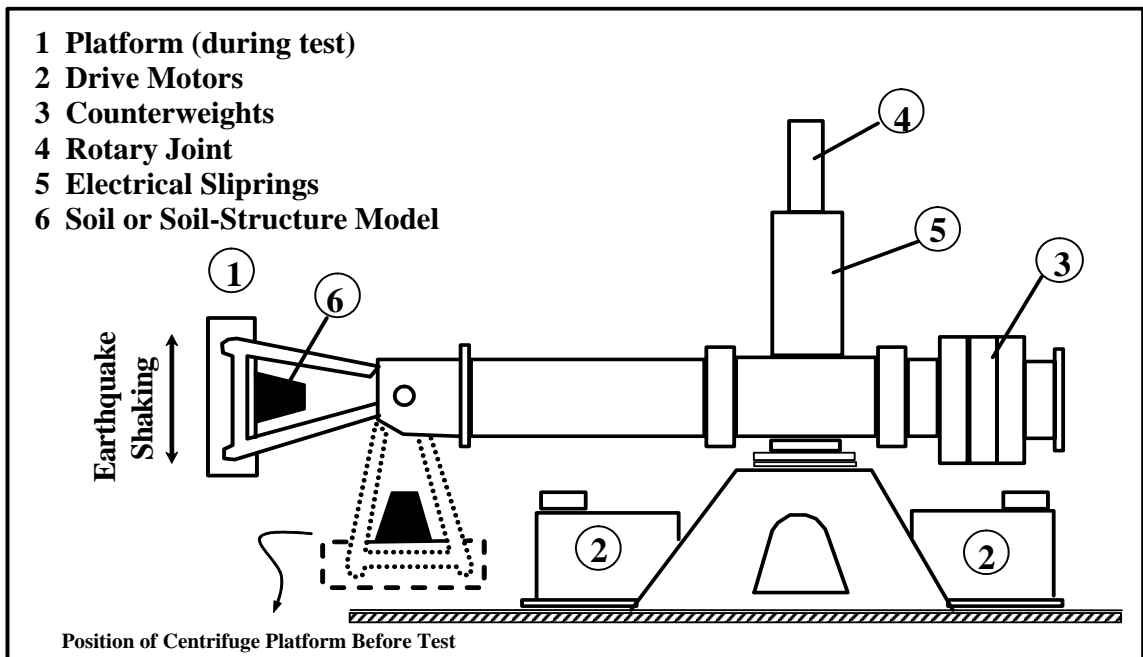
Figure 2.2: RPI geotechnical facility’s layout

The upgraded earthquake engineering centrifuge capability also included: a) 2-D in-flight shaker with two horizontal components, b) 2-D laminar box container, c) centrifuge in-flight robot and associated software, d) 128-channel data acquisition system with Internet capability, e) client-server data acquisition/control software, including server software for web-based teleobservation and teleoperation of centrifuge experiments from locations outside RPI, f) advanced and improved sensors, g) high-speed cameras and image processing software, and h) additional box containers, sensors, etc., to increase the number of centrifuge models that can be constructed simultaneously. The four degrees of freedom robot is capable of performing in flight operations such as construction and excavation, pile driving, ground remediation, cone penetration, and static and cyclic loading test without stopping the centrifuge.

This new equipment allows the users to: a) perform more realistic in flight earthquake simulations, b) conduct a number of operations in flight in a more realistic manner without having to stop the centrifuge, and c) monitor tests more closely and produce more and better data sets, providing a higher resolution picture of model response. The use of advanced sensors and high-speed cameras will provide high resolution of model response and will be especially useful for test visualization, system identification and numerical simulations.



(a)



(b)

Figure 2.3: RPI geotechnical centrifuge, (a) picture, (b) schematic

Table 2.2: RPI centrifuge specifications

Centrifuge platform	
Length	100 cm
Width	100 cm
Radius from centrifuge axis to platform	300 cm
Radius from centrifuge axis to pivot point	200 cm
Load	
Nominal maximum platform payload mass	1500 kg
Nominal maximum mass of soil in a model	800 kg
Speed	
Maximum speed for nominal maximum payload mass	265 rpm
Time required to slow from maximum to zero speed	10 min
Time required to increase from zero to maximum speed	10 min

More information on the NEES earthquake simulation and networking capabilities at RPI centrifuge can be found at Zeghal et al., 2000. The following sections present detailed information on the equipments, data acquisition system, sensors, instruments, and soil material used in this research.

2.3 In-Flight 1-D Large Shaker

Generating earthquake-like shaking on a model in flight on a centrifuge requires a power source or actuator. This equipment has to be able to operate under high centrifugal forces and provide high peak power at high frequencies. This requirement for high frequency excitation arises from the scaling of time for dynamic events. Dominant frequencies of typical earthquakes may range between 0.2 Hz and 5 Hz. At a centrifugal acceleration of 100 g the actuator has to be able to generate controllable motion at frequencies as high as 500 Hz.

The RPI large shaker used in this study is the ES-18 shaker, designed to provide one-dimensional base input motion for centrifuge models of up to 400 kg (Van Laak, 1996). This centrifuge shaker is an electro-hydraulic servo-controlled device, which is the second simulator built for the RPI centrifuge. Figure 2.4a shows the basic layout of this shaker. The overall width of the ES-18 is 0.9 m, able to accommodate a model container width of 0.45 m. This shaker can be

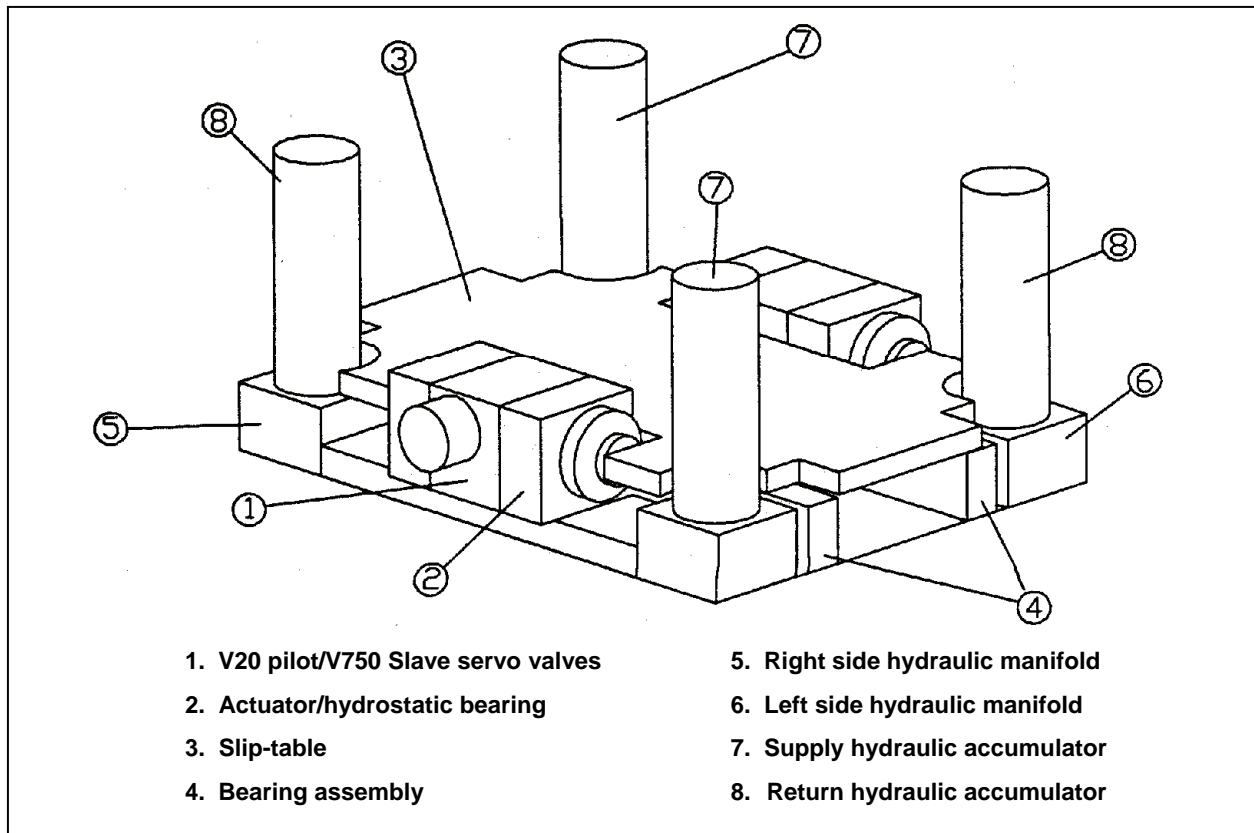
disassembled into 4 main parts: a) the slip table, b) the left and right hydraulic manifolds with attached actuators, and c) the central bearings support assembly.

Shaking force is produced by two TEAM Integrated Hydroshakers, which are double acting high performance servo-hydraulic actuators. They are configured to act in parallel, with each actuator producing a maximum force of 40 kN when supplied with 3000-psi hydraulic oil. Electronic control of the shaker is accomplished by a displacement closed loop feedback system. An LVDT displacement transducer is mounted internally for measuring the relative displacement between the actuator piston and housing, providing accurate measurements over the frequency range 0-1000 Hz. This shaker accepts either standard input signals from a function generator or arbitrary input signals generated by a computer. The technical specifications of the ES-18 shaker are outlined in Table 2.3. Figure 2.4b presents the frequency response magnitude of the in-flight shaker without payload. This frequency response characteristic must be taken into account when preparing an excitation signal. More detailed information about this shaker is presented by Van Laak (1996).

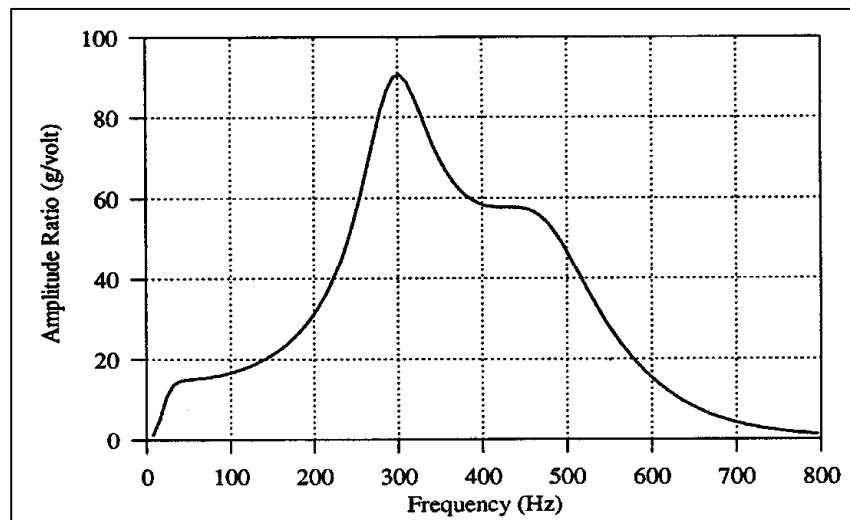
2.4 1-D Large Laminar Box

2.4.1 Design Philosophy

A state-of-the-art rectangular laminar container was built at RPI in 2002 for improved modeling of earthquake phenomena in soil. This box was design to accommodate a wide range of cyclic and permanent lateral deformations occurring in the soil model. Whitman and Lambe (1986) stated that a laminar container can simulate the shear beam conditions in the soil during vertical shear wave propagation. Such a container must be relatively weightless, perfectly flexible in the longitudinal direction, rigid in the transversal direction, dissipates no energy, and has enough friction with the soil and enough vertical strength in the confining walls to provide the necessary complementary shear stresses. If the mass of the laminar box is similar to the contained soil mass, the inertia forces of the box will influence the model deformation. The container should also maintain a constant horizontal cross section during the test to prevent undesirable horizontal normal straining of the soil. Thin rings are used in order to increase flexibility and accommodate possible shear strain concentrations. As the main use of the laminar box at RPI is modeling liquefaction and lateral spreading, it was design to allow large lateral displacements.



(a)



(b)

Figure 2.4: RPI 1-D large shaker, (a) schematic, (b) frequency response (Van Laak, 1996)

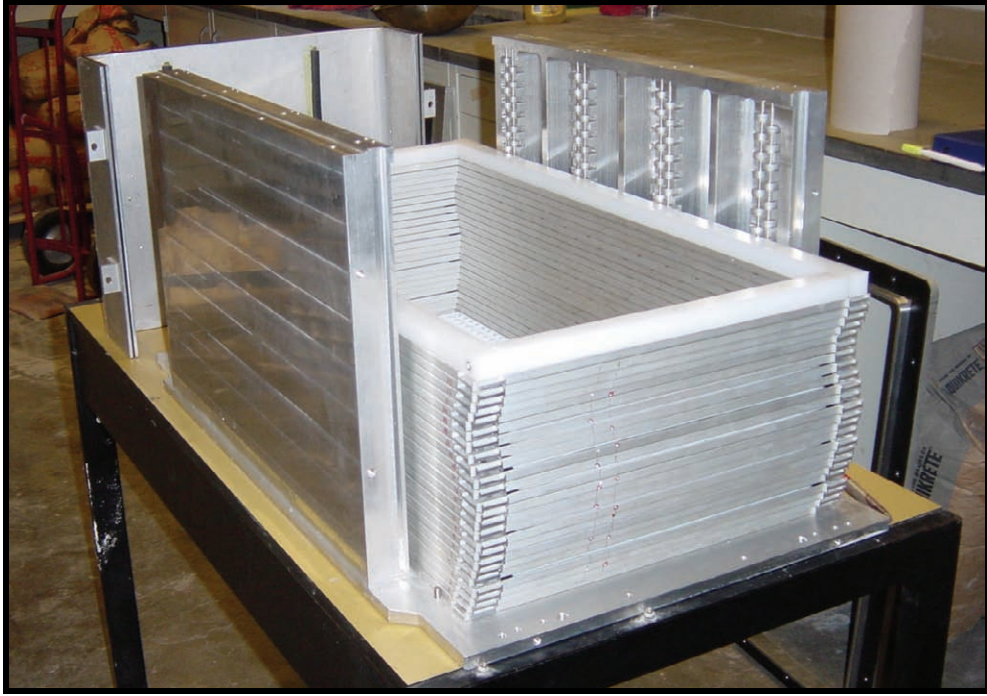
Table 2.3: RPI 1-D large shaker technical specifications (Van Laak, 1996)

Max. payload	400 kg
Available length	90 cm
Available width	45 cm
Available height	50 cm
Peak slip table displacement	± 12 mm
Peak slip table velocity	± 750 mm/sec
Peak slip table acceleration	± 22 g
Max. actuation force	10 ton
Frequency bandwidth	0-600 Hz
Operating range	Up to 120 g centrifuge acceleration

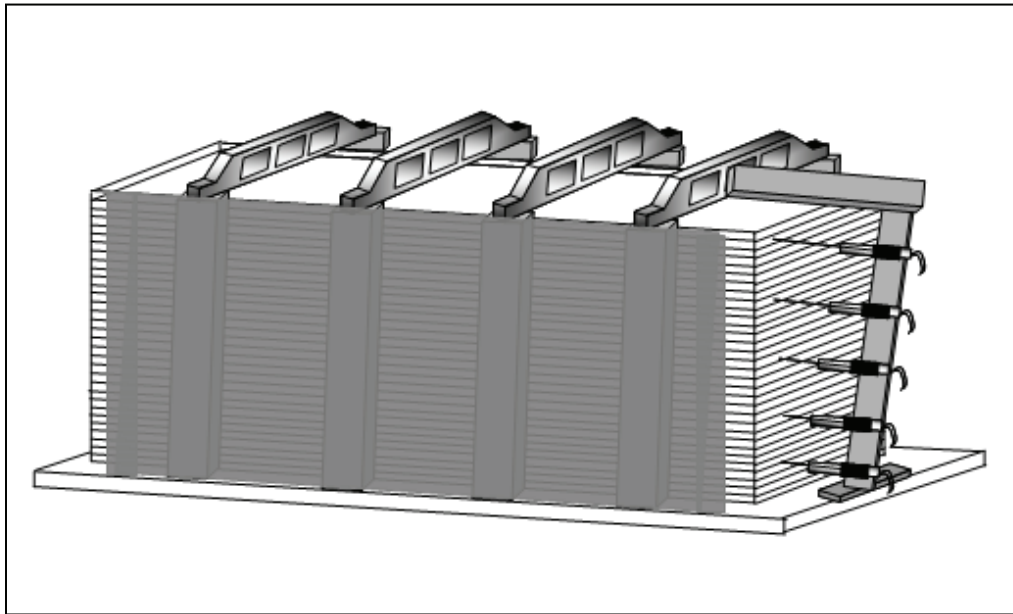
2.4.2 1-D Large Laminar Box Description

The 1-D large laminar box used in this research (Fig. 2.5) consists of a stack of up to 38 rectangular rings separated by linear roller bearings, arranged to permit relative movement between rings in the longitudinal direction with minimal friction. The 86 rollers that separate two adjacent rings are properly aligned and spaced by bearing cages. A plan view of an individual ring showing the dimensions and arrangement of the roller bearings is presented in Fig. 2.6a. A cross-section of the laminar box is shown in Fig. 2.6b. A clamp fitted is placed on top of the stack to prevent uplifting of the rings during shaking. The box, made of high strength aluminum alloy, weight about 80 kg and has internal dimensions of 35.5 cm in width, 71 cm in length, and 35.5 cm in height.

The friction coefficient between rings was measured by Taboada (1995) as 0.006 under 8kN vertical load. The lateral support bars and side rollers (Fig. 2.6b) were design to limit the horizontal strain in the box to 0.02% for a soil with a lateral stress coefficient $K_0 = 0.3$.

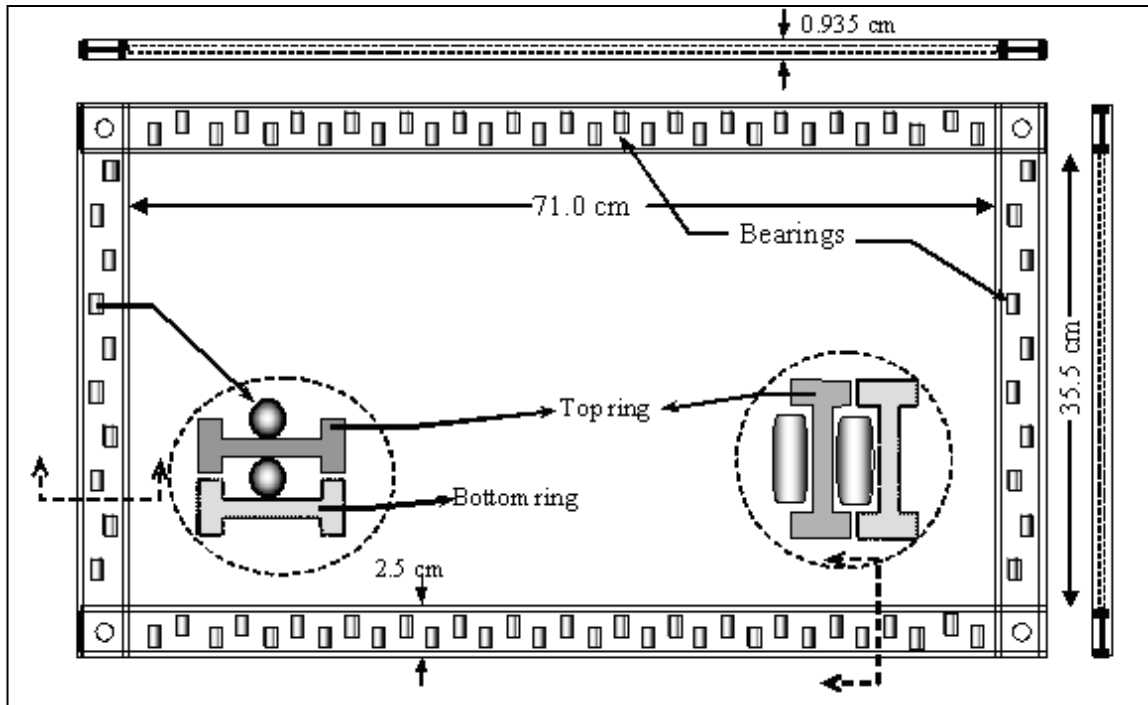


(a)

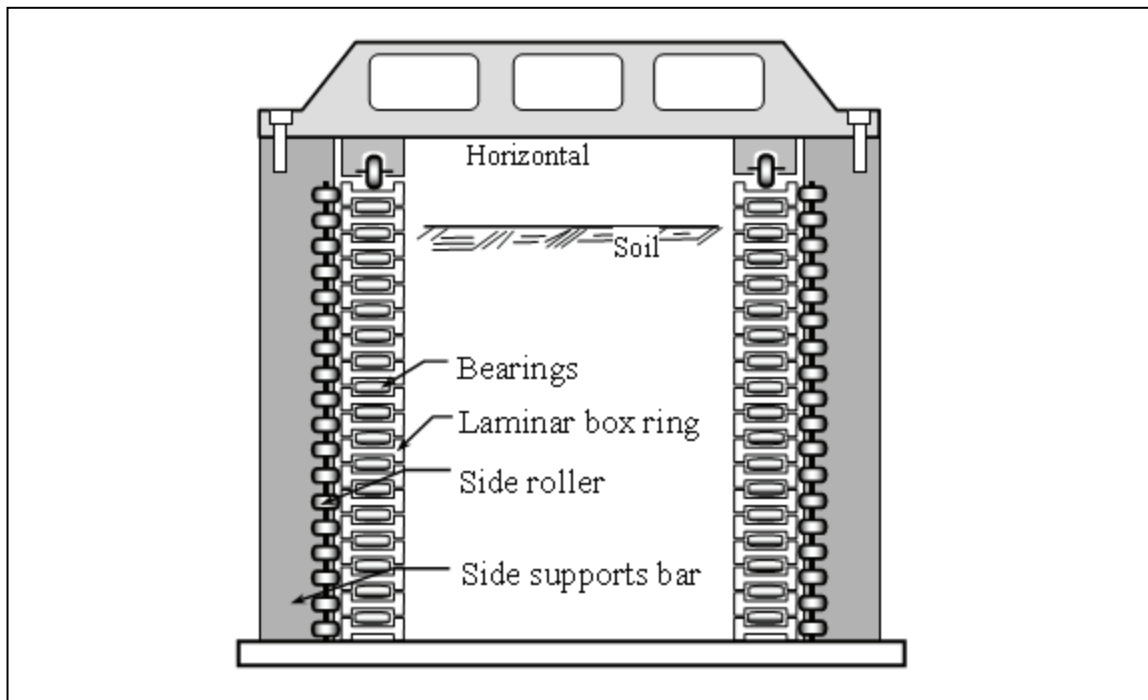


(b)

Figure 2.5: RPI 1-D large laminar box, (a) picture, (b) schematic



(a)



(b)

Figure 2.6: RPI 1-D large laminar box, (a) plan view, (b) cross section (after Pamuk, 2004)

2.5 Data Acquisition System

Data acquisition requires signal conditioning before a computer-based measurement system can effectively and accurately acquire the signal. The signal conditioning system used in the centrifuge includes functions such as signal amplification, attenuation, filtering, electrical isolation, simultaneous sampling, and multiplexing. In addition, many transducers require excitation currents or voltages, bridge completion, linearization, or high amplification for proper and accurate operation. This process is done by a SCXI (Signal Conditioning eXtensions for Instrumentation) system, which consists in a rugged chassis that houses shielded signal conditioning modules. Three SCXI chassis were used for this study, units that were located in a platform next to the basket, as close as possible to the sensors (Fig. 2.7). Each SCXI chassis has space for four signal-conditioning modules, which were selected depending on the combination of sensors that were used in each test. Since each module has 8 analog input channels, the capability of the system in this case was 96 channels.

Once the analog signal is filtered and amplified, it is converted into digital signal in the Data Acquisition device (DAQ) board, which is located in the PXI (PCI eXtensions for Instrumentation) unit. The PXI unit, located in the center of the centrifuge, consists in a Pentium III PC, four 6052E DAQ boards, one 6711 analog output board, and one 2562 general purpose relay switch board. Once the acquisition is triggered, the data is stored in the PC located in the PXI. Both SCXI and PXI units are manufactured by National Instruments Corporation.

A voltage time history representing the earthquake motion is sent to the shaker through the 6711 analog output board 1 second after the acquisition is triggered. The signal generation and data acquisition processes are controlled from the control room using a wireless connection. Figure 2.8 shows the state-of-the-art control and teleparticipation room, which comprises four plasma screen that allow to control and monitor the centrifuge operations and data acquisition process. A custom made software developed by Bloomy Controls Inc., using LabView (a graphic-based programming language) was used to control the data acquisition process.

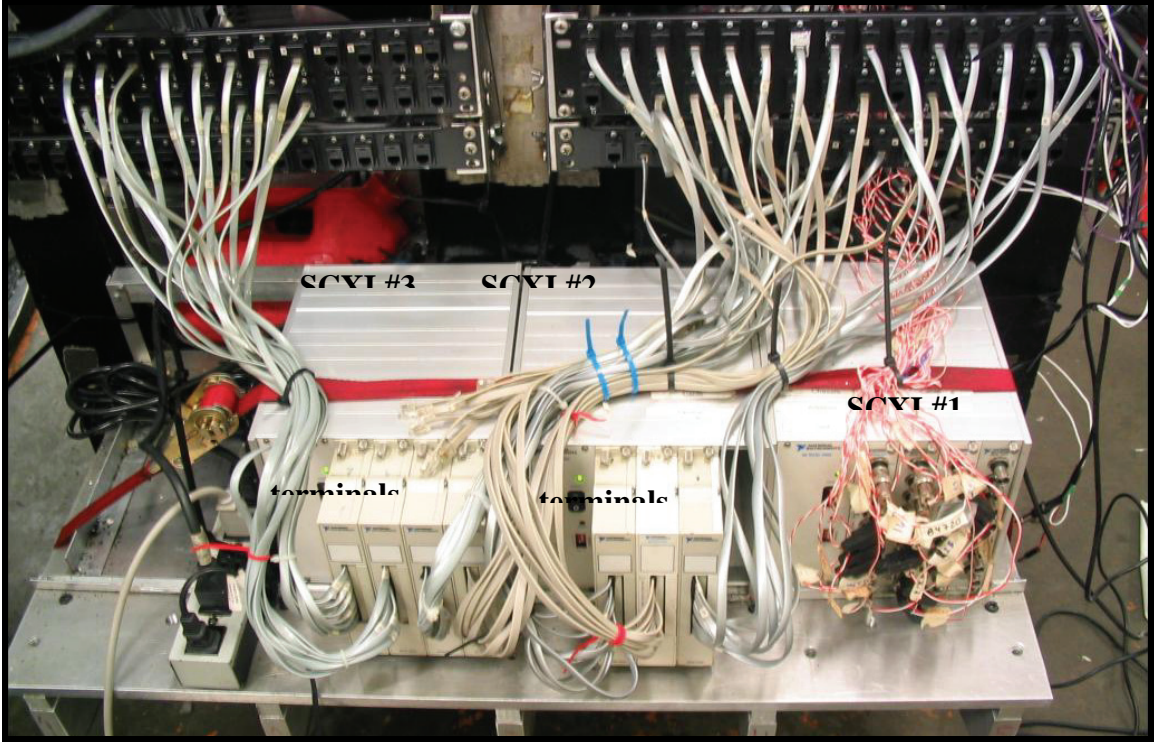


Figure 2.7: Signal conditioning system



Figure 2.8: Control and teleparticipation room

2.6 Sensors used in Centrifuge Models

Transducers and sensors are devices that convert one type of physical phenomenon, such as temperature, strain, pressure, or light into a measurable unit. The most common transducers convert physical quantities to electrical quantities, such as voltage or resistance. Figure 2.9 shows a picture of the type of accelerometer, LVDT, and pore pressure transducer used in the RPI centrifuge.

2.6.1 Accelerometers

Accelerometers Model A353B17/AC from PCB Piezotronics were used for acceleration measurements. These accelerometers, 8 mm in diameter and 12 mm in length, consist of a known mass attached to a piezoelectric element. As the accelerometer moves, the mass applies force to the element and generates a charge. Piezoelectric accelerometers measure the acceleration along one axis, so proper alignment was needed. Accelerometers are available in two types, passive and active. Passive accelerometers, similar to the ones currently used in the RPI centrifuge, send out the charge generated by the piezoelectric element. Since the signal is very small, passive accelerometers require a charge amplifier to boost the signal and serve as a very high impedance buffer for the measurement device. Active accelerometers include internal circuitry to convert the accelerometer charge into a voltage signal, but require a constant current source to drive the circuitry (National Instruments, 2001a). The specifications of the accelerometer Model A353B17/AC are shown in Table 2.4.




	<p><u>Accelerometer</u> Model A353B17/AC (PCB Piezotronics)</p>
	<p><u>LVDT</u> Model MHR-500 & Model MHR-1000 (Lucas Systems)</p>
	<p><u>Pore pressure transducer</u> Model PDCR 81 (Druck)</p>

Figure 2.9: Sensors used in centrifuge models

Table 2.4: Accelerometer specifications (after Pamuk, 2004)

Range (for ± 5 V)	50 g
Resolution	0.01 g
Sensitivity (nominal)	10 mV/g
Resonant frequency	70 kHz
Frequency range ($\pm 5\%$)	1~10000
Linearity	1%
Weight	2 grams
Model	PCB A353B17/AC
Manufacturer	PCB Piezotronics, Inc

2.6.2 LVDTs

The lateral displacements and the vertical settlements were measured by LVDTs (Linear Variable Differential Transducer) Model MHR-500 and MHR-1000, manufactured by Schaevitz Engineering. These types of LVDTs consist of a stationary coil assembly and a movable core. The coil assembly houses a primary and two secondary windings. The core is a steel rod of high magnetic permeability, smaller in diameter than the internal bore of the coil assembly; this contact free configuration eliminates measurement errors due to friction. When an AC excitation voltage is applied to the primary winding, a voltage is induced in each secondary winding through the magnetic core. The position of the core determines how strongly the excitation signal couples to each secondary winding. When the core is in the center, no signal is created. As the core travels to the left or to the right of center, an output voltage proportional to the displacement is created (National Instruments, 2001a). The nominal linear ranges of the LVDTs used in this study were ± 12.7 mm and ± 25.4 mm.

2.6.3 Pore Pressure Transducers

The pore fluid pressure was measured by pore pressure transducers (PPT) Model PDCR-81, manufactured by Druck Inc. These sensors are strain gauge type transducers with a full bridge configuration and a fundamental frequency of 56 kHz. The ceramic porous stone located at the tip was removed and replaced by a thin and permeable membrane, to ensure fully saturation of the PPT, particularly in the models saturated with viscous fluid. The transducers used in the centrifuge models, 6 mm in diameter and 10 mm in length, had ranges of 50 and 100 psi.

2.6.4 Strain Gages

Strain gages were installed along the surface of some of the model piles to measure the bending moments and axial forces. These strain gages, type CEA-13-032UW-120 and purchased from Measurements Group Inc., consist of a very fine foil grid or wire. The electrical resistance of the grid varies linearly with the strain applied to the device. Since strain measurement requires detecting relatively small changes in resistance, the Wheatstone bridge circuit is almost always used. The Wheatstone bridge circuit consists of four resistive elements with a voltage excitation supply applied to the ends of the bridge. Strain gauges can occupy one (quarter bridge configuration), two (half bridge configuration), or four arms of the bridge (full bridge configuration), with any remaining positions filled with fixed resistors. A quarter bridge configuration can measure both axial and bending strains, while a half bridge configuration can measure just bending strains. The specifications for this type of strain gages are summarized in Table 2.5. The next section describes the construction process and calibration of the instrumented model piles.

2.7 Construction Process and Calibration of Model Piles

In the first series of centrifuge tests, conducted to study the effect of soil permeability on pile response to lateral spreading, the model piles had to simulate prototype piles with an EI of the order of 10,000 kN-m². The material used to build these model piles was Ultem 1000, a polymer purchased from Quadrant Engineering Plastic Products. This material has been used successfully in the past at RPI in several centrifuge tests (Abdoun 1997; Wang, 2001; Pamuk, 2004). In the second series of centrifuge tests, conducted to study the effect of pile pinning on lateral spreading, the model piles had to simulate very stiff prototype piles with an EI of the order of 90,000 kN-m². The material used to build these model piles was aluminum.

2.7.1 Construction Process of Model Piles

The construction process for all eight model piles made is illustrated in Fig. 2.10. After each rod was cut and clean, strain gages were attached along two sides, called sides a and b. Thin wires were used to connect the strain gages, either in quarter bridge or half bridge configurations (Fig. 2.10a). Afterwards, the thin wires were protected by a shrink tube and connected to telephone cables (Fig. 2.10b). At this stage the model piles were calibrated to: a) determine the material stiffness, b) evaluate the linear-elastic behavior of the material, and c) verify the strain gages were properly installed. Once the calibration process was done, the piles were covered with a thin layer of wax for protection (Fig. 2.10c). Finally, the piles were covered with a soft shrink tube and sand grains were glued to the sides to develop an adequate pile-soil roughness (Fig. 2.10d).

Table 2.5: Strain gage specifications (after Pamuk, 2004)

Type	Uniaxial
Grid width	1.52 mm
Overall width	3.05 mm
Matrix width	4.8 mm
Gage length	4.57 mm
Overall length	4.57 mm
Gage resistance	120 ± 0.3 Ohm
Gage factor	2.1 ± 1.0%
Strain range	Max ± 5%
Model No.	CAE-13-032UW-120
Manufacturer	Micro-Measurements, Inc

2.7.2 Calibration of Model Piles Type U1

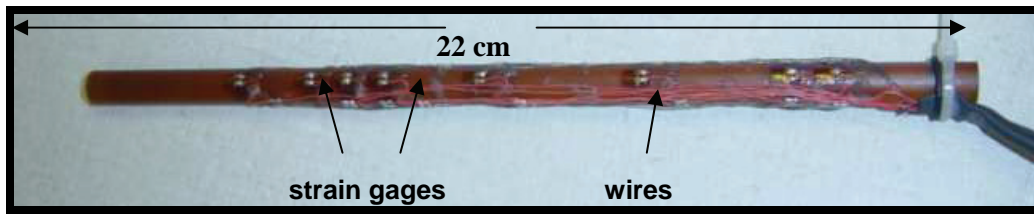
The first series of two piles build, called type U1, were made of Ultem 1000. These piles, 0.95 cm in diameter, were instrumented with 5 pair of strain gages. Fig. 2.11 shows the strain gage locations and configurations of these two piles (piles #1 and #2), used in Model 2x2-w, 2x2-v, 3x1-w, and 3x1-v.

The piles were first calibrated in bending by applying a known load (weight) on one extreme of the pile, while the other was perfectly clamped (Fig. 2.12). The strains were measured at both sides and plotted for three different weights. Fig. 2.12 shows the measured strain versus distance for pile #2, demonstrating the linear behavior of the material and the good attachment of the strain gages.

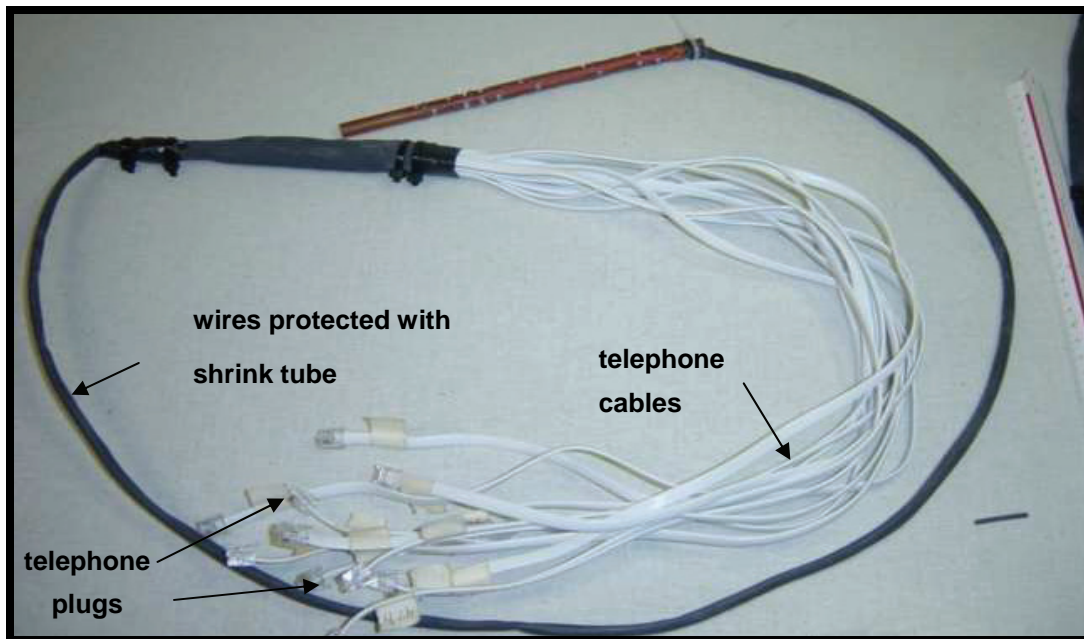
The estimated bending stresses at the location of each pair of strain gage were plotted versus the measured strain at those locations (Fig. 2.13). The slopes of the fitted lines represent the modulus of elasticity in bending of piles #1 and #2, with values of 3,958,000 kN/m² and 3,963,000 kN/m² respectively.

Table 2.6: Summary of model pile properties

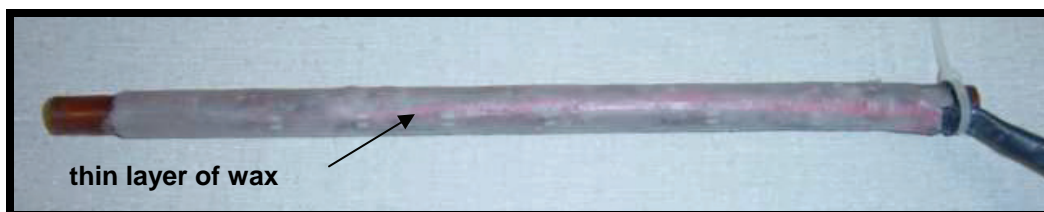
Pile type	U1		U2		A			
Material	Ultem 1000 (polyetherimide)		Ultem 1000 (polyetherimide)		Aluminum			
Diameter [cm]	0.95		0.95		0.79			
# of pairs of strain gages	4		6		9			
# of pile	# 1	# 2	# 1	# 2	# 1	# 2	# 3	# 4
Modulus of elasticity in bending [kN/m ²] x 10 ⁶	3,96	3,96	3,84	3,86	69,6	69,0	69,7	69,2
Modulus of elasticity in axial [kN/m ²] x 10 ⁶	3,91	3,98	3,72	3,88	/	/	/	/
Piles used in Models	2x2-w 2x2-v 3x1-w 3x1-v		1x1-w 1x1-v 3x1-w 3x1-v		p-0 p-3x2 p-6x2 p-3x1			



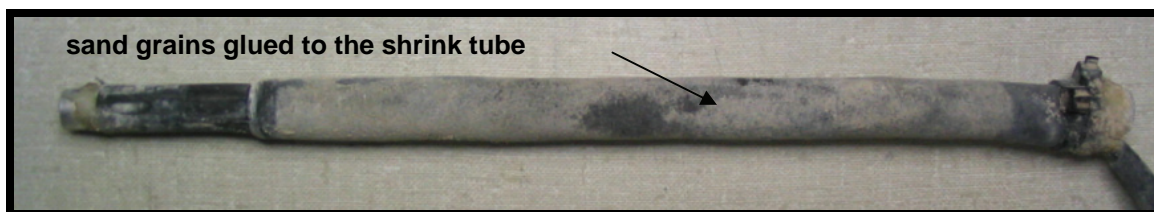
(a)



(b)



(c)



(d)

Figure 2.10: Construction process for model piles, (a) strain gages attachment and wiring, (b) phone cables connection, (c) wax application, (d) a shrink tube with glued sand covers the pile

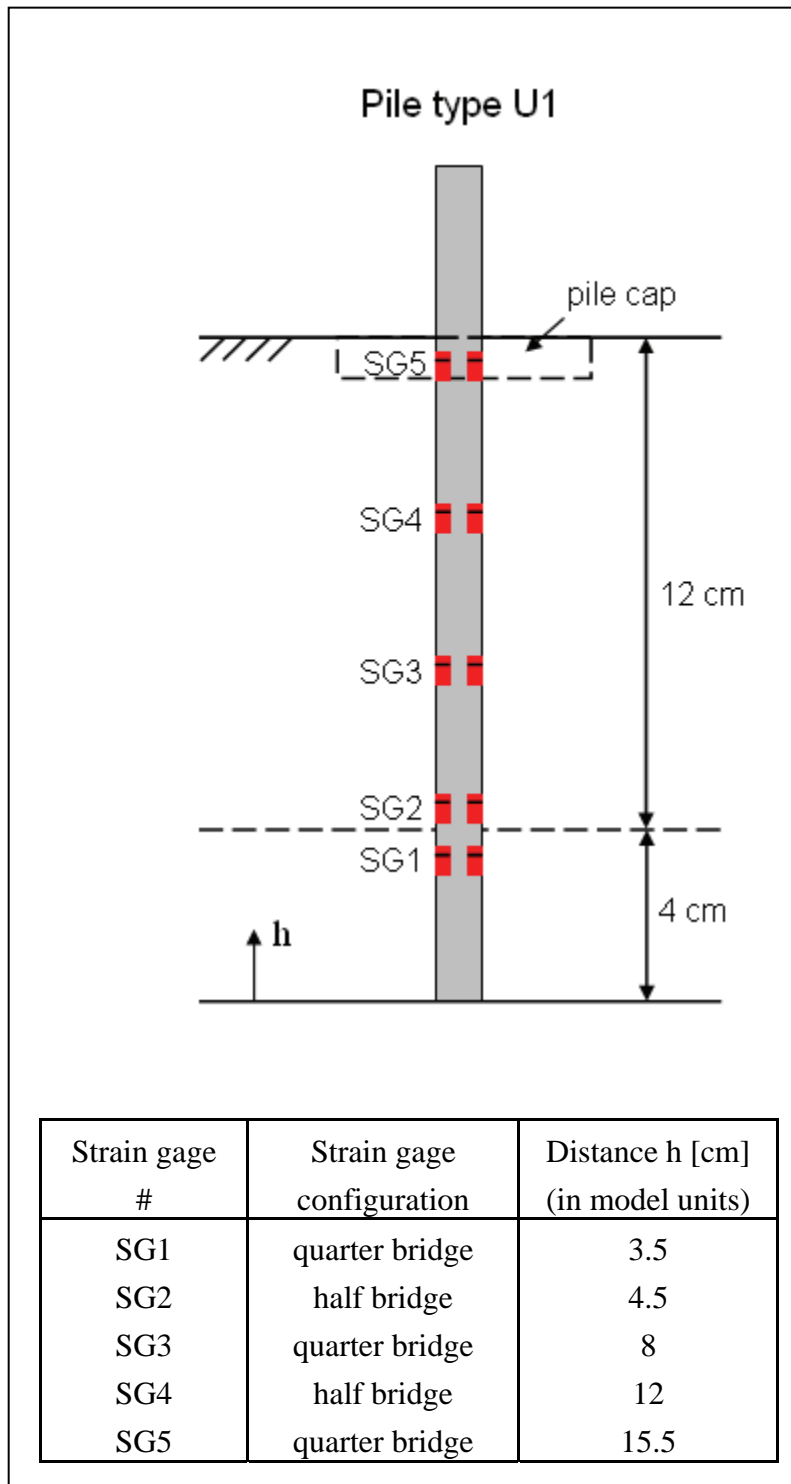


Figure 2.11: Diagram of model pile type U1 configuration, used in Model 2x2-w and 2x2-v, and in Model 3x1-w and 3x1-v (3x1 pile group)

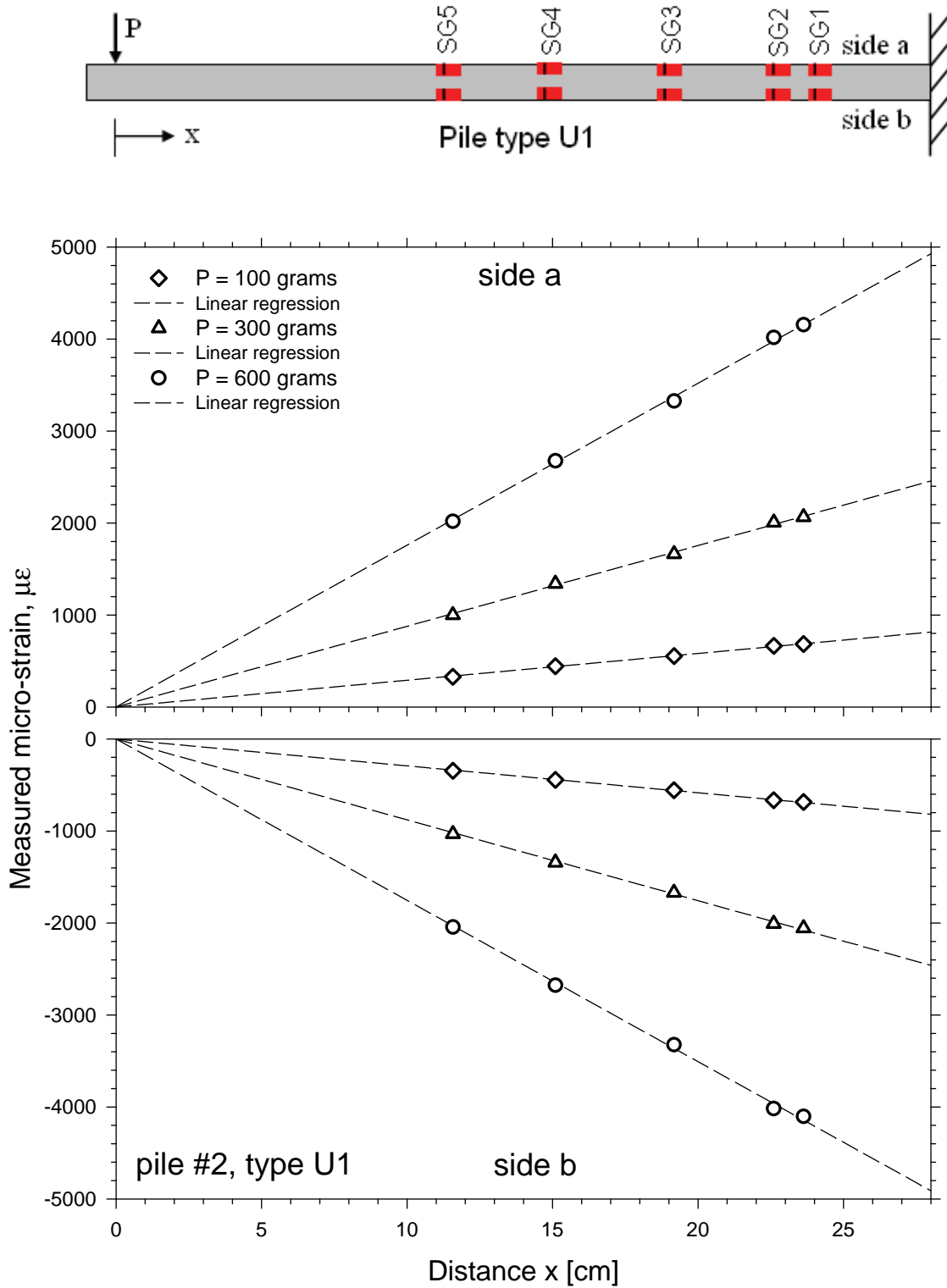


Figure 2.12: Model pile calibration under bending, pile #2 type U1 (in model units)

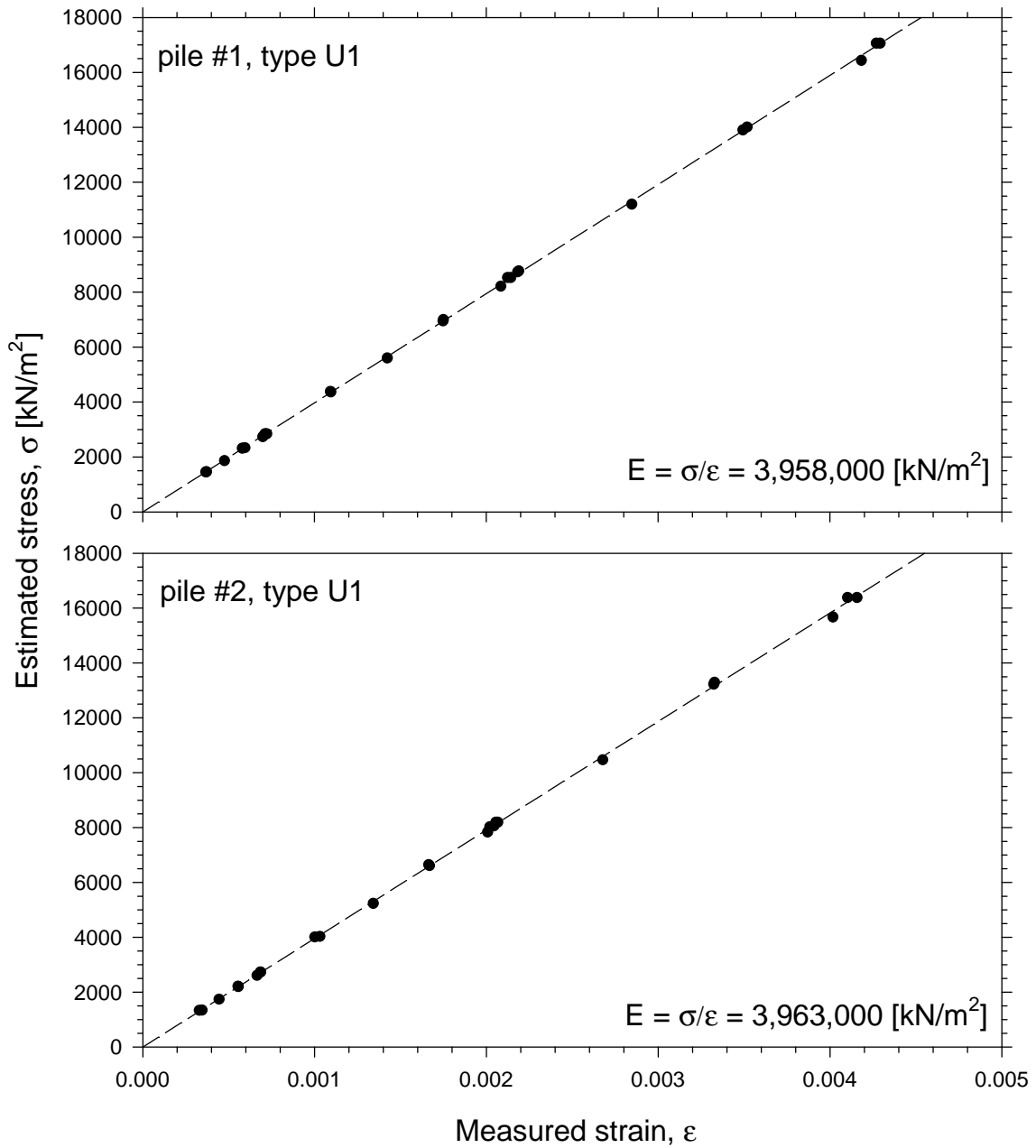


Figure 2.13: Modulus of elasticity (in bending) of model pile #1 and #2, type U1

The piles were also tested axially, with the setup shown in Fig. 2.14. The estimated bending stresses for the three different loads were plotted versus the measured axial strains (Fig. 2.14). The slopes of the fitted lines represent the modulus of elasticity under axial loading of piles #1 and #2, with values of 3,910,000 kN/m² and 3,980,000 kN/m² respectively. A small offset of the axial loads seems to have induced small bending strains, causing some scattering. However, by averaging the values, the modulus of elasticity are in very good agreement with the ones obtain from the bending test.

2.7.3 Calibration of Model Piles Type U2

The second series of two piles build, called type U2, were made of Ultem 1000. These piles, 0.95 cm in diameter, were instrumented in this case with 6 pair of strain gages. Fig. 2.15 shows the strain gage locations and configurations of these two piles (piles #1 and #2), used in Model 3x1-w, 3x1-v, 1x1-w, and 1x1-v.

The piles were first calibrated in bending following the same procedure used for model piles type U1 (Fig. 2.16). The strains were measured at both sides and plotted for three different weights. Fig. 2.16 shows the measured strain versus distance for pile #1, demonstrating once again the linear behavior of the material and the good attachment of the strain gages.

Figure 2.17 shows the estimated bending stresses at the location of each pair of strain gage versus the measured strain at those locations. The slopes of the fitted lines represent the modulus of elasticity in bending of piles #1 and #2, with values of 3,840,000 kN/m² and 3,860,000 kN/m² respectively.

The piles were also tested axially, with the setup shown in Fig. 2.18. The estimated bending stresses for the three different loads were plotted versus the measured axial strains (Fig. 2.18). The slopes of the fitted lines represent the modulus of elasticity under axial loading of piles #1 and #2, with values of 3,715,000 kN/m² and 3,880,000 kN/m² respectively. As previously explained, a small offset of the axial loads seems to have induced small bending strains, causing some scattering.

2.7.4 Calibration of Model Piles Type A

The last series of piles build, called type A, were made of solid aluminum. These piles, 0.79 cm in diameter, were instrumented with 9 pair of strain gages. Fig. 2.19 shows the strain gage locations and configurations of these four piles (piles #1, #2, #3, and #4), used in Model p-3x2, p-6x2, and p-3x1.

These piles were also calibrated in bending, following the same procedure already described (Fig. 2.20). The strains were measured at both sides and plotted for three different weights. Fig. 2.20 shows the measured strain versus distance for pile #3, demonstrating the linear behavior of this aluminum and the good attachment of the strain gages.

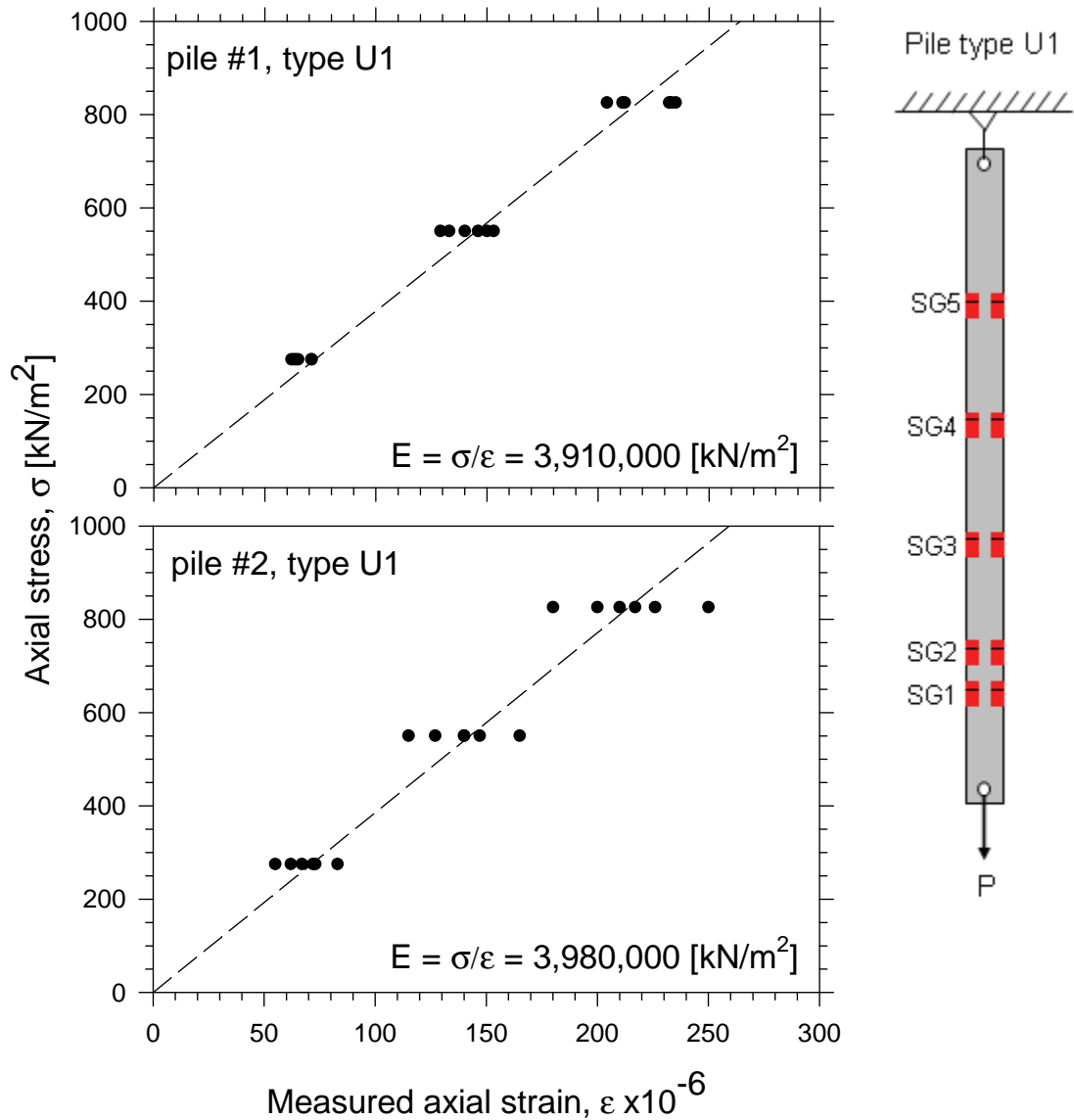


Figure 2.14: Modulus of elasticity (in axial) of model pile #1 and #2, type U1

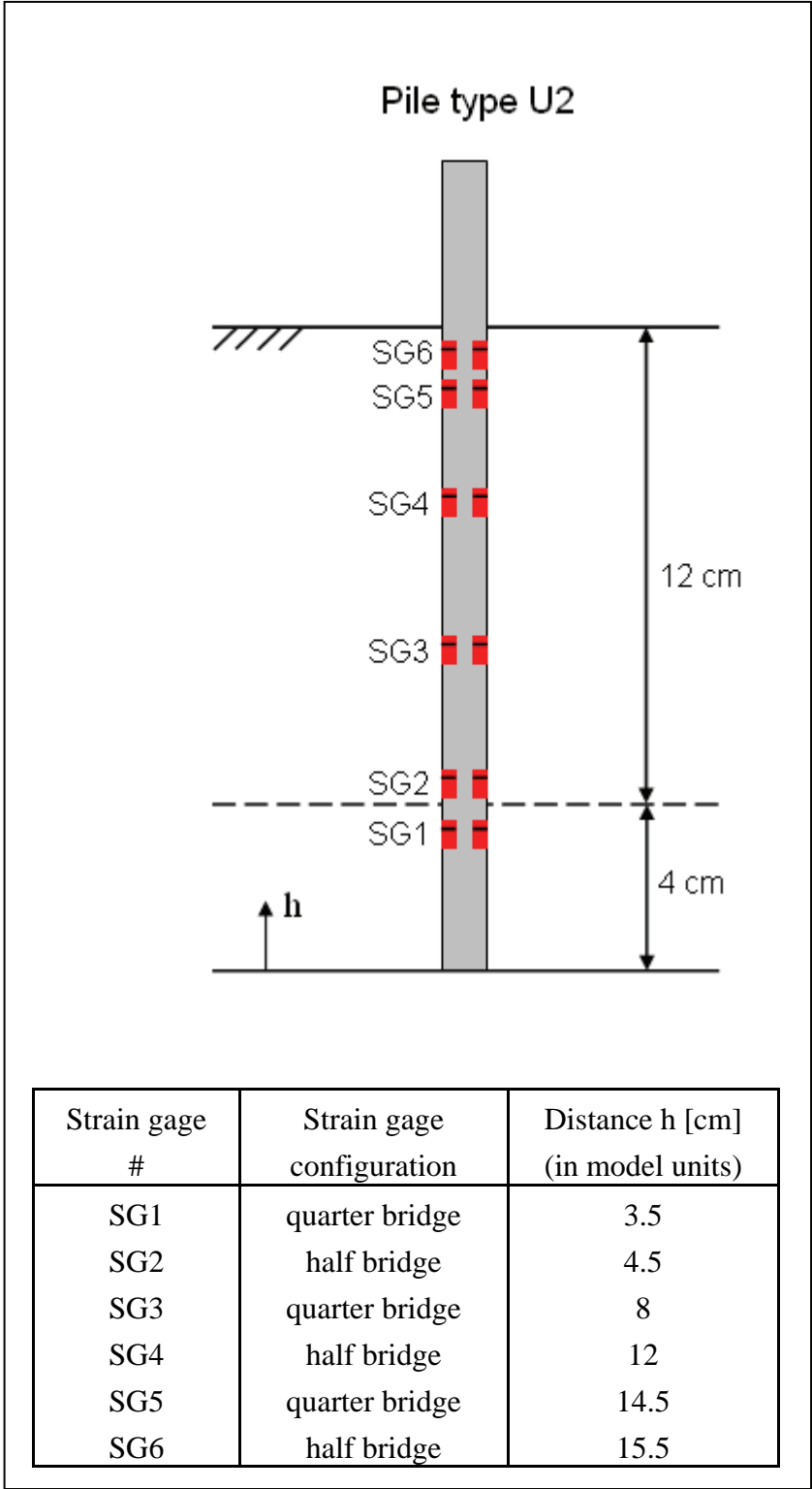


Figure 2.15: Diagram of model pile type U2 configuration, used in Model 1x1-w and 1x1-v, and in Model 3x1-w and 3x1-v (single pile)

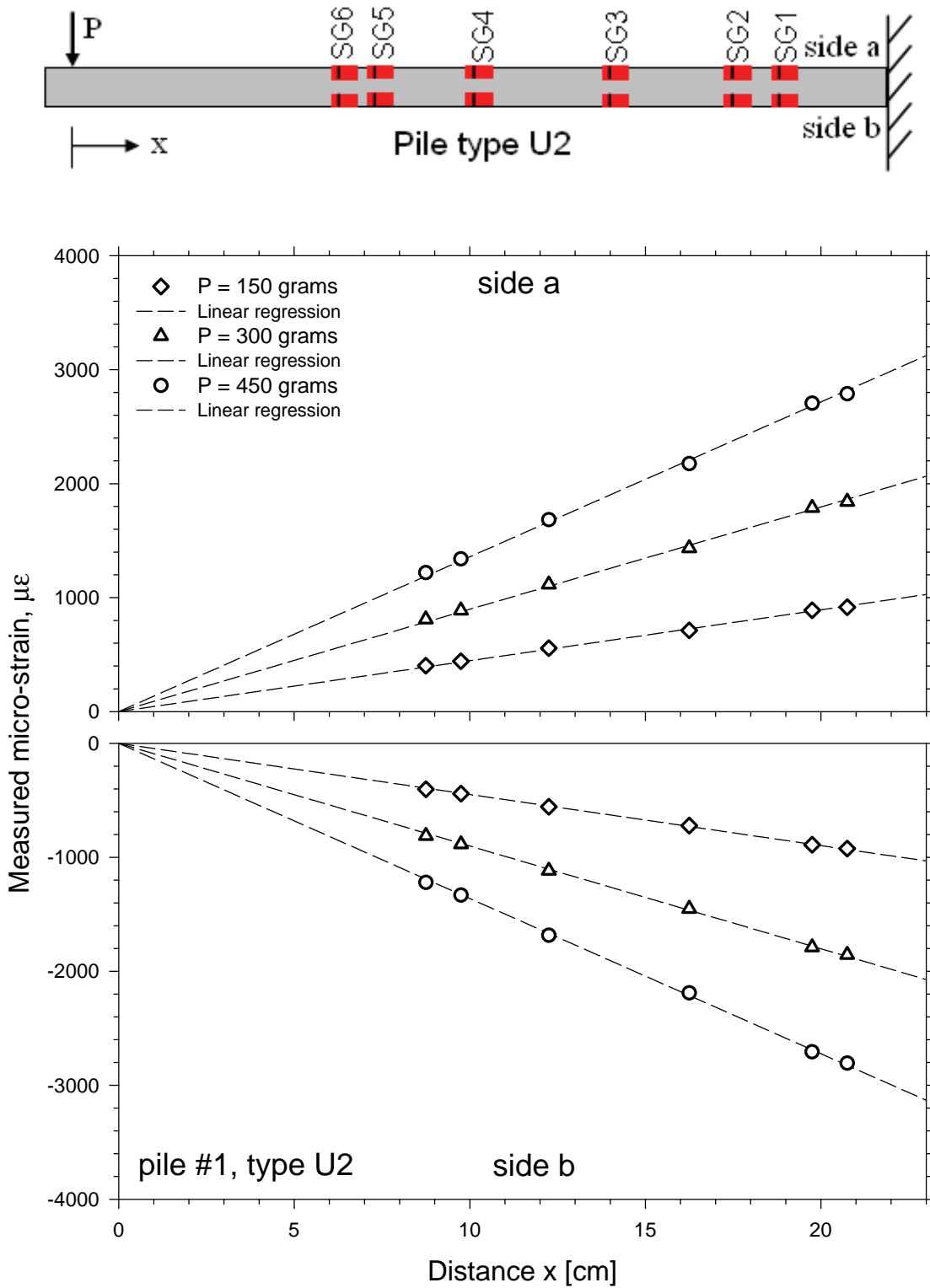


Figure 2.16: Model pile calibration under bending, pile #1 type U2 (in model units)

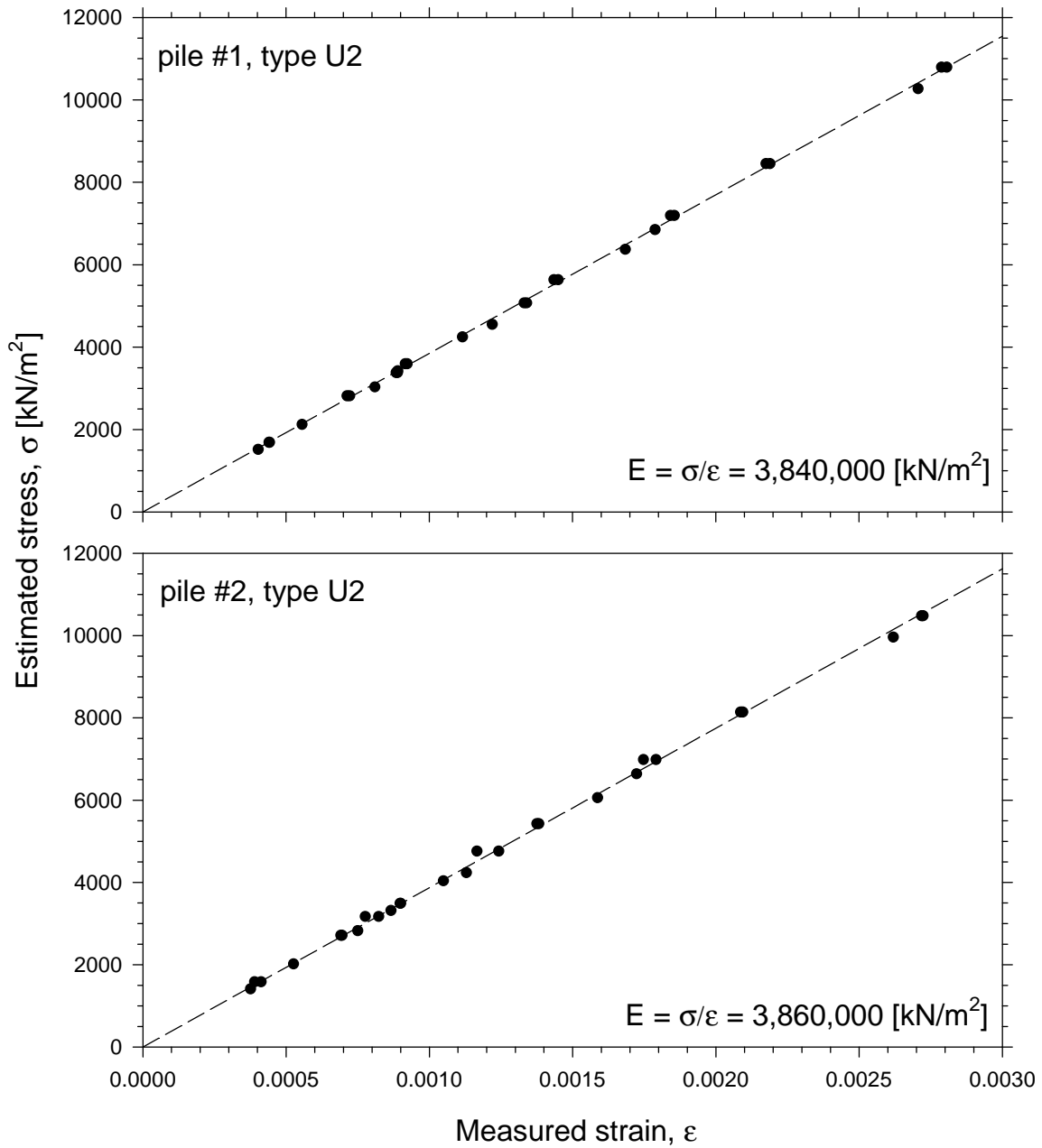


Figure 2.17: Modulus of elasticity (in bending) of model pile #1 and #2, type U2

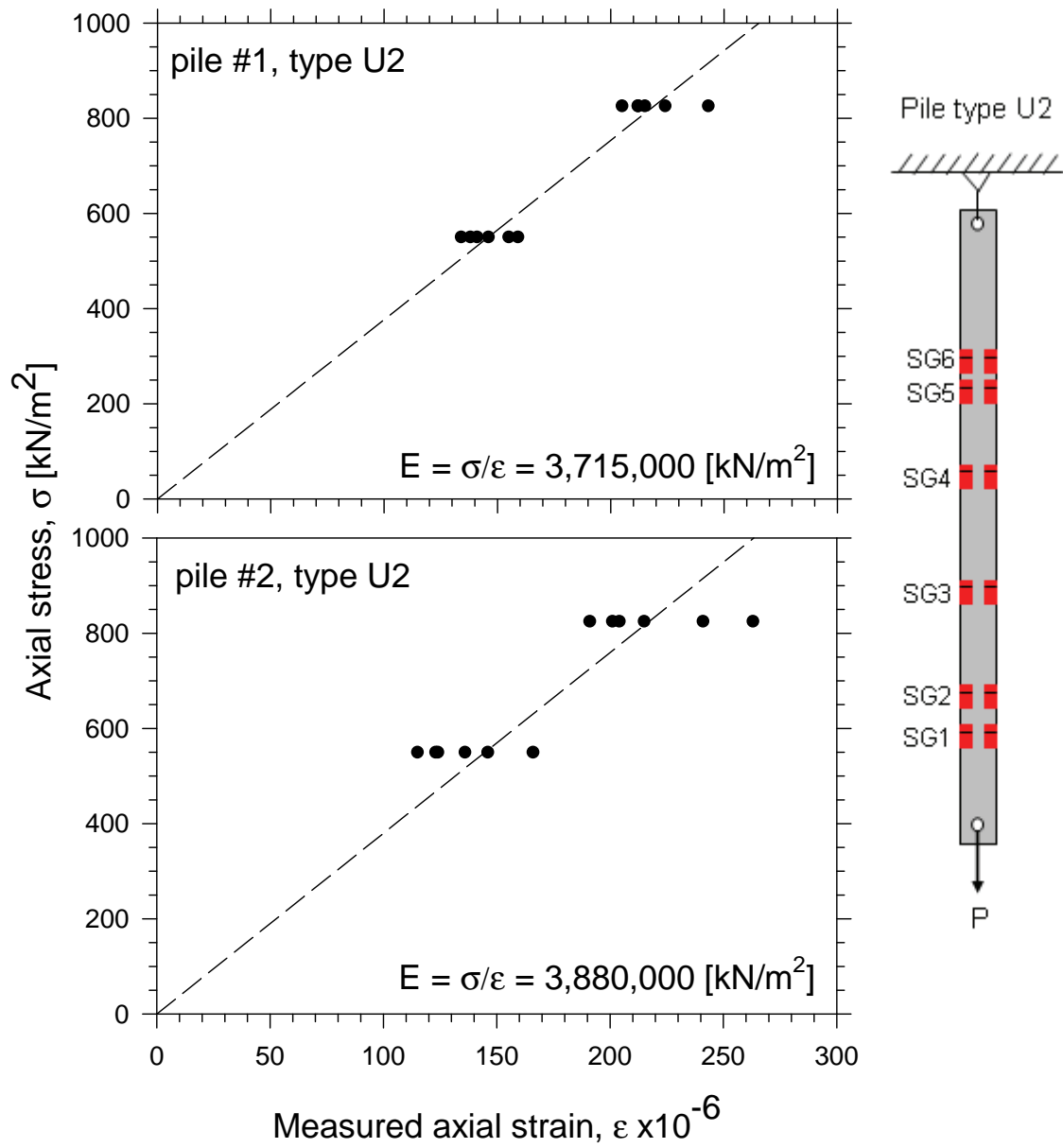


Figure 2.18: Modulus of elasticity (in axial) of model pile #1 and #2, type U2

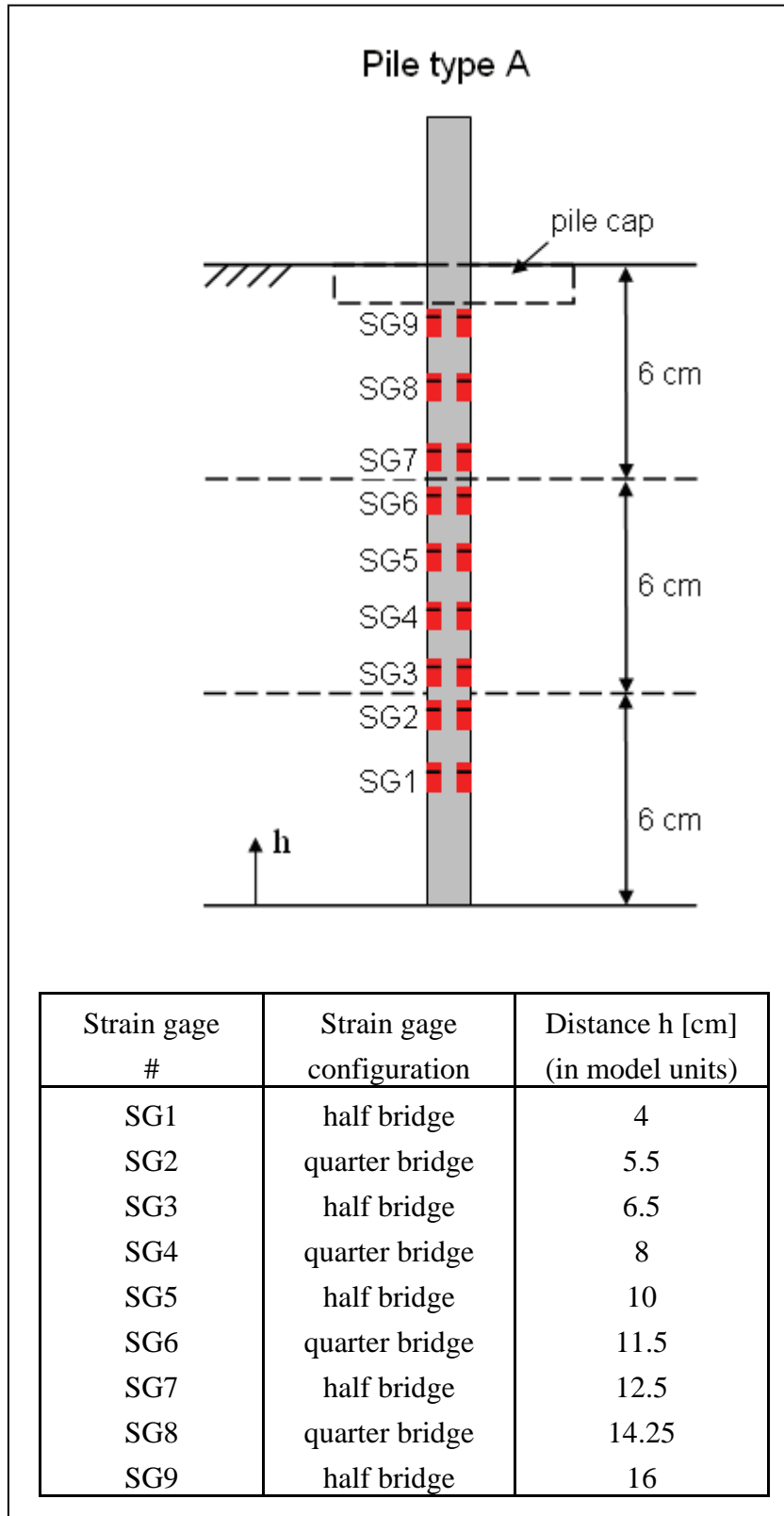


Figure 2.19: Diagram of model pile type A configuration, used in Model p-0, p-3x2, p-6x2 and p-3x1

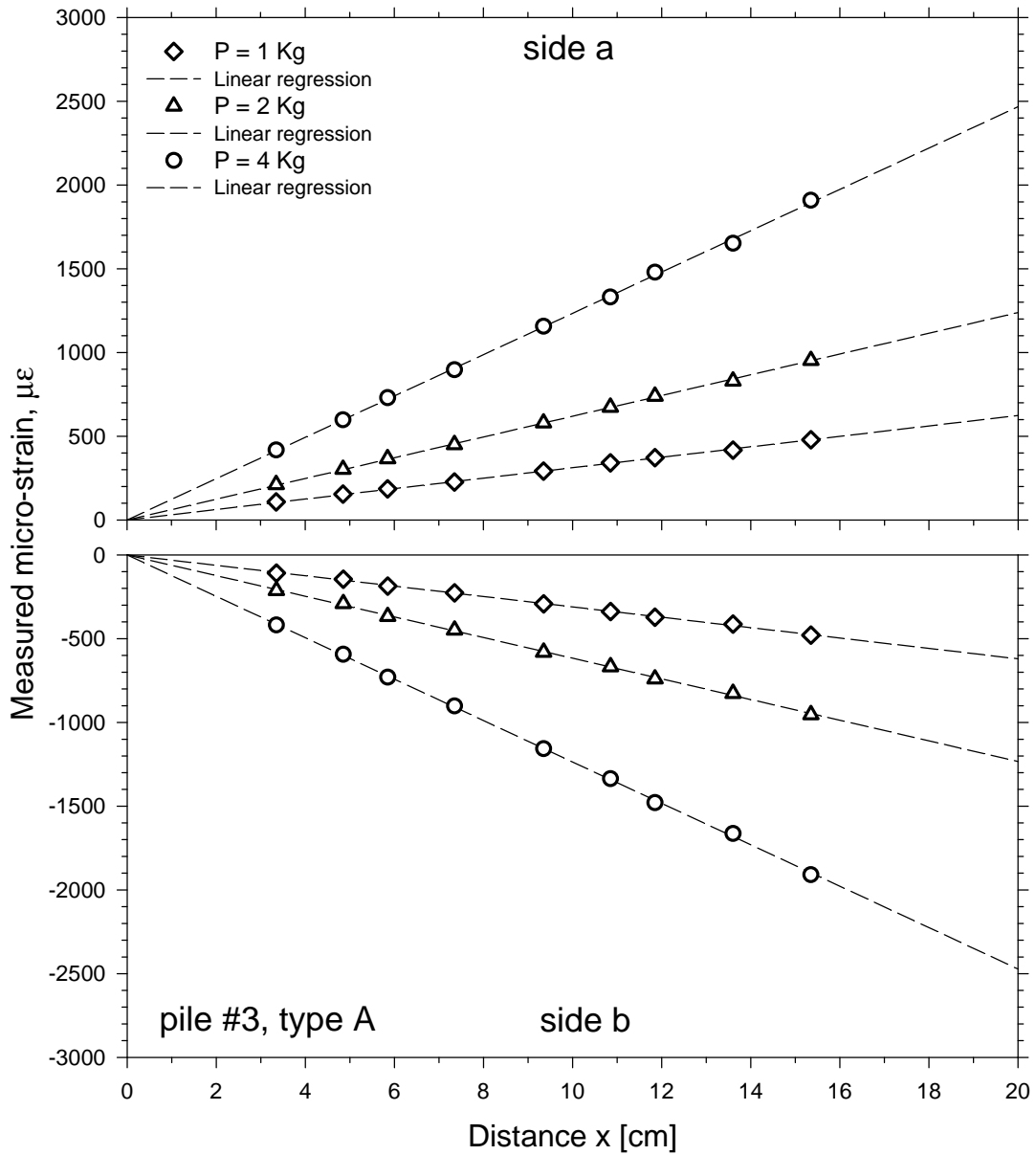
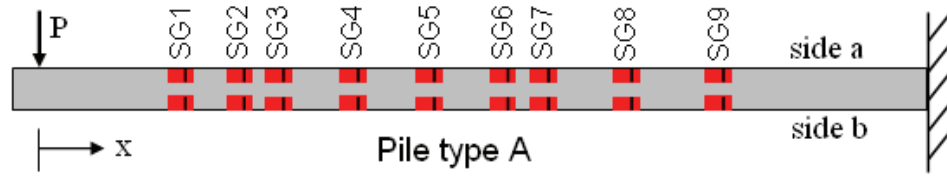


Figure 2.20: Model pile calibration under bending, pile #3, type A (in model units)

Figures 2.21 and 2.22 show the estimated bending stresses at the location of each pair of strain gage versus the measured strain at those locations. The slopes of the fitted lines represent the modulus of elasticity in bending of piles #1 and #2 (Fig. 2.21) and of piles #3 and #4 (Fig. 2.22), with an average value of 69,400,000 kN/m².

2.8 Soil Properties

2.8.1 Nevada Sand

The sand used in all centrifuge models in this research was Nevada sand, purchased from Gordon Sand Company of Compton, California. This sand was used in the VELACS project (Arulandan, 1993; and Taboada, 1995), and its properties have been extensively investigated. Nevada sand has been used extensively at RPI to study a variety of geotechnical problems (Taboada, 1995; Adalier; 1996; Abdoun, 1997; Ramos, 1999; Sharp, 1999; Wang, 2001, Pamuk, 2004).

EARTH Technology Corporation carried out general laboratory tests which included sieve analyses, specific gravity tests, maximum and minimum density tests, and constant-head permeability tests (Arulmoli et al., 1992). The specific gravity of Nevada sand was determined to be 2.67 and the maximum and minimum dry densities were estimated as 17.33 kN/m³ and 13.87 kN/m³ respectively. The corresponding minimum and maximum void ratios were $e_{\min} = 0.511$ and $e_{\max} = 0.887$. Tables 2.7 and 2.8 summarize the results from the laboratory tests and Fig. 2.23 shows the grain size distribution for Nevada sand. Constant-head permeability tests were performed using reconstituted samples (Arulmoli et al., 1992). The permeability corresponding to a relative density of $D_r = 40\%$, was $k = 6.6 \times 10^{-5}$ m/sec. The hydraulic conductivity versus relative density is plotted in Fig. 2.24, whereas Table 2.9 summarizes these results.

2.8.2 Slightly Cemented Sand

Partially saturated sands in the field have little liquefaction potential. Since it has been difficult to simulate in the centrifuge these nonliquefiable layers, Abdoun (1997) proposed and tested a method using weak cementation in the sand, giving properties comparable to a dense non-cemented sand in the field with small apparent cohesion. This method, used also by Ramos (1999), Wang (2001), and Pamuk (2004) was used in the centrifuge tests conducted in this study. This slightly cemented sand consisted of a dry mixture of Nevada sand and cement (quick-setting cement), purchased from Quikrete Company. The percentage of cement added to the mixture was 10% by weight of the clean Nevada sand. The total density of the saturated slightly cemented sand was estimated as 21.3 kN/m³ (Abdoun, 1997).

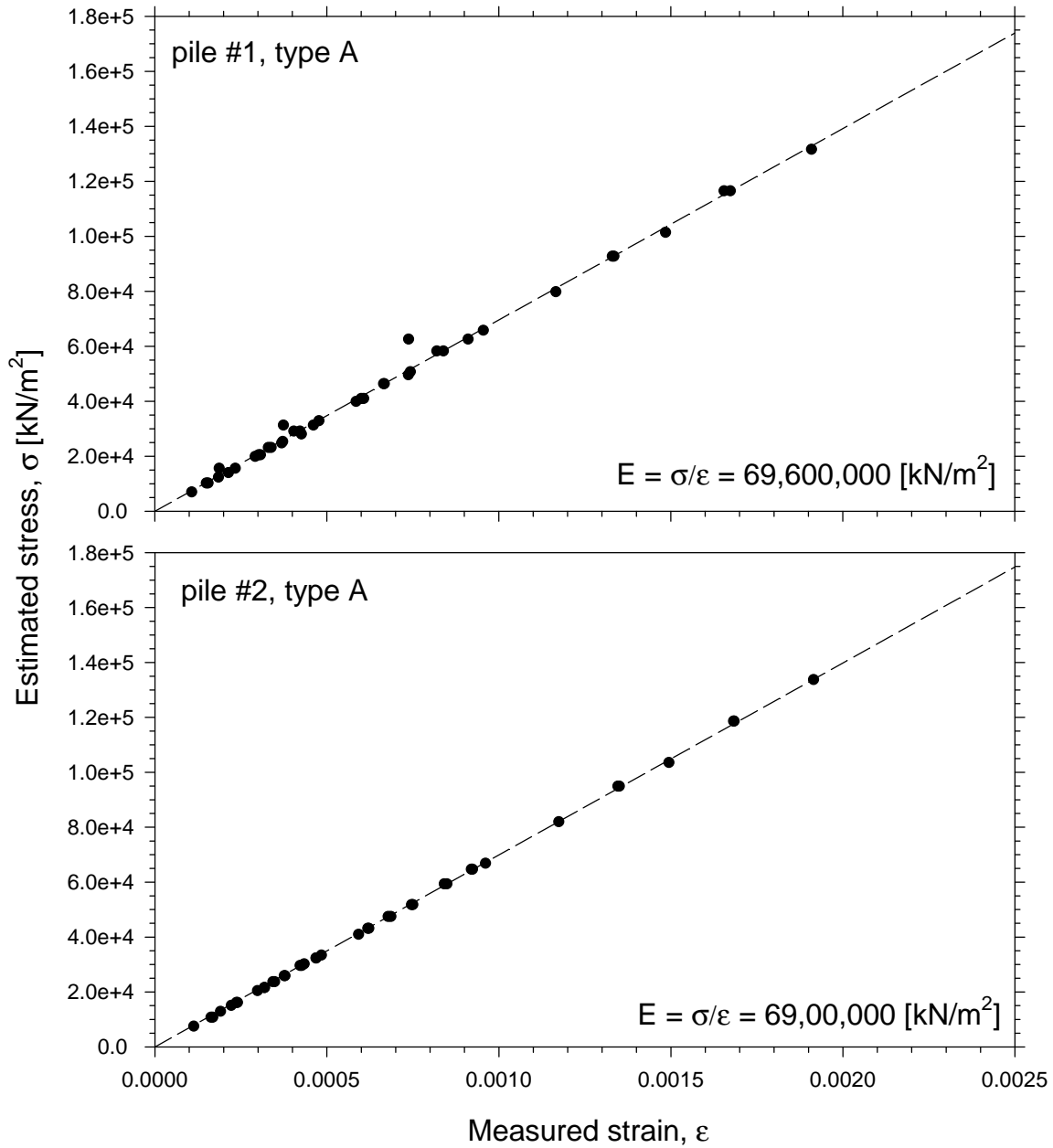


Figure 2.21: Modulus of elasticity (in bending) of model pile #1 and #2 (type A)

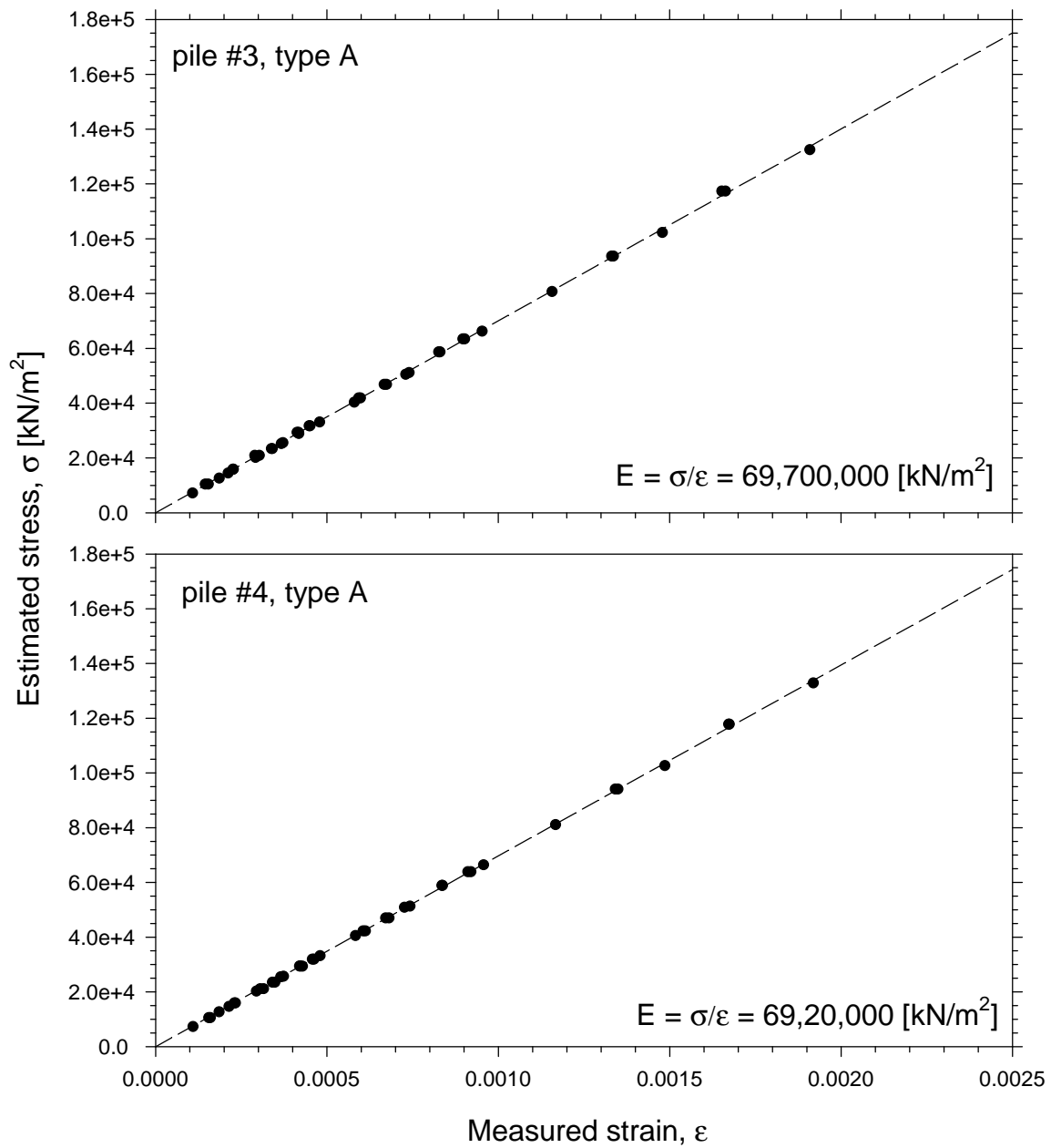


Figure 2.22 Modulus of elasticity (in bending) of model pile #3 and #4, type A

Table 2.7: General test results for Nevada sand (Arulmoli et al., 1992)

D_{10}	0.08 mm
D_{50}	0.15 mm
Specific gravity, G_s	2.67
Max. void ratio, e_{max}	0.887
Min. void ratio, e_{min}	0.511
Max. dry density	17.33 kN/m ³
Min. dry density	13.87 kN/m ³

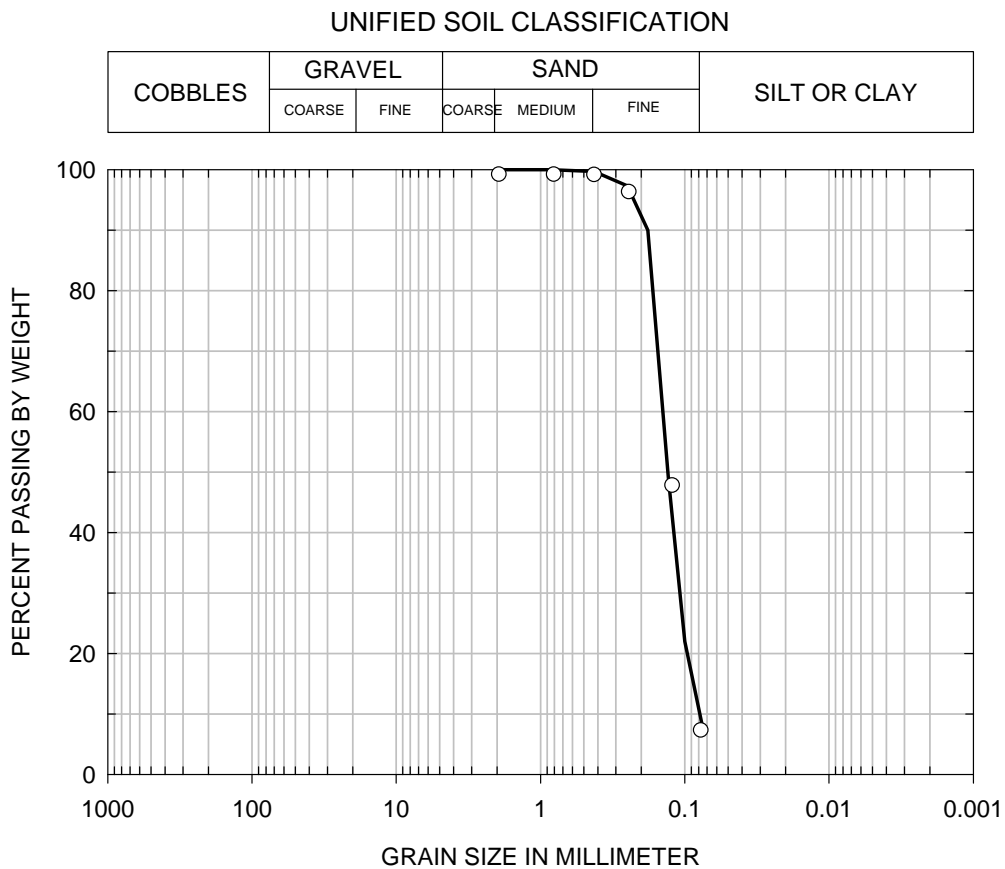


Figure 2.23: Grain size distribution for Nevada sand (after Arulmoli et al., 1992)

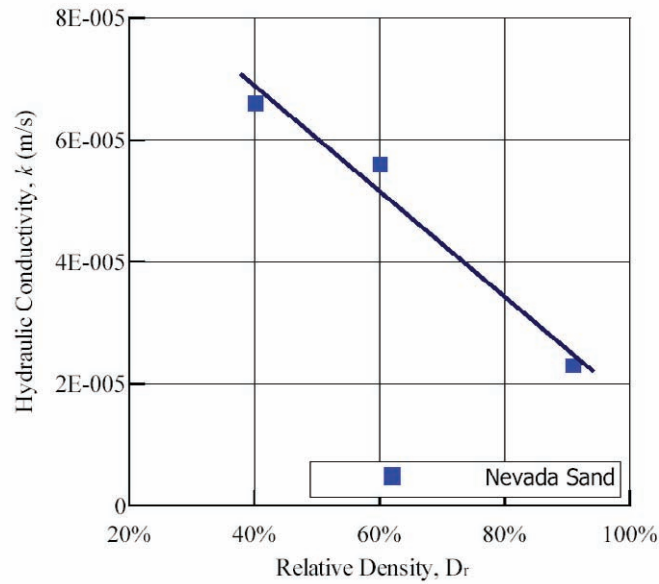


Figure 2.24: Hydraulic conductivity versus relative density for Nevada sand (after Arulmoli et al., 1992)

Table 2.8: Sieve analysis for Nevada sand (Arulmoli et al., 1992)

Sieve number	10	20	40	60	100	200
Sieve size (mm)	2	0.84	0.42	0.25	0.15	0.075
Percent passing through sieve	100	100	99.7	97.3	49.1	7.7

Table 2.9: Constant-head permeability tests results for Nevada sand (Arulmoli et al., 1992)

Test No.	Dry density (kN/m ³)	Void ratio	Relative density (%)	Permeability (m/sec)
1	16.95	0.55	91	2.3 x 10 ⁻⁵
2	15.08	0.742	40.2	6.6 x 10 ⁻⁵
3	15.76	0.667	60.1	5.6 x 10 ⁻⁵

A series of consolidated-drained triaxial tests on the slightly cemented sand was conducted by Abdoun (1997). The procedure used to prepare the soil sample was similar to the procedure used to build the slightly cemented sand layers in the centrifuge models. First, a cylindrical sample was built in three layers from a dry mixture of slightly cemented sand. Each layer was compacted using an aluminum rod dropped from a distance of 2 cm. The final dimensions of the sample were 5 cm in diameter and 10 cm in length. After about 40% of the slightly cemented sand voids were filled with water, the sample was allowed to set for about 12 hours before testing. Figure 2.25 shows the stress-strain curves obtained for the slightly cemented sand at different cell pressures (σ_3). The cell pressures used were representative of the range of stresses exerted on the models during the tests. The results of these tests are summarized in the p-q diagram shown in Fig. 2.26. The K_f – line had an inclination $\alpha = 29.5^\circ$ and an intercept $a = 4.3$ kPa (0.044 kg/cm²), which corresponds to a drained friction angle $\phi = 34.5^\circ$ and cohesion $c = 5.2$ kPa (0.053 kg/cm²). These values are considered still valid for this study, since the same process was followed to build the slightly cemented layer.

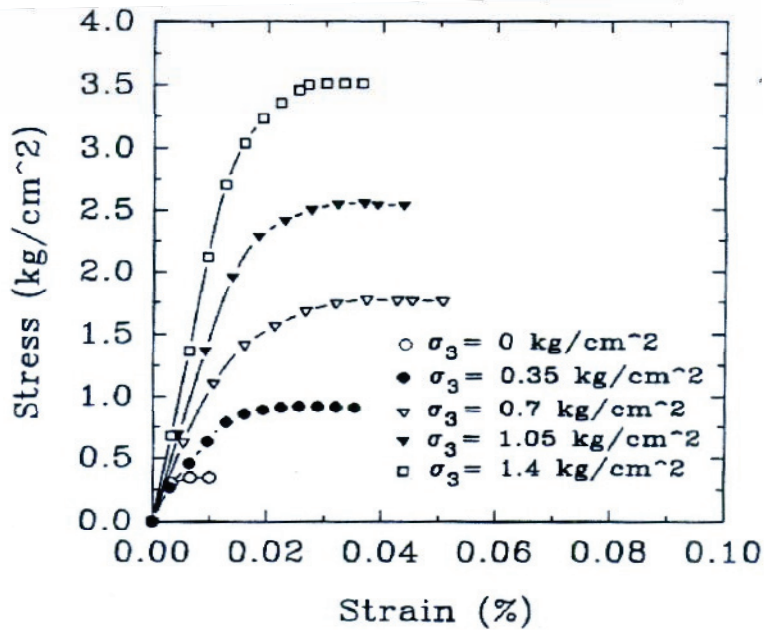


Figure 2.25: Stress-strain curves for cemented sand (Abdoun, 1997)

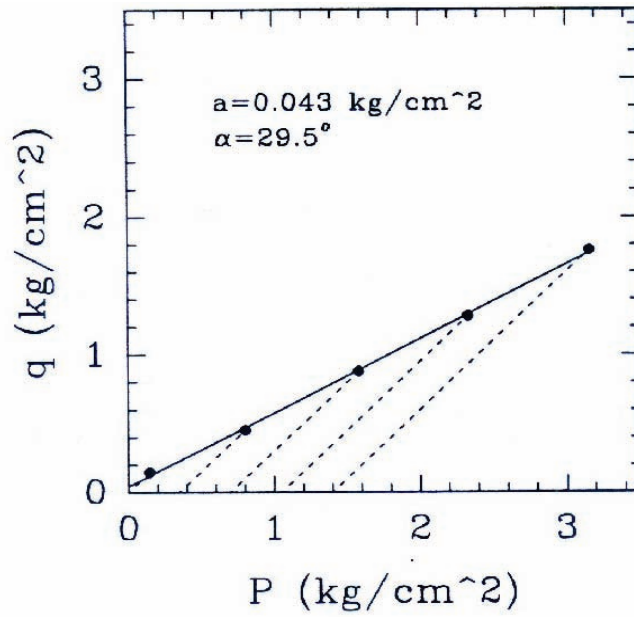


Figure 2.26: Triaxial test results for cemented sand plotted on p-q diagram (Abdoun, 1997)

CHAPTER 3

EFFECT OF SOIL PERMEABILITY ON SINGLE PILE RESPONSE TO LATERAL SPREADING

3.1 Introduction

Liquefaction-induced lateral spreading of sloping ground and near waterfronts continues to be a major cause of damage to deep foundations. Even though various foundation analyses and design methods are used in engineering practice, and extensive research has been conducted, there are still significant uncertainties associated with the maximum lateral pressures and forces applied by the liquefied soil. Furthermore, recent centrifuge and 1g shaking table tests (small and full scale) of single piles and pile groups indicate that the permeability of the liquefied sand is an extremely important and poorly understood factor. A series of centrifuge tests were conducted in this study to investigate the effect of soil permeability in the response of single piles and pile groups to lateral spreading. More specifically, six models simulating a mild infinite slope with a 6 m thick loose sand layer on top of a 2 m thick cemented sand layer were tested in a large laminar box. Three models consisting of a single pile, a 3x1 pile group, and a 2x2 pile group were tested using water as pore fluid. Since in centrifuge modeling of liquefaction there is a conflict with the consolidation and dynamic processes, these models consolidated much faster than desired, hence simulating a loose layer of coarse sand. These models were then repeated, using the same fine Nevada sand, but saturated this time with a viscous fluid (metulose), hence simulating a loose layer of fine sand. As a result, these models simulate deposits of wide different permeability in the field. The suitability of metulose as been study extensively by other researchers; for instance, Dewoolkar et al. (1999) conducted a series of experimental tests to examine the suitability of metulose, concluding that the constitutive behavior of saturated sand specimens is not significantly altered with this substitute pore fluid. Nevertheless, further investigations were recommended to study the effect of strain rates and damping properties of metulose. Madabhushi (1994) concluded that damping is rather less sensitive to the viscosity of pore fluid, thus justifying the use of high viscosity pore fluids in centrifuge tests. Increasing the viscosity of the fluid or decreasing the permeability of a liquefiable soil profile may however affect the rate of pore-pressure buildup and subsequent dissipation during and after earthquake excitation. Consequently, effective soil confinement and available resistance to shear deformations may be significantly dependent on permeability in many practical situations.

This chapter presents in detail the results of two centrifuge tests conducted at the RPI centrifuge to investigate the effect of soil permeability on the response of single piles due to lateral spreading. The models simulate a single pile embedded in a two layer soil system, consisting of a liquefiable layer on top of a nonliquefiable layer (Fig. 3.1). The slightly inclined models were excited by practically the same input motion, so the results can be compared. A main feature of these two models is the large number of pore pressure transducers placed far away, close and

next to the pile models, as shown in Fig. 3.1. The pile is instrumented with 6 pair of strain gages so p-y curves can be back-calculated. Besides, grids of colored sand were placed at different depths to observe the change in pattern of soil deformation with depth. The only difference is that Model 1x1-w is saturated with de-aired/de-ionized water, whereas Model 1x1-v is saturated with a methylcellulose-water solution (metulose) having about 40 times the viscosity of water. Consequently, at a centrifugal acceleration of 50g, these models simulate deposits with very different permeability in the field (Table 3-1).

The steps to prepare the models are described in section 3.2, whereas a description of both models is presented in section 3.3. Experimental results of Models 1x1-w and 1x1-v are presented and discussed in sections 3.4 and 3.5 respectively. A p-y curve analyses is conducted to back-calculate the soil pressure against the piles, and a basic limit equilibrium analysis is developed to estimate the maximum bending moments and pile lateral displacement due to lateral spreading. Section 3.6 compares both models and discusses the difference in response due to the soil permeability effect.

3.2 Model Preparation

This section describes the preparation of the two centrifuge models (Models 1x1-w and 1x1-v), using Fig. 3.2. While Fig. 3.2 refers to the 2x2 pile group tests discussed in chapter 5, the model preparation was very similar in all cases and hence Fig. 3.2 is also applicable to Models 1x1-w and 1x1-v. The 1-D large laminar box, described in section 2.4, was used in this series of tests.

First, a 0.02 cm thick latex membrane is placed inside the laminar box to prevent leakage of the saturated soil. Afterwards, the external side of the container is sealed and a vacuum pump is connected to remove the air from the outer chamber, as shown in Fig. 3.2a. The external vacuum forces the latex membrane to flush against the rings, facilitating placement of the soil. At this stage the pile group is properly located and aligned in the box. Figure 3.2a shows the construction of the bottom slightly cemented layer. A dry mixture of slightly cemented sand is pluviated into the laminar box in three sublayers. Each sublayer is compacted by dropping an aluminum block five times from a height of 2 cm, ending up with a cemented layer of about 4.2 cm high. The soil in the pile group area is compacted following the same procedure, but using a smaller aluminum block and dropping it eight times from the same height of 2 cm (Fig. 3.2a). An accelerometer is placed at an intermediate elevation at the proper orientation. This slightly cemented sand layer is believed to represent a medium-dense layer in the field (Abdoun, 1997).

A cover is placed on top of the laminar box and de-ionized water is slowly introduced from the corners of the cover until the whole layer is wet (Fig. 3.2b). Once the cement is set, after approximately 12 hours, the cover is removed and the surface is flattened and carefully scraped to ensure a uniform height of 4 cm.

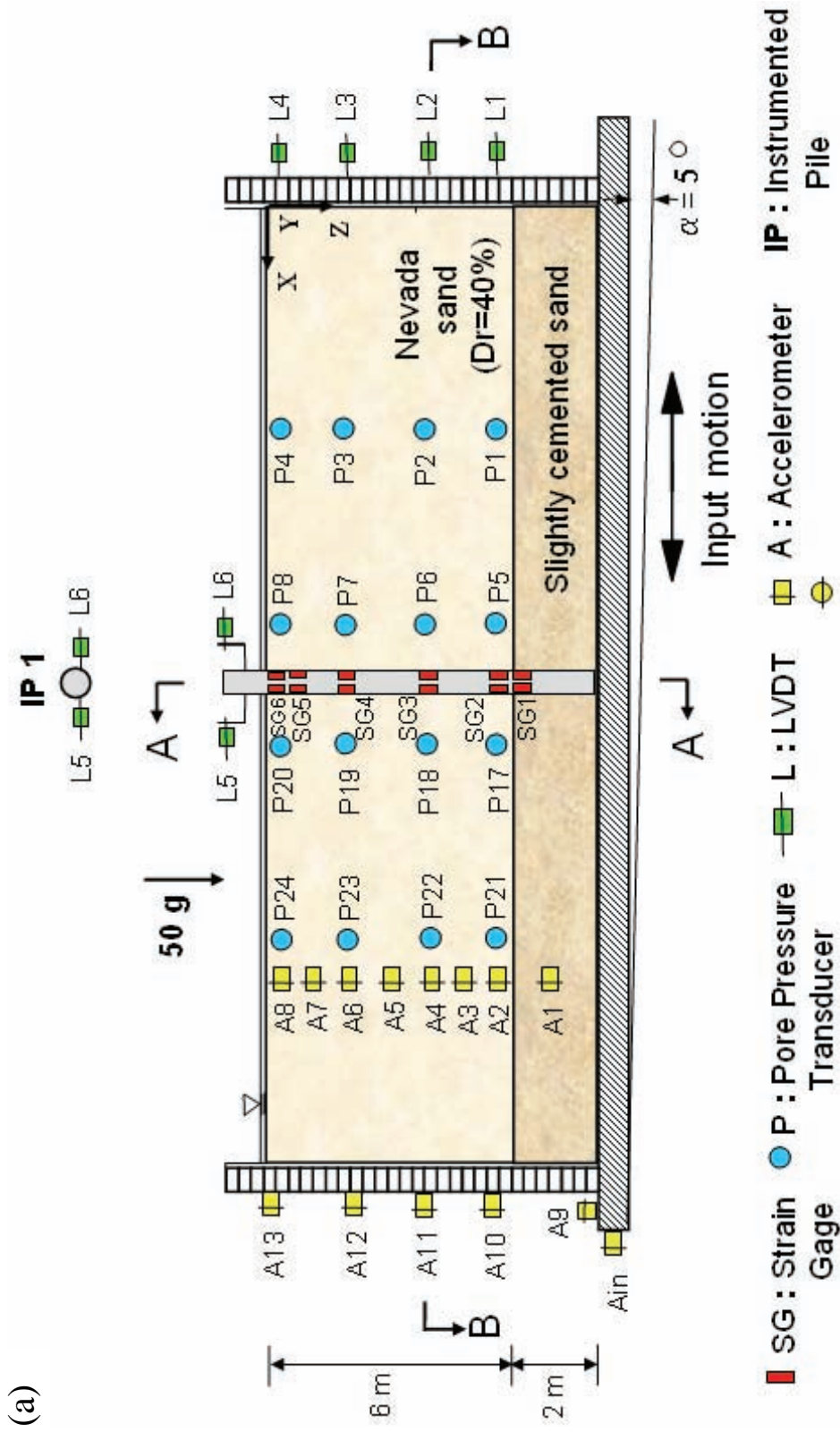


Figure 3.1: (a) Setup and instrumentation used in Models 1x1-w and 1x1-v, (in prototype units)

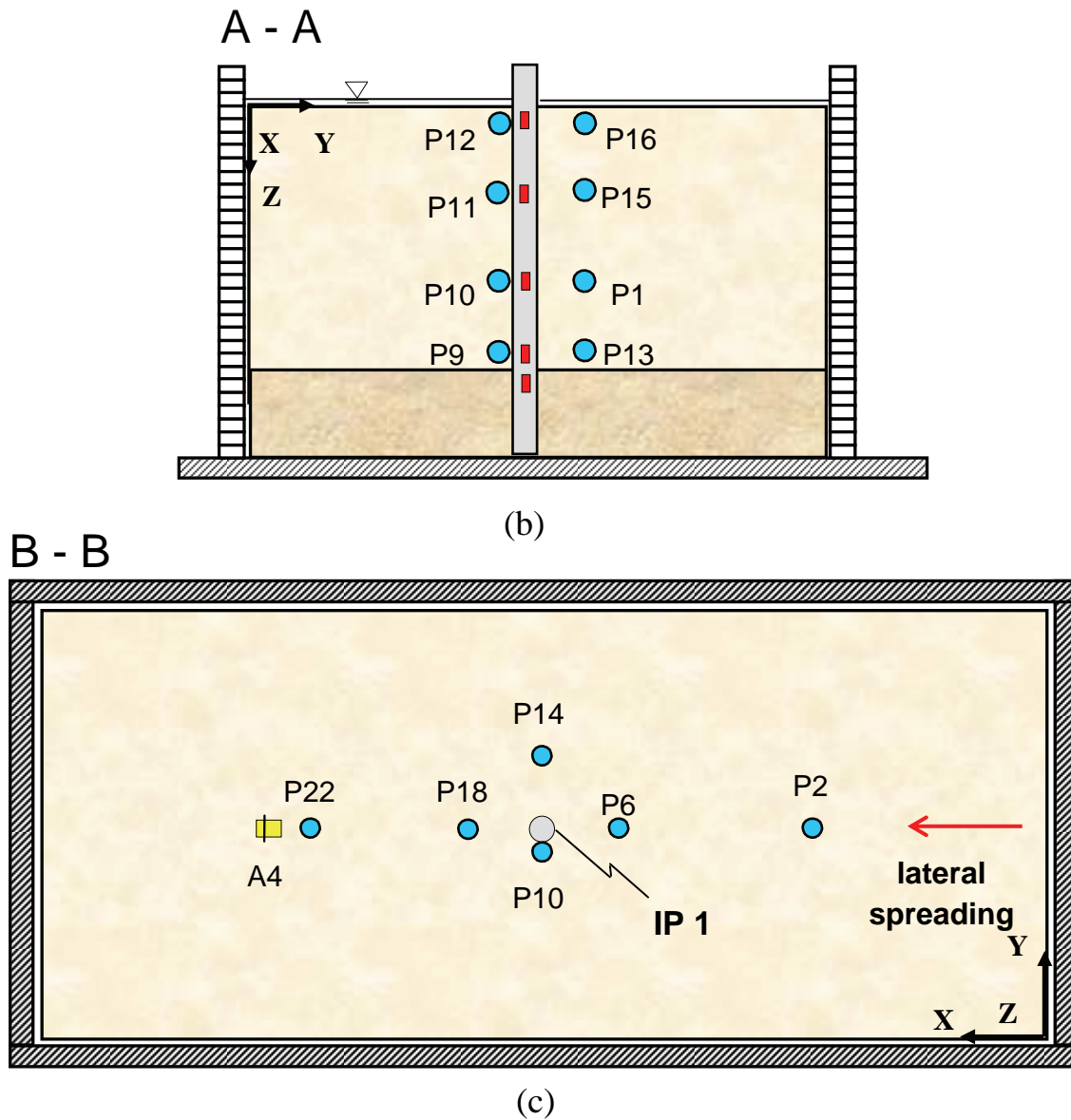
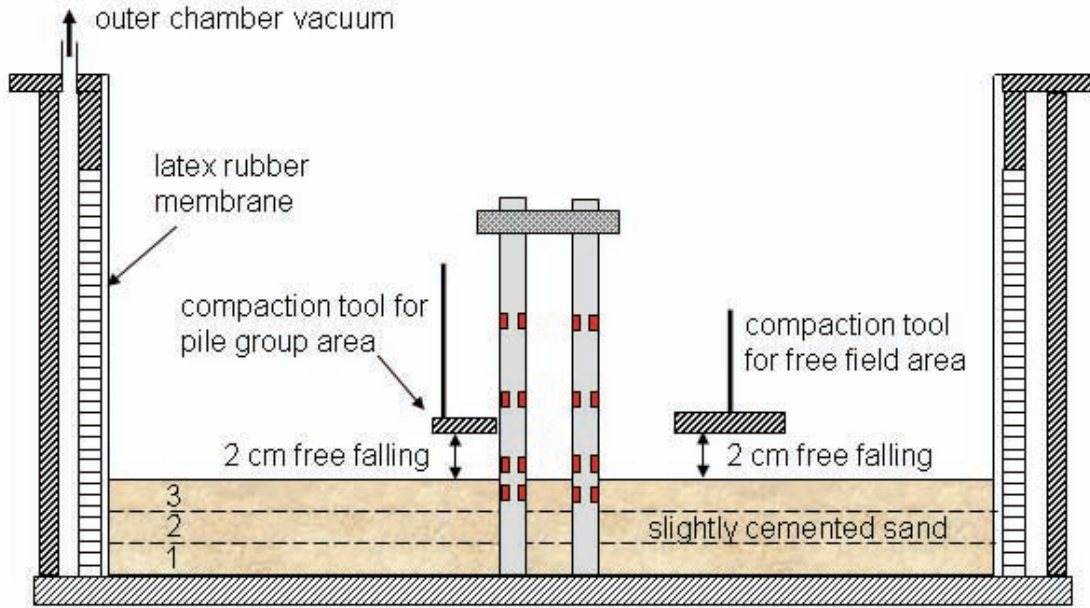


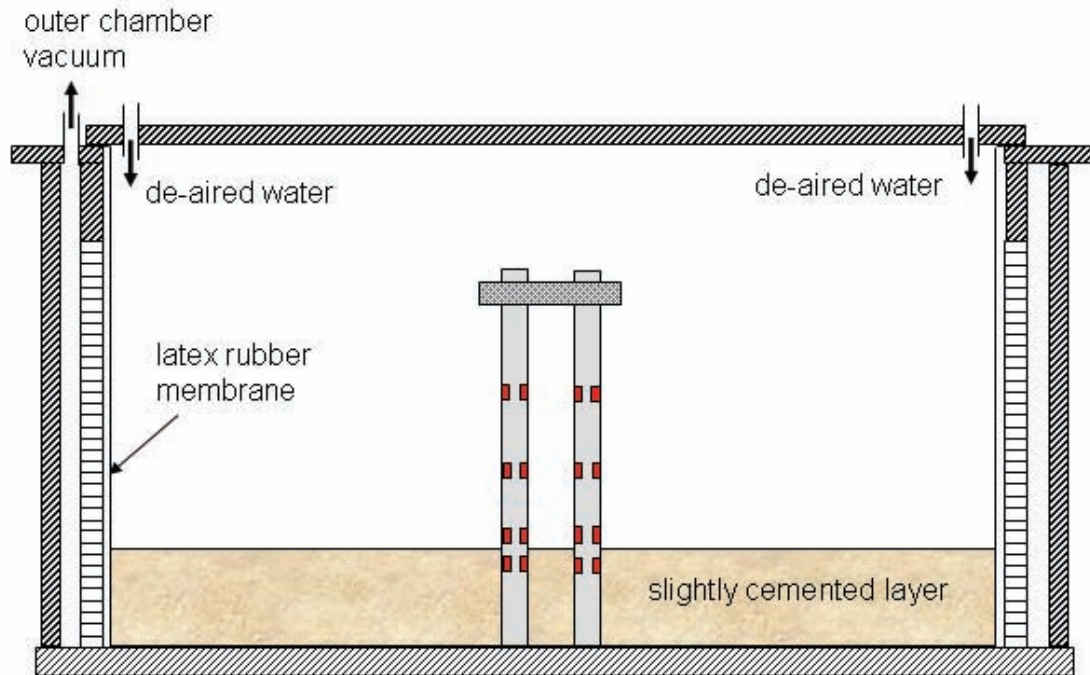
Figure 3.1 (cont): (b) Transversal and (c) horizontal sections of Models 1x1-w and 1x1-v

Table 3.1: Testing properties of centrifuge Models 1x1-w and 1x1-v

Model	Pile configuration	# of piles	# of instrument. piles	Pile cap	# of layers	Fluid viscosity (μ_w)
1x1-w	single pile	1	1	no	2	1
1x1-v	single pile	1	1	no	2	42

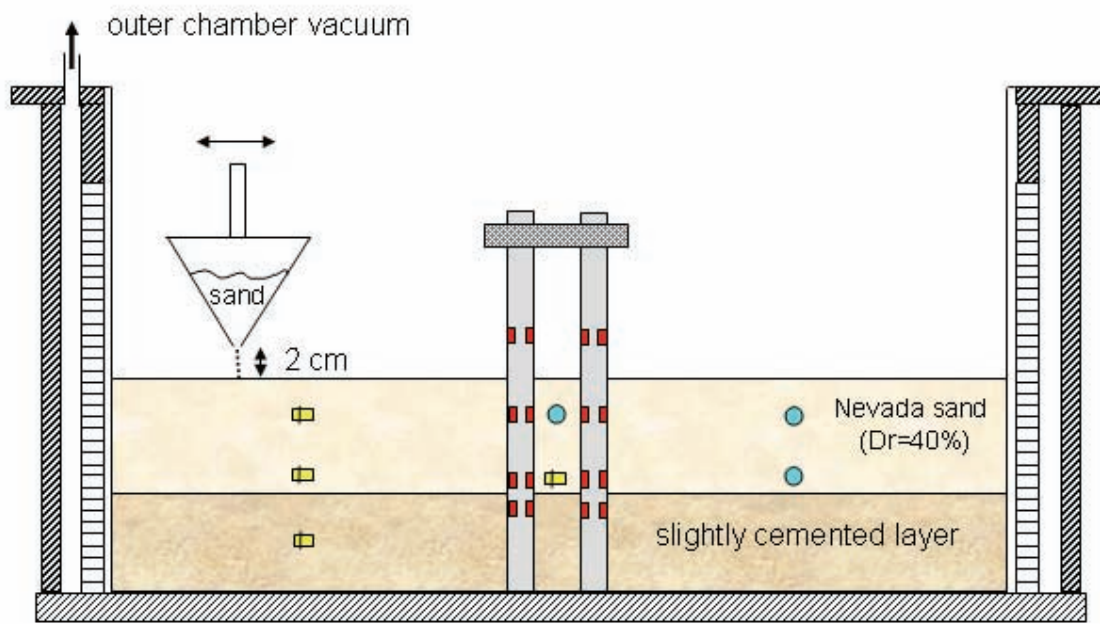


(a)

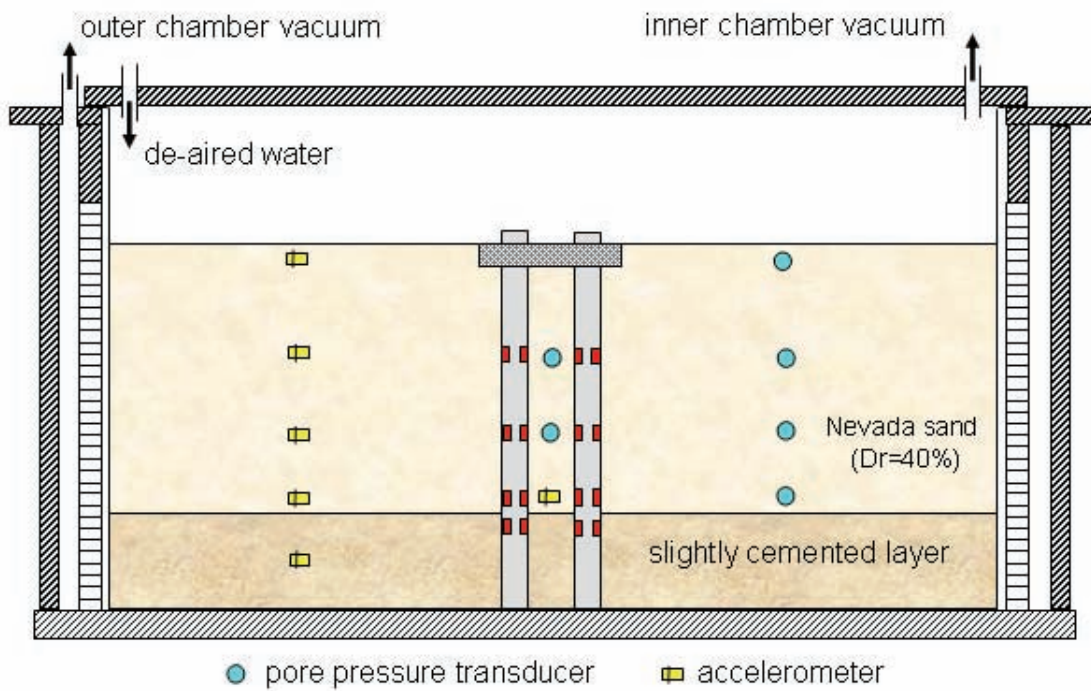


(b)

Figure 3.2: (a) Preparation of slightly cemented sand later, (b) saturation of the cemented sand layer



(c)



(d)

Figure 3.2 (cont.): (c) Pluviation of Nevada sand, (d) saturation of the model

Figure 3.2c illustrates the construction of the liquefiable layer. Dry Nevada sand is poured into the laminar box by dry pluviation to a height of 12 cm above the slightly cemented layer. A funnel with a row of holes is used to place the sand in the free field, whereas a small cone connected to a thin tube is used to fill the pile group area. The falling distance and speed of movement in both methods were previously calibrated to ensure the desired 40% relative density. The width of the funnel was approximately one third the width of the laminar box. The funnel is manually moved back and forth along the longest dimension of the box, with a free falling distance of about 2 cm. Accelerometers and pore pressure transducers are installed at proper locations and orientations. Colored sand is also placed at intermediate depths using a plastic grid that serve as mold.

Once the thickness of the loose Nevada sand is exactly 12.0 cm, an airtight cover is placed on top of the laminar box to seal the inner chamber. The vacuum pump for the outer chamber is turned off and the laminar box is carefully moved to the centrifuge platform. Once the laminar box is fixed to the inclined table, on top of the shaker, the vacuum pump is reconnected to the outer chamber, until a vacuum of 30 in of mercury is reached. A second vacuum pump is then connected to the inner chamber to apply a vacuum of about 26 in of mercury, as shown in Fig. 3.2d. This differential vacuum is required to keep the latex membrane tight against the rings. After maintaining the inner vacuum for an hour, the second pump is turned off and carbon dioxide is slowly introduced into the box during approximately half an hour until atmospheric pressure is reached in the inner chamber. The purpose of using CO₂ is to help dissolving the remaining oxygen in the water. At this time, the fluid is introduced very slowly to the model from four dripping pipes located on each corner of the cover. This process continues for about 10 hours until the pore fluid covers the model surface. The inner and outer vacuums are slowly released and the airtight cover is removed. The rigid sides of the laminar box are also removed and the remaining sensors are attached to the side of the laminar box. The model is finally tested between 24 and 48 hours after the saturation process is completed.

3.3 Model Description

The setup and instrumentation used in Models 1x1-w and 1x1-v are presented in Fig. 3.1. These models simulate a single pile embedded in the nonliquefiable layer. The prototype profile consists of a 6 m thick Nevada sand layer placed at a relative density of about 40%, on top of a 2 m thick nonliquefiable cemented layer. The models, inclined 2° to the horizontal (4.8° after instrumental correction; Taboada, 1995), simulate an infinite mild ground slope. The only difference between both models is that Model 1x1-w is saturated with de-aired/de-ionized water, whereas Model 1x1-v is saturated with a methylcellulose-water solution (metulose) having about 40 times de viscosity of water. At a centrifugal acceleration of 50g the loose Nevada sand in Model 1x1-w simulates a coarse sand, whereas in Model 1x1-v it simulates a fine sand.

The embedded pile has a prototype diameter (d) of 60 cm and a prototype bending stiffness (EI) of approximately 9000 kN-m². Figure 3.3 shows a picture of the single pile and the transducers during model preparation. Grids of colored sand were placed as well at intermediate depths to observe the pattern of soil displacement around the pile (Fig. 3.4).

The models were excited by 30 cycles of a 100 Hz sinusoidal acceleration with uniform amplitude of about 15g. At a centrifugal acceleration of 50g this corresponds to a frequency of 2 Hz and peak acceleration of about 0.3g.

The instrumentation used in Models 1x1-w and 1x1-v is shown in Fig. 3.2 and listed in Table 3.2. The models were instrumented with 14 accelerometers, 24 pore pressure transducers, and 6 LVDTs. The pile (IP1) was instrumented with 6 pairs of strain gages. Detailed information about the strain gage configuration and the pile (type U2) used in these models is presented in section 2.7. Accelerations in the soil and outside the laminar box, excess pore water pressure, lateral displacement of the soil and the pile head, and bending moments were measured during the tests.

3.4 Model 1x1-w

3.4.1 Recorded Accelerations

Figure 3.5 shows the recorded input acceleration and soil acceleration time histories in the free field at different depths. As expected, the measured input acceleration had a uniform amplitude of 0.3g. Near the ground surface the soil acceleration dropped significantly after one cycle due to the dynamic isolation of the shallower layers. At deeper elevations, large negative spikes developed due to the dilative behavior of the saturated loose sand during lateral spreading. Therefore, the records indicate the loose sand layer liquefied and displaced in the downslope direction during shaking. On the other hand, the acceleration of the bottom layer (A1) was identical to the input acceleration, indicating that no sliding occurred between this layer and the base of the laminar box. The acceleration records on laminar rings (Fig. 3.6) exhibit a drop in positive amplitude and spikes in the negative direction, showing a good agreement with the soil acceleration.

3.4.2 Recorded Excess Pore Pressures

Excess pore pressure time histories in the free field, near field, and next to the pile, are shown in Figs. 3.7, 3.8 and 3.9 respectively. These records reveal that practically the whole sand layer liquefied at the beginning of shaking. However, a decrease in excess pore pressure took place near the ground surface, with this tendency being stronger next to the pile than in the free field. On the other hand, the high permeability of the loose sand layer was illustrated by the fast dissipation process, which started during the excitation and took only a few seconds.

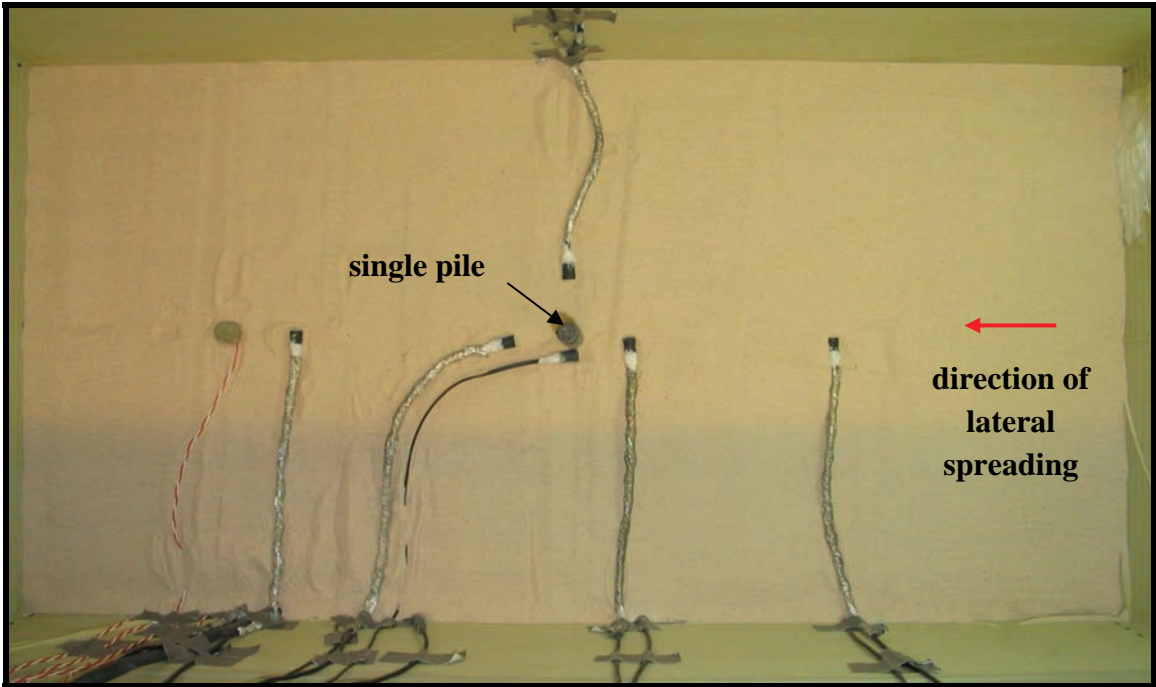


Figure 3.3: Model during preparation, Models 1x1-w and 1x1-v

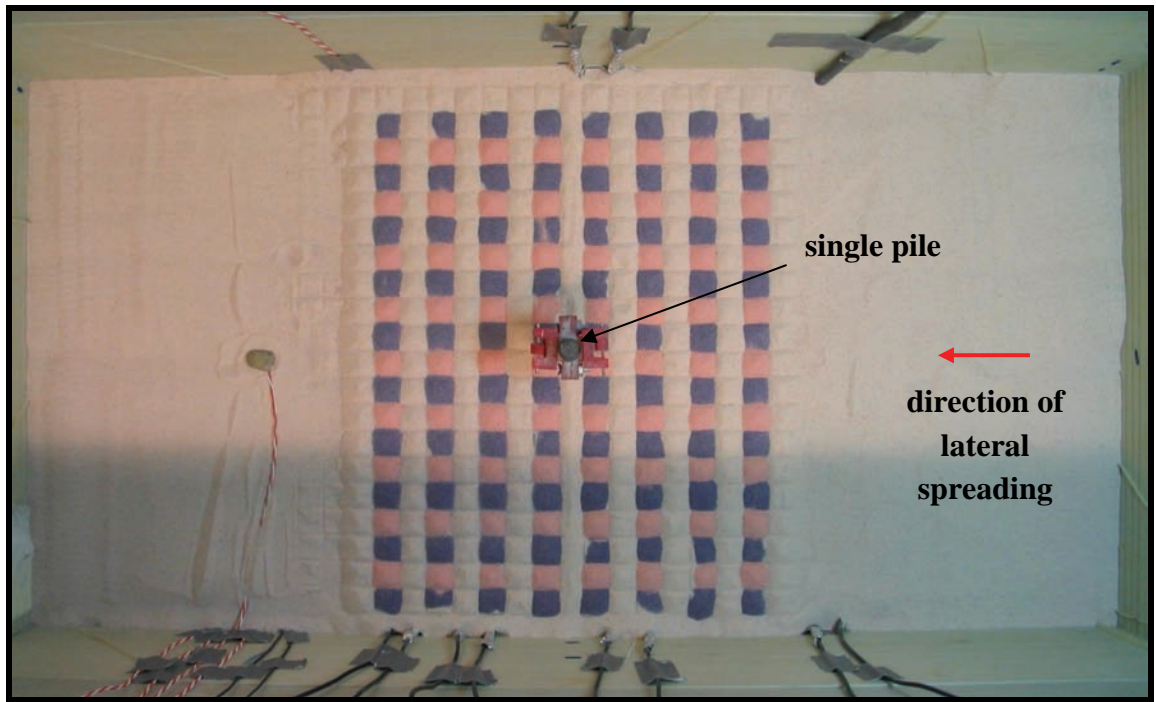


Figure 3.4: Colored sand placed at an intermediate depth, Models 1x1-w and 1x1-v

Table 3.2: Location of instruments in Models 1x1-w and 1x1-v (in model units)

Transducer	Sensor name	Coordinates [cm]		
		X	Y	Z
Accelerometer	Ain	73.5	17.75	16.5
	A1	55	17.75	14
	A2	55	17.75	11
	A3	55	17.75	9.5
	A4	55	17.75	8
	A5	55	17.75	6
	A6	55	17.75	4
	A7	55	17.75	2.5
	A8	55	17.75	1
	A9	72.5	17.75	16
	A10	71	17.75	11
	A11	71	17.75	8
	A12	71	17.75	4
	A13	71	17.75	1
Pore pressure transducer	P1	17.75	17.75	11
	P2	17.75	17.75	8
	P3	17.75	17.75	4
	P4	17.75	17.75	1
	P5	32	17.75	11
	P6	32	17.75	8
	P7	32	17.75	4
	P8	32	17.75	1
	P9	35.5	16.75	11
	P10	35.5	16.75	8
	P11	35.5	16.75	4
	P12	35.5	16.75	1
	P13	35.5	21.25	11
	P14	35.5	21.25	8
	P15	35.5	21.25	4
	P16	35.5	21.25	1
	P17	39	17.75	11
	P18	39	17.75	8
	P19	39	17.75	4
	P20	39	17.75	1
	P21	53	17.75	11
	P22	53	17.75	8
	P23	53	17.75	4
	P24	53	17.75	1

Table 3.2 (cont.): Location of instruments in Models 1x1-w and 1x1-v (in model units)

Transducer	Sensor name	Coordinates [cm]		
		X	Y	Z
LVDT	L1	0	17.75	11
	L2	0	17.75	8
	L3	0	17.75	4
	L4	0	17.75	0.5
	L5	36.5	17.75	-2
	L6	34.5	17.75	-2
Strain gage		IP 1	IP 1	IP 1
	SG1	35.5	17.75	12.5
	SG2	35.5	17.75	11.5
	SG3	35.5	17.75	8
	SG4	35.5	17.75	4
	SG5	35.5	17.75	1.5
	SG6	35.5	17.75	0.5

3.4.3 Recorded Lateral Displacements

The recorded soil lateral displacement in the free field (Fig. 3.10) shows that the liquefied layer displaced gradually during shaking, reaching a maximum displacement of approximately 165 cm at the end of shaking. The single pile on the other hand, bounced back after reaching a maximum lateral displacement of 28 cm.

The profiles of soil lateral displacement in the free field were obtained by interpolating the LVDT measurements, after filtering out the cyclic component (Fig. 3.11). As soon as the loose sand liquefied at the beginning of shaking, the deposit started moving downslope, with the maximum displacement taking place always on the ground surface.

3.4.4 Pattern of Soil Displacement around the Single Pile

Grids of colored sand were placed at intermediate depths to observe the pattern of soil displacement around the pile. Figure 3.12 shows pictures of the soil condition at two different depths, after carefully removing the soil on top. The liquefied sand moved around the pile, affecting the soil pattern close to the pile itself. Therefore, the characteristic width perpendicular to the flow was the diameter of the pile. Even though the area of influence was very small, it is possible to observe a larger area of influence at shallower elevations.

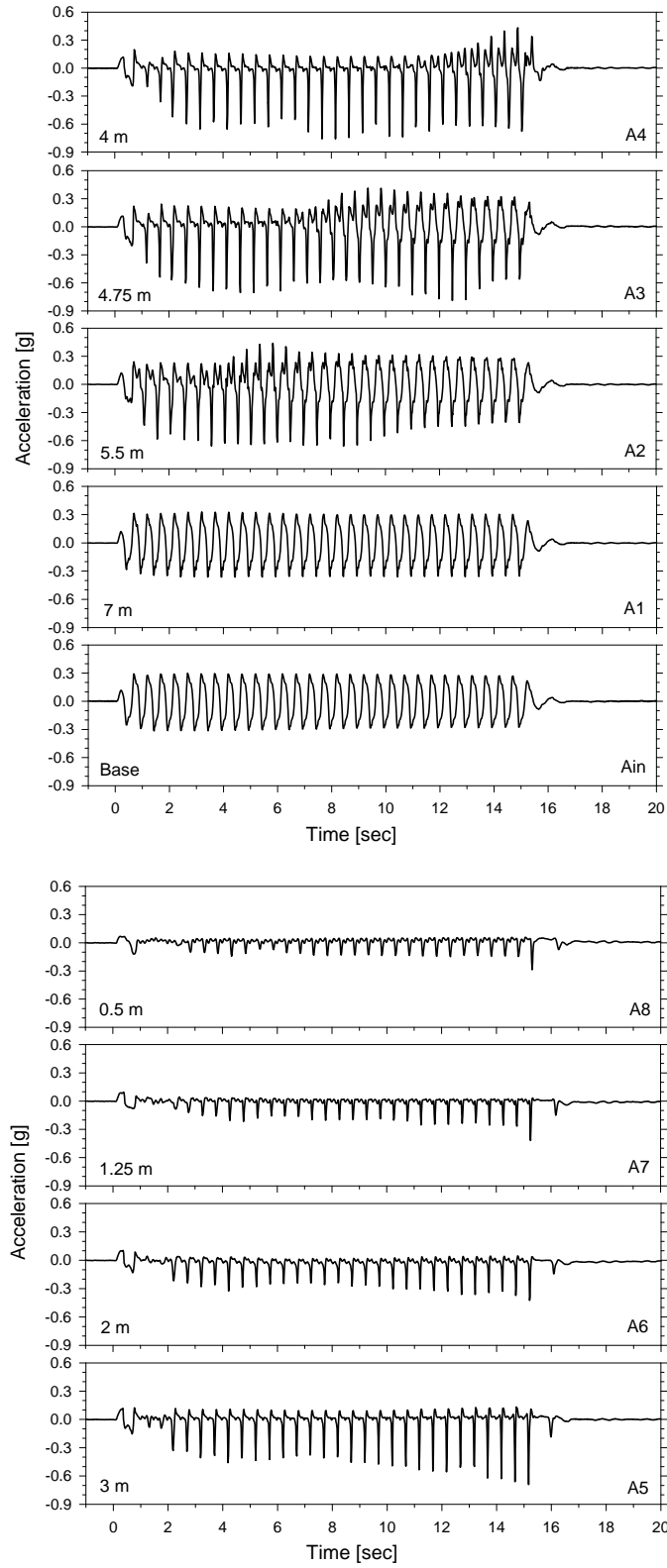


Figure 3.5: Soil acceleration time histories in the free field, Model 1x1-w

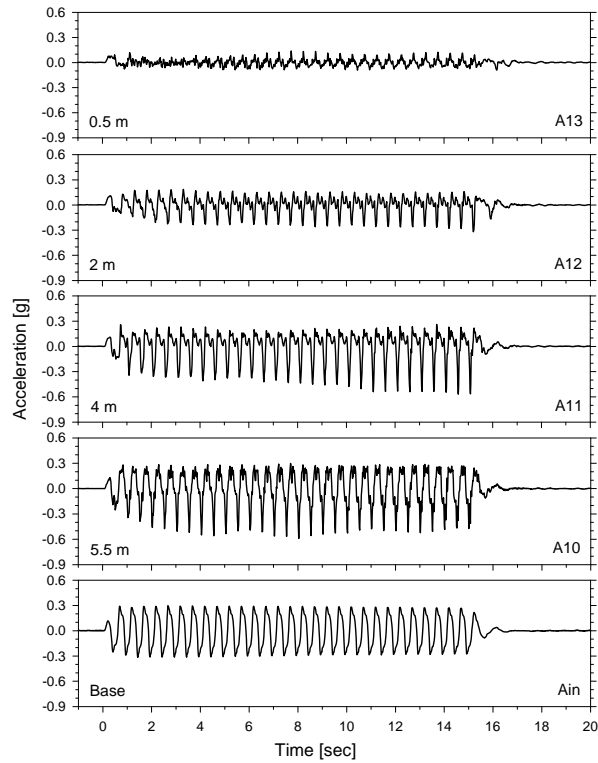


Figure 3.6: Accelerations recorded on the laminar rings, Model 1x1-w

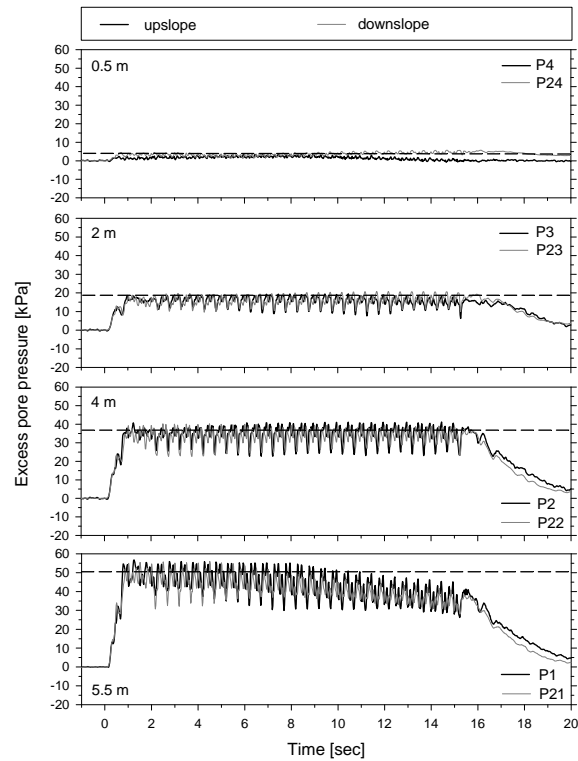


Figure 3.7: Excess pore pressure time histories in the free field, the dashed lines correspond to initial liquefaction, Model 1x1-w

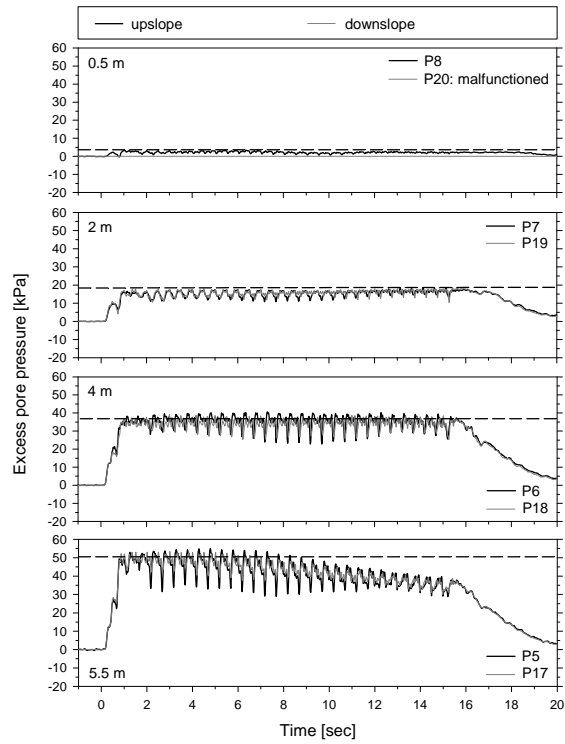


Figure 3.8: Excess pore pressure time histories close to the pile, upslope and downslope, Model 1x1-w

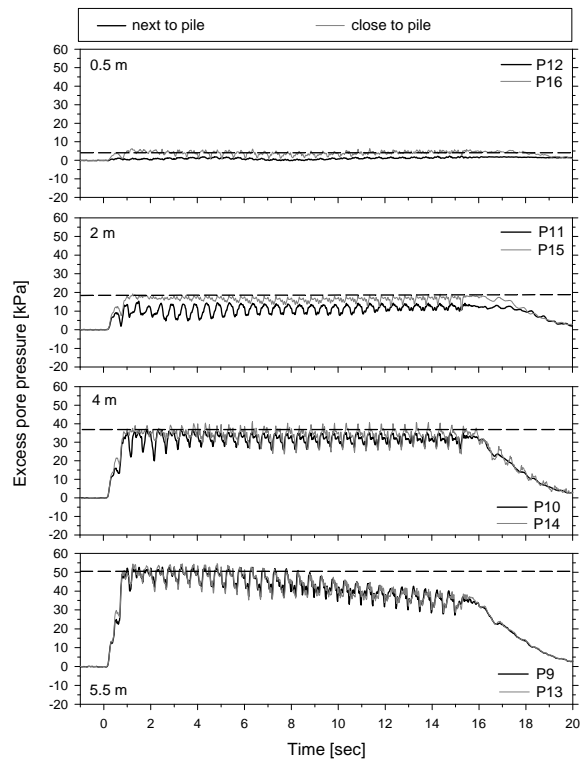


Figure 3.9: Excess pore pressure time histories close and next to the pile, Model 1x1-w

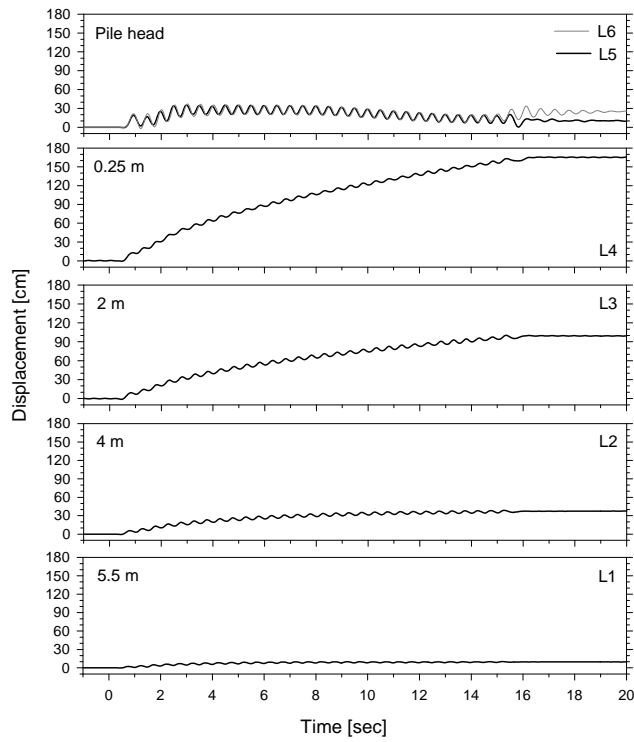


Figure 3.10: Lateral displacement time histories, Model 1x1-w

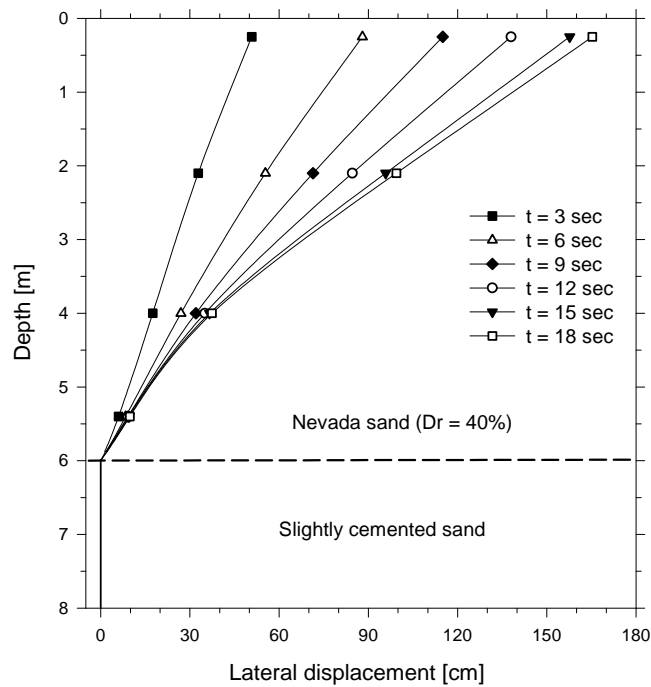


Figure 3.11: Profiles of soil lateral displacement in the free field, Model 1x1-w

3.4.5 Recorded Bending Moments

Figure 3.13 shows prototype bending moments measured in the single pile, whereas the profiles of bending moments are shown in Fig. 3.14, after filtering out the cyclic component. The maximum moment at any given time occurred closed to the base of the liquefied layer, reaching a maximum value at about 6 sec, which is also the time at which the pile reached its maximum deflection. Afterwards, the bending moments decreased despite the displacement of the liquefied layer kept increasing until the end of shaking. There is a strong indication that after 6 sec the liquefied soil started flowing around the pile, thus decreasing the exerted soil pressure on the pile. This general pattern of bending moment and pile displacement is typical of many centrifuge models of single piles and pile groups conducted at RPI using water as pore fluid (Abdoun, 1997).

Figure 3.15 shows the measured bending moment at the base of the liquefiable layer versus the measured pile head lateral displacement, after filtering out the cyclic component. The pile reached a maximum lateral displacement and bending moment and then bounced back during shaking. The almost linear relationship between bending moment and pile head displacement indicates a linear elastic behavior of the pile-fixation system.

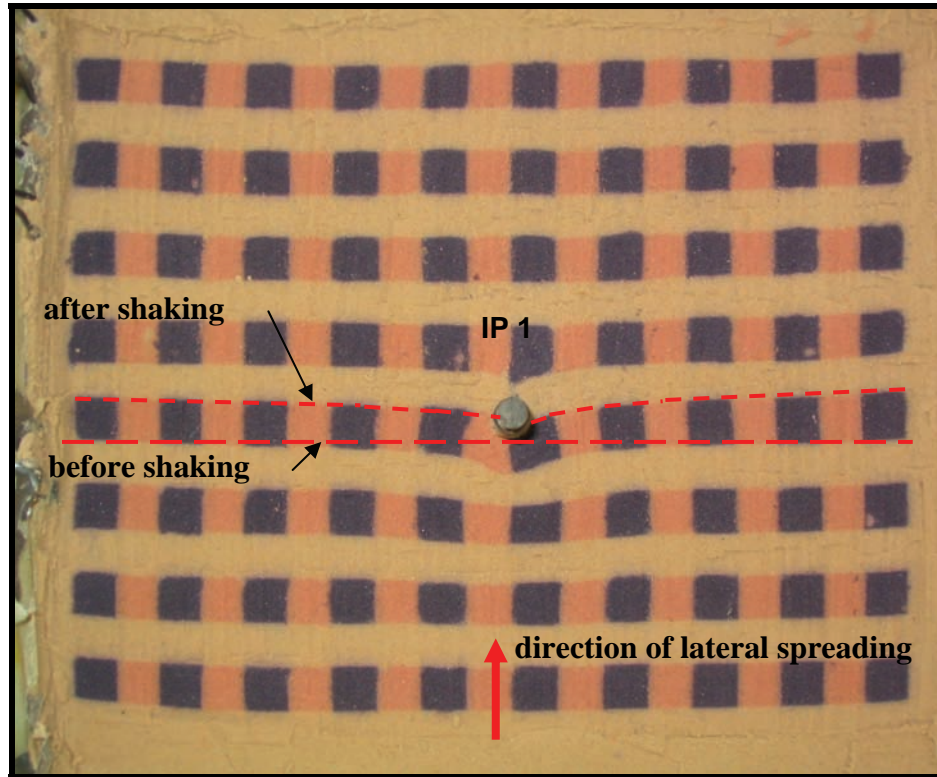
3.4.6 P-y Curve Analysis

To further investigate the pile-soil-fluid interaction during lateral spreading, p-y curves were estimated along the pile. The profiles of pile displacement were calculated as a first approximation by double integrating the bending moment distributions along the height of the pile, according to equation:

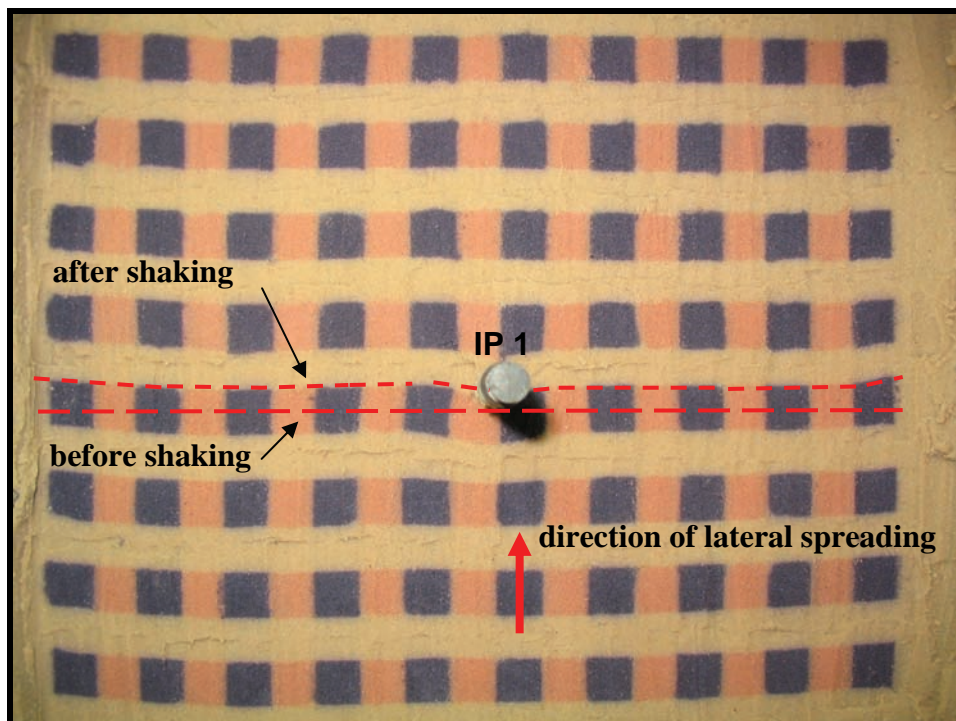
$$y_p = \iint \frac{M(h)}{EI} dh \quad [3.1]$$

where y_p is the pile lateral deformation, EI is the pile bending stiffness, M is the pile bending moment after filtering out the cyclic component, and h is the height measured from the bottom of the loose sand layer. However, the estimated lateral displacement (LD_E) at the location of the LVDTs differed considerably from the one measured with the transducers L5 and L6 (LD_M), indicating that the slightly cemented layer was not able to provide an infinite constrain. The rotation of the pile at the base of the liquefiable layer (θ_{base}) was hence estimated using the following expression:

$$\theta_{base} = \frac{LD_M - LD_E}{dh} \quad [3.2]$$



(a)



(b)

Figure 3.12: Pattern of soil displacement around the pile, (a) $z = 1$ m, (b) $z = 3$ m, Model 1x1-w

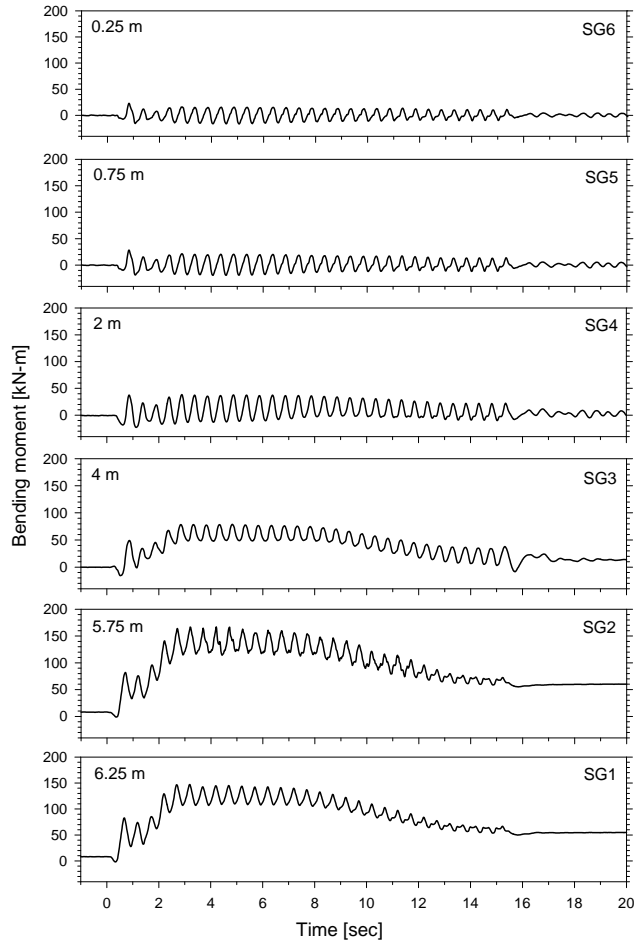


Figure 3.13: Bending moment time histories, Model 1x1-w

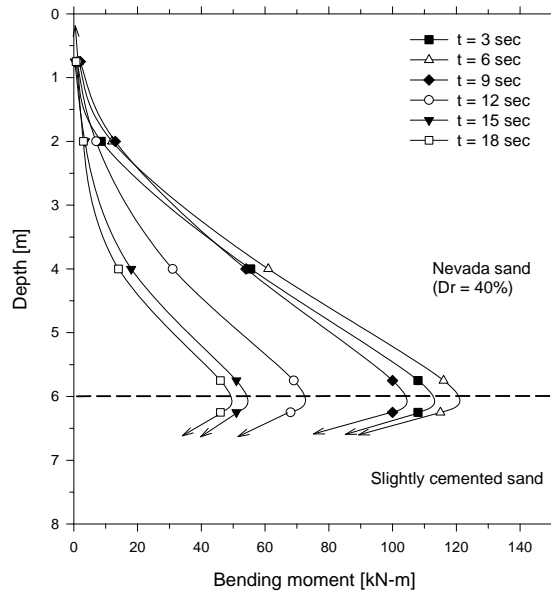


Figure 3.14: Profiles of bending moment, Model 1x1-w

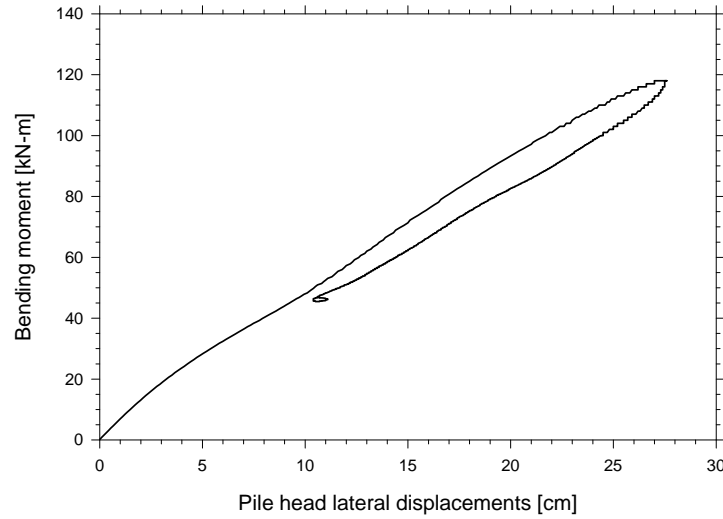


Figure 3.15: Bending moment at the base of the liquefiable layer versus pile head lateral displacement, Model 1x1-w

where dh is the distance between the bottom of the liquefiable layer and the LVDTs L5 and L6. At each time instant, the rotational stiffness provided by the bottom cemented layer was estimated by dividing the pile bending moment at the base of the liquefiable layer by the rotation of the pile (θ_{base}). Figure 3.16 shows the back-calculated rotational stiffness of the cemented sand around the pile versus the bending moment at the base of the liquefiable layer. The rotational stiffness at the beginning of the excitation was approximately 12000 kN-m/rad. As the bending moment started increasing, the cemented sand around the pile started to yield and the fixation was reduced to some extent. Probably a tiny gap developed between the cemented sand and the pile causing the rotational stiffness to drop when the pile bounced back.

Figure 3.17 shows the large difference between the measured pile head lateral displacement and the estimated displacement assuming no rotation at the base. However, the back-calculated pile head displacement agrees very well with the measured one using a constant rotational stiffness of 8000 kN-m/rad. The pile lateral displacement profiles were hence obtained considering the deformation by curvature and rotation. Finally, the relative lateral displacement profiles (y) were estimated by simple subtraction of the pile lateral displacement profiles from the free field lateral displacement profiles.

On the other hand, the lateral resistance (p) on the pile was obtained from the bending moment distributions $M(z)$, using the simple beam theory according to the equation:

$$p = \frac{\partial^2}{\partial z^2} M(z) \quad [3.3]$$

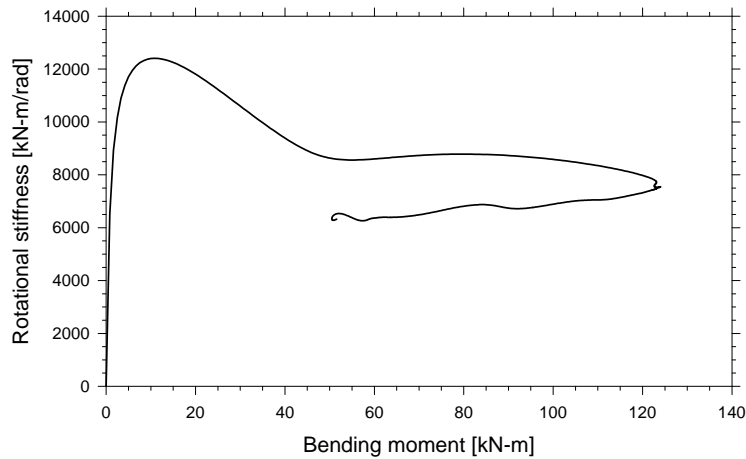


Figure 3.16: Back-calculated rotational stiffness of the cemented sand around the pile versus bending moment at the base of the liquefiable layer, Model 1x1-w

where z is the depth measured from the ground surface. The discrete measurements of bending moments along the pile were interpolated using a cubic spline interpolation technique. A cubic spline is perhaps the simplest interpolation of discrete values that can be double differentiated (Wilson, 1998); however since the spline fits every point exactly, the interpolation is affected by the dynamic component upon differentiation. Therefore, the cyclic component of the bending moment records was filtered out before obtaining the bending moment distributions.

The p - y curves shown in Fig. 3.18 indicate that the lateral resistance on the pile reached values between 5 and 15 kN/m. In the upper 3 m however, the liquefied soil was not able to sustain this pressure during the excitation, losing most of its strength and explaining the pile rebound. On the other hand, the estimated lateral resistance at a depth of 4 m did not decrease, probably due to the fact that the relative displacement (y) was smaller at deeper elevations.

3.4.7 Limit Equilibrium Analysis

A limit equilibrium analysis was conducted to estimate the liquefied soil pressure acting on the single pile. A student version of the software AVwin was used to model the pile subjected to the lateral force induced by lateral spreading. The pile was modeled with 30 elements, having a bending stiffness of 9000 kN-m^2 . The slightly cemented layer was modeled with a rotational springs at the base of the liquefiable layer, using the stiffness of 8000 kN-m/rad back-calculated in the p - y curve analysis.

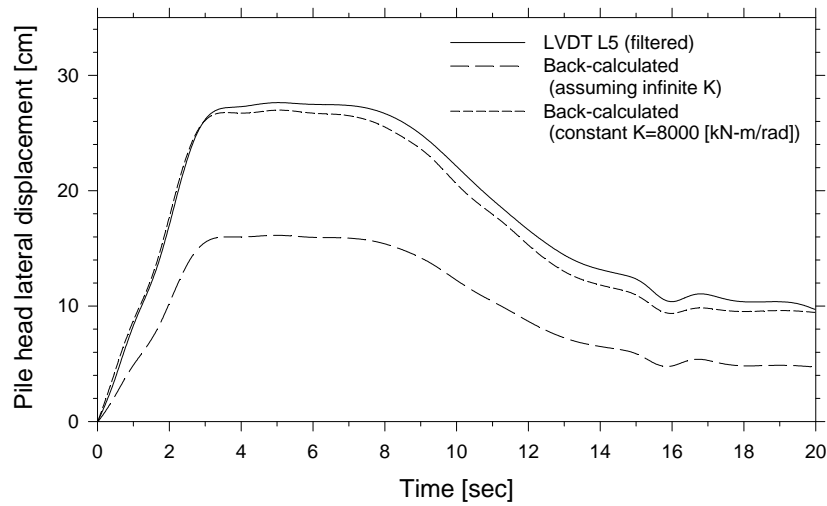


Figure 3.17: Back-calculated pile head lateral displacement, Model 1x1-w

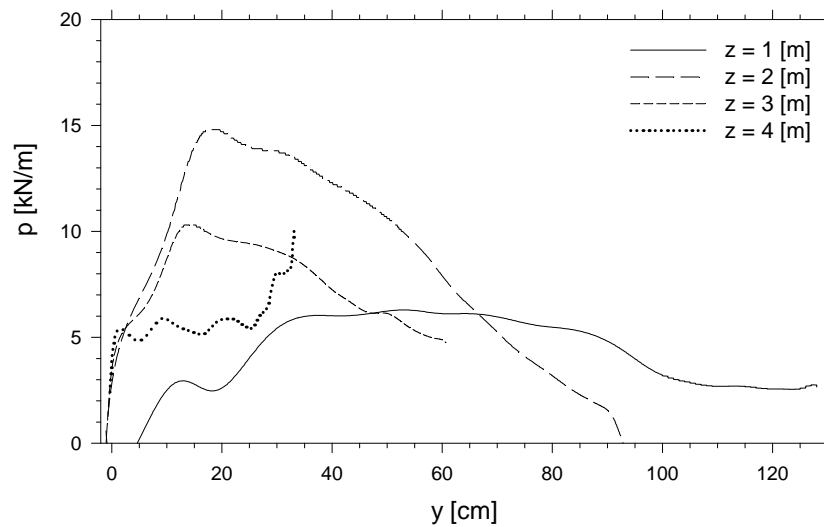


Figure 3.18: Back-calculated p-y curves, Model 1x1-w

The pattern of soil deformation in Fig. 3.12 shows that the liquefied sand moved around the pile, affecting the soil pattern close to the pile itself. Therefore, the liquefied soil pressure was assumed to act only on the pile, which represents an effective area of 3.6 m^2 , as shown in Fig. 3.19a. This pressure was assumed to be constant and independent of depth, and the force on each node was obtained by multiplying this soil pressure by the corresponding area. A liquefied soil pressure of 11.5 kN/m^2 was found to provide the best estimations of the maximum moment and pile head displacement. For a pile diameter of 0.6 m , the soil pressure corresponds to a lateral soil resistance (p) of 7 kN/m , which is within the 5 to 15 kN/m range back-calculated in the p-y

curve analysis. The liquefied soil pressure is in excellent agreement with the 10 kPa estimated by Dobry et al. (2002) based on a limit equilibrium analysis on a single pile.

The back-calculated bending moment at the base of the liquefiable layer was 125 kN-m, very close to the 120 kN-m measured during the test. The calculated pile head lateral displacement was 27 cm, one centimeter less than the maximum value measured during the test. Table 3.3 summarizes some of the parameters used in the limit equilibrium analysis, as well as measured and calculated values, showing an excellent agreement.

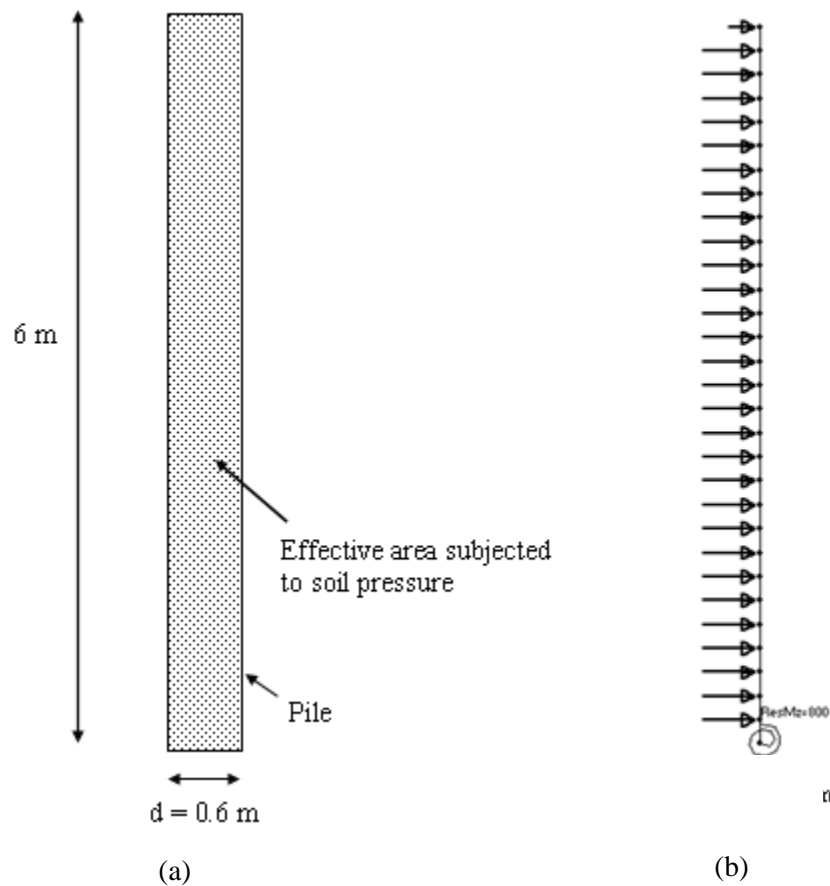


Figure 3.19: (a) Effective area subjected to liquefied soil pressure and (b) lateral view of the model used for limit equilibrium analyses, Model 1x1-w

Table 3.3: parameters used in the limit equilibrium analysis, as well as measured and calculated values, Models 1x1-w and 1x1-v

Model	Liquefied soil pressure [kN/m ²]	e_a [m ²]	Rotational stiffness [kN-m/rad]	Max. bending moment [kN-m]		Max. pile cap disp. [cm]	
				Measured	Calculated	Measured	Calculated
1x1-w	11.5	3.6	8000	120	125	28	27
1x1-v	11.5	7.6	8000	360	350	85	87

Max. bending moments measured and calculated at the base of the liquefiable layer

e_a : Effective area subjected to liquefied soil pressure

3.5 Model 1x1-v

3.5.1 Recorded Accelerations

Figure 3.20 shows the recorded input acceleration and soil acceleration time histories in the free field at different depths. As expected, the measured input acceleration (A_{in}) had a prototype amplitude of 0.3g. The acceleration records exhibit the same trends observed in Model 1x1-w, indicating the loose sand layer did liquefy during the excitation and the bottom cemented layer did not slide with respect to the base. The acceleration records on the laminar rings (Fig. 3.21) exhibit a drop in positive amplitude and spikes in the negative direction, showing a good agreement with the soil acceleration in the free field.

3.5.2 Recorded Excess Pore Pressures

The excess pore pressure records reveal that the loose sand in the free field liquefied after one or two cycles of shaking (Fig. 3.22). One of the records near the ground surface however, shows a decrease in excess pore pressure. Large shear strains developed under low confinement and a slow dissipation process appear to be responsible for this phenomenon.

Figure 3.23 shows excess pore pressures measured at a distance of 2d from the pile, in the upslope and downslope direction. Excess pore pressures recorded at a distance of 2d on one side, and next to the pile on the other side, are presented in Fig. 3.24. As expected, the records near the ground surface exhibit a reduction in excess pore pressure. The excess pore pressure close to the pile decreased up to values of the order of -10 kPa during shaking. This tendency was much stronger next to the pile, with the excess pore pressure dropping up to -20 kPa at the end of shaking. The reduction in lateral stress on the downslope side of the pile, as well as large shear strains with an undrained dilative response of the liquefied soil close to the pile, seem to have been responsible for this phenomenon. Moreover, it seems that due to the low permeability, the flow from the free field was not fast enough to dissipate the increments of negative pore pressure developed next to pile. This decrease in pore pressure appears to have stiffened the soil around

the pile, thus increasing the effective area subjected to the lateral pressure of the liquefied soil, explaining the large bending moments and pile displacement.

Figure 3.25 presents long term excess pore pressures at various depths, in the free field and next to the pile. The dissipation process in the free field is consistent with previous centrifuge tests conducted at RPI. Near the pile however, the negative excess pore pressure developed at shallow elevations generated a large vertical hydraulic gradient. This gradient was responsible for a much faster dissipation process around the pile.

3.5.3 Visualization of Pore Pressure Build-up and Dissipation

The excess pore pressure records discussed above are very revealing; however, it may not be easy to understand the complex set of data generated by the large number of pore pressure transducers by analyzing time histories of measured excess pore pressures. Therefore, a visual animation was created to further analyze the dynamic response of the model, particularly the pore pressure build-up and dissipation around the pile. The software used was Tecplot 10, a commercial tool with extensive 2-D and 3-D capabilities for visualizing data.

The 2-D visualization involves pore pressure ratios and lateral displacement of the soil and pile in the longitudinal direction. The soil lateral displacement was obtained by interpolating the LVDT measurements, whereas the pile deformation was estimated considering the curvature and rotation following the procedure presented below in section 3.5.7. These displacements were amplified by a factor of 2 for visual clarity. The field of pore pressure ratio was obtained by interpolating the measurements provided by 20 pore pressure transducers, located far from the pile (P1 - P4, P21 – P24), close to the it (P5 – P9, P17 – P20), and next to the it (P9 – P12).

Figure 3.26 shows snapshots of the animation at selected time instants during the excitation. After one second the whole loose sand layer was practically liquefied, except near the surface where negative excess pore pressure developed and sustained during all the excitation. These very low pore pressures, particularly around the pile, must have stiffened the liquefied soil in this zone. On the other hand, these negative excess pore pressures created a large vertical gradient close to the pile. Figure 3.27 shows snapshots of the animation after the shaking stopped. The dissipation process started around the pile, with the free field still being liquefied. The expelled water ended up liquefying the soil on the downslope side of the pile, as shown in Fig. 3.27b.

Figure 3.28 shows the ground surface, after carefully removing the fluid above it. Unexpectedly, several sand boils developed on the downslope side of the pile, even though the model was fully saturated. This phenomenon validates the hypothesis of a non-liquefied crust developed close to the pile. As the water started being expelled, it broke through this crust carrying some of the colored sand that was placed below the surface. The snapshots in Fig. 3.27 clearly illustrate that the dissipation process was not only in the vertical direction, but also toward the pile; process that took more than five minutes, confirming the low permeability of the model.

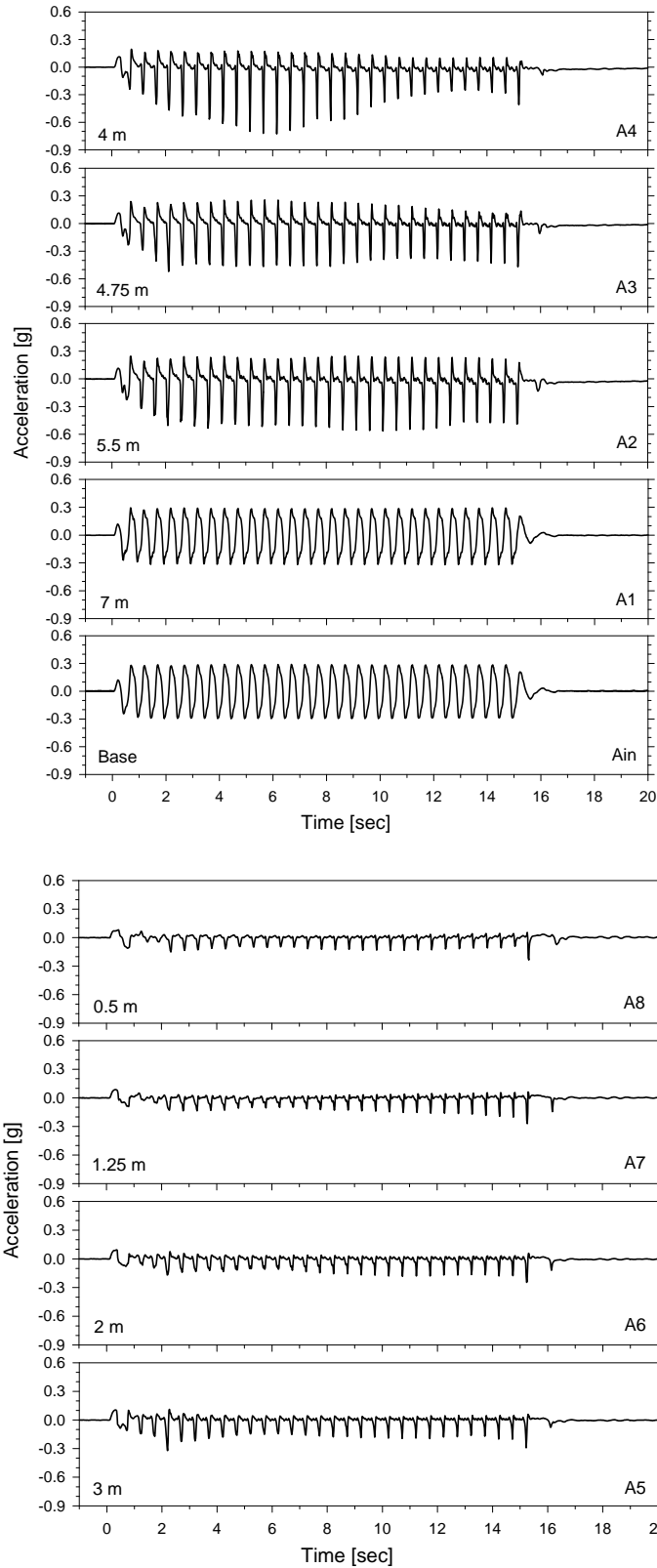


Figure 3.20: Soil acceleration time histories in the free field, Model 1x1-v

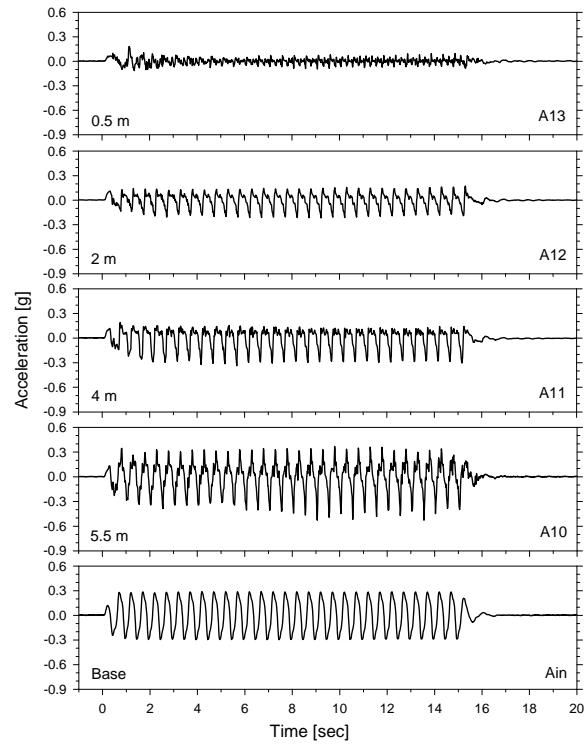


Figure 3.21: Accelerations recorded on the laminar rings, Model 1x1-v

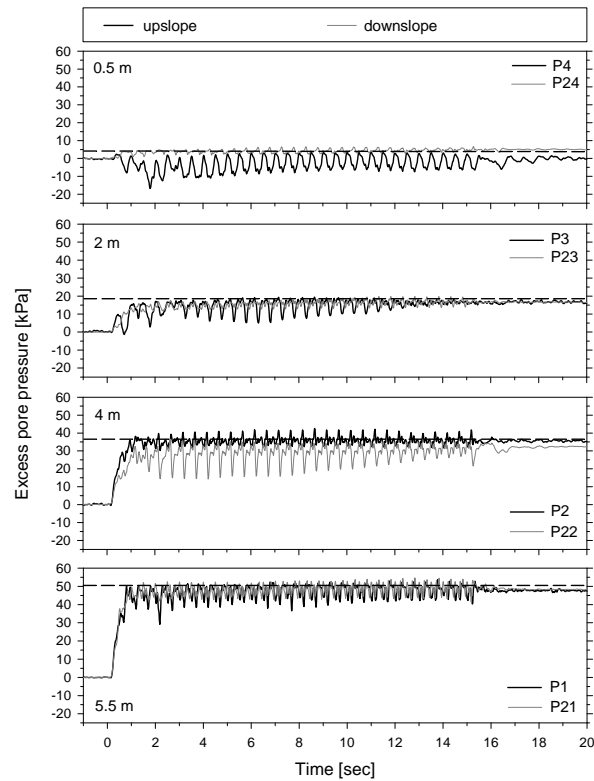


Figure 3.22: Excess pore pressure time histories in the free field, the dashed lines correspond to initial liquefaction, Model 1x1-v

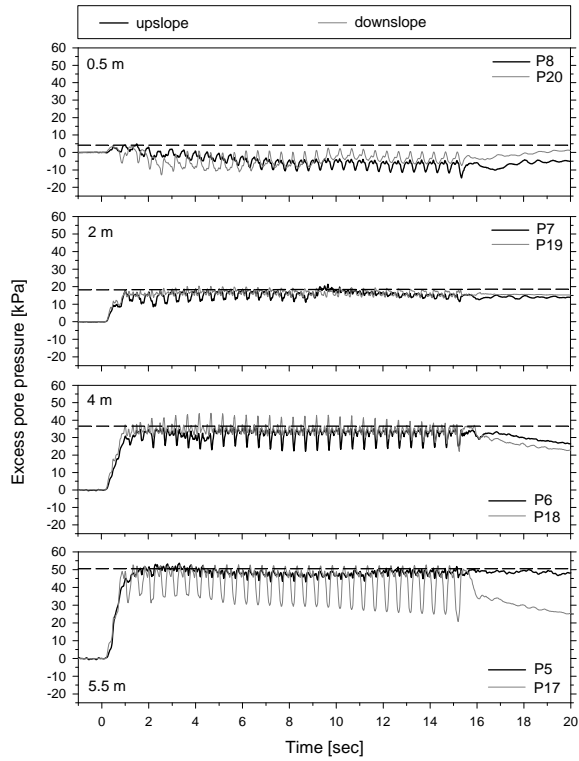


Figure 3.23: Excess pore pressure time histories close to the pile, upslope and downslope, Model 1x1-v

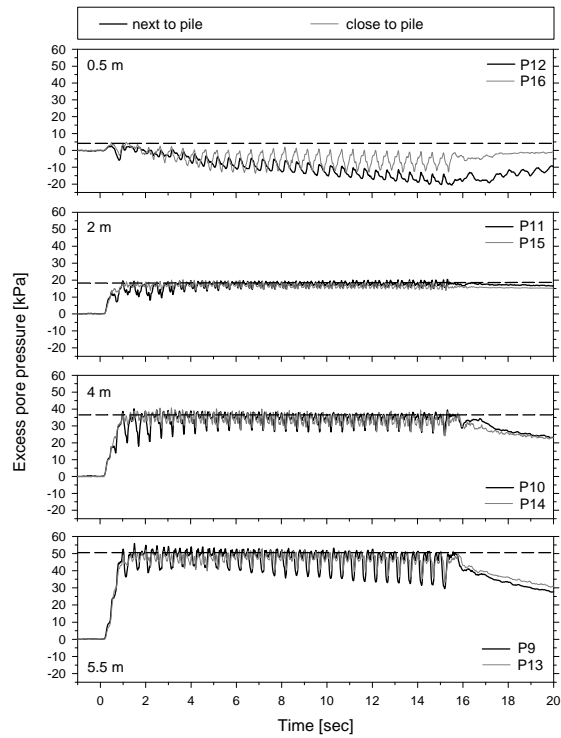


Figure 3.24: Excess pore pressure time histories close and next to the pile, Model 1x1-v

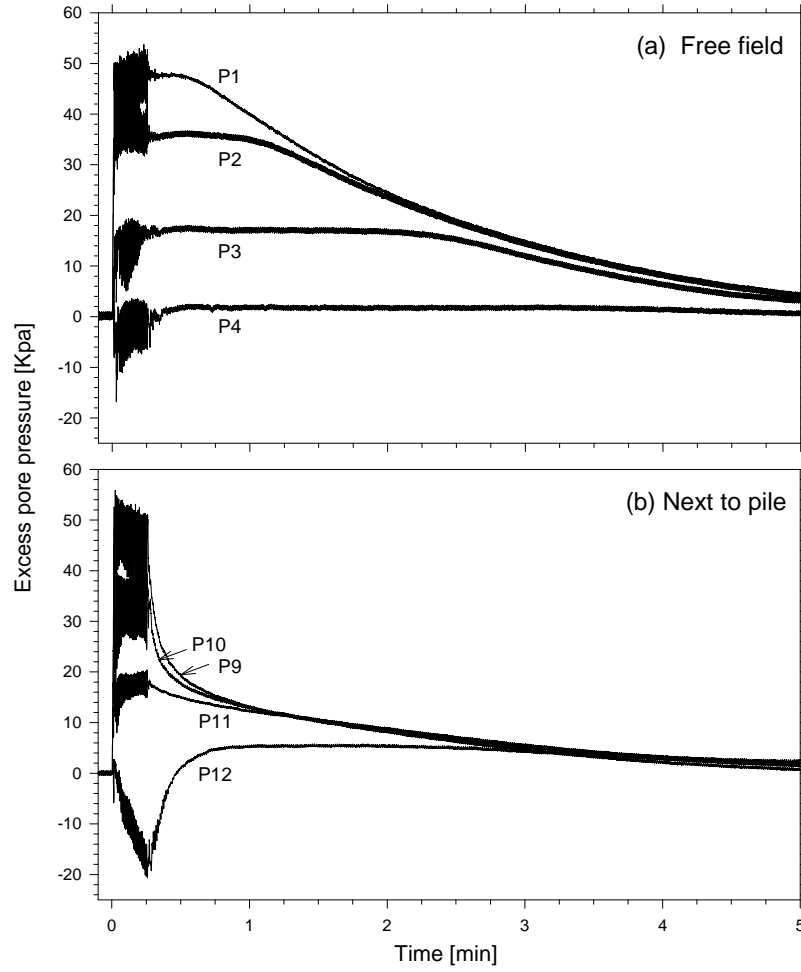
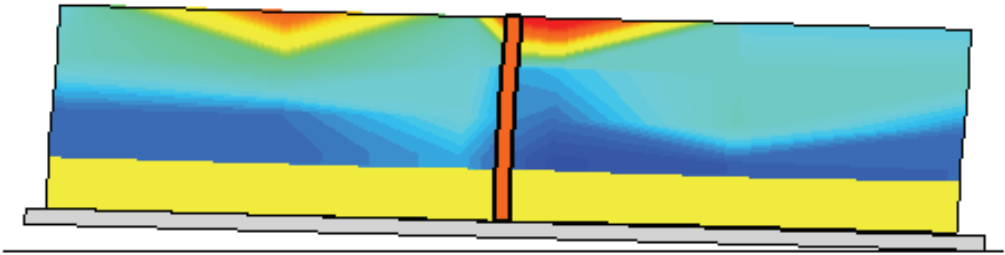
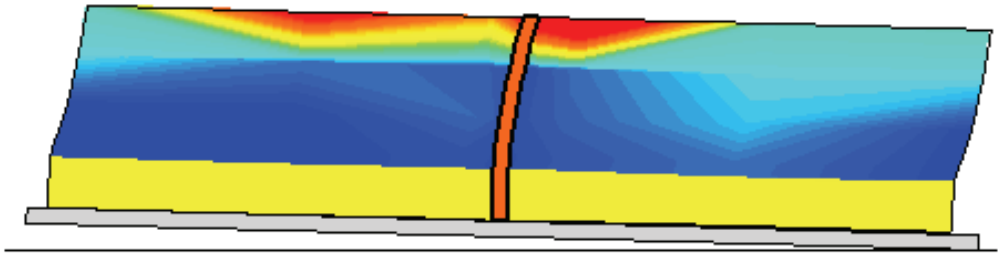


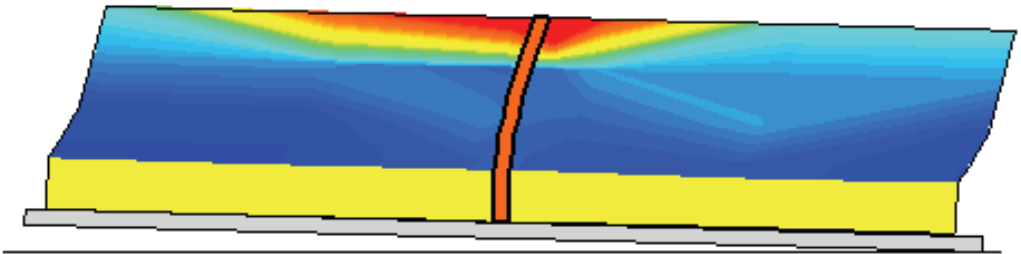
Figure 3.25: Long term excess pore pressure time histories, (a) free field and (b) next to the pile, Model 1x1-v



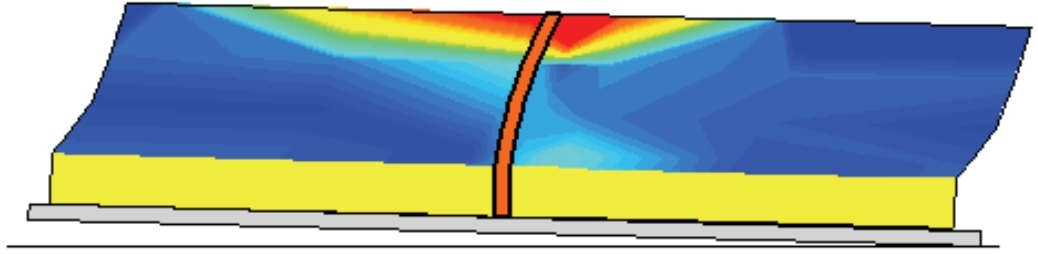
(a) $t = 1$ sec



(b) $t = 5$ sec



(c) $t = 10$ sec



(d) $t = 16$ sec

Figure 3.26: Short term excess pore pressure ratios and lateral displacements for selected time instants, Model 1x1-v

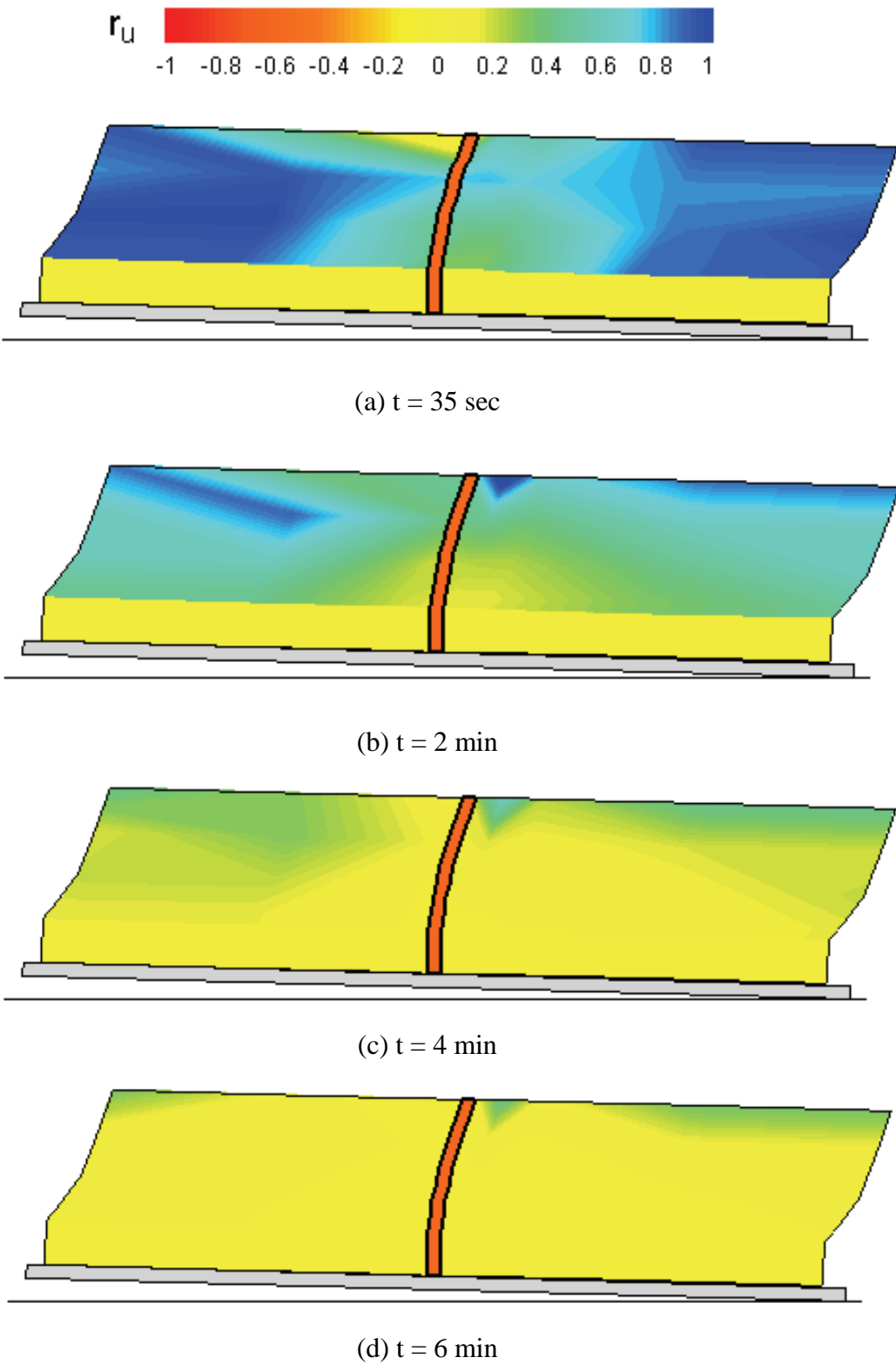
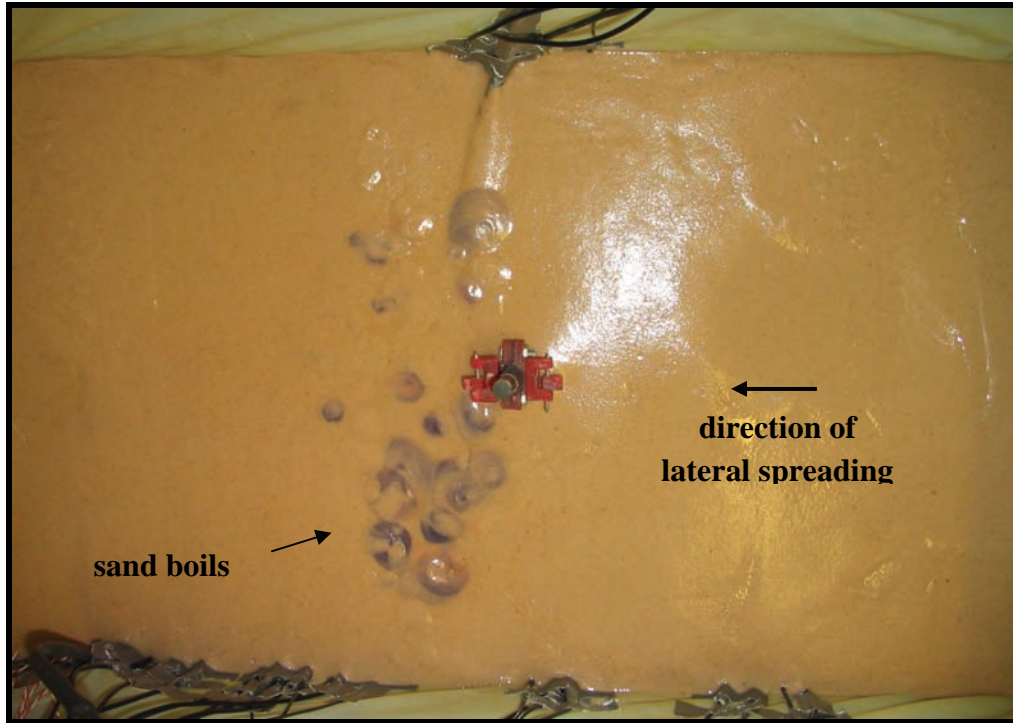
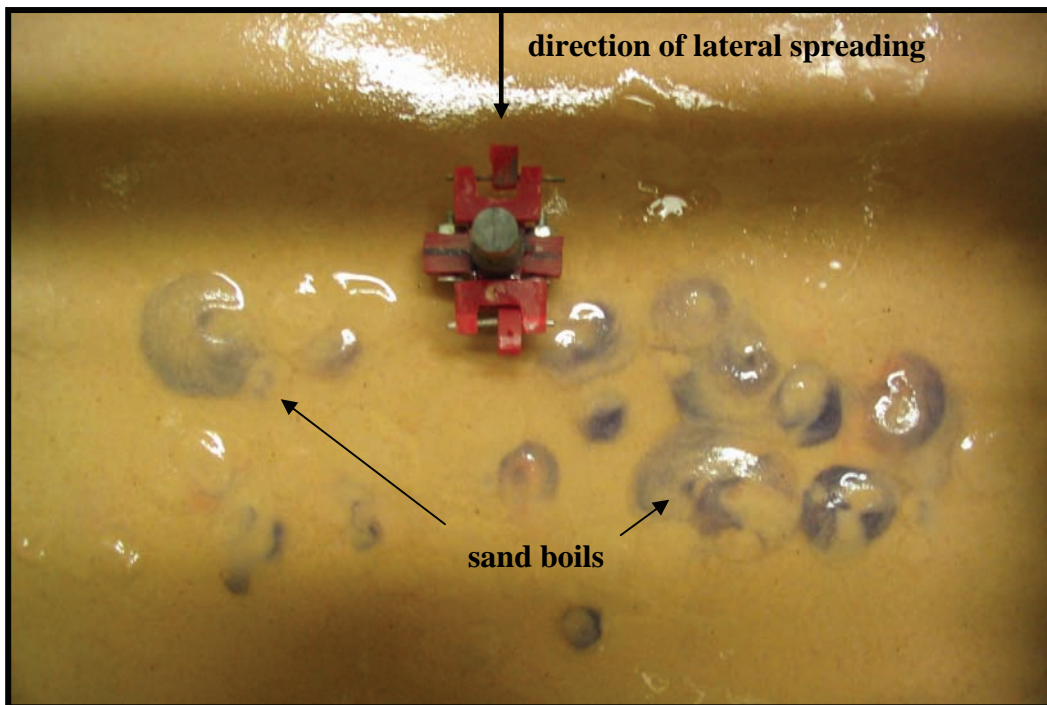


Figure 3.27: Long term excess pore pressure ratios and lateral displacements for selected time instants, Model 1x1-v



(a)



(b)

Figure 3.28: Sand boils on the downslope side of the pile, (a) far view, (b) close view, Model 1x1-v

3.5.4 Recorded Lateral Displacements

The recorded soil lateral displacement in the free field (Fig. 3.29) shows that the liquefied layer displaced gradually during shaking. Once the excitation ended, the lateral displacement stopped immediately even though the loose sand was still liquefied. This phenomenon is consistent with previous centrifuge tests (Abdoun, 1997; Pamuk, 2004), and confirms that the inertia forces due to shaking are necessary for the ground deformation to continue (Okamura et al., 2001). The single pile displaced laterally during shaking without ever bouncing back, reaching a maximum displacement at the end of shaking of about 85 cm.

The profiles of soil lateral displacement in the free field were obtained by interpolating the LVDT measurements, after filtering out the cyclic component (Fig. 3.30). As soon as the loose sand liquefied at the beginning of shaking, the deposit started moving downslope, with the ground surface reaching a maximum displacement of approximately 140 cm at the end of shaking.

3.5.5 Pattern of Soil Displacement around the Single Pile

Grids of colored sand were placed at intermediate depths to observe the pattern of soil displacement around the pile. Figure 3.31 shows pictures of the soil condition at two different depths, after carefully removing the soil on top. The liquefied sand moved around the pile, affecting the soil pattern up to a considerable distance at both sides of the pile. Therefore, the characteristic width perpendicular to the flow was much larger than the diameter of the piles. The comparison of soil deformation patterns at different elevations evidences a larger area of influence around the pile at the shallower depth.

3.5.6 Recorded Bending Moments

Figure 3.32 shows prototype bending moments measured in the single pile. The profiles of bending moments are shown in Fig. 3.33, after filtering out the cyclic component. The maximum moment at any given time occurred close to the base of the liquefied layer, reaching a maximum value at the end of the excitation, being consistent with the pile displacement.

Figure 3.34 shows the measured bending moment at the base of the liquefiable layer versus the measured pile head lateral displacement, after filtering out the cyclic component. The linear relationship between bending moment and pile displacement evidences the linear behavior of the pile-fixation system.

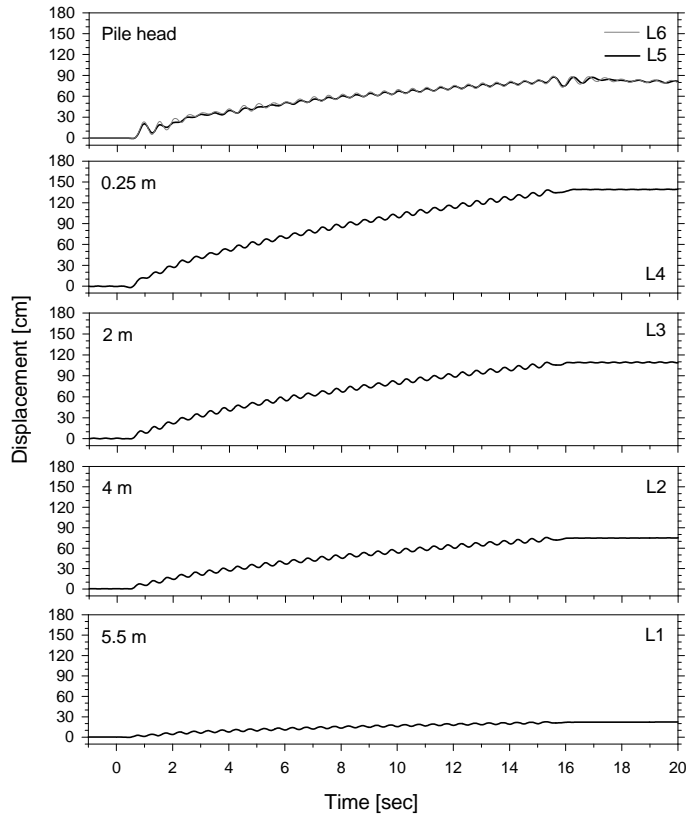


Figure 3.29: Lateral displacement time histories, Model 1x1-v

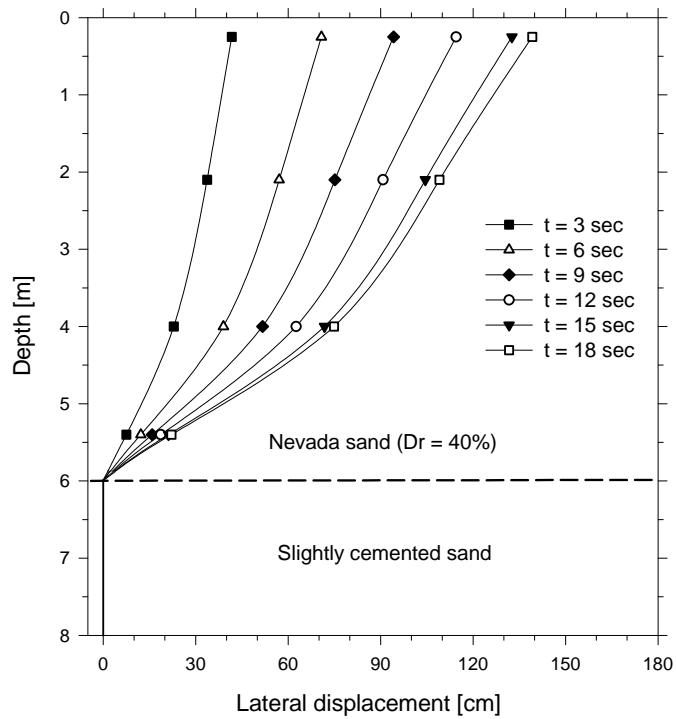
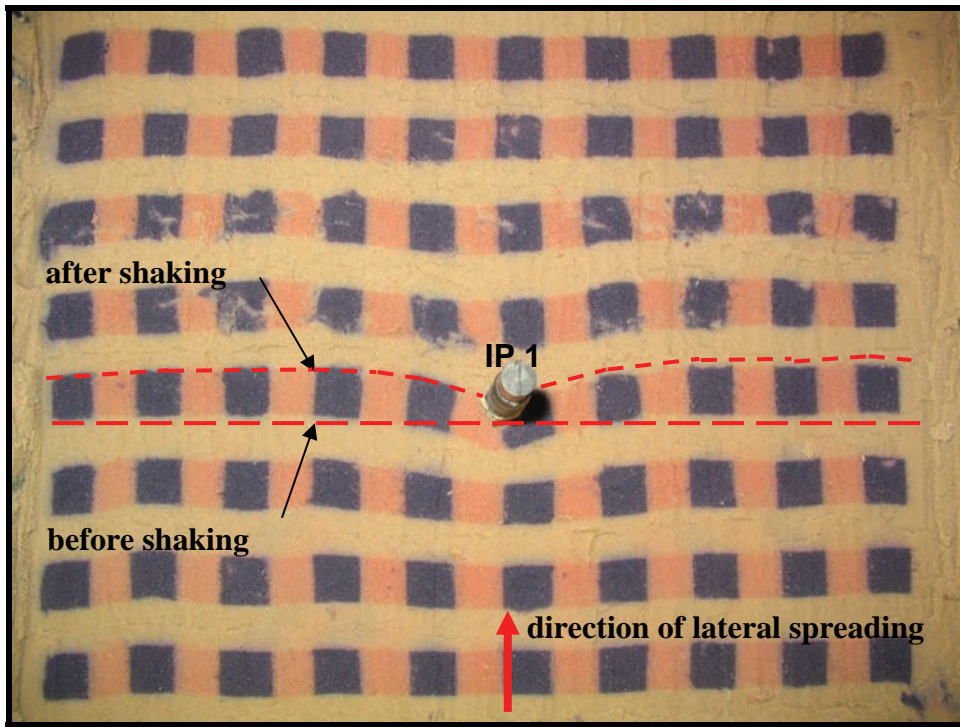
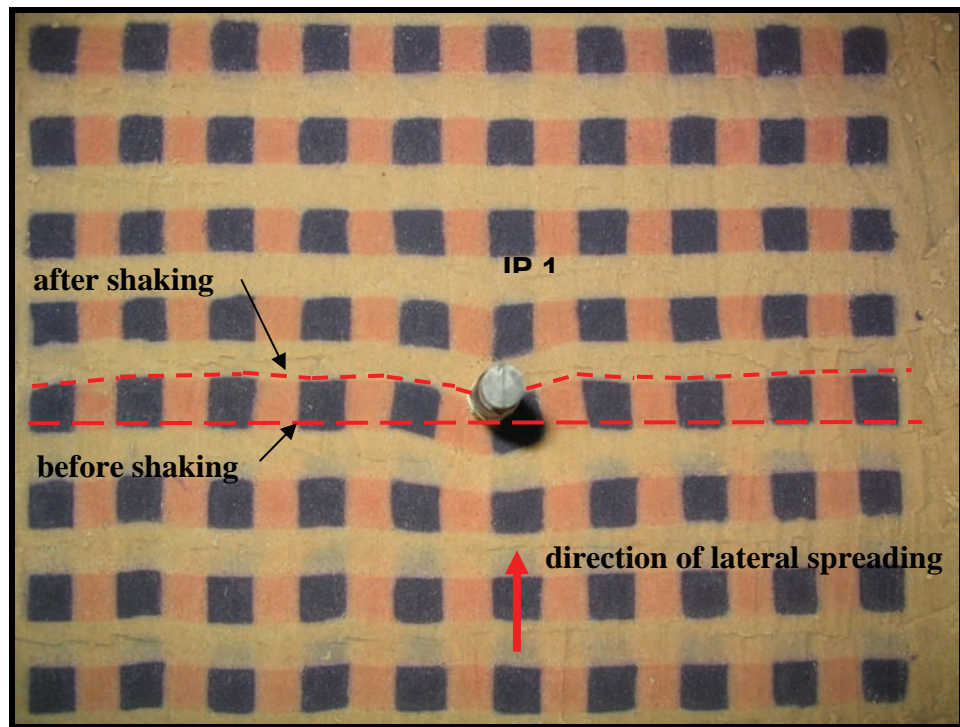


Figure 3.30: Profiles of soil lateral displacement in the free field, Model 1x1-v



(a)



(b)

Figure 3.31: Pattern of soil displacement around the pile, (a) $z = 1$ m, (b) $z = 3$ m, Model 1x1-v

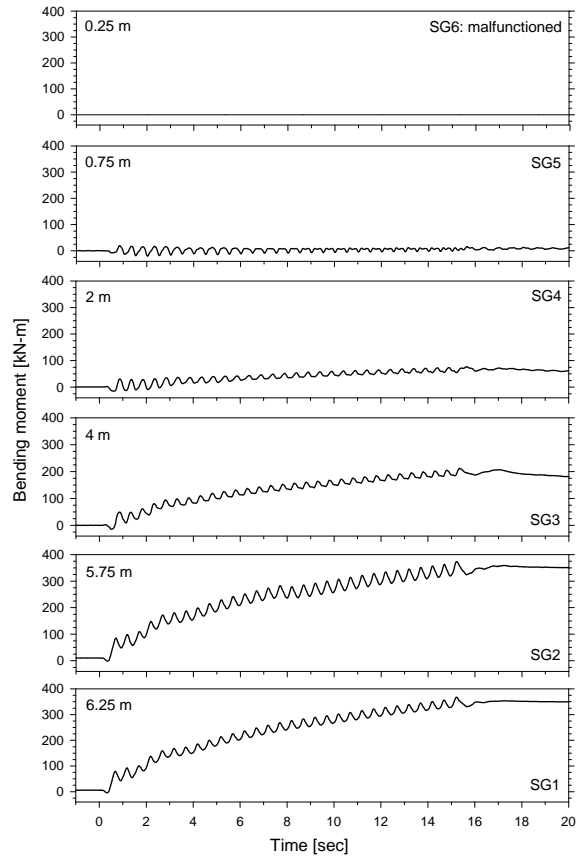


Figure 3.32: Bending moment time histories, Model 1x1-v

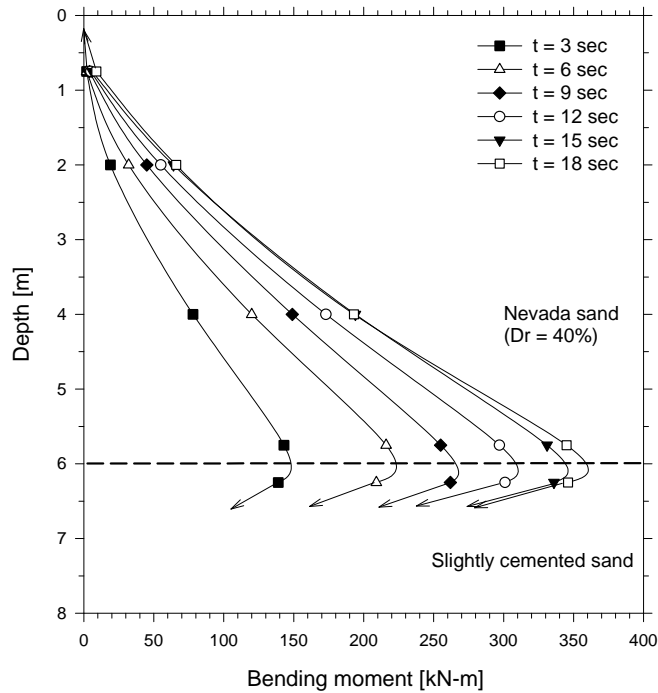


Figure 3.33: Profiles of bending moment, Model 1x1-v

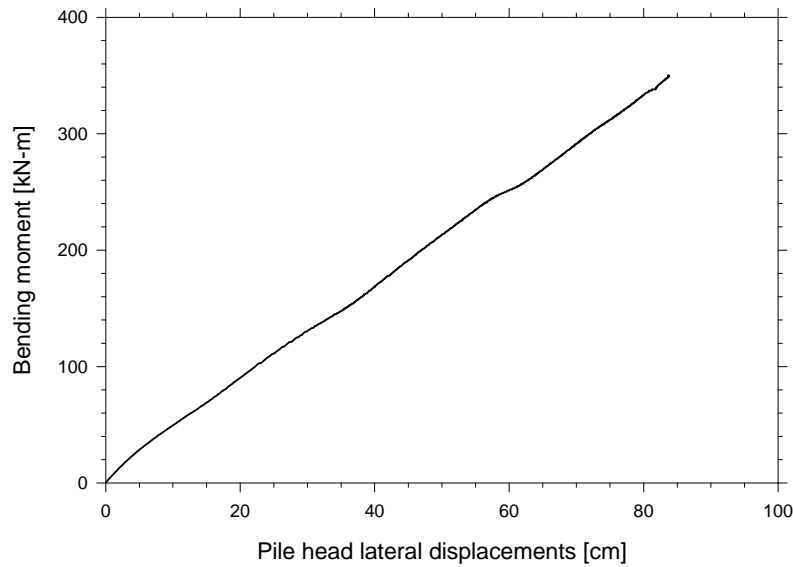


Figure 3.34: Bending moment at the base of the liquefiable layer versus pile head lateral displacement, Model 1x1-v

3.5.7 P-y Curve Analysis

The profiles of pile displacement were calculated as a first approximation by double integrating the bending moment distributions along the height of the pile, according to equation 3.1. Like in Model 1x1-w (Section 3.4.6), the estimated lateral displacement at the location of the LVDTs differed considerably from the one measured with the transducers L5 and L6, indicating that the slightly cemented layer was not able to provide an infinite constrain. The rotation of the pile at the base of the liquefiable layer (θ_{base}) was hence estimated using the equation 3.2. At each time instant, the rotational stiffness provided by the bottom cemented layer was estimated dividing the pile bending moment at the base of the liquefiable layer by the rotation of the pile (θ_{base}). Figure 3.35 shows the back-calculated rotational stiffness of the cemented sand around the pile versus the bending moment at the base of the liquefiable layer.

Ignoring the large value generated at the beginning of shaking, the rotational stiffness in the elastic range was approximately 14000 kN-m/rad. As the bending moment started increasing, the cemented sand around the pile lost part of its strength and the rotational stiffness decreased and stabilized at about 8000 kN-m/rad.

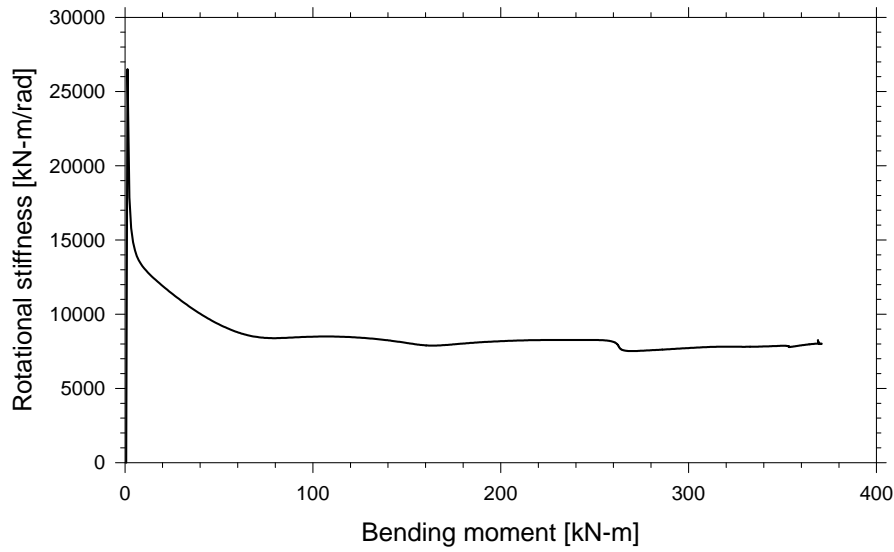


Figure 3.35: Back-calculated rotational stiffness of the cemented sand around the pile versus bending moment at the base of the liquefiable layer, Model 1x1-v

Figure 3.36 shows the large difference between the measured pile head lateral displacement and the estimated displacement assuming no rotation at the base. However, the back-calculated pile head displacement fits exactly the measured one if a constant rotational stiffness of 8000 kN-m/rad is considered, which is in excellent agreement with the value estimated in the p-y curve analysis in Model 1x1-w. The pile lateral displacement profiles were hence obtained considering the deformation by curvature and rotation. Finally, the relative lateral displacement profiles (y) were estimated by simple subtraction of the pile lateral displacement profiles from the free field lateral displacement profiles.

On the other hand, the lateral resistance (p) on the pile was obtained from the bending moment distributions $M(z)$, using equation 3.3. The p-y curves shown in Fig. 3.37 indicate that below 2 m the lateral resistance reached approximately 10 kN/m, being consistent with estimated values in Model 1x1-w. Near the ground surface however, the resistance of the liquefied soil increased almost linearly up to about 45 kN/m at the end of shaking. This huge lateral pressure near the surface, associated to the decrease in excess pore pressure, would explain the large bending moment and pile lateral displacement.

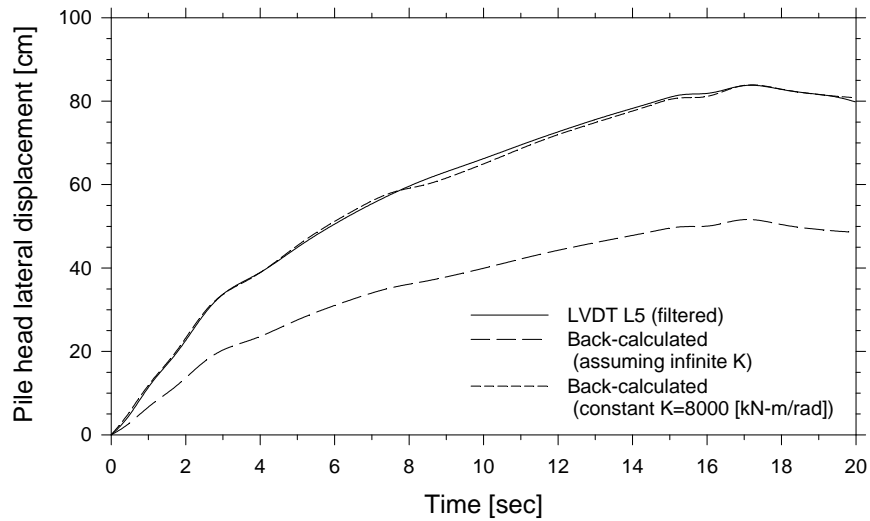


Figure 3.36: Back-calculated pile head lateral displacement, Model 1x1-v

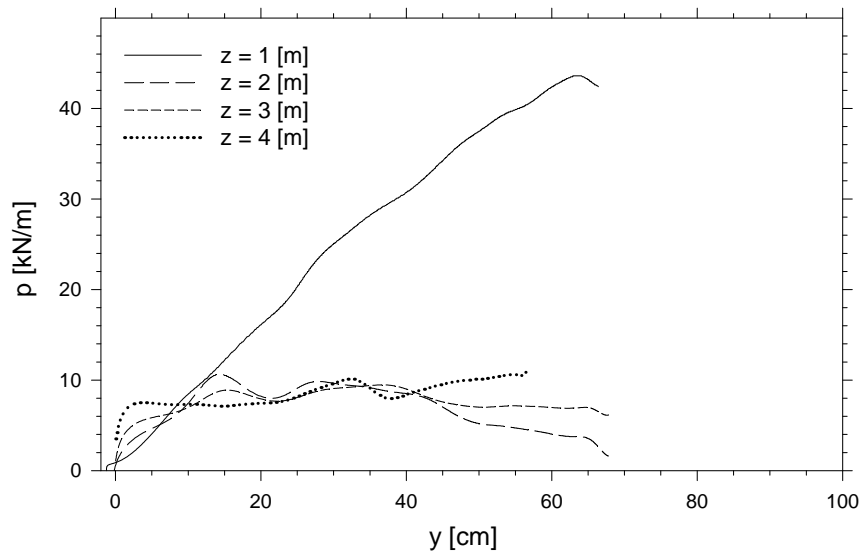


Figure 3.37: Back-calculated p-y curves, Model 1x1-v

3.5.8 Limit Equilibrium Analysis

A limit equilibrium analysis was conducted to back-calculate the maximum measured bending moment and pile head displacement. A student version of the software AVwin was used to model the single pile subjected to the lateral force induced by lateral spreading. The pile was modeled with 30 elements, having a bending stiffness of $9000 \text{ kN}\cdot\text{m}^2$. The slightly cemented layer was modeled with a rotational springs at the base of the liquefiable layer, using the stiffness

of 8000 kN-m/rad back-calculated in the previous section. The force on each node was obtained by multiplying the soil pressure by the corresponding effective area.

The liquefied soil pressure used in the analysis was the 11.5 kN/m² estimated in Model 1x1-w. This pressure corresponds to a lateral resistance (p) of 7 kN/m, which agrees very well with the back-calculated values below 2 m depth, as shown in Fig. 3.37. The pattern of soil displacement (Fig. 3.31) shows that the liquefied sand moved around the pile, affecting the soil pattern up to a considerable distance at both sides of the pile, especially near the ground surface. Therefore, at shallow depths, the characteristic width perpendicular to the flow was much larger than the diameter of the pile. This response is consistent with the huge lateral resistance obtained in the p - y curve analysis at a depth of 1 m. Figure 3.38c shows a snapshot of a visual animation of the model in the transversal direction. The negative excess pore pressures (in red color) developed next to the pile in the upper 2 m must have stiffened the soil in a conical zone. Therefore, considering the triangular area subjected to the liquefied soil pressure shown in Fig. 3.38a, the estimated maximum bending moment and pile head lateral displacement agree very well with the measured values. The back-calculated bending moment was 405 kN-m, close to the 425 kN-m measured at the base of the liquefiable layer. The calculated pile cap lateral displacement was 90 cm, very similar to the 85 cm measured during the test. Table 3.3 summarizes some of the parameters used in the limit equilibrium analysis, as well as measured and calculated values.

3.6 Comparison of Free Field Results between Model 1x1-w and 1x1-v

This section compares some of the free field results obtained in Models 1x1-w and 1x1-v, such as: soil accelerations, excess pore pressures and soil lateral displacements. A detailed comparison of the recorded results from all centrifuge tests as well as a discussion of the effect of soil permeability on pile foundation response to lateral spreading is presented in chapter 6. The centrifuge models 1x1-w and 1x1-v simulated the response of a single pile embedded in a two layer soil profile subjected to lateral spreading. The only difference between these models is that the first one was saturated with water, while the second one was saturated with a viscous fluid, simulating hence deposits of very different permeability in the field. A sketch of the setup and instrumentation used in both cases is presented in Fig. 3.2.

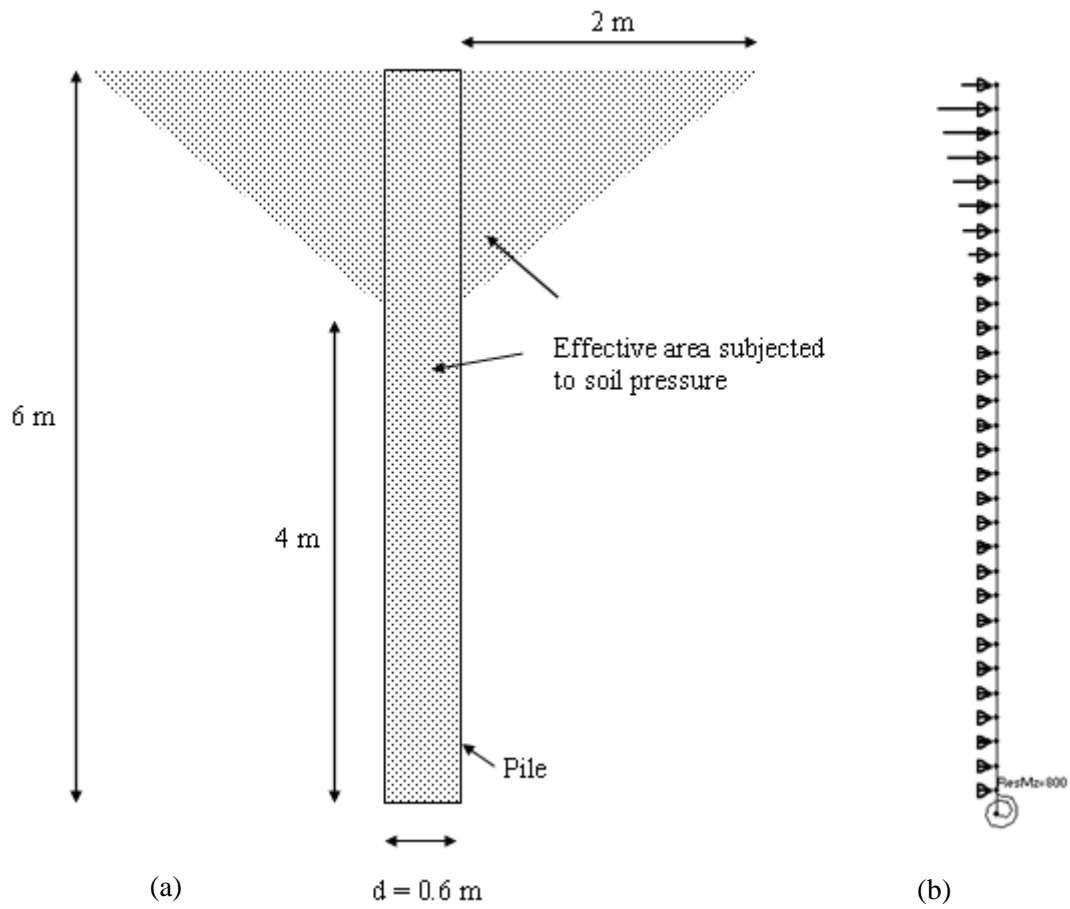


Figure 3.38: (a) Effective area subjected to liquefied soil pressure, (b) lateral view of model used for limit equilibrium analyses, (c) snapshot of excess pore pressures during shaking taking from visualization in transversal direction, Model 1x1-v

3.6.1 Comparison of Free Field Soil Accelerations

Figure 3.39 compares the free field soil accelerations measured in both centrifuge tests. The measured input accelerations indicate that both models were subjected to the same base excitation, which shows the excellent repeatability and validates the direct comparison between the tests. The soil acceleration records in the loose sand layer exhibit in both cases a drop in positive amplitude after the first cycle of shaking due to the liquefaction process and dynamic isolation of the shallower layers. These records also contain large negative spikes in each cycle due to the dilative behavior of the saturated loose layer during lateral spreading, with the spikes being slightly larger in Model 1x1-w. Nevertheless, the results indicate that soil acceleration in the free field was not significantly affected by the fluid viscosity or soil permeability.

3.6.2 Comparison of Excess Pore Pressures

Figure 3.40 compares the excess pore pressures measured in the free field in Models 1x1-w and 1x1-v. In both tests, the records show that the sand in the free field liquefied after about one or two cycles of shaking. In Model 1x1-v however, the excess pore pressure near the ground surface dropped to values below zero, displaying large fluctuations. Large shear strains developed under low confinement and a slow dissipation process appear to be responsible for this phenomenon.

Figure 3.41 compares the excess pore pressures measured next to the single pile. Near the ground surface, there was practically no excess pore pressure in the model saturated with water. However in Model 1x1-v, this tendency was much stronger, with the excess pore pressure decreasing gradually to values way below zero. The reduction in lateral stress on the downslope side of the pile, as well as the large shear strains with an undrained dilative response of the liquefied soil close to the pile, seem to have been responsible for this phenomenon. At deeper elevations, the records indicate that the soil close to the pile was liquefied during most of the excitation. Therefore, the records indicate that the excess pore pressure build-up near the ground surface, in the free field and close to the pile, is significantly affected by the soil permeability.

As expected, the dissipation process was highly dependent on the soil permeability. While it took about five minutes in Model 1x1-v, it took only a few seconds in the water-saturated Model 1x1-w. The process of dissipation in Model 1x1-w was mainly vertical, whereas in Model 1x1-v, the water in the free field moved toward the surface and toward the pile to compensate for the negative and low excess pore pressure in this area.

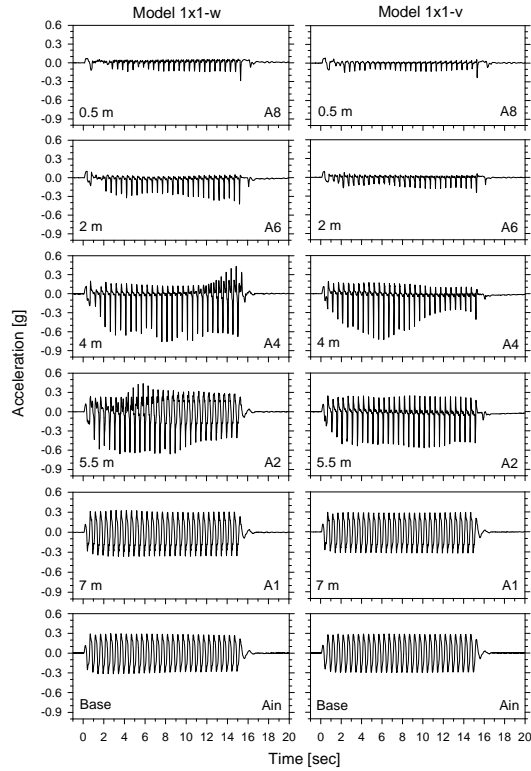


Figure 3.39: Comparison of soil acceleration in the free field between Model 1x1-w and 1x1-v

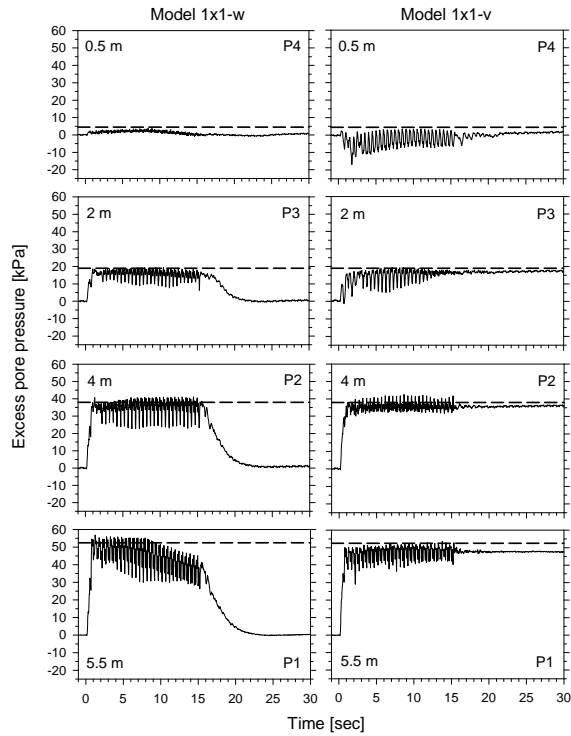


Figure 3.40: Comparison of excess pore pressure in the free field between Model 1x1-w and 1x1-v

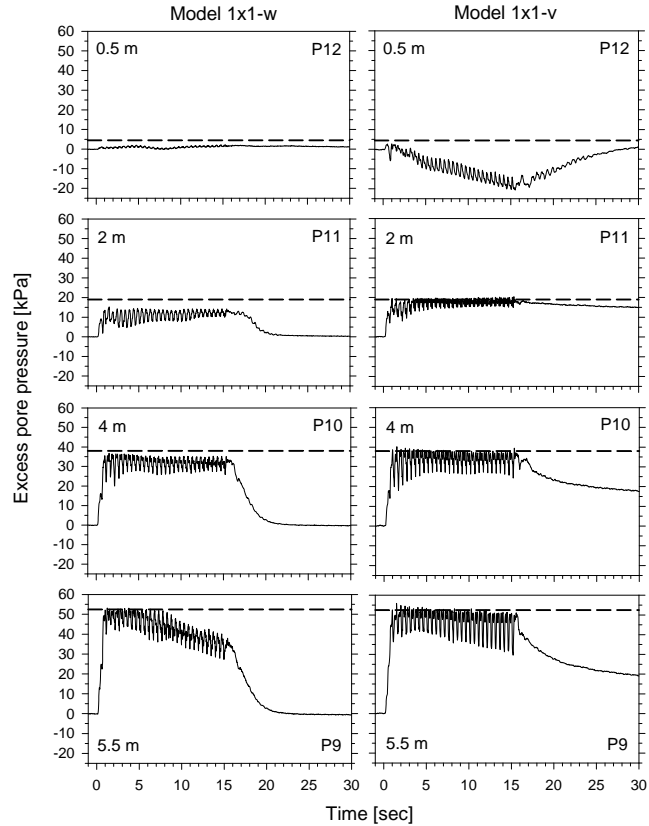


Figure 3.41: Comparison of excess pore pressure next to the pile between Model 1x1-w and 1x1-v

3.6.3 Comparison of Free Field Lateral Displacements

Figure 3.42 compares the free field lateral displacement profiles between Models 1x1-w and 1x1-v. In both tests, the loose layer started moving downslope as soon as it liquefied at the beginning of shaking, with the maximum displacement at all times measured at the ground surface. Even though the ground surface deformation at all times was very similar, the profiles tended to have a different shape. In the water-saturated model, the shear strains tended to increase with height, whereas in Model 1x1-v the shear strains tended to decrease with height. The loose sand layer in Model 1x1-w was so permeable that the dissipation process started before the end of shaking, as shown in Fig. 3.41. This reduction in pore pressure must have increased the soil stiffness near the bottom of the sand layer, explaining the lower shear strains compared to the ones in Model 1x1-v. On the other hand, the reduction in pore pressure near the surface in the Model 1x1-v appears to have been responsible for the low shear strains developed at shallow elevations.

The cemented sand in both models did not experience permanent displacement and acted as a solid layer during the excitation, as illustrated by its acceleration record being very similar to the input.

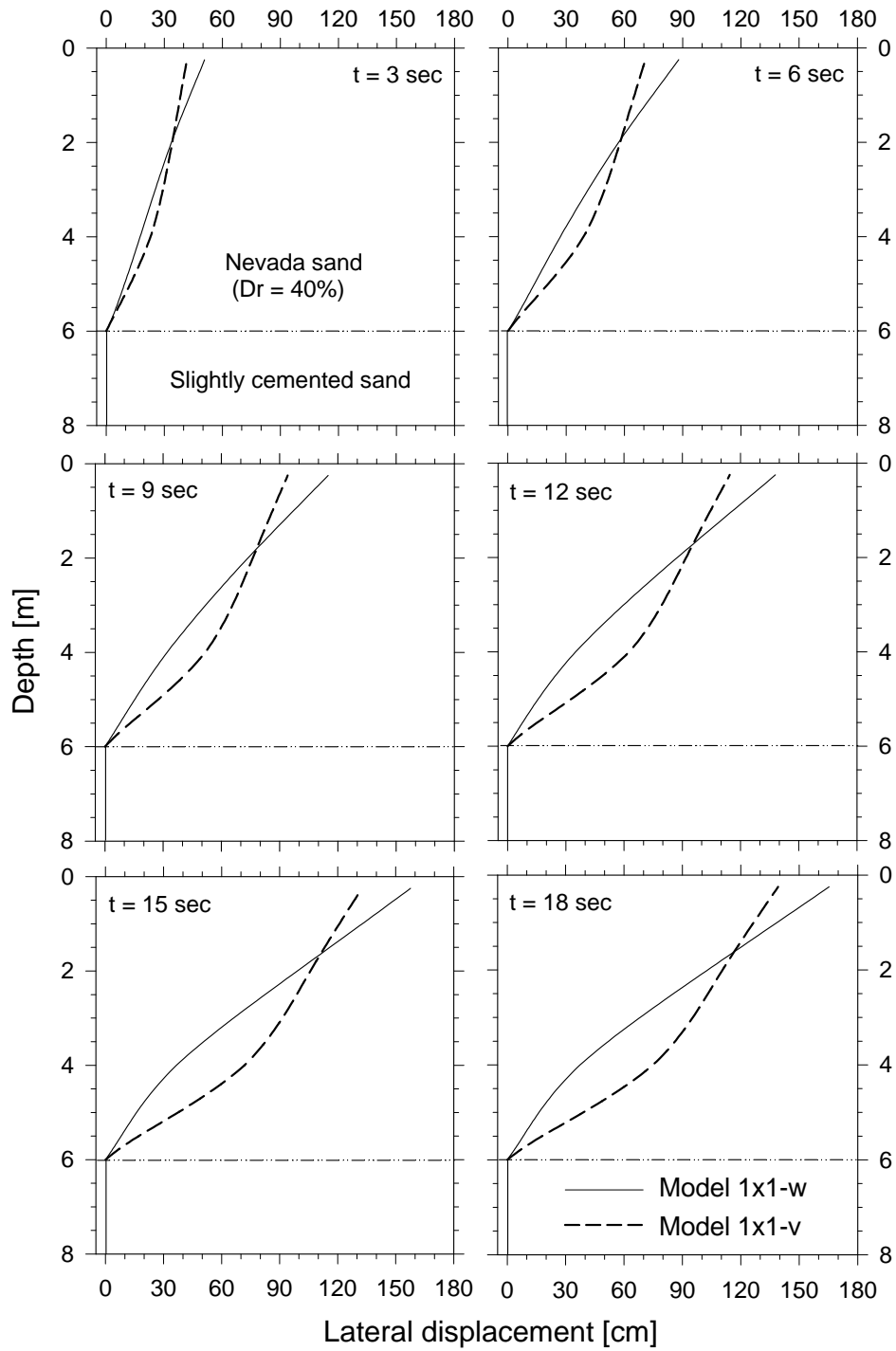


Figure 3.42: Comparison of free field lateral displacement profiles between Model 1x1-w and 1x1-v

CHAPTER 4
EFFECT OF SOIL PERMEABILITY ON 3x1 PILE GROUP + SINGLE PILE
RESPONSE TO LATERAL SPREADING

4.1 Introduction

In the previous chapter, the results revealed that the liquefied soil permeability played an extremely important factor in the pile group response subjected to lateral spreading. In Model 1x1-w (saturated with water) the single pile reached a maximum lateral displacement and bending moments and then bounced back during the excitation, being consistent with previous centrifuge tests conducted at RPI. In Model 1x1-v (saturated with viscous fluid) however, the single pile reached a maximum displacement and bending moments at the end of shaking, without ever bouncing back. The bending moments and lateral displacement were 3 times larger than those measured in Model 1x1-w, clearly illustrating the uncertainty and poor understating of the complex behavior of the liquefied soil in the vicinity of the foundations (Table 4.1).

Table 4.1: Testing properties of centrifuge Models 3x1-w and 3x1-v

Model	Pile configuration	# of piles	# of instrument. piles	Pile cap	# of layers	Fluid viscosity (μ_w)
3x1-w	(3 x 1) + 1	4	3	in 3 x 1	2	1
3x1-v	(3 x 1) + 1	4	3	in 3 x 1	2	40

This chapter presents in detail the results of two centrifuge tests conducted to further investigate the pile foundation response to lateral spreading. These models simulate a 3x1 pile group and a single pile embedded in a two layer soil system, as shown in Fig. 4.1. The profile is the same one used in Models 1x1-w and 1x1-v, consisting of a liquefiable layer on top of a nonliquefiable layer. The slightly inclined models were excited by practically the same input motion, so the results can be compared. Pore pressure transducers were located next to the pile group (Fig. 4.1b) to elucidate the soil-fluid interaction next to the piles. Besides, grids of colored sand were placed at an intermediate elevation to observe the pattern of soil deformation around the piles. Once again, the only difference between both models is that Model 3x1-w is saturated with de-aired/de-ionized water, whereas Model 3x1-v is saturated with a methylcellulose-water solution (metulose) having about 40 times de viscosity of water. Consequently, at a centrifugal acceleration of 50g, these models simulate deposits of wide different permeability in the field.

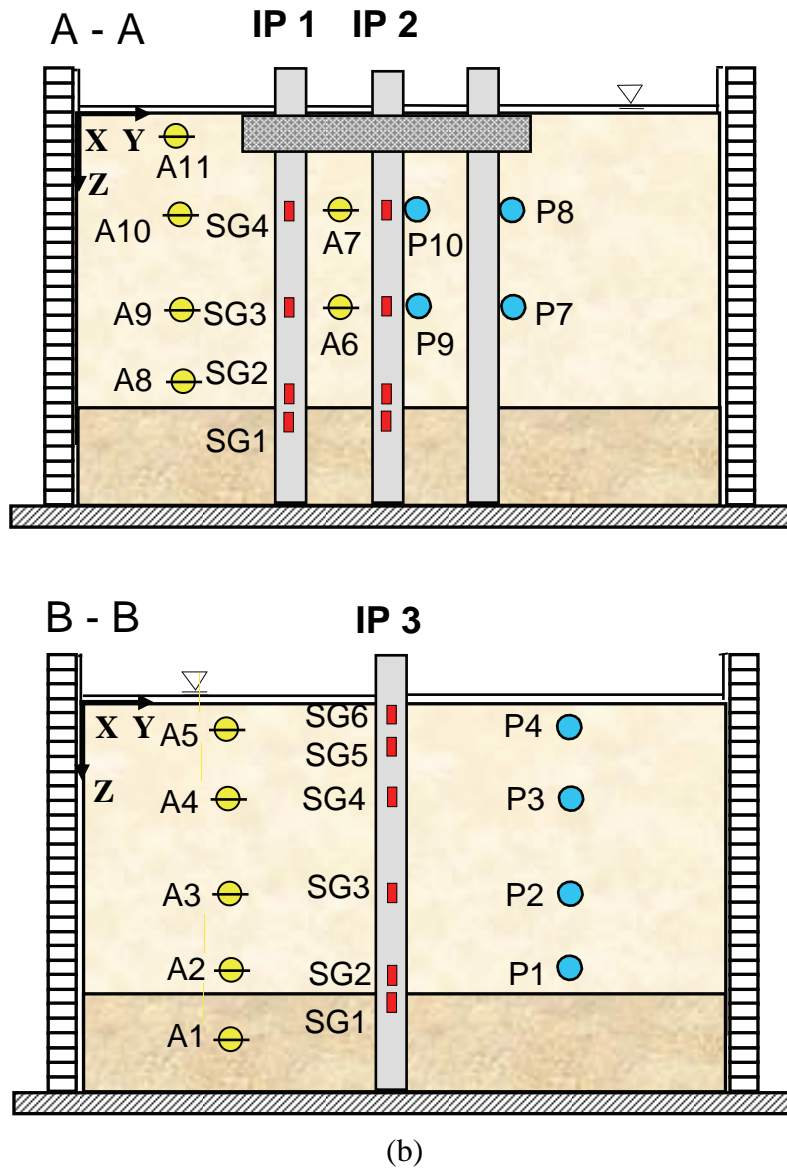


Figure 4.1 (cont.): (b) Transversal sections of Models 3x1-w and 3x1-v

A description of the models is presented in section 4.3, whereas the model preparation followed the same steps already described in section 3.2. Experimental results of Models 3x1-w and 3x1-v are presented and discussed in sections 4.4 and 4.5 respectively. Also, a basic limit equilibrium analysis is developed to back-calculate the maximum bending moments and pile group lateral displacement due to lateral spreading. Section 4.6 compares the two tests and discusses the difference in response due to the soil permeability effect.

4.2 Model Preparation

Preparation of Models 3x1-w and 3x1-v followed the same steps already described in section 3.2. In both models a single pile and a 3x1 pile group were placed before the soil was pluviated, attempting to simulate piles installed with minimal disturbance to the surrounding soil, as may be the case when a pile is inserted into a pre-augered hole.

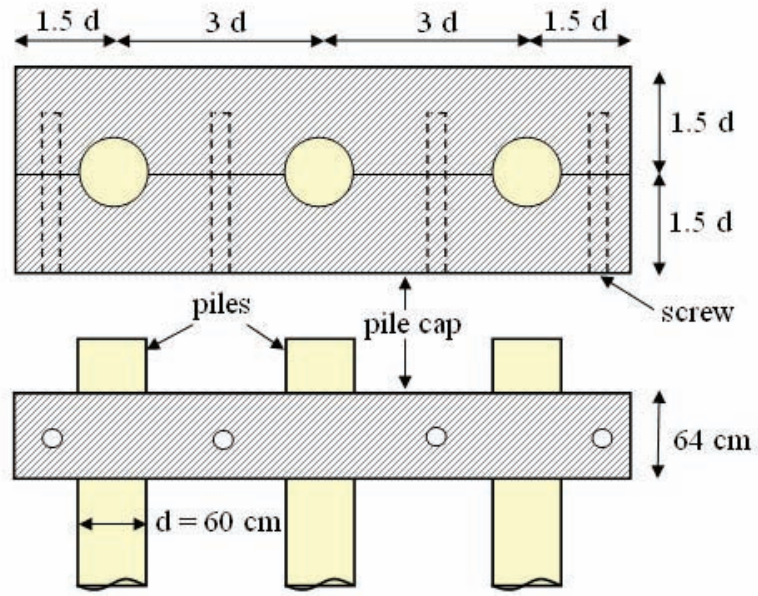
4.3 Model Description

The setup and instrumentation used in Models 3x1-w and 3x1-v are presented in Fig. 4.1. These models simulate a single pile and a line of three piles connected with a pile cap perpendicular to the direction of lateral spreading. The prototype profile consists of a 6 m thick Nevada sand layer placed at a relative density of about 40%, on top of a 2 m thick nonliquefiable cemented layer. The models, inclined 2° to the horizontal (4.8° after instrumental correction; Taboada, 1995), simulate an infinite mild ground slope. The main and only difference between both models is that Model 3x1-w is saturated with de-aired/de-ionized water, whereas Model 3x1-v is saturated with a methylcellulose-water solution (metulose) having about 40 times the viscosity of water. At a centrifugal acceleration of 50g the loose Nevada sand in Model 3x1-w simulates a coarse sand, whereas in Model 3x1-v it simulates a fine sand.

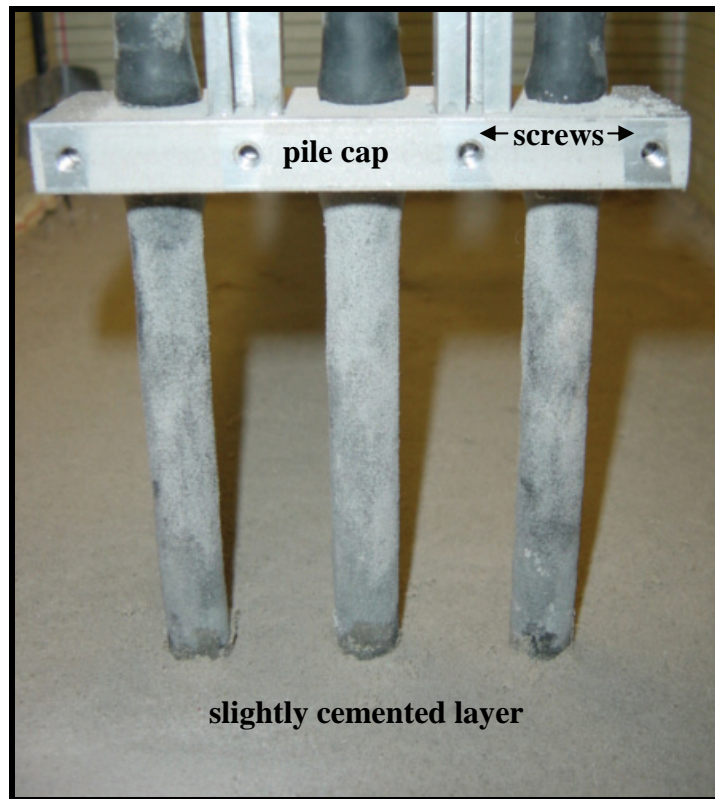
The embedded piles have a prototype diameter (d) of 60 cm and a prototype bending stiffness (EI) of approximately $9000 \text{ kN}\cdot\text{m}^2$. The aluminum cap, embedded in the loose Nevada sand, has prototype dimensions of 1.8 m in width, 5.4 m in length, and 0.64 m in height. Figure 4.2 displays a picture and schematic of the pile-cap-structure, showing the spacing between piles (3d). Figure 4.3 shows a picture of the single pile, 3x1 pile group, and transducers during model preparation. Grids of colored sand were placed as well at intermediate depths to observe the pattern of soil displacement around the piles (Fig. 4.4).

The models were excited by 30 cycles of a 100 Hz sinusoidal acceleration with uniform amplitude of about 15g. At a centrifugal acceleration of 50g this corresponds to a frequency of 2 Hz and peak acceleration of about 0.3g.

The instrumentation used in Models 3x1-w and 3x1-v is shown in Fig. 4.1 and listed in Table 4.2. The models were instrumented with 21 accelerometers, 12 pore pressure transducers, and 8 LVDTs. Three instrumented piles (IP1, IP2 and IP3) were used in these models, as shown in Fig. 4.1. Detailed information about the strain gage configuration and the piles used (types U1 and U2) is presented in section 2.7. Accelerations in the soil and outside the laminar box, excess pore water pressure, lateral displacement of the soil and the pile heads, bending moments, and axial forces were measured during the tests.



(a)



(b)

Figure 4.2: Pile-cap-structure, (a) schematic, (b) picture, Models 3x1-w and 3x1-v

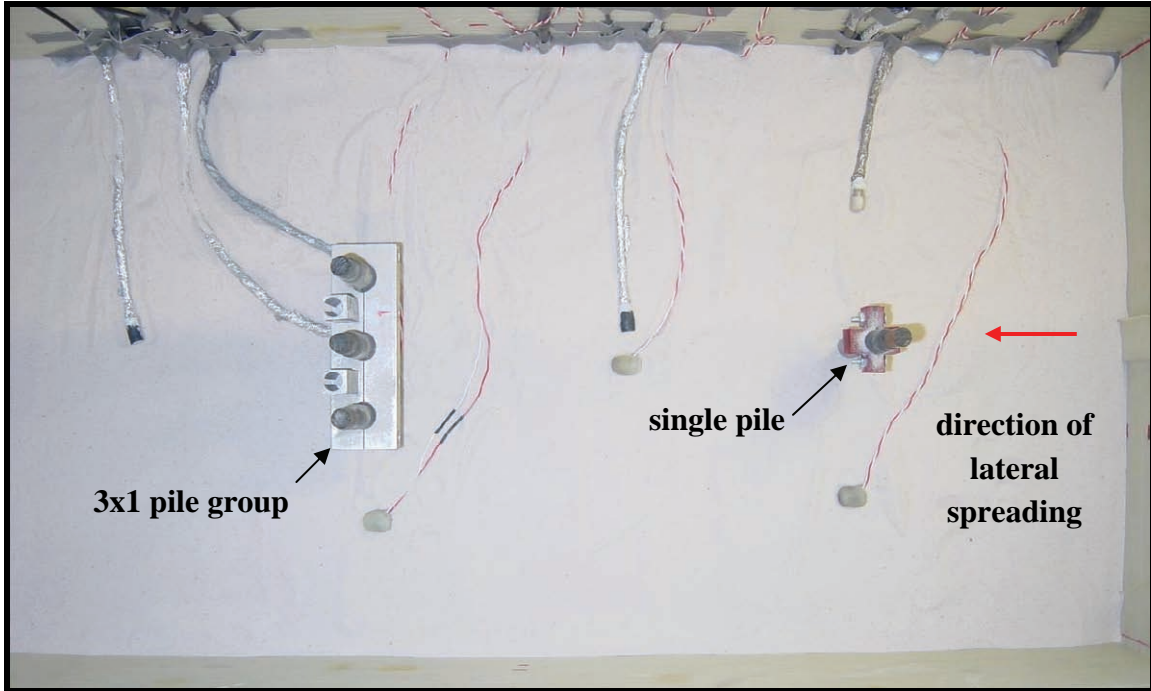


Figure 4.3: Model during preparation, Models 3x1-w and 3x1-v

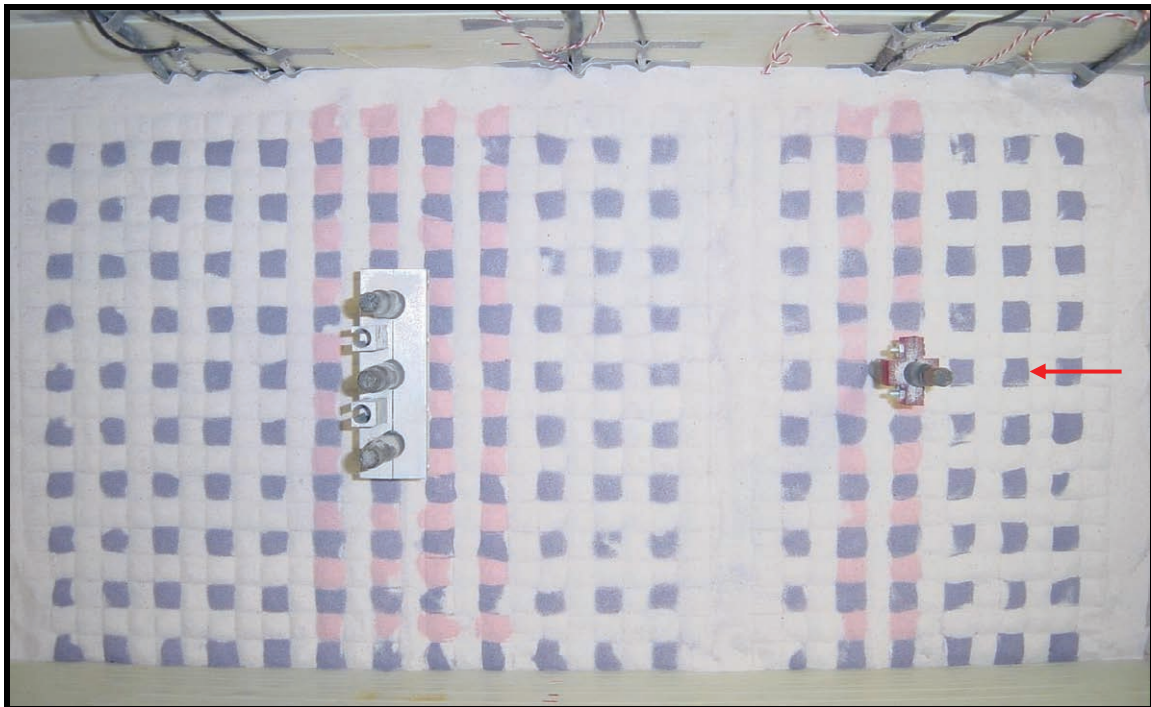


Figure 4.4: Colored sand placed at an intermediate depth, Models 3x1-w and 3x1-v

Table 4.2: Location of instruments in Models 3x1-w and 3x1-v (in model units)

Transducer	Sensor name	Coordinates [cm]		
		X	Y	Z
Accelerometer	Ain	73.5	17.75	16.5
	A1	15	9	14
	A2	15	9	11
	A3	15	9	8
	A4	15	9	4
	A5	15	9	1
	A6	43	16	8
	A7	43	16	4
	A8	43	7	11
	A9	43	7	8
	A10	43	7	4
	A11	43	7	1
	A12	44.75	41.25	0.63
	A13	41.25	41.25	0.63
	A14	43	43	0.63
	A15	42	42	0
	A16	72.5	17.75	16
	A17	71	17.75	11
	A18	71	17.75	8
	A19	71	17.75	4
A20	71	17.75	1	
Pore pressure transducer	P1	15	26.5	11
	P2	15	26.5	8
	P3	15	26.5	4
	P4	15	26.5	1
	P5	30	17.75	8
	P6	30	17.75	4
	P7	43	22.25	8
	P8	43	22.25	4
	P9	43	18.75	8
	P10	43	18.75	4
	P11	57	17.75	8
	P12	57	17.75	4

Table 4.2(cont.): Location of instruments in Models 3x1-w and 3x1-v (in model units)

Transducer	Sensor name	Coordinates [cm]		
		X	Y	Z
LVDT	L1	0	17.75	11
	L2	0	17.75	8
	L3	0	17.75	4
	L4	0	17.75	0.5
	L5	44.75	16	-2
	L6	44.75	19.5	-2
	L7	15	16.5	-2
	L8	15	19	-2
Strain gage		IP 1	IP 1	IP 1
	SG1	43	14.25	12.5
	SG2	43	14.25	11.5
	SG3	43	14.25	8
	SG4	43	14.25	4
		IP 2	IP 2	IP 2
	SG1	43	17.75	12.5
	SG2	43	17.75	11.5
	SG3	43	17.75	8
	SG4	43	17.75	4
		IP 3	IP 3	IP 3
	SG1	15	17.75	12.5
	SG2	15	17.75	11.5
	SG3	15	17.75	8
	SG4	15	17.75	4
	SG5	15	17.75	1.5
SG6	15	17.75	0.5	

4.4 Model 3x1-w

4.4.1 Recorded Accelerations

Figure 4.5 shows the recorded input acceleration and soil acceleration time histories in the free field at different depths. As expected, the measured input acceleration (A_{in}) had a uniform prototype amplitude of 0.3g. Near the ground surface the soil acceleration dropped significantly after one cycle due to the dynamic isolation of the shallower layers. At deeper elevations, large negative spikes developed due to the dilative behavior of the saturated loose sand during lateral spreading. Therefore, the records indicate the loose sand layer liquefied and displaced in the downslope direction during shaking. On the other hand, the acceleration of the bottom layer (A_1) was very similar to the input acceleration, with the exception of small spikes probably caused by a very small vibration of this layer with respect to the base.

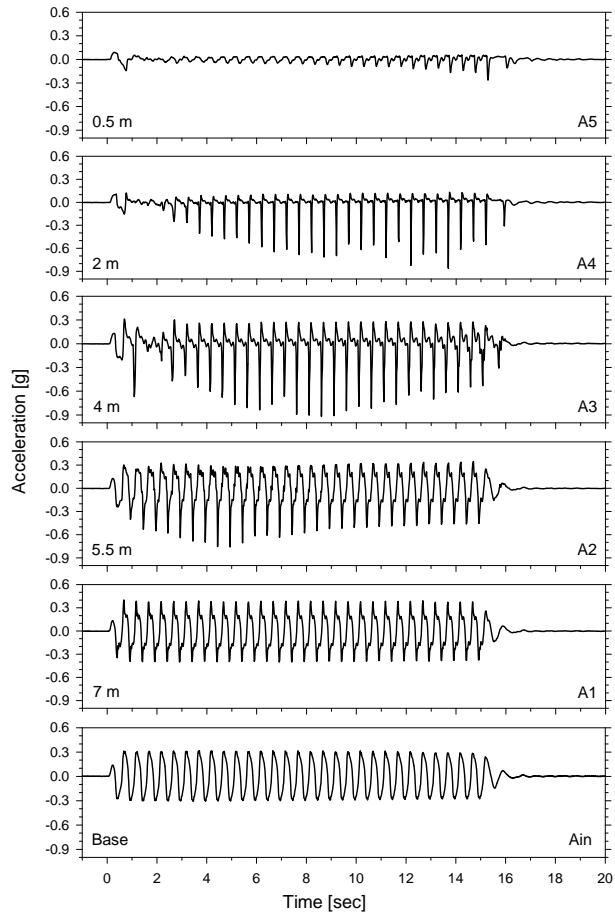


Figure 4.5: Soil acceleration time histories in the free field, Model 3x1-w

Figure 4.6 shows soil acceleration time histories close to the pile group and between piles in the pile group. These records exhibit a drop in positive amplitude and spikes in the negative direction, indicating the soil in the near field liquefied too. The negative spikes reveal a less dilative behavior compared to the one in the free field.

Figure 4.7 presents acceleration time histories on the pile cap, as well as the measured horizontal and vertical acceleration at the base of the box. The large vertical acceleration may have been caused by a combined effect of the vertical acceleration at the base and an interaction with the liquefied soil. The acceleration in the lateral spreading direction was even larger and had the same frequency than the input motion. The recorded acceleration on the laminar rings (Fig. 4.8) is in good agreement with the soil acceleration, showing a drop in positive amplitude and spikes in the negative direction.

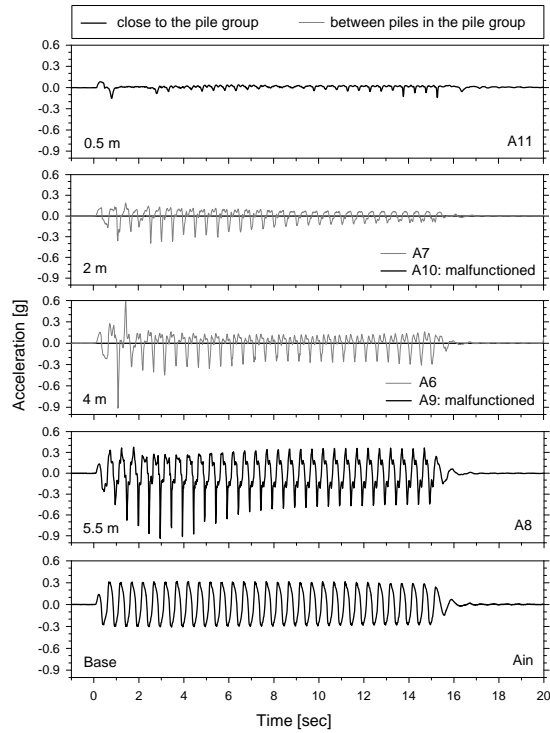


Figure 4.6: Soil acceleration time histories in the near field, Model 3x1-w

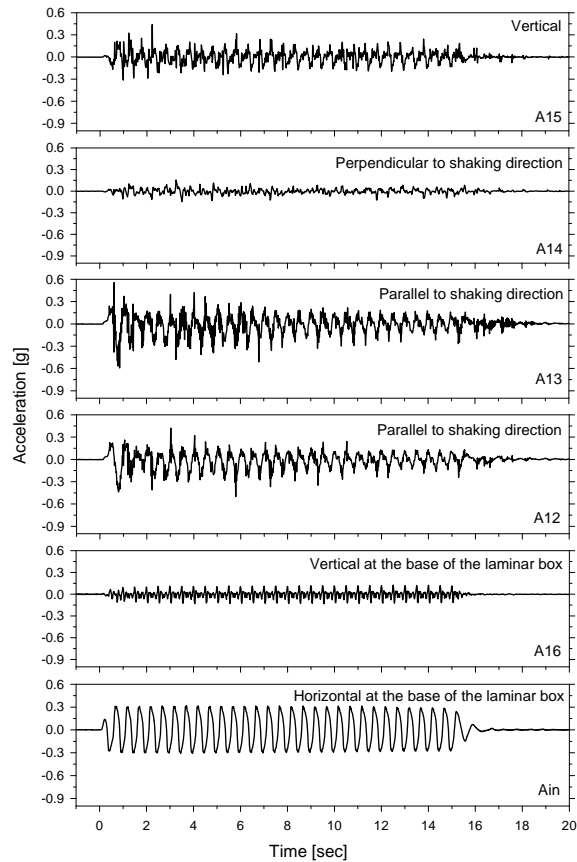


Figure 4.7: Accelerations recorded on the pile cap, Model 3x1-w

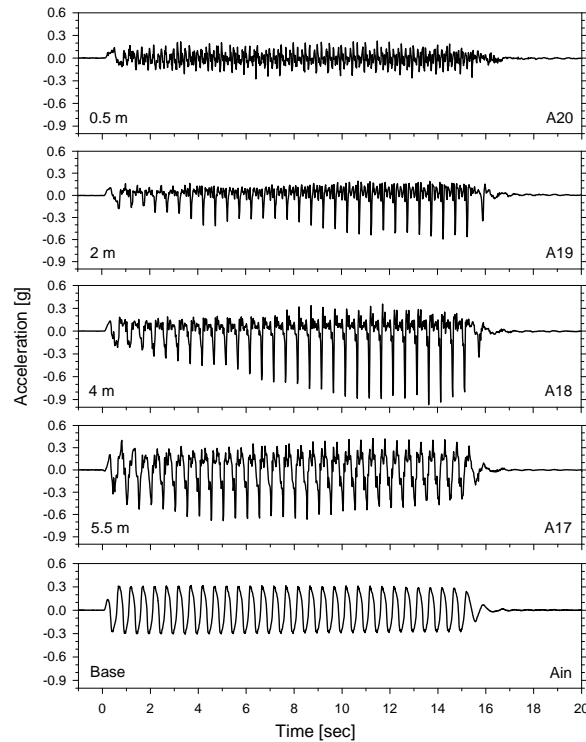


Figure 4.8: Accelerations recorded on the laminar rings, Model 3x1-w

4.4.2 Recorded Excess Pore Pressures

Excess pore pressure time histories in the free field, next to the piles, and close to the pile group, are shown in Figs. 4.9, 4.10, and 4.11 respectively. Except for a slight decrease in excess pore pressure measured next to the external pile at a depth of 2 m in the 3x1 pile group, the records indicate that the loose sand layer liquefied after about one cycle of shaking. The dissipation process took only a few seconds, confirming the high permeability of the model.

4.4.3 Recorded Lateral Displacements

The recorded soil lateral displacement in the free field (Fig. 4.12) shows that the liquefied layer displaced gradually during shaking, reaching a maximum displacement of approximately 155 cm at the end of shaking. The single pile and pile group on the other hand, bounced back after reaching a maximum lateral displacement of 35 and 26 cm respectively. This response is consistent with the single pile displacement in Model 1x1-w, indicating the liquefied soil was flowing around the piles.

The profiles of soil lateral displacement in the free field were obtained by interpolating the LVDT measurements, after filtering out the cyclic component (Fig. 4.13). As soon as the loose sand liquefied at the beginning of shaking, the deposit started moving downslope, with the maximum displacement taking place always on the ground surface.

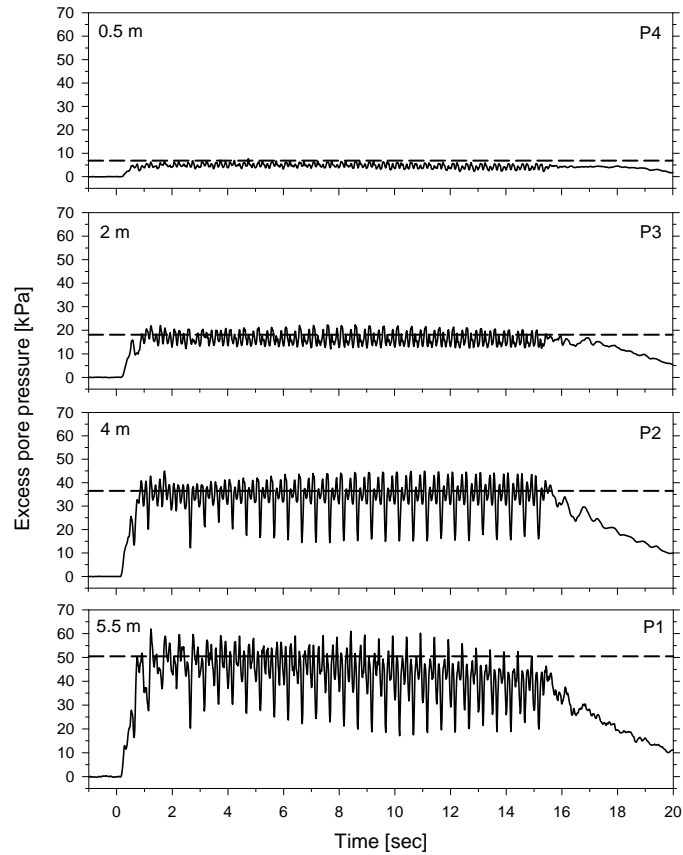


Figure 4.9: Excess pore pressure time histories in the free field, the dashed lines correspond to initial liquefaction, Model 3x1-w

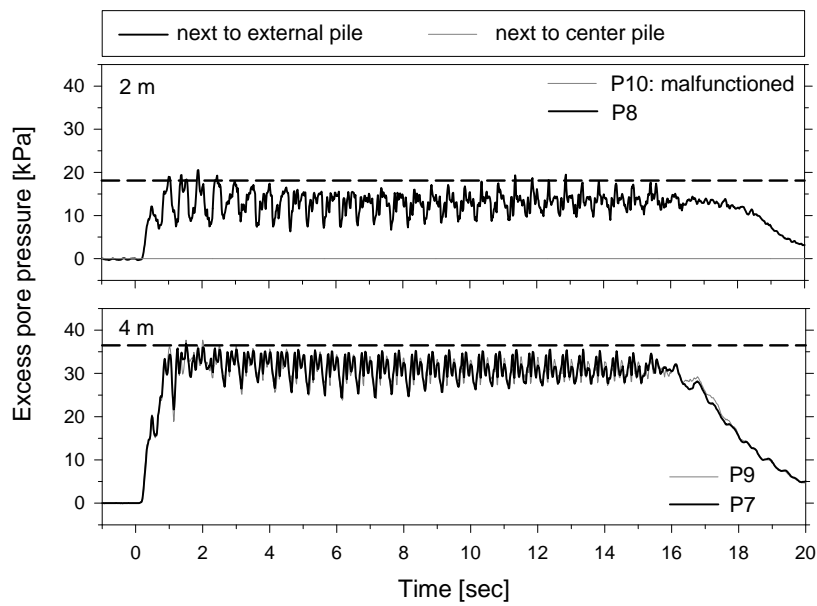


Figure 4.10: Excess pore pressure time histories next to pile group, Model 3x1-w

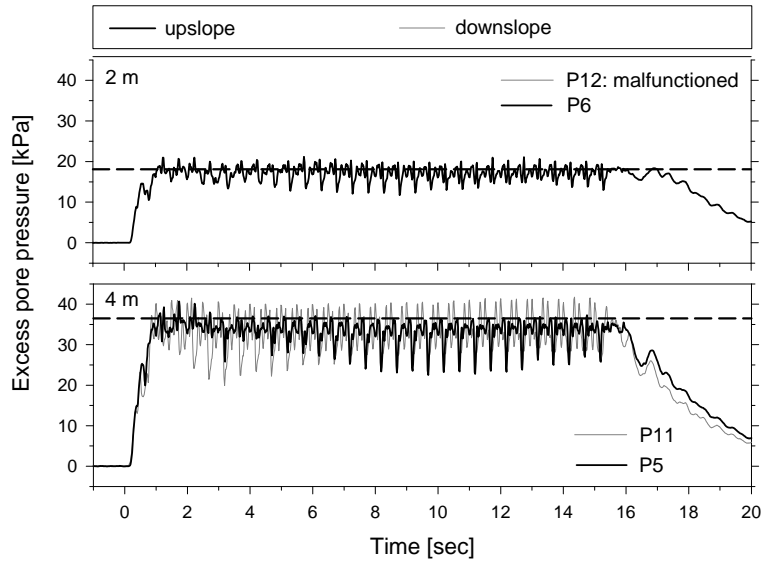


Figure 4.11: Excess pore pressure time histories downslope and upslope from pile group, Model 3x1-w

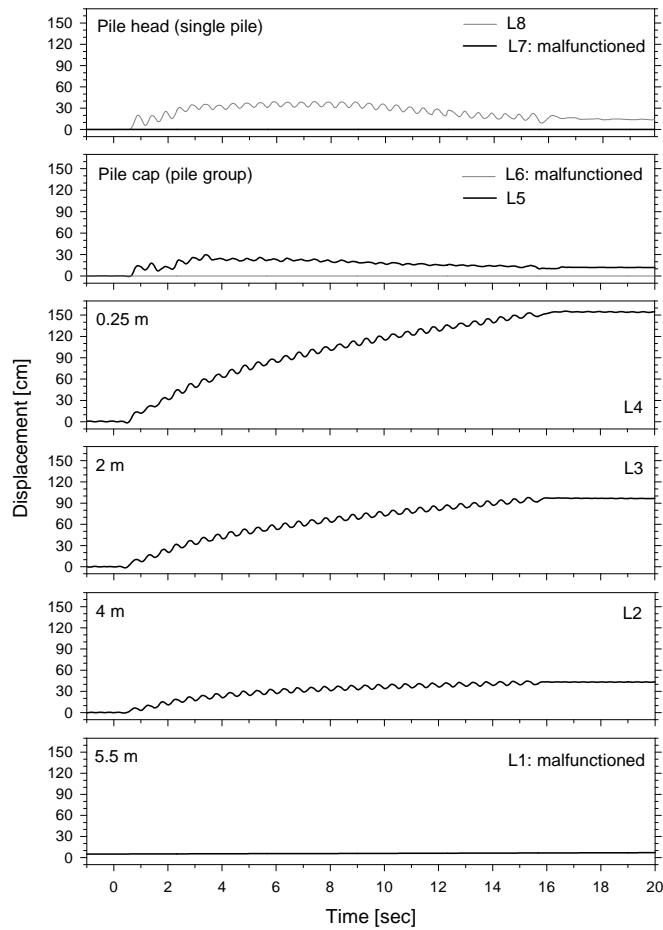


Figure 4.12: Lateral displacement time histories, Model 3x1-w

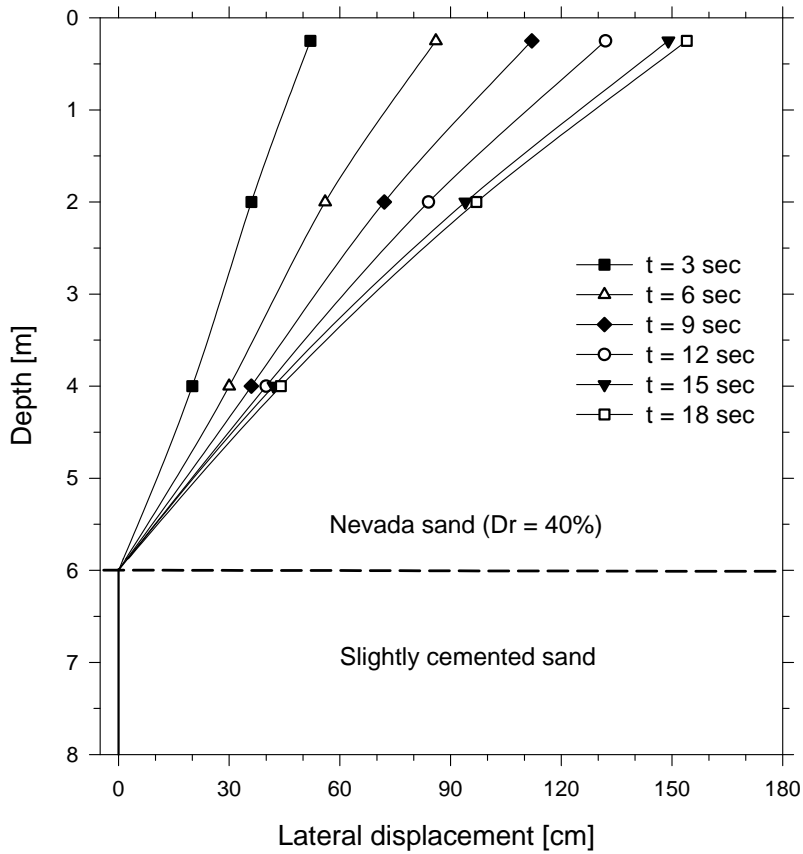
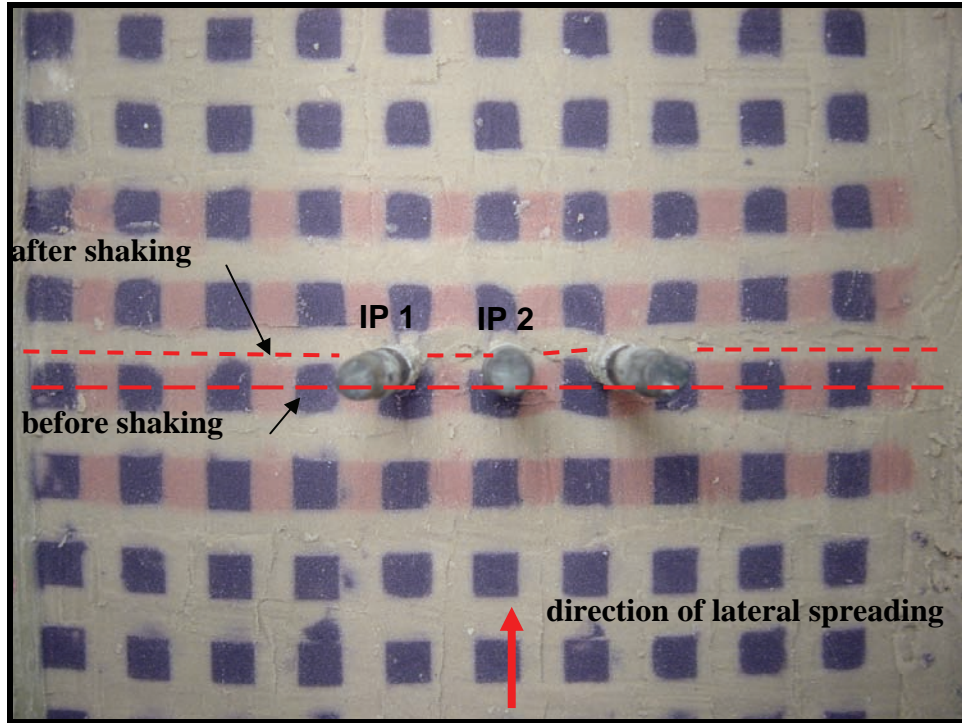


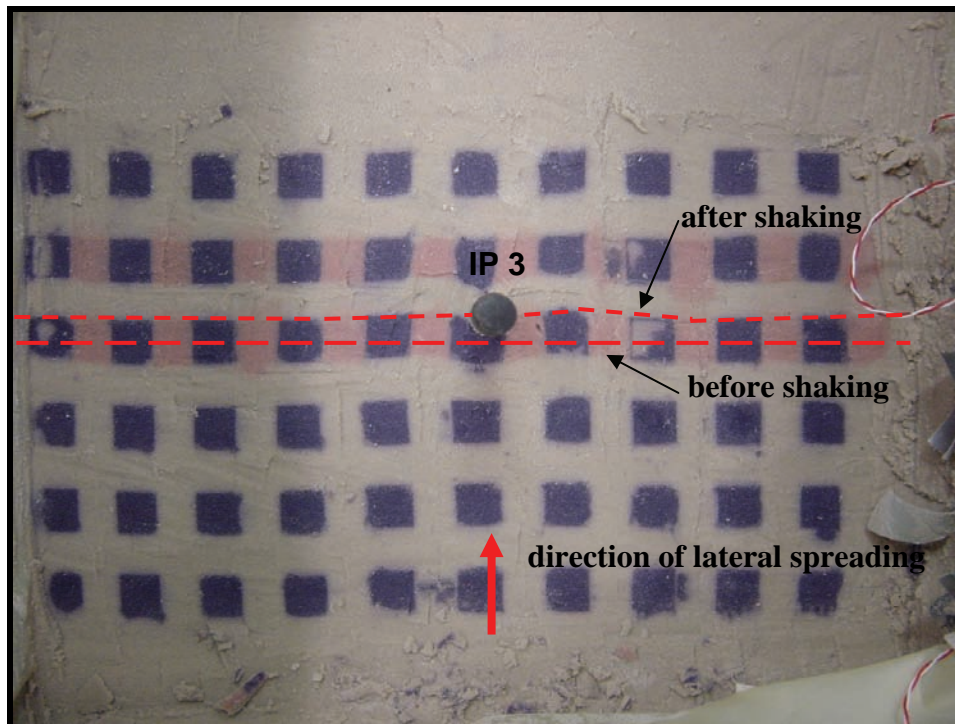
Figure 4.13: Profiles of soil lateral displacement in the free field, Model 3x1-w

4.4.4 Pattern of Soil Displacement around Piles

Grids of colored sand were placed at an intermediate depth to observe the pattern of soil displacement around the piles. Figure 4.14 shows pictures of the soil condition around the single pile and the pile group, after carefully removing the soil on top. The liquefied sand moved around the individual piles, affecting the soil pattern very close to the piles themselves. Therefore, the characteristic width perpendicular to the flow was the diameter of the piles. This would indicate that the pressure of the liquefied soil acts only on the individual piles and not on the soil in between.



(a)



(b)

Figure 4.14: Pattern of soil displacement around piles at a depth of 3 m, (a) pile group, (b) single pile, Model 3x1-w

4.4.5 Recorded Bending Moments

Prototype bending moments measured in the pile group and single pile are presented in Figs. 4.15, 4.16, and 4.17. Profiles of bending moments in the center pile (IP2) are shown in Fig. 4.18, after filtering out the cyclic component. These profiles are representative of all piles in the pile group, since the bending moments in the center and external piles were practically the same. The maximum moment at any given time occurred closed to the base of the liquefied layer, reaching a maximum value at about 3 sec, which is also the time at which the pile group reached its maximum deflection. Afterwards, the bending moment decreased despite the deformation of the liquefied layer kept increasing until the end of shaking. Clearly after 3 sec the liquefied soil started flowing around the piles, thus decreasing the exerted pressure on the piles.

Profiles of bending moment in the single pile (IP3) are shown in Fig. 4.19. The response of the single pile was similar to the one of the pile group, with the bending moment reaching a maximum value and decreasing afterwards. Even though the soil was liquefied during practically all the excitation, it was able to push the pile at the beginning but then it softened and allowed the pile to bounce back.

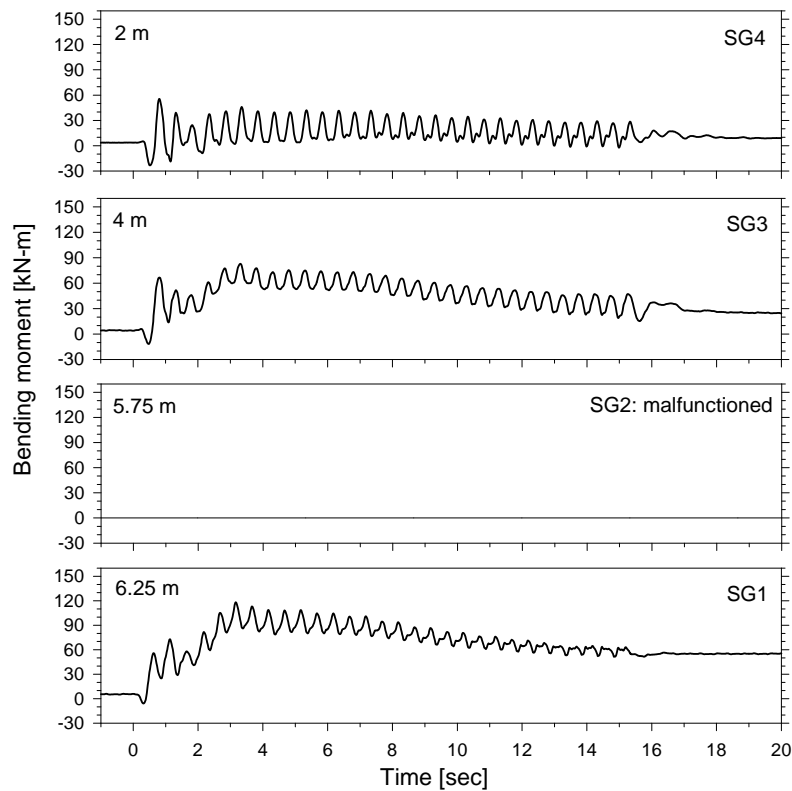


Figure 4.15: Bending moment time histories, external pile (IP 1), Model 3x1-w

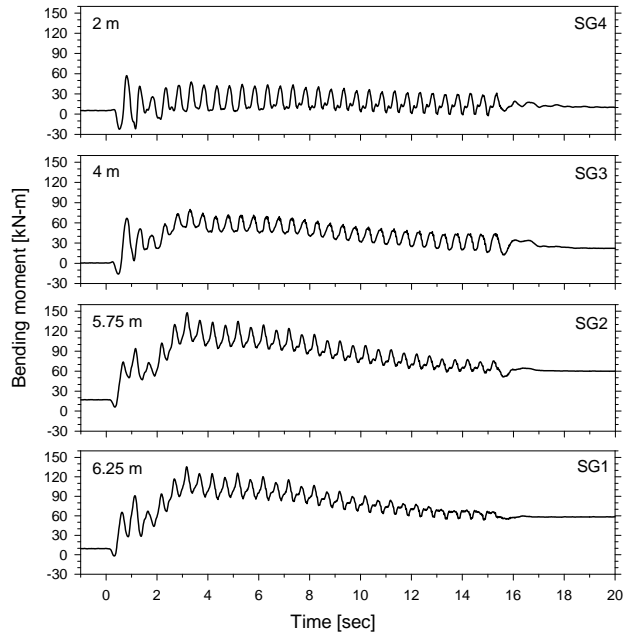


Figure 4.16: Bending moment time histories, center pile (IP 2), Model 3x1-w

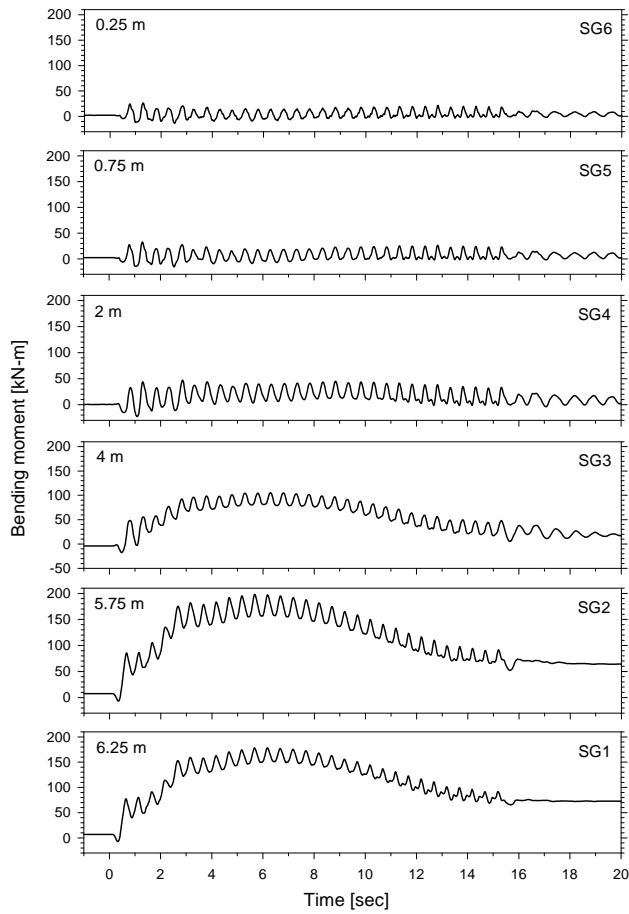


Figure 4.17: Bending moment time histories, single pile (IP 3), Model 3x1-w

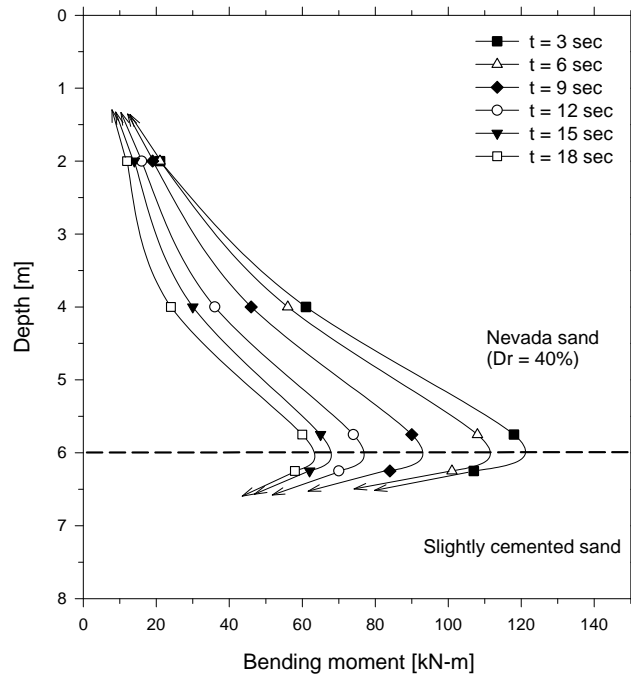


Figure 4.18: Profiles of bending moment, center pile (IP 2), Model 3x1-w

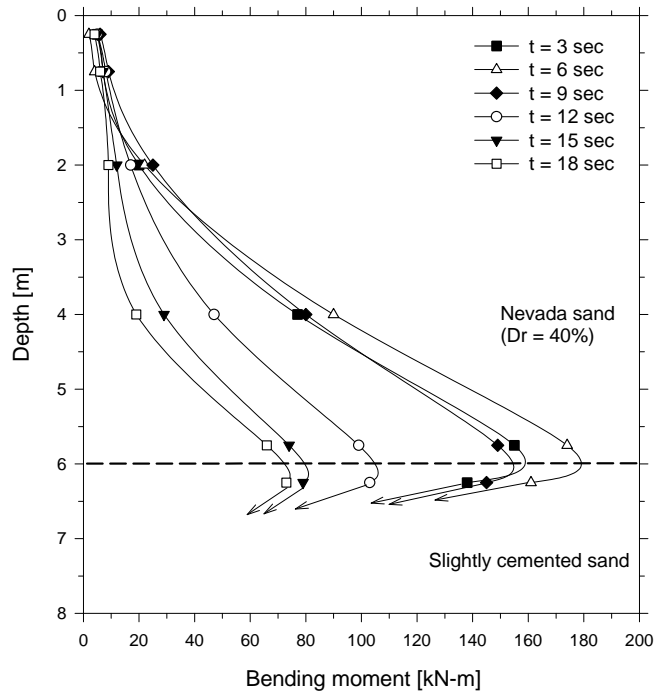


Figure 4.19: Profiles of bending moment, single pile (IP 3), Model 3x1-w

Figure 4.20 shows the measured bending moment at the base of the liquefiable layer versus the measured pile cap lateral displacement, after filtering out the cyclic component. The pile group reached a maximum lateral displacement and bending moment and then bounced back during shaking. The linear relationship between bending moment and pile cap displacement evidences the linear elastic behavior of the pile-group-fixation system.

4.4.6 Limit Equilibrium Analysis

A limit equilibrium analysis was conducted to estimate the liquefied soil pressure acting on the 3x1 pile group. A student version of the software AVwin was used to model the pile group subjected to the lateral force induced by lateral spreading. Given the fact that the bending moments in all three piles were very similar and they were connected by a cap, only one pile was modeled including one third of the cap, as shown in Fig. 4.21b. The pile was modeled with 30 elements, having a bending stiffness of $9000 \text{ kN}\cdot\text{m}^2$, and the slightly cemented layer was modeled with a rotational springs at the base of the liquefiable layer.

The pattern of soil deformation in Fig. 4.14 shows that the liquefied sand moved around each pile, affecting the soil pattern close to the piles themselves. Therefore, the liquefied soil pressure was assumed to act only on the piles and pile cap, which represents an effective area of 13.1 m^2 , as shown in Fig. 4.21a. This pressure was assumed to be constant and independent of depth. The force on each node was finally obtained by multiplying the soil pressure by the associated area. A liquefied soil pressure of 8.3 kN/m^2 and a rotational stiffness of $8000 \text{ kN}\cdot\text{m}/\text{rad}$ at the base of each pile were found to provide the best estimations of the maximum moment and pile cap displacement. This is the same value used in the limit equilibrium analyses on the single pile in chapter 3, showing the excellent repeatability of the models. The back-calculated bending moment at the base of the liquefiable layer was $120 \text{ kN}\cdot\text{m}$, the same value measured during the test. The calculated pile cap lateral displacement was 27 cm , compared to the 26 cm measured during the test. Table 4.3 summarizes some of the parameters used in the limit equilibrium analysis, as well as measured and calculated values, showing an excellent agreement.

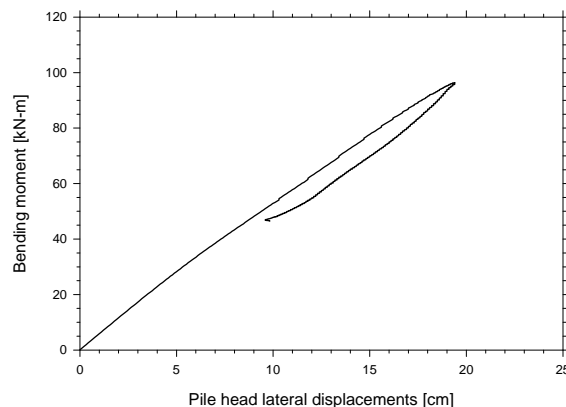


Figure 4.20: Bending moment at the base of the liquefiable layer versus pile cap lateral displacement, pile group, Model 3x1-w

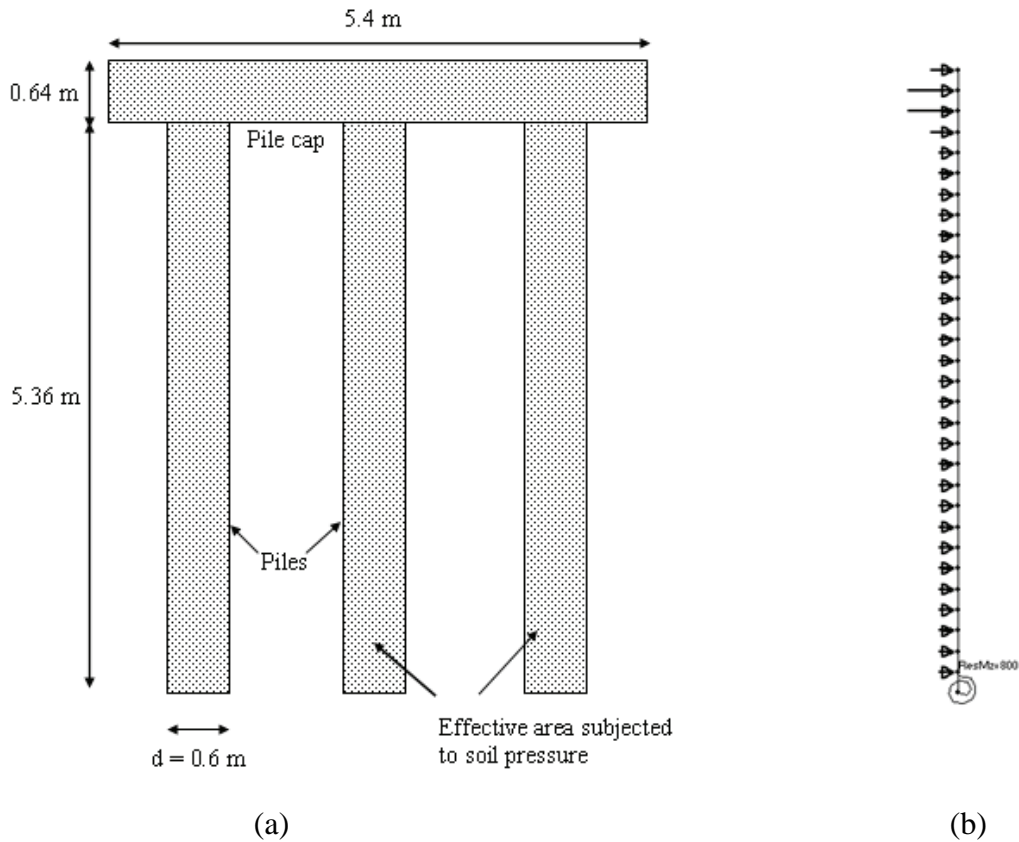


Figure 4.21: (a) Effective area subjected to liquefied soil pressure and (b) lateral view of the model used for limit equilibrium analyses, Model 3x1-w

Table 4.3: Parameters used in the limit equilibrium analysis, as well as measured and calculated values, Models 3x1-w and 3x1-v

Model	Liquefied soil pressure [kN/m ²]	e_a [m ²]	Rotational stiffness [kN-m/rad]	Max. bending moment [kN-m]		Max. pile cap disp. [cm]	
				Measured	Calculated	Measured	Calculated
3x1-w	8.3	13.1	8000	120	120	26	27
3x1-v	8.3	39.3	8000	425	405	85	90

Max. bending moments measured and calculated at the base of the liquefiable layer

e_a : effective area subjected to liquefied soil pressure

4.5 Model 3x1-v

4.5.1 Recorded Accelerations

Figure 4.22 shows the recorded input acceleration and soil acceleration time histories in the free field at different depths. The input acceleration had a uniform amplitude of 0.33g, slightly more than in Model 3x1-w. The acceleration records in the loose sand layer show a drop in positive amplitude and large spikes in the negative direction, indicating this layer liquefied and displaced in the downslope direction during shaking. On the other hand, the acceleration of the bottom cemented layer (A1) was very similar to the input acceleration, with the exception of small spikes probably caused by a very small vibration of this layer with respect to the base. The soil acceleration close to the pile group and between piles in the pile group (Fig. 4.23) exhibited the same behavior than in the free field.

The acceleration records on the pile cap and on the laminar rings, as shown in Figs. 4.24 and 4.25 respectively, are consistent with the trends observed in Model 3x1-w.

4.5.2 Recorded Excess Pore Pressures

The excess pore pressure records in the free field (Fig. 4.26) reveal that the soil did liquefy after one or two cycles of shaking. Near the ground surface however, the excess pore pressure decreased after a couple of cycles to values close to zero. As previously discussed in chapter 3, large shear strains developed under low confinement and a slow dissipation process appear to be responsible for this phenomenon.

The excess pore pressure records next the pile group are very revealing, especially at shallower depths where a strong negative excess pore pressure developed early in the shaking (Fig. 4.27). Even though the records at a deeper elevation do not exhibit such a dramatic response, exceptional large spikes developed during the first half of shaking (Fig. 4.28).

Figure 4.29 shows excess pore pressure records in the free field and near field at a depth of 2 m, after filtering out the cyclic component. As expected, the excess pore pressure in the free field represents the upper limit. On the other hand, the negative excess pore pressure developed next to the external pile corresponds to the lower limit.

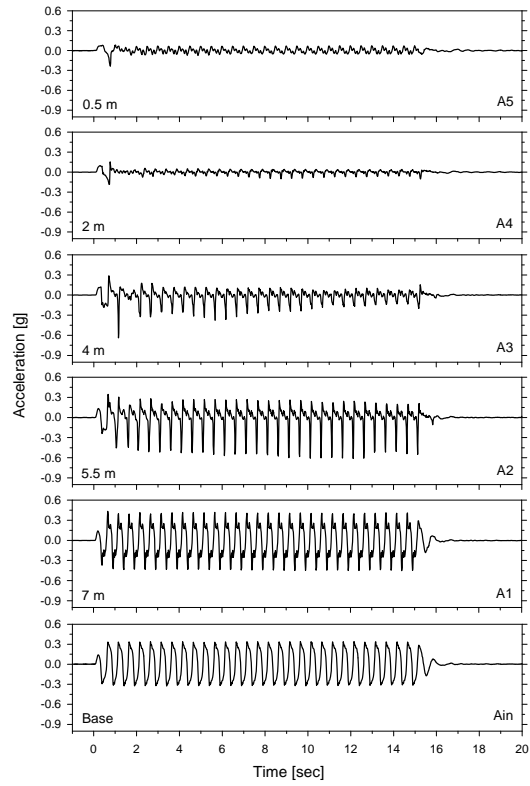


Figure 4.22: Soil acceleration time histories in the free field, Model 3x1-v

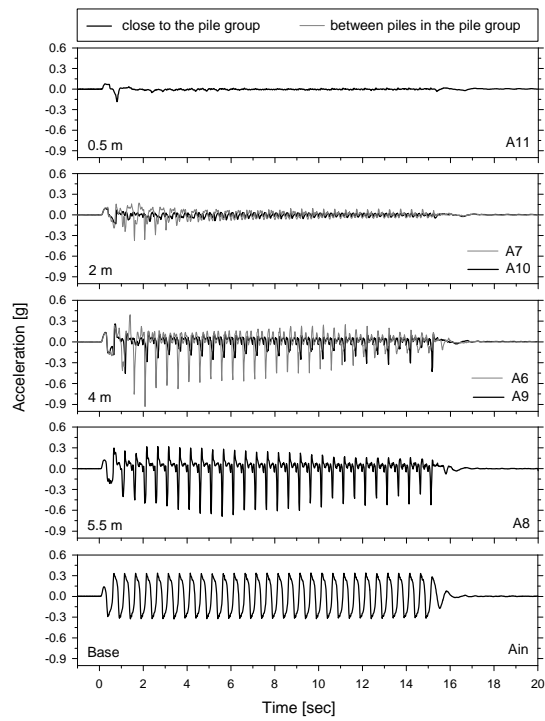


Figure 4.23: Soil acceleration time histories in the near field, Model 3x1-v

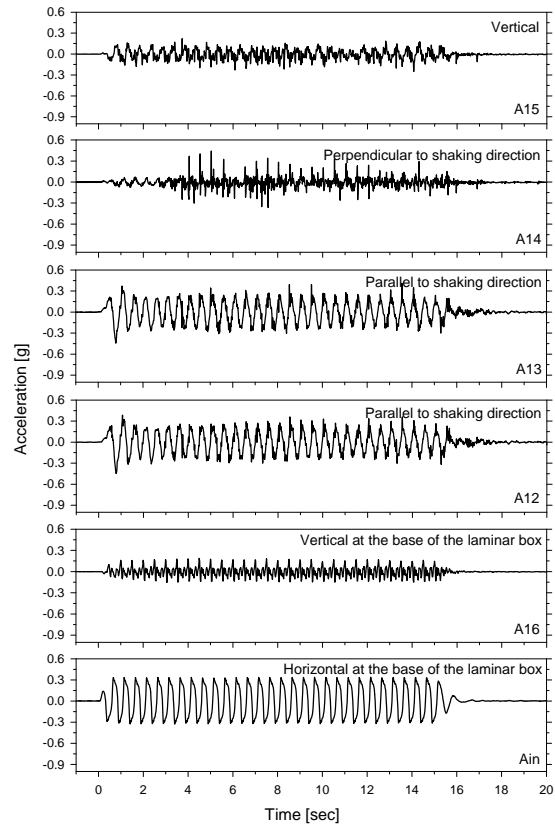


Figure 4.24: Accelerations recorded on the pile cap, Model 3x1-v

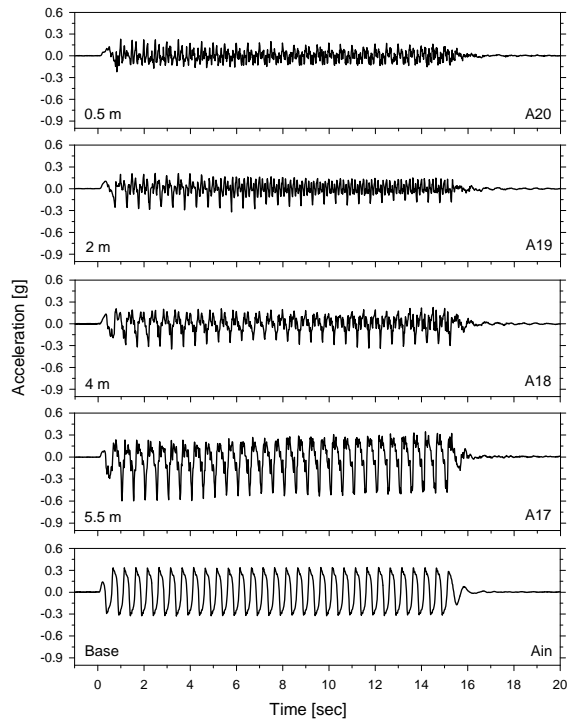


Figure 4.25: Accelerations recorded on the laminar rings, Model 3x1-v

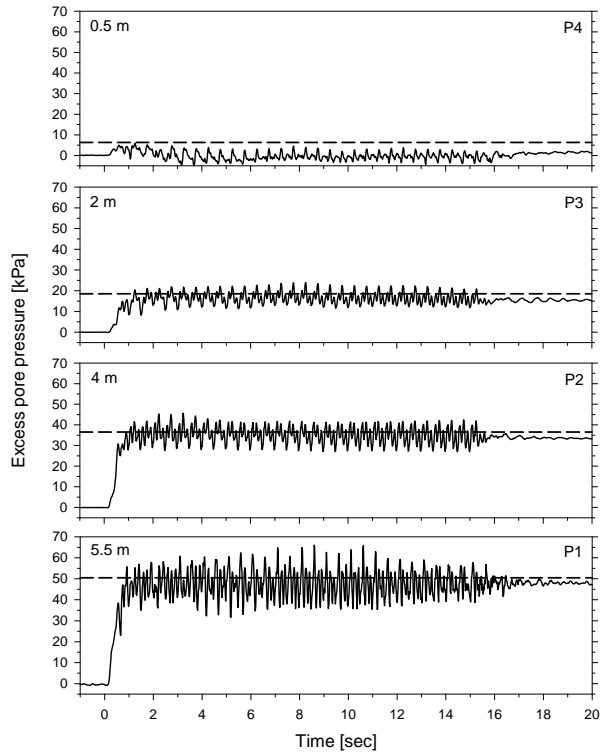


Figure 4.26: Excess pore pressure time histories in the free field, the dashed lines correspond to initial liquefaction, Model 3x1-v

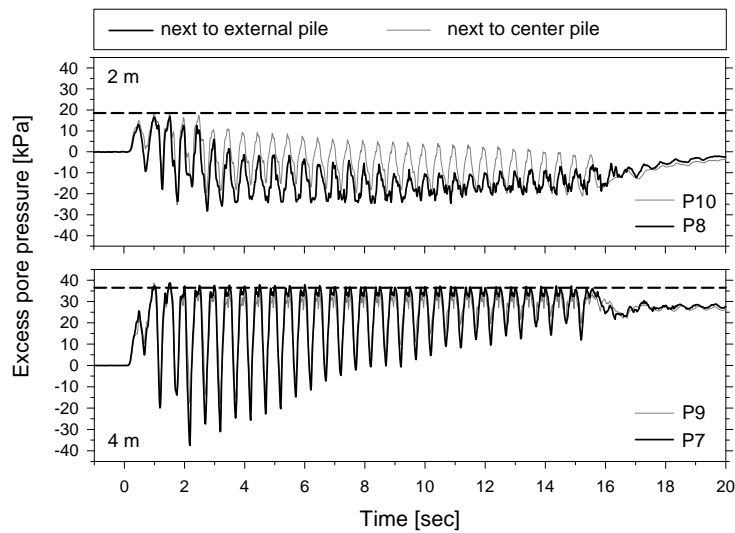


Figure 4.27: Excess pore pressure time histories next to pile group, Model 3x1-v

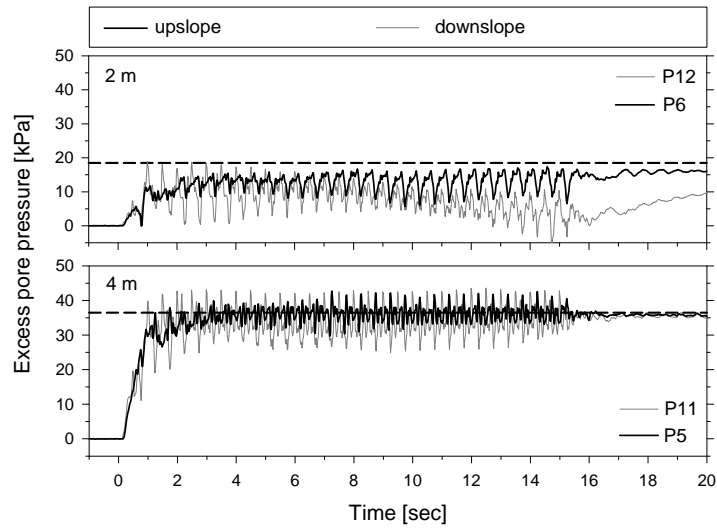


Figure 4.28: Excess pore pressure time histories downslope and upslope from pile group, Model 3x1-v

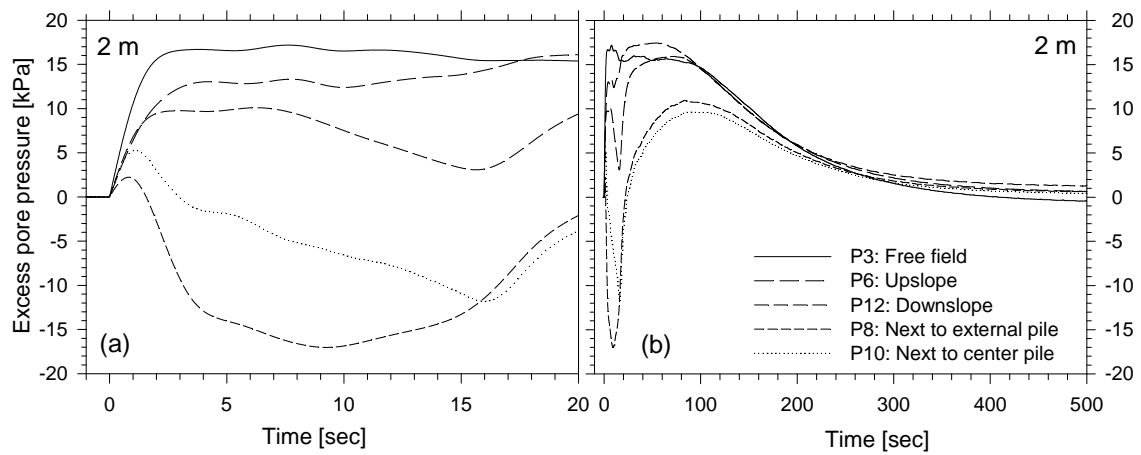


Figure 4.29: Filtered excess pore pressure time histories at 2 m depth, (a) short term and (b) long term, Model 3x1-v

If large shear strains under an undrained dilative response around the piles are largely responsible for the development of negative excess pore pressures, the recorded pore pressure next to the center and external piles should have been similar. However, the movement of colored sand in Fig. 4.33a shows that the liquefied soil did not flow between the piles, indicating the shear strains generated next to the center pile were smaller than the ones next to the external piles. Therefore, it seems that the fluid was not able to flow fast enough from the free field to dissipate the increments of negative pore pressure developed next to the external piles. As a result, these increments built up generating large hydraulic gradients in the horizontal plane toward these piles, gradients that must have induced a reduction of pore pressure next to the center pile early in the shaking. This zone of influence appears to have expanded during the excitation, reaching at about 7 sec the pore pressure transducer (P12) located on the downslope side of the pile group.

Once the shaking process stopped, pore fluid from the free field moved toward the pile group to compensate the negative and low excess pore pressure in this area. Figure 4.29b shows the dissipation process, with the pore pressure slowly rising to the positive value existing at the same depth in the free field. The excess pore pressure records expose a complex pile-soil-fluid interaction, and probably the response involves other effects like the reduction in lateral stress on the downslope side of the pile group.

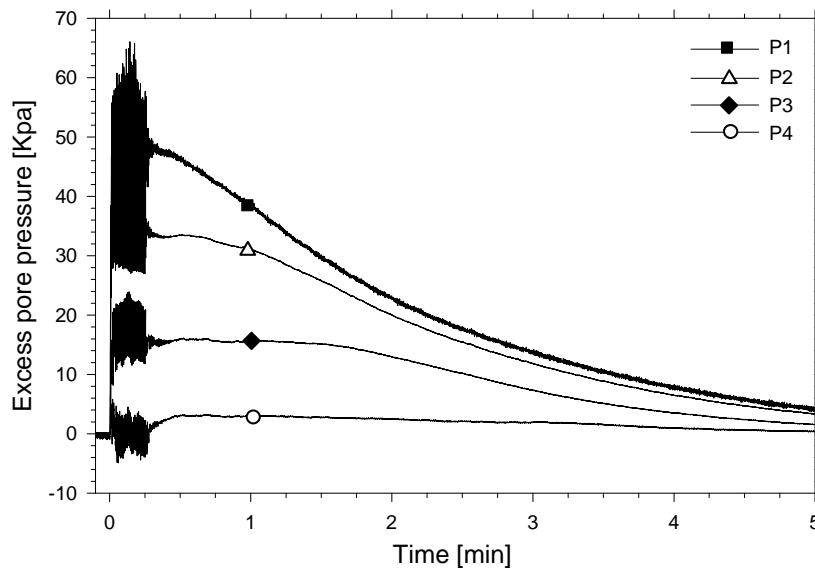


Figure 4.30: Long term excess pore pressure time histories in the free field, Model 3x1-v

4.5.3 Recorded Lateral Displacements

The recorded soil lateral displacement in the free field shows that the liquefied layer displaced gradually during shaking. Once the excitation ended, the lateral displacement stopped immediately even though the loose sand was still liquefied. The single pile and pile group displaced laterally during shaking without ever bouncing back, reaching a maximum displacement at the end of shaking of about 120 and 85 cm respectively. In fact, the single pile head and ground surface lateral displacements were similar, suggesting the higher fluid viscosity or lower soil permeability had a dramatic effect in the soil behavior close to the piles.

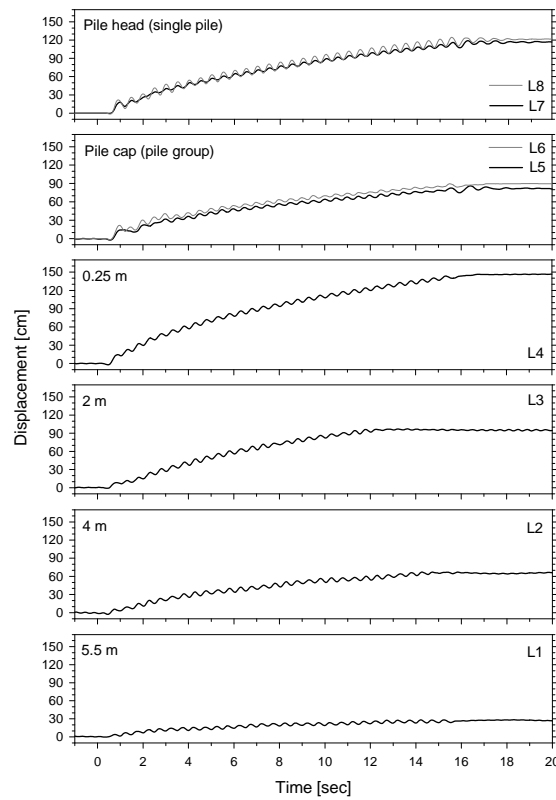


Figure 4.31: Lateral displacement time histories, Model 3x1-v

The profiles of soil lateral displacement in the free field were obtained by interpolating the LVDT measurements, after filtering out the cyclic component. As soon as the loose sand liquefied at the beginning of shaking, the deposit started moving downslope, with the ground surface reaching a maximum displacement of approximately 145 cm at the end of shaking.

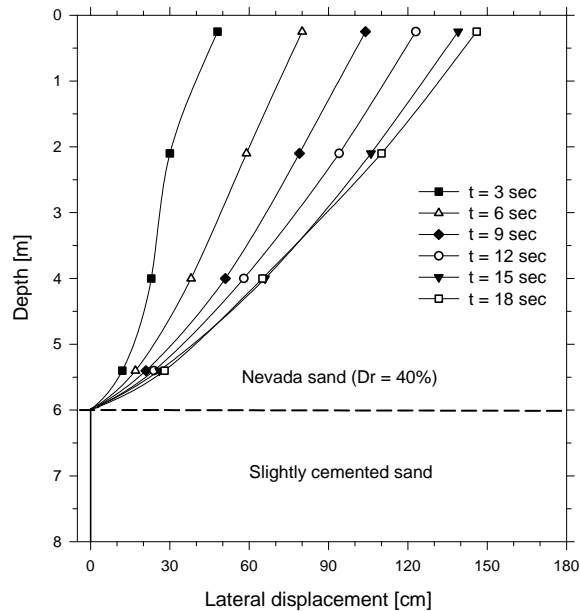


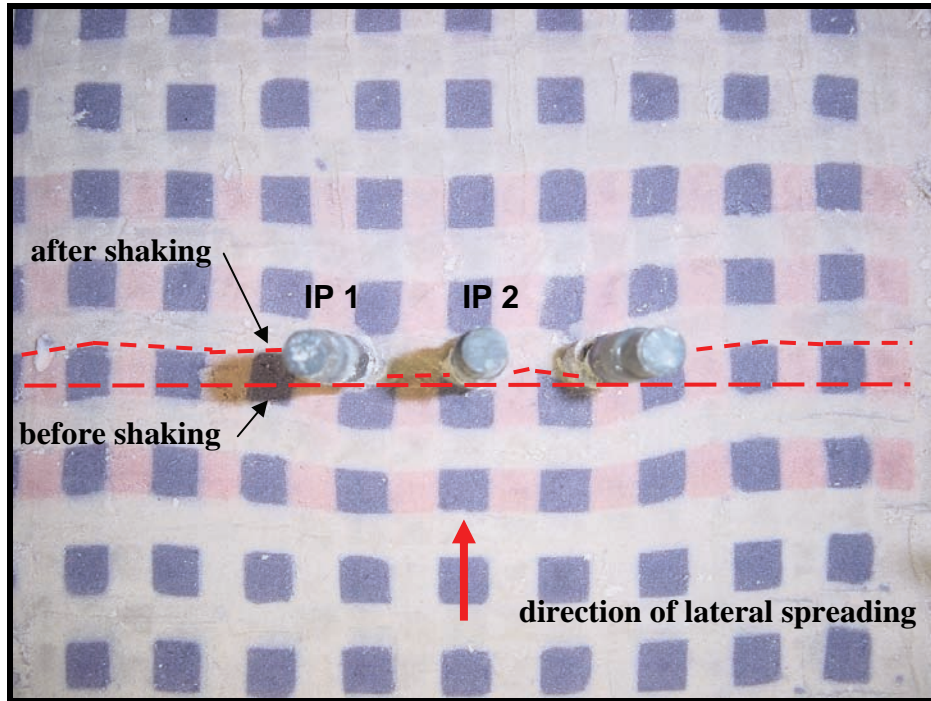
Figure 4.32: Profiles of soil lateral displacement in the free field, Model 3x1-v

4.5.4 Pattern of Soil Displacement around Piles

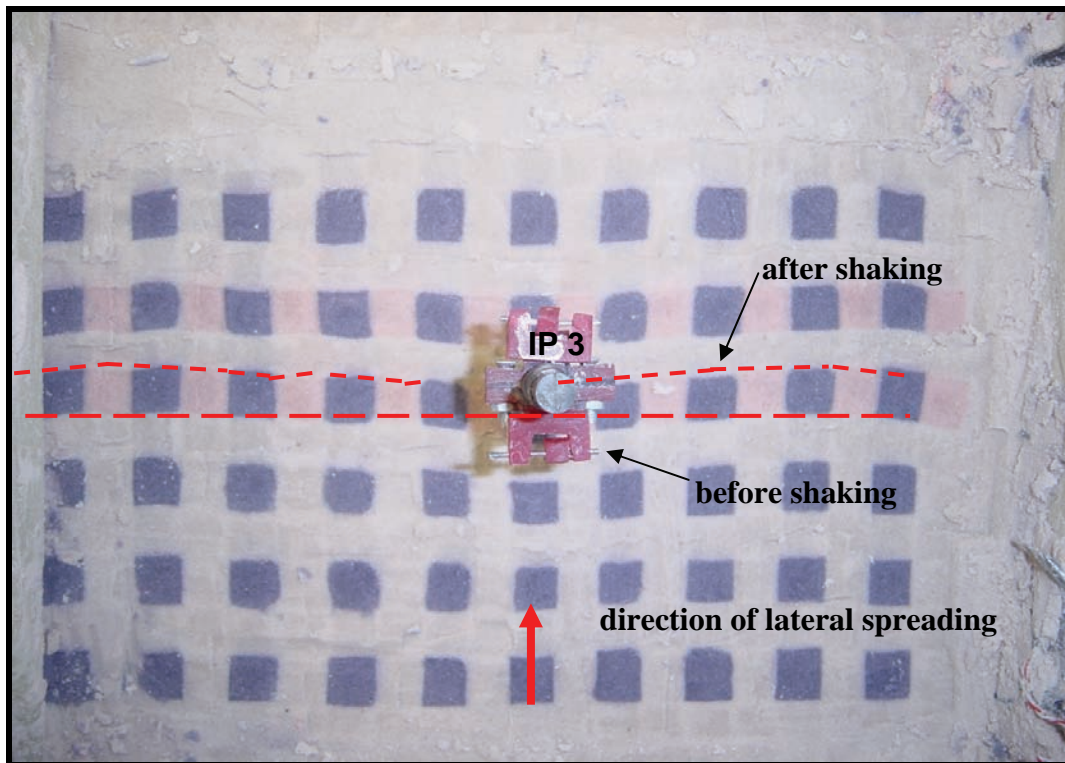
Grids of colored sand were placed at an intermediate depth to observe the pattern of soil displacement around the piles. Figure 4.33 shows pictures of the soil condition around the single pile and the pile group, after carefully removing the soil on top. Figure 4.33a shows that the liquefied soil did not flow between the piles. As a result, the soil had to flow around the pile group instead of around each individual pile, indicating the characteristic width perpendicular to the flow was at least the width of the whole pile group. This tends to support the hypothesis that the pressure of the liquefied soil acts on both piles and soil in between (Yokoyama et al., 1997), with significant increase in lateral loads and pile bending moments. Figure 4.33b shows that the pattern of soil deformation was affected up to a considerable distance at both sides of the single pile, corroborating the existence of a larger area of influence than the pile width itself.

4.5.5 Recorded Bending Moments

Prototype bending moments measured in the pile group and single pile are presented in Figs. 4.34, 4.35, and 4.36. The profiles of bending moments in the center pile are representative of all piles in the pile group, since the bending moments in the center and external piles were practically the same. As expected, the maximum moment at any given time occurred close to the base of the liquefied layer, reaching a maximum value at the end of shaking.



(a)



(b)

Figure 4.33: Pattern of soil displacement around piles at a depth of 3 m, (a) pile group, (b) single pile, Model 3x1-v

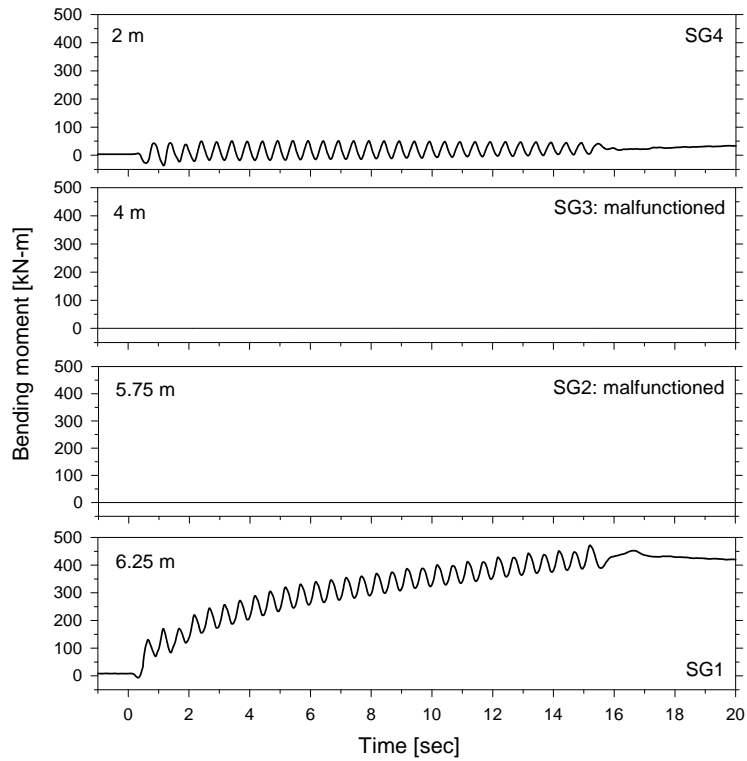


Figure 4.34: Bending moment time histories, external pile (IP 1), Model 3x1-v

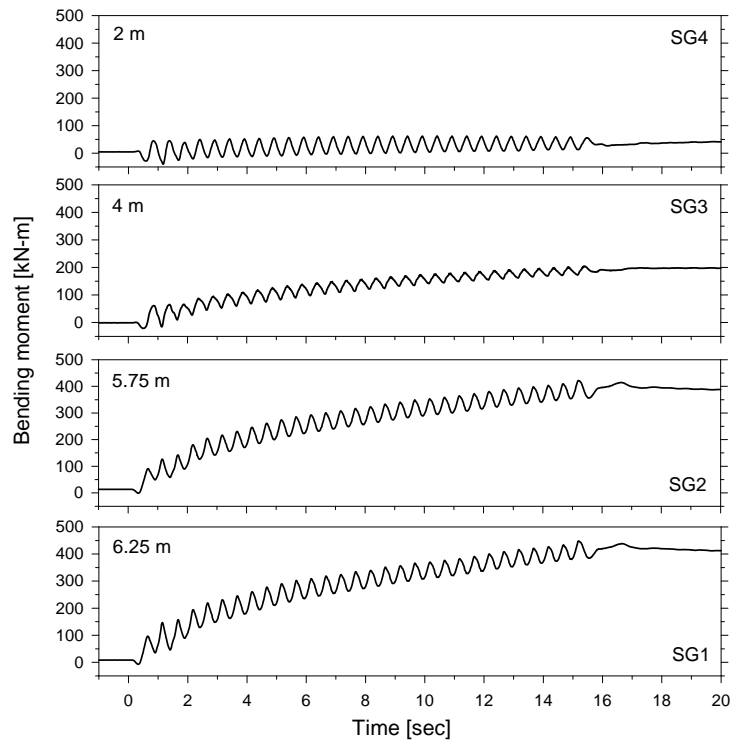


Figure 4.35: Bending moment time histories, center pile (IP 2), Model 3x1-v

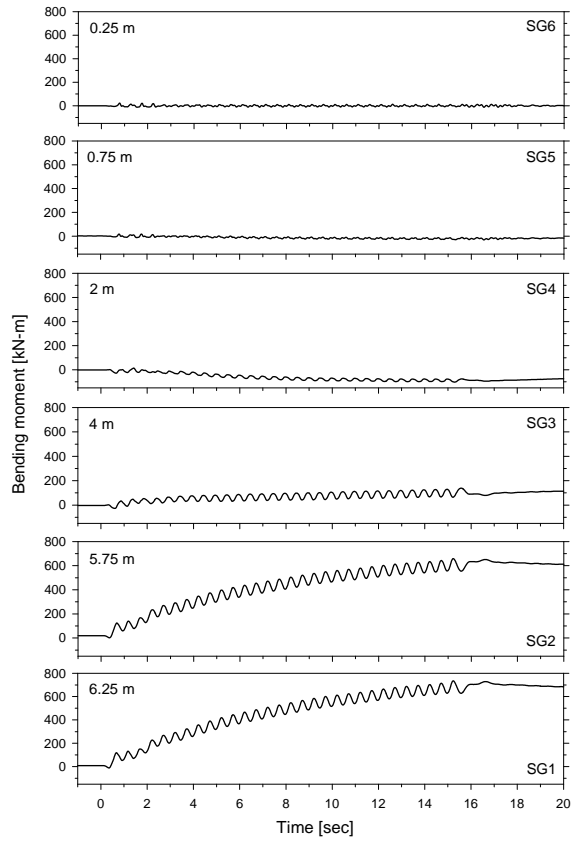


Figure 4.36: Bending moment time histories, single pile (IP 3), Model 3x1-v

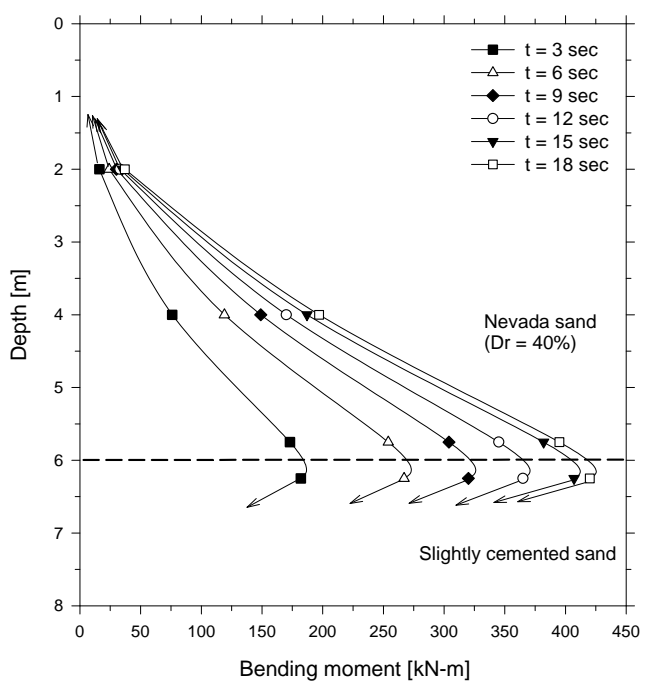


Figure 4.37: Profiles of bending moment, center pile (IP 2), Model 3x1-v

On the other hand, the profiles of bending moment in Fig. 4.38 reveal a much different response for the single pile. At deep elevations, the bending moment reached a very large positive value at the end of shaking. In the upper 3 m however, the bending moment was negative during the excitation. These profiles suggest that the soil near the ground surface behaved like a non-liquefied layer. Probably, negative excess pore pressure developed near the surface stiffened the soil next to the pile, generating a large force and restriction for the rotation of the pile head. This force would also explain the large bending moment and pile displacement. However, it appears that the large nonliquefied zone developed around the 3x1 pile group influenced the response of the single pile, given the fact that no negative moments were measured in Model 1x1-v, which simulates a single pile only, without a pile group nearby.

Figure 4.39 shows the measured bending moment at the base of the liquefiable layer versus the measured pile cap lateral displacement, after filtering out the cyclic component. The almost linear relationship between bending moment and pile cap displacement evidences the linear behavior of the pile-group-fixation system.

4.5.6 Limit Equilibrium Analysis

A limit equilibrium analysis was conducted to back-calculate the maximum measured bending moments and pile cap displacement. A student version of the software AVwin was used to model the 3x1 pile group subjected to the lateral force induced by lateral spreading. Since the bending moments of all three piles were very similar and they were connected by a cap, only one pile was modeled including one third of the cap, as shown in Fig. 4.40b. The pile was modeled with 30 elements, having a bending stiffness of $9000 \text{ kN}\cdot\text{m}^2$, whereas the slightly cemented layer was modeled with a rotational springs at the base of the liquefiable layer.

The liquefied soil pressure used in the analysis was the same $8.3 \text{ kN}/\text{m}^2$ previously estimated in Model 3x1-w, and the force acting on each node was obtained by multiplying this pressure by the corresponding area. Figure 4.33a clearly shows that the liquefied sand moved around the pile group, affecting the soil pattern up to a considerable distance at both sides of the foundation, suggesting that the liquefied soil pressure acted on the pile group, soil in between, and on the sides to some extent. The area of influence on the sides must be related to the negative excess pore pressure developed next to the piles, trend that was stronger at shallower depths. Therefore, a good solution is to consider a triangular area of influence on both sides of the pile group subjected to the soil pressure, as shown in Fig. 4.40a. Assuming a uniform pressure, an effective area of 39.3 m^2 was found to provide the best estimate for the maximum bending moment at the base of the liquefiable layer. On the other hand, the same rotational stiffness for each pile of $8000 \text{ kN}\cdot\text{m}/\text{rad}$ back-calculated in Model 3x1-w provided the best estimation for the maximum pile cap lateral displacement.

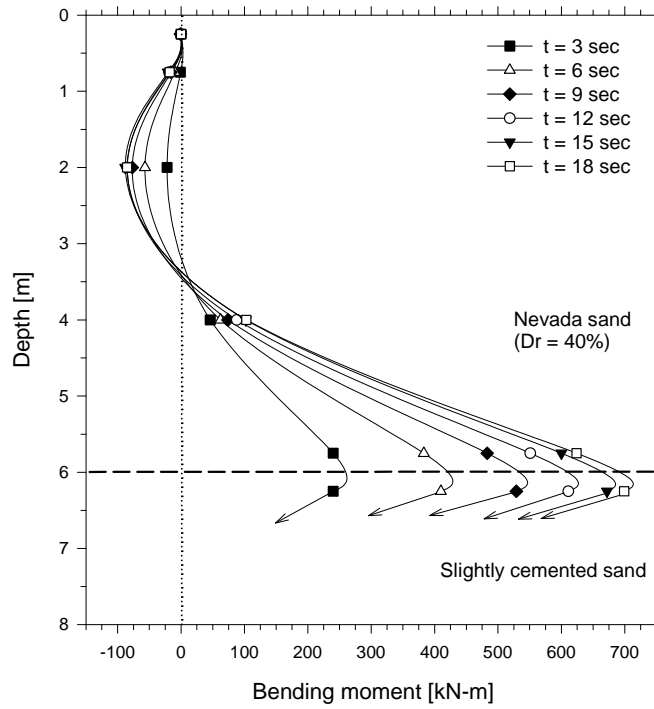


Figure 4.38: Profiles of bending moment, single pile (IP 3), Model 3x1-v

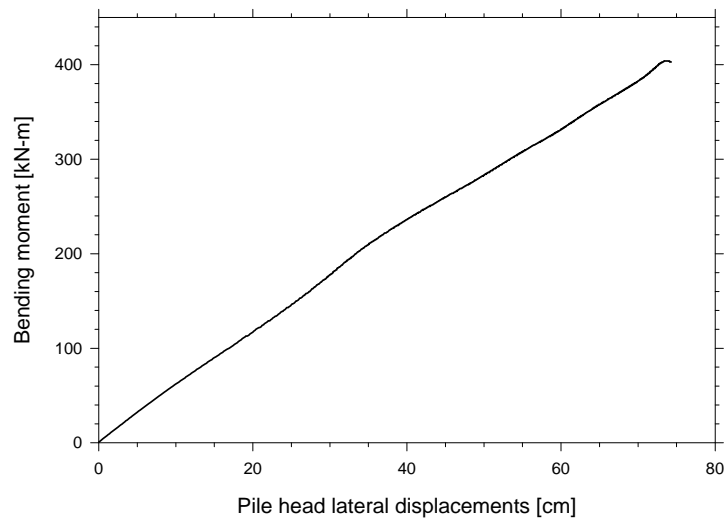


Figure 4.39: Bending moment at the base of the liquefiable layer versus pile cap lateral displacement, pile group, Model 3x1-v

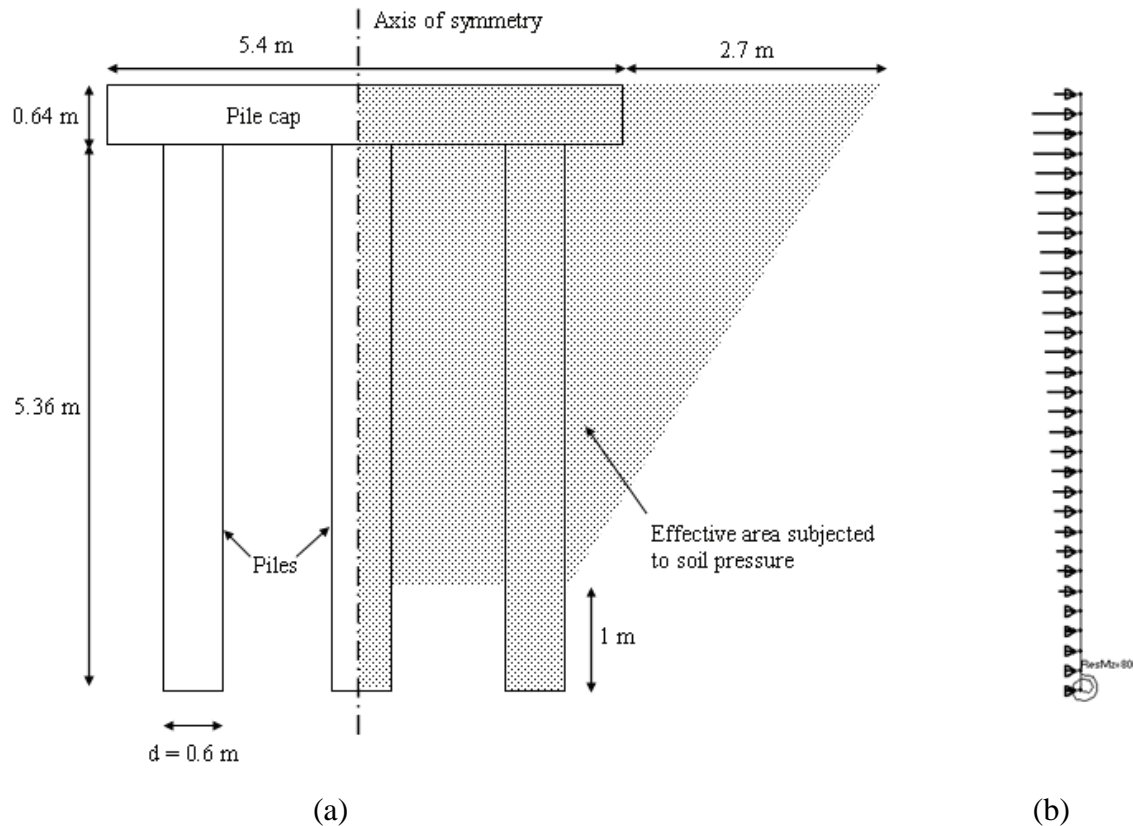


Figure 4.40: (a) Effective area subjected to liquefied soil pressure and (b) lateral view of the model used for limit equilibrium analyses, Model 3x1-v

The back-calculated bending moment was 405 kN-m, compared to 425 kN-m measured at the base of the liquefiable layer. The calculated pile cap lateral displacement was 90 cm, very similar to the 85 cm measured during the test. Table 4.3 summarizes some of the parameters used in the limit equilibrium analysis, as well as measured and calculated values, showing an excellent agreement.

4.6 Comparison of Free Field Results between Model 3x1-w and 3x1-v

This section compares some of the free field results obtained in Models 3x1-w and 3x1-v, such as: soil accelerations, excess pore pressures and soil lateral displacements. A detailed comparison of the recorded results from all centrifuge tests as well as a discussion of the effect of soil permeability on pile foundation response to lateral spreading is presented in Chapter 6. The centrifuge models 3x1-w and 3x1-v simulated the response of a 3x1 pile group and a single pile embedded in a two layer soil profile subjected to lateral spreading. The only difference between these models is that the first one was saturated with water, while the second one was saturated with a viscous fluid, simulating hence deposits of very different permeability in the field. A sketch of the setup and instrumentation used in both cases is presented in Fig. 4.1.

4.6.1 Comparison of Free Field Soil Accelerations

Figure 4.41 compares the free field soil accelerations measured in both centrifuge tests. The measured input accelerations indicate that both models were subjected to practically the same base excitation, which shows the very good repeatability and validates the direct comparison between the tests. The soil acceleration records in the loose sand layer exhibit in both cases a drop in positive amplitude after the first cycle of shaking due to the liquefaction process and dynamic isolation of the shallower layers. These records also contain large negative spikes during most of the excitation, with the spikes being considerably larger in the model saturated with water, suggesting that the simulated coarse sand exhibited a more dilative behavior, particularly near the ground surface. These phenomenon seems to be related with the fact that the shear strains at shallow elevations were larger in Model 3x1-w, as discussed below.

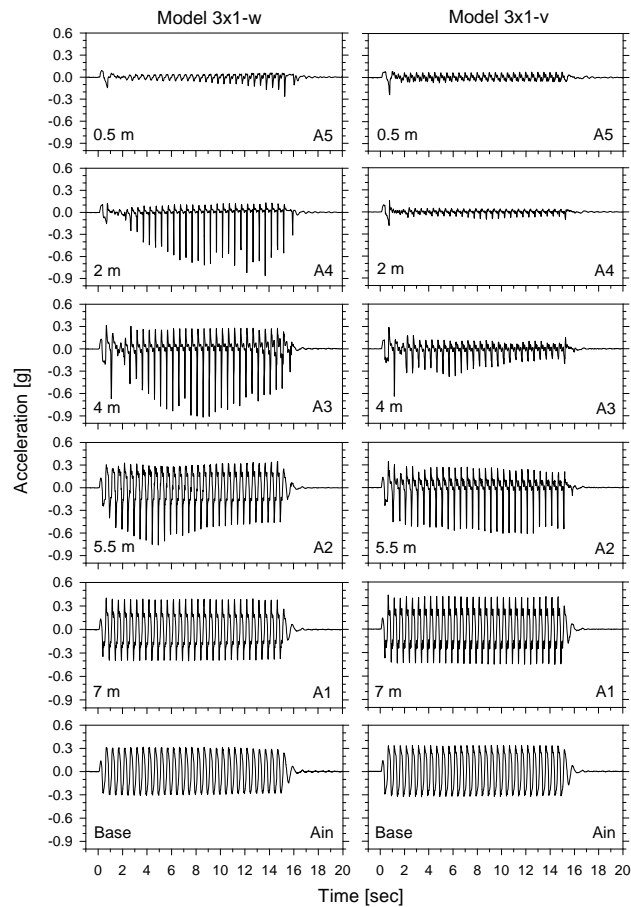


Figure 4.41: Comparison of soil acceleration in the free field between Model 3x1-w and 3x1-v

4.6.2 Comparison of Excess Pore Pressures

Figure 4.42 compares the excess pore pressures measured in the free field in Models 3x1-w and 3x1-v. In both tests, the records show that the in the free field the soil liquefied after about one or two cycles of shaking, which is in agreement with the trend exhibited by the acceleration time histories. In Model 3x1-v however, the excess pore pressure near the ground surface dropped and stayed around zero. At deeper elevations, the records in the water-saturated model exhibit larger negative spikes than in Model 3x1-v, being in some way consistent with the acceleration records.

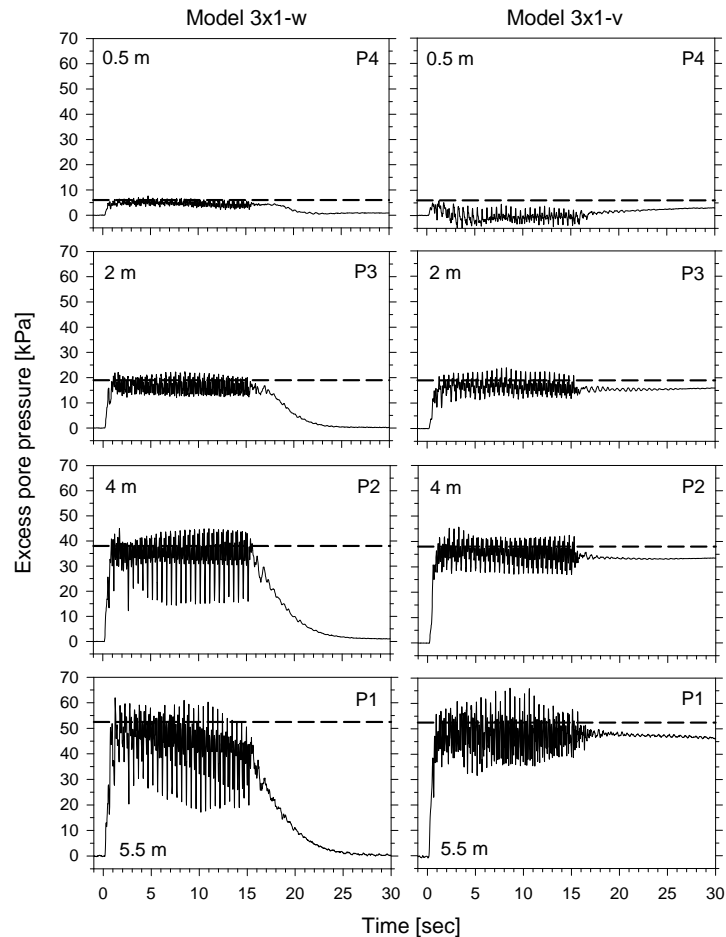


Figure 4.42: Comparison of excess pore pressure in the free field between Model 3x1-w and 3x1-v

Figure 4.43 compares the excess pore pressures measured next to one of the external piles in the pile group. In the model saturated with water, the soil close to the piles liquefied at the very beginning of shaking. In Model 3x1-v however, a strong negative excess pore pressure developed early in the shaking, pressure that was sustained until the end of the excitation. Even though the record at a deeper elevation does not exhibit such a dramatic response, exceptional large spikes developed during the first half of shaking. These records indicate that the excess

pore pressure build-up near the ground surface in the free field, and close to the piles, is significantly affected by the soil permeability. Most probably this negative excess pore pressure stiffened the soil close to the piles, enabling it to maintain a strong force near the pile cap, which would explain the large pile group displacement and bending moments. Even though there are no pore pressure measurements next to the single pile, the response must have been similar in order to explain the large pile displacement and shape of the bending moment profiles. As expected, the dissipation process was highly dependent on the soil permeability; it took only a few seconds in the simulated coarse sand layer (Model 3x1-w) and about five minutes in the simulated fine sand layer (Model 3x1-v). The process of dissipation in Model 3x1-w was mainly vertical. In Model 3x1-v however, besides the vertical dissipation, pore fluid from the free field moved toward the pile group to compensate the negative and low excess pore pressure in this area.

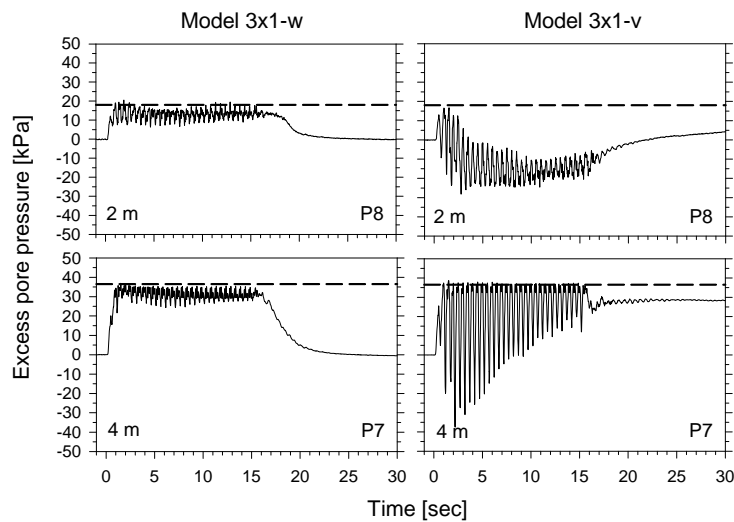


Figure 4.43: Comparison of excess pore pressure next to the external pile in the pile group, between Model 3x1-w and 3x1-v

4.6.3 Comparison of Free Field Lateral Displacements

Figure 4.44 compares the free field lateral displacement profiles between Models 3x1-w and 3x1-v. In both tests, the loose layer started moving downslope as soon as it liquefied at the beginning of shaking, with the maximum displacement at all times measured at the ground surface. Even though the magnitude of the deformation at all times was very similar, the profiles tended to have a different shape. In the water-saturated model, the shear strains had a tendency to increase with height, whereas in Model 3x1-v the shear strains tended to decrease with height. This trend is consistent with the response observe in the models simulating the single pile. The loose sand layer in Model 3x1-w was so permeable that the dissipation process started before the end of shaking, as shown in Fig. 4.42. This reduction in pore pressure must have increased the soil stiffness near the bottom of the sand layer, explaining the lower shear strains compared to the ones in Model 3x1-v. On the other hand, the reduction in pore pressure near the surface in

Model 3x1-v appears to have been responsible for the low shear strains developed at shallow elevations.

The cemented sand in both models did not experience permanent displacement and acted as a solid layer during the excitation, as illustrated by its acceleration record being very similar to the input.

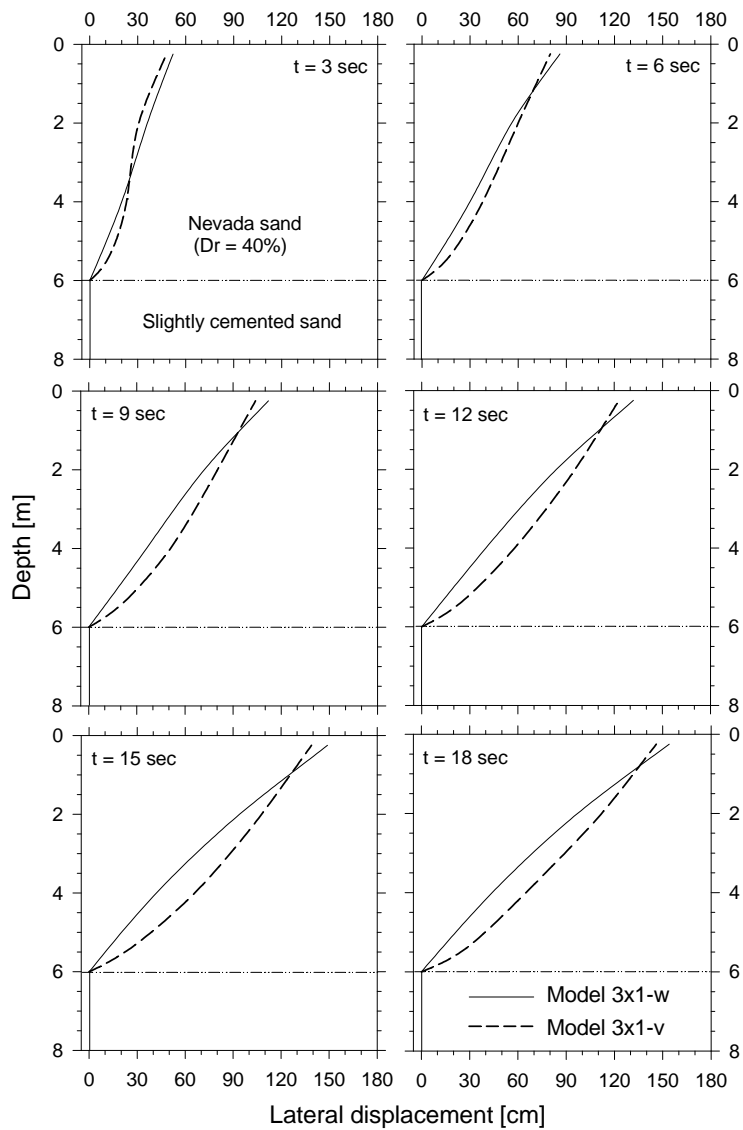


Figure 4.44: Comparison of free field lateral displacement profiles, between Model 3x1-w and 3x1-v

CHAPTER 5

EFFECT OF SOIL PERMEABILITY ON 2X2 PILE GROUP RESPONSE TO LATERAL SPREADING

5.1 Introduction

In the previous chapters, the results revealed that the liquefied soil permeability played an extremely important factor in the pile foundation response subjected to lateral spreading. The pile foundations in the models saturated with water reached maximum lateral displacements and bending moments and then bounced back during the excitation, whereas in the models saturated with water the foundations did not bounce back, reaching much larger lateral displacements and bending moments. Negative excess pore pressure developed close to the piles at shallow depths, allowing an hypothesis on the reasons for the huge variation in overall response, especially lateral displacement and bending moments.

This chapter presents in detail the results of two centrifuge tests conducted to investigate the response of a 2x2 pile group to lateral spreading. These models simulate a 2x2 pile group embedded in a two layer soil system, as shown in Fig. 5.1. The profile is the same one used in the previous models, consisting of a liquefiable layer on top of a nonliquefiable layer.

The slightly inclined models were excited by practically the same input motion, so the results can be compared. The only difference is that Model 2x2-w is saturated with de-aired/de-ionized water, whereas Model 2x2-v is saturated with a methylcellulose-water solution (metulose) having about 40 times the viscosity of water. Consequently, at a centrifugal acceleration of 50g, these models simulate deposits with very different permeability in the field.

A description of the models is presented in section 5.3, whereas the model preparation followed the same steps already described in section 3.2. Experimental results of Models 2x2-w and 2x2-v are presented and discussed in sections 5.4 and 5.5 respectively. Also, a basic limit equilibrium analysis is developed to back-calculate the maximum bending moments and pile group lateral displacement due to lateral spreading. Section 5.6 compares the two tests and discusses the difference in response due to the soil permeability effect.

5.2 Model Preparation

Preparation of Models 2x2-w and 2x2-v followed the same steps already described in section 3.2. In both models a single pile was placed before the soil was pluviated, attempting to simulate a pile installed with minimal disturbance to the surrounding soil, as may be the case when a pile is inserted into a pre-augered hole.

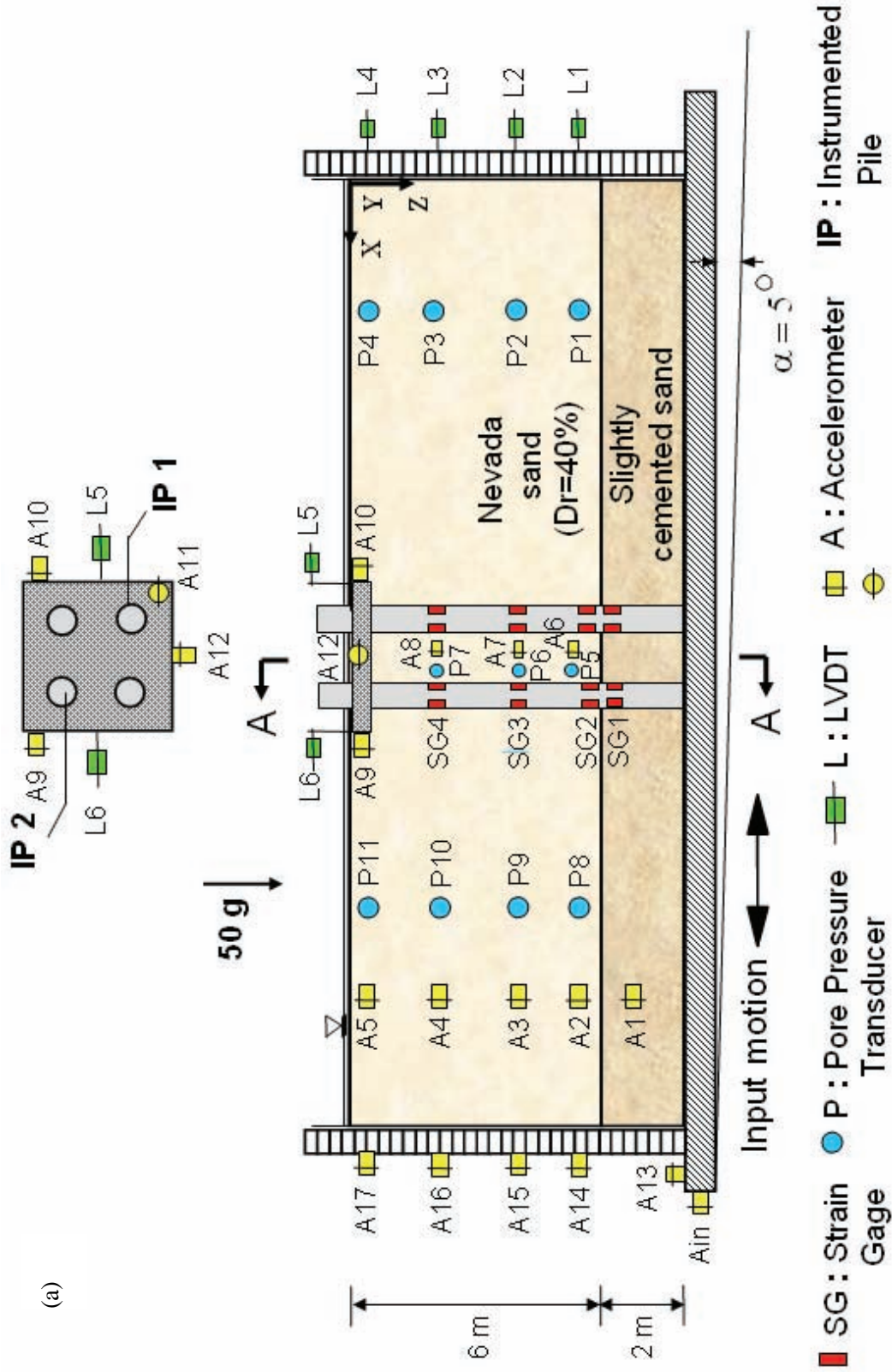
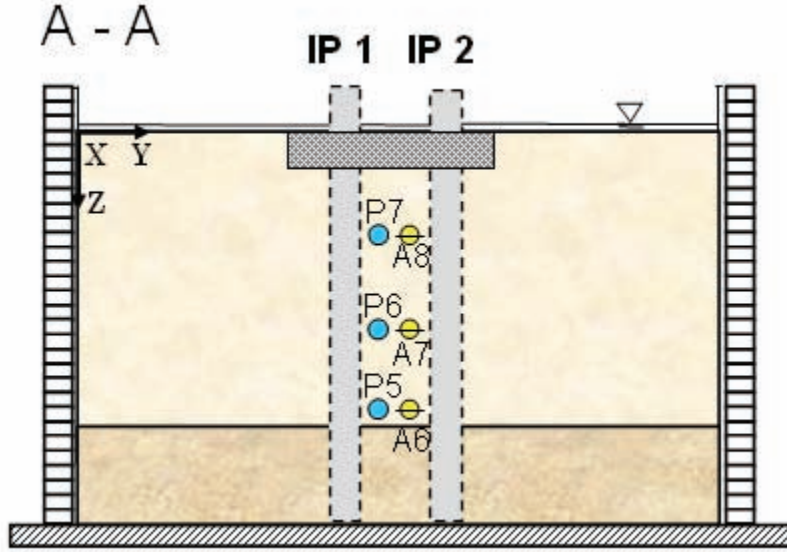


Figure 5.1: (a) Setup and instrumentation used in Models 2x2-w and 2x2-v, (in prototype units)



(b)

Figure 5.1 (cont.): (b) Transversal section of Models 2x2-w and 2x2-v

Table 5.1: Testing properties of centrifuge Models 2x2-w and 2x2-v

Model	Pile configuration	# of piles	# of instrument. piles	Pile cap	# of layers	Fluid viscosity (μ_w)
2x2-w	2 x 2	4	2	yes	2	1
2x2-v	2 x 2	4	2	yes	2	38

5.3 Models Description

The setup and instrumentation used in Models 2x2-w and 2x2-v are presented in Fig. 5.1. These models simulate a 2x2 pile group connected with a pile cap. The prototype profile consists of a 6 m thick Nevada sand layer placed at a relative density of about 40%, on top of a 2 m thick nonliquefiable cemented layer. The models, inclined 2° to the horizontal (4.8° after instrumental correction; Taboada, 1995), simulate an infinite mild ground slope. The main and only difference between both models is that Model 2x2-w is saturated with de-aired/de-ionized water, whereas Model 2x2-v is saturated with a methylcellulose-water solution (metulose) having about 40 times the viscosity of water. At a centrifugal acceleration of 50g the loose Nevada sand in Model 2x2-w simulates a coarse sand, whereas in Model 2x2-v it simulates a fine sand.

The embedded piles have a prototype diameter (d) of 60 cm and a prototype bending stiffness (EI) of approximately $9000 \text{ kN}\cdot\text{m}^2$. The square aluminum cap, embedded in the loose Nevada

sand, has prototype dimensions of 3.6 m in width, and 0.64 m in height. Figure 5.2 displays a picture and schematic of the pile-cap-structure, showing the spacing between piles ($3d$). Figure 5.3 shows a picture of the pile group and transducers during model preparation. Colored sand was placed as well at an intermediate depth to observe the pattern of soil displacement around the piles (Fig. 5.4).

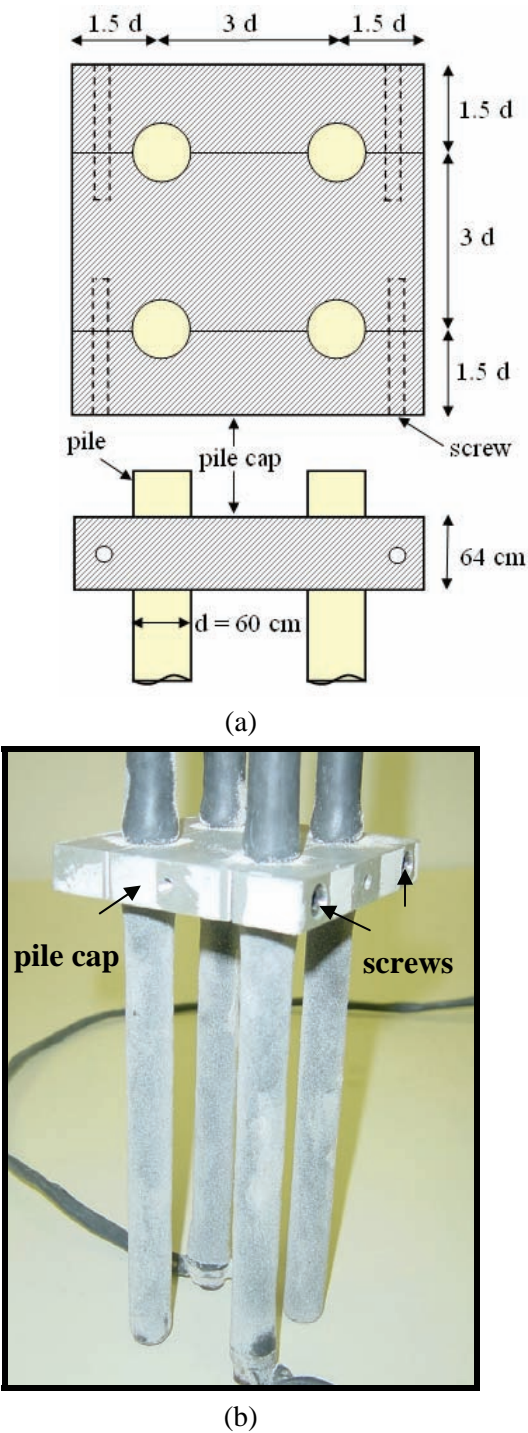


Figure 5.2: Pile-cap-structure, (a) schematic, (b) picture, Models 2x2-w and 2x2-v

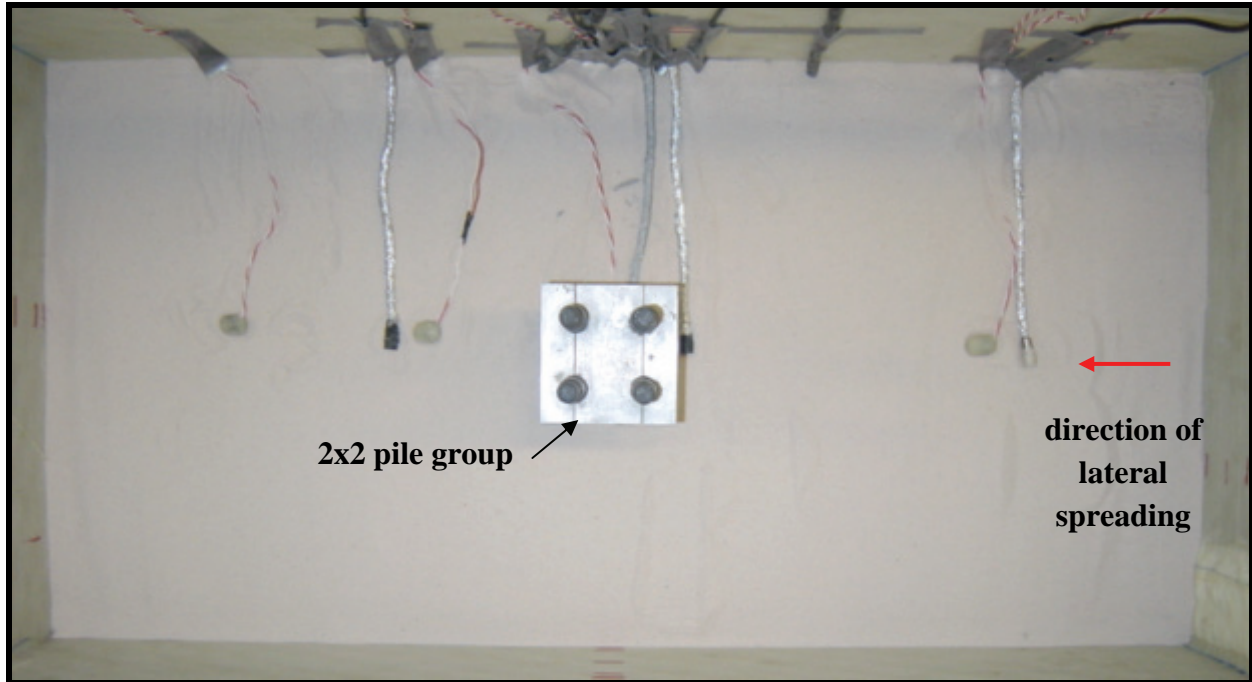


Figure 5.3: Model during preparation, Models 2x2-w and 2x2-v

Both models were excited by 30 cycles of a 100 Hz sinusoidal acceleration with uniform amplitude of about 15g. At a centrifugal acceleration of 50g this corresponds to a frequency of 2 Hz and peak acceleration of about 0.3g.

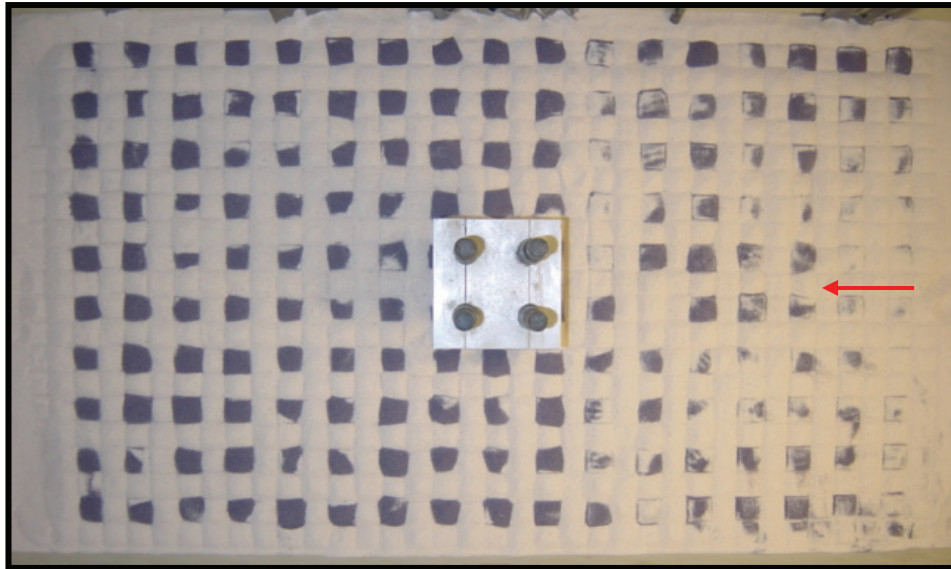
The instrumentation used in Models 2x2-w and 2x2-v is shown in Fig. 5.1 and listed in Table 5.2. The models were instrumented with 18 accelerometers, 11 pore pressure transducers, and 6 LVDTs. Two instrumented piles (IP1 and IP2) were used in the pile group foundation, as shown in Fig. 5.1a. Detailed information about the strain gage configuration and the piles (type U1) used in these models is presented in section 2.7. Accelerations in the soil and outside the laminar box, excess pore water pressure, lateral displacement of the soil and the pile cap, bending moments, and axial forces were measured during the tests.

5.4 Model 2x2-w

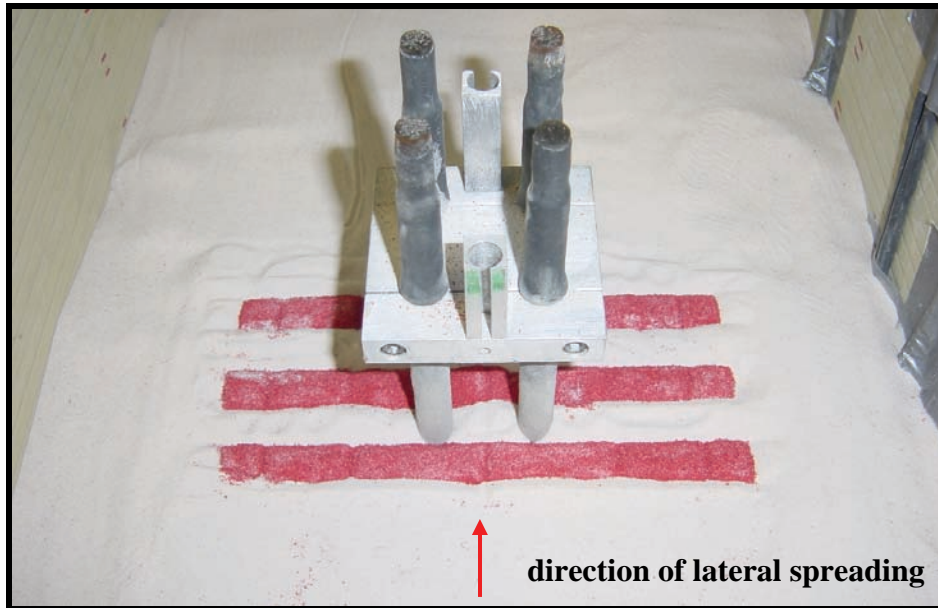
5.4.1 Recorded Accelerations

Figure 5.5 shows the recorded input acceleration and soil acceleration time histories in the free field (far from the pile group) at different depths. As expected, the measured input acceleration (A_{in}) had a uniform prototype amplitude of 0.3g. The acceleration records in the loose sand layer show a drop in positive amplitude and large spikes in the negative direction, indicating this layer did liquefy during the excitation. This decrease in positive amplitude is related to the difficulty shear waves have in traveling through the liquefied soil due to its significant reduction in

stiffness and strength. On the other hand, the acceleration of the bottom layer was very similar to the input acceleration, indicating no sliding occurred between this layer and the base of the laminar box. The soil acceleration between piles dropped after one or two cycles, as shown in Fig. 5.6, indicating that liquefaction occurred in this area too. However, the smaller spikes compared to the ones in the free field seems to be related to the confining effect of the pile group. The increase in acceleration at a depth of 5.5 m was probably caused by the influence of one of the piles, as that accelerometer (A7) was moving downslope during shaking.



(a)



(b)

Figure 5.4: Colored sand placed at an intermediate depth, (a) Model 2x2-w, (b) Model 2x2-v

Table 5.2: Location of instruments in Models 2x2-w and 2x2-v (in model units)

Transducer	Sensor name	Coordinates [cm]		
		X	Y	Z
Accelerometer	Ain	73.5	17.75	16.5
	A1	60	17.75	14
	A2	60	17.75	11
	A3	60	17.75	8
	A4	60	17.75	4
	A5	60	17.75	1
	A6	35	18.25	11
	A7	35	18.25	8
	A8	35	18.25	4
	A9	39	20.5	0.63
	A10	32	20.5	0.63
	A11	32.75	15	0
	A12	35.5	14.25	0.63
	A13	72.5	17.75	16
	A14	71	17.75	11
	A15	71	17.75	8
	A16	71	17.75	4
A17	71	17.75	1	
Pore pressure transducer	P1	10	17.75	11
	P2	10	17.75	8
	P3	10	17.75	4
	P4	10	17.75	1
	P5	36	17.25	11
	P6	36	17.25	8
	P7	36	17.25	4
	P8	50	17.75	11
	P9	50	17.75	8
	P10	50	17.75	4
	P11	50	17.75	1

Table 5.2 (cont.): Location of instruments in Models 2x2-w and 2x2-v (in model units)

Transducer	Sensor name	Coordinates [cm]			
		X	Y	Z	
LVDT	L1	0	17.75	11	
	L2	0	17.75	8	
	L3	0	17.75	4	
	L4	0	17.75	0.5	
	L5	32	17.75	-2	
	L6	39	17.75	-2	
Strain gage	SG1	IP 1	IP 1	IP 1	
		33.75	16	12.5	
		SG2	33.75	16	11.5
		SG3	33.75	16	8
	SG4	33.75	16	4	
		IP 2	IP 2	IP 2	
		SG1	37.25	19.5	12.5
		SG2	37.25	19.5	11.5
	SG3	37.25	19.5	8	
		SG4	37.25	19.5	4

Figure 5.7 presents accelerations recorded on the pile cap, as well as the measured horizontal and vertical acceleration at the base of the laminar box. As expected, the vertical and perpendicular accelerations of the pile cap were very small. The acceleration in the lateral spreading direction was larger and had the same frequency of the input motion. The acceleration records on laminar rings (Fig. 5.8) exhibit a drop in positive amplitude and spikes in the negative direction, showing a good agreement with the free field soil accelerations of Fig. 5.5.

5.4.2 Recorded Excess Pore Pressures

The excess pore pressure records reveal that the loose sand in the free field (far from the pile group) liquefied after about one or two cycles of shaking (Fig. 5.9), in agreement with the trend exhibited by the acceleration time histories. However near the ground surface, the pore pressure on the downslope side of the pile group (P11) did not increase during shaking. The fact that the pore pressure did not raise just after the excitation due to the dissipation process, suggests that this pore pressure (P11) must have moved toward the surface at the beginning of the excitation.

The excess pore pressure time histories between piles indicate the soil in this area also liquefied (Fig. 5.10). The excess pore pressures were slightly lower than in the free field, probably related to the fact the initial vertical effective stresses were smaller below the pile cap. The dissipation process took only a few seconds, confirming the high permeability of the model.

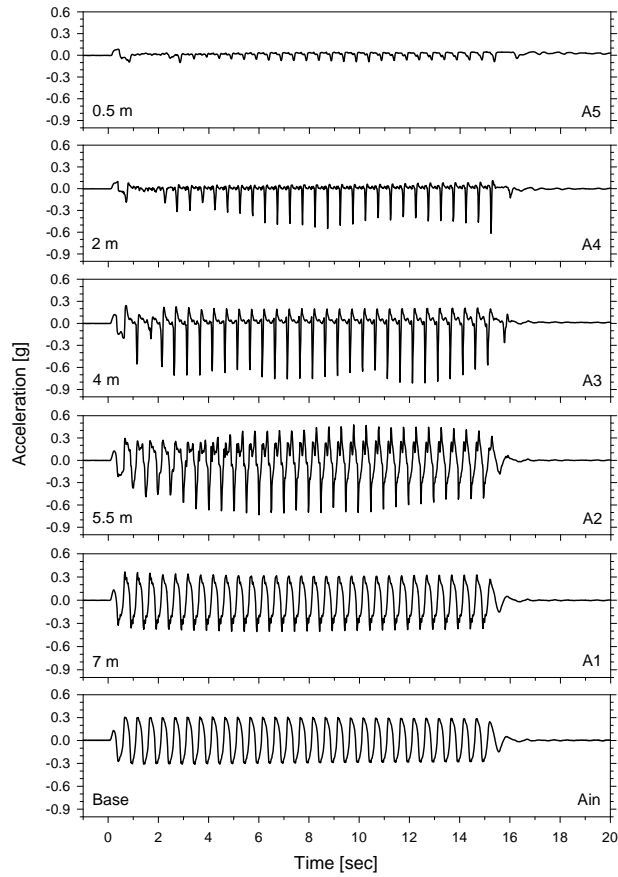


Figure 5.5: Soil accelerations time histories in the free field, Model 2x2-w

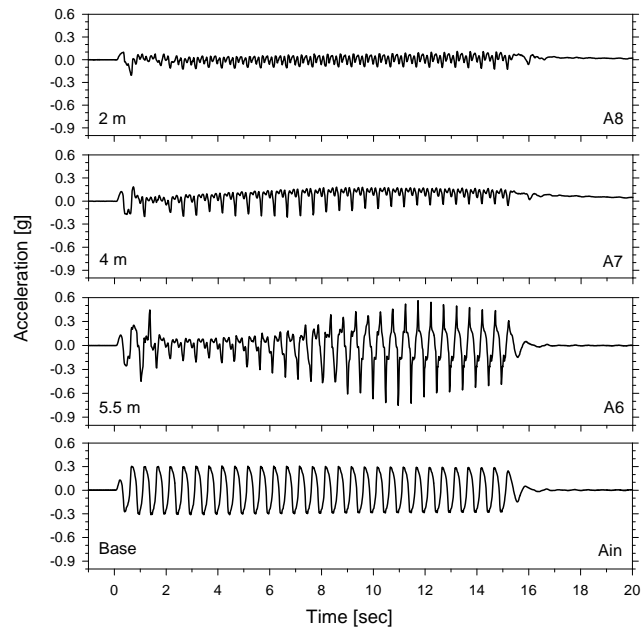


Figure 5.6: Soil acceleration time histories between piles, Model 2x2-w

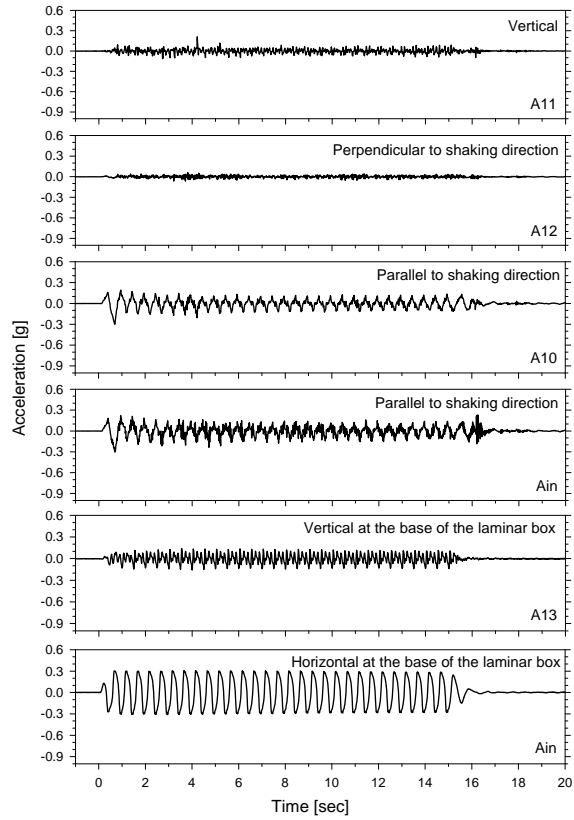


Figure 5.7: Accelerations recorded on the pile cap, Model 2x2-w

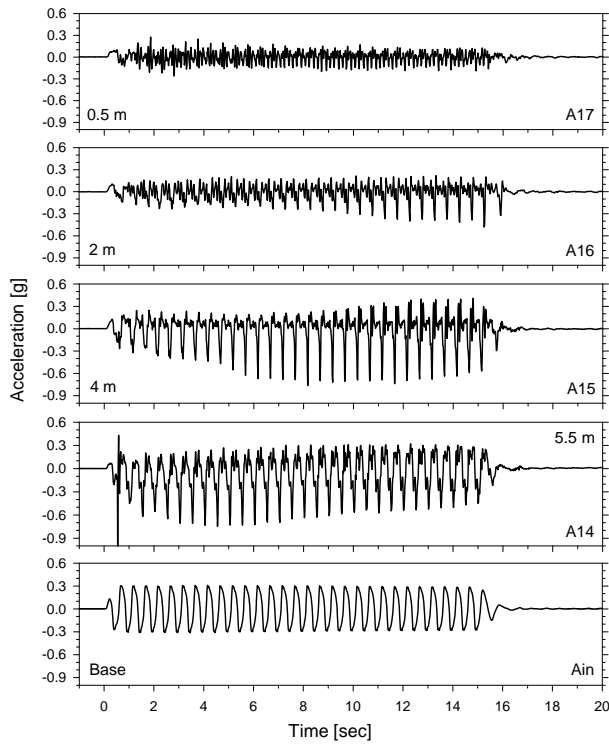


Figure 5.8: Accelerations recorded on the laminar rings, Model 2x2-w

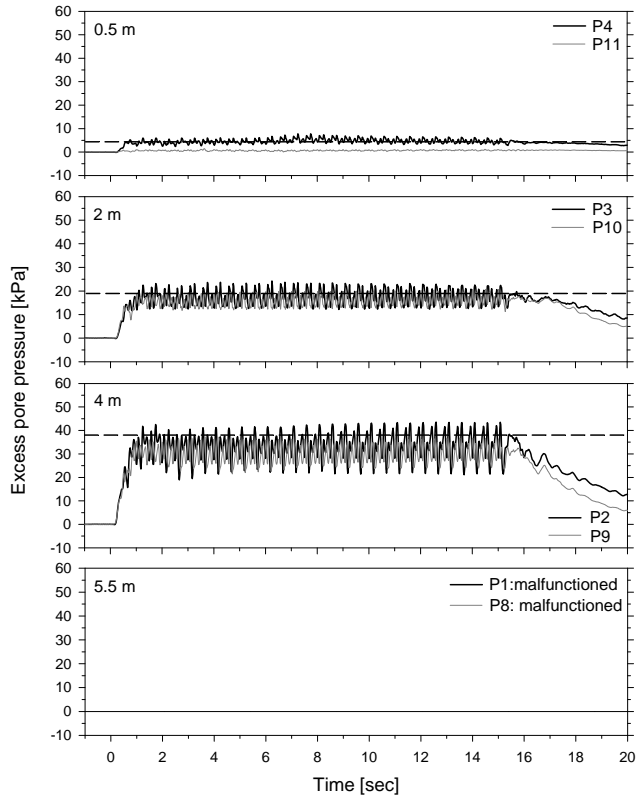


Figure 5.9: Excess pore pressure time histories in the free field, the dashed lines correspond to initial liquefaction, Model 2x2-w

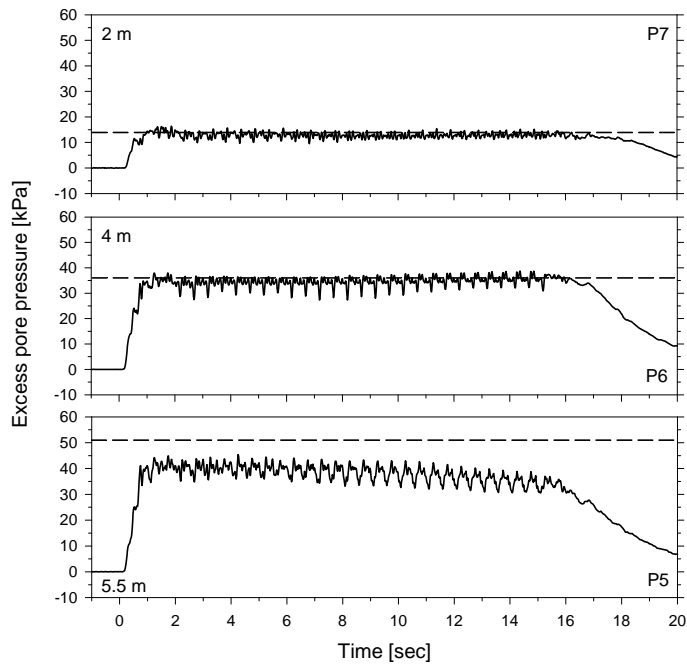


Figure 5.10: Excess pore pressure time histories between piles, the dashed lines correspond to initial liquefaction, Model 2x2-w

5.4.3 Recorded Lateral Displacements

The recorded soil lateral displacement in the free field (Fig. 5.11) shows that the liquefied layer displaced gradually during shaking, reaching a maximum displacement of approximately 150 cm at the end of shaking. The pile cap on the other hand, bounced back after reaching a maximum lateral displacement of approximately 7 cm at the beginning of the excitation. This decrease in displacement occurred despite the fact the free field deformation kept increasing until the end of shaking, indicating clearly that the liquefied soil was flowing around the foundation.

The profiles of soil lateral displacement in the free field were obtained by interpolating the LVDT measurements, after filtering out the cyclic component (Fig. 5.12). As soon as the loose sand liquefied at the beginning of shaking, the deposit started moving downslope, with the maximum displacement taking place always on the ground surface.

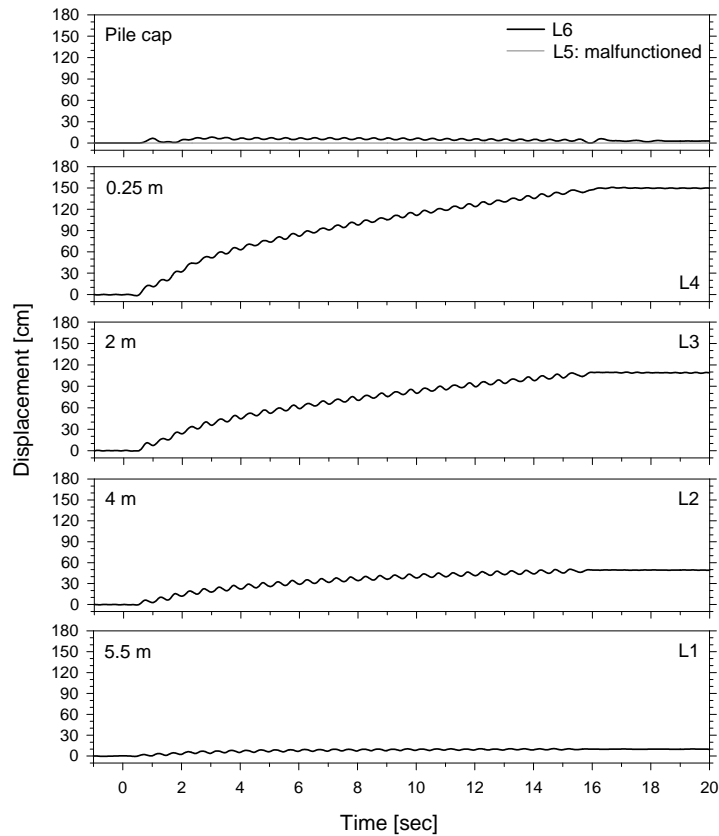


Figure 5.11: Lateral displacement time histories, Model 2x2-w

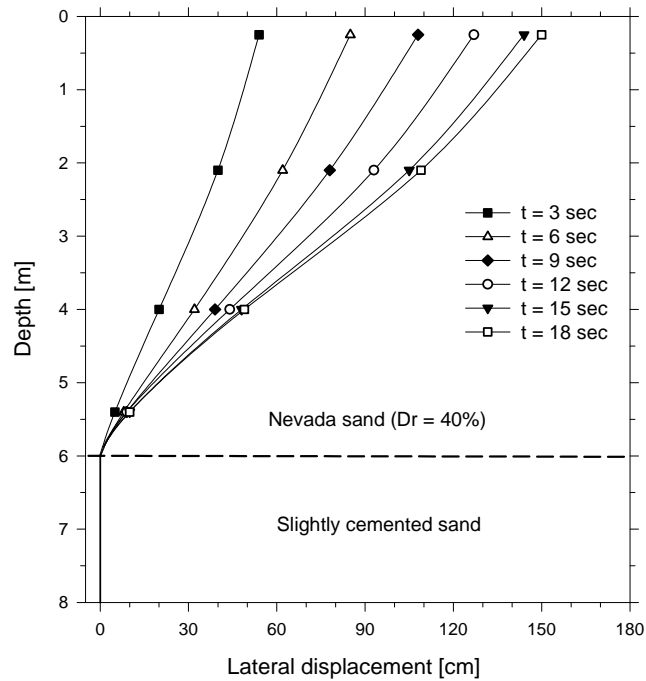


Figure 5.12: Profiles of soil lateral displacement in the free field, Model 2x2-w

5.4.4 Pattern of Soil Displacement around Piles

Figure 5.13 shows the pattern of soil displacement around the pile group at an intermediate elevation. Even though it is not possible to observe in this picture (Fig. 5.13) the soil condition around each pile, the soil close to the pile group moved the same amount that in the free field. This indicates that the liquefied soil moved around each individual pile, instead of around the pile group. Therefore, the characteristic width perpendicular to the flow was the diameter of the piles. This would tend to support the hypothesis that the pressure of the liquefied soil acts only on the individual piles and not on the soil in between, contrary to the recommendation by Yokoyama et al. (1997) discussed in chapter 1.

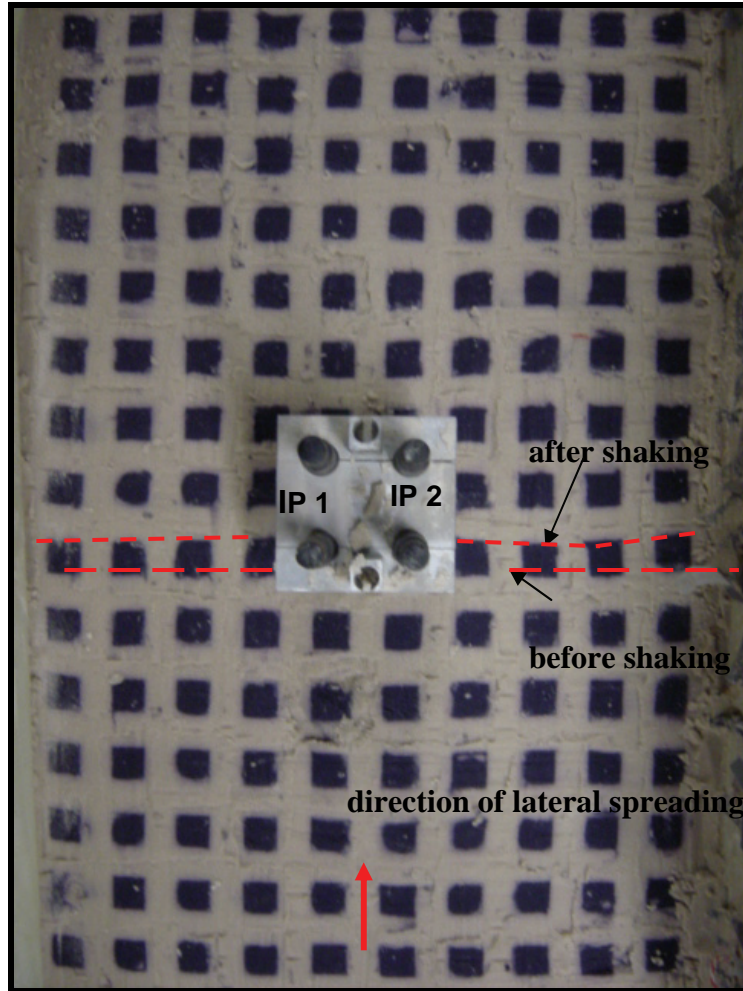


Figure 5.13: Pattern of soil displacement around pile group at a depth of 4 m, Model 2x2-w

5.4.5 Recorded Bending Moments

Prototype bending moments were obtained with the strain gage measurements at different elevations. Since bending moments can be estimated from quarter and half bridge configurations, four records were obtained for the upslope pile IP1 and downslope pile IP2, as shown in Figs. 5.14 and 5.15 respectively. Profiles of bending moments for both piles are presented in Fig. 5.16, after filtering out the cyclic component. The profiles in the upslope and downslope piles are practically the same, with the maximum moments taking place close to the base of the liquefied layer and at the connection with the pile cap. The bending moments reached a maximum value at about 3 sec, which is also the time at which the pile cap reached its maximum deflection. Afterwards, the bending moments decreased despite the fact that the free field deformation associated with the lateral spreading kept increasing until the end of shaking. After 3 sec the liquefied soil seemed to be flowing around the piles, following the same trend observed in the previous centrifuge tests using water as pore fluid.

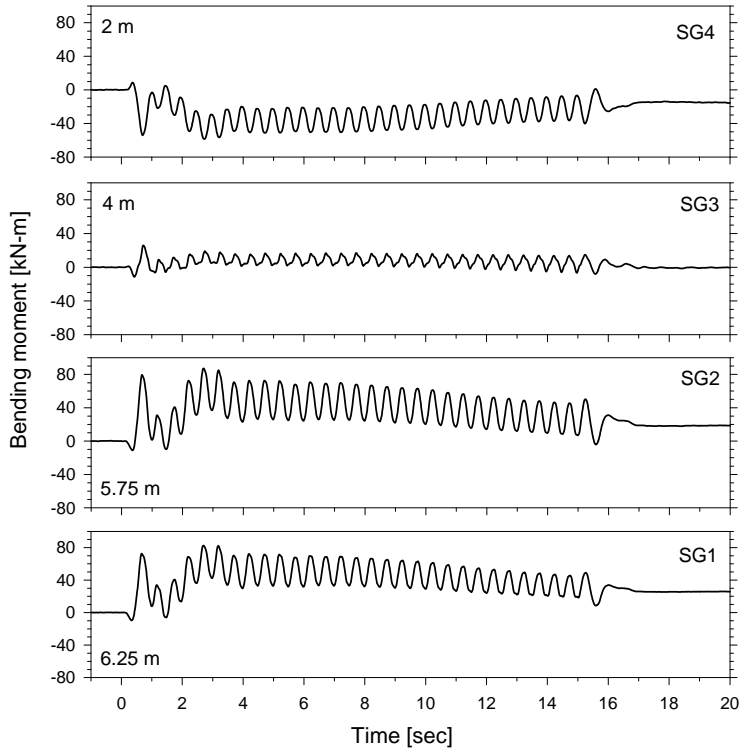


Figure 5.14: Bending moment time histories, upslope pile (IP 1), Model 2x2-w

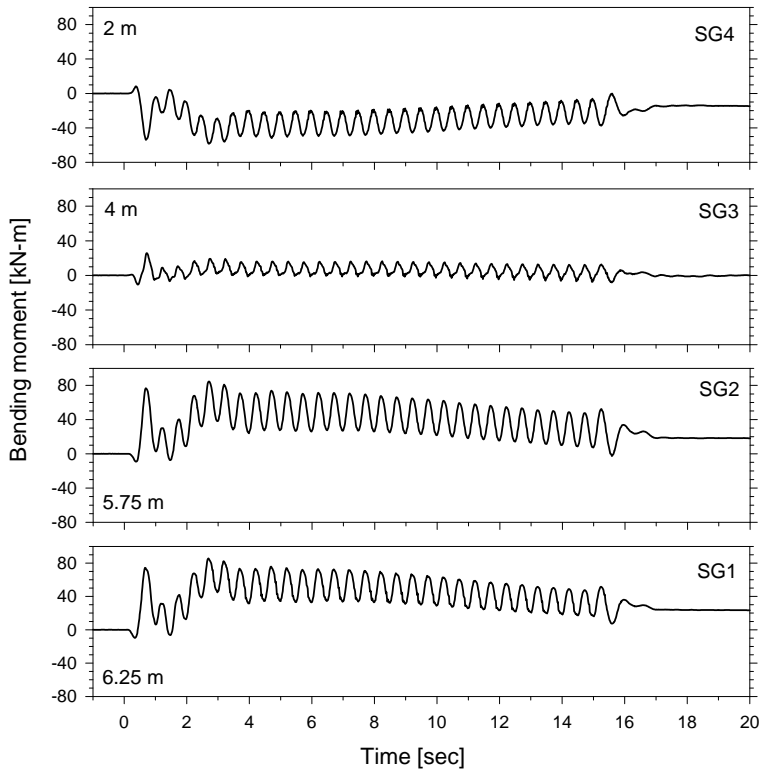


Figure 5.15: Bending moment time histories, downslope pile (IP 2), Model 2x2-w

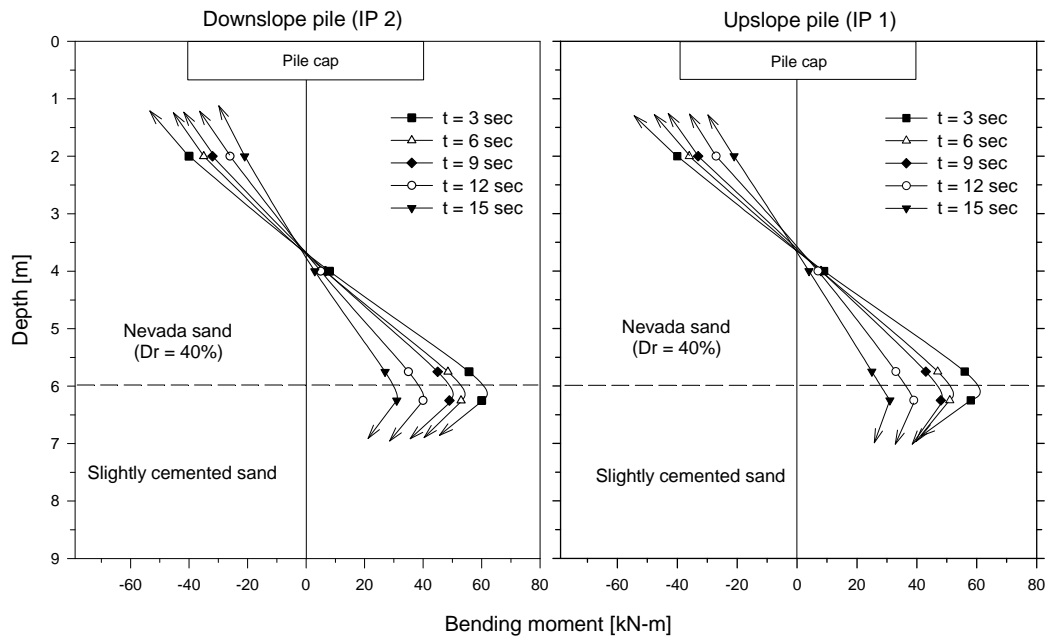


Figure 5.16: Profiles of bending moment, upslope (IP 1) and downslope (IP 2) piles, Model 2x2-w

Figure 5.17 shows the measured pile bending moment at the base of the liquefiable layer versus the measured pile cap lateral displacement, after filtering out the cyclic component. The pile group reached a maximum lateral displacement and bending moment and then bounced back during shaking. The almost linear relationship between bending moment and pile cap displacement indicates an approximately linear elastic behavior of the pile-group-fixation system.

5.4.6 Recorded Axial Forces

Prototype axial force time histories were also obtained with the strain gage measurements. Since axial forces can be estimated only from a quarter bridge configuration, two measurement histories were obtained for the upslope pile IP1 and downslope pile IP2, as shown in Figs. 5.18 and 5.19 respectively. Positive values represent tension while negative ones represent compression. The axial forces were zeroed at the beginning of shaking, and therefore represent the change in axial force during the excitation.

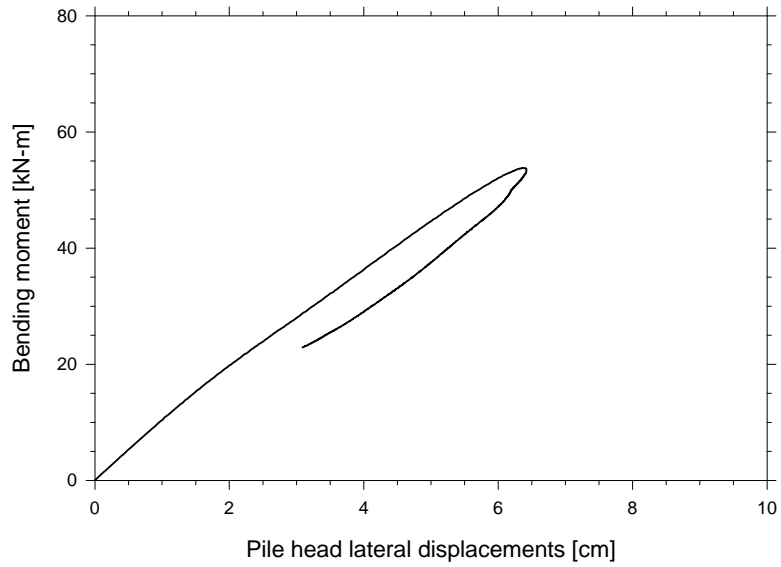


Figure 5.17: Bending moment at the base of the liquefiable layer versus pile cap lateral displacement, Model 2x2-w

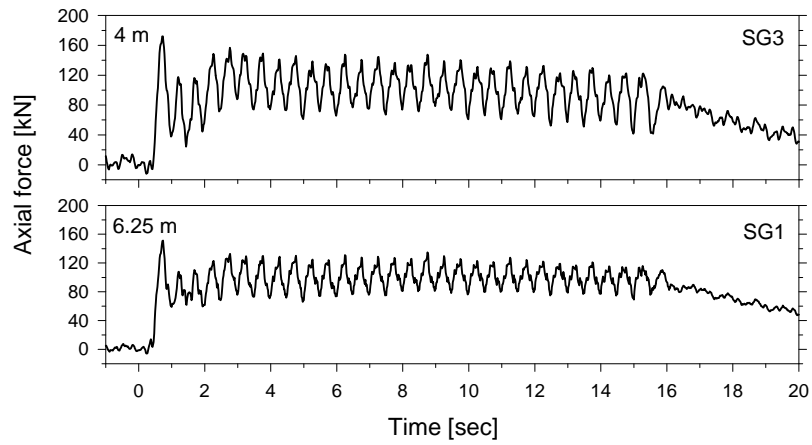


Figure 5.18: Axial force time histories, upslope pile (IP 1), Model 2x2-w

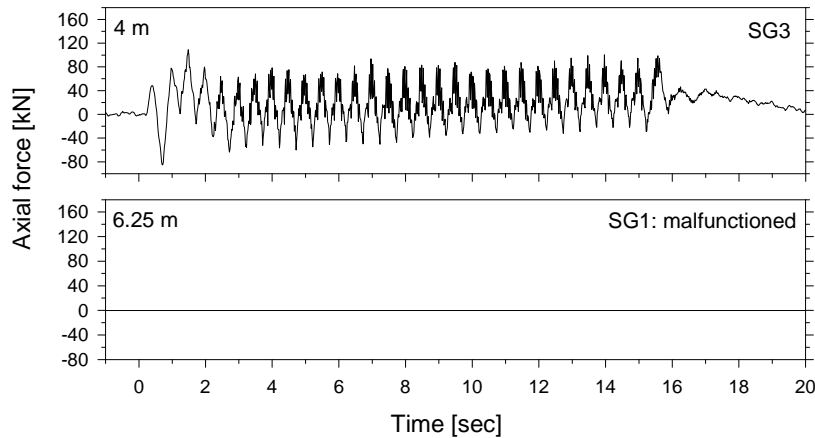


Figure 5.19: Axial force time histories, downslope pile (IP 2), Model 2x2-w

As expected, the upslope pile IP1 was in tension during the excitation, averaging a force of 100 kN. The measured force in the downslope pile was also positive, with an average value of 10 kN, suggesting that the whole pile group was pulled upwards during the shaking. The excess pore pressure must have applied a large pressure under the pile cap, generating tensional forces on the pile that were added to the ones induced by the frame effect. As a result, a tensional force in each pile of about + 55 kN appears to have superimposed to the ± 45 kN forces generated by the frame effect.

5.4.7 Limit equilibrium analysis

A limit equilibrium analysis was conducted to estimate the liquefied soil pressure acting on the pile group. A student version of the software AVwin was used to model the pile group subjected to the lateral force induced by lateral spreading. A 2-D analysis of this 3-D system could be conducted due to the symmetry of the 2x2 pile group, as shown in Fig. 5.20b. Each pile was modeled with 31 elements, having a bending stiffness of $9000 \text{ kN}\cdot\text{m}^2$, whereas the pile cap was modeled with three rigid elements. Since the measured bending moments in the upslope and downslope piles were very similar, articulated elements were used to transfer part of the lateral load from the upslope to the downslope pile. The slightly cemented layer was modeled with rotational springs at the base of the liquefiable layer.

The pattern of soil deformation in Fig. 5.13 showed that the liquefied sand moved around each pile, affecting the soil pattern close to the piles themselves. Therefore, the liquefied soil pressure was assumed to act only on the upslope piles and pile cap, which represents a total effective area of 8.6 m^2 , as shown in Fig. 5.20a. This pressure was assumed to be constant and independent of depth. The force on each node was finally obtained by multiplying the soil pressure by the

associated area. A liquefied soil pressure of 16 kN/m^2 and a rotational stiffness of 8000 kN-m/rad at the base of each of the two piles in Fig. 5.20b were found to provide the best estimations of the maximum pile bending moment and pile cap displacement. The back-calculated bending moment was 56 kN-m , very similar to the 58 kN-m measured at the base of the liquefiable layer. The calculated pile cap lateral displacement was 5 cm , compared to the 7 cm measured during the test. The calculated axial force was 63 kN in the upslope pile and -63 kN in the downslope pile, compared to the $\pm 45 \text{ kN}$ estimated in the test, after subtracting the vertical force acting on the pile group, as discussed in the previous section. Table 5.3 summarizes some of the parameters used in the limit equilibrium analysis, as well as measured and calculated values, showing very good agreement.

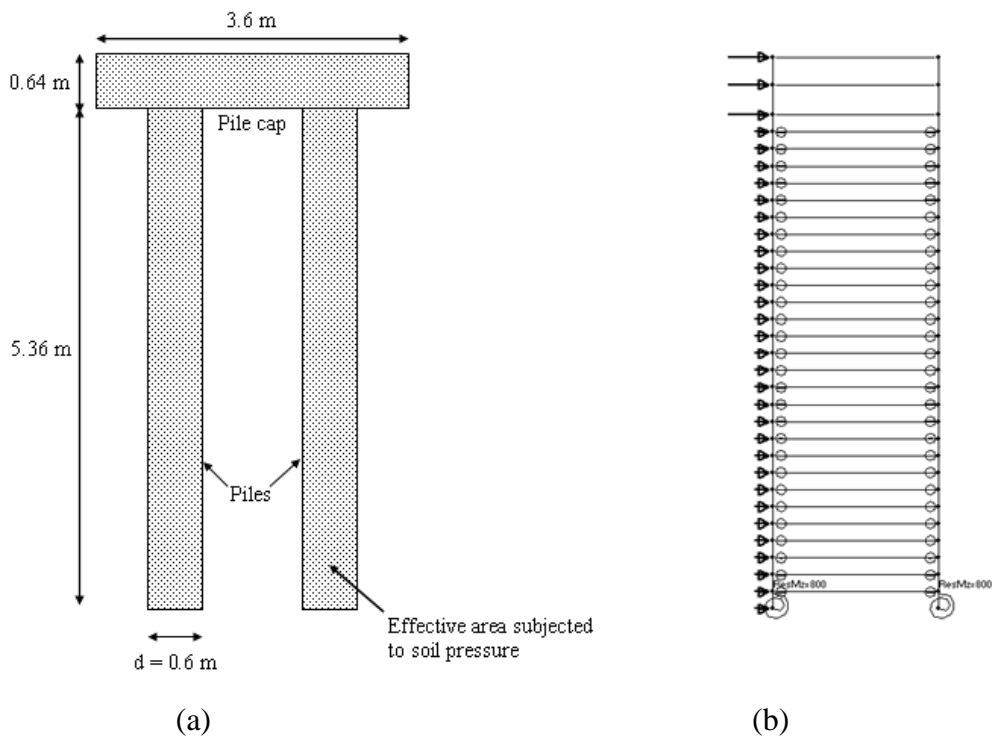


Figure 5.20: (a) Effective area subjected to liquefied soil pressure and (b) lateral view of the model used for limit equilibrium analyses, Model 2x2-w

5.5 Model 2x2-v

5.5.1 Recorded Accelerations

Figure 5.21 shows the recorded input acceleration and soil acceleration time histories in the free field (far from the pile group) at different depths. The input acceleration had a uniform amplitude of $0.27g$, slightly less than in Model 2x2-w. The acceleration records in the loose sand layer show a drop in positive amplitude and large spikes in the negative direction, spikes that are

related to the dilative behavior of the saturated loose sand during lateral spreading. Therefore, these records indicate the loose sand layer liquefied and displaced in the downslope direction during shaking. On the other hand, the acceleration of the bottom layer was identical to the input acceleration, indicating no sliding occurred between this layer and the base of the laminar box.

The soil acceleration between piles (Fig. 5.22) was very similar to the one in the free field, giving evidence of liquefaction in the pile group area. Figure 5.23 presents accelerations recorded on the pile cap, as well as horizontal and vertical acceleration at the base of the laminar box. As expected, the vertical and perpendicular acceleration of the pile cap were small. In the direction of lateral spreading however, the acceleration record contains large spikes. The acceleration records on the laminar rings (Fig. 5.24) exhibit a drop in positive amplitude and spikes in the negative direction, showing a good agreement with the soil acceleration.

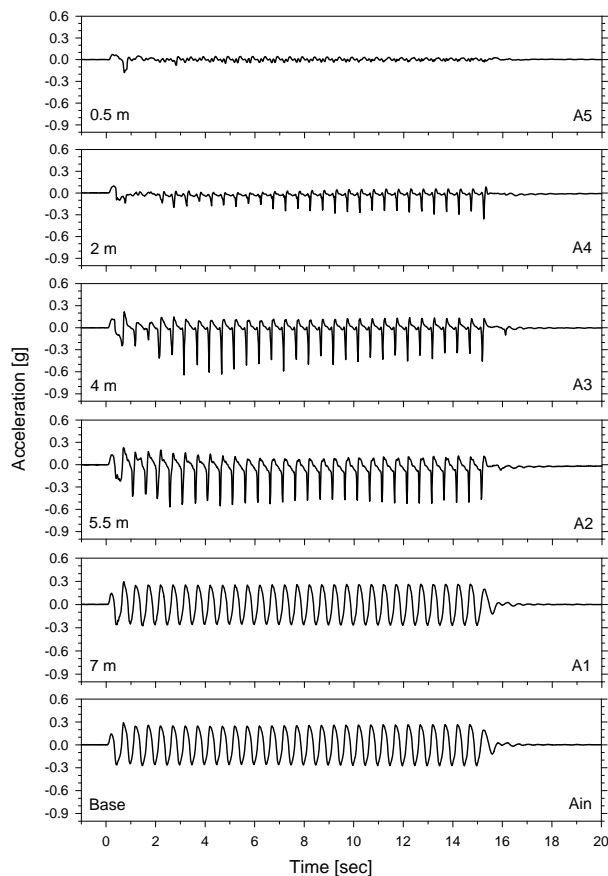


Figure 5.21: Soil acceleration time histories in the free field, Model 2x2-v

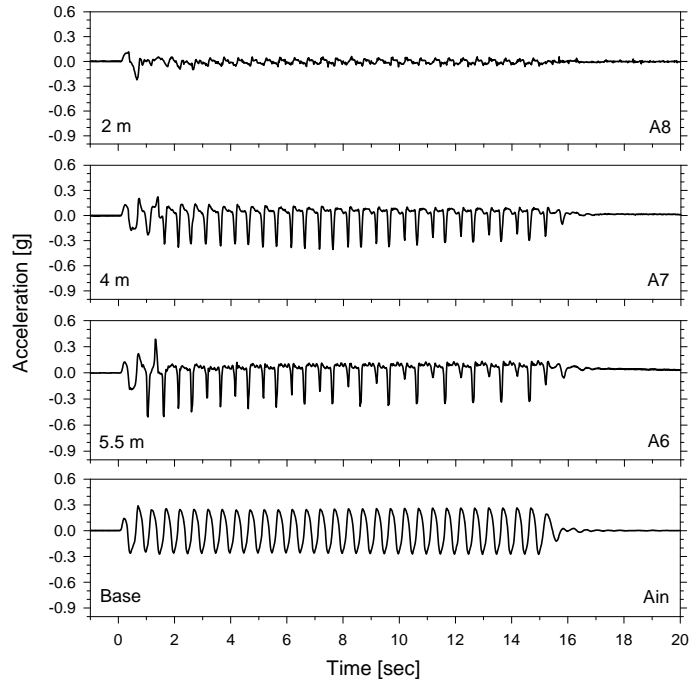


Figure 5.22: Soil acceleration time histories between piles, Model 2x2-v

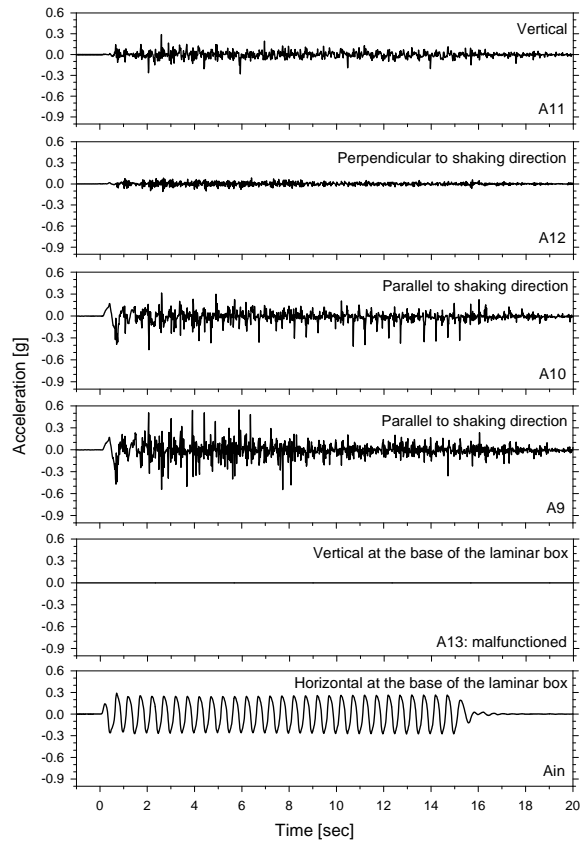


Figure 5.23: Accelerations recorded on the pile cap, Model 2x2-v

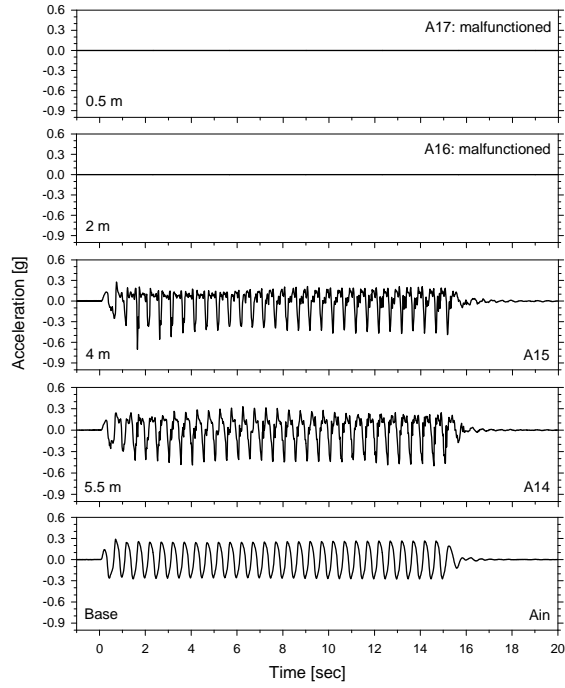


Figure 5.24: Accelerations recorded on the laminar rings, Model 2x2-v

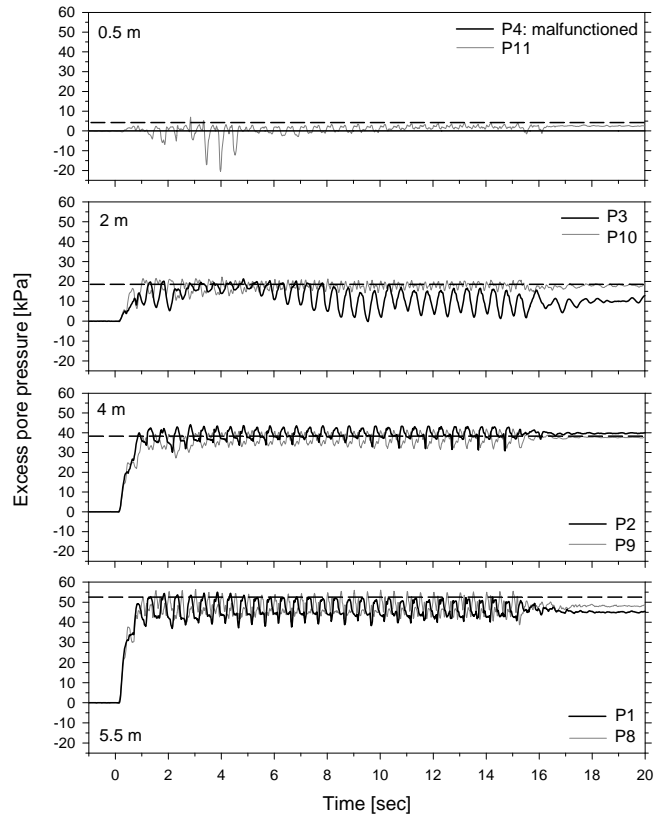


Figure 5.25: Excess pore pressure time histories in the free field, the dashed lines

5.5.2 Recorded Excess Pore Pressures

The excess pore pressure time histories in the free field reveal that the loose sand layer liquefied after about one or two cycles of shaking. Near the ground surface however, the excess pore pressure record on the downslope side of the pile group exhibits large negative spikes. This reduction in pore pressure seems to be related to a decrease in lateral stress on the downslope side of the pile cap. The excess pore pressure records between piles indicate that at least below 4 m the soil in this area did liquefy after about two cycles (Fig. 5.26), in agreement with the acceleration records.

The long term excess pore pressure records in the free field show that the dissipation process progressed from the bottom up toward the ground surface (Fig. 5.27). Each layer of soil remained liquefied until the excess pore pressure at deeper elevations dissipated to the extent of reaching the same value of that layer. The dissipation process took more than five minutes, in prototype units, confirming the low permeability of the model.

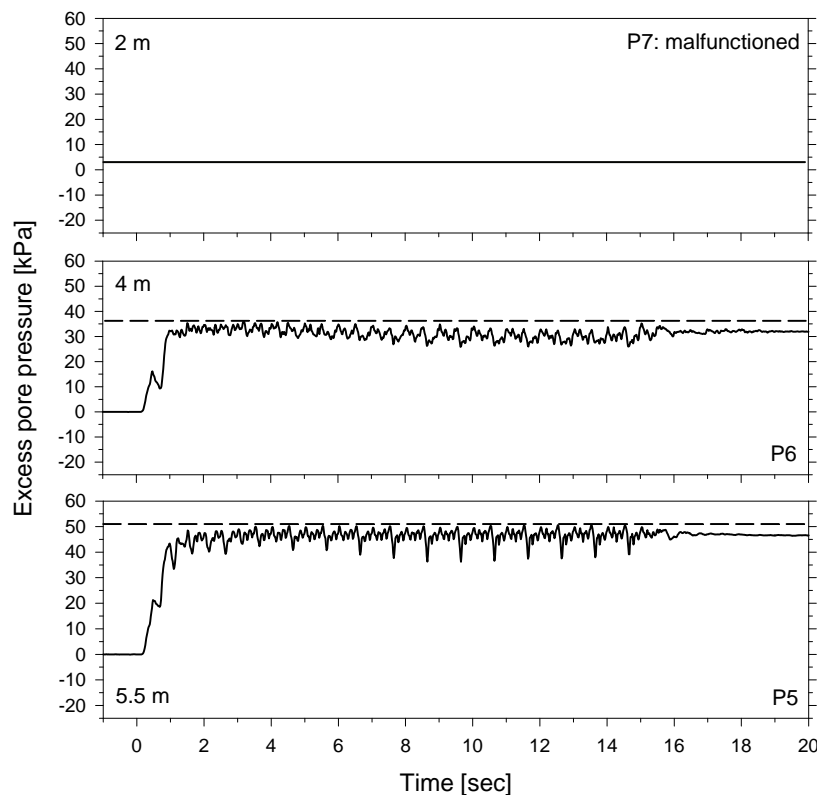


Figure 5.26: Excess pore pressure time histories between piles, the dashed lines correspond to initial liquefaction, Model 2x2-v

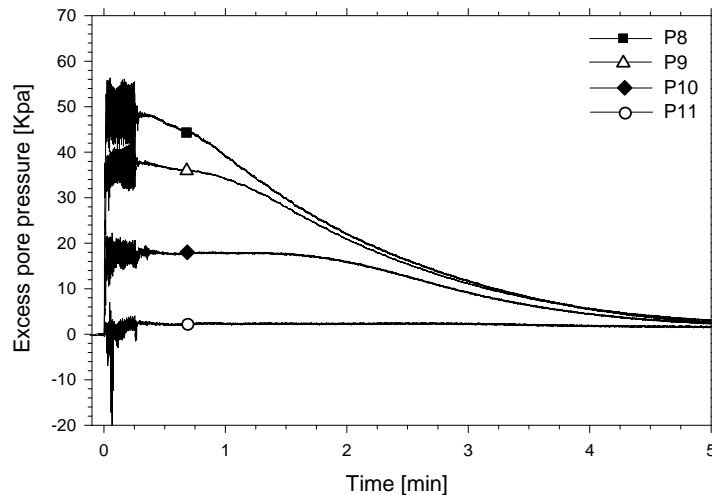


Figure 5.27: Long term excess pore pressure time histories in the free field, Model 2x2-v

5.5.3 Recorded Lateral Displacements

The recorded soil lateral displacement in the free field (Fig. 5.28) shows that the liquefied layer displaced gradually during shaking. Once the excitation ended, the lateral displacement stopped immediately even though the loose sand was still liquefied. The pile group displaced laterally during shaking without ever bouncing back, reaching a maximum displacement of about 45 cm at the end of shaking.

The profiles of soil lateral displacement in the free field were obtained by interpolating the LVDT measurements, after filtering out the cyclic component (Fig. 5.29). As soon as the loose sand liquefied at the beginning of shaking, the deposit started moving downslope, with the ground surface reaching a maximum displacement of approximately 125 cm at the end of shaking.

5.5.4 Pattern of Soil Displacement around Piles

The colored sand movement at an intermediate depth (Fig. 5.30) clearly shows that the liquefied soil did not flow between the piles, indicating the soil moved around the pile group instead of around each individual pile. Consequently, the characteristic width perpendicular to the flow was at least the width of the whole pile group. This tends to support the hypothesis that the pressure of the liquefied soil acts on both piles and soil in between, with significant increase in lateral loads and pile bending moments, in agreement with the recommendation by Yokoyama et al. (1997).

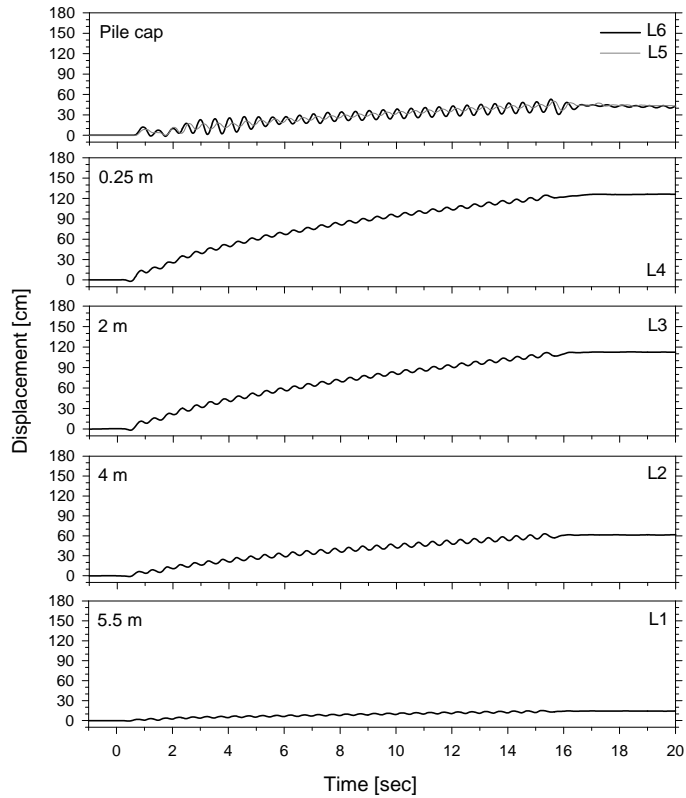


Figure 5.28: Lateral displacement time histories, Model 2x2-v

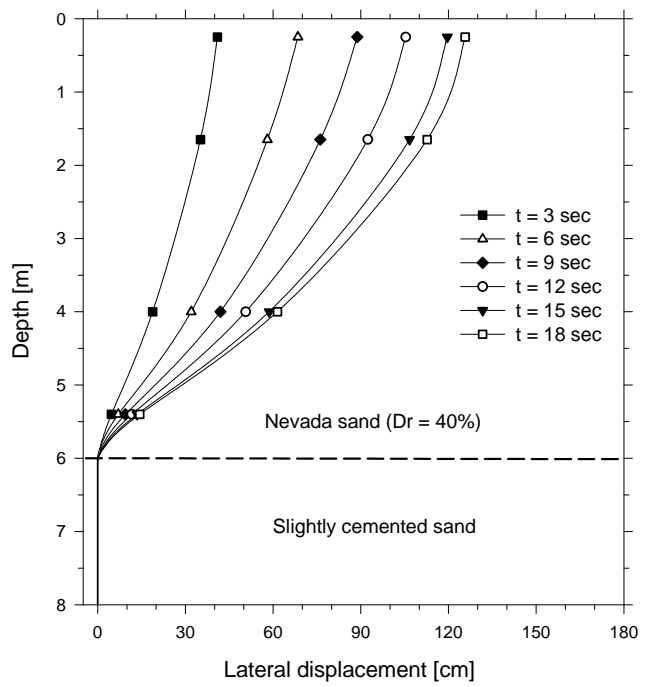


Figure 5.29: Profiles of lateral displacement in free field, Model 2x2-v

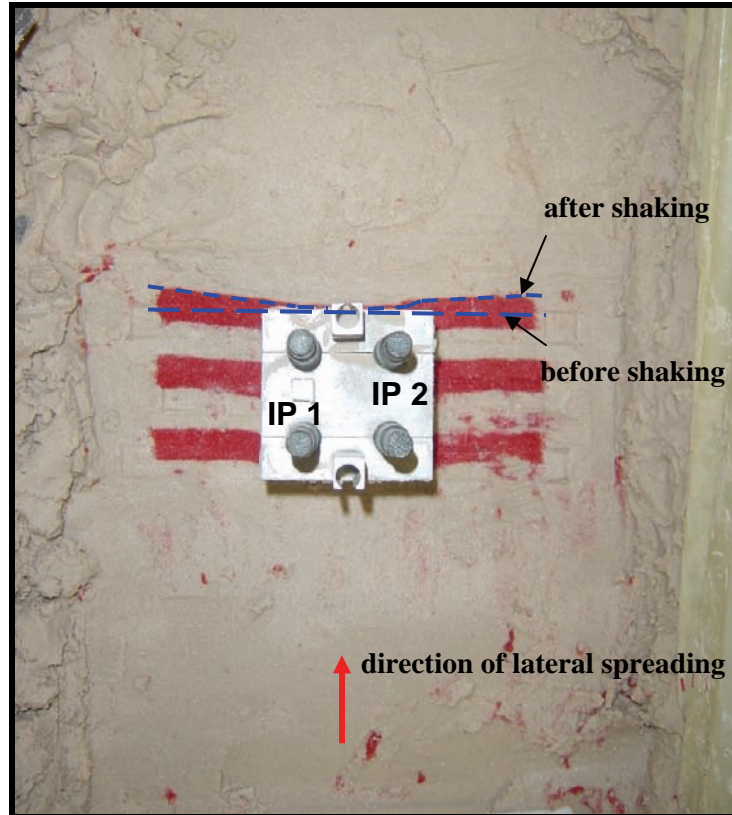


Figure 5.30: Pattern of soil displacement around pile group at a depth of 4 m, Model 2x2-v

5.5.5 Recorded Bending Moments

Prototype bending moments measured in the upslope pile IP1 and downslope pile IP2 are presented in Figs. 5.31, and 5.32 respectively. The bending moment profiles in the upslope and downslope piles (Fig. 5.33) are practically the same, with the maximum moments taking place close to the base of the liquefied layer and at the connection with the pile cap. The bending moments reached a maximum value of about 380 kN-m at the end of shaking, without ever bouncing back, being consistent with the pile cap displacement.

Figure 5.34 shows the measured bending moment at the base of the liquefiable layer versus the measured pile cap lateral displacement, after filtering out the cyclic component. The almost linear relationship between bending moment and pile displacement evidences the linear behavior of the pile-group-fixation system.

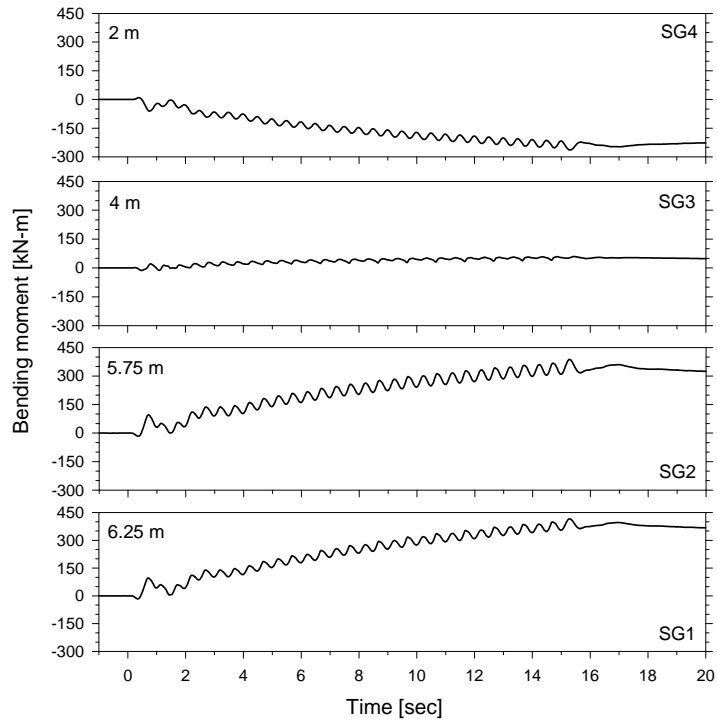


Figure 5.31: Bending moment time histories, upslope pile (IP 1), Model 2x2-v

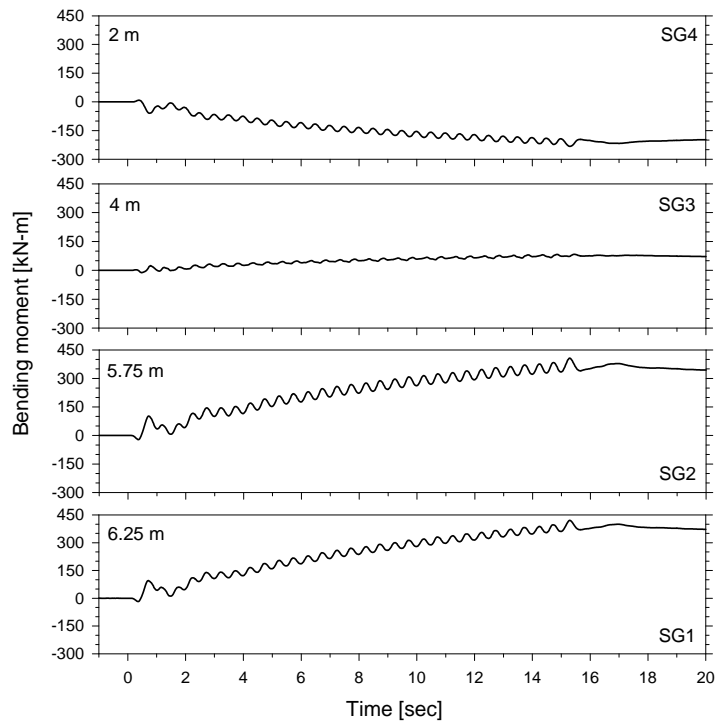


Figure 5.32: Bending moment time histories, downslope pile (IP 2), Model 2x2-v

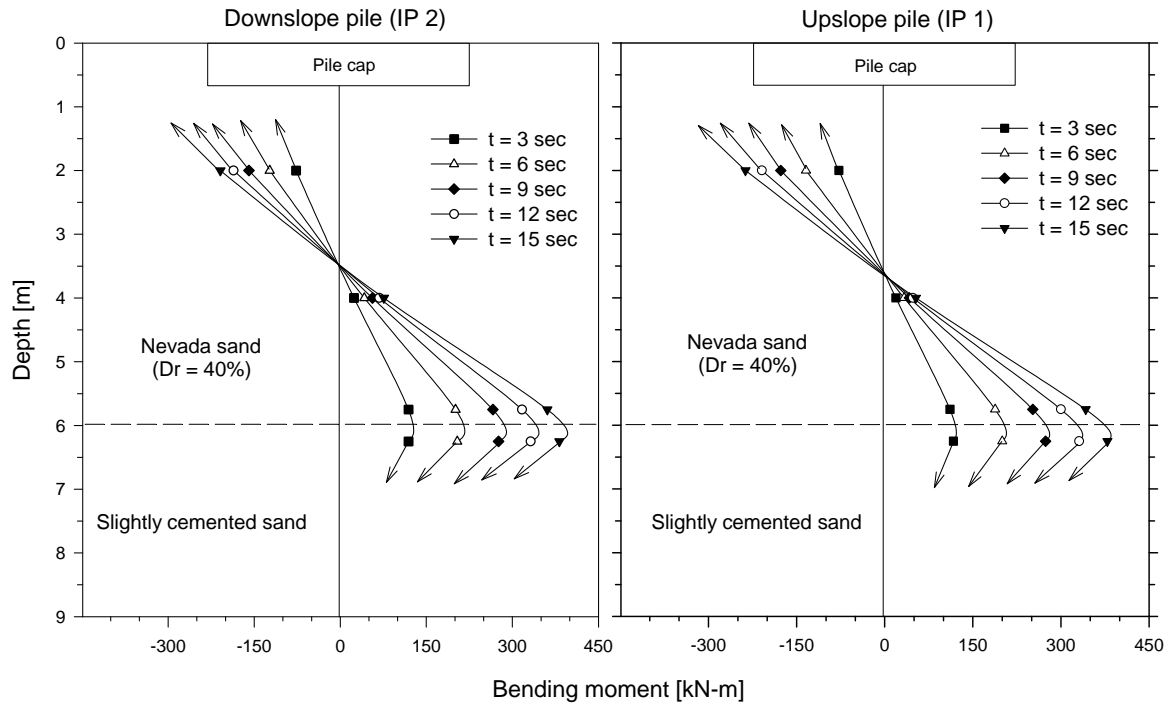


Figure 5.33: Profiles of bending moment, upslope (IP 1) and downslope (IP 2) piles, Model 2x2-v

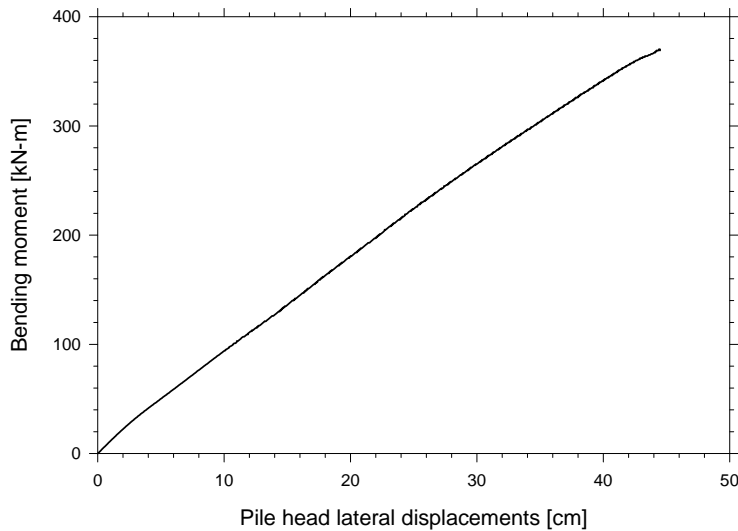


Figure 5.34: Bending moment at the base of the liquefiable layer versus pile cap lateral displacement, Model 2x2-v

5.5.6 Recorded Axial Forces

Prototype axial force time histories were obtained with the strain gage measurements. Since axial forces can be estimated only from a quarter bridge configuration, two measurement histories were obtained for the upslope pile IP1 and downslope pile IP2, as shown in Figs. 5.35 and 5.36 respectively. Positive values represent tension while negative ones represent compression. The axial forces were zeroed at the beginning of shaking, and therefore represent the change in axial force during the excitation.

As expected, the upslope pile IP1 was in tension during the excitation, reaching a maximum force of about 500 kN. The downslope pile IP2 was under compression, reaching a force of about - 350 kN at the end of the excitation. This difference in forces would tend to support the hypothesis discussed in section 5.4.6 that the pile group is pushed upward during shaking by the excess pore pressure under the pile cap. Consequently, a tensional force in each pile of about +75 kN appears to have superimposed to the ± 425 kN forces generated by the frame effect. This force does not differ much from the 55 kN estimated in Model 2x2-w.

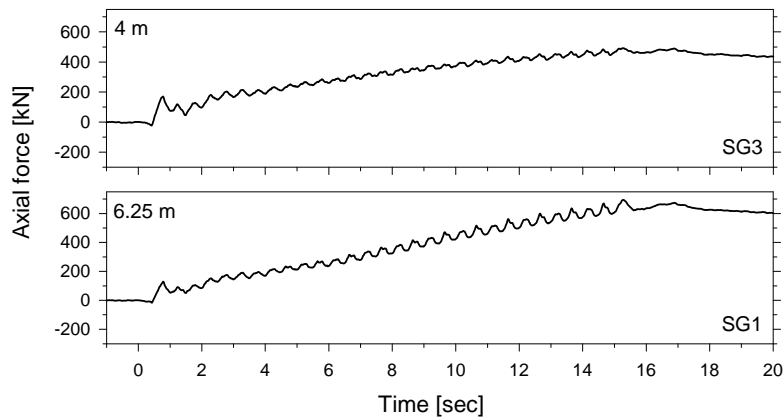


Figure 5.35: Axial force time histories, upslope pile (IP 1), Model 2x2-v

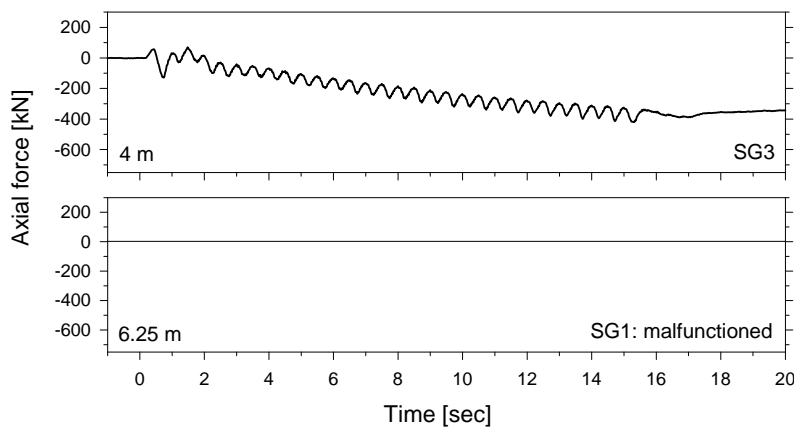


Figure 5.36: Axial force time histories, downslope pile (IP 2), Model 2x2-v

5.5.7 Limit equilibrium analysis

A limit equilibrium analysis was conducted to back-calculate the maximum measured bending moments and pile cap displacement (Fig. 5.37). A student version of the software AVwin was used to model the pile group subjected to the lateral force induced by lateral spreading. A 2-D analysis was conducted due to the symmetry of the 2x2 pile group, as shown in Fig. 5.37b. Each pile was modeled with 31 elements, having a bending stiffness of $9000 \text{ kN}\cdot\text{m}^2$, whereas the pile cap was modeled with three rigid elements. Since the measured bending moments in the upslope and downslope piles were very similar, articulated elements were used to transfer part of the lateral load from the upslope to the downslope pile. The slightly cemented layer was modeled with rotational springs at the base of the liquefiable layer.

The liquefied soil pressure used in the analysis was the same $16 \text{ kN}/\text{m}^2$ estimated in Model 2x2-w, and the force acting on each node was obtained by multiplying this pressure by the corresponding area. Figure 5.30 clearly shows that the liquefied sand moved around the pile group, affecting the soil pattern up to a considerable distance at both sides of the foundation, suggesting that the liquefied soil pressure acted on the pile group, soil in between, and on the sides to some extent. Following the same assumption used on the single pile (section 3.5.8) and 3x1 pile group (section 4.5.6), the soil pressure was considered to act also on a triangular area, as shown in Fig. 5.37a. If the pressure is assumed to be uniform and independent of depth, an effective area of 46.2 m^2 was found to provide the best estimation for the maximum bending moment at the base of the liquefiable layer. On the other hand, a rotational stiffness of $5000 \text{ kN}\cdot\text{m}/\text{rad}$ at the base of each of the piles gave the best estimation for the maximum pile cap lateral displacement.

The back-calculated bending moment was $340 \text{ kN}\cdot\text{m}$, close to the $375 \text{ kN}\cdot\text{m}$ measured at the base of the liquefiable layer. The calculated pile cap lateral displacement was 42 cm , very similar to the 45 cm measured during the test. The calculated axial force was 480 kN in the upslope pile and -480 kN in the downslope pile, compared to the $\pm 435 \text{ kN}$ estimated in the test, after subtracting the vertical force acting on the pile group, as discussed in section 5.5.6. Table 5.3 summarizes some of the parameters used in the limit equilibrium analysis, as well as measured and calculated values, showing very good agreement.

5.6 Comparison of Free Field Results between Model 2x2-w and 2x2-v

This section compares some of the free field results obtained in Models 2x2-w and 2x2-v such as: soil accelerations, excess pore pressures and soil lateral displacements. A detailed comparison of the recorded results from all centrifuge tests as well as a discussion of the effect of soil permeability on pile foundation response to lateral spreading is presented in Chapter 6. The centrifuge models 2x2-w and 2x2-v simulated the response of a 2x2 pile group embedded in a two layer soil profile subjected to lateral spreading. The only difference between these models is

that the first one was saturated with water, while the second one was saturated with a viscous fluid, simulating hence deposits of very different permeability in the field. A sketch of the setup and instrumentation used in both cases is presented in Fig. 5.1.

5.6.1 Comparison of Free Field Soil Accelerations

Figure 5.38 compares the free field soil accelerations measured in both centrifuge tests. The measured input accelerations indicate that both models were subjected to practically the same base excitation, which shows very good repeatability and validates the direct comparison between the tests. The soil acceleration records in the loose sand layer exhibit in both cases a drop in positive amplitude after the first cycle of shaking due to the liquefaction process and dynamic isolation of the shallower layers. These records also contain large negative spikes during most of the excitation, with the spikes being slightly larger in the model saturated with water. Nevertheless, the results indicate that soil acceleration in the free field was not significantly affected by the fluid viscosity or soil permeability.

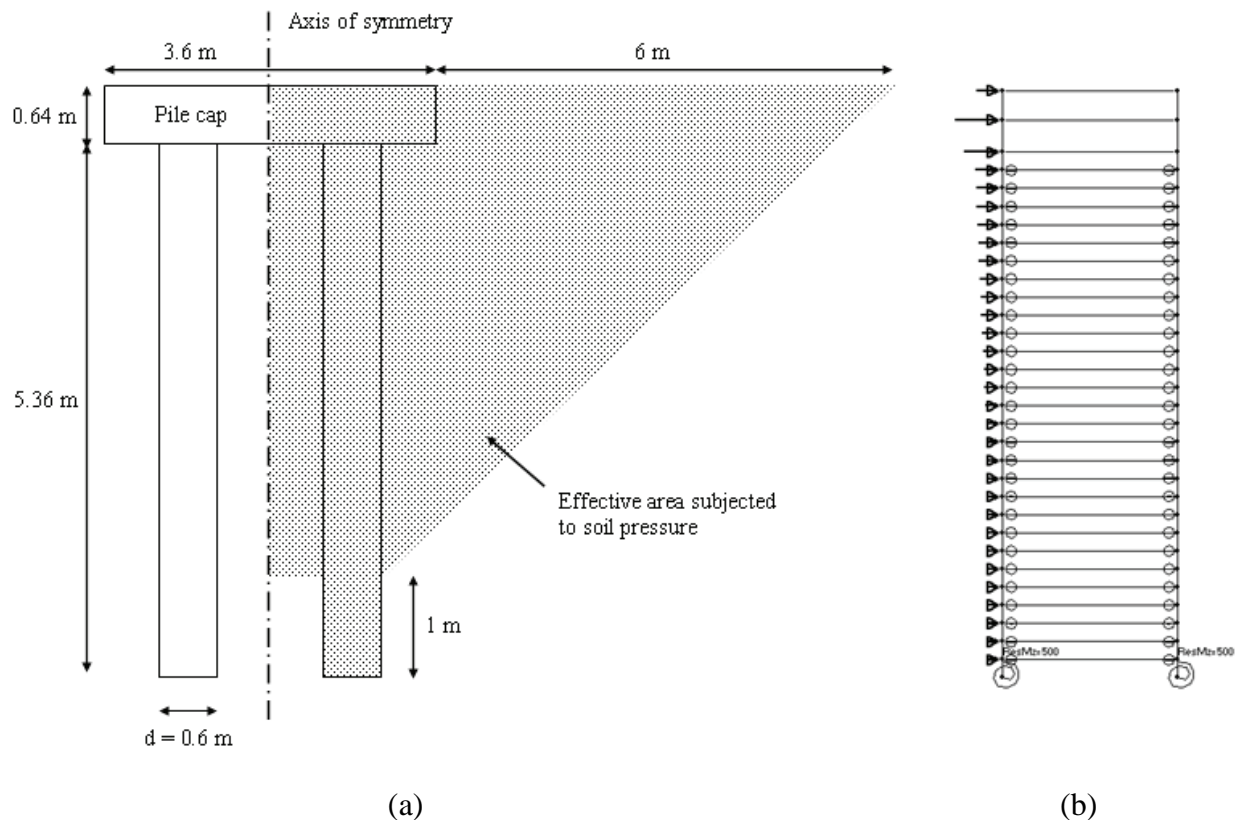


Figure 5.37: (a) Effective area subjected to liquefied soil pressure and (b) lateral view of the model used for limit equilibrium analyses, Model 2x2-v

Table 5.3: Parameters used in the limit equilibrium analysis, as well as measured and calculated values, Models 2x2-w and 2x2-v

Model	Liquefied soil pressure [kN/m ²]	e _a [m ²]	Rotational stiffness [kN-m/rad]	Max. bending moment [kN-m]		Max. pile head disp. [cm]		Max. axial load [kN]			
				Measured	Calculated	Measured	Calculated	Upslope		Downslope	
2x2-w	16	8.6	8000	58	56	7	5	45	63	-45	-63
2x2-v	16	46.2	5000	375	340	45	42	425	480	-425	-480

Maximum bending moments measured and calculated at the base of the liquefiable layer

e_a: effective area subjected to liquefied soil pressure

Measured axial force after subtracting vertical force acting on the pile group, as discussed in sections 3.4.6 and 3.5.6

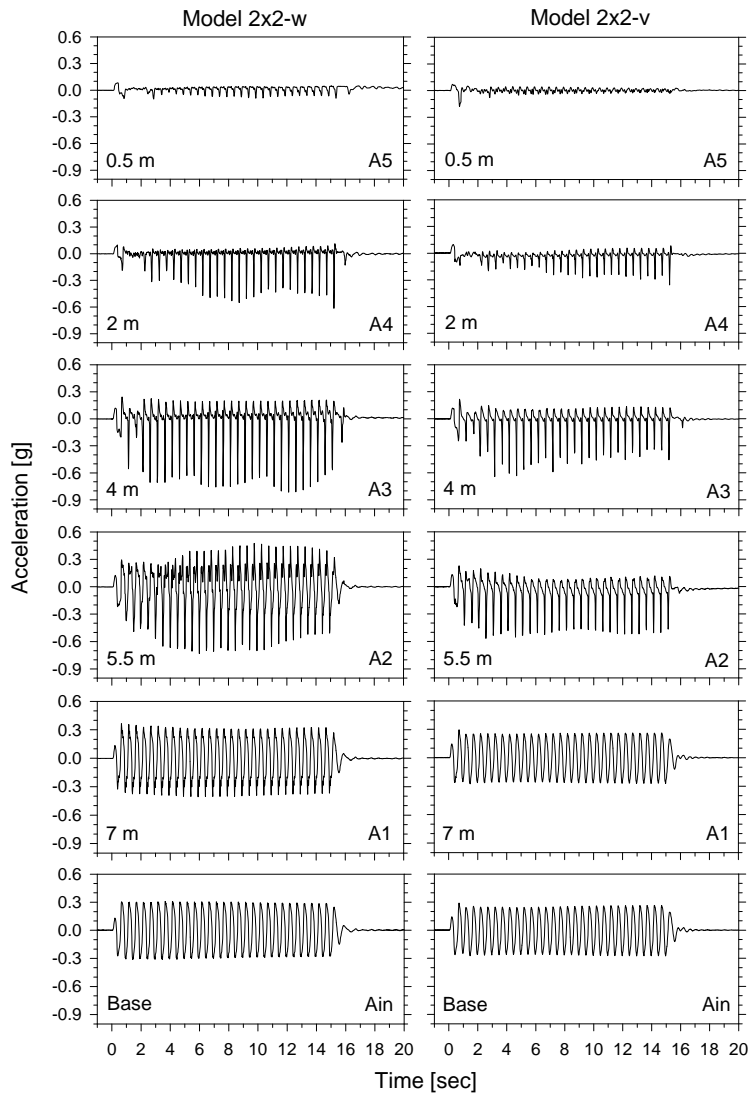


Figure 5.38: Comparison of soil acceleration in the free field between Model 2x2-w and 2x2-v

5.6.2 Comparison of Excess Pore Pressures

Figure 5.39 compares the excess pore pressures measured in the free field in Models 2x2-w and 2x2-v. In both tests, the records show that the sand in the free field liquefied after about one or two cycles of shaking, which is in agreement with the trend exhibited by the acceleration time histories. Near the ground surface however, the pore pressure on the downslope side of the pile group (P11) was lower than expected, exhibiting even negative spikes at the beginning of shaking in Model 2x2-v. In Model 2x2-w, as explained in section 5.4.2, the pore pressure transducer appears to have moved towards the surface. However, in the model saturated with viscous fluid, this response seems to be related to a reduction in lateral stress on the downslope

side of the cap, since on the upslope side the soil did liquefy (P4 in Fig. 5.9). The excess pore pressure time histories recorded between piles indicate that the soil in this area liquefied at the beginning of shaking, as shown in Fig. 5.40. Unfortunately, the pore pressure transducer at 2 m depth (P7) in Model 2x2-v malfunctioned.

These records indicate that the excess pore pressure build-up in the free field and at least below 4 m depth inside the pile group area was not significantly affected by the soil permeability. The dissipation process however, was highly dependent on the permeability; it took only a few seconds in the simulated coarse sand layer (Model 2x2-w), and about five minutes in the simulated fine sand layer (Model 2x2-v).

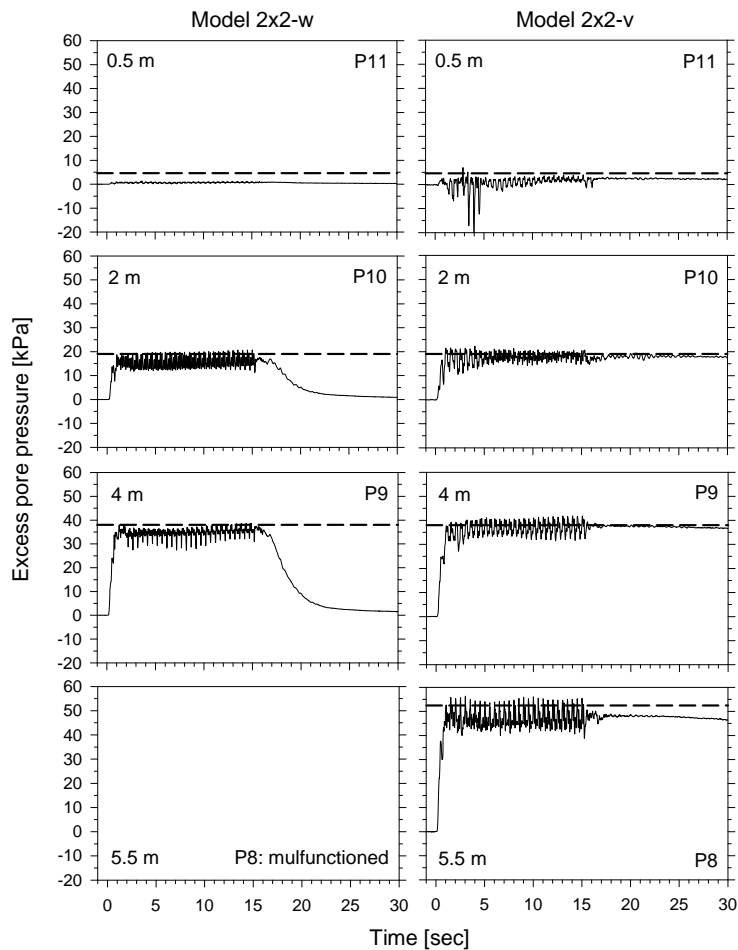


Figure 5.39: Comparison of excess pore pressure in the free field between Model 2x2-w and 2x2-v

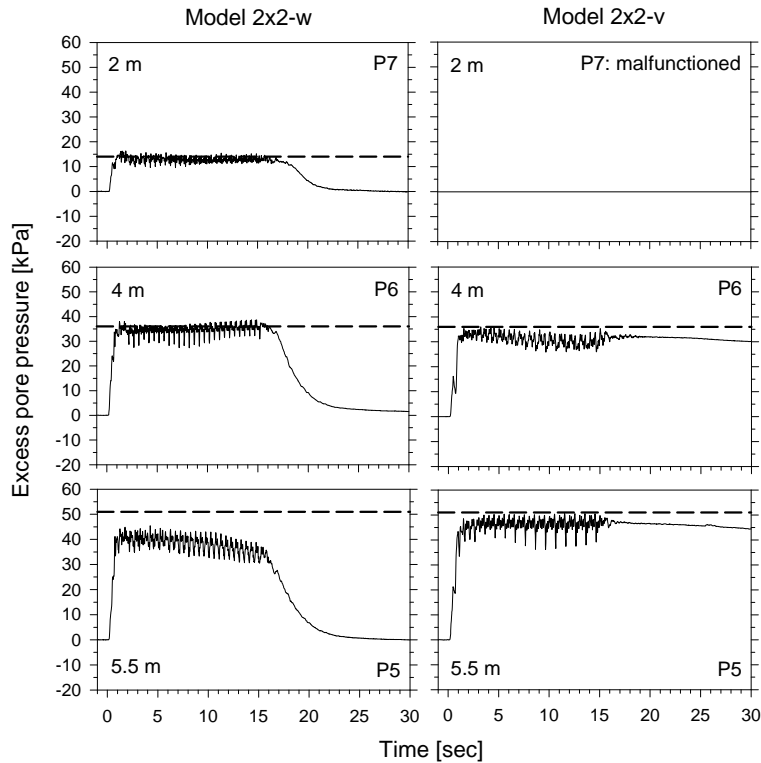


Figure 5.40: Comparison of excess pore pressure between piles, between Model 2x2-w and 2x2-v

5.6.3 Comparison of Free Field Lateral Displacements

Figure 5.41 compares the free field lateral displacement profiles between Models 2x2-w and 2x2-v. In both tests, the loose layer started moving downslope as soon as it liquefied at the beginning of shaking, with the maximum displacement at all times measured at the ground surface. Even though the magnitude of the deformation at all times was very similar, the profiles in Model 2x2-v tended to be more curved than the ones in the water saturated model. This trend is consistent with the response observe in the previous centrifuge tests conducted in this study. The loose sand layer in Model 2x2-w was so permeable that the dissipation process started before the end of shaking, as shown in Fig. 5.40. This reduction in pore pressure must have increased the soil stiffness near the bottom of the sand layer, explaining the lower shear strains compared to the ones in Model 2x2-v. On the other hand, the reduction in pore pressure near the surface in the Model 2x2-v appears to have been responsible for the low shear strains developed at shallow elevations.

The cemented sand in both models did not experience permanent displacement and acted as a solid layer during the excitation, as illustrated by its acceleration record being essentially identical to the input shaking.

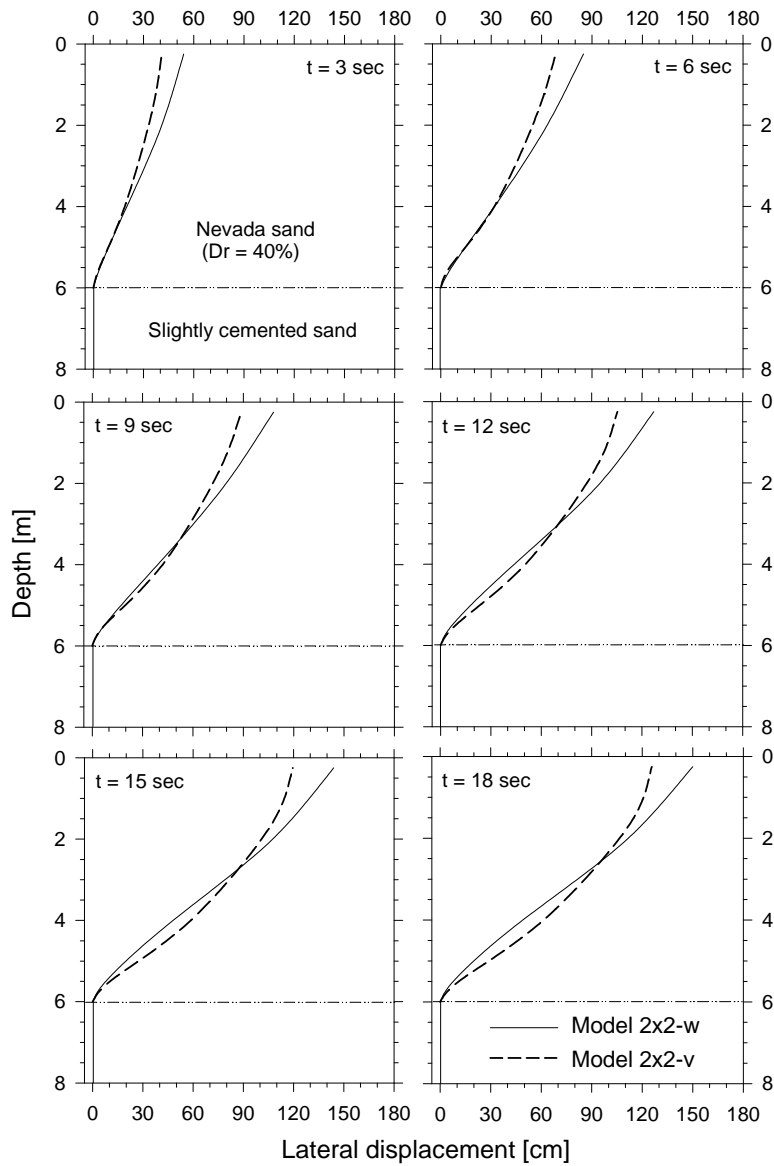


Figure 5.41: Comparison of free field lateral displacement profiles between Model 2x2-w and 2x2-v

CHAPTER 6

SUMMARY AND DISCUSSIONS ON SOIL PERMEABILITY EFFECT ON PILE RESPONSE TO LATERAL SPREADING

6.1 Introduction

A series of centrifuge tests were conducted to study the effect of soil permeability on pile foundation response to lateral spreading. Three model setups consisting of a single pile, a 3x1 pile group, and a 2x2 pile group were tested using fine Nevada sand saturated with water as pore fluid, simulating a liquefiable coarse sand layer. These models were then repeated, using the same fine Nevada sand, but saturated with a viscous fluid, hence simulating a loose layer of fine sand. Chapters 3, 4 and 5 presented the experimental results, data interpretation and analyses of these models. Special attention was put on the following parameters during model preparation and testing to ensure a good repeatability of the tests: amplitude of the input acceleration, relative density of the liquefiable layer, compaction of the slightly cemented layer, and viscosity of the pore fluid. The instrumentation within the liquefiable layer consisted of accelerometers and pore pressure transducers placed close and far from the foundations, pairs of strain gages along the piles, and grids of colored sand placed at intermediate elevations.

This chapter summarizes the results and trends observed in these six centrifuge tests, providing evidence of the important effect of soil permeability on the response of single piles and pile groups subjected to lateral spreading, in particular to the bending moments and pile displacements. This summary is divided into the following subsections: soil acceleration in the free field, excess pore pressure development, piles and soil lateral displacement, soil pattern displacement around piles, pile bending moments, bending moment versus pile displacement, limit equilibrium analysis, and p-y curve analysis on the single pile. Table 6.1 summarizes the properties and measurements from the centrifuge tests, while Table 6.2 summarizes the results obtained in the limit equilibrium analysis. Conclusions and recommendations are presented in chapter 9.

6.2 Summary of Soil Acceleration in the Free Field

The measured input accelerations in the six centrifuge tests provide evidence that the models were excited by practically the same input motion, with the amplitude of the sinusoidal acceleration being very close to 0.3g in prototype units, as summarized in Table 6.1. This shows very good repeatability of the large 1-D shaker and validates the direct comparison between the tests. Some of the trends observed from the soil acceleration records in the free field, as shown in Figs. 3.39, 4.41 and 5.38, are that: (i) the positive amplitude decreased significantly at the beginning of shaking due to the liquefaction process, especially at shallow elevations where the soil became isolated from the base motion; (ii) the acceleration records contain large negative spikes due to the dilative behavior of the saturated loose sand during lateral spreading, with the

spikes being larger at deeper elevations due to the higher confinement, and usually being larger in the models saturated with water than in the ones saturated with viscous fluid; and (iii) the acceleration of the bottom layer was very similar to the input acceleration, indicating no sliding occurred between this layer and the base of the laminar box, being consistent with the fact that the bottom laminar ring was fixed to the base.

The larger spikes observed in the models saturated with water, especially at about 2 m depth, appear to be related with the larger shear strains developed in these models near the ground surface. Except for this behavior, the soil acceleration in the free field does not seem to have been significantly affected by the soil permeability.

6.3 Summary of Excess Pore Pressure Development

As already mentioned, soil permeability is one of the most important parameters in this series of tests. Since fluid viscosity is very sensitive to temperature, before each saturation process the methylcellulose-water mixture (metulose) was calibrated using a standard glass capillary viscometer. The viscous fluid used in Models 1x1-v, 3x1-v and 2x2-v had approximately 40 times the viscosity of water, as summarized in Table 6.1, simulating hence a fine sand with a permeability very close to the one of Nevada sand in the field. The dissipation process in these models was very similar, as illustrated in Fig. 6.1, confirming that the permeability of the loose sand layer was practically the same.

Table 6.1: Summary of properties and measurements from centrifuge tests

Model	1x1-w	1x1-v	3x1-w	3x1-v	2x2-w	2x2-v
Pile configuration	1 x 1 (single)		3 x 1 ^a		2 x 2 ^b	
Pile cap	No	No	Yes	Yes	Yes	Yes
Fluid viscosity (μ_w : viscosity of water)	1	42	1	40	1	38
Measured input acceleration amplitude [g]	0.3	0.3	0.3	0.33	0.3	0.27
Max. free field displacement [cm]	165	140	155	145	150	125
Max. pile displacement [cm]	28	85	26	85	7	45
Time occurring max. pile displacement [sec]	6	16	3	16	3	16
Max. bending moment [kN-m]	120	360	120	425	58	375
Time occurring max. bending moment [sec]	6	16	3	16	3	16

Notes:

All measurements presented are in prototype units, and evaluated after filtering out the cyclic component.

^a The maximum bending moment is representative of all piles in the 3x1 pile group.

^b The maximum bending moment was measured at the base of the liquefiable layer and is representative of all piles in the 2x2 pile group.

Table 6.2: Parameters used in the limit equilibrium analyses, as well as measured and calculated values

Model	Liquefied soil pressure [kN/m ²]	Ap [m ²]	Rotational stiffness [kN-m/rad]	Max. bending moment [kN-m]		Max. pile head disp. [cm]		Max. axial load [kN]			
				Measured	Calculated	Measured	Calculated	Upslope		Downslope	
								Measured	Calculated	Measured	Calculated
1x1-w	11.5	3.6	8000	120	125	28	27				
1x1-v	11.5	7.6	8000	360	350	85	87				
3x1-w	8.3	13.1	8000	120	120	26	27				
3x1-v	8.3	39.3	8000	425	405	85	90				
2x2-w	16	8.6	8000	58	56	7	5	45	63	-45	-63
2x2-v	16	46.2	5000	375	340	45	42	425	480	-425	-480

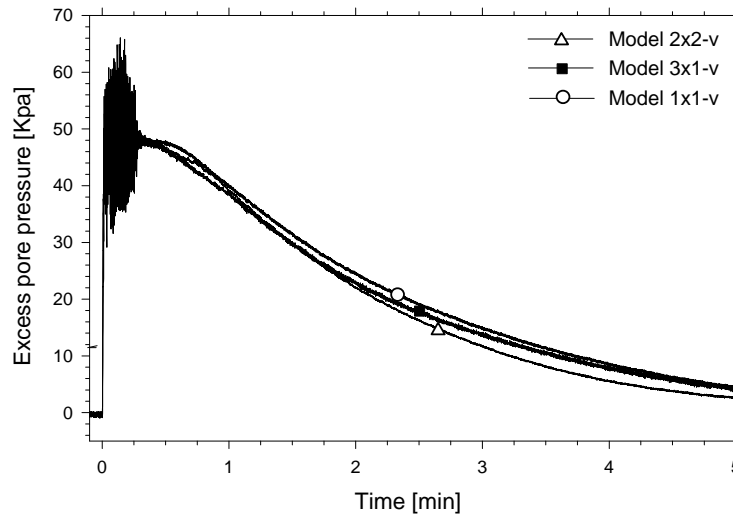


Figure 6.1: Comparison of excess pore pressure dissipation in the models saturated with viscous fluid

The summary of the observed trends of the recorded excess pore pressure is divided in three groups: short-term in the free field (far from the piles), short-term in the near field (close to the piles), and long term (dissipation process).

6.3.1 Short-Term in the Free Field

In the water-saturated models the pore pressure records indicate that the soil in the free field did liquefy after about one or two cycles of shaking, in agreement with the trend exhibited by the acceleration records. A similar response was observed in the models saturated with viscous fluid; however, near the ground surface the excess pore pressure decreased after a couple of cycles to values below or close to zero. Shear strains developed under low confinement and a slow dissipation process appears to be responsible for this phenomenon. Figures 3.40, 4.42 and 5.39 summarize the free field excess pore pressure records in all the centrifuge tests.

6.3.2 Short-Term in the Near Field

Figures 3.41, 4.43 and 5.40 summarize the effect of soil permeability in the excess pore pressure development close to the piles in all the centrifuge tests. At deeper elevations, the records indicate that the soil close to the piles liquefied after about one or two cycles of shaking, independently of the soil permeability. However, at shallow elevations the records are very revealing, showing a huge effect of the fluid viscosity or soil permeability on the excess pore pressure development.

In the models saturated with water the pore pressure near the piles exhibited some tendency to decrease during shaking, especially near the ground surface. However, the permeability of the

soil was so high, that water flowed fast from the free field dissipating the potential negative increments in pore pressure. In the models saturated with viscous fluid this tendency was much stronger, with the excess pore pressure reaching large negative values, particularly at shallow elevations. The reduction in lateral stress on the downslope side of the piles, as well as large shear strains with a dilative response of the liquefied soil close to the foundations, seems to have been responsible for the negative increments of pore pressure developed near the piles. Besides, the pore fluid flow from the free field was not fast enough to dissipate these negative increments, allowing a nonliquefied zone to develop and expand during the excitation, particularly at shallow elevations. In Model 1x1-v, this nonliquefied zone around the single pile had at the end of the excitation the approximate shape of an inverted cone, reaching a depth of about 1.5 m, as illustrated in the snapshots taken from the visualizations (Figs. 3.26d and 3.38c). Even though no visualization was made for Model 3x1-v, the pore pressure records suggest that the nonliquefied zone around the 3x1 pile group had also an approximate inverted cone shape. This zone was however much wider and deeper than the one in Model 1x1-v, reaching a depth of about 3 to 4 m next to the piles. Unfortunately, no pore pressure transducers were placed next to the 2x2 pile group and single pile in Model 3x1-v. However, it is speculated that negative excess pore pressure must have developed close to the piles at shallow elevations in order to explain the pile foundation response.

6.3.3 Long-Term (Dissipation Process)

In the water-saturated models, the dissipation process was very fast, starting to dissipate even before the end of shaking, as shown in Figs. 3.41, 4.43 and 5.40. This vertical water-flow toward the surface seems to have kept the upper layers liquefied during shaking. In the models saturated with viscous fluid, the dissipation process was very complex, as illustrated in Figs. 3.25b and 3.27 of Model 1x1-v and Fig. 4.29b of Model 3x1-v. The negative excess pore pressure developed close to the piles at shallow elevations created a large vertical gradient close to the foundation. Therefore, the dissipation process around the piles was much faster than in the free field. As the fluid started flowing toward the surface, it broke through the nonliquefied zone around the foundations near the surface, creating even sand boils in Models 1x1-v and 3x1-v. Meanwhile the pore fluid in the free field moved upward and toward the foundation to compensate for the negative and low positive excess pore pressure in this area, as clearly shown in Fig. 4.29b. The dissipation of excess pore pressure was far from being a one-dimensional process, that took about five minutes, confirming the low permeability of these models.

6.4 Summary of Soil Lateral Displacement

Figure 6.2 summarizes the free field soil lateral displacement measured in all the centrifuge tests, by plotting profiles at different times, after filtering out the cyclic component. The profiles in the water-saturated models and the ones in the viscous-fluid-saturated models are plotted separately

to observe the effect of soil permeability. In all tests the loose layer started moving downslope as soon as it liquefied at the beginning of shaking, with the maximum displacement measured at all times at the ground surface. These profiles are consistent with the assumption that these soil measurements indeed correspond to free field soil response, being practically unaffected by the presence of the foundations. They also confirm that the relative density of the loose sand layer must have been very similar in order to have this excellent repeatability of lateral spreading. Even though the ground surface deformation was very similar in all tests, the profiles in Figure 6.2 reveal a difference in shape due to the change in the soil permeability. In the water-saturated models, the shear strains tended to decrease with depth, whereas in the models simulating a fine sand layer, the shear strains tended to increase with depth. Since in the simulated coarse sand layer the dissipation process started before the end of shaking, as discussed in section 6.3, the reduction in pore pressure must have increased the soil stiffness near the bottom of the sand layer, explaining the lower shear strains compared to the ones in the models saturated with viscous fluid. On the other hand, the reduction in pore pressure near the surface in the models that simulate a fine sand layer appears to have been responsible for the low shear strains developed at shallow elevations. A similar trend in the shape of the profiles was observed by Ubilla (2004, unpublished) in centrifuge tests conducted at RPI as part of the US-Japan project mentioned in section 1.3.2. Some of the centrifuge models were tested using water and some using viscous fluid to try to replicate full-scale shaking table tests.

6.5 Summary of Piles Lateral Displacement

A summary of the ground surface and pile cap/head lateral displacement measured in all tests is presented in Fig. 6.3. The ground surface displacement increased gradually during shaking, reaching an average value of about 145 cm at the end of the excitation (Fig. 6.3a). In the models saturated with water, the pile foundations reached a maximum lateral displacement after a few seconds of shaking, bouncing back afterwards. This decrease in displacement occurred despite the fact that the free field deformation kept increasing until the end of shaking. Clearly after a few seconds the liquefied soil was flowing around the individual piles. In the models saturated with viscous fluid, however, the lateral displacement of the pile foundations increased gradually during the excitation and never bounced back, reaching lateral displacements much larger than the ones observed in the models saturated with water. These measurements suggest that the higher fluid viscosity or lower soil permeability had a dramatic effect in the soil-foundation response, increasing the pile head displacements as much as 6 times. The decrease in pore pressure near the piles must have stiffened the soil, enabling it to maintain a strong force near the pile heads, explaining the large pile displacements, as well as the lack of piles rebound. Table 6.1 summarizes the ground surface and pile head lateral displacements measured in all models.

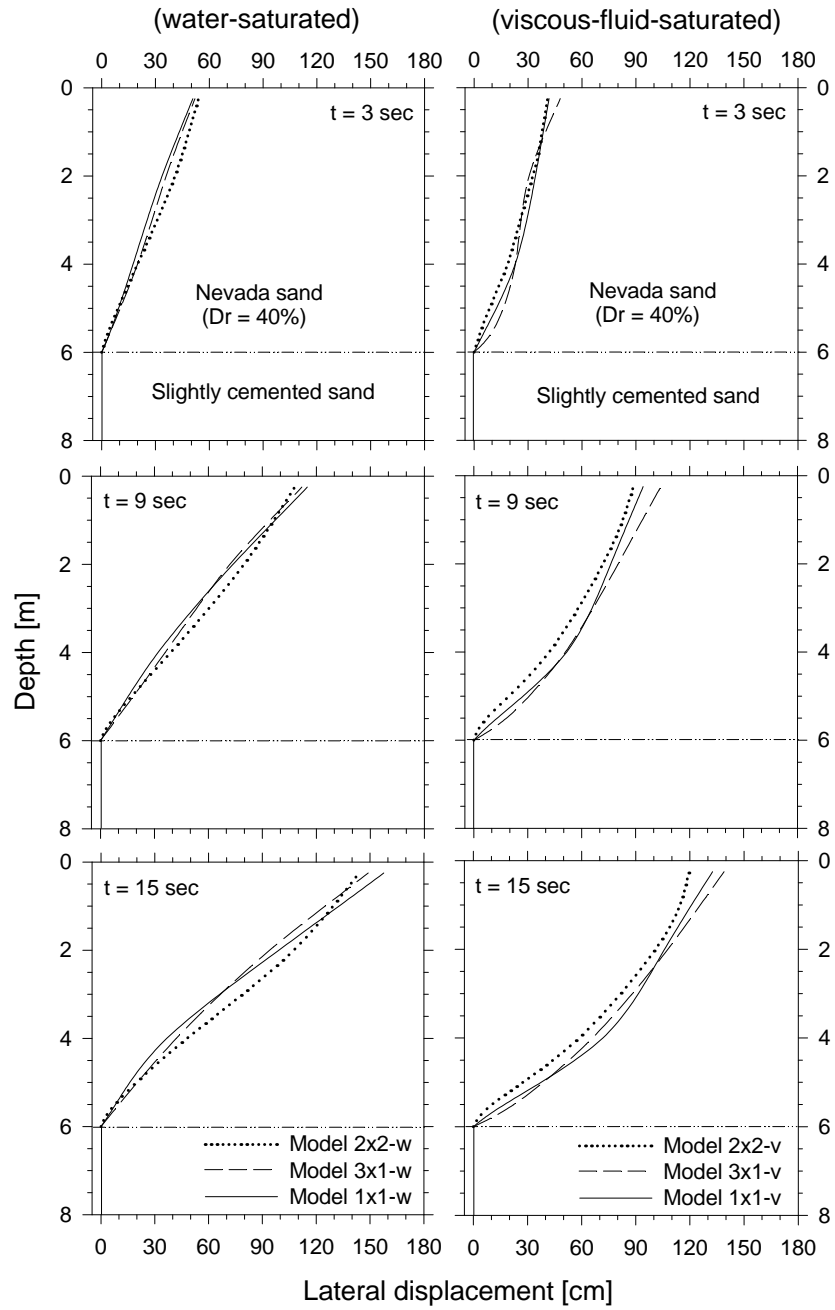


Figure 6.2: Summary of free field lateral displacement profiles

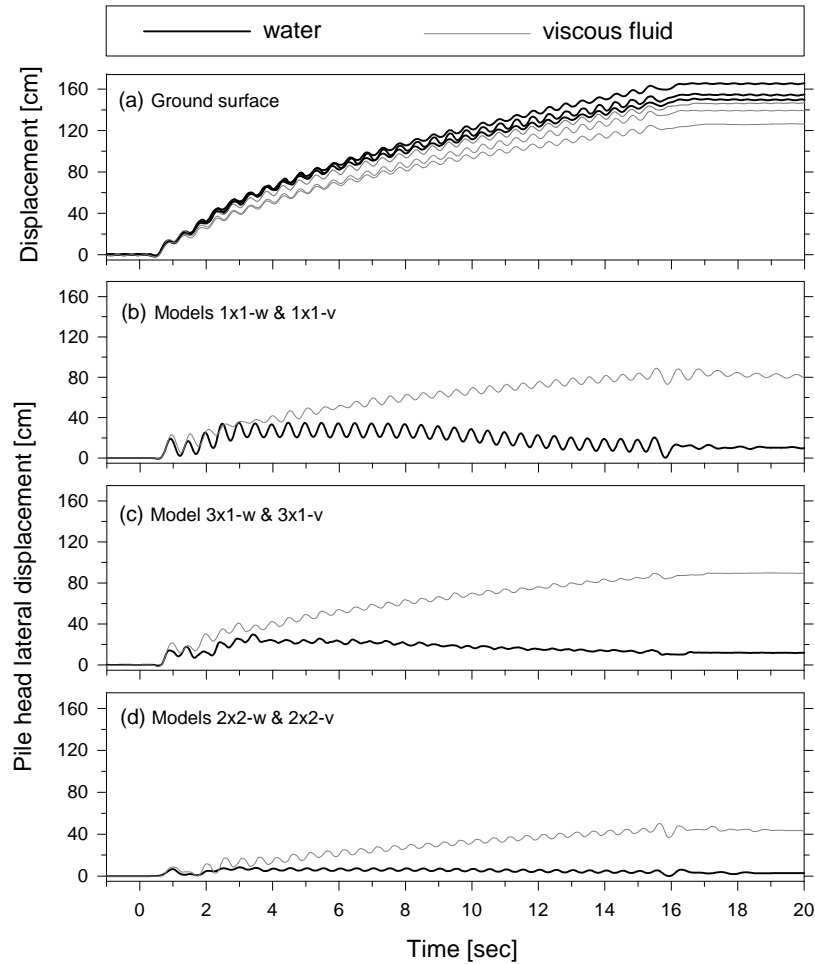


Figure 6.3: Summary of ground surface and pile head lateral displacements (the lateral displacements in figures (c) correspond to the 3x1 pile group)

6.6 Summary of Soil Pattern Displacement around Piles

Figure 6.4 summarizes the effect of soil permeability on the pattern of soil displacement around the piles. This figure presents a set of pictures of the colored sand taken after each test at an intermediate depth. The arrows indicate the direction of lateral spreading during shaking. In the models that simulate a coarse sand layer (saturated with water), the liquefied sand moved around the individual piles, affecting the soil pattern close to the piles themselves. Therefore, the effective width perpendicular to the flow was the diameter of the individual piles. This is true even for the pile groups in Models 3x1-w and 2x2-w (Figs. 6.4c and 6.4e), supporting the hypothesis that the pressure of the liquefied soil acts only on the individual piles and not on the soil in between.

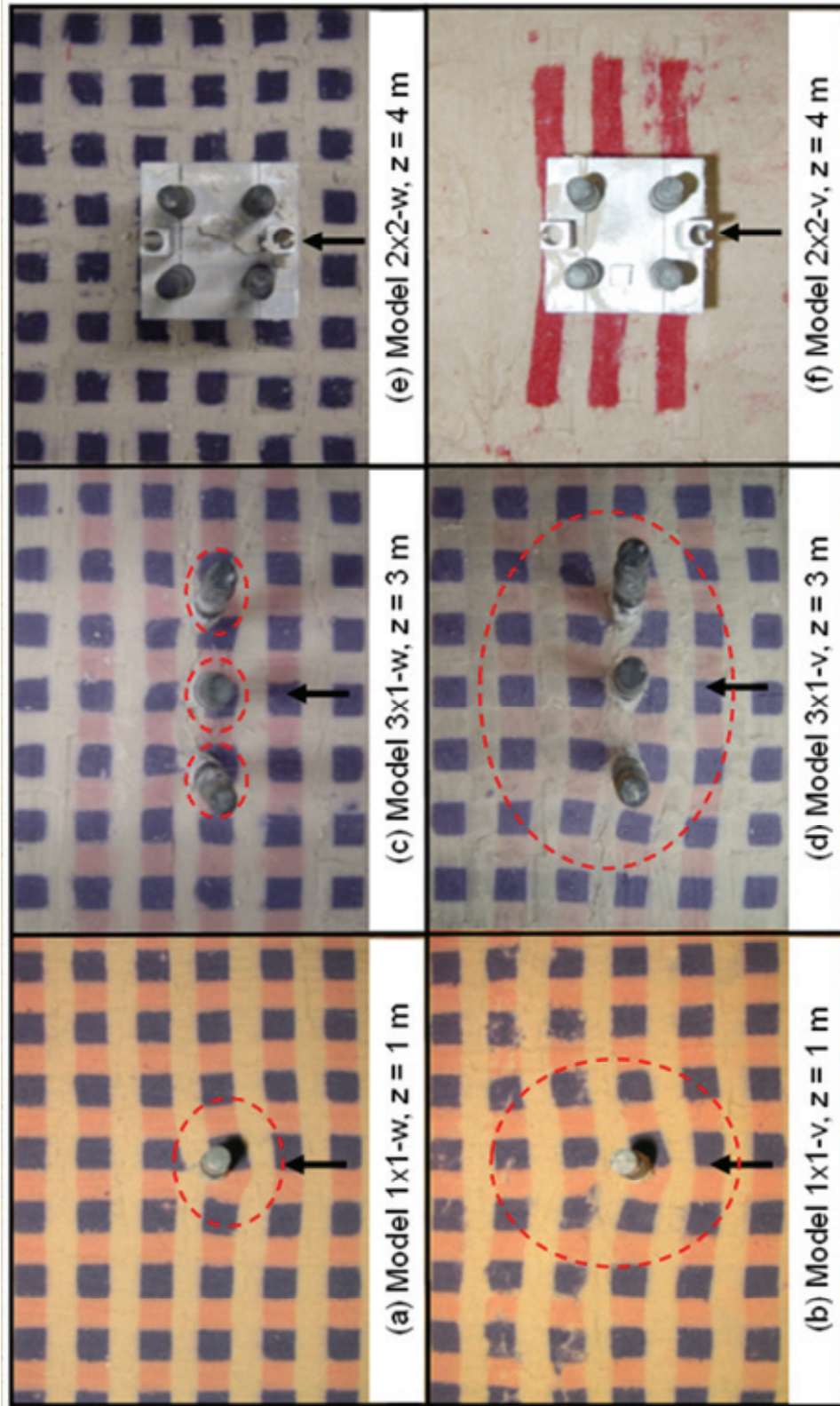


Figure 6.4: Summary of soil pattern displacement around piles (the arrows indicate the direction of lateral spreading; the dashed lines show the area of influence around the piles)

A completely different liquefied flow pattern is observed in the models that simulate a fine sand layer. In Model 1x1-v the pattern of soil deformation was affected up to a considerable distance at both sides of the single pile (Fig. 6.4b), revealing the existence of a larger area of influence than the pile width itself, at least at a depth of 1 m. An even more significant effect in the soil deformation pattern was observed in Models 3x1-v and 2x2-v, where the liquefied soil did not flow between the piles (Fig. 6.4d and 6.4f). The soil had to flow around the pile groups, affecting the soil pattern up to a considerable distance at both sides of the foundations. This tends to support the hypothesis that the pressure of the liquefied soil acts on the piles, soil in between in the pile groups, and soil to some extent on both sides of the foundation. The comparison of soil deformation patterns at different elevations around the single pile (Fig. 5.30) indicates that the area of influence decreases with depth, suggesting an inverted conical shape around the foundations. This observation indicates that the affected soil pattern must be directly related to the nonliquefied zone around the piles; as the soil became stiffer near the foundation, the liquefied soil in the free field had to move around it.

6.7 Summary of Bending Moment Profiles

A summary of pile bending moment profiles in all tests, after filtering out the cyclic component, is presented in Fig. 6.5. In all cases the maximum moment at any given time occurred at or close to the base of the liquefied layer, as expected. In the 2x2 pile group the piles were subjected to double curvature, with the maximum moments taking place at the base of the liquefied layer and at the connection with the pile cap. The bending moment records in the upslope and downslope piles in the 2x2 pile group were practically the same, hence the profiles in Figs. 6.5e and 6.5f are representative of all four piles. Similarly, the profiles in Figs. 6.5c and 6.5d are representative of all piles in the 3x1 pile group.

In the water-saturated models the bending moments reached a maximum value after a few seconds of excitation, at the same time when the pile heads reached their maximum deflection. Afterwards, the bending moments decreased despite the fact that the free field deformation associated with the lateral spreading kept increasing until the end of shaking. Clearly the liquefied soil was flowing around the piles, which was confirmed by the pictures in Figs. 6.4a, 6.4c and 6.4e. This general pattern of pile displacement and bending moment is typical of many centrifuge models of single piles and pile groups conducted at RPI using water as pore fluid (Abdoun, 1997).

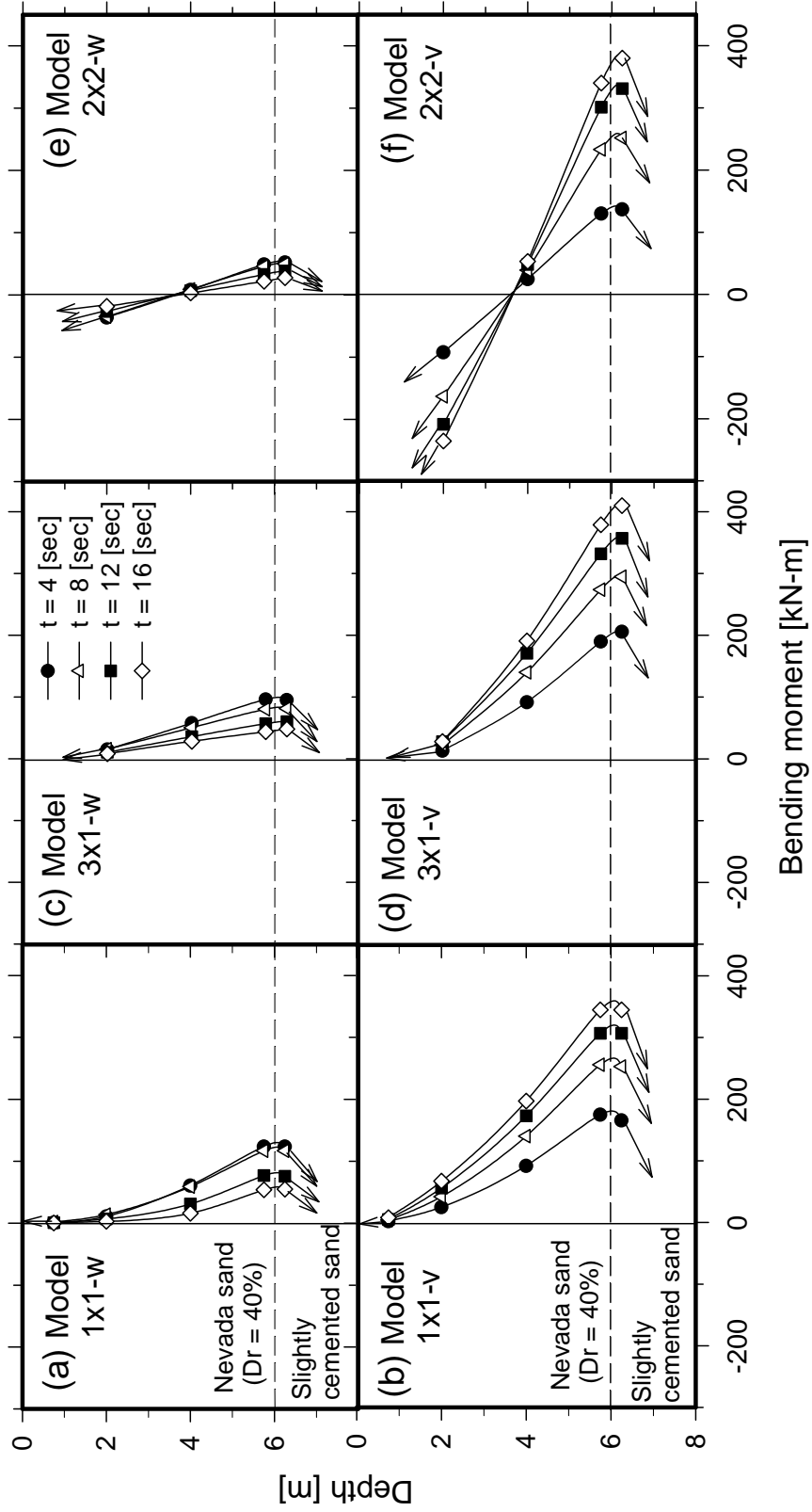


Figure 6.5: Summary of bending moment profiles (the bending moment profiles in figures (c) and (d) correspond to the 3x1 pile group)

On the other hand, in the models saturated with viscous fluid the piles reached a maximum bending moment at the end of shaking, without ever bouncing back, being consistent with the pile head displacements. Certainly, the soil permeability had a huge impact on the pile foundation response during lateral spreading, increasing the bending moments as much as 6 times. Table 6.1 summarizes the maximum bending moments measured in all models, after filtering out the cyclic component.

6.8 Summary of the Relationship between Bending Moment and Pile Displacement

Figure 6.6 shows the measured bending moments at the base of the liquefiable layer versus the measured pile head/cap lateral displacements, summarizing the response of all models. These curves were obtained after filtering out the cyclic component. In the models saturated with water the piles reached a maximum lateral displacement and bending moment then bounced back, following a quite linear relationship. In the models saturated with viscous fluid, the bending moments and pile head displacements followed essentially the same linear relationships, without bouncing back and reaching much larger values at the end of the excitation.

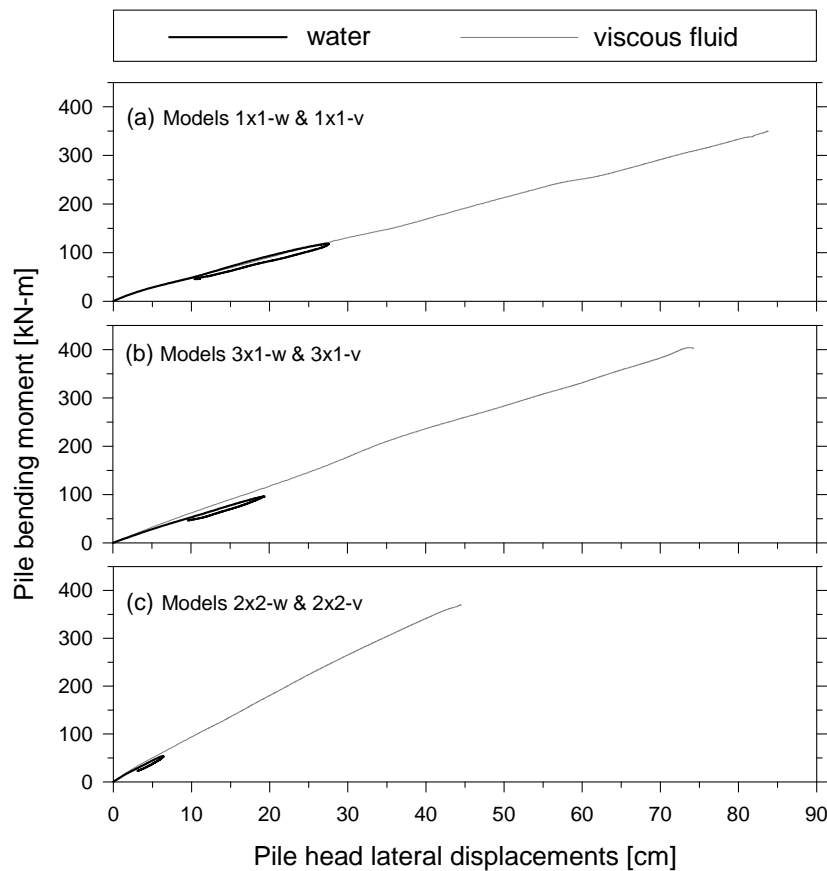


Figure 6.6: Summary of measured pile bending moment versus measured pile head lateral displacement (figure (b) corresponds to the 3x1 pile group)

The virtually linear relationship between bending moment and pile head displacement evidences three characteristics of the soil-foundation interaction: (i) the elastic behavior of the piles, (ii) the position of the resultant force against the foundations did not change considerably during shaking and was not noticeably affected by soil permeability, and (iii) the fixation provided by the cemented layer was quite constant during the excitation. The first point was actually proved during the pile calibration tests (section 2.7), and the third point was demonstrated by the p-y curve analyses on the single pile in Models 1x1-w (section 3.4.6) and 1x1-v (section 3.5.7), and by the limit equilibrium analyses, where the back-calculated rotational stiffness at the base of each pile was practically the same in all cases.

6.9 Summary of Limit Equilibrium Analysis

Limit equilibrium analyses were carried out using structural software to estimate the liquefied soil pressure, effective area subjected to the soil pressure, and the rotational stiffness provided by the cemented sand layer (Fig. 6.7). Since in the water-saturated models the liquefied soil flowed around the individual piles (Figs. 6.4a, 6.4c and 6.4e), the soil pressure was considered to act only on the foundations. The lateral pressure was assumed to be constant and independent of depth, following the approach used by Abdoun (1997). The back-calculated soil pressures in the 3x1 pile group (section 4.4.6) and in the single pile (section 3.4.8) were very similar, averaging a value of 10 kN/m^2 , which is very close to the liquefied soil pressure of 9.25 kN/m^2 estimated by Abdoun (1997). In the 2x2 pile group however, the estimated value was 16 kN/m^2 . Another iteration was done in this case assuming the liquefied soil pressure acting on both upslope and downslope piles. However, the estimated soil pressure did not change much, with the bending moment distributions and pile head displacements being very different from the measured ones. A rotational stiffness of 8000 kN-m/rad was found to provide the best prediction for the measured pile head/cap displacements, in excellent agreement with the values back-calculated in the p-y curve analyses in Models 1x1-w and 1x1-v (Fig. 6.8).

In the models saturated with viscous fluid the liquefied sand moved around the foundations, affecting the soil pattern up to a considerable distance at both sides. It appears that as the soil became stiffer in the nonliquefied zone around the foundations, the liquefied soil in the free field had to flow around it. Hence, a valid assumption was to consider the liquefied soil pressure to be acting on this inverted cone zone of solidified soil. Therefore, it was assumed that the soil pressure in the viscous fluid-saturated models was acting on the piles, on the soil in between the pile groups, and on a triangular area at both sides of the foundations, hence a trapezoidal area. The height of these trapezoids was estimated based on the pore pressure measurements, and the width was obtained matching the bending moments using limit equilibrium analyses. Figure 6.7 shows the effective areas that were found to give the best predictions for the maximum bending moments (not perfectly drawn on scale). The horizontal dashed lines correspond to the affected pattern of soil displacement, information that was not used in the limit equilibrium analyses. The

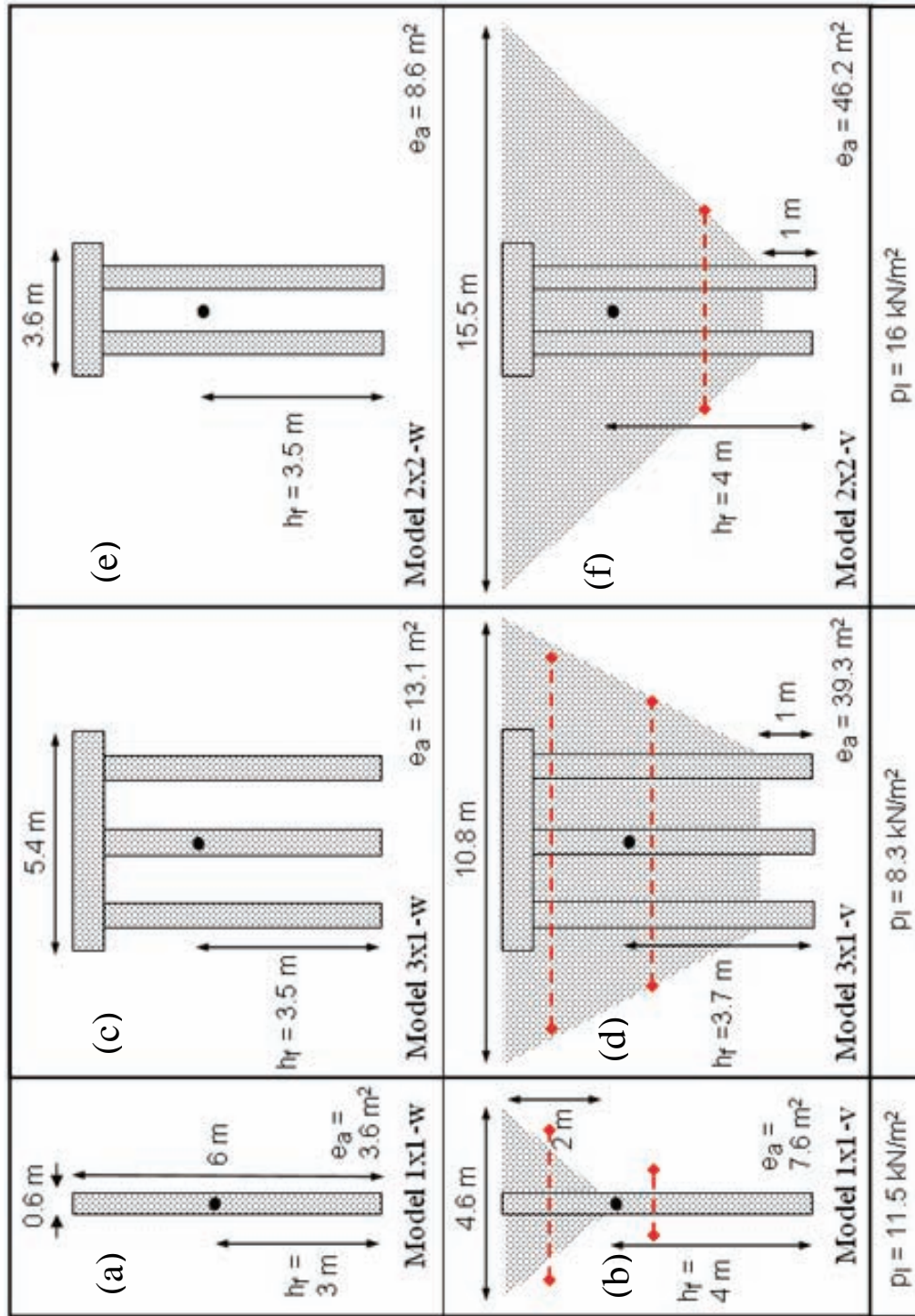


Figure 6.7: Summary of the effective areas used in the limit equilibrium analyses (not perfectly on scale), e_a : effective area corresponding to shadow zone, h_r : distance to the resultant force, p_i : liquefied soil pressure

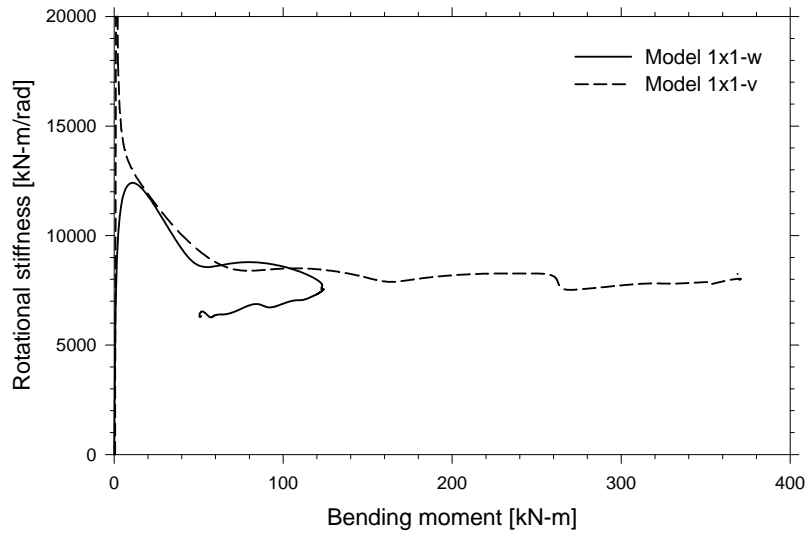


Figure 6.8: Back-calculated rotational stiffnesses (with the p-y approach) provided by the cemented sand in Models 1x1-w and 1x1-v

very good agreement between the pattern of soil displacement and the estimated area subjected to liquefied soil pressure validates the relationship between the nonliquefied zone developed around the foundations, movement of the liquefied soil around these zones, and the larger area subjected to the liquefied soil pressure.

It was found that a rotational stiffness of 8000 kN-m/rad provided the best estimation for the single pile and 3x1 pile group lateral displacements, in excellent agreement with the estimated value in the water-saturated models. In the 3x1 and 2x2 pile groups the location of the resultant force did not change significantly, being consistent with the fact that the relationship between moment and pile cap displacement practically did not change with the soil permeability. Table 6.2 summarizes most of the parameters used in the limit equilibrium analyses, as well as measured and calculated values, and Figure 6.7 summarizes the estimated effective areas and the location of the resultant forces.

6.10 Summary of p-y Curve Analysis on the Single Pile

To further investigate the pile-soil-fluid interaction during lateral spreading, p-y curves analyses were carried out for the single pile. Sections 3.4.6 and 3.5.7 present in detail the results of the p-y curve analysis obtained for Models 1x1-w and 1x1-v respectively. This section summarizes the effect of soil permeability on the lateral resistance against the single pile. Figure 6.9 shows profiles of bending moment, back-calculated lateral resistance (p), and excess pore pressure next to the pile, after filtering out the cyclic component for both models.

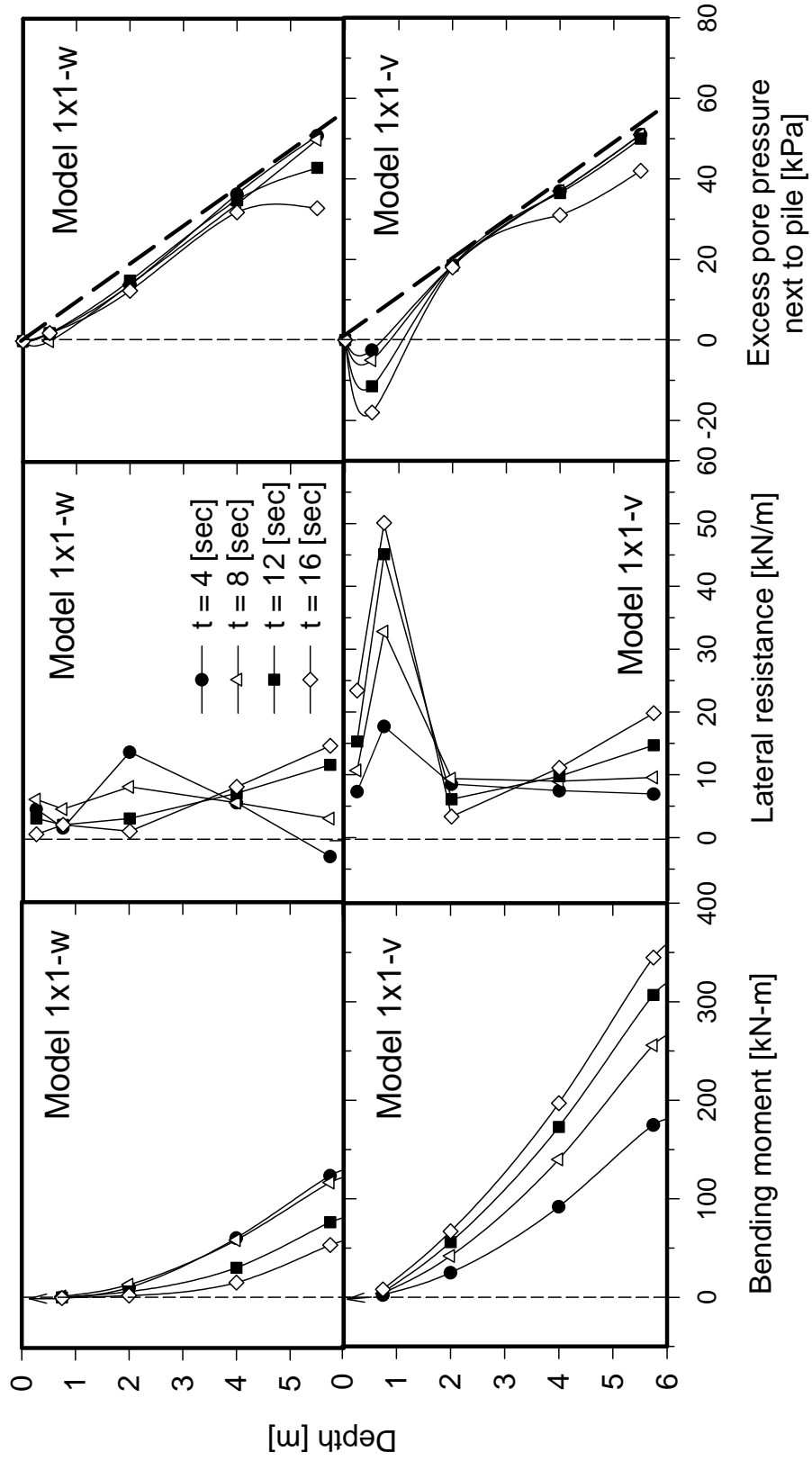


Figure 6.9: Summary of single pile response

In the water-saturated model the bending moment reached its maximum value at the beginning of shaking, decreasing afterwards (Fig.6.9a). This response is clearly associated with the lateral pressure on the pile, which in the upper 3 m it reached values of about 10-15 kN/m at the beginning of shaking, decreasing afterwards to values close to zero (Fig. 6.9c). Near the bottom of the liquefiable layer however, the lateral resistance increased up to a value of around 15 kN/m, without ever decreasing. It appears that the reduction in pore pressure due to the fast dissipation (Fig. 6.9e) and the smaller pile-soil relative displacement at deeper elevations were responsible for this phenomenon. The liquefied soil pressure of 11.5 kN/m^2 estimated in the limit equilibrium analysis, which corresponds to a lateral resistance of 7 kN/m, is in good agreement with the back-calculated lateral resistance along the pile. At the beginning of shaking however, when the bending moment is maximum, the lateral resistance is larger at a depth of 2 m.

In the model saturated with viscous fluid the back-calculated lateral resistance, shown in Figure 6.9d, confirms the significant effect of soil permeability. In the bottom half of the loose sand layer the profiles are very similar to the ones estimated in Model 1x1-w, where the soil next to the pile remained liquefied during most of the shaking. However, near the ground surface, the lateral resistance increased gradually up to values of about 50 kN/m, without ever decreasing. These back-calculated profiles are in excellent agreement with the force per unit length used in the equilibrium analysis, constant in the lower 4 m and increasing with height in the upper 2 m. This increase in lateral resistance appears to be inversely proportional to the decrease in pore pressure, particularly in the upper 2 m, as shown in Fig. 6.9f. Therefore, as the soil started stiffening around the pile near the surface, the liquefied soil in the free field was pushing a much larger effective area, which explains the larger bending moments and lack of pile rebound in the models saturated by the viscous fluid.

CHAPTER 7

PILE PINNING EFFECT ON LIQUEFACTION INDUCED LATERAL SPREADING

7.1 Introduction

The vulnerability of highway bridges to earthquake-induced ground failures arising from liquefaction has been clearly demonstrated by the extensive damage observed in past earthquakes. Damage has been primarily associated with either large translational flow slides and related embankment deformations, or progressive but limited lateral spread embankment deformation. Damage modes associated with such lateral deformations are related to displacement demands on abutments and piers leading to possible pile damage and/or span collapse (Martin et al., 2002)

Whereas the evaluation of the mode and magnitude of liquefaction induced lateral ground deformations involves considerable uncertainty, the current state of practice utilizes the Newmark sliding block approach on an assumed dominant failure plane within the liquefied zone. Once the geometry of the failure and magnitude of the liquefaction induced lateral deformation are estimated, an assessment should be made to see if the foundation is able to withstand the displacement demands and the superstructure can accommodate those deformations. A refinement of this approach is to consider the reinforcing or pinning effect the piles or pile group have on the lateral stability, by representing the pile shear forces at the location of the failure plane as an equivalent shear strength in the calculation of yield accelerations used in the Newmark analyses.

A series of four centrifuge tests were conducted at the 150 g-ton RPI centrifuge facility to study the pinning effect of pile foundation systems on the reduction of lateral spreading. The centrifuge models, conducted using a slightly inclined laminar box subjected to in-flight base shaking, simulate a mild infinite ground slope. The prototype profiles consist of a 3 m thick layer of liquefiable Nevada sand on top and below a 3 m thick nonliquefiable layer. The first centrifuge model (Model p-0) does not include piles and is considered the benchmark experiment to simulate lateral spreading in the free field. Using a similar setup, Models p-3x2, p-6x2, and p-3x1 simulate the response of a 3x2, 6x2, and 3x1 pile group, respectively, placed in a soil profile similar to that used in Model p-0. Soil accelerations, excess pore water pressure, lateral deformations, and bending moments were some of the measurements recorded during the tests.

Testing properties of the centrifuge models are summarized in Table 7.1, and a description of model preparation is presented in section 7.2. Experimental results, data interpretation and basic analyses are presented in sections 7.3 through 7.6. A comparison of all tests and a practical analysis approach are presented in section 8.

Table 7.1: Testing properties of centrifuge models

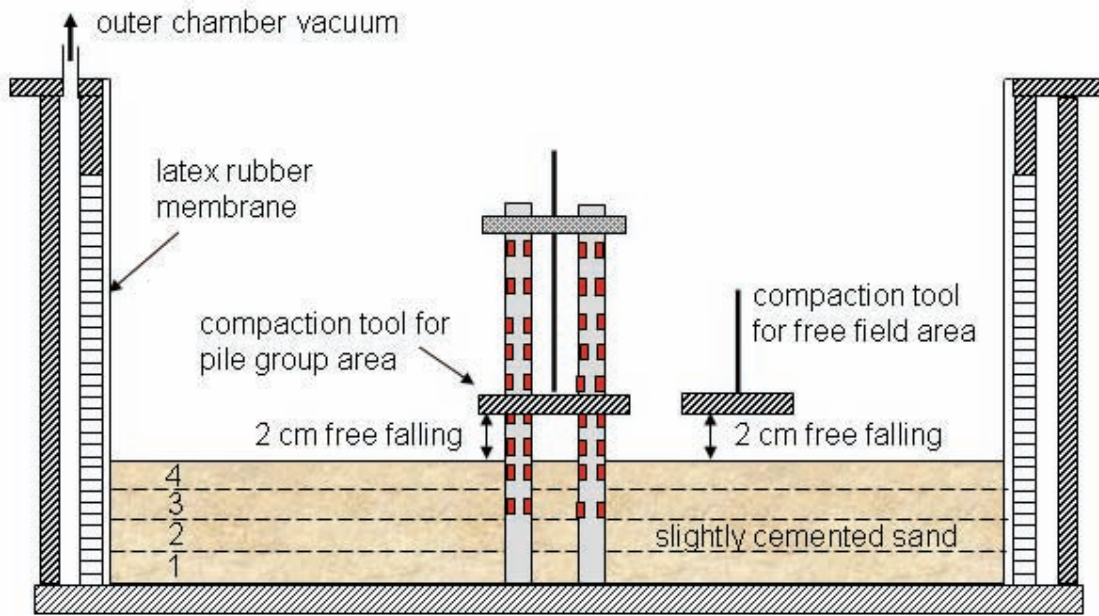
Model	Pile configuration	# of piles	# of instrument. piles	Pile cap	# of layers	Fluid viscosity (μ_w)
p-0	No foundation	0	0	–	3	1
p-3x2	3 x 2	6	2	yes	3	1
p-6x2	6 x 2	12	3	yes	3	1
p-3x1	3 x 1	3	2	yes	3	1

7.2 Model Preparation

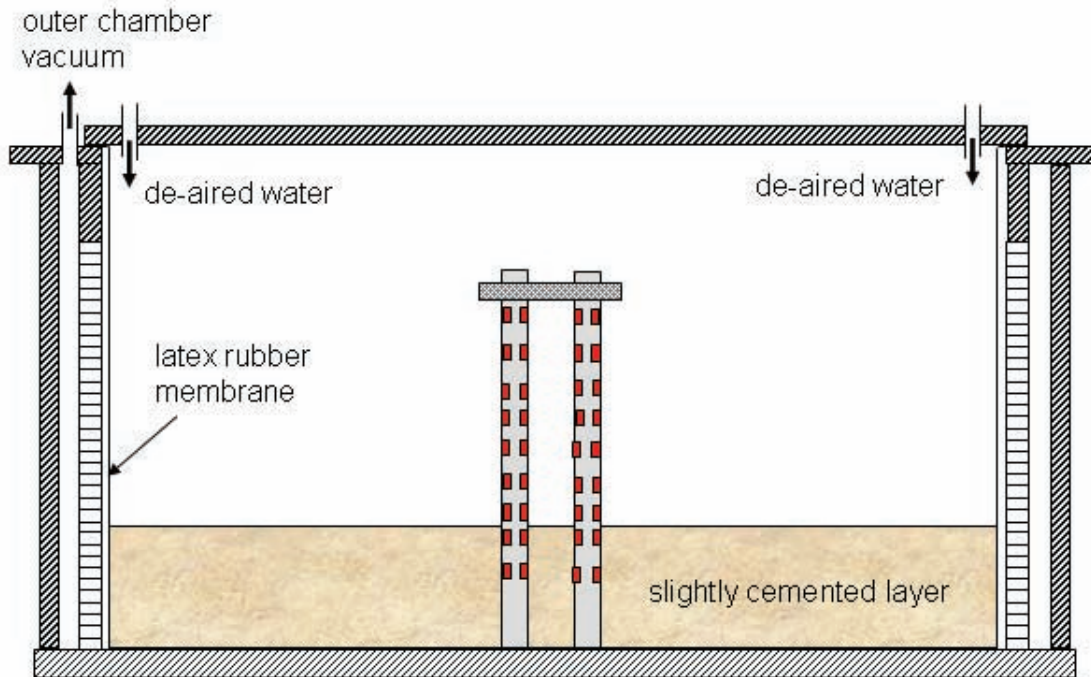
This section describes the preparation of the centrifuge models listed above. Even though there were some differences regarding the pile group foundations, the model preparation was very similar in all cases. The 1-D large laminar box, described in section 2.4, was used in this series of tests.

First, a 0.02 cm thick latex membrane is placed inside the laminar box to prevent leakage of the saturated soil. Afterwards, the external side of the container is sealed and a vacuum pump is connected to remove the air from the outer chamber, as shown in Fig. 7.1a. This forces the latex membrane to flush against the rings, facilitating placement of the soil. At this stage the pile group (in Models p-3x2, p-6x2, and p-3x1) is properly located and aligned in the box. Figure 7.1a shows the construction of the bottom slightly cemented layer. A dry mixture of slightly cemented sand is pluviated into the laminar box in four sublayers. Each sublayer is compacted by dropping an aluminum block three times from a height of 2 cm, ending up with a cemented layer of about 6.2 cm high. The soil in the pile group area is compacted following the same procedure, but using an aluminum block with holes slightly larger than the diameter of the piles (Fig. 7.1a). An accelerometer is placed at an intermediate elevation at the proper orientation. This slightly cemented sand layer is believed to represent a medium-dense layer in the field (Abdoun, 1997).

A cover is placed on top of the laminar box and de-ionized water is slowly introduced from the corners of the cover until the whole layer is wet (Fig. 7.1b). Once the cement is set, after approximately 12 hours, the cover is removed and the surface is flattened and carefully scraped to ensure a uniform height of 6 cm.

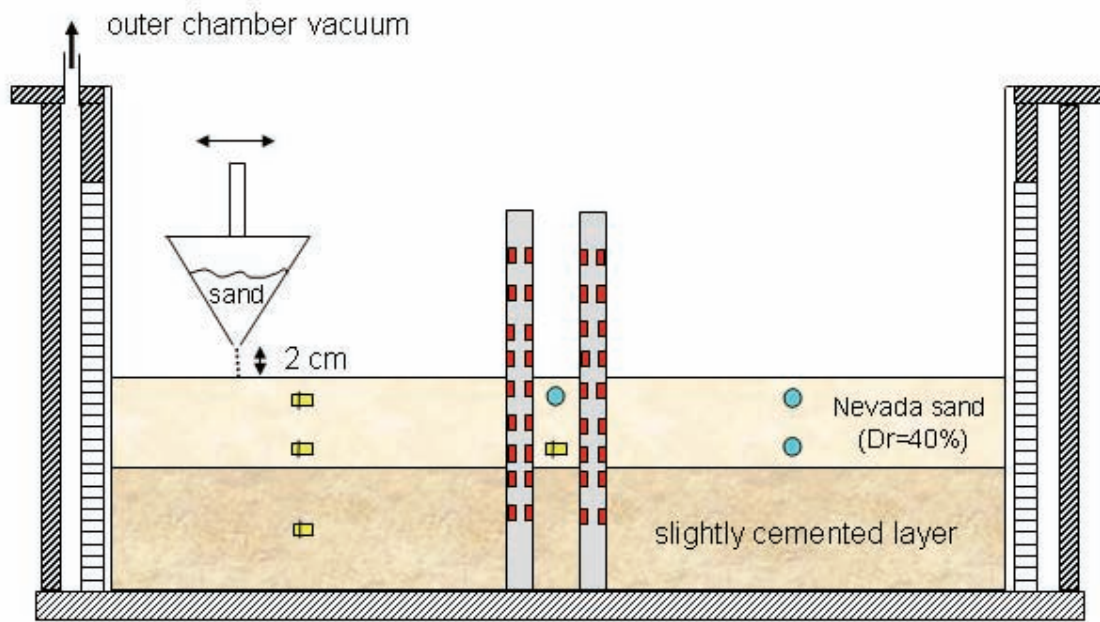


(a)

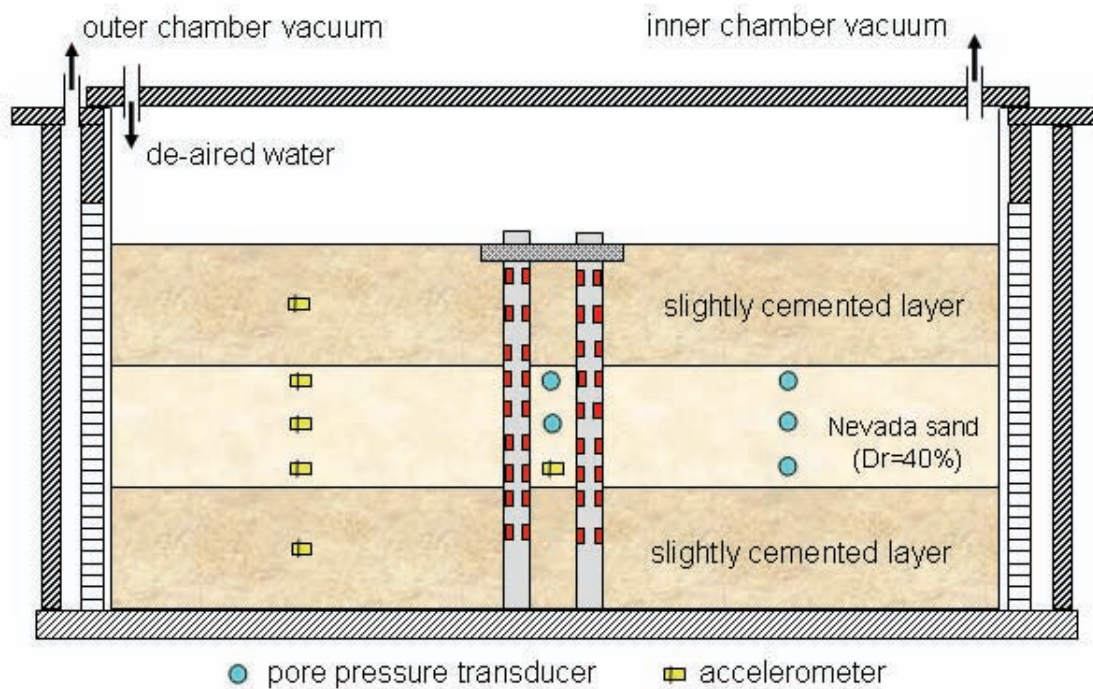


(b)

Figure 7.1: (a) Preparation of slightly cemented sand later, (b) saturation of the cemented sand layer



(c)



(d)

Figure 7.1 (cont.): (c) Pluviation of Nevada sand, (d) saturation of the model

At this stage, the pile cap is removed to facilitate pluviation of the soil. Figure 7.1c illustrates the construction of the liquefiable layer. Dry Nevada sand is poured into the laminar box by dry pluviation to a height of 6 cm above the bottom cemented layer. A funnel with a row of holes is used to place the sand in the laminar box, except in the pile group area where a small cone connected to a thin tube is used. The falling distance and speed of movement in both methods were previously calibrated to ensure the desired 40% relative density. The width of the funnel was approximately one third the width of the laminar box. The funnel is manually moved back and forth along the longest dimension of the box, with a free falling distance of about 2 cm. Accelerometers and pore pressure transducers are installed at proper locations and orientations. In Models p-6x2 and p-3x1 lines of colored sand are placed at intermediate depths, using a plastic grid that serve as mold.

Once the thickness of the loose Nevada sand is exactly 6.0 cm, four shrink tubes are placed at each side of the long dimension of the box. These tubes serve as drainage for the dissipation of excess pore pressure developed in the liquefiable layer during shaking. The construction process of the top cemented layer is very similar to that of the bottom layer. The only difference is that the first sublayer is carefully compacted without dropping the aluminum block, avoiding the compaction of the liquefiable layer. In Models p-6x2 and 3x1 thin layers of colored cemented sand are placed at various elevations. After the third sublayer is pluviated and properly compacted, the pile cap is reattached. Finally, once the fourth layer is poured and compacted, the ground surface is carefully flattened to ensure an exact thickness of 6 cm.

An airtight cover is placed on top of the laminar box, sealing the inner chamber. The vacuum pump for the outer chamber is turned off and the laminar box is carefully moved to the centrifuge platform. Once the laminar box is fixed to the inclined table, on top of the shaker, the vacuum pump is reconnected to the outer chamber, reaching a vacuum of 30 in of mercury. A second vacuum pump is then connected to apply a vacuum of about 26 in of mercury to the inner chamber, as shown in Fig. 7.1d. This differential vacuum is required to keep the latex membrane tight against the rings. After maintaining the inner vacuum for an hour, the second pump is turned off and carbon dioxide is slowly introduced into the box during approximately half an hour until atmospheric pressure is reached in the inner chamber. The purpose of using CO₂ is to help dissolving the remaining oxygen in the water. Then, de-ionized/de-aired water is introduced very slowly to the model from two dripping pipes located on the downslope side of the cover. This process continues for about 24 hours until the water table reaches the model surface. The inner and outer vacuums are slowly released and the airtight cover is removed. The rigid sides of the laminar box are also removed and the remaining sensors are attached. The model is finally tested between 24 and 30 hours after the saturation process is completed.

7.3 Model p-0 (free field)

7.3.1 Model Description

The setup and instrumentation used in Model p-0 are presented in Fig. 7.2. The model height is 18 cm, simulating at 50g a 9 m soil deposit. The profile consists of a 3 m thick Nevada sand layer placed at a relative density of about 40%, between two 3 m thick nonliquefiable slightly cemented layers. The model is inclined 2° to the horizontal and saturated with de-ionized/de-aired water. At a centrifugal acceleration of 50g the loose Nevada sand simulates a coarse sand layer, and the inclination becomes 4.8° after instrumental correction (Taboada, 1995). Since this model does not include a pile foundation, it simulates the lateral deformation in a free field condition.

The purpose of this test is to simulate a lateral spreading between 1 and 1.5 m. Based on previous centrifuge tests conducted at RPI, a sinusoidal acceleration of 30 cycles, amplitude of 12g and frequency of 100 Hz was estimated as an appropriate input signal. At a 50g centrifugal acceleration, this corresponds to a frequency of 2 Hz and peak acceleration of 0.24g. However, to avoid repeating the test with a different input signal in case of measuring less lateral spreading than the targeted displacement, the number of the input cycles was increased to 50.

The instrumentation used in Model p-0 is shown in Fig. 7.2 and listed in Table 7.2. The model was instrumented with 12 accelerometers, 5 pore pressure transducers, and 6 LVDTs. Accelerations in the soil and outside the laminar box, excess pore water pressure in the liquefiable layer, ground surface settlement, and lateral displacement of the soil were measured during the test.

7.3.2 Recorded Accelerations

Figure 7.3 shows the recorded input acceleration and soil acceleration time histories at different depths. The acceleration record of the top cemented layer shows uniform amplitude of about 0.1g during the shaking process, indicating that this layer did not liquefy. Acceleration records in the liquefiable layer show a drop in positive amplitude, exhibiting as well large spikes in the negative direction after about two cycles of shaking. At the bottom of this layer however, no significant drop in acceleration is observed. The acceleration records indicate the loose sand layer did liquefy, with the decrease in positive amplitude due to the difficulty shear waves have in traveling through the liquefied soil because of significant reduction in its stiffness and strength. The large negative spikes are related to the dilative behavior of the saturated loose sand during lateral spreading.

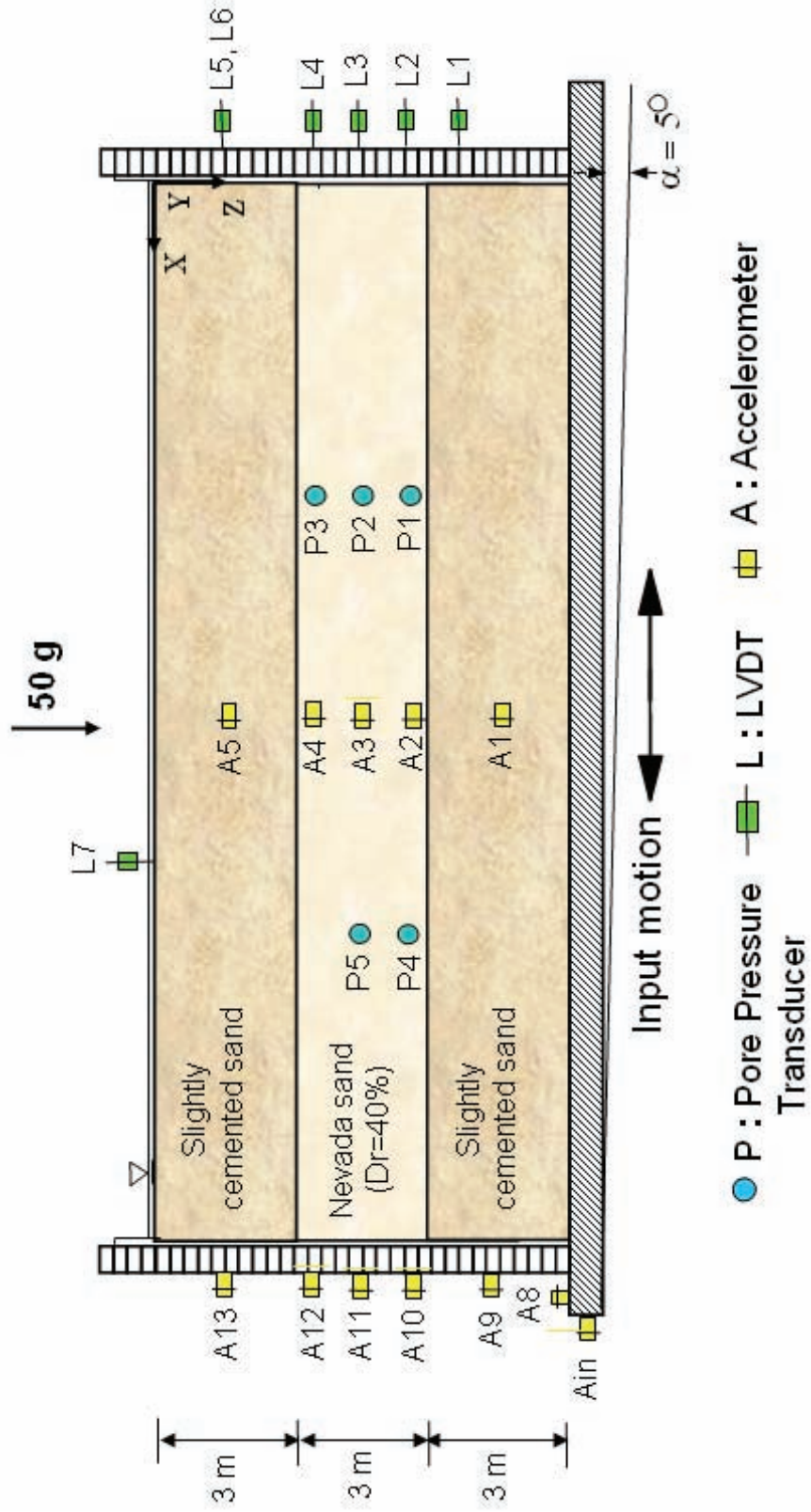


Figure 7.2: Setup and instrumentation used in Model p-0, (in prototype units)

Table 7.2: Location of instruments in Model p-0 (in model units)

Transducer	Sensor name	Coordinates [cm]		
		X	Y	Z
Accelerometer	Ain	73.5	17.75	18.5
	A1	35.5	17.75	15
	A2	35.5	17.75	11
	A3	35.5	17.75	9
	A4	35.5	17.75	7
	A5	35.5	17.75	3
	A8	72.5	17.75	18
	A9	71	17.75	15
	A10	71	17.75	11
	A11	71	17.75	9
	A12	71	17.75	7
	A13	71	17.75	3
	Pore pressure transducer	P1	18	17.75
P2		18	17.75	9
P3		18	17.75	7
P4		53	17.75	11
P5		53	17.75	9
LVDT	L1	0	24	14
	L2	0	12	11
	L3	0	24	9.1
	L4	0	12	7.2
	L5	0	24	3
	L6	0	12	3
	L7	45	18	0

At 4.5 m the acceleration amplitude (A3) increased considerable after about 16 sec. This phenomenon, related to the soil lateral displacement, is discussed below in section 7.3.4. The recorded acceleration of the bottom cemented layer is very similar to the input acceleration, indicating that no sliding occurred between this layer and the base of the laminar box.

Figure 7.4 shows accelerations recorded on laminar rings at the same elevations than the ones of the accelerometers in the soil. Next to the cemented layers, the ring accelerations are very similar to the soil accelerations. However, next to the liquefiable layer, ring accelerations do not show either a significant drop in amplitude nor large spikes.

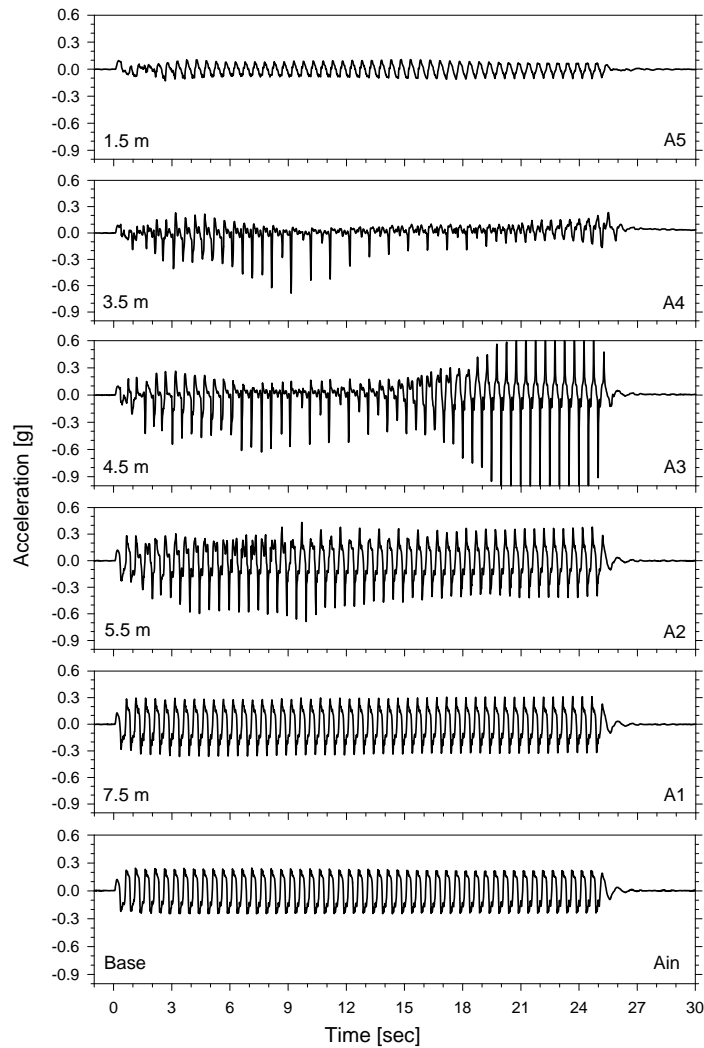


Figure 7.3: Soil acceleration time histories in the free field, Model p-0

7.3.3 Recorded Excess Pore Pressures

Figure 7.5 presents excess pore pressure time histories at different depths within the loose sand layer. These records reveal that the whole layer liquefied after a few seconds of excitation, and the dissipation process started before the end of shaking. The low permeability of the slightly cemented layer, including the drainages tubes, compared to the one of Nevada sand, and the settlement process of the top cemented layer, seem to have been responsible for: a) an increase in excess pore pressure after the loose sand was liquefied, and b) a slow dissipation process during approximately the first 45 sec. Actually, the settlement rate of the top cemented layer decreased noticeably at about 45 sec (Fig. 7.10b), increasing the dissipation rate of the remaining excess pore pressure.

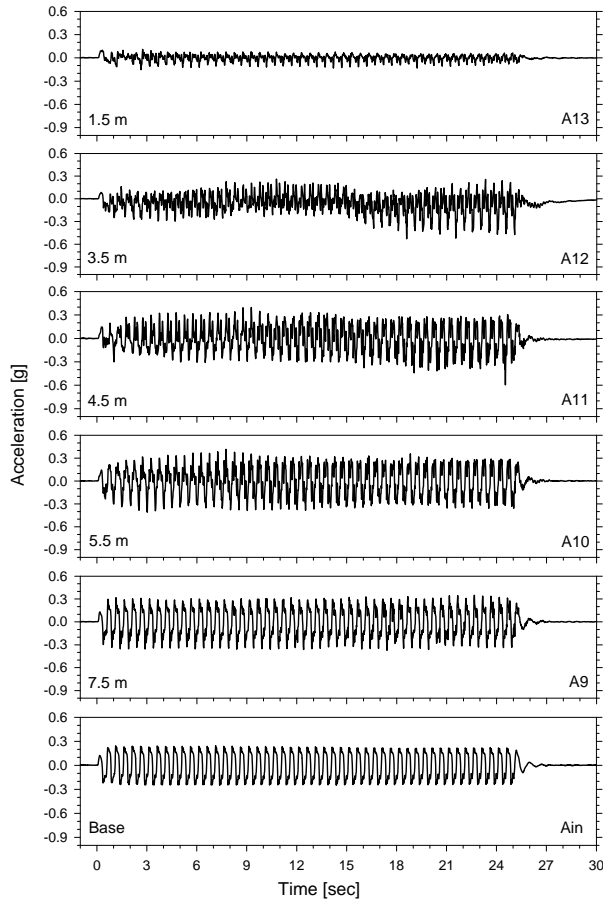


Figure 7.4: Acceleration time histories on the laminar rings, Model p-0

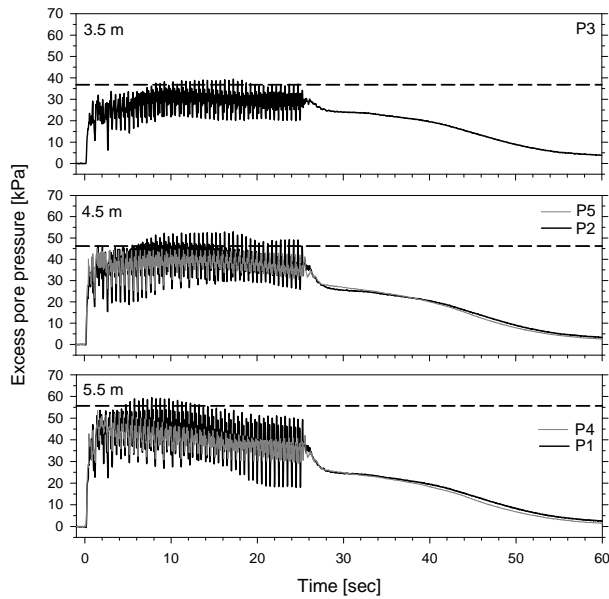


Figure 7.5: Short and long term excess pore pressure time histories in the free field, the dashed lines correspond to initial liquefaction, Model p-0

7.3.4 Recorded Lateral Displacements

Figure 7.6 shows the recorded lateral displacement of the model at different depths. The liquefied layer and the top cemented layer displaced gradually during shaking. On the other hand, the bottom cemented layer did not move, being consistent with the acceleration record at that elevation. Once the shaking stopped, the lateral displacement stopped immediately, even though the loose layer was still liquefied. This phenomenon is consistent with previous centrifuge tests (Abdoun, 1997; Pamuk, 2004), and confirms that the inertia forces due to shaking are necessary for the ground deformation to continue (Okamura et al., 2001).

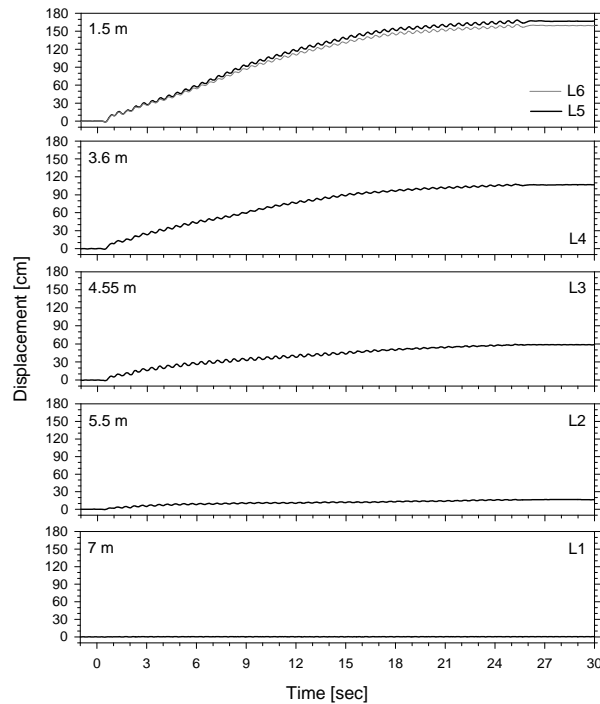


Figure 7.6: Soil lateral displacement time histories in the free field, Model p-0

Visual inspection of the model after the test revealed that the relative displacement between some of the rings reached the limit of about 4.5 mm, corresponding to 22.5 cm in prototype units. Figure 7.7 shows relative displacement time histories between the rings attached to the LVDTs, where the dashed lines represent the allowable relative displacement between these rings. The relative displacement $\Delta 1$ corresponds to two adjacent rings, while $\Delta 2$, $\Delta 3$, and $\Delta 4$ correspond to two rings separated by another one, representing an allowable relative displacement of 45 cm. Figure 7.7 confirms that in the upper half of the liquefied layer the relative displacements ($\Delta 3$ and $\Delta 4$) reached the limit after about 30 cycles of shaking, time at which the lateral displacement on the ground surface was approximately 135 cm (Fig. 7.6). Since this level of lateral spreading is within the expected range, only the first 30 cycles are considered.

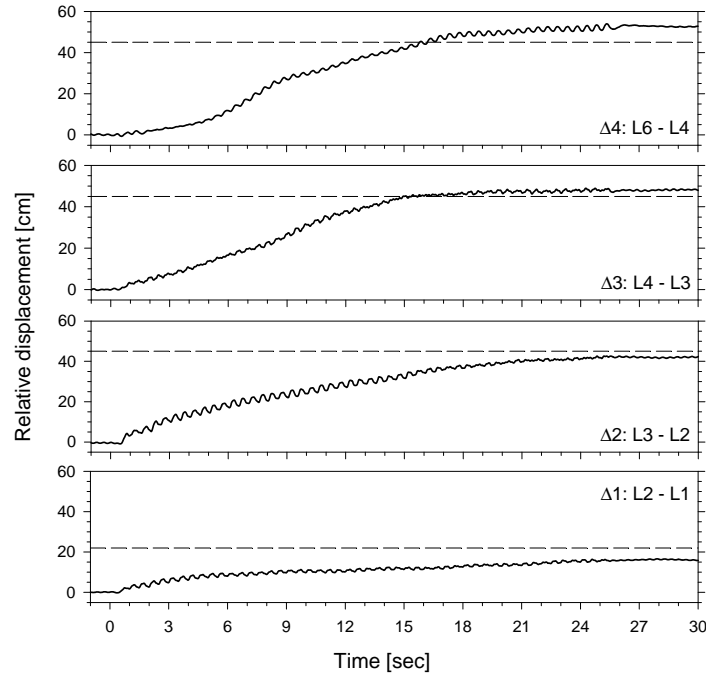


Figure 7.7: Relative displacement time histories between the rings attached to the LVDTs, the dashed lines represent the allowable relative displacement between these rings in prototype units, Model p-0

Figure 7.8 shows the soil lateral displacement time histories considering the first 30 cycles of shaking, data that can be directly compared to the soil displacement measured in the following centrifuge tests.

Figure 7.9 presents profiles of soil lateral displacement in the free field at different times during shaking, after filtering out the cyclic component. The ground surface settlement time history in the short and long term is presented in Fig. 7.10. During the shaking process the top cemented layer settled about 6 cm, mainly due to the rearrangement of particles induced by shear strain. Once the shaking finished, the settlement continued due to the consolidation process of the liquefied layer, reaching a value of about 15 cm. Figure 7.11 shows a picture and schematic of a longitudinal crack developed on the ground surface during the test. The excess pore pressure developed in the middle layer fractured the top cemented layer along the longitudinal direction, evidenced also by the sand boils observed along this crack.

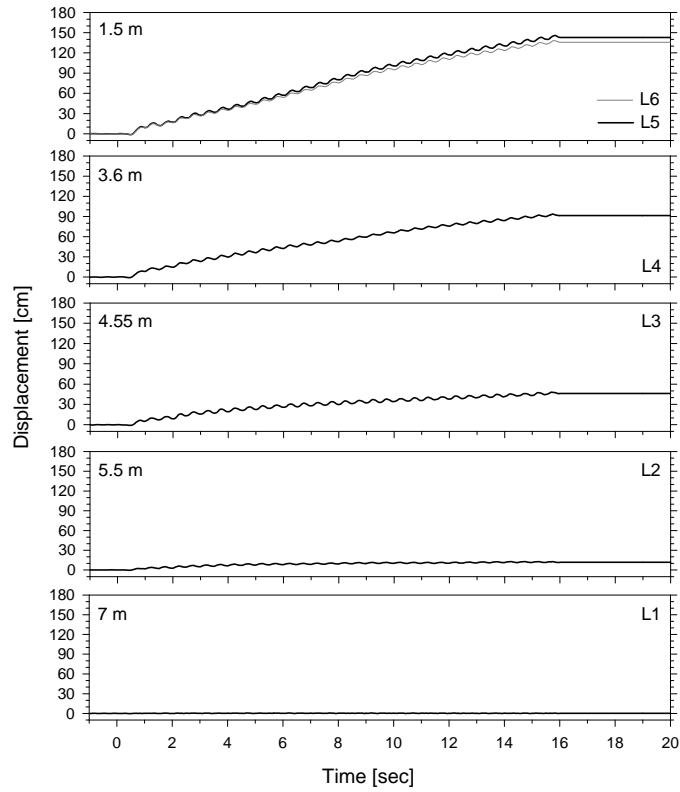


Figure 7.8: Soil lateral displacement time histories in the free field, considering the first 30 cycles of shaking, Model p-0

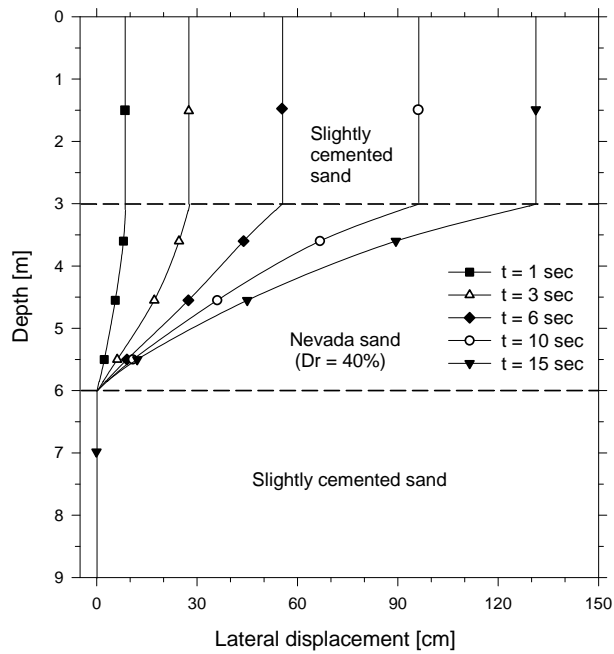
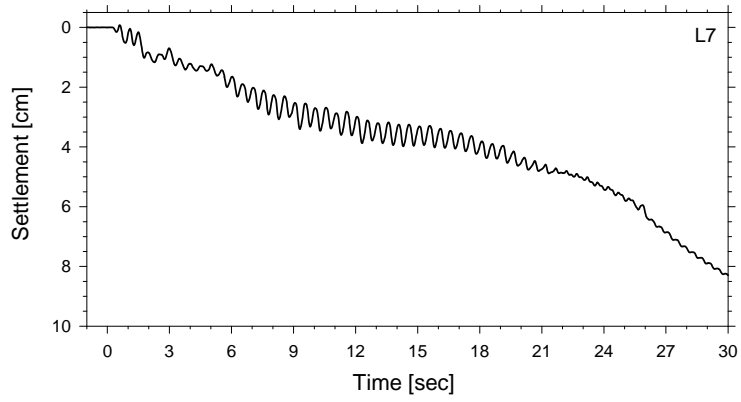
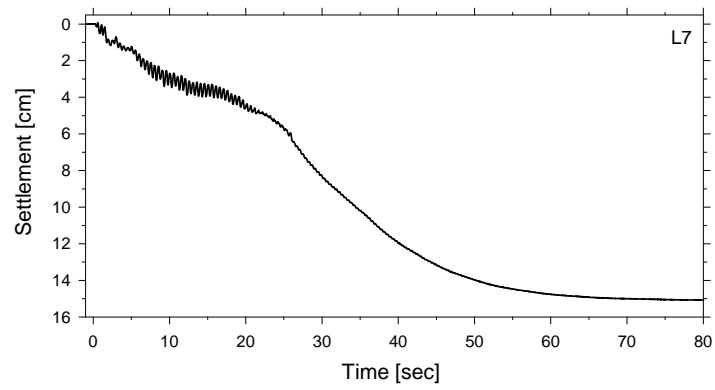


Figure 7.9: Profiles of soil lateral displacement in the free field, Model p-0

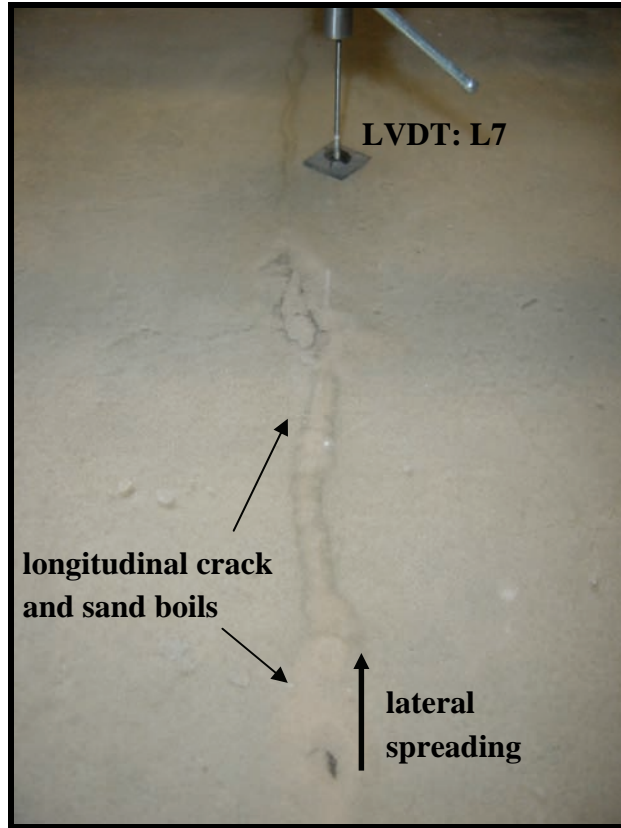


(a)

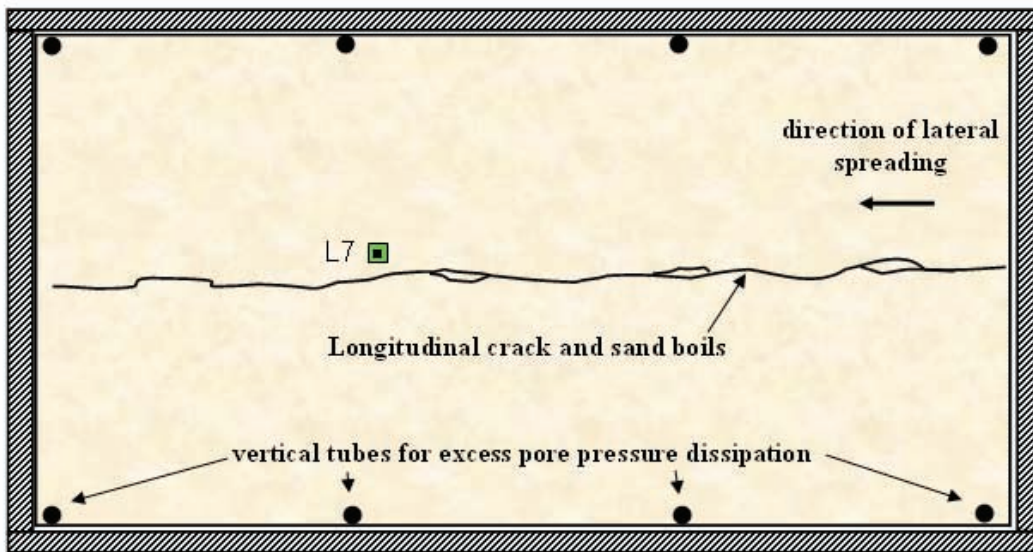


(b)

Figure 7.10: Ground surface settlement time history, (a) short term, (b) long term, Model p-0



(a)



(b)

Figure 7.11: Longitudinal crack and sand boils developed on the surface, (a) picture, (b) schematic, Model p-0

7.4 Model p-3x2

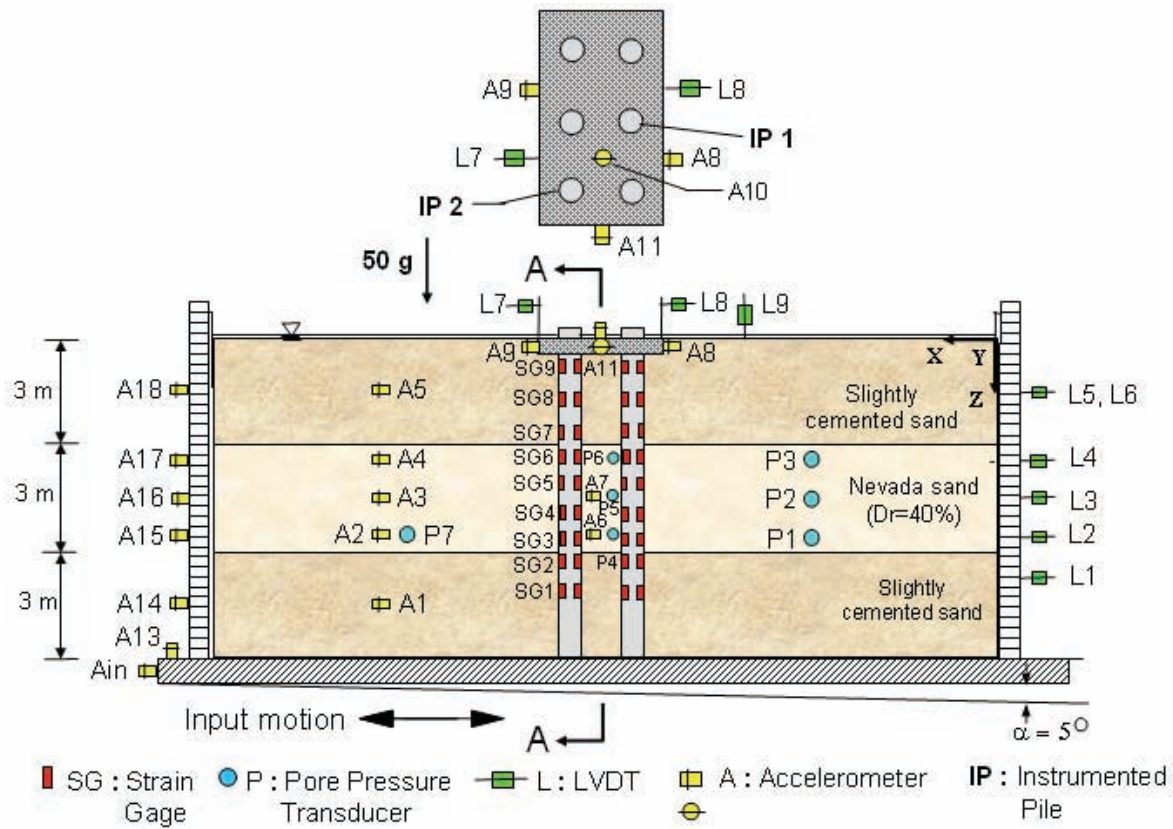
7.4.1 Model Description

The setup and instrumentation used in Model p-3x2 are presented in Fig. 7.12. This model simulates a 3x2 pile group connected with a pile cap perpendicular to the direction of lateral spreading. The prototype profile consists of a 3 m thick Nevada sand layer placed at a relative density of about 40%, on top and below a 3 m thick nonliquefiable cemented layer. The model is inclined 2° to the horizontal and saturated with de-ionized/de-aired water. At a centrifugal acceleration of 50g the loose Nevada sand simulates a coarse sand layer, and the inclination becomes 4.8° after instrumental correction.

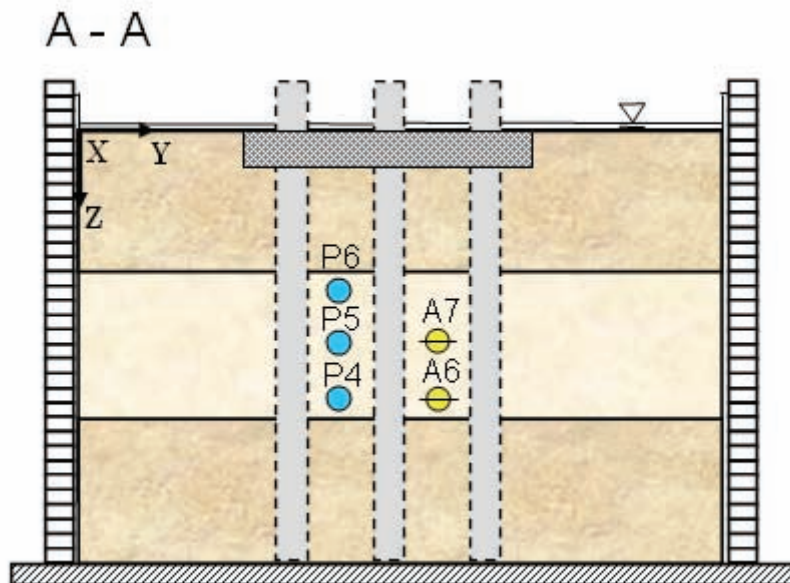
The embedded piles have a prototype diameter of 55 cm and a bending stiffness (EI) of approximately $78000 \text{ kN}\cdot\text{m}^2$. The aluminum cap, embedded in the top cemented layer, has prototype dimensions of 3.3 m in width, 4.95 m in length, and 0.64 m in height. Figure 7.13 displays a picture and schematic of the pile-cap-structure, showing the spacing between piles (3d), as well as the aluminum block used to compact the cemented sand around the piles. Figure 7.14 shows a picture of the model during preparation, with the dashed line representing the location of the pile cap.

Based on the measured results of Model p-0, the model was excited by 30 cycles of a 100 Hz sinusoidal acceleration with uniform amplitude of about 12g. At a centrifugal acceleration of 50g this corresponds to a frequency of 2 Hz and peak acceleration of 0.24g.

The instrumentation used in Model p-3x2 is shown in Fig. 7.12 and listed in Table 7.3. The model was instrumented with 18 accelerometers, 7 pore pressure transducers, and 9 LVDTs. Two instrumented piles (IP1 and IP2) were used in the pile group foundation, as shown in Fig. 7.12a. Detailed information about the strain gage configuration and the aluminum piles (type A) used in this model is presented in section 2.7. Accelerations in the soil and outside the laminar box, excess pore water pressure, lateral displacement of the soil and the pile cap, ground surface settlement, bending moments, and axial forces were measured during this test.

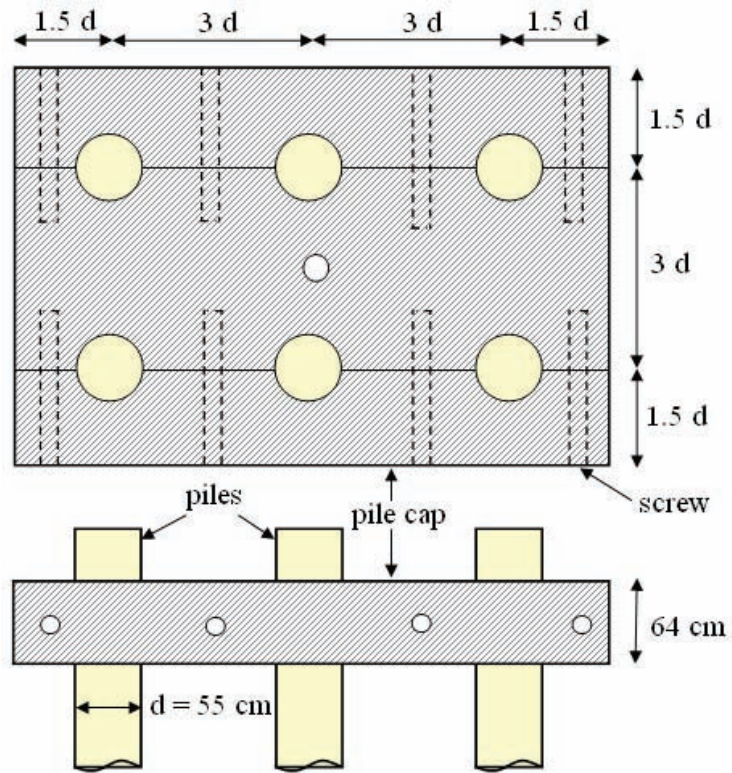


(a)

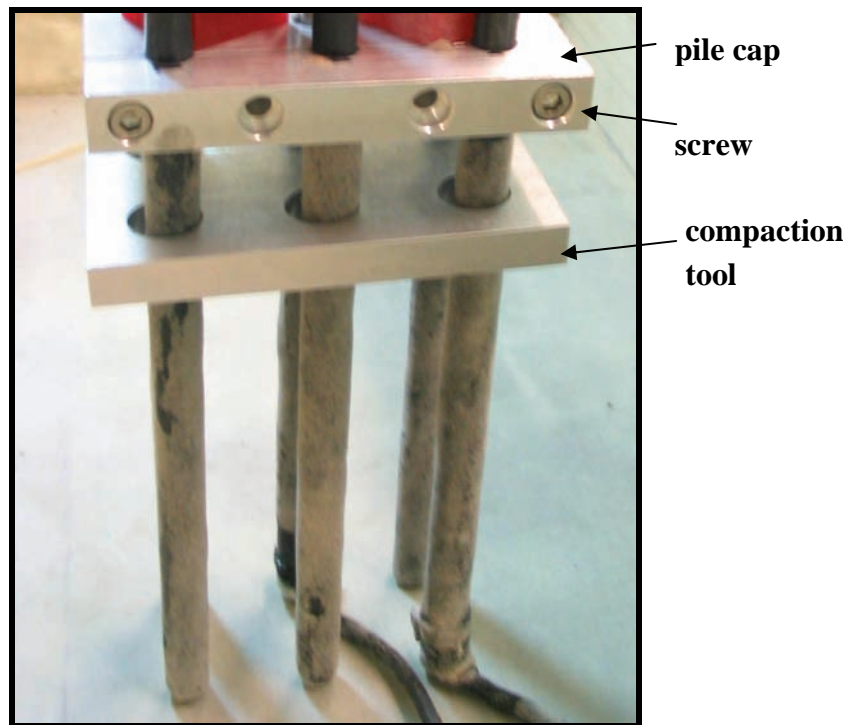


(b)

Figure 7.12 (a) Setup and instrumentation used in Model p-3x2, (in prototype units)
(b) Transversal section of Model p-3x2



(a)



(b)

Figure 7.13: Pile-cap-structure, (a) schematic, (b) picture, Model p-3x2

Table 7.3: Location of instruments in Model p-3x2 (in model units)

Transducer	Sensor name	Coordinates [cm]		
		X	Y	Z
Accelerometer	Ain	73.5	17.75	18.5
	A1	53	17.75	15
	A2	53	17.75	11
	A3	53	17.75	9
	A4	53	17.75	7
	A5	53	17.75	3
	A6	35.5	19.5	11
	A7	35.5	19.5	9
	A8	32.5	16	0.63
	A9	39	19.5	0.63
	A10	35.5	16	0
	A11	35.5	12.75	0.63
	A13	72.5	17.75	18
	A14	71	17.75	15
	A15	71	17.75	11
	A16	71	17.75	9
	A17	71	17.75	7
	A18	71	17.75	3
Pore pressure transducer	P1	18	17.75	11
	P2	18	17.75	9
	P3	18	17.75	7
	P4	35.5	16	11
	P5	35.5	16	9
	P6	35.5	16	7
	P7	51	17.75	11
LVDT	L1	0	24	14
	L2	0	12	11
	L3	0	24	9.1
	L4	0	12	7.2
	L5	0	24	3
	L6	0	12	3
	L7	39	16	-2
	L8	32.5	19.5	-2
	L9	24	27	0

Table 7.3 (cont.): Location of instruments in Model p-3x2 (in model units)

Transducer	Sensor name	Coordinates [cm]			
		X	Y	Z	
Strain gage		IP 1	IP 1	IP 1	
	SG1	34.25	17.75	14	
	SG2	34.25	17.75	12.5	
	SG3	34.25	17.75	11.5	
	SG4	34.25	17.75	10	
	SG5	34.25	17.75	8	
	SG6	34.25	17.75	6.5	
	SG7	34.25	17.75	5.5	
	SG8	34.25	17.75	3.75	
	SG9	34.25	17.75	2	
			IP 2	IP 2	IP 2
	SG1	37.25	14.5	14	
	SG2	37.25	14.5	12.5	
	SG3	37.25	14.5	11.5	
	SG4	37.25	14.5	10	
	SG5	37.25	14.5	8	
	SG6	37.25	14.5	6.5	
	SG7	37.25	14.5	5.5	
SG8	37.25	14.5	3.75		
SG9	37.25	14.5	2		

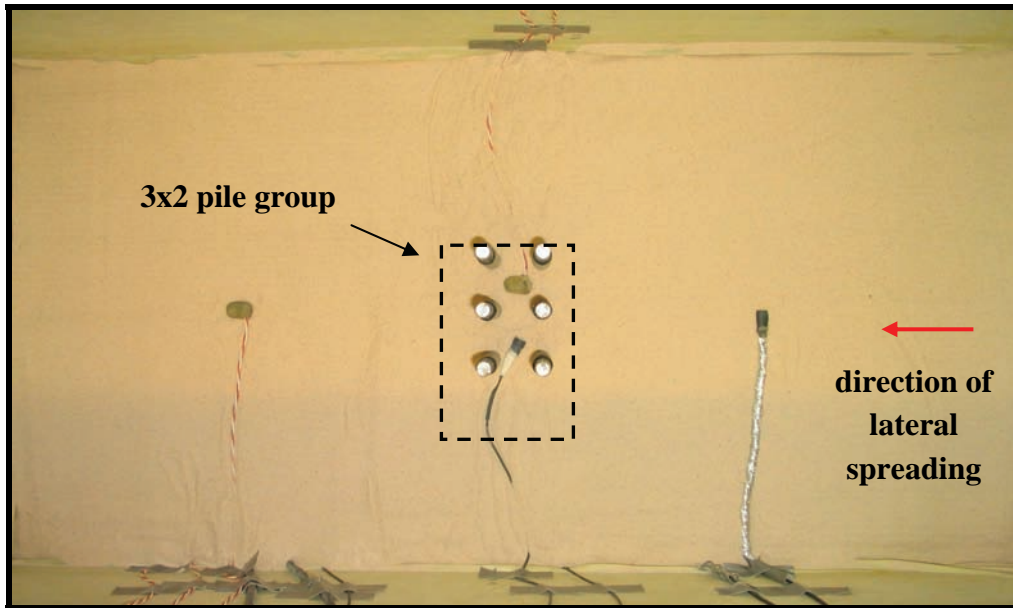


Figure 7.14: Model during preparation, the dashed line represents the pile cap, Model p-3x2

7.4.2 Recorded Accelerations

Figure 7.15 shows the recorded input acceleration and soil acceleration time histories far from the pile group at different depths. Acceleration records in the loose sand layer show a drop in positive amplitude, exhibiting as well large spikes in the negative direction after a couple of cycles of shaking. At the bottom of this layer however, the positive acceleration did not drop significantly, probably due to the boundary effect of the bottom layer. This effect has been observed in previous centrifuge tests conducted by the author (Gonzalez, 2002). Nevertheless, the acceleration records indicate the loose sand layer liquefied and displaced in the downslope direction during shaking. The recorded acceleration in the top cemented layer (A5) shows a considerable drop in amplitude after the first cycle of shaking, indicating a dynamic isolation of this layer once the loose layer liquefied, despite the fact that the pile group was embedded in this layer. The acceleration record of the bottom cemented layer is very similar to the input acceleration, indicating no sliding occurred between this layer and the base of the laminar box.

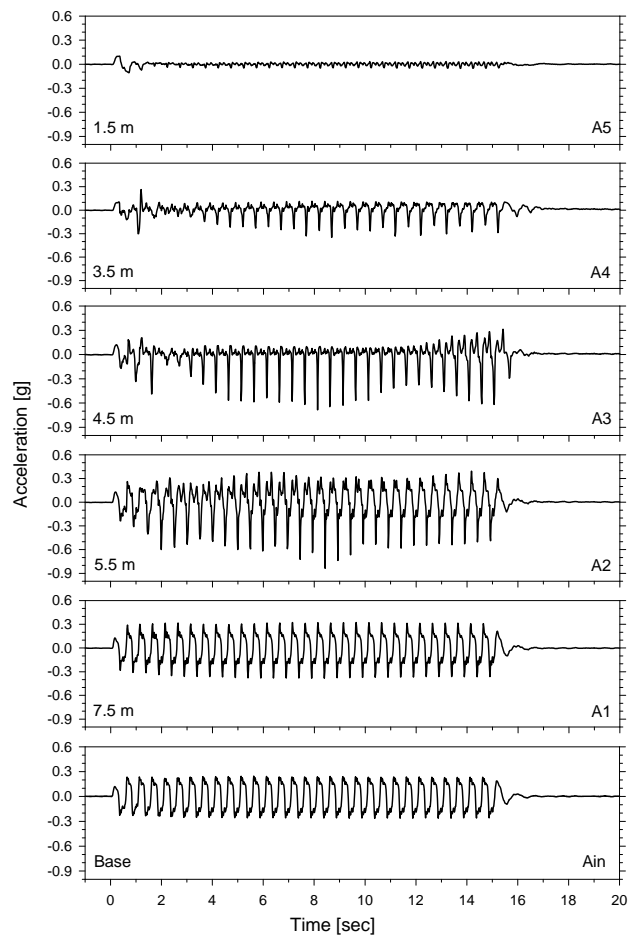


Figure 7.15: Soil acceleration time histories far from the pile group, Model p-3x2

Soil acceleration time histories between piles at two different depths are presented in Fig. 7.16. The soil acceleration at 4.5 m dropped substantially after a few cycles, indicating the soil in this area did liquefy. As the excitation continued however, the acceleration amplitude started increasing significantly. The accelerometer (A7) apparently moved close to one of the piles during lateral spreading, being influenced by the pile movement. At 5.5 m the acceleration record is similar to the one in the soil far from the pile group, confirming the boundary condition effect.

Figure 7.17 presents the acceleration time histories on the pile cap, as well as the measured horizontal and vertical acceleration at the base of the box. The cap vertical acceleration seems to be related to the vertical acceleration at the base of the model. The acceleration perpendicular to the direction of lateral spreading consists of small spikes generated by the pile group vibration during shaking. On the other hand, the acceleration record in the direction of lateral spreading contains large high frequency spikes generated by the interaction between the pile group and the top cemented layer.

Laminar ring accelerations recorded at two elevations are presented in Fig. 7.18. Unfortunately some accelerometers were not properly attached and got pulled during the test. The ring accelerations at 5.5 and 7.5 m are very similar to the ones recorded in the soil at the same depths.

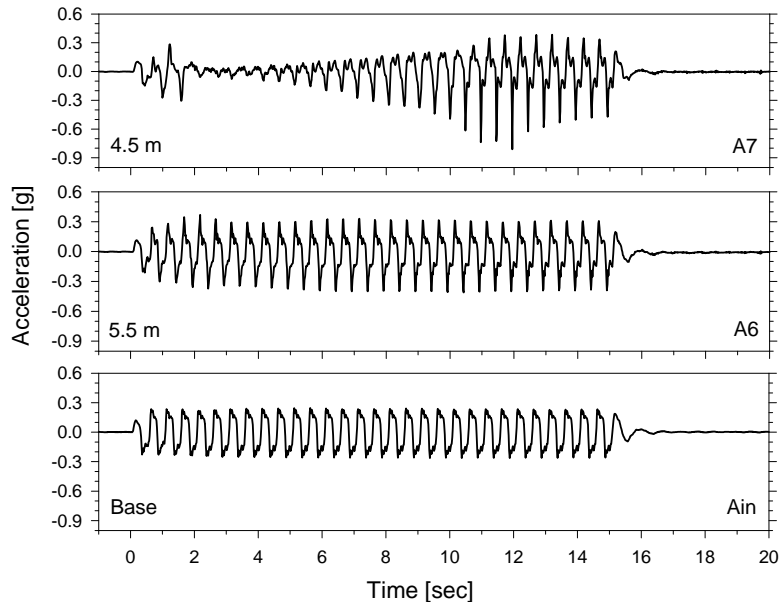


Figure 7.16: Soil acceleration time histories between piles, Model p-3x2

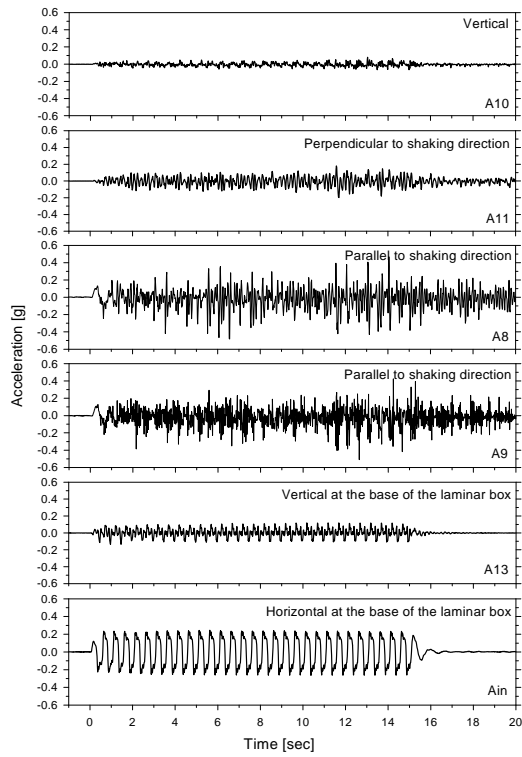


Figure 7.17: Acceleration time histories on the pile cap, Model p-3x2

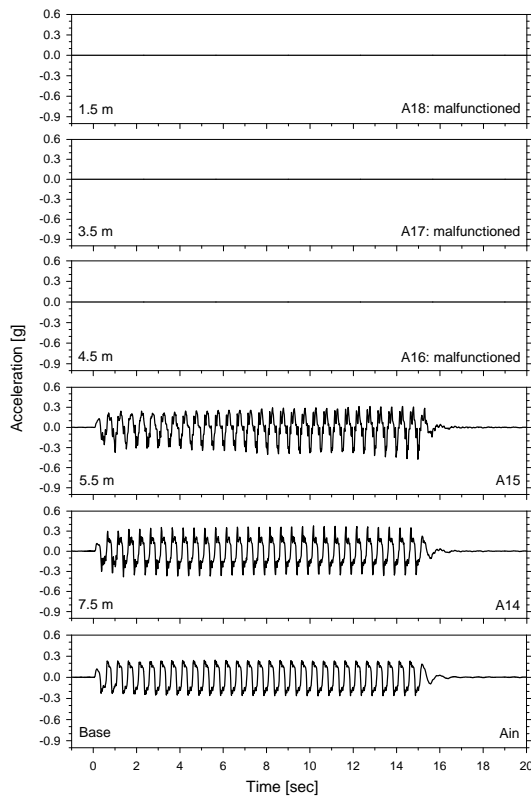


Figure 7.18: Acceleration time histories on the laminar rings, Model p-3x2

7.4.3 Recorded Excess Pore Pressures

The excess pore pressure records reveal that the loose sand layer liquefied after a couple of cycles (Fig. 7.19). In the free field, a slight increase in excess pore pressure during the excitation and a slow dissipation process seem to be associated to the low permeability and settlement of the top cemented layer, as discussed in section 7.3.3. In the pile group area, the smaller thickness of cemented layer below the cap generated a lower excess pore pressure than in the free field. In addition, gaps developed on the downslope side of the pile group (Fig. 7.27b) seem to have slightly increased the dissipation rate in this area (Fig. 7.20).

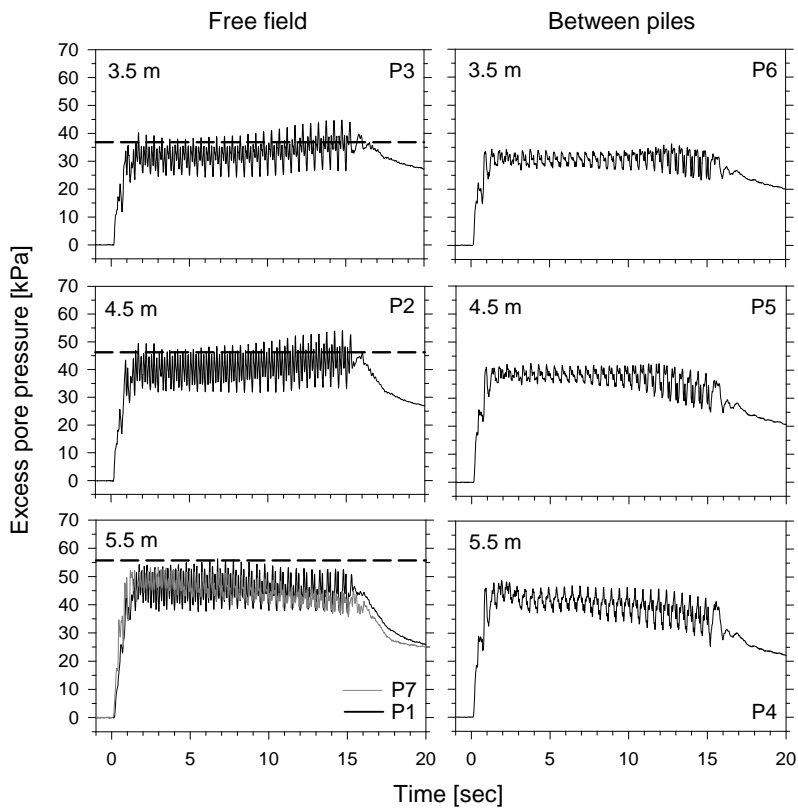


Figure 7.19: Short term excess pore pressure time histories in the free field and between piles, the dashed lines correspond to initial liquefaction, Model p-3x2

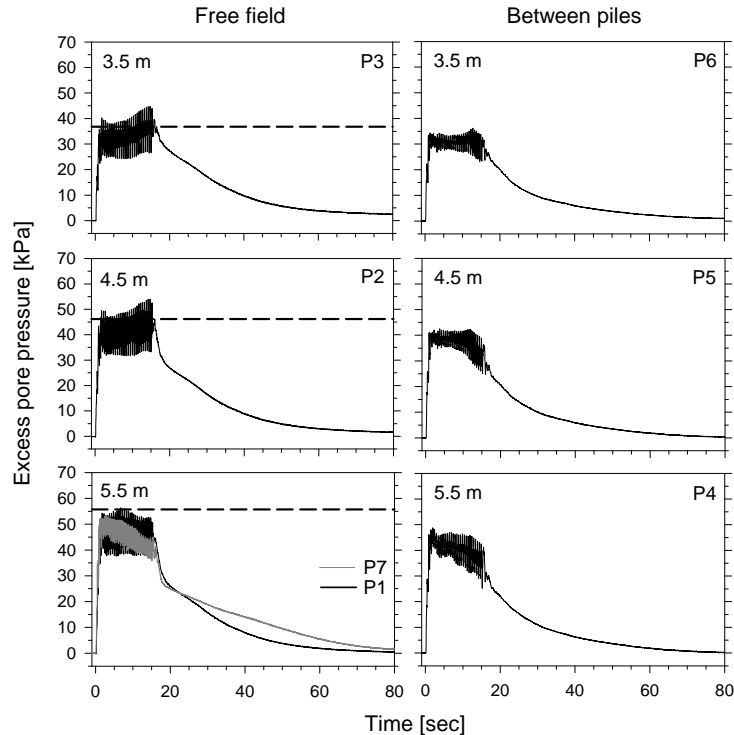


Figure 7.20: Long term excess pore pressure time histories in the free field and between piles, the dashed lines correspond to initial liquefaction, Model p-3x2

7.4.4 Recorded and Back-calculated Lateral Displacements

Figure 7.21 shows the recorded lateral displacement of the pile cap and soil at various depths. The liquefied layer and top cemented layer displaced gradually during shaking. The records also show that the bottom cemented layer did not move, being consistent with the acceleration record at that elevation. Once the shaking process finished, the soil lateral displacement stopped immediately. The pile cap on the other hand, remained vibrating for a short period of time.

The profiles of soil lateral displacement were obtained interpolating the LVDT measurements, after filtering out the cyclic component (Fig. 7.22). As soon as the loose sand liquefied at the beginning of shaking, the deposit started moving downslope, with the top cemented layer reaching a maximum displacement of approximately 65 cm at the end of shaking, 70 cm less than the case without piles (Model p-0). Therefore, the pile group was able to reduce the amount of lateral spreading in more than 50%.

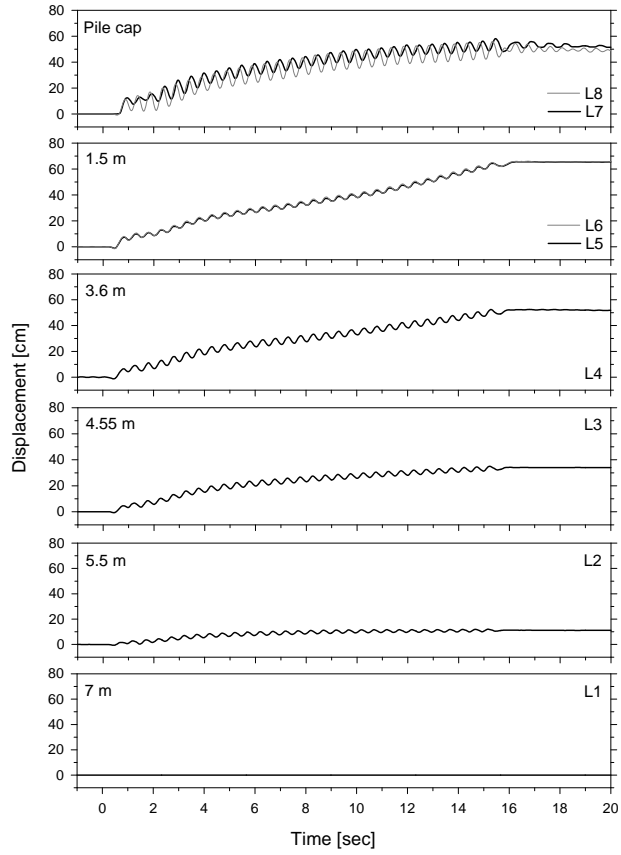


Figure 7.21: Soil and pile cap lateral displacement time histories, Model p-3x2

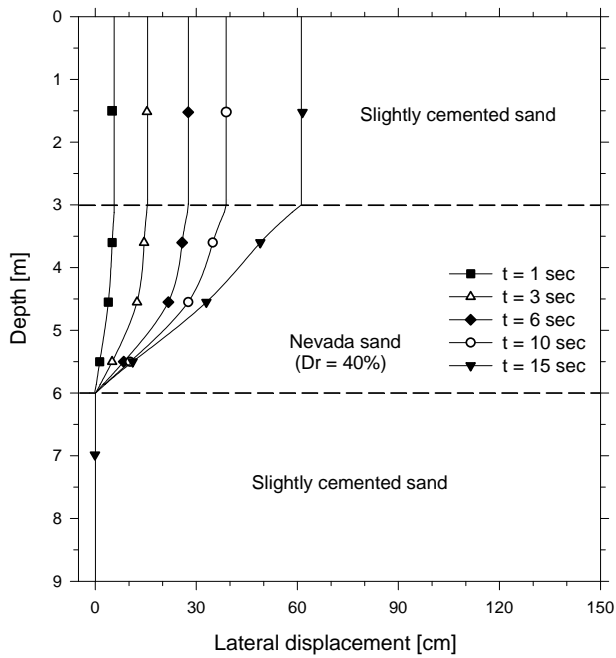


Figure 7.22: Profiles of soil lateral displacement, Model p-3x2

Even though the method and equations to estimate the deformation and rotation of the piles were presented in section 3.4.6, they are included again in this section. The displacement profiles of the upslope (IP1) and downslope (IP2) piles were first calculated by double integrating the bending moment distributions along the height of the piles, according to equation:

$$y_p = \iint \frac{M(h)}{EI} dh \quad [7.1]$$

where y_p is the pile lateral deformation, EI is the pile bending stiffness, M is the pile bending moment after filtering out the cyclic component, and h is the height measured from the bottom of the Nevada sand layer. However, the estimated lateral displacement (LD_E) at the location of the LVDTs differed considerably from the one measured with the transducers L7 and L8 (LD_M), indicating that the bottom cemented layer was not able to provide infinite constrain to the piles. The rotation of each pile at the base of the liquefiable layer (θ_{base}) was hence estimated using the following expression:

$$\theta_{base} = \frac{LD_M - LD_E}{dh} \quad [7.2]$$

where dh is the distance between the bottom of the liquefiable layer and the LVDTs L7 and L8. At each time instant, the rotational stiffness provided by the bottom cemented layer was estimated dividing the pile bending moment at the base of the liquefiable layer by the rotation of the corresponding pile (θ_{base}). Figure 7.23 shows the back-calculated rotational stiffness provided by the bottom cemented layer around the instrumented piles IP1 and IP2 versus the corresponding bending moment at the base of the liquefiable layer.

After ignoring the indetermination generated by very small rotations of the upslope pile IP1 at the beginning of shaking, the rotational stiffness in the elastic range was approximately 45000 kN-m/rad. As the bending moment increased, the bottom cemented sand around the pile lost strength and the confinement decreased drastically. The cemented sand around the downslope pile IP2 provided a similar stiffness in the elastic range. In this case however, the rotational stiffness did not decrease so dramatically, with the cemented sand being able to withstand larger bending moments. This difference in response seems to be related to the fact that the upslope piles were under tension forces, and therefore the cemented sand around them was being unloaded in the vertical direction.

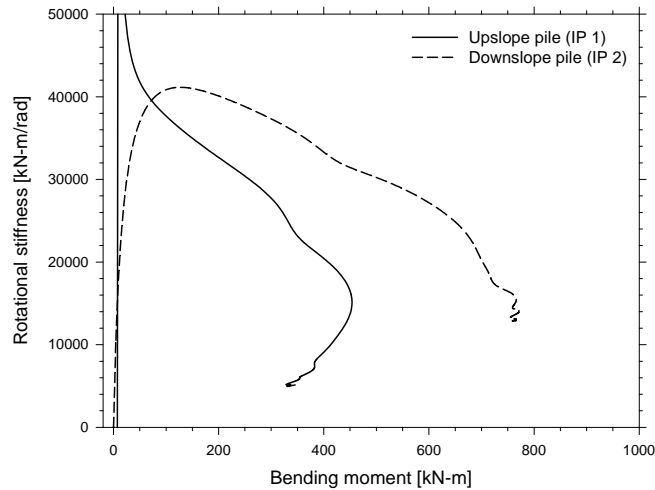


Figure 7.23: Back-calculated rotational stiffness provided by the bottom cemented layer versus bending moment at the base of the liquefiable layer, Model p-3x2

Since LVDTs L7 and L8 were located 2 cm above the ground surface, the correct pile cap lateral displacement was obtained by subtracting the increment in displacement above the pile cap from the LVDT measurements. Figure 7.24 compares the lateral displacement of the pile cap and top cemented layer during shaking. In the firsts 10 sec the displacement of the pile cap and top cemented layer, without considering the cyclic component, was practically the same. As the excitation continued, a gap started developing on the downslope side of the pile group.

Finally, the lateral displacement profiles of the piles were obtained considering the deformation by curvature and rotation. Figure 7.25 shows the lateral displacement profiles of the upslope pile IP1 and the soil at different times. Since the piles were connected by a cap and most of the displacement was due to the rotation at the base, these profiles are considered representative of the pile group lateral displacement. Given the fact that the top cemented layer moved as a rigid block, the pile group tried to break the soil around it as soon as it started rotating at the beginning of shaking ($t = 1$ sec). Near the ground surface, the pile cap slightly snapped the cemented sand in the downslope direction. At deeper elevations within the top layer, the pile group offered such a great resistance that it ended up inducing a passive failure in the upslope direction, as shown in the following sections. As this failure progressed, the top cemented layer far from the pile group displaced more than the pile cap did, inducing gaps on the downslope side of the cap.

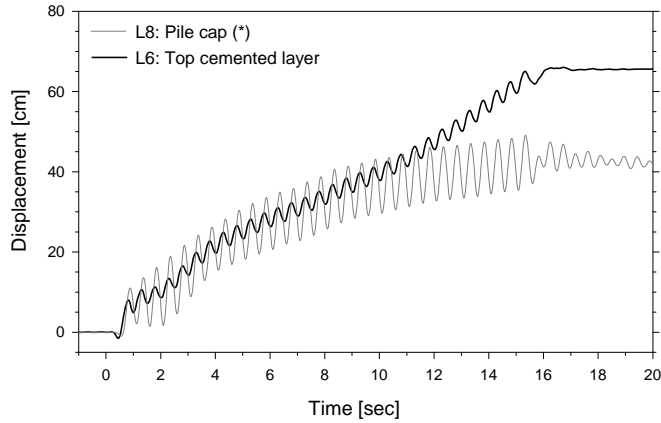


Figure 7.24: Lateral displacement time histories of the pile cap and top cemented layer, (*) after subtracting the increment in displacement above the pile cap, Model p-3x2

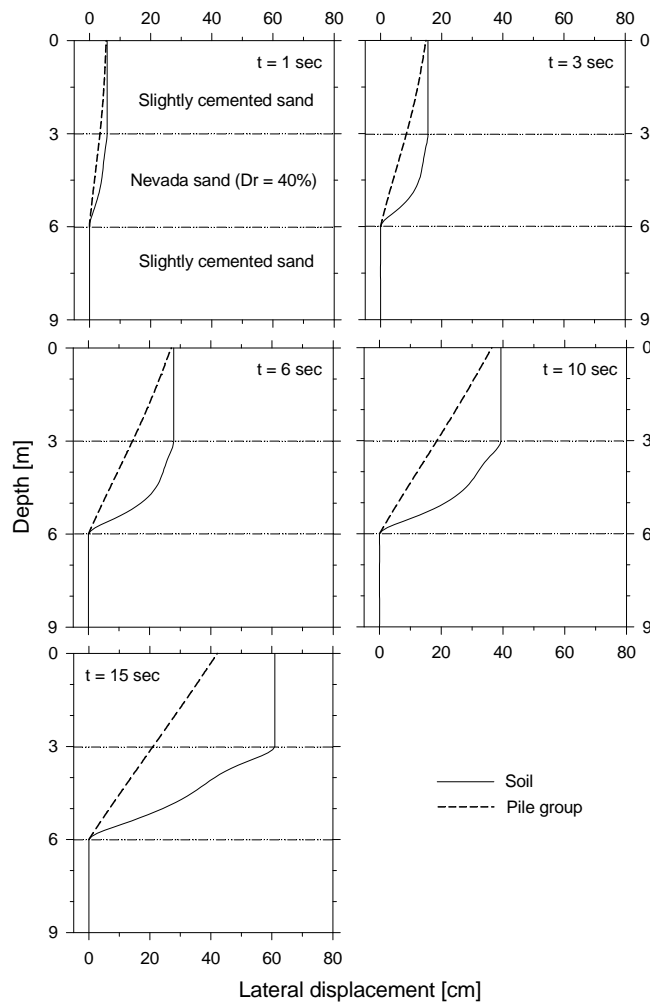
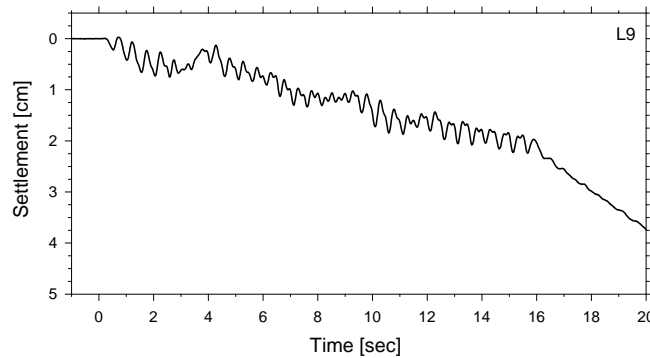
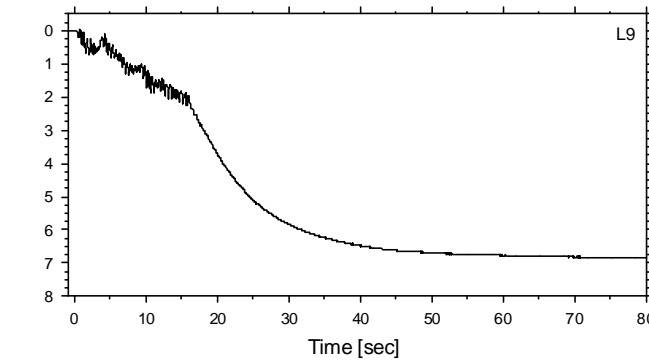


Figure 7.25: Profiles of soil and pile group lateral displacement, Model p-3x2

The ground surface settlement time history on the upslope side of the pile group is presented in Fig. 7.26. This area of the ground surface settled about 2 cm during shaking. A visual inspection after the test revealed that the transducer used to record this settlement (L9) was located just outside the passive wedge; therefore this measurement does not represent either the passive wedge vertical movement or the ground surface settlement. Once the shaking stopped, the ground surface continued settling due to the consolidation process.



(a)

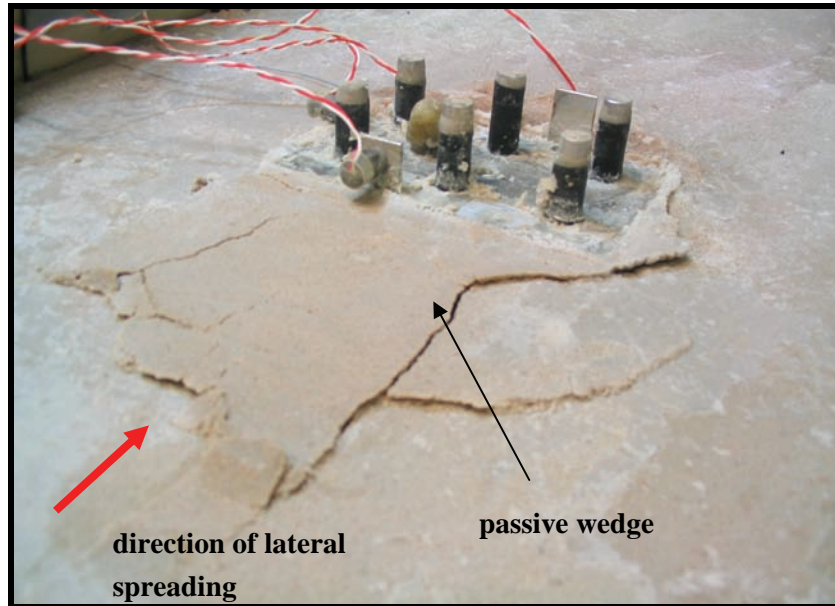


(b)

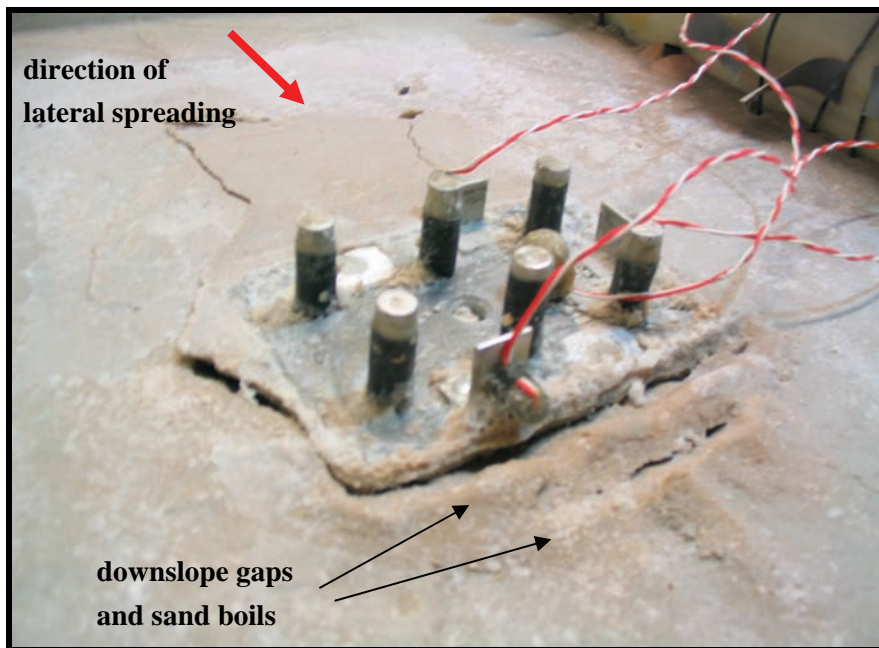
Figure 7.26: Ground surface settlement time history close to the pile group, (a) short term, (b) long term, Model p-3x2

7.4.5 Soil Condition around Pile Cap

Figure 7.27 shows pictures of the ground surface condition around the pile cap after the test. The cracks on the upslope side of the pile group confirm the development of a passive failure. As this failure progressed, two gaps developed on the downslope side of the cap; illustrated also by the sand boils along the gaps



(a)



(b)

Figure 7.27: Ground surface condition around pile cap after the test, (a) upslope, (b) downslope, Model p-3x2

7.4.6 Recorded Bending Moments

Prototype bending moment time histories were obtained from the strain gage measurements. Since bending moments can be estimated from a quarter and half bridge configuration, nine measurement histories were obtained for the upslope pile IP1 and downslope pile IP2, as shown in Figs. 7.28 and 7.29 respectively. Profiles of bending moment for both piles are presented in Fig. 7.30, after filtering out the cyclic component.

The profiles at 1 sec indicate that at the very beginning of the excitation the cemented sand around the piles was in the elastic range, with the upper and lower moments being very similar and with the point of zero moment located near the middle of the loose layer. The profiles at 3 sec show that the bending moments in the upper part kept increasing, with the maximum value taking place near the cap, suggesting that the cemented sand started failing locally around each individual pile. At about 6 sec the upper bending moments started decreasing, indicating the passive failure in the top cemented layer was developing. In the second half of the excitation the bending moments in the upper part kept decreasing, with the maximum moment taking place just below the pile cap. The fact that the upper bending moments were decreasing while the pile group was still moving downslope suggests the frame effect was disappearing. The passive failure on the top layer and the decrease of confinement on the bottom layer allowed the pile group to rotate slightly.

In the lower part, the bending moments tended to be larger than in the upper part. In the downslope pile the maximum moment was reached at about 10 sec, whereas the moments in the upslope pile were smaller and bounced back after a few seconds of shaking. At the end of shaking the bending moment in the downslope pile was 780 kN-m, while it was 350 kN-m in the upslope pile. This big difference was apparently caused by a pseudo p - Δ effect; since the compression forces in the downslope piles tend to increase even more the bending moments as the lateral displacement increases, while the tension forces on the upslope piles tend to decrease the bending moments. If the moments caused by the axial forces are subtracted, at the end of the excitation the bending moment in the upslope pile would be 630 kN-m, while in the downslope piles it would be a similar value of 715 kN-m. The fact that the bending moment in the downslope pile did not increase after 10 sec must be related with the passive failure of the top cemented layer.

At all times the bending moment on both piles varied approximately linearly with depth within the loose sand layer, indicating the pressure applied by the liquefied soil was negligible compared to the one applied by the top cemented layer.

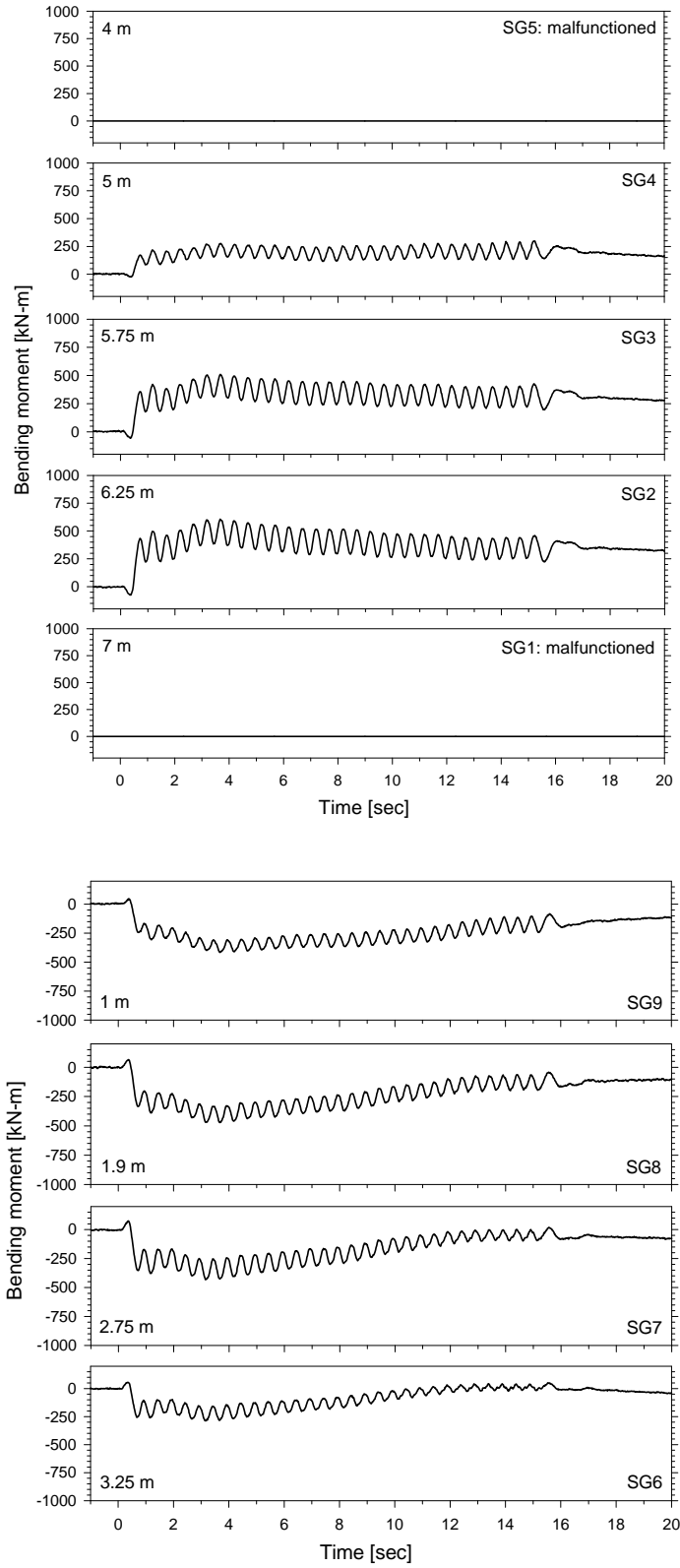


Figure 7.28: Bending moment time histories, upslope pile (IP 1), Model p-3x2

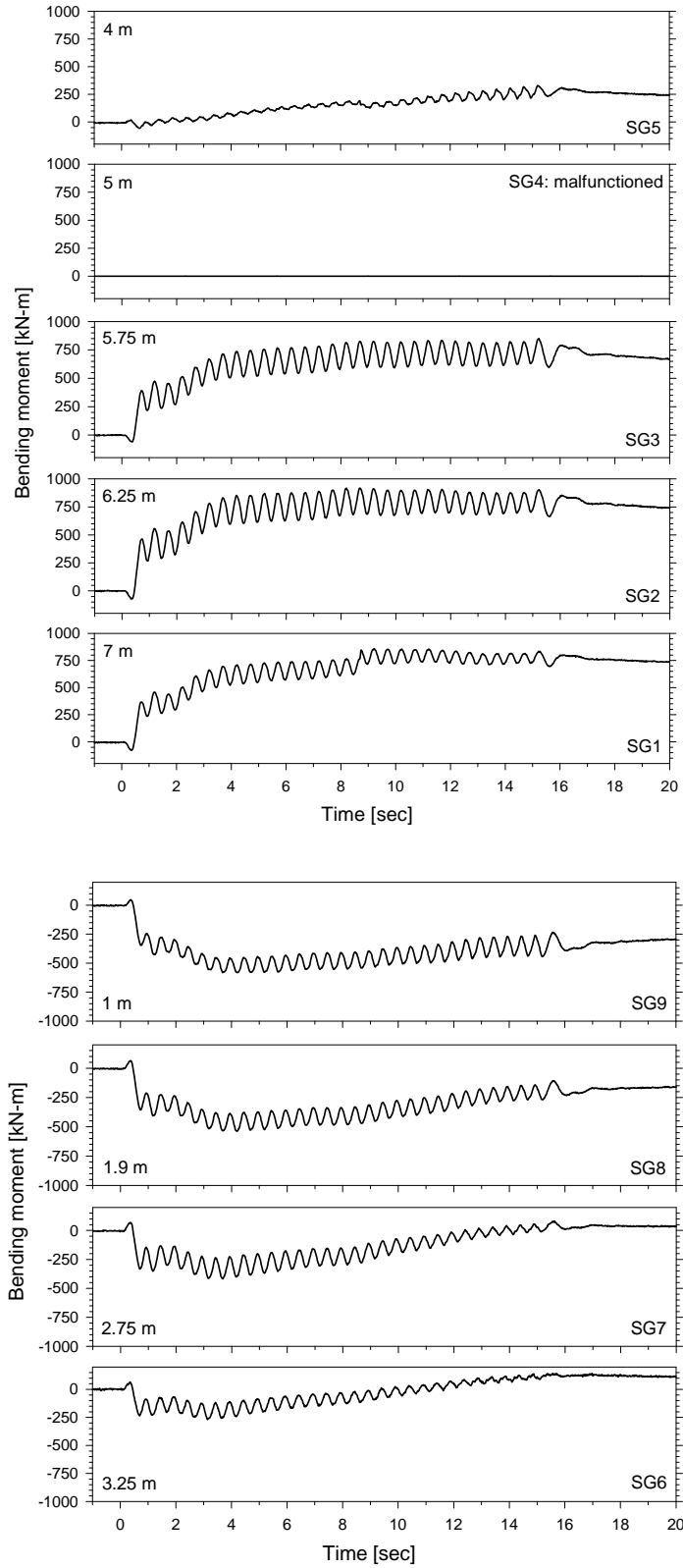


Figure 7.29: Bending moment time histories, downslope pile (IP 2), Model p-3x2

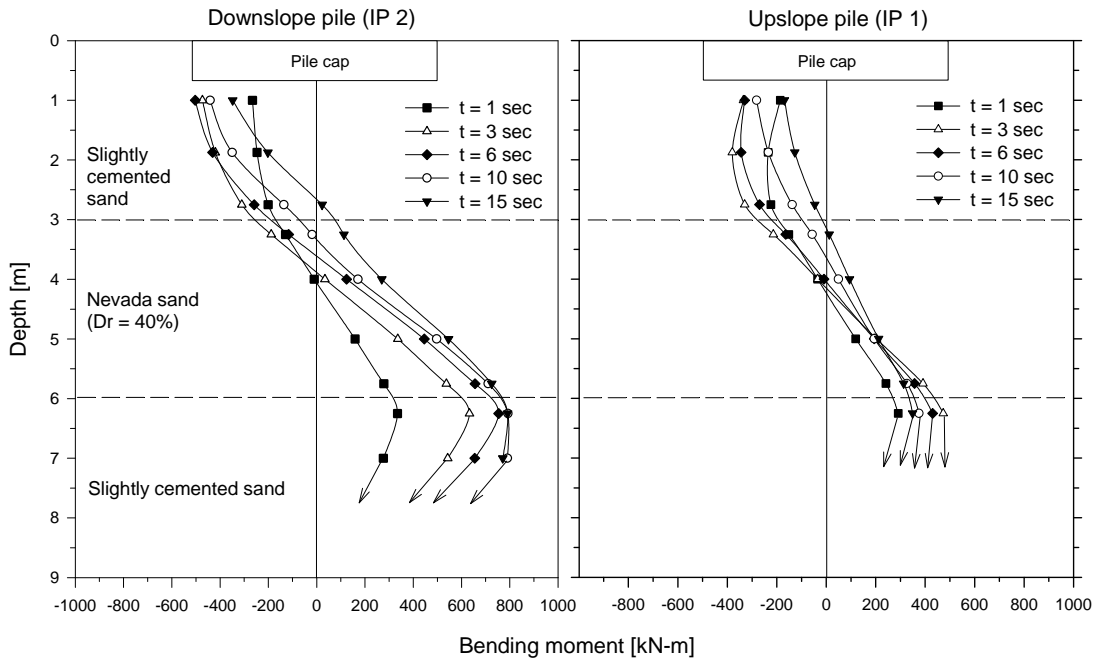


Figure 7.30: Profiles of bending moment, upslope (IP 1) and downslope (IP 2) piles, Model p-3x2

7.4.7 Recorded Axial Forces

Prototype axial force time histories were obtained with the strain gage measurements. Since axial forces can be estimated only from a quarter bridge configuration, four measurement histories were obtained for the upslope pile IP1 and downslope pile IP2, as shown in Figs. 7.31 and 7.32 respectively. Positive values represent tension while negative ones represent compression. The axial forces were zeroed at the beginning of shaking, and therefore represent the change in axial force during the excitation. Profiles of the axial force in both piles are shown in Fig. 7.33, after filtering out the cyclic component.

As expected, during shaking the upslope piles were subjected to tension forces, while the downslope piles were in compression. At the beginning of shaking the forces in compression and tension were very similar, about 500 kN. As shaking continued however, the tension force kept increasing up to about 650 kN, while the compression force decreased up to approximately 150 kN. This difference in the magnitude of the axial forces is consistent with the trend observed in the centrifuge models simulating a 2x2 pile group presented in chapter 5. It seems that the excess pore water pressure below the pile cap and the vertical movement of the passive wedge created a large vertical force in the pile group during shaking, force that is superimposed to the ones generated from the frame effect.

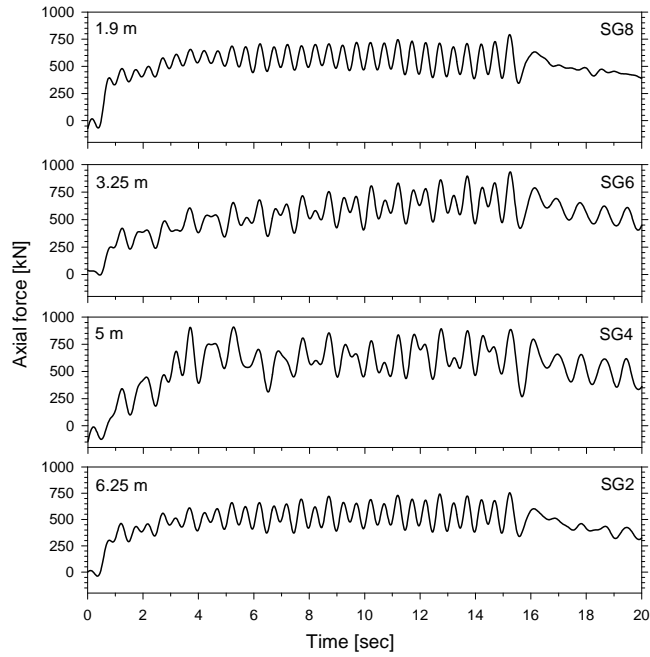


Figure 7.31: Axial force time histories, upslope pile (IP 1), Model p-3x2

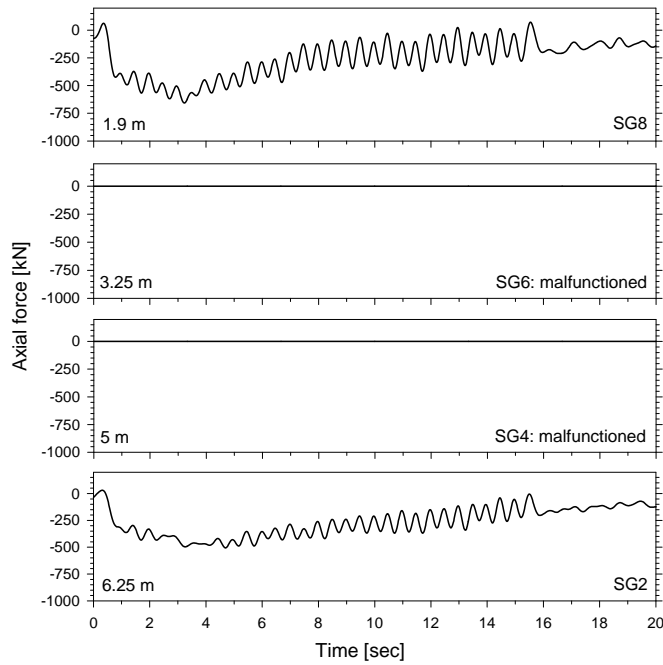


Figure 7.32: Axial force time histories, downslope pile (IP 2), Model p-3x2

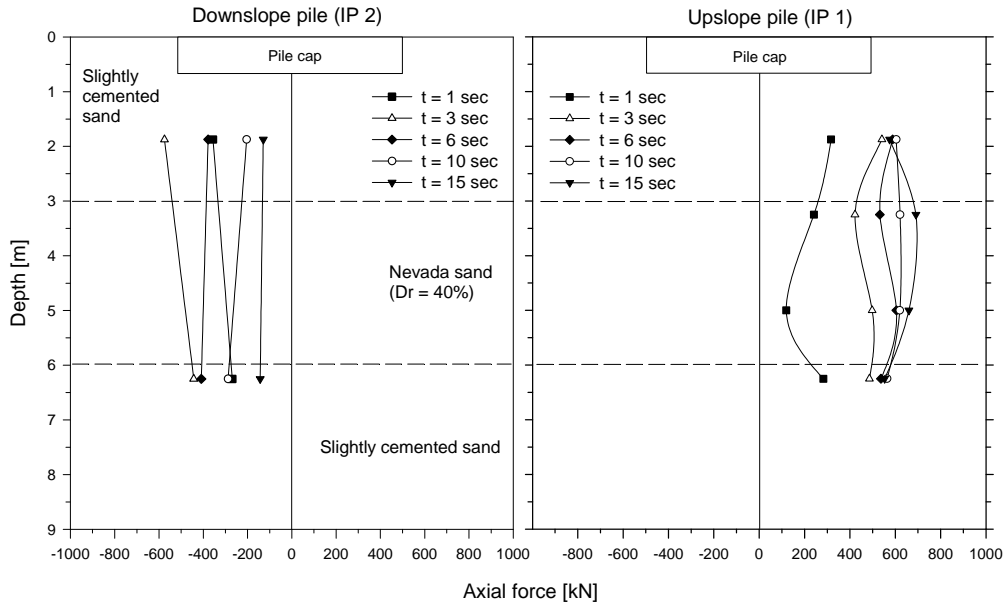


Figure 7.33: Profiles of axial force, upslope (IP 1) and downslope (IP 2) piles, Model p-3x2

7.4.8 Lateral Force against Piles

In order to further investigate the soil-pile-group interaction during lateral spreading, back-calculated lateral resistance (p) on the upslope pile IP1 and downslope pile IP2 were obtained from the bending moment distributions $M(z)$, using the simple beam theory according to the equation:

$$p = \frac{\partial^2}{\partial z^2} M(z) + P \frac{\partial^2 x}{\partial z^2} \quad [7.3]$$

where z is the depth measured from the ground surface, x is the pile deformation, and P is the axial load. Even though the axial forces were relatively large and the pile group displacement was large as well, the deformation of the piles was mainly caused by the rotation at the base. Hence, the second derivative of the deformation with respect to height was very small and the second term in equation 7.3 was negligible and was not used in the analyses. The discrete measurements of bending moments along the pile were interpolated using a cubic spline interpolation technique. A cubic spline is perhaps the simplest interpolation of discrete values that can be double differentiated (Wilson, 1998); however since the spline fits every point exactly, the interpolation is affected by the dynamic component upon differentiation. Therefore, the cyclic component of the bending moment records was filtered out before obtaining the bending moment distributions. Figure 7.34 shows profiles of the back-calculated lateral resistance against piles IP1 and IP2. As expected, the lateral resistance of the liquefied sand was very small compared to the one of the top cemented layer.

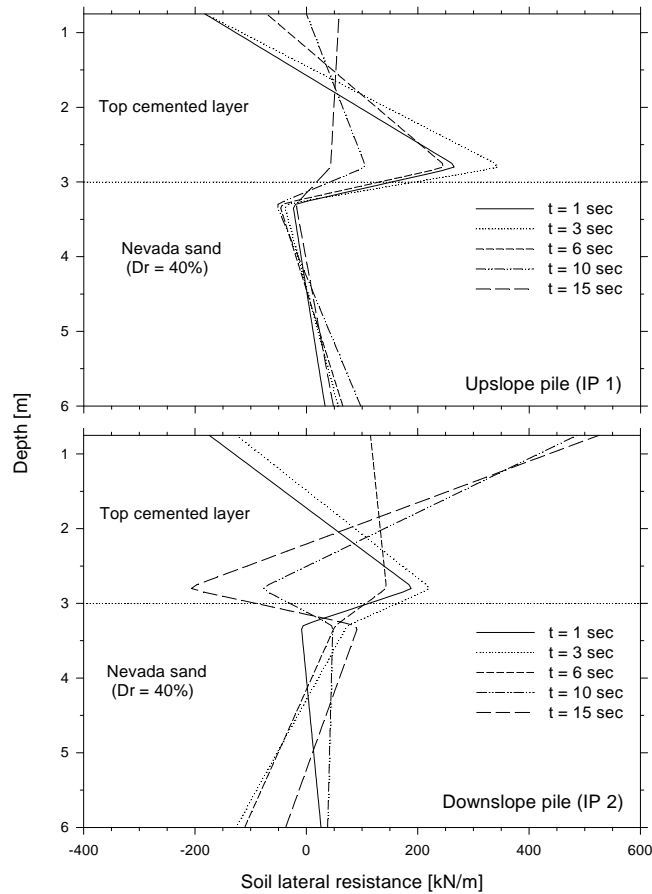


Figure 7.34: Profiles of back-calculated soil lateral resistance, Model p-3x2

The lateral resistance corresponding to the elastic range ($t = 1$ sec) was very similar in both piles. The soil resistance varied linearly from approximately 200 kN/m at the bottom of the top layer to -200 kN/m below the cap. These positive and negative values correspond to the resistance of the cemented sand to the pile rotation. The reduction in resistance near the ground surface must be related to the gap developed on the downslope side of the cap. As the passive failure developed, the lateral resistance of the cemented sand decreased.

The force time history applied by the top cemented layer was obtained by integrating the lateral resistance along the top cemented layer for each time instant. Figure 7.35 shows the back-calculated lateral force time histories against the piles. Assuming the force applied to each upslope and downslope pile is the same, the lateral force against the pile group was estimated as the sum of the forces against IP1 and IP2, multiplied by 3. Figure 7.35 shows that the pile-group-soil system was in the linear elastic range during the first second of shaking. Then, the force kept increasing with a smaller lateral stiffness, reaching 1600 kN at about 4 sec. At that time the cemented sand started to yield and the force decreased gradually up to 800 kN at the end of

shaking. The downslope piles were subjected to larger forces than the upslope piles during most of the excitation.

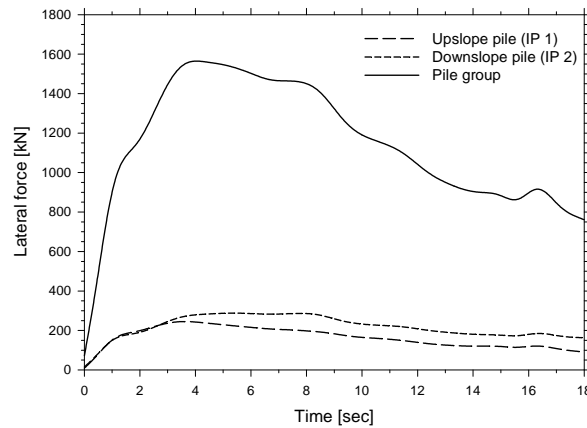


Figure 7.35: Back-calculated lateral force time histories against the piles, Model p-3x2

7.5 Model p-6x2

7.5.1 Model Description

The setup and instrumentation used in Model p-6x2 are presented in Fig. 7.36. This model simulates a 6x2 pile group connected with a pile cap perpendicular to the direction of lateral spreading. The prototype profile consists of a 3 m thick Nevada sand layer placed at a relative density of about 40%, on top and below a 3 m thick nonliquefiable slightly cemented layer. The model is inclined 2° to the horizontal and saturated with de-ionized/de-aired water. At a centrifugal acceleration of 50g the loose Nevada sand simulates a coarse sand layer, and the inclination becomes 4.8° (Taboada, 1995).

The embedded piles have a prototype diameter of 55 cm and a bending stiffness (EI) of approximately $78000 \text{ kN}\cdot\text{m}^2$. The aluminum cap, embedded in the top cemented sand layer, has prototype dimensions of 3.3 m in width, 9.9 m in length, and 0.64 m in height. Figure 7.37 displays a picture and schematic of the pile-cap-structure, showing the spacing between piles (3d), as well as the aluminum block used to compact the cemented sand around the piles. Figure 7.38 shows a picture of the model during preparation, with the dashed line representing the pile cap. Lines of colored sand were placed at intermediate depths within the liquefiable layer (Fig. 7.39) to observe the pattern of soil deformation around the piles. Thin layers of colored cemented sand were placed as well at different elevations within the top cemented layer to observe the soil condition after the test.

The model was excited by 30 cycles of a 100 Hz sinusoidal acceleration with uniform amplitude of about 12g. At a centrifugal acceleration of 50g this corresponds to a frequency of 2 Hz and peak acceleration of 0.24g.

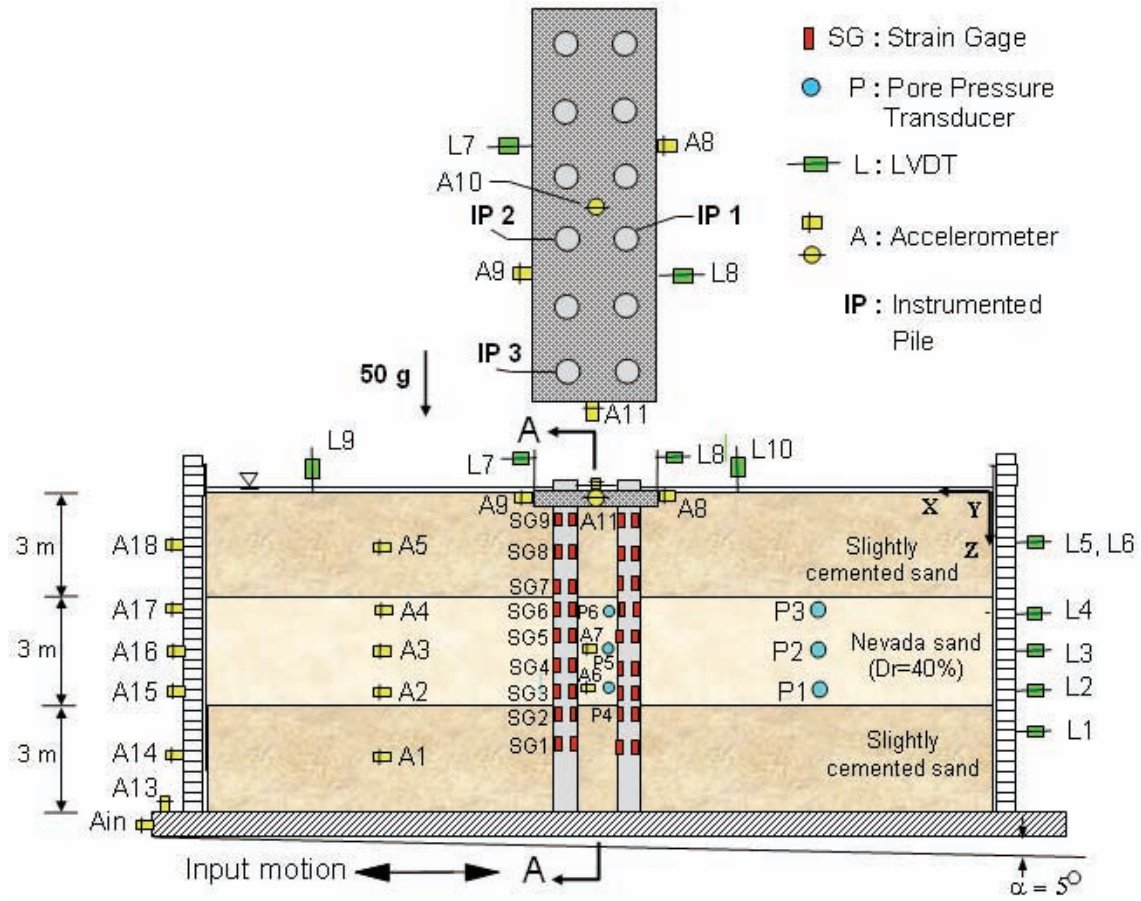
The instrumentation used in Model p-6x2 is shown in Fig. 7.36 and listed in Table 7.4. The model was instrumented with 18 accelerometers, 6 pore pressure transducers, and 10 LVDTs. Three instrumented piles (IP1, IP2, and IP3) were used in the pile group foundation, as shown in Fig. 7.36a. Detailed information about the strain gage configuration and the aluminum piles (type A) used in this model is presented in section 2.7. Accelerations in the soil and outside the laminar box, excess pore water pressure, lateral displacement of the soil and the pile cap, ground surface settlement, bending moments, and axial forces were measured during the test.

7.5.2 Recorded Accelerations

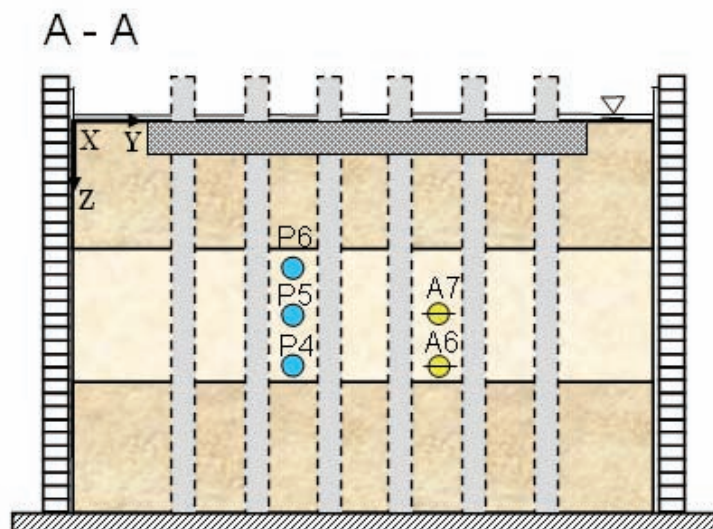
Figure 7.40 shows the recorded input acceleration and soil acceleration time histories far from the pile group at different depths. Acceleration amplitudes in the loose sand layer dropped significantly after the first cycle of shaking due to liquefaction. Since the amount of lateral spreading in this model was significantly reduced by the pile group, as shown in the following sections, the negative spikes were not as large as in the other centrifuge tests. At the bottom of the loose layer the acceleration increased during shaking, probably due to the boundary effect of the bottom layer. The recorded acceleration in the top cemented layer (A5) shows a substantial drop in amplitude after the first cycle of shaking, evidencing a sort of isolation of this layer once the loose layer liquefied, despite the fact the pile group was embedded in this layer. The acceleration record of the bottom cemented layer (A1) is very similar to the input acceleration; the small spikes in each cycle must have been caused by a very small vibration of this layer.

The soil acceleration time histories between piles at two different depths are presented in Fig. 7.41. At 4.5 m the record is very similar to the one in the soil far from the pile group at the same depth, indicating the soil did liquefy in the pile group area. Close to the bottom layer, the acceleration record shows the same type of amplification observed at a certain distance from the foundation.

Figure 7.42 presents the acceleration time histories on the pile cap, as well as the measured horizontal and vertical acceleration at the base of the box. In this case the vertical acceleration of the cap was much smaller than the vertical acceleration at the base. The acceleration perpendicular to the direction of lateral spreading consists of small spikes generated by the pile group vibration during shaking. On the other hand, one of the acceleration records in the direction of lateral spreading contains high frequency spikes generated by the interaction between the cap and the top cemented layer. Laminar ring accelerations recorded at various elevations are presented in Fig. 7.43. These acceleration records are in reasonable agreement with those measured in the soil in Fig. 7.40.

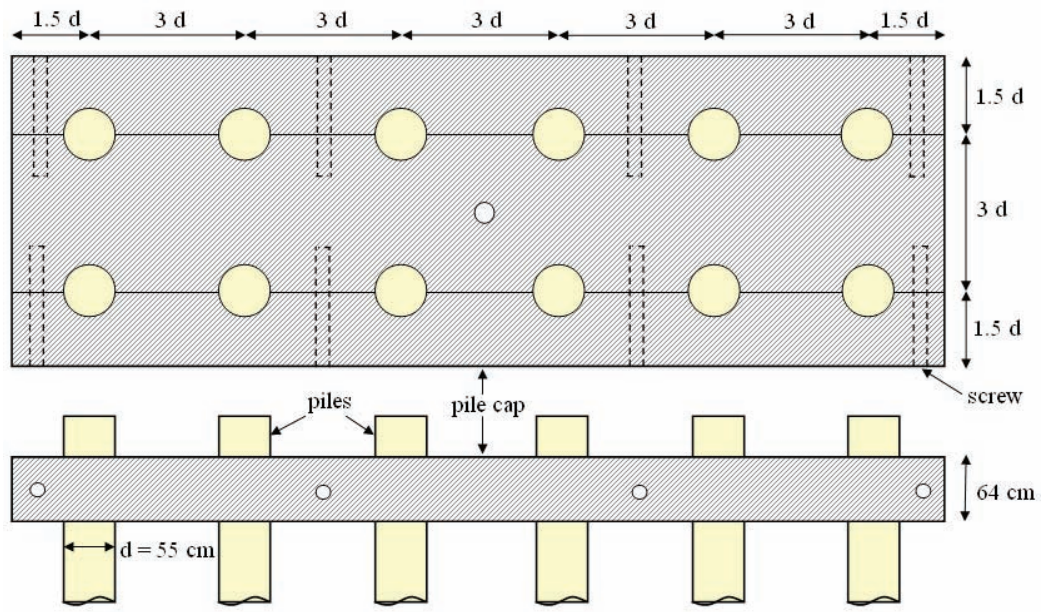


(a)



(b)

Figure 7.36: (a) Setup and instrumentation used in Model p-6x2, (in prototype units);
 (b) Transversal section of Model p-6x2



(a)



(b)

Figure 7.37: Pile-cap-structure, (a) schematic, (b) picture, Model p-6x2

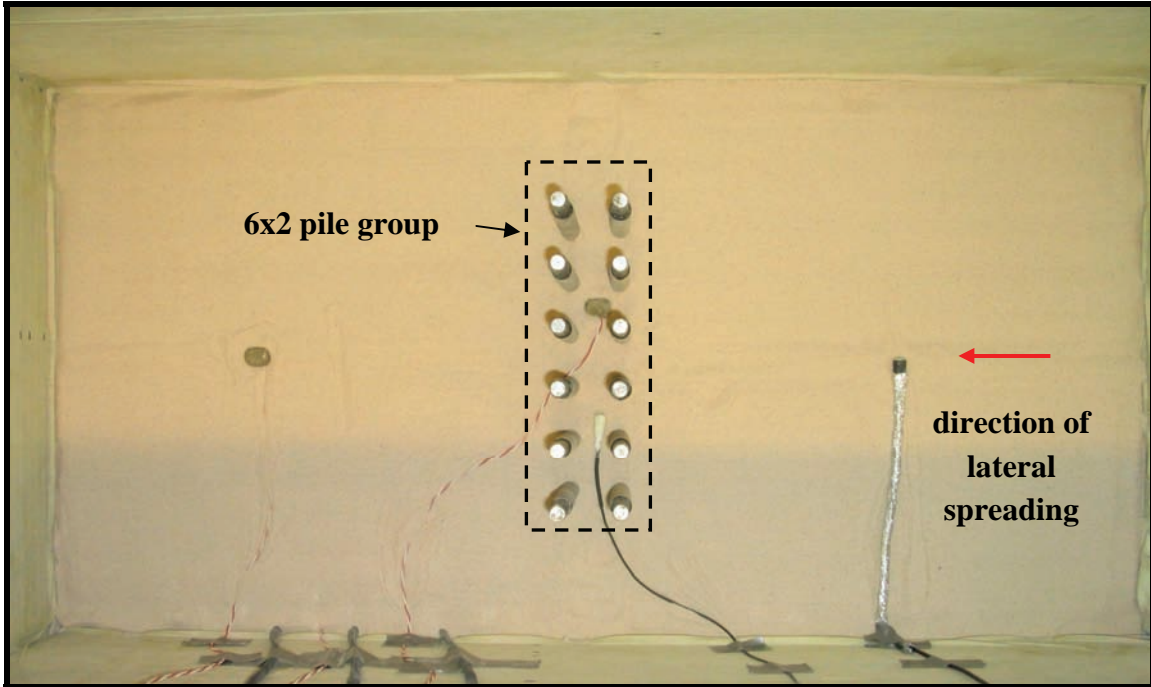


Figure 7.38: Model during preparation, the dashed line represents the pile cap, Model p-6x2

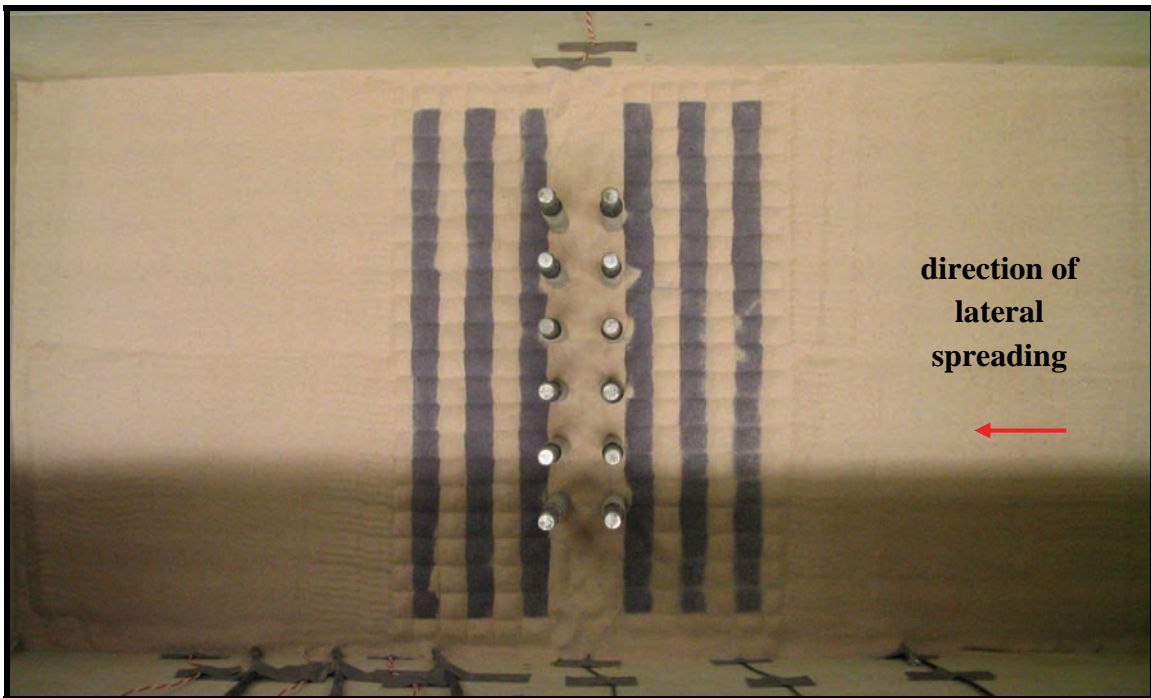


Figure 7.39: Colored sand placed at an intermediate depth, Model p-6x2

Table 7.4: Location of instruments in Model p-6x2 (in model units)

Transducer	Sensor name	Coordinates [cm]		
		X	Y	Z
Accelerometer	Ain	73.5	17.75	18.5
	A1	55	17.75	15
	A2	55	17.75	11
	A3	55	17.75	9
	A4	55	17.75	7
	A5	55	17.75	3
	A6	35.5	21	11
	A7	35.5	21	9
	A8	32.5	21	0.63
	A9	39	14.5	0.63
	A10	35.5	17.75	0
	A11	35.5	8	0.63
	A13	72.5	17.75	18
	A14	71	17.75	15
	A15	71	17.75	11
	A16	71	17.75	9
	A17	71	17.75	7
	A18	71	17.75	3
Pore pressure transducer	P1	17	17.75	11
	P2	17	17.75	9
	P3	17	17.75	7
	P4	35.5	14.5	11
	P5	35.5	14.5	9
	P6	35.5	14.5	7
LVDT	L1	0	24	14
	L2	0	12	11
	L3	0	24	9.1
	L4	0	12	7.2
	L5	0	24	3
	L6	0	12	3
	L7	39	21	-2
	L8	32.5	14.5	-2
	L9	63	8	0
	L10	26	24	0

Table 7.4 (cont.): Location of instruments in Model p-6x2 (in model units)

Transducer	Sensor name	Coordinates [cm]			
		X	Y	Z	
Strain gage		IP 1	IP 1	IP 1	
	SG1	34.25	16	14	
	SG2	34.25	16	12.5	
	SG3	34.25	16	11.5	
	SG4	34.25	16	10	
	SG5	34.25	16	8	
	SG6	34.25	16	6.5	
	SG7	34.25	16	5.5	
	SG8	34.25	16	3.75	
	SG9	34.25	16	2	
			IP 2	IP 2	IP 2
	SG1	37.25	16	14	
	SG2	37.25	16	12.5	
	SG3	37.25	16	11.5	
	SG4	37.25	16	10	
	SG5	37.25	16	8	
	SG6	37.25	16	6.5	
	SG7	37.25	16	5.5	
	SG8	37.25	16	3.75	
	SG9	37.25	16	2	
			IP 3	IP 3	IP 3
	SG1	37.25	9.75	14	
	SG2	37.25	9.75	12.5	
	SG3	37.25	9.75	11.5	
	SG4	37.25	9.75	10	
	SG5	37.25	9.75	8	
	SG6	37.25	9.75	6.5	
SG7	37.25	9.75	5.5		
SG8	37.25	9.75	3.75		
SG9	37.25	9.75	2		

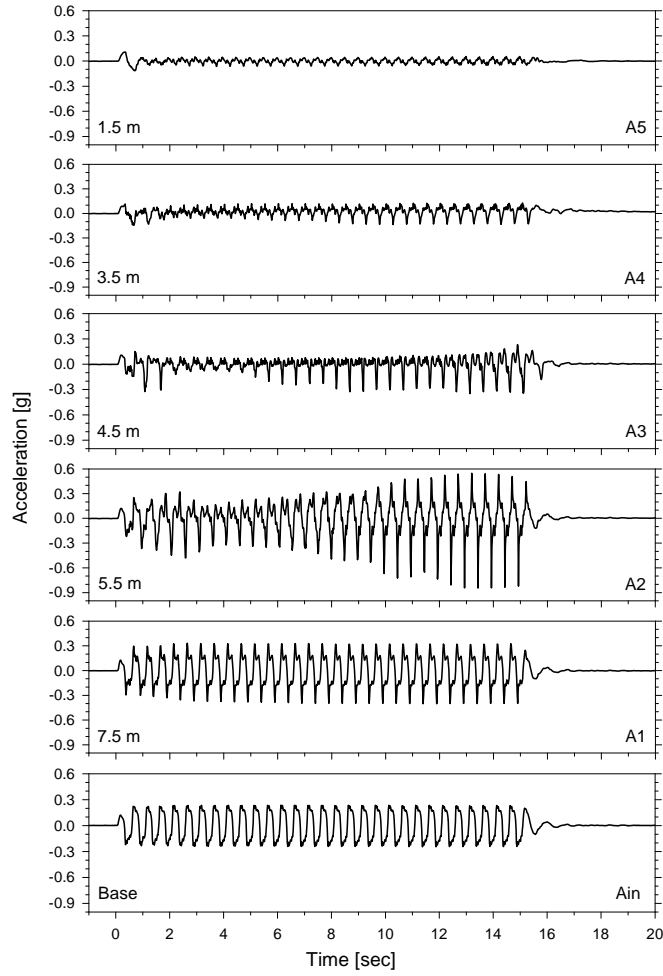


Figure 7.40: Soil acceleration time histories far from the pile group, Model p-6x2

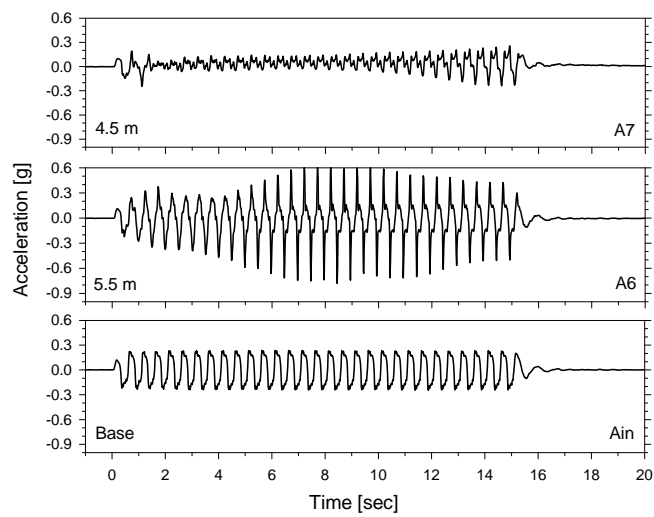


Figure 7.41: Soil acceleration time histories between piles, Model p-6x2

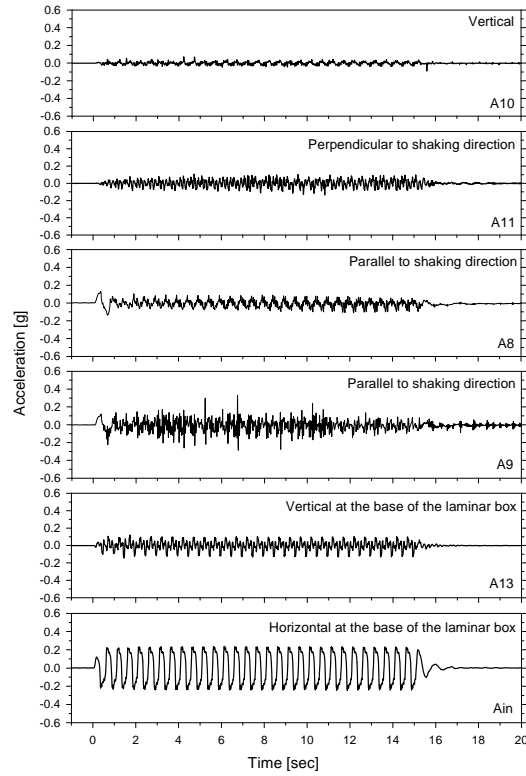


Figure 7.42: Accelerations time histories on the pile cap, Model p-6x2

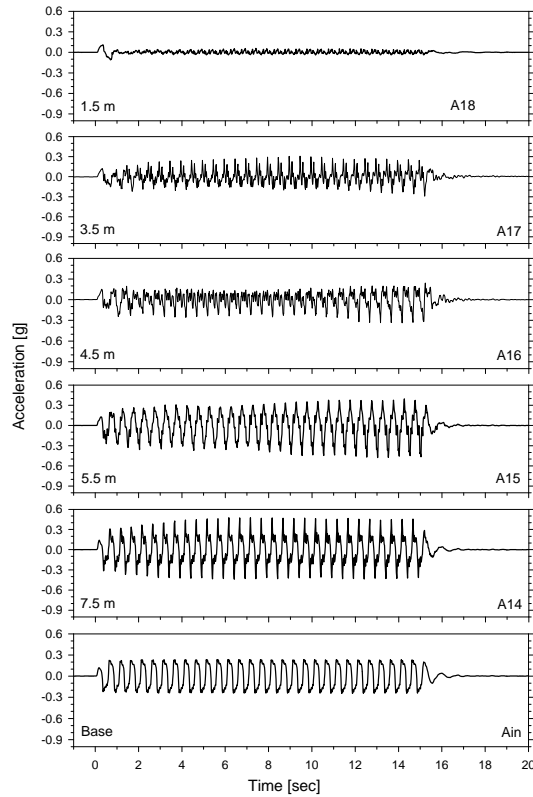


Figure 7.43: Accelerations time histories on the laminar rings, Model p-6x2

7.5.3 Recorded Excess Pore Pressures

Excess pore pressure time histories in the short and long term are presented in Figs 7.44 and 7.45 respectively. These records reveal that the loose sand layer liquefied after about two cycles of excitation. Like in the other models, vertical tubes were installed on both sides of the top layer to help dissipate the excess pore water pressures. However, the lower permeability of this layer compared to the one of Nevada sand, and the settlement process of the top cemented layer, seem to have been responsible for: a) a slight increase in excess pore pressure after the soil was liquefied, and b) a slow dissipation process during approximately the first 55 sec. Being consistent with the other centrifuge tests, the excess pore pressure in the pile group area was slightly smaller than in the free field, and the dissipation process in this area was slightly faster than in the free field.

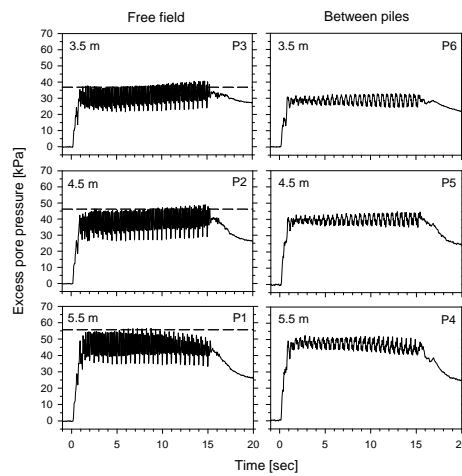


Figure 7.44: Short term excess pore pressure time histories in the free field and between piles, the dashed lines correspond to initial liquefaction, Model p-6x2

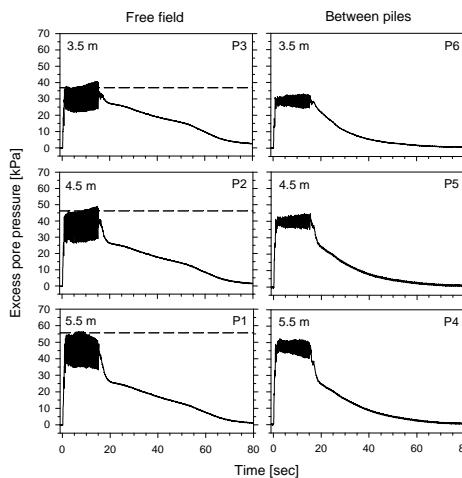


Figure 7.45: Long term excess pore pressure time histories in the free field and between piles, the dashed lines correspond to initial liquefaction, Model p-6x2

7.5.4 Recorded and Back-calculated Lateral Displacements

Figure 7.46 shows that the liquefied layer and top cemented layer displaced gradually during shaking. Once the shaking process was finished, the soil lateral displacement stopped. On the other hand, the recorded displacement of the bottom layer shows a very small vibration during shaking, being consistent with the acceleration record at that elevation.

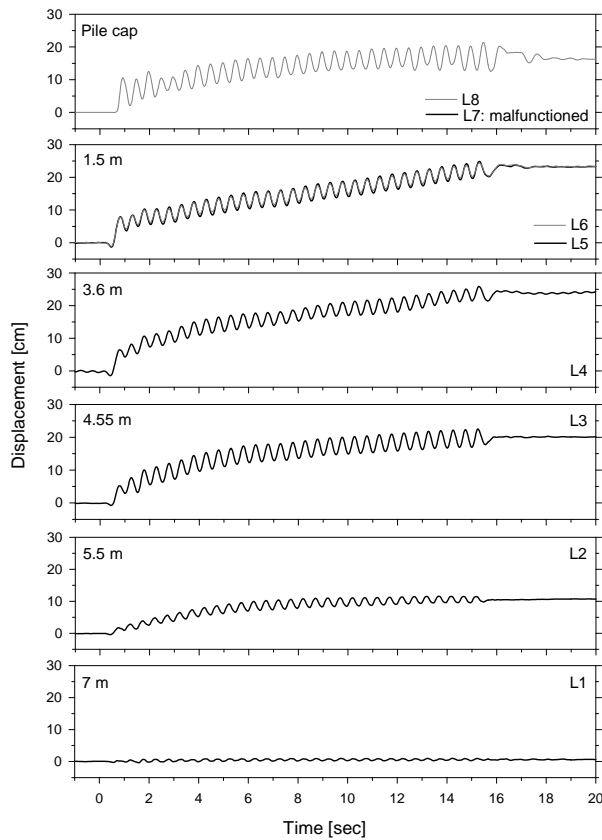


Figure 7.46: Soil and pile cap lateral displacement time histories, Model p-6x2

The profiles of soil lateral displacement were obtained by interpolating the LVDT measurements, after filtering out the cyclic component (Fig. 7.47). As soon as the loose sand liquefied at the beginning of shaking, the deposit started moving downslope, with the top cemented layer reaching a maximum displacement of approximately 23 cm at the end of shaking, compared to 135 cm of displacement in the case without piles (Model p-0). Therefore, the pile group was able to reduce the measured lateral spreading by more than 80%.

The pile displacement profiles of the upslope pile IP1 and downslope pile IP3 were back-calculated following the procedure presented in section 7.4.4. Figure 7.48 shows the back-calculated rotational stiffness provided by the bottom cemented layer around the piles IP1 and IP3 versus the corresponding bending moment at the base of the liquefiable layer.

The stiffness provided at the base of the upslope pile IP1 was approximately 35000 kN-m/rad in the elastic range. As the bending moment increased, the stiffness decreased linearly up to 23000 kN-m/rad, moment at which the cemented sand around the pile lost most of its strength. The cemented sand around the downslope pile IP2 provided a larger constraint than around the upslope pile. This trend was also observed in Model p-3x2 as discussed in section 7.4.4.

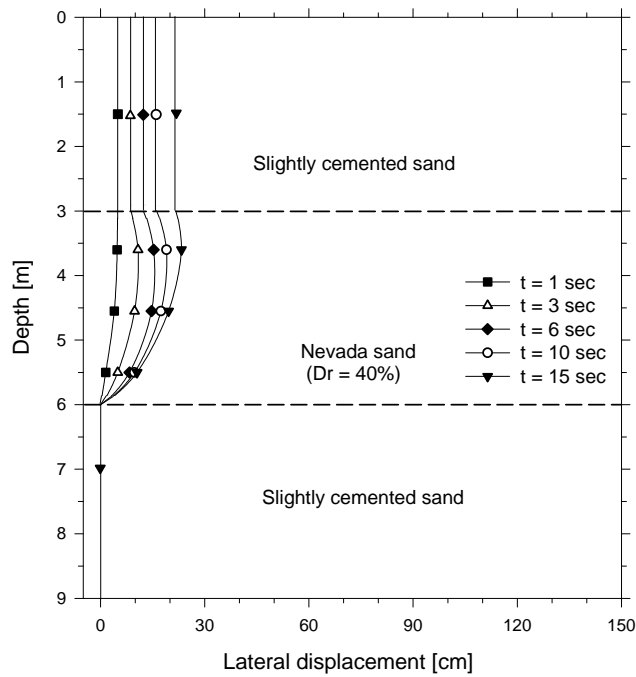


Figure 7.47: Profiles of soil lateral displacement, Model p-6x2

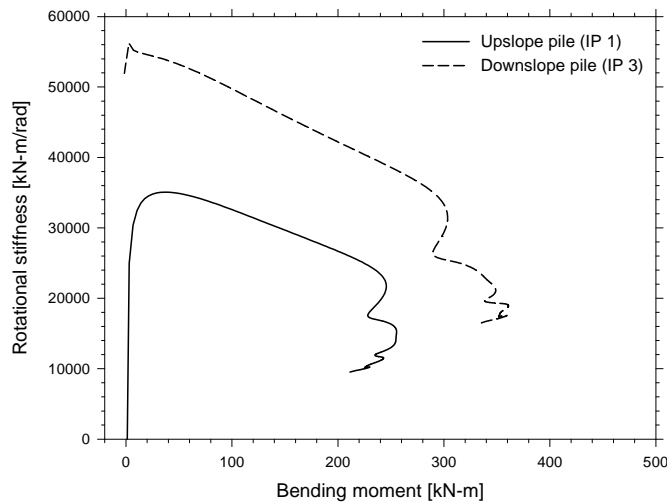


Figure 7.48: Back-calculated rotational stiffness provided by the bottom cemented layer versus bending moment at the base of the liquefiable layer, Model p-6x2

Since LVDTs L7 and L8 were located 2 cm above the ground surface, the correct pile cap lateral displacement was obtained by subtracting the increment in displacement above the pile cap from the LVDT measurements. Figure 7.49 compares the lateral displacement of the pile cap and top cemented layer during shaking. During approximately the first 8 sec the displacement of the pile cap and top cemented layer, without considering the cyclic component, were very similar. As the excitation continued, a gap started developing on the downslope side of the pile group.

Finally, the lateral displacement profiles of the piles were obtained considering the deformation by curvature and rotation. Figure 7.50 shows the lateral displacement profiles of the upslope pile IP1 and the soil at different times. Since the piles were connected by a cap and most of the displacement was due to the rotation at the base, these profiles are considered representative of the pile group lateral displacement. As soon as the shaking started, the pile group offered a great opposition against lateral spreading. This resistance induced a passive failure on the upslope side of the cap, as shown in Fig. 7.53. The relative displacement developed during shaking between the pile group and the top layer ($t = 15$ sec) is confirmed by the gaps on the downslope side of the cap, as shown in Fig. 7.52.

The ground surface settlement time histories far from the pile group and on the upslope side of the pile group (close to the pile group) are presented in Fig. 7.51. During the shaking process the top cemented layer far from the foundation settled 7 cm, mainly due to the rearrangement of particles induced by shear strain. Once the shaking stopped, the settlement was caused by the consolidation process of the liquefied layer, reaching a value of 14.5 cm. The ground surface on the upslope side of the cap settled 5 cm during the excitation. However, a visual inspection after the test revealed that the transducer used to record this settlement (L10) was located just outside the passive wedge, and therefore this measurement does not represent the passive wedge vertical movement.

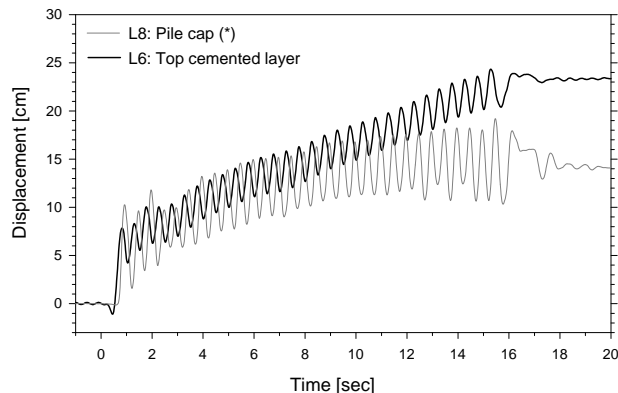


Figure 7.49: Lateral displacement time histories of the pile cap and top cemented layer, (*) after subtracting the increment in displacement above the pile cap, Model p-6x2

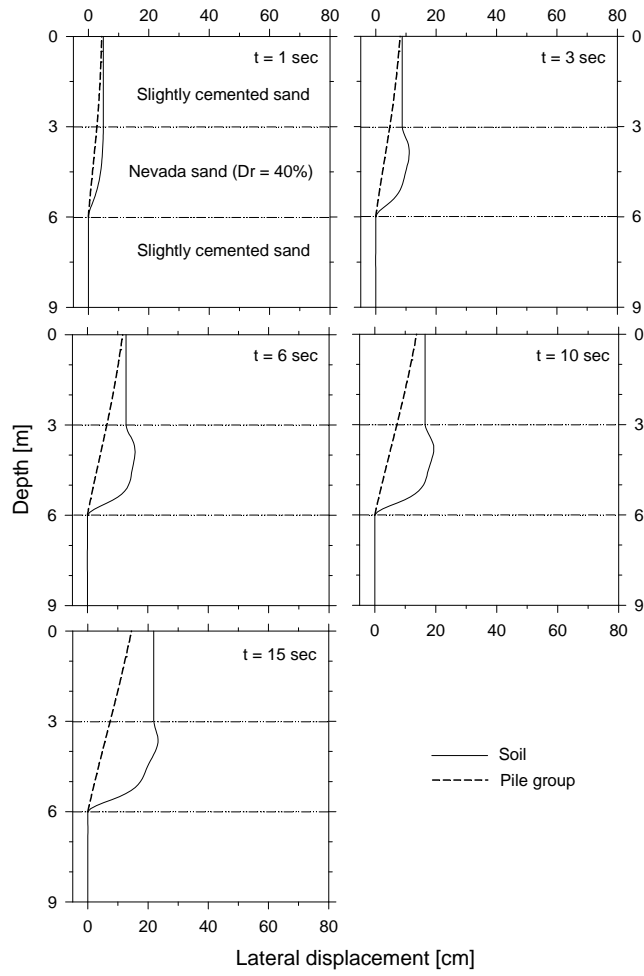
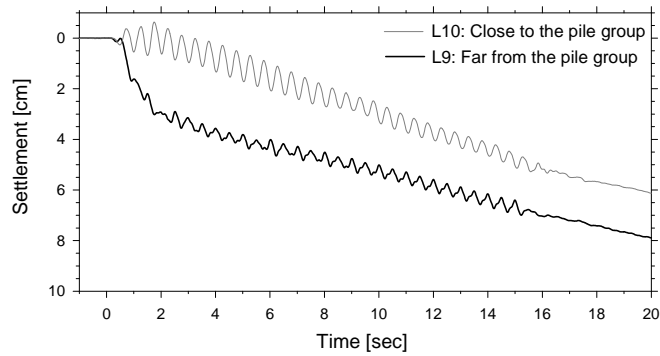
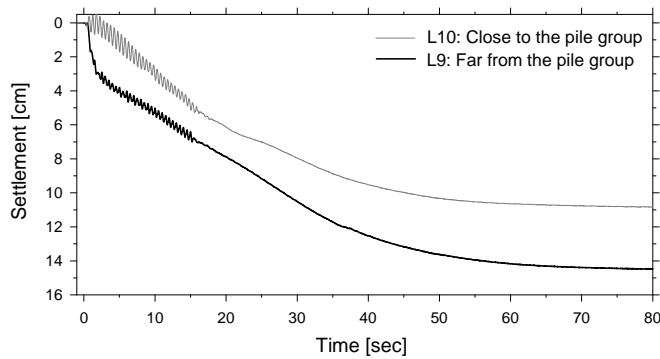


Figure 7.50: Profiles of soil and pile group lateral displacement, Model p-6x2



(a)



(b)

Figure 7.51: Ground surface settlement time histories far and close from the pile group, (a) short term, (b) long term, Model p-6x2

7.5.5 Soil Condition around Pile Cap

Figure 7.52 shows the ground surface condition around the pile cap after the test. The cracks on the upslope side of the pile group confirm the development of a passive failure. On the downslope side, two gaps developed parallel to the pile cap. Since the pile group did neither displace nor rotate much, the pile cap did not fail the soil on the downslope side.

Figure 7.53 shows a lateral view of the top cemented layer after carefully removing part of the soil. The colored cemented sand placed at different elevations clearly identifies the passive failure plane on the upslope side, which has an angle of 59° with the vertical. On the downslope side the soil does not look very disturbed and there is no clear evidence of an active type of failure.

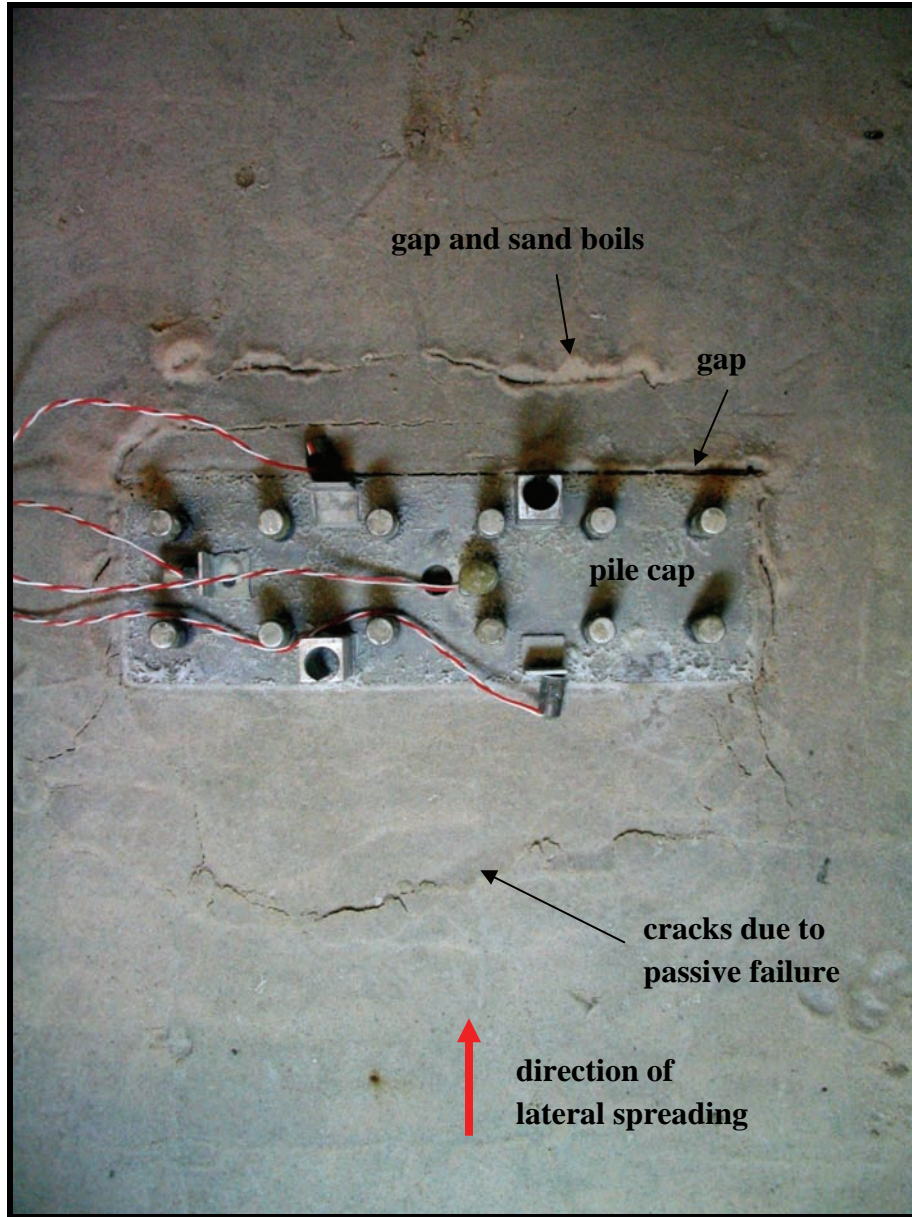


Figure 7.52: Ground surface condition around pile cap after the test, Model p-6x2

7.5.6 Pattern of Soil Displacement around Piles

Lines of colored sand were placed at intermediate depths to observe the pattern of soil displacement around the piles. Figure 7.54 shows a picture of the soil condition taken after the test, with the arrow indicating the direction of lateral spreading. The liquefied sand moved around the individual piles, affecting the soil pattern close to the piles themselves. The movement of the soil beyond this immediate neighborhood of the individual piles was very close to that far from the piles. Therefore, the characteristic width perpendicular to the flow determining the flow pattern was the diameter of the individual piles.

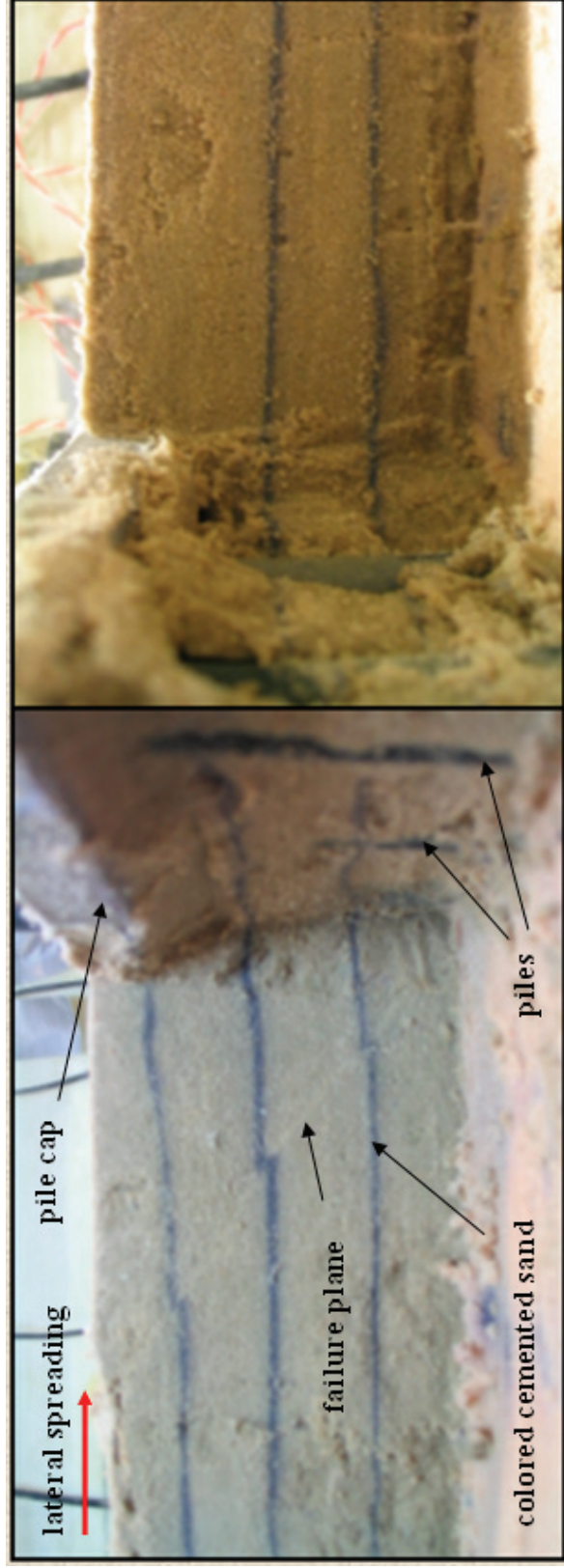


Figure 7.53: Soil condition in the top cemented layer after the test, Model p-6x2

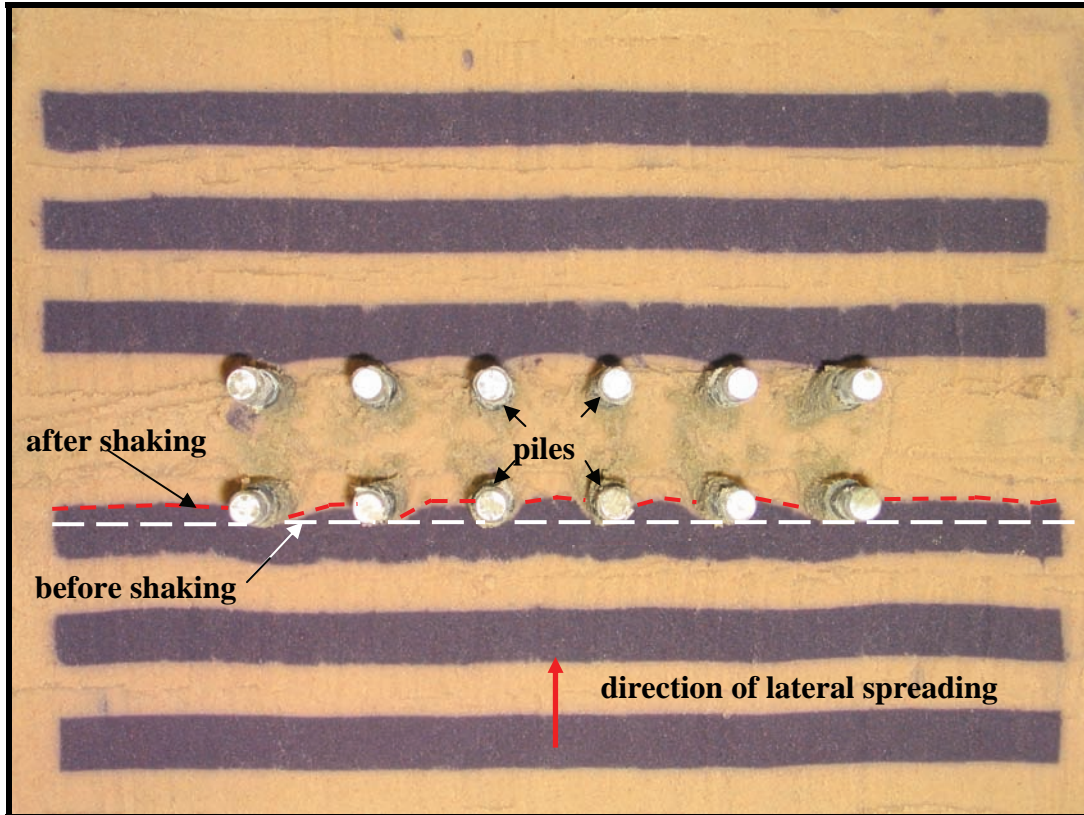


Figure 7.54: Pattern of soil displacement around pile group, Model p-6x2

7.5.7 Recorded Bending Moments

Prototype bending moment time histories measured in the upslope pile IP1 and downslope piles IP2 and IP3 are presented in Figs. 7.55, 7.56, and 7.57 respectively. Bending moment profiles for the upslope pile IP1 and downslope pile IP3 are shown in Fig. 7.58, after filtering out the cyclic component.

The profiles at 1 sec indicate that at the very beginning of the excitation the cemented sand around the piles was in the elastic range, with the upper and lower moments being very similar and the point of zero moment near the middle of the loose sand layer. The profiles at 3 sec show that the moments in the upper part kept increasing slightly, with the maximum values taking place near the middle of the top layer. This suggests that at the beginning of shaking the top cemented sand started failing locally around each individual pile. At about 6 sec the upper bending moment started decreasing, indicating that the passive failure in the top cemented layer was developing. In the second half of the excitation the bending moments in the upper part kept decreasing, with the maximum values taking place just below the pile cap.

In the lower part, the bending moments in both piles bounced back in the middle of the excitation after reaching a maximum value. The moments were larger in the downslope pile than in the

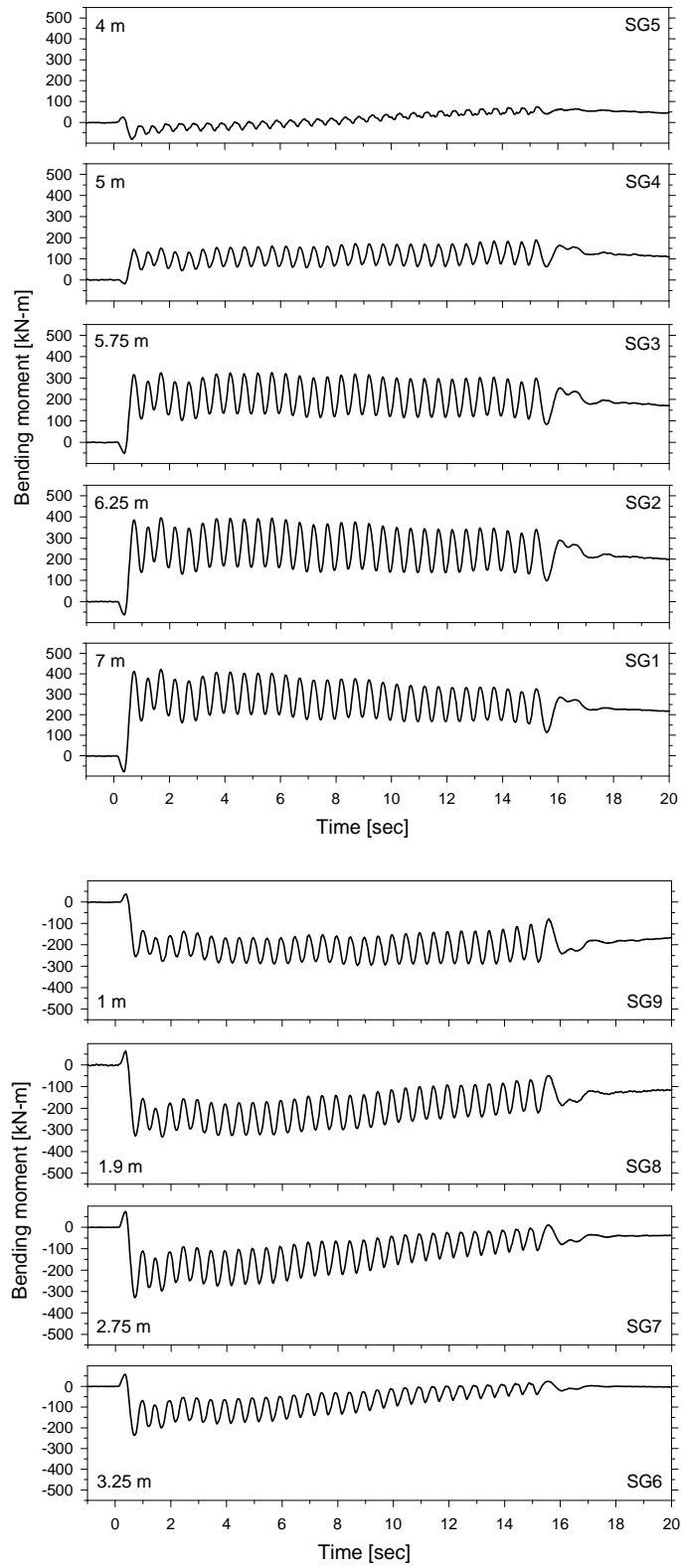


Figure 7.55: Bending moment time histories, upslope pile (IP 1), Model p-6x2

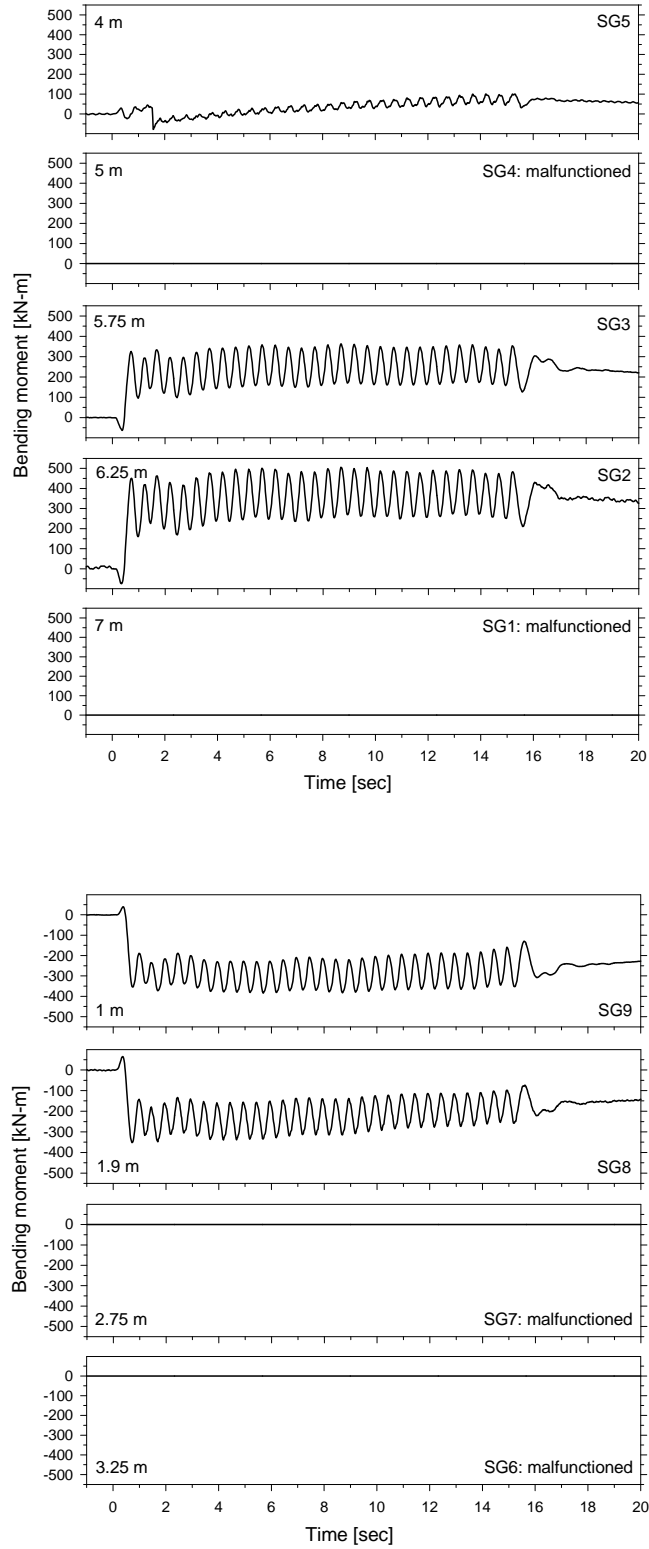


Figure 7.56: Bending moment time histories, downslope pile (IP 2), Model p-6x2

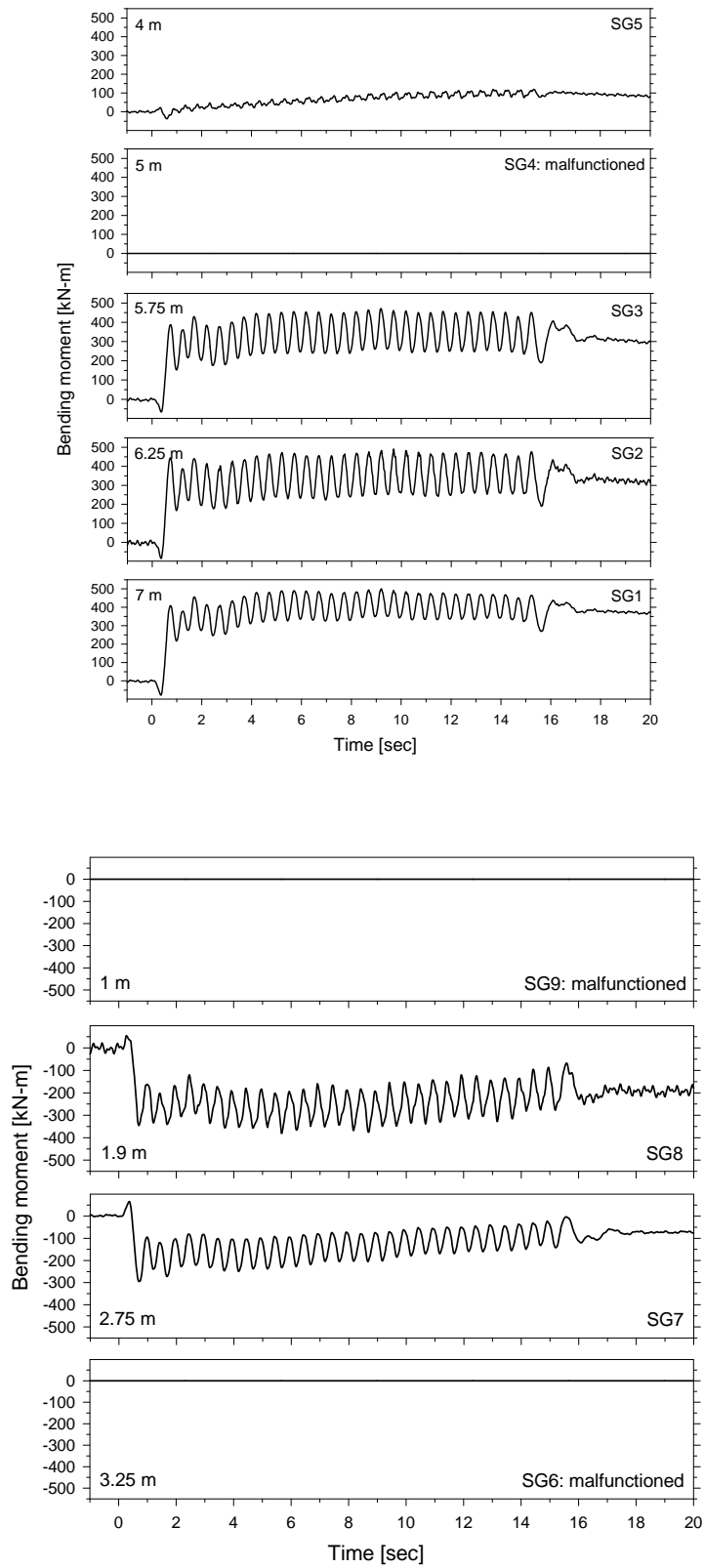


Figure 7.57: Bending moment time histories, downslope pile (IP 3), Model p-6x2

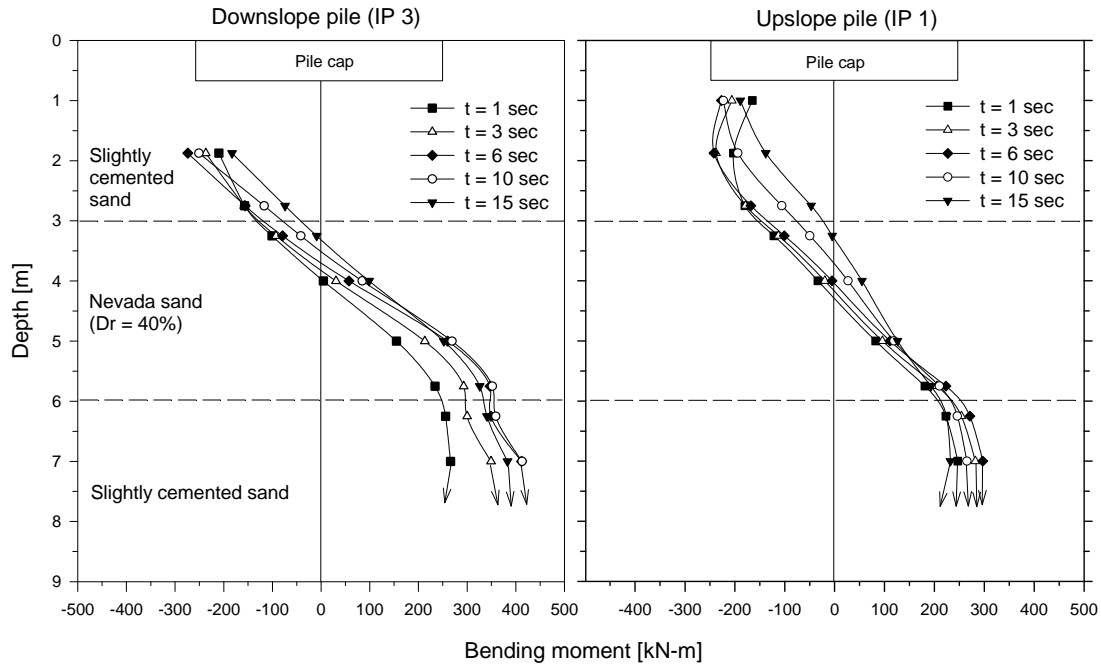


Figure 7.58: Profiles of bending moment, upslope (IP 1) and downslope (IP 3) piles, Model p-6x2

upslope pile, following the same trend observed in the 3x2 pile group. However, since the pile group lateral displacement was much smaller, the pseudo p - Δ effect was not that significant. The fact that the bending moment in the downslope pile did not increase after 10 sec must be related to the passive failure of the top cemented layer. The bending moment on both piles varied linearly with depth within the loose sand layer, indicating that the pressure applied by the liquefied soil was negligible compared to the one applied by the top cemented layer.

7.5.8 Recorded Axial Forces

Figure 7.59 shows prototype axial force time histories obtained for the upslope pile IP1. The axial force was zeroed at the beginning of shaking, and therefore represents the change in axial force during the excitation. Profiles of axial force are shown in Fig. 7.60, after filtering out the cyclic component. As expected the upslope pile was in tension during the excitation. Without considering the values measured at 5 m depth, the axial force was in very good agreement with the one measured in the upslope pile in Model p-3x2.

7.5.9 Lateral Force against Piles

The back-calculated lateral resistance was obtained following the same procedure described in section 7.4.8. In this case the pile group displacement was smaller than in Model p-3x2, and the effect of the axial load on the lateral resistance was also negligible.

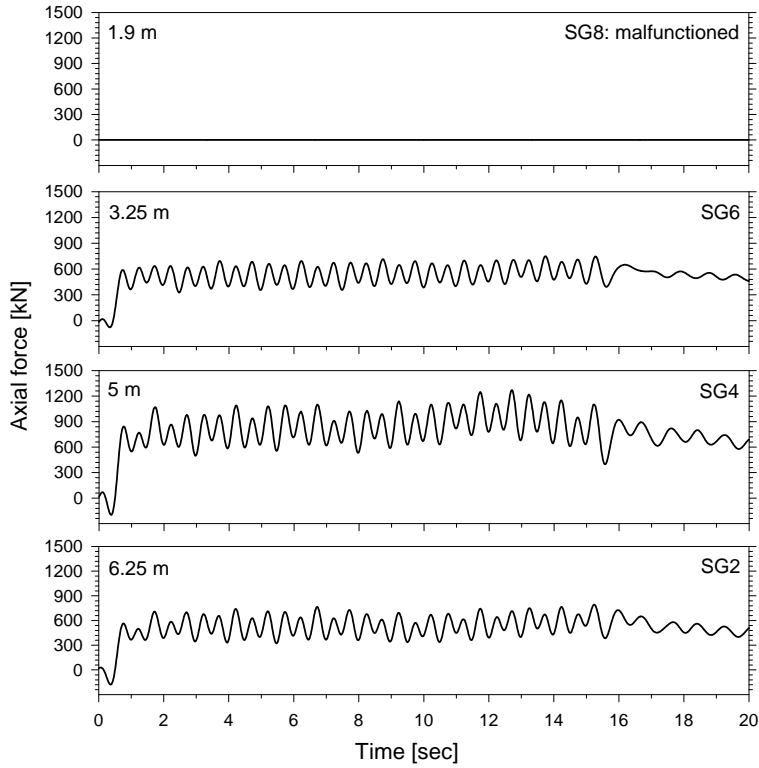


Figure 7.59: Axial force time histories, upslope pile (IP 1), Model p-6x2

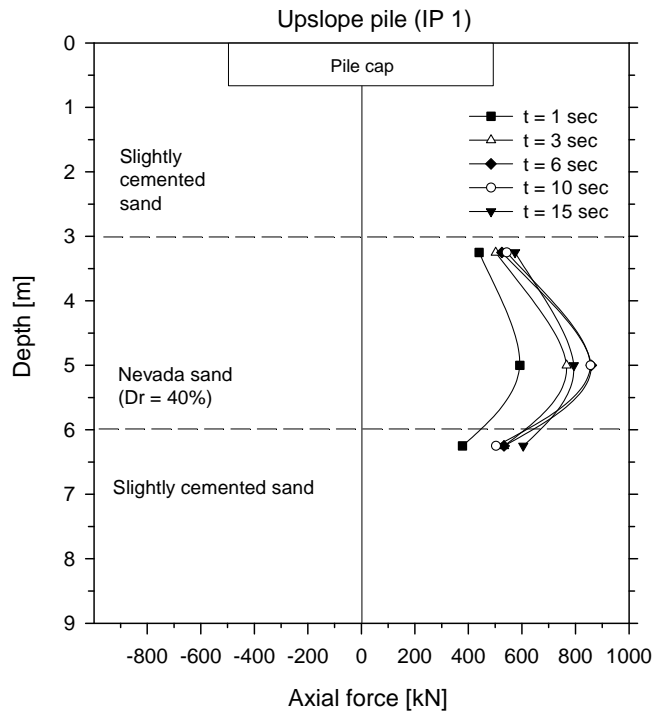


Figure 7.60: Profiles of axial force, upslope pile (IP 1), Model p-6x2

Figure 7.61 shows the profiles of soil lateral resistance against the upslope pile IP1 and downslope pile IP3. As expected, the lateral resistance of the liquefied sand was very small compared to the one of the top cemented layer. At the beginning of shaking the lateral resistance was about 100 kN/m at the bottom of the top layer and slightly negative below the pile cap. These smaller values for the elastic range, compared to the ones obtained in Models p-3x2 and p-3x1, seem to be related with the fact the 6x2 pile group did not displaced and rotated much. As the passive failure progressed, the lateral resistance at the lower part decreased. At shallower elevations the lateral resistance at the end of shaking was about 150 kN/m.

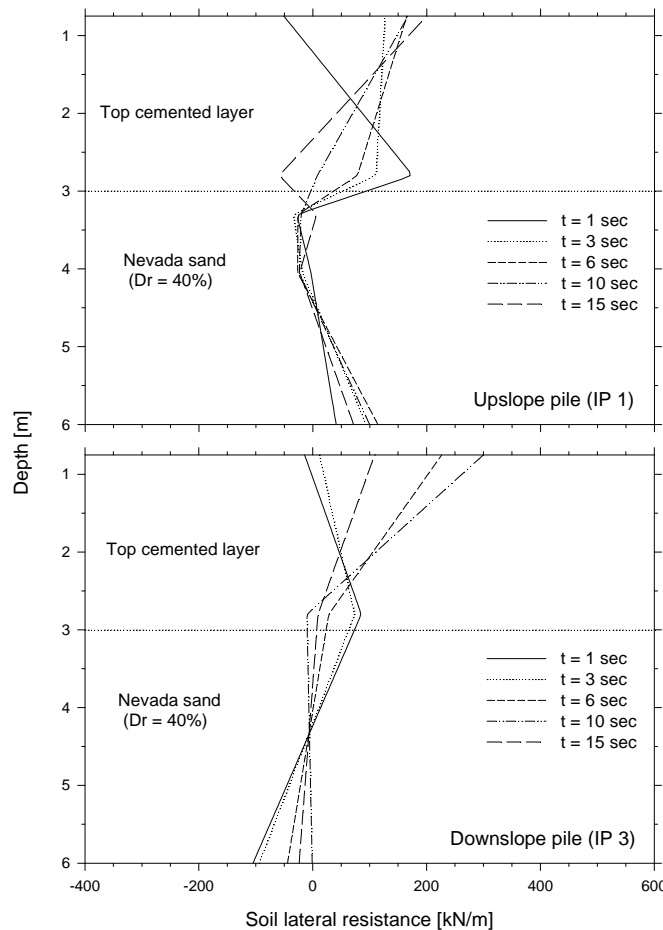


Figure 7.61: Profiles of back-calculated soil lateral resistance, Model p-6x2

The force time history applied by the top cemented layer was obtained by integrating the lateral resistance along the top cemented layer for each time instant. Figure 7.62 shows the back-calculated lateral force time histories against the piles IP1 and IP3. Assuming the force applied to each upslope and downslope piles is the same, the lateral force against the pile group was estimated as the sum of the forces against piles IP1 and IP3, multiplied by 6. Figure 7.62 shows that the pile-group-soil system was in the linear elastic range the first second of shaking, presenting a very large lateral stiffness. Then, the force increased slightly up to 1800 kN at about

4 sec. At that time the cemented sand was not able to withstand more stress and the force decreased gradually up to 1300 kN at the end of shaking. Like in Model p-3x2, the downslope piles were subjected to larger forces than the upslope piles during most of the excitation.

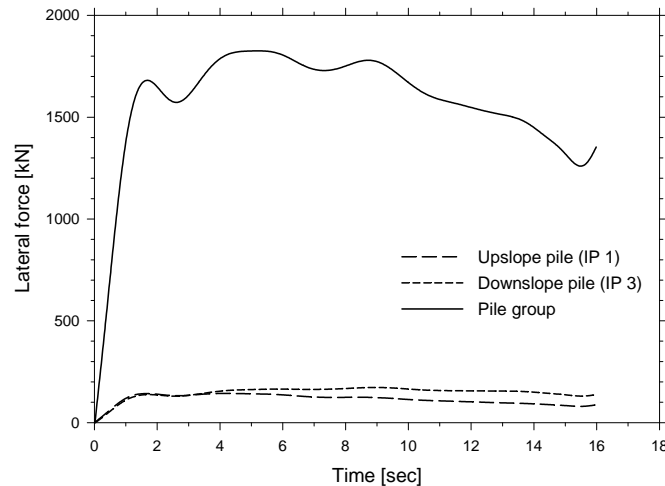


Figure 7.62: Back-calculated lateral force time histories against the piles, Model p-6x2

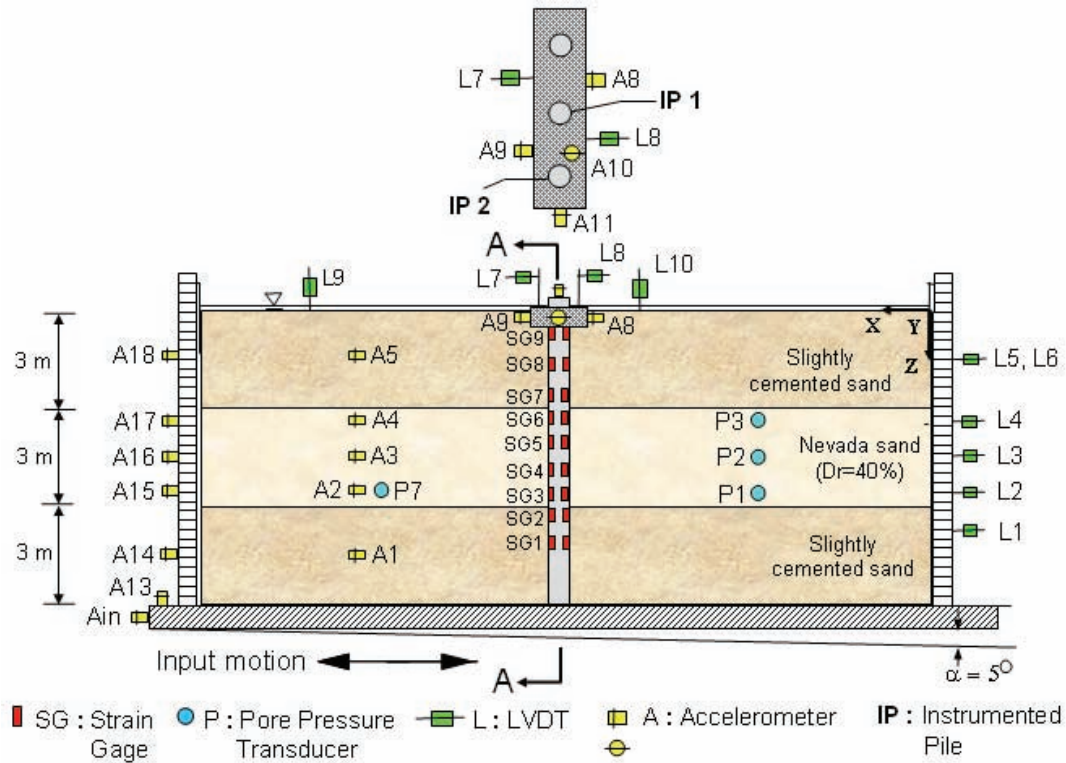
7.6 Model p-3x1

7.6.1 Model Description

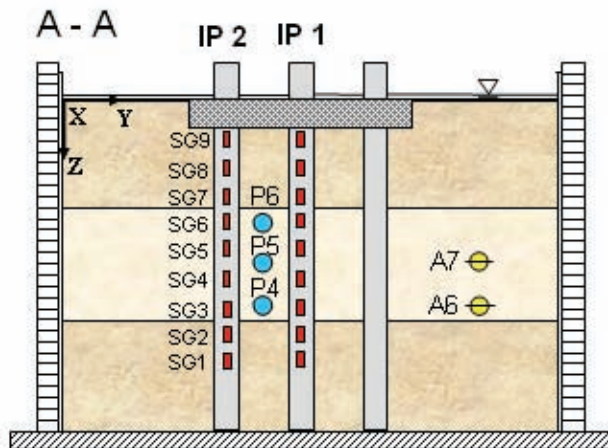
The setup and instrumentation used in Model p-3x1 are presented in Fig. 7.63. This model simulates a line of three piles connected with a pile cap perpendicular to the direction of lateral spreading. Like the previous models, the prototype profile consists of a 3 m thick Nevada sand layer with a relative density of 40%, on top and below a 3 m thick nonliquefiable slightly cemented layer. The model is inclined 2° to the horizontal and saturated with de-ionized/de-aired water. At a centrifugal acceleration of 50g the fine Nevada sand simulates a coarse sand layer, and the inclination becomes 4.8° (Taboada, 1995).

The embedded piles have a prototype diameter of 55 cm and a bending stiffness (EI) of approximately 78000 kN-m². The aluminum cap, embedded in the top cemented sand layer, has prototype dimensions of 1.65 m in width, 4.95 m in length, and 0.64 m in height. Figure 7.64 displays a picture and schematic of the pile-cap-structure, showing the spacing between piles (3d), as well as the aluminum block used to compact the cemented layers. Figure 7.65 shows a picture of the model during preparation, with the dashed line representing the pile cap. Lines of colored sand were placed at intermediate depths within the liquefiable layer (Fig. 7.66) to observe the pattern of soil deformation around the piles. Thin layers of colored cemented sand were placed as well at different elevations within the top cemented layer to observe the soil condition after the test.

The model was excited by 30 cycles of a 100 Hz sinusoidal acceleration with uniform amplitude of about 12g. At a centrifugal acceleration of 50g this corresponds to a frequency of 2 Hz and peak acceleration of 0.24g.



(a)



(b)

Figure 7.63: (a) Setup and instrumentation used in Model p-3x1, (in prototype units)
(b) Transversal section of Model p-3x1

The instrumentation used in Model p-3x1 is shown in Fig. 7.63 and listed in Table 7.5. The model was instrumented with 18 accelerometers, 7 pore pressure transducers, and 10 LVDTs. Two instrumented piles (IP1 and IP2) were used in the pile group foundation, as shown in Fig. 7.63b. Detailed information about the strain gage configuration and the aluminum piles (type A) used in this model is presented in section 2.7. Accelerations in the soil and outside the laminar box, excess pore water pressure, lateral displacement of the soil and the pile cap, ground surface settlement, bending moments, and axial forces were measured during the test.

Table 7.5: Location of instruments in Model p-3x1 (in model units)

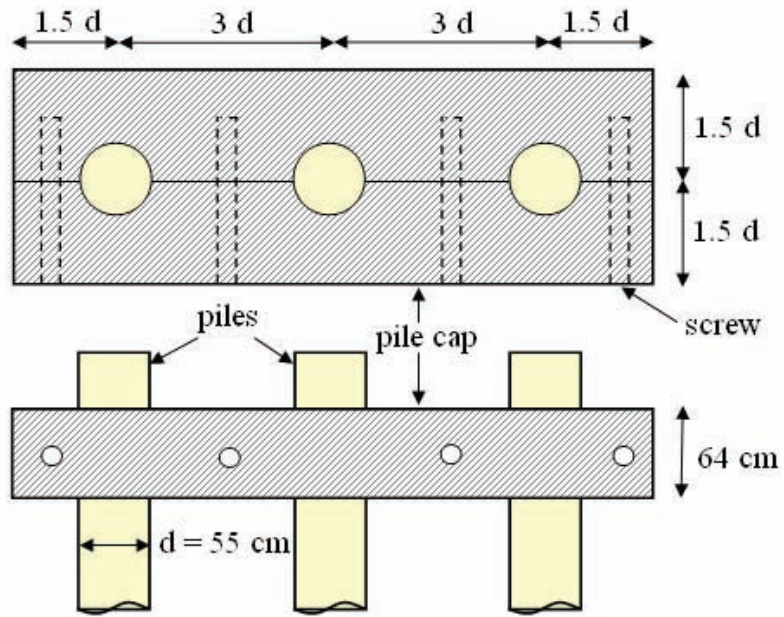
Transducer	Sensor name	Coordinates [cm]		
		X	Y	Z
Accelerometer	Ain	73.5	17.75	18.5
	A1	55	17.75	15
	A2	55	17.75	11
	A3	55	17.75	9
	A4	55	17.75	7
	A5	55	17.75	3
	A6	35.5	21	11
	A7	35.5	21	9
	A8	32.5	21	0.63
	A9	39	14.5	0.63
	A10	35.5	17.75	0
	A11	35.5	8	0.63
	A13	72.5	17.75	18
	A14	71	17.75	15
	A15	71	17.75	11
	A16	71	17.75	9
	A17	71	17.75	7
	A18	71	17.75	3
Pore pressure transducer	P1	17	17.75	11
	P2	17	17.75	9
	P3	17	17.75	7
	P4	35.5	14.5	11
	P5	35.5	14.5	9
	P6	35.5	14.5	7
LVDT	L1	0	24	14
	L2	0	12	11
	L3	0	24	9.1
	L4	0	12	7.2
	L5	0	24	3
	L6	0	12	3
	L7	39	21	-2
	L8	32.5	14.5	-2
	L9	63	8	0
	L10	26	24	0

Table 7.5 (cont): Location of instruments in Model p-3x1 (in model units)

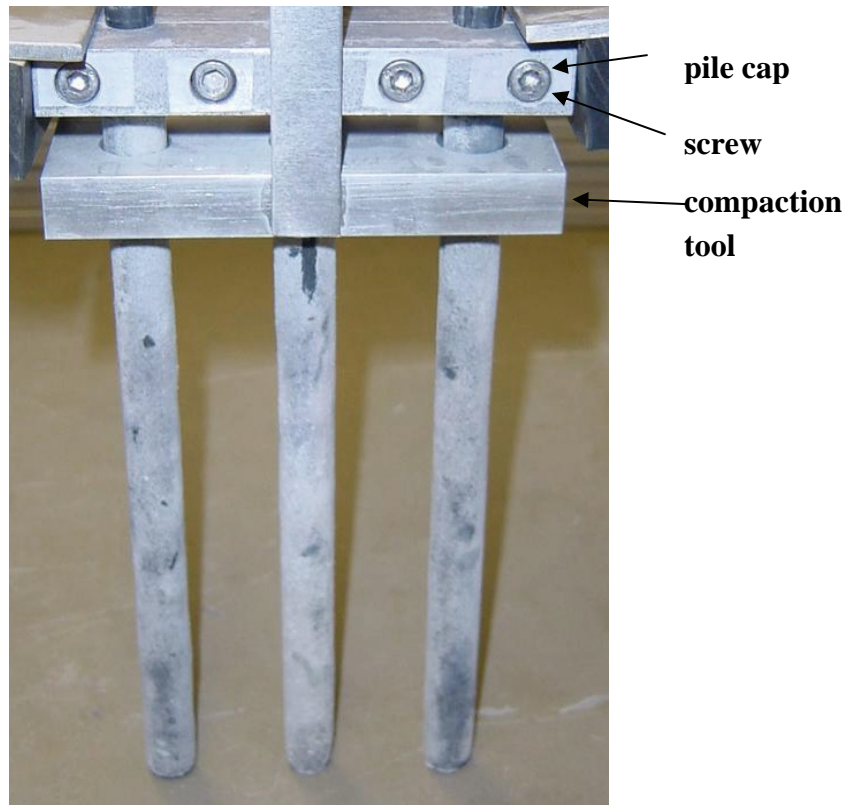
Transducer	Sensor name	Coordinates [cm]		
		X	Y	Z
		IP 1	IP 1	IP 1
Strain gage		IP 2	IP 2	IP 2
	SG1	35.5	14.5	14
	SG2	35.5	14.5	12.5
	SG3	35.5	14.5	11.5
	SG4	35.5	14.5	10
	SG5	35.5	14.5	8
	SG6	35.5	14.5	6.5
	SG7	35.5	14.5	5.5
	SG8	35.5	14.5	3.75
	SG9	35.5	14.5	2

7.6.2 Recorded Accelerations

Figure 7.67 shows the recorded input acceleration and soil acceleration time histories far from the pile group at different depths. Acceleration records in the loose sand show a drop in positive amplitude, exhibiting as well large spikes in the negative direction after one or two cycles of shaking. At the bottom of this layer however, the positive acceleration did not drop significantly, probably due to the boundary effect of the bottom layer. The acceleration records indicate the loose sand layer liquefied and displaced in the downslope direction during shaking. The recorded acceleration in the top cemented layer (A5) evidences the dynamic isolation of this layer. The bottom cemented layer acceleration was very similar to the input acceleration, indicating that no sliding occurred between the bottom layer and the base of the laminar box. The soil acceleration close to the external pile (A6), as shown in Fig. 7.68, was very similar to the one recorded in the soil far from the piles at the same elevation (A2), indicating no large area of influence was induced by the foundation.



(a)



(b)

Figure 7.64: Pile-cap-structure, (a) schematic, (b) picture, Model p-3x1

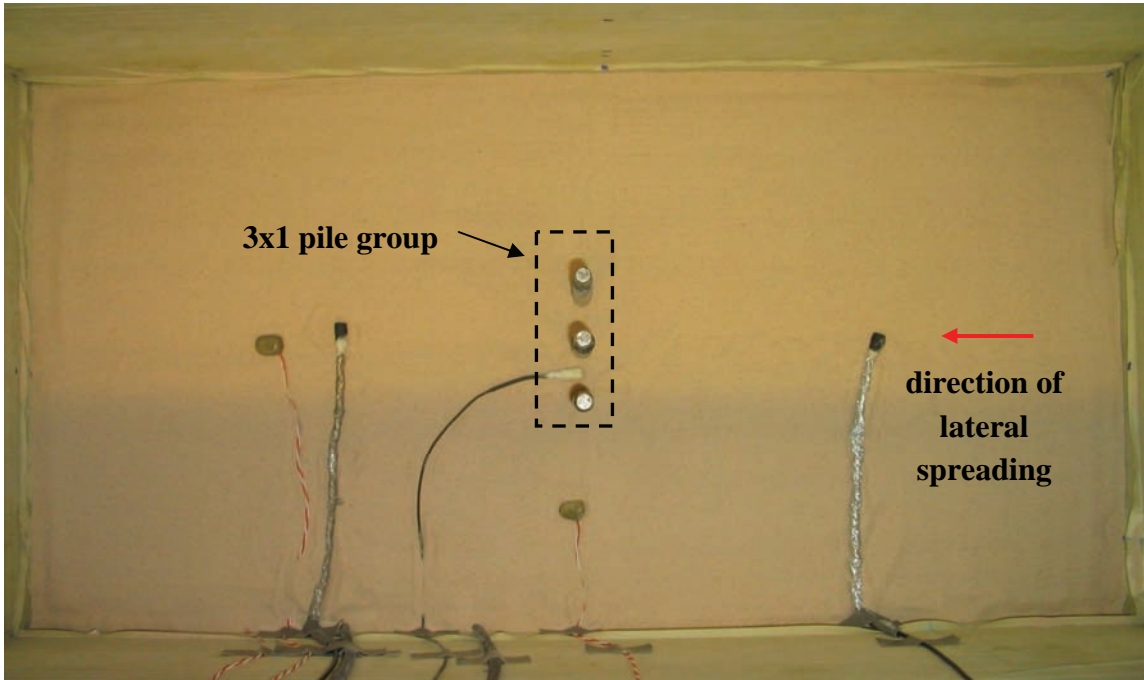


Figure 7.65: Model during preparation, the dashed line represents the pile cap, Model p-3x1

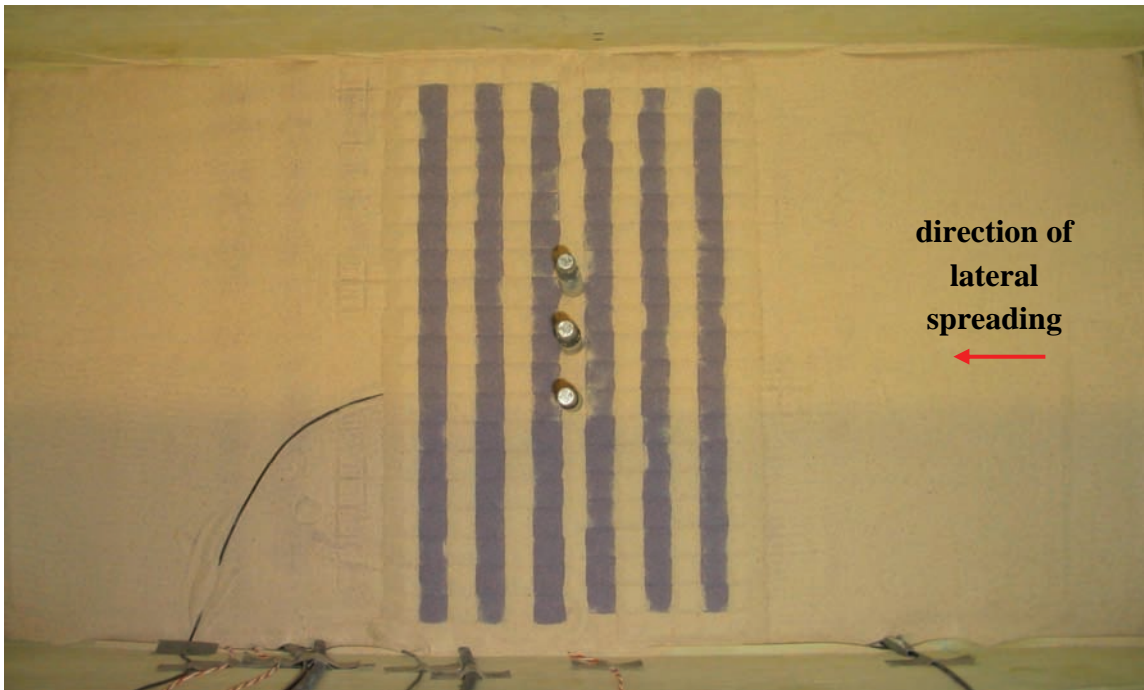


Figure 7.66: Colored sand placed at an intermediate depth, Model p-3x1

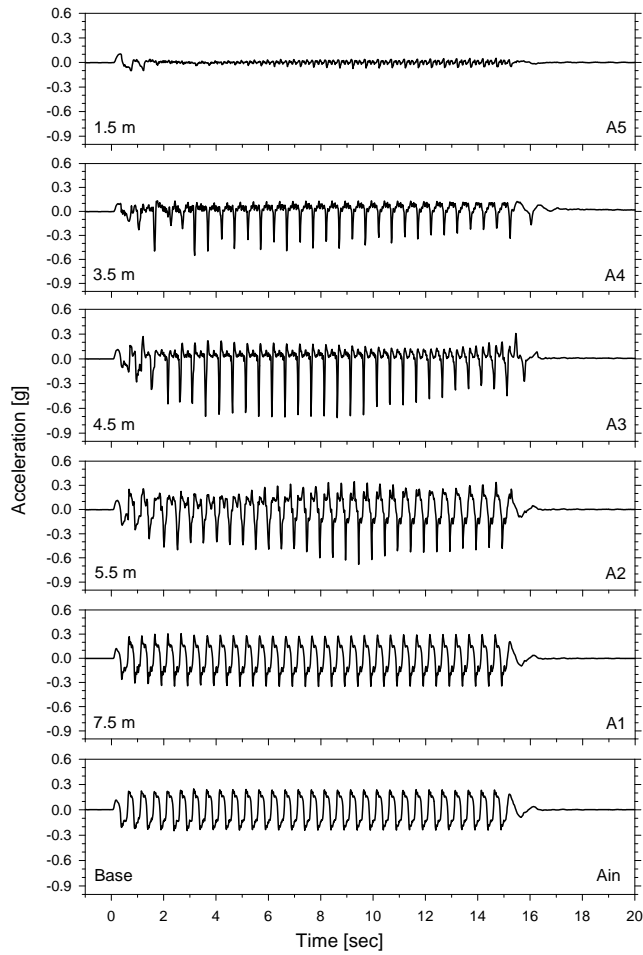


Figure 7.67: Soil acceleration time histories far from the pile group, Model p-3x1

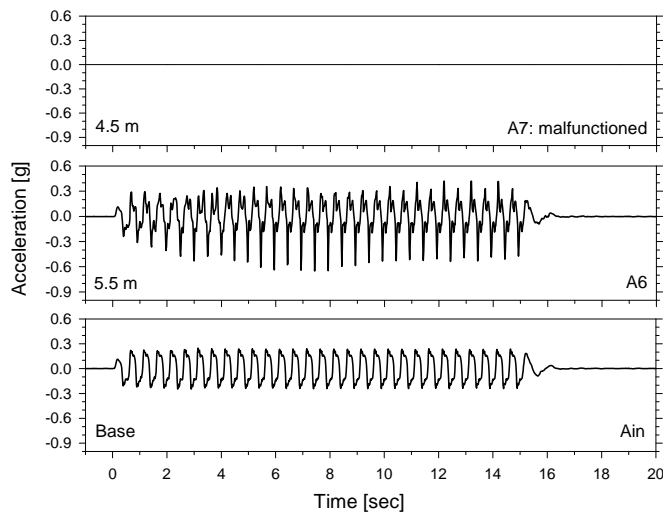


Figure 7.68: Soil acceleration time histories close to the external pile, Model p-3x1

Figure 7.69 presents the acceleration time histories on the pile cap, as well as the measured horizontal and vertical acceleration at the base of the laminar box. The vertical acceleration of the pile cap seems to be related to the vertical acceleration at the base of the model. The acceleration perpendicular to the direction of lateral spreading consists of small spikes generated by the vibration of the pile group. On the other hand, the cap acceleration in the direction of lateral spreading contains large high frequency spikes generated by the interaction between the pile group and the top cemented layer. Laminar ring accelerations recorded at various elevations are presented in Fig. 7.70. These acceleration records are in reasonable agreement with the ones in the soil in Fig. 7.67.

7.6.3 Recorded Excess Pore Pressures

The excess pore pressure records reveal that the loose sand layer liquefied after about two or three cycles of excitation. In the free field, the excess pore pressure slightly increased after liquefaction was reached. On the other hand, the excess pore pressure in the pile group area was slightly lower than in the free field. These trends, as well as the low dissipation rate in the free field, are consistent with the results obtained in the previous centrifuge models (Models p-3x2 and p-6x2) and were already discussed. (Figures 7.71 and 7.72)

7.6.4 Recorded and Back-calculated Lateral Displacements

Figure 7.73 shows the recorded lateral displacement of the pile cap and soil at various depths. The liquefied layer and top cemented layer displaced gradually during shaking. The records also show that the bottom cemented layer practically did not move, being consistent with the acceleration record at that elevation. Once the shaking process finished, the soil lateral displacement stopped immediately. The pile cap on the other hand, remained vibrating for a short period of time.

The profiles of soil lateral displacement were obtained interpolating the LVDT measurements, after filtering out the cyclic component (Fig. 7.74). As soon as the loose sand liquefied at the beginning of shaking, the top cemented layer started moving downslope, reaching a maximum displacement of approximately 75 cm at the end of shaking, 60 cm less than the in the case without piles (Model p-0). Therefore, the pile group was able to reduce the amount of lateral spreading in almost 50%.

The pile displacement profiles of the center pile (IP1) was back-calculated following the procedure presented in section 7.4.4. Figure 7.75 shows the back-calculated rotational stiffness provided by the bottom cemented around the center pile layer versus the corresponding bending moment at the base of the liquefiable layer.

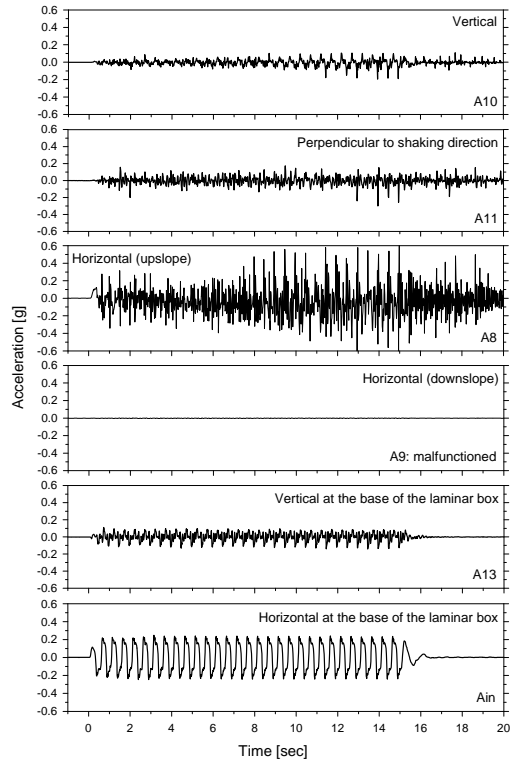


Figure 7.69: Acceleration time histories on the pile cap, Model p-3x1

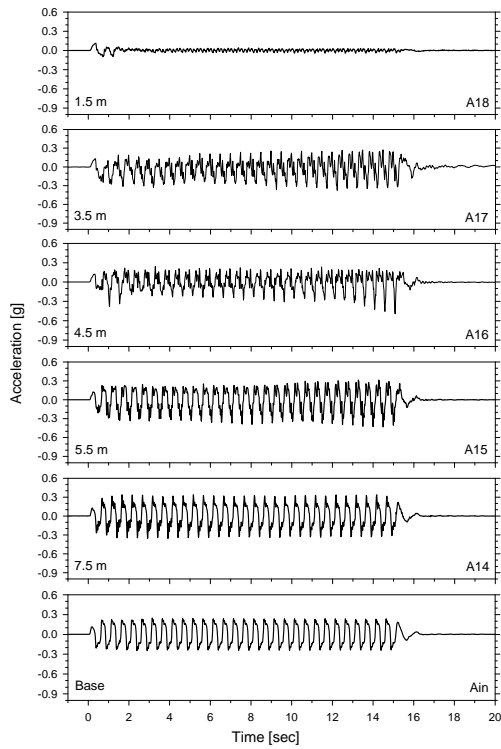


Figure 7.70: Acceleration time histories on the laminar rings, Model p-3x1

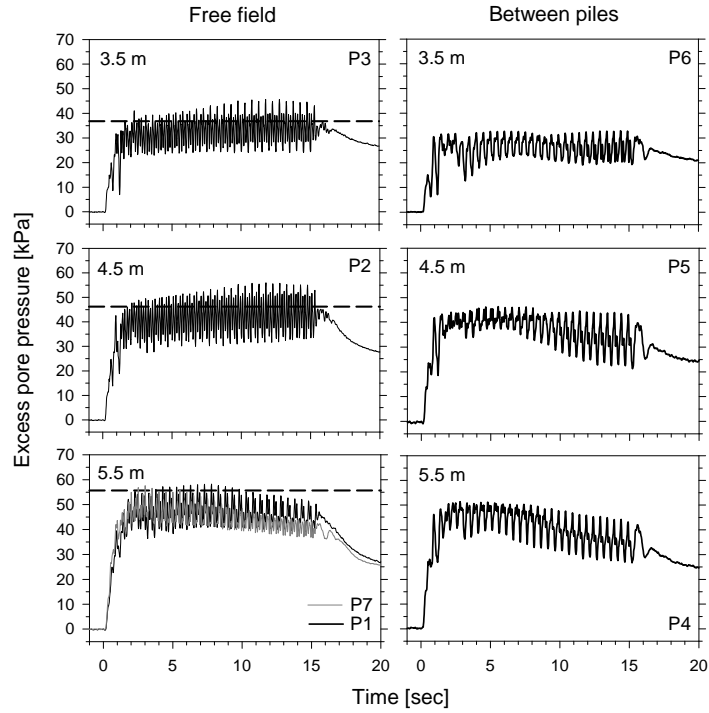


Figure 7.71: Short term excess pore pressure time histories in the free field and between piles, the dashed lines correspond to initial liquefaction, Model p-3x1

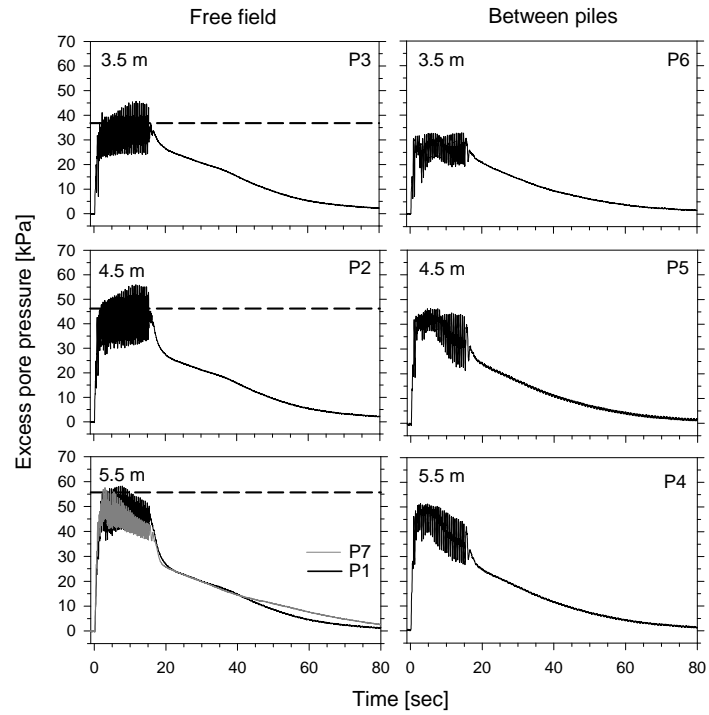


Figure 7.72: Long term excess pore pressure time histories in the free field and between piles, the dashed lines correspond to initial liquefaction, Model p-3x1

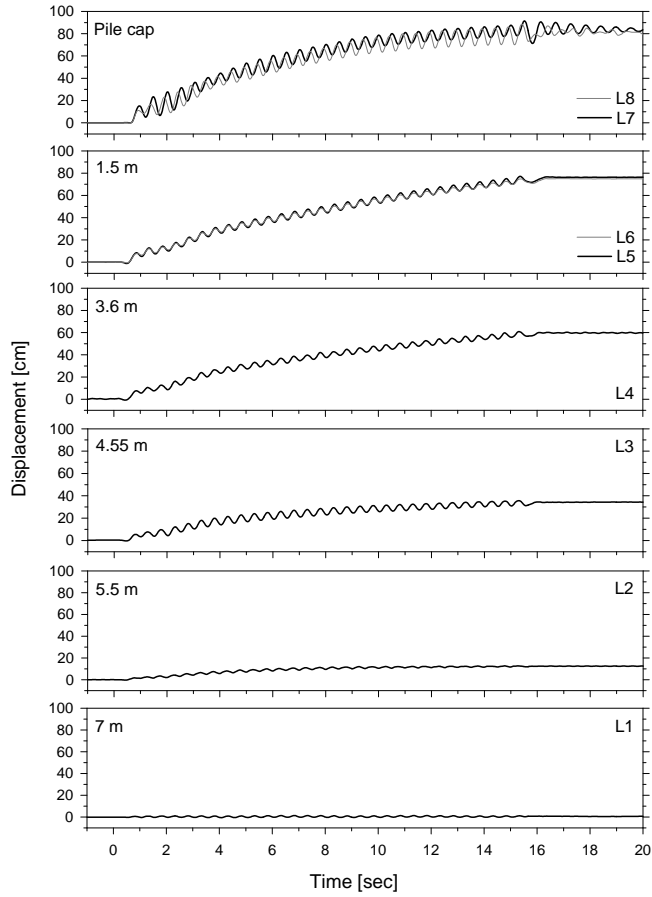


Figure 7.73: Soil and pile cap lateral displacement time histories, Model p-3x1

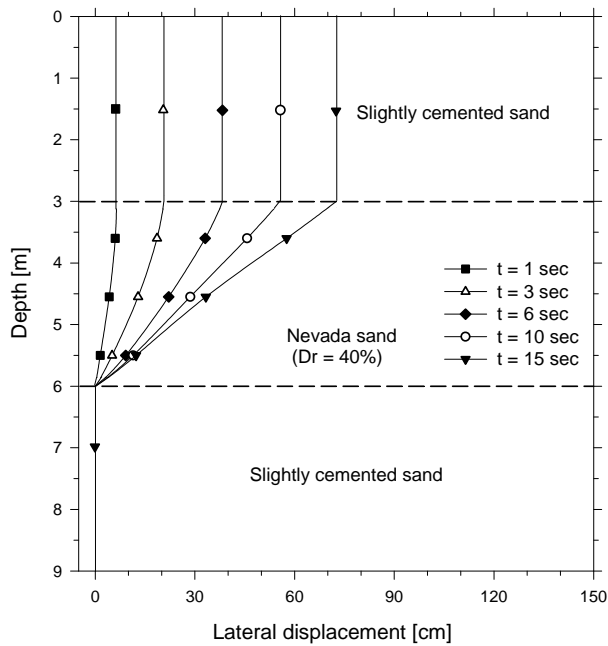


Figure 7.74: Profiles of soil lateral displacement, Model p-3x1

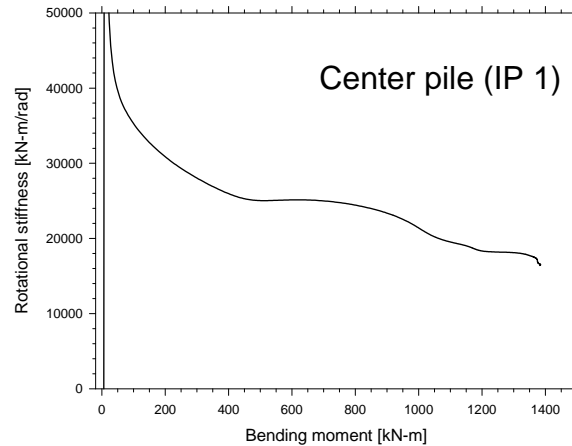


Figure 7.75: Back-calculated rotational stiffness provided by the bottom cemented layer versus bending moment at the base of the liquefiable layer, Model p-3x1

After ignoring the indetermination generated by very small rotations of the pile at the beginning of shaking, the rotational stiffness in the elastic range was approximately 40000 kN-m/rad, which is similar to the values estimated in Models p-3x2 and p-6x2. As the bending moment increased, the stiffness around the pile decreased gradually up to about 20000 kN-m/rad without showing an excessive lost in strength, even though the bending moments were much larger than the ones measured in Models p-3x2 and p-6x2.

Since the LVDTs L7 and L8 were located 2 cm above the ground surface, the correct pile cap lateral displacement was obtained by subtracting the increment in displacement above the pile cap from the LVDT measurements. Figure 7.76 compares the lateral displacement of the pile cap and top cemented layer during shaking. During approximately the firsts 9 sec the displacement of the pile cap and top cemented layer, without considering the cyclic component, were very similar. As the excitation continued, a gap started developing on the downslope side of the pile group.

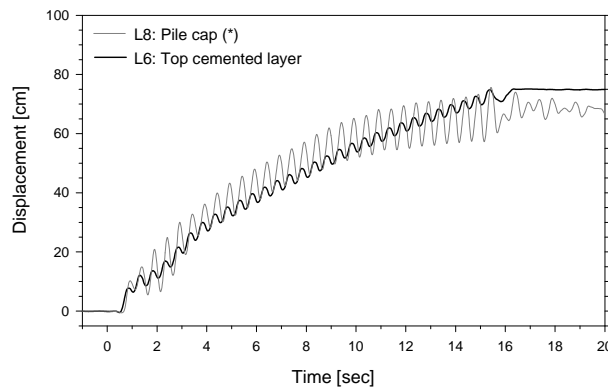


Figure 7.76: Lateral displacement time histories of the pile cap and top cemented layer, (*) after subtracting the increment in displacement above the pile cap, Model p-3x1

Finally, the profiles of the pile lateral displacement were obtained considering the deformation by curvature and rotation. Figure 7.77 shows the lateral displacement profiles of the pile group and the soil at different times. The piles were so stiff, compared to the bottom cemented layer, that a large percentage of the pile lateral displacement was caused by the rotation at the base. Since the top cemented layer moved as a rigid block, the pile group tried to break the soil around it as soon as it started rotating at the beginning of shaking, as shown in Fig. 7.77. Near the ground surface, the pile cap snapped the cemented sand in the downslope direction. At deeper elevations within the top layer, the pile group tried to break the cemented sand in the upslope direction. In this case however, the pile group induced a passive failure, as shown in the following sections. As passive failure progressed, the top cemented layer far from the pile group ended up displacing more than the pile cap ($t = 15$ sec).

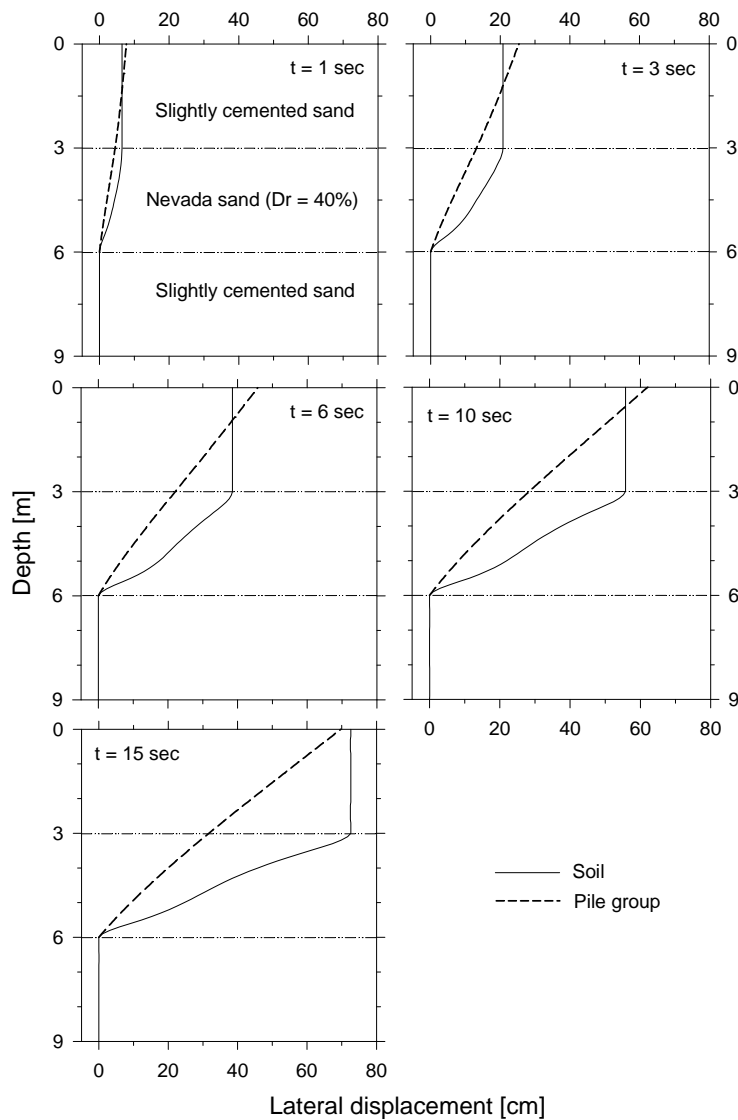
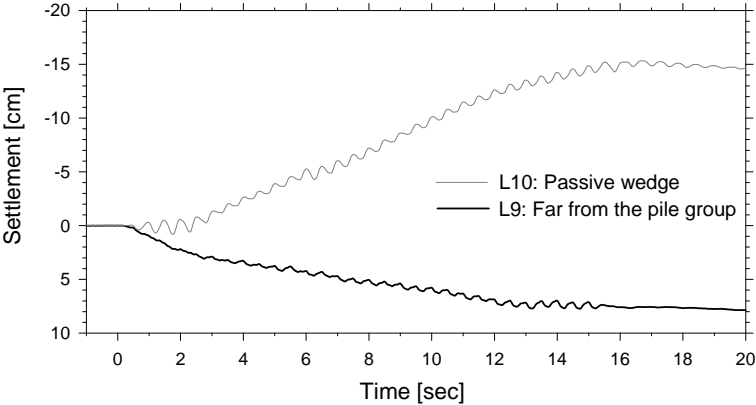
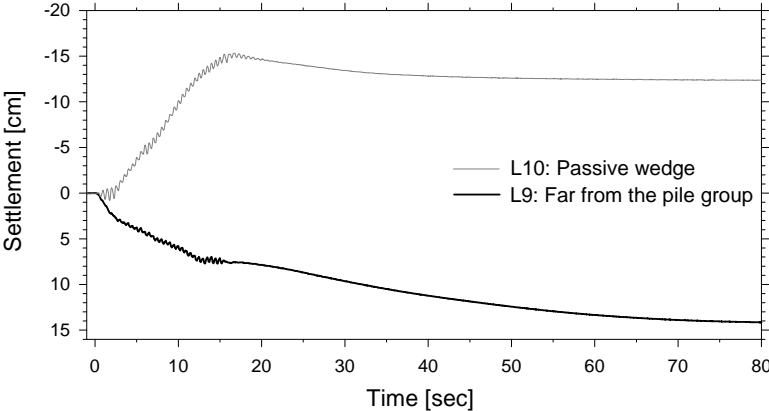


Figure 7.77: Profiles of soil and pile group lateral displacement, Model p-3x1

The ground surface settlement time histories far from the foundation and on the upslope side of the pile group (close to the cap) are presented in Fig. 7.78. During the shaking process the top cemented layer far from the piles settled 7.5 cm. Once the shaking stopped, the settlement continued due to the consolidation process of the liquefied layer, reaching a value of 14 cm after about 80 sec. These values are in very good agreement with the ones measured in the other models. On the other hand, the ground surface on the upslope side of the pile group moved up during the excitation. This measurement, corresponding to the passive wedge, indicates that the passive failure developed gradually during the excitation process. Once the shaking stopped, the passive wedge started settling with a similar rate than the one far from the pile group.



(a)

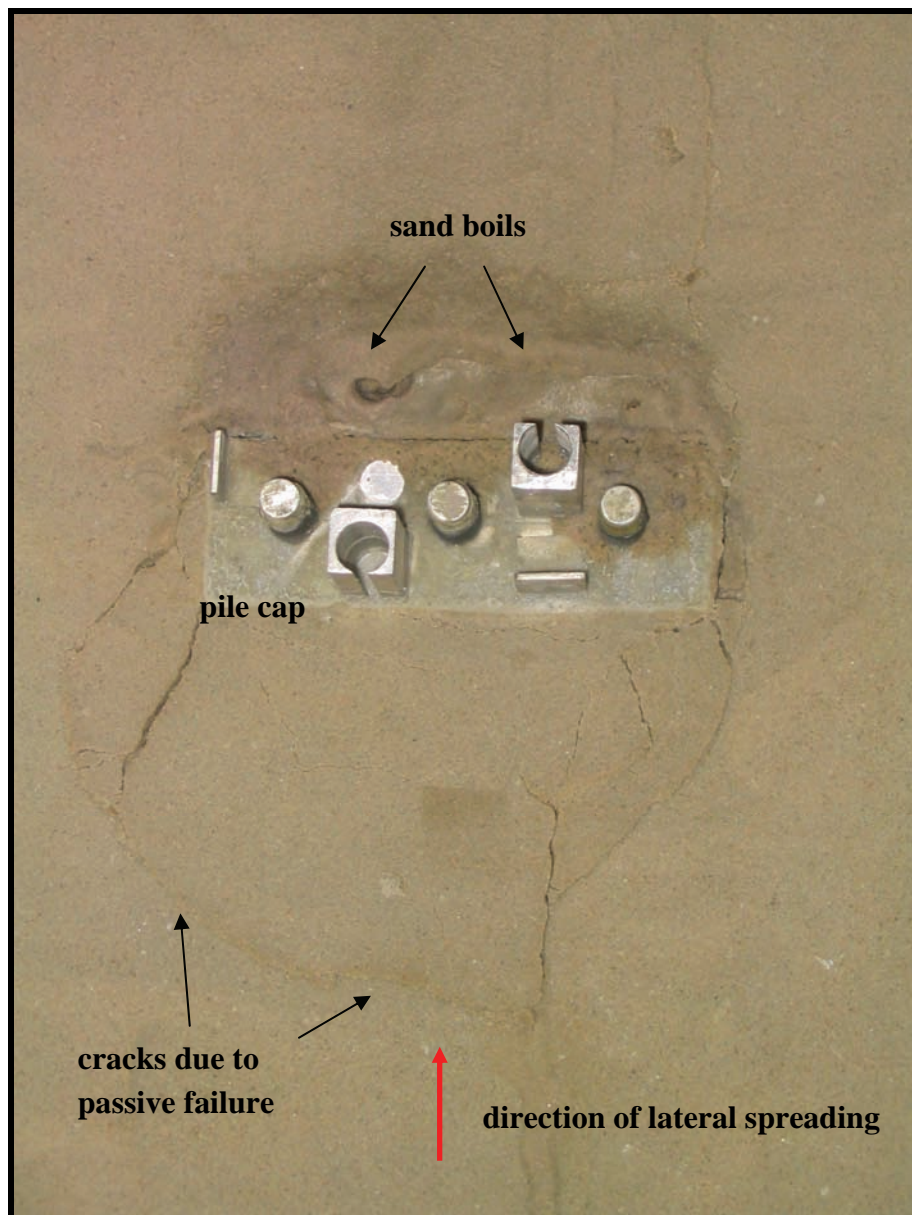


(b)

Figure 7.78: Ground surface settlement time histories far from the pile group and on the passive wedge, (a) short term, (b) long term, Model p-3x1

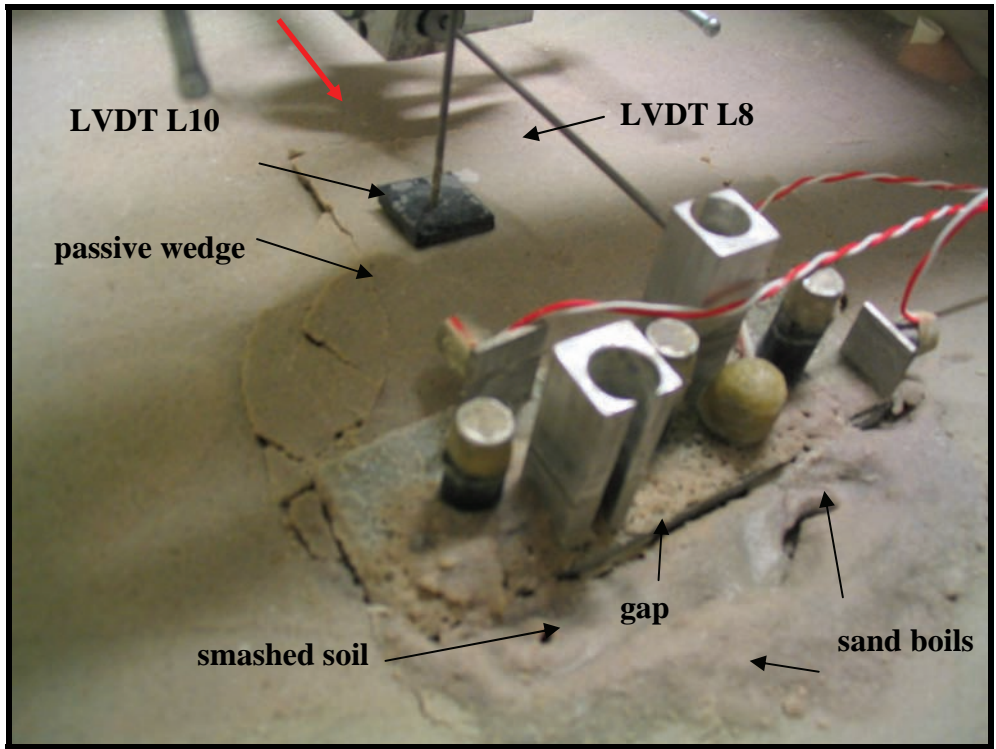
7.6.5 Soil Condition around Pile Cap

Figure 7.79 shows pictures of the ground surface condition after the test. The cracks on the upslope side of the pile group confirm the development of a passive failure. On the downslope side of the cap the soil was excessively damaged after it was pushed by the pile cap. The sand boils on the downslope side are evidence of the gaps that developed as the passive failure progressed. The permanent deformation of the pile group is displayed in Fig. 7.79c.

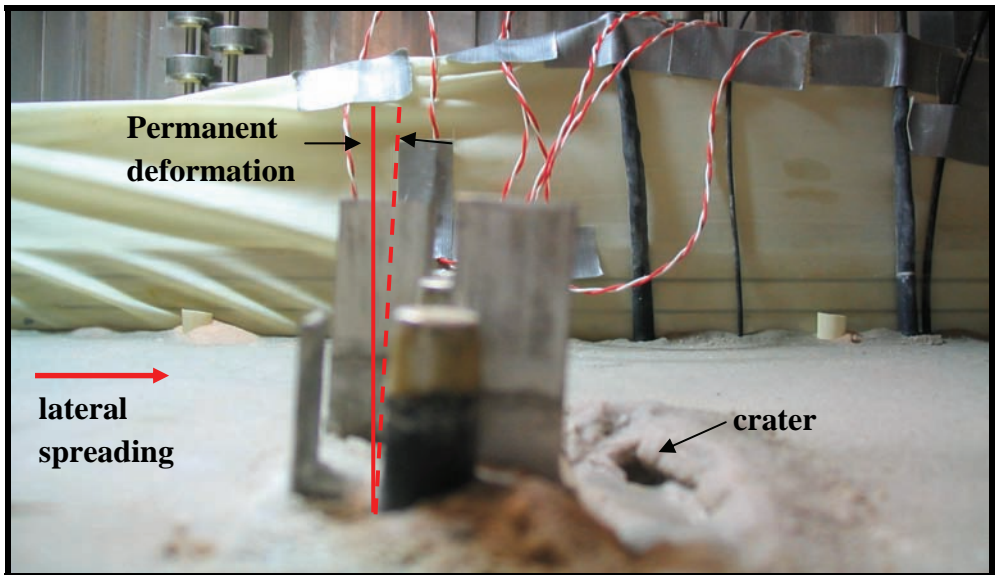


(a)

Figure 7.79: Ground surface condition around pile cap after the test, (a) top view, Model p-3x1



(b)



(c)

Figure 7.79(cont.): Ground surface condition around pile cap after the test, (b) inclined view, (c) lateral view, Model p-3x1

Figure 7.80 shows a lateral view of the top cemented layer after carefully removing part of the soil. The colored cemented sand placed at different elevations clearly identifies the passive failure plane, which has an angle of 56° with the vertical. No active or passive type of failure is observed on the downslope side of the pile group. Near the pile cap however, the soil looks very disturbed. The gaps developed on the downslope side of the cap induced a path for the dissipation of excess pore pressure, as shown in Fig. 7.80.

7.6.6 Pattern of Soil Displacement around Piles

Lines of colored sand were placed at intermediate depths to observe the pattern of soil displacement around the piles. Figure 7.81 shows a picture of the soil condition taken after the test, with the arrow indicating the direction of lateral spreading. The liquefied sand moved around the individual piles, affecting the soil pattern close to the piles themselves.

7.6.7 Recorded Bending Moments

Prototype bending moment time histories measured in the center pile IP1 and external pile IP2 are presented in Figs. 7.82 and 7.83, respectively. Bending moment profiles for both piles are shown in Fig. 7.84, after filtering out the cyclic component. The bending moments near the bottom of the liquefiable layer increased monotonically in both piles, reaching a maximum value of approximately 1400 kN-m in the center pile and 1550 kN-m in the external pile. This difference indicates the cemented sand around the external piles offered slightly more constrain than the soil around the center pile. On the other hand, the bending moments in the upper part were very similar.

The profiles at 1 sec suggest that at the very beginning of the excitation the cemented sand around the piles was in the elastic range, with the upper and lower moments being very similar and the point of zero moment near the middle of the loose layer. The profiles at 3 sec show that the moments in the upper part kept increasing, with the maximum moments taking place near the middle of the cemented layer, suggesting the cemented sand started failing locally around each individual pile. At about 6 sec the profiles show that the top cemented layer was failing around the pile group, with the upper bending moments decreasing and the maximum values taking place just below the pile cap. In the second half of the excitation, the bending moments below the pile cap were practically zero, indicating the pile group head was able to rotate almost freely without much resistance from the top cemented layer.

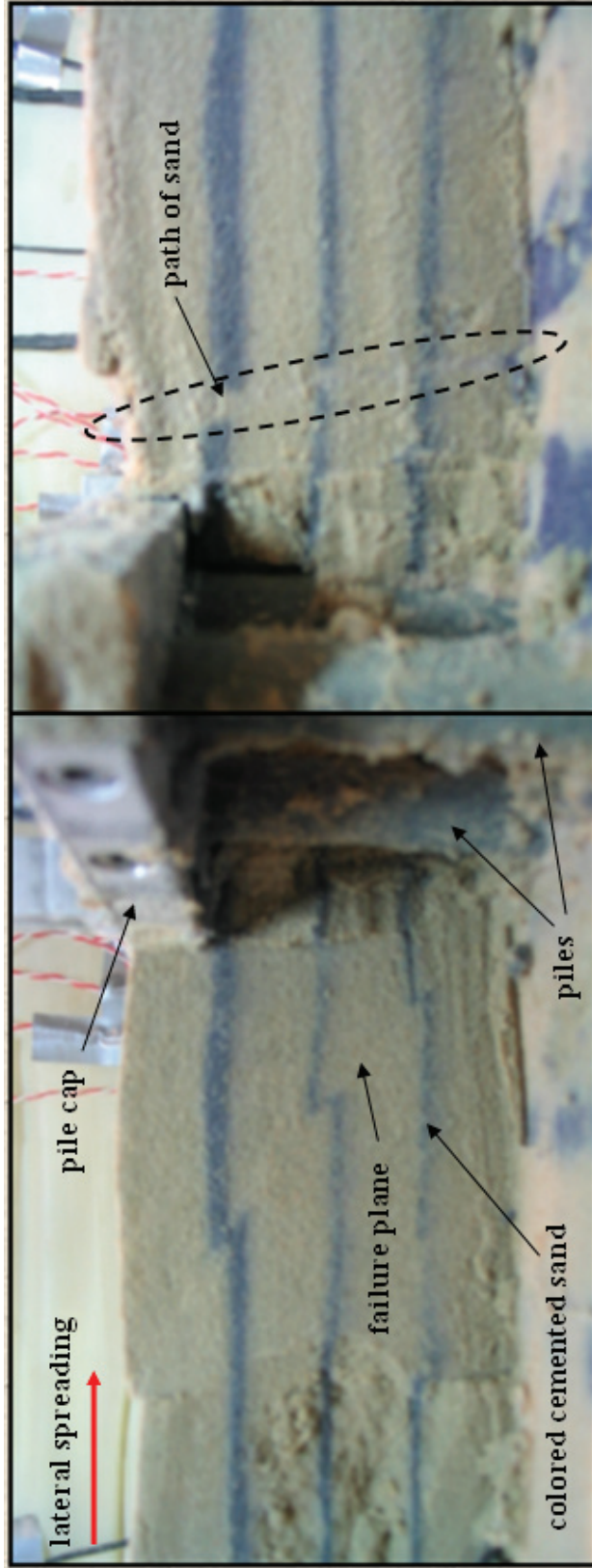


Figure 7.80: Soil condition in the top cemented layer after the test, Model p-3x1

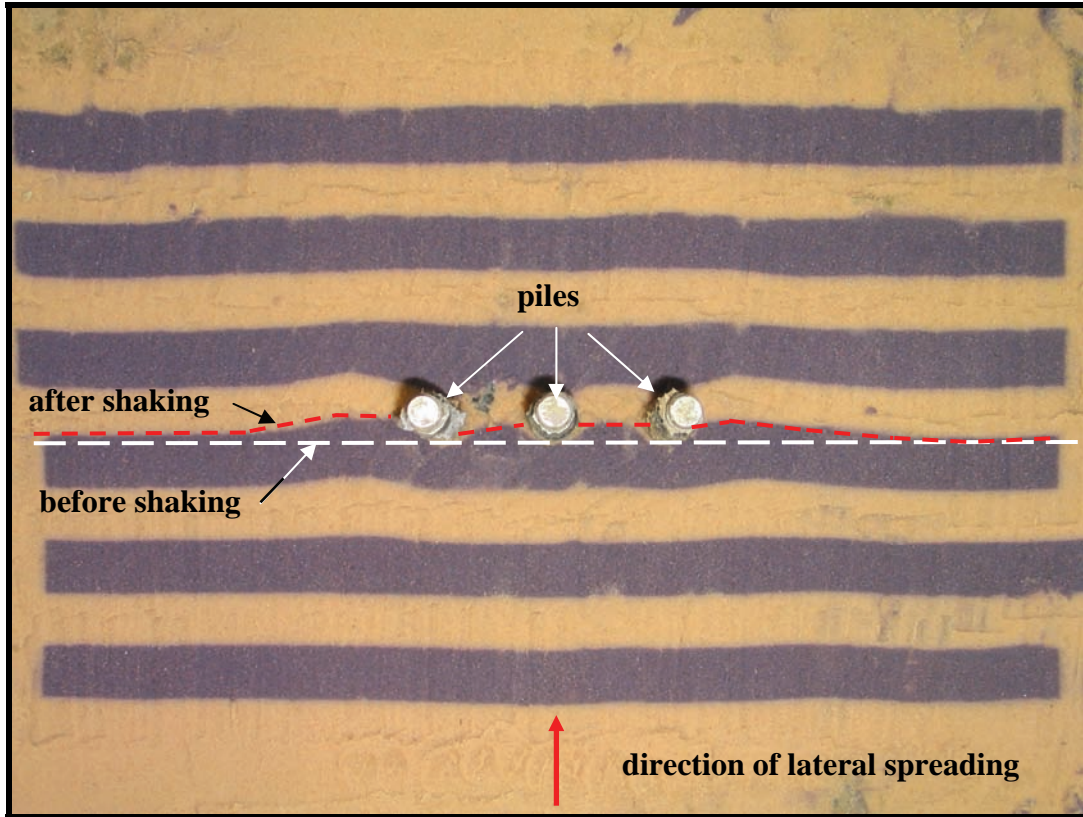


Figure 7.81: Pattern of soil displacement around pile group, Model p-3x1

At all times the bending moment on both piles varied approximately linearly with depth within the loose sand layer, indicating that the pressure applied by the liquefied soil was negligible compared to the one applied by the top cemented layer. The bending moments seems to indicate that at the beginning of shaking the resistance was controlled by the soil around each individual pile, but as the passive failure developed, the resistance on the piles was controlled mainly by the soil around the pile group.

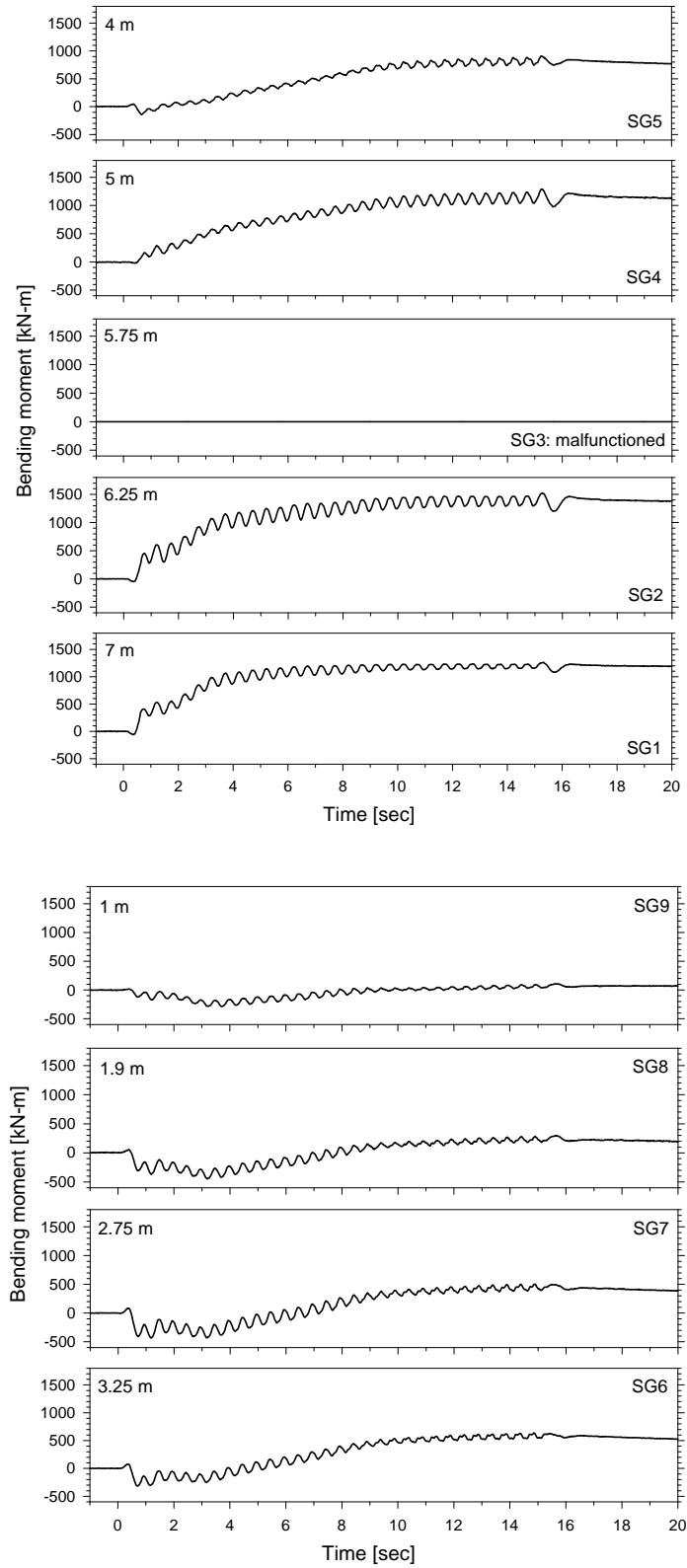


Figure 7.82: Bending moment time histories, center pile (IP 1), Model p-3x1

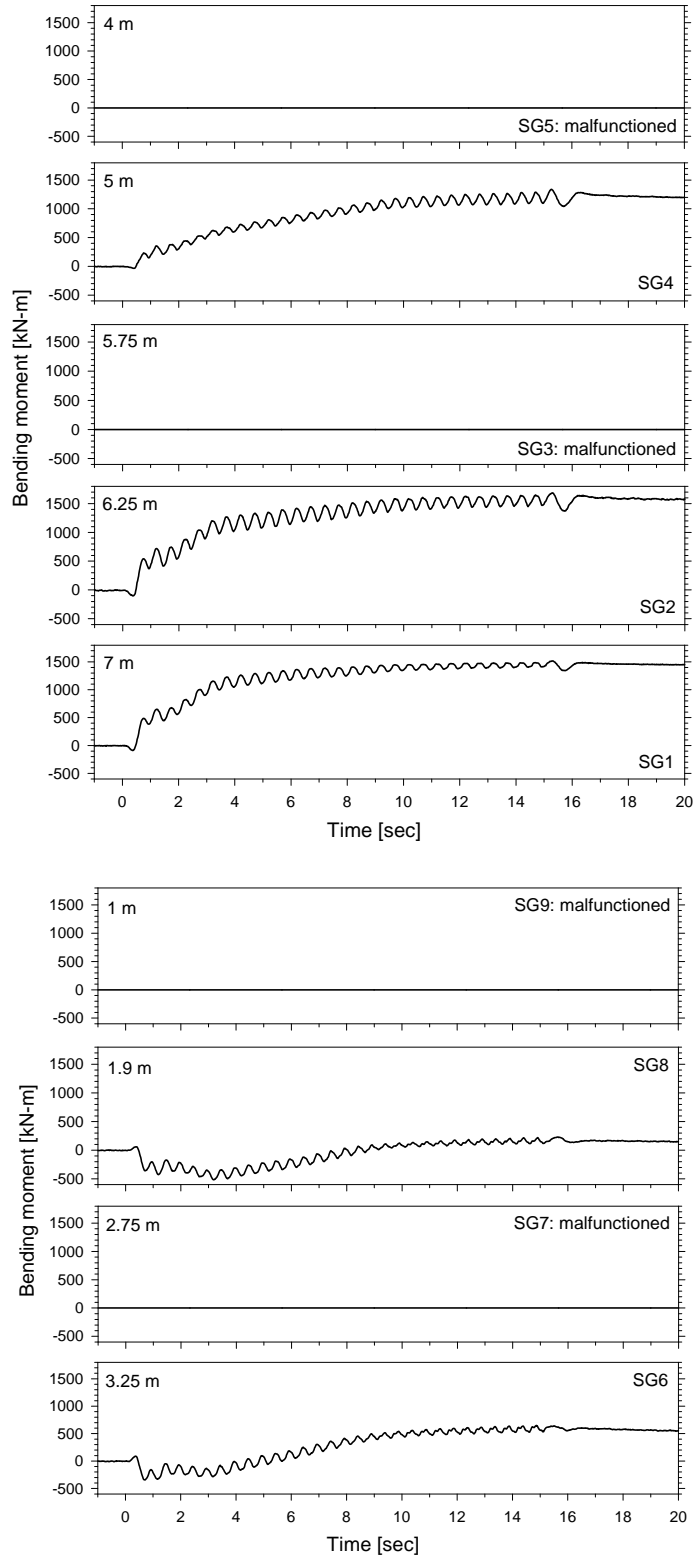


Figure 7.83: Bending moment time histories, external pile (IP 2), Model p-3x1

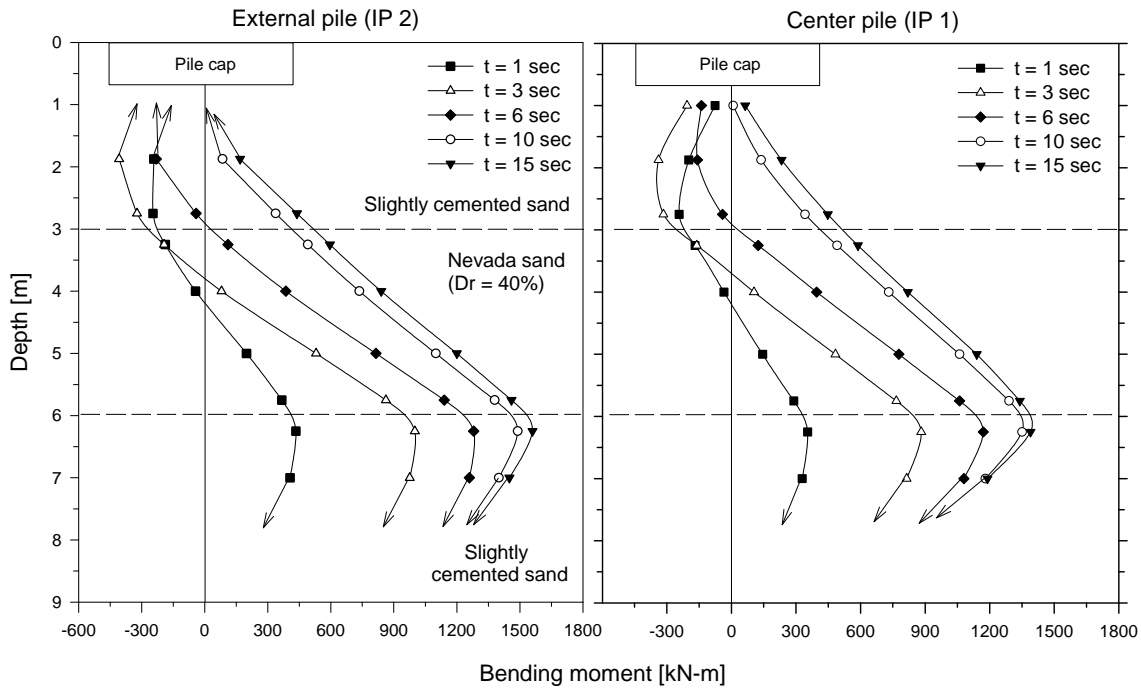


Figure 7.84: Profiles of bending moment, center (IP 1) and external (IP 2) piles, Model p-3x1

7.6.8 Recorded Axial Forces

Figures 7.85 and 7.86 show prototype axial force time histories obtained for the center and external pile respectively. Positive values represent tension while negative values represent compression. The axial forces were zeroed at the beginning of shaking, and therefore represent the change in axial force during the excitation. The axial force was very similar in both piles. In the first couple of seconds the piles were subjected to compression forces, reaching a value of about 150 kN. This force is related to the weight of the top cemented layer that was supported in part by the pile group once the loose sand layer liquefied. As lateral spreading continued, the piles started being pushed up. This result is consistent with the net vertical force measured in the 3x2 pile group, probably caused by the excess pore pressure in the liquefied layer and the vertical movement of the passive wedge.

7.6.9 Lateral Force against Piles

The back-calculated lateral resistance was obtained following the same procedure described in section 7.4.8. Fig. 7.87 shows the profiles of soil lateral resistance against the center pile. As expected, the lateral resistance of the liquefied sand was negligible compared to the one of the top cemented layer. At the beginning of the excitation, the soil resistance in the elastic range varied linearly from approximately 400 kN/m at the bottom of the top layer to -400 kN/m below

the cap. These values evidence the large resistance of the cemented sand to the pile rotation at the beginning of shaking. The reduction in resistance near the ground surface must be related to the low strength of the smashed soil, and the gap developed on the downslope side. As passive failure progressed, the cemented sand around the pile group did not offer too much resistance.

The force time history applied by the top cemented layer was obtained by integrating the lateral resistance along the top cemented layer for each time instant. Figure 7.88 shows the back-calculated lateral force time history against the center pile. Since the bending moment at the base of the liquefiable layer in the external pile was about 10% larger than in the center pile, the lateral force against the pile group was obtained by multiplying the force against the center pile by a factor of 3.2. The pile-group-soil system response was in the linear elastic range the first second of shaking. Then, the force kept increasing with a smaller lateral stiffness, reaching 1100 kN at about 4 sec. At that time the cemented sand was not able to withstand more stress and the force decreased gradually up to 900 kN at the end of shaking.

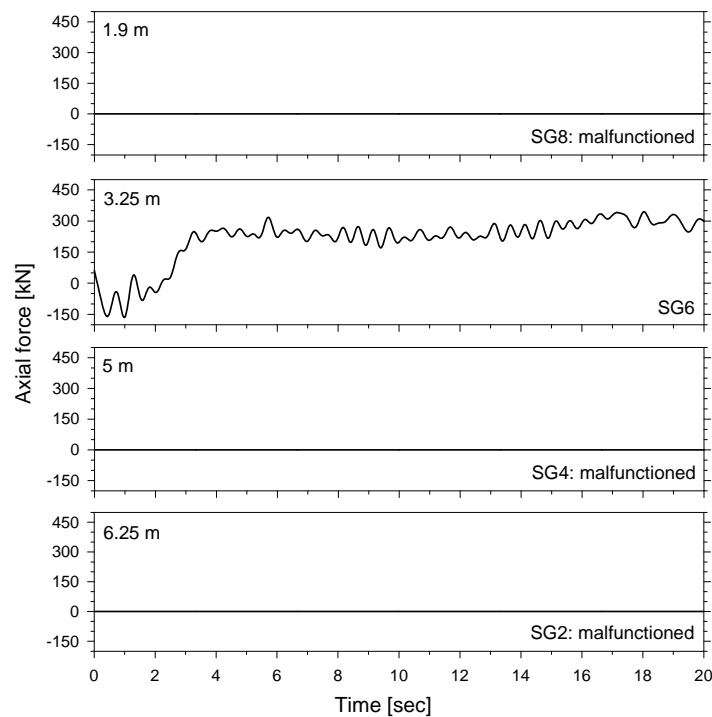


Figure 7.85: Axial force time histories, center pile (IP 1), Model p-3x1

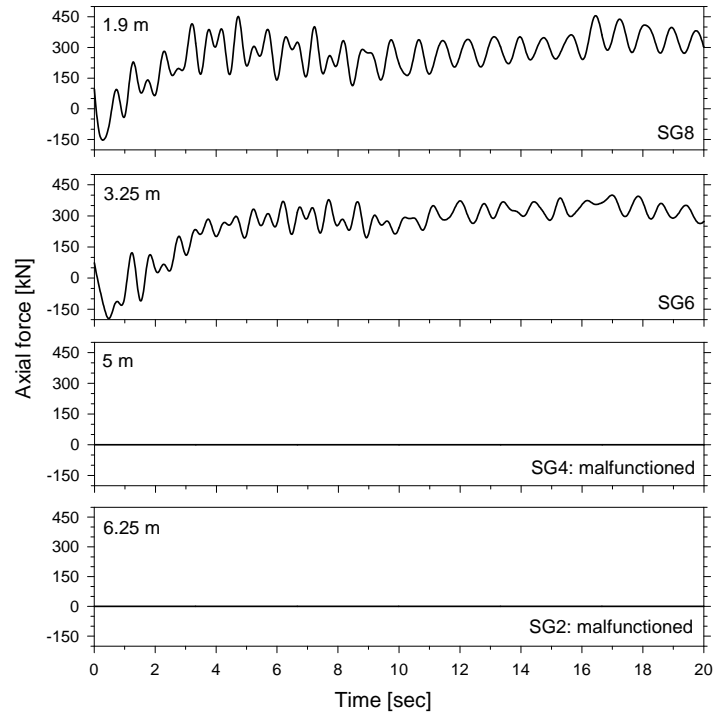


Figure 7.86: Axial force time histories, external pile (IP 2), Model p-3x1

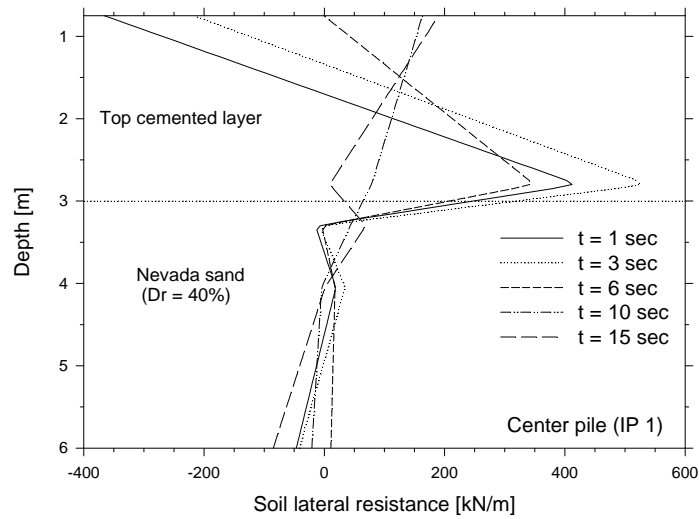


Figure 7.87: Profiles of back-calculated soil lateral resistance, Model p-3x1

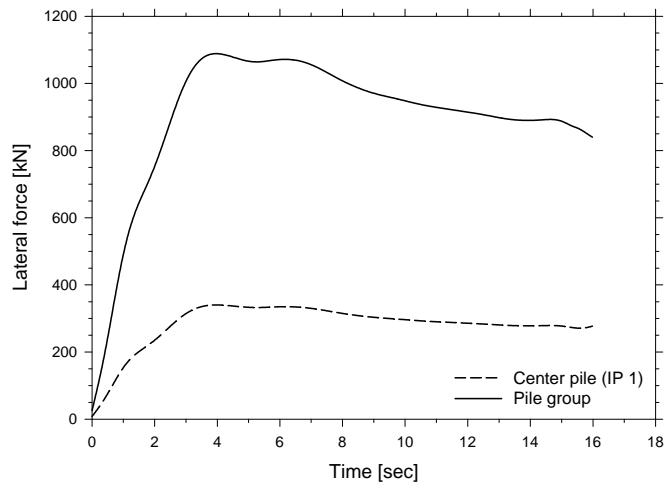


Figure 7.88: Back-calculated lateral force time histories against the piles, Model p-3x1

CHAPTER 8
SUMMARY, ANALYSES AND DISCUSSIONS ON PILE PINNING EFFECT ON
LATERAL SPREADING

8.1 Introduction

A series of four centrifuge tests were conducted at the 150 g-ton RPI centrifuge facility to study the reinforcing or pinning effect the pile groups have on the lateral spreading. The centrifuge models, discussed in detailed in chapter 7, were conducted on a slightly inclined laminar box subjected to in-flight base shaking, and they simulate the case of a nonliquefied crust riding on top of a liquefied sand layer. The prototype profiles consist of a 3 m thick layer of liquefiable Nevada sand on top and below a 3 m thick slightly cemented sand layer. The first centrifuge test (Model p-0) did not include piles and was the benchmark experiment to simulate lateral spreading in the free field. Using a similar setup, the other centrifuge tests simulated the response of a 3x2, 6x2, and 3x1 pile group respectively. The pile groups were connected by a cap and embedded in the three layer soil profile. In this type of soil profiles, the load applied to the foundations is essentially controlled by the top nonliquefiable layer, with the pressure of the liquefied soil being negligible. Therefore, the models were saturated with water instead of viscous pore fluid. The instrumentation within the model consisted of accelerometers and pore pressure transducers placed close and far from the foundations, 9 pairs of strain gages along the instrumented piles, and color sand placed at intermediate elevations within the liquefiable layer as well as in the top cemented layer.

This chapter summarizes the results and trends observed in these four centrifuge tests, providing evidence of the reinforcing effect that pile foundations have on liquefaction induced lateral spreading. An analysis approach based on the back-calculated forces acting on the pile groups is also presented in this chapter. Table 8.1 summarizes the properties and measurements from the centrifuge tests. Conclusions and recommendations are presented in chapter 9.

Table 8.1: Summary of properties and measurements from centrifuge tests

Model	p-0	p-3x2	p-6x2	p-3x1
Pile configuration	No foundation	3x2	6x2	3x1
Pile cap	—	Yes	Yes	Yes
Fluid viscosity (μ_w : viscosity of water)	1	1	1	1
Input acceleration amplitude [g]	0.24	0.24	0.24	0.24
Max. free field displacement [cm]	135	65	23	75
Max. pile cap displacement [cm]	—	43	15	67
Estimated pile cap displacement [cm]	—	41	14	63

Estimated pile cap displacement with the approach presented in section 8.10

8.2 Summary of Soil Accelerations

The measured input acceleration in all four centrifuge tests has a maximum amplitude of 0.24g in prototype units, showing once again the excellent repeatability of the large 1-D shaker. Some of the trends observed from the recorded soil acceleration (Figs. 7.3, 7.15, 7.40 and 7.67) could be summarized as follows: (i) in the loose sand layer the positive amplitude decreased significantly at the beginning of shaking due to the liquefaction process; (ii) in the liquefied layer the records contain large negative spikes due to the dilative behavior of the saturated loose sand during lateral spreading, with the amplitude of the spikes being slightly smaller in the models with less lateral spreading; (iii) in the top cemented layer the records show a considerable drop in amplitude after the first cycle of shaking, indicating dynamic isolation once the loose sand liquefied, and (iv) in the bottom cemented later the acceleration was very similar to the input acceleration, indicating no sliding occurred between this layer and the base of the laminar box.

8.3 Summary of Excess Pore Pressure Development

In order to improve the dissipation process during the tests, small vertical tubes were placed during model preparation at each side of the top cemented layer. Some of the trends observed from the excess pore pressure records (Figs. 7.5, 7.19, 7.44 and 7.71) could be summarized as follows: (i) the loose sand in the free field and pile group area liquefied after a few cycles of excitation, in agreement with the trend exhibited by the acceleration records; (ii) the excess pore pressure kept increasing slightly after the loose sand was liquefied due to the low permeability and the settlement of the top layer; (iii) the dissipation process was slowed by the low permeability and the settlement of the top layer; and (iv) the dissipation process in the pile group area was slightly faster than in the free field (far from the pile groups) due to small gaps developed on the top cemented layer close to the pile groups, as shown in Fig. 8.4.

8.4 Summary of Soil Lateral Displacement and Ground Settlement

Figure 8.1 shows the lateral displacement of the top cemented layer measured in the four centrifuge tests. In all the cases the top layer started displacing as soon as the loose sand liquefied at the beginning of shaking. Once the excitation finished, the lateral displacement stopped immediately, even though the loose sand layer was still liquefied. This phenomenon confirms that the inertia forces due to shaking are necessary for the ground deformation to continue. Figure 8.1 and Table 8.1 illustrate very well the reinforcing effect of pile groups against lateral spreading. In the model without piles (Model p-0), the top layer reached a lateral displacement of 135 cm, whereas in the models with pile groups the top layer lateral displacement was reduced up to 80%. As expected, the largest reduction was in Model p-6x2, where the maximum displacement was only 23 cm. In Model p-3x2 the reduction of lateral spreading was close to 50%. It is interesting that the 3x1 pile group was able to reduce the lateral spreading almost as much as the 3x2 pile group did, even though it did not have the frame effect.

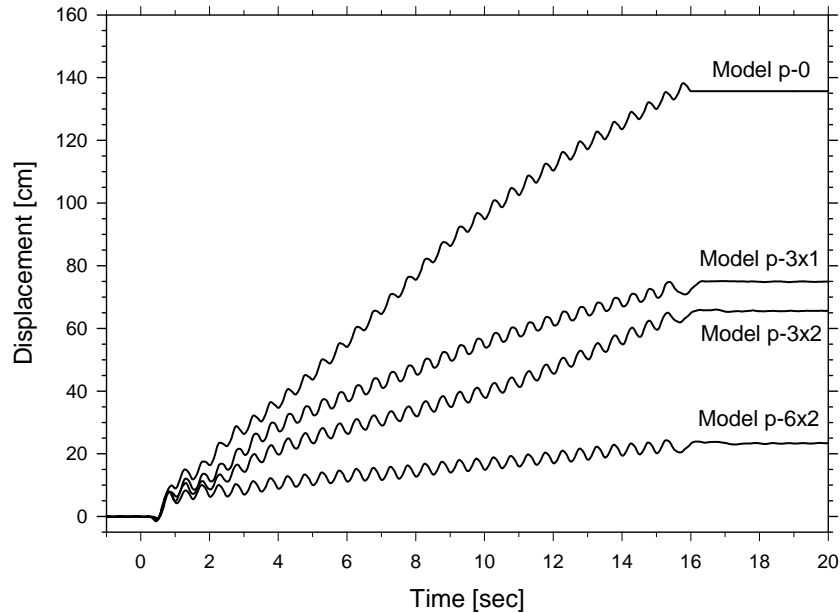


Figure 8.1: Summary of ground surface lateral displacements

Figure 8.2 compares the profiles of soil lateral displacement measured in the four centrifuge tests. As expected, the soil deformation took place in the liquefied layer, with the bottom and top cemented layers behaving as rigid blocks. The profiles show that the lateral displacement of the liquefied layer was significantly affected by the top layer displacement. In Model p-0, it seems that the inertial forces tended to increase the lateral displacement of the top cemented layer. As a result, the top layer started pulling the liquefied sand in the downslope direction, affecting the profile in the top meter within the loose sand layer. On the other hand, as the displacement of the cemented layer was being reduced by the presence of the pile groups, the liquefied sand was pulled back by the top layer. This effect is clearly demonstrated in Model p-6x2, where the maximum displacement took place within the liquefied layer instead of at the ground surface. The profiles also show that the influence of the top cemented layer did not reach the bottom of the liquefiable layer.

Figure 8.3 shows the settlement of the ground surface in three of the four centrifuge tests, as measured with LVDT transducers. In Models p-6x2 and p-3x1 the settlement at the end of excitation was about 7 cm. The vertical movement of the ground surface in Model p-0 was apparently affected by a longitudinal fracture developed in the top cemented layer during the excitation, as previously discussed in section 7.3.4. However, once the consolidation process of the liquefied layer finished, the settlement in the three tests was very similar, showing a good repeatability.

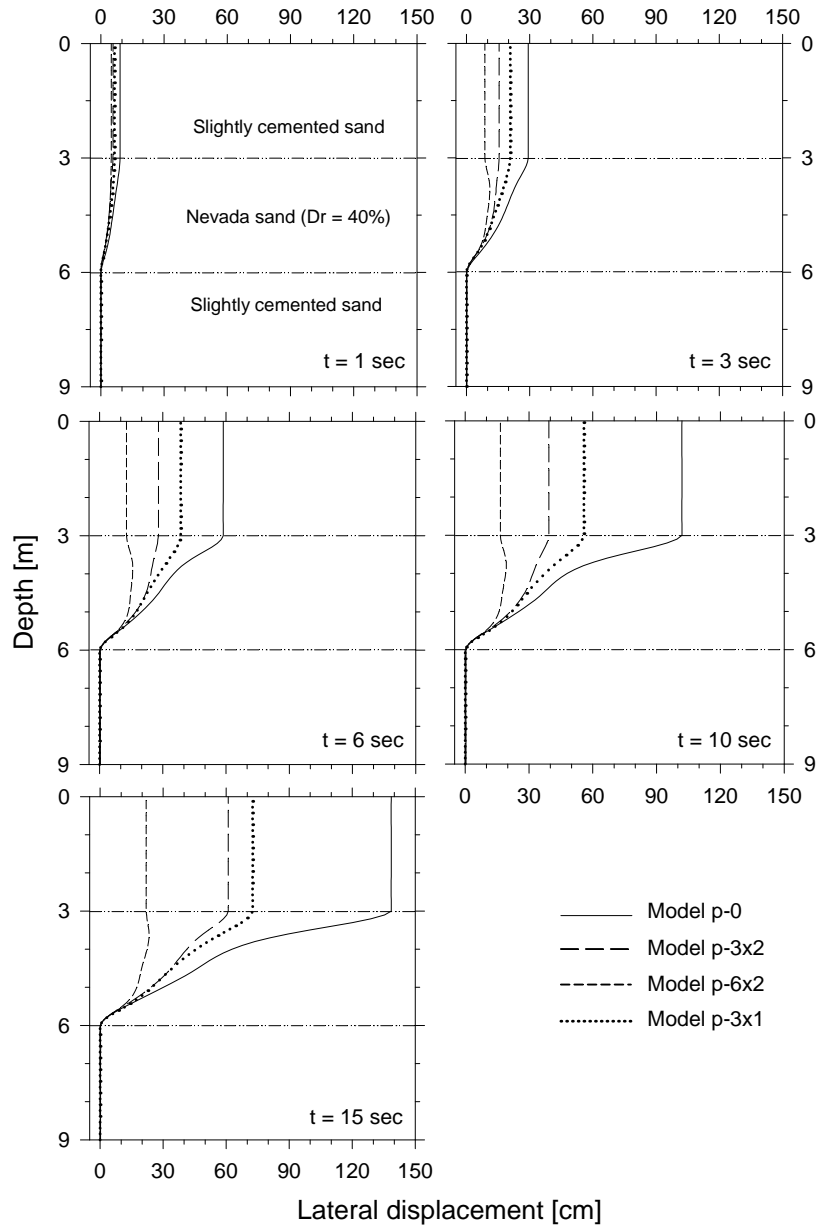


Figure 8.2: Summary of soil lateral displacement profiles

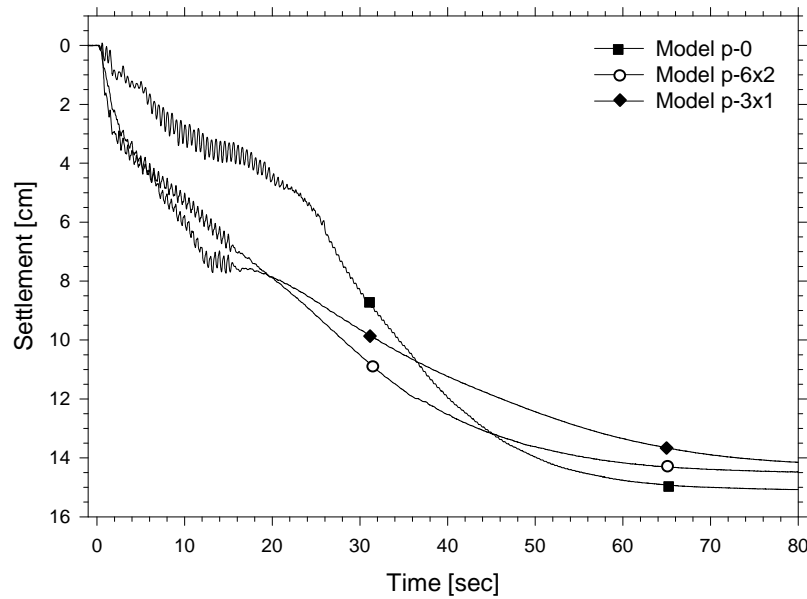


Figure 8.3: Summary of ground surface settlement

8.5 Summary of Soil Condition around Pile Groups

The displacement profiles of the piles were obtained in a first approximation considering only the curvature due to bending moment. However, the estimated lateral displacements differed considerably from the ones measured by the LVDTs during the test. It was very clear that as the piles were very stiff compared to the bottom cemented layer, most of the displacement was caused by pile rotation at the base. This rotation was hence back-calculated by matching the estimated and measured lateral displacements. The displacement profiles of the piles and soil corresponding to Models p-3x2, p-6x2, and p-3x1 are plotted in Figs. 7.25, 7.50 and 7.77 respectively.

Since the top cemented layer moved as a rigid block in the free field, the pile groups tended to stop the soil movement and break the soil around it as soon as the soil movement increased and the piles started rotating at the beginning of shaking. Near the ground surface, the pile caps tended to push into the cemented sand in the downslope direction. This tendency was stronger in Model p-3x1, where the pile group deformed so much that it broke the cemented sand near the surface. On the other hand, the displacement and rotation of the 6x2 pile group was much smaller and the phenomenon was not observed. At deeper elevations within the top cemented layer, the pile groups offered such a large restriction in the upslope direction that they induced a passive failure in the soil.

Figure 8.4 summarizes the soil condition on the ground surface around the pile groups, where the cracks on the upslope side of the pile groups are evidence of the soil passive failures. Moreover, the passive failure planes were clearly identified on the vertical cuts done on the cemented layer after the tests, as shown in Figs. 7.53 and 7.80. On the other hand, the vertical movement of the passive wedge in Model p-3x1 (Fig. 7.78) indicated that the passive failure developed gradually during the excitation, instead of being sudden. As the failure progressed, the top layer in the free

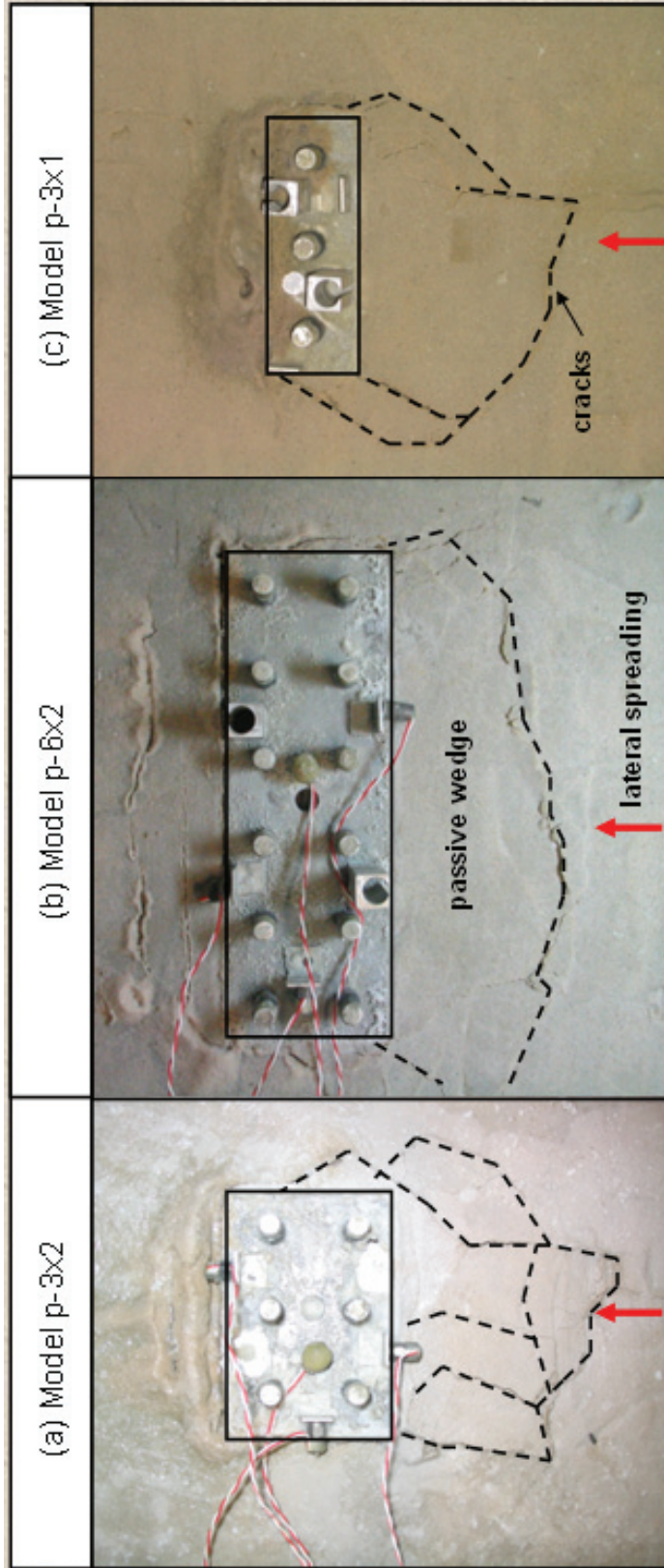


Figure 8.4: Summary of ground surface condition around pile caps

field started displacing more than the pile caps (Figs. 7.25, 7.50 and 7.77), inducing gaps on the downslope side of the pile groups. These gaps served as drainages for the excess pore pressure, as evidenced by the sand boils shown in Fig. 8.4.

8.6 Summary of the Rotational Stiffness Provided by the Bottom Cemented Layer

The rotational stiffness provided by the bottom cemented layer was estimated by dividing the piles bending moment at the base of the liquefiable layer by the rotation of the corresponding piles. Figure 8.5 summarizes the back-calculated rotational stiffness versus bending moment at the base of the liquefiable layer, stiffness that was obtained in sections 7.4.4, 7.5.4 and 7.7.4. After ignoring the indetermination generated by very small rotations of the piles at the beginning of shaking, the rotational stiffness in the elastic range was in the order of 40000 kN-m/rad. In Model p-3x1, the stiffness provided by the cemented sand around each pile decreased gradually up to approximately 20000 kN-m/rad, without showing an excessive lost in strength. In the other models however, the rotational stiffness decreased drastically during shaking, with the bottom cemented sand being able to withstand much smaller bending moments than in Model p-3x1. On the other hand, the fact that the piles behaved linearly under bending moments of at least 800 kN-m, based on the pile calibration tests, support that the rotations at the base were caused by a reduction in the fixation rather than by plastic hinges on the piles.

The huge difference in response between the 3x1 pile group and the other pile groups appears to be related to the frame action. Under relatively small bending moments, the cemented sand around each pile provided support. However, it appears that at some point the cemented sand between the upslope and downslope piles started “moving” with the piles without providing much support. In other words, in terms of bottom fixation each frame of two piles behaved as a single and wider pile.

A similar phenomenon may have happened in the transverse direction, since the back-calculated rotational stiffnesses in the 6x2 pile group are smaller than the ones in the 3x2 pile group. It seems that at some point in time the cemented sand between piles in the transversal direction also started “moving” with the piles, proving less support. The cemented sand next to the external piles was not affected by this phenomenon, hence explaining the difference in response between the 3x2 pile group (4 out of 6 are external piles) and the 6x2 pile group (4 out of 12 are external piles). The fact that the maximum bending moment in the external pile in the 3x1 pile group was about 15% larger than in the center pile tends to support this hypothesis, as shown in Fig. 7.84.

It is interesting also to highlight that the rotational stiffness provided to the downslope piles was considerably larger than that provided to the upslope piles, as shown in Fig. 8.5. This difference in response seems to be related to the fact that the upslope piles were under tension, and therefore the cemented sand around them was being unloaded in the vertical direction hence providing less confinement.

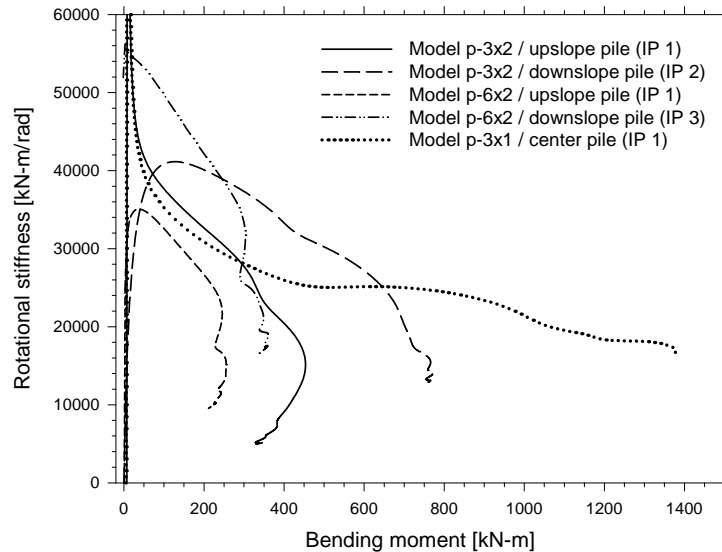


Figure 8.5: Back-calculated rotational stiffness provided by the bottom cemented layer versus bending moment at the base of the liquefiable layer

8.7 Summary of Bending Moments

Figure 8.6 summarizes the profiles of bending moments obtained in the centrifuge tests, after filtering out the cyclic component. The profiles correspond to the upslope and downslope piles from the 3x2 and 6x2 pile groups, and the center and external piles from the 3x1 pile group. The most important trends and findings are that: (i) at the very beginning of the excitation the cemented sand around the piles was in the elastic range, with the upper and lower bending moments being very similar; (ii) once the passive failure started developing after a few seconds of shaking the upper bending moments started decreasing; (iii) in the 3x1 pile group the upper bending moments decreased down to zero once the passive failure allowed the pile head to rotate; (iv) the pseudo p - Δ effect increased the bending moments in the downslope piles and decreased the moments in the upslope piles, as the pile group displacement was increasing; and (v) at all times the bending moment varied essentially linearly within the loose sand layer, indicating that the pressure applied by the liquefied soil was negligible compared to the one applied by the top cemented layer.

8.8 Summary of Lateral Resistance against Pile Groups

In order to further investigate the soil-pile-group interaction during lateral spreading, back-calculated lateral resistances against the piles were obtained from the bending moment distributions. As discussed in sections 7.4.8 and 7.5.9, the axial force did not have a significant effect on the lateral resistance and therefore was not considered in the analyses. Figure 8.7 summarizes the lateral resistance profiles obtained for the 3x2, 6x2, and 3x1 pile groups.

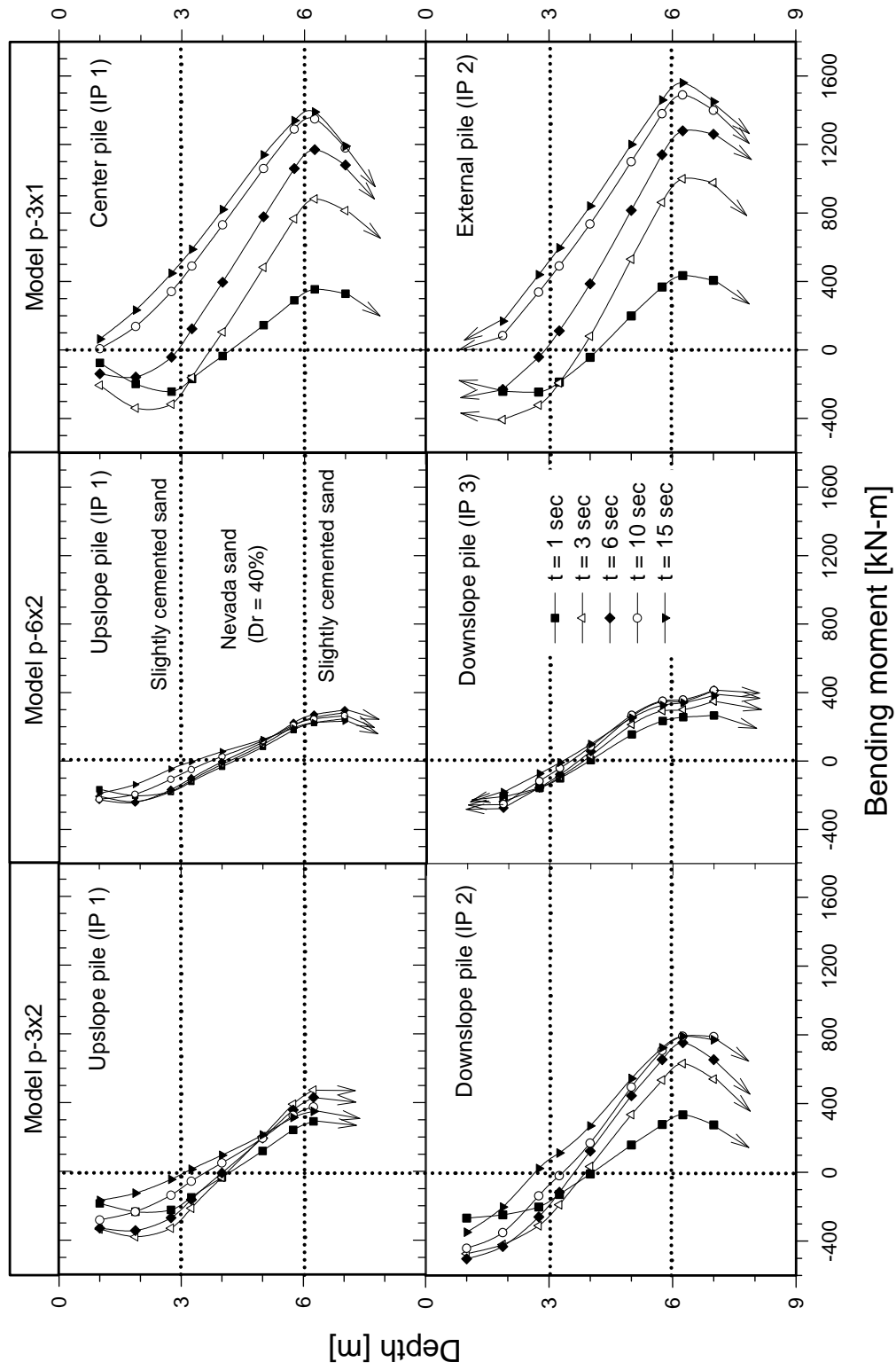


Figure 8.6: Summary of bending moment profiles

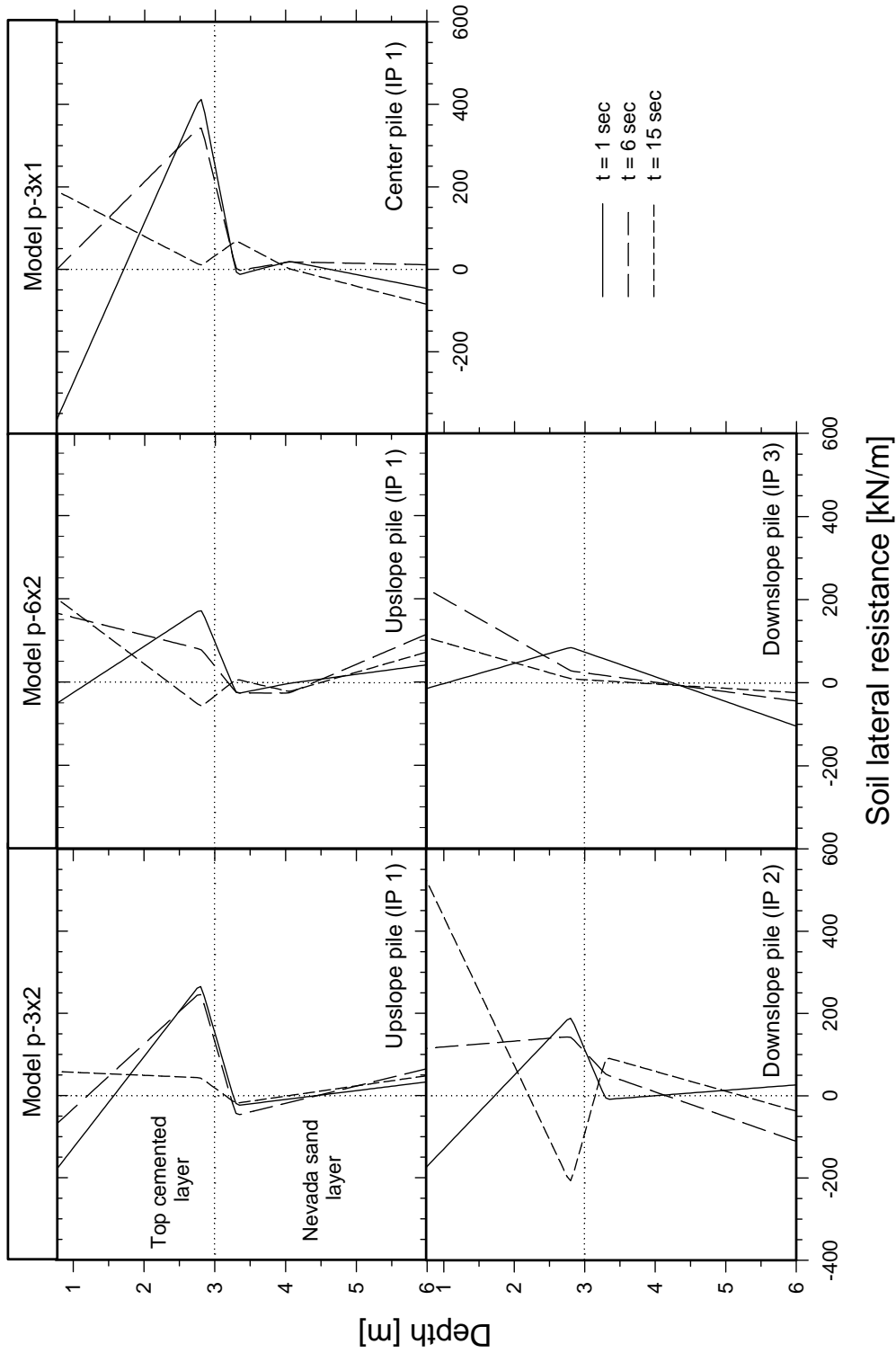


Figure 8.7: Summary of back-calculated lateral resistance profiles

As expected, the lateral resistance of the liquefied sand was very small compared to that of the top cemented layer. At the very beginning of the excitation, the soil resistance in the top cemented layer varied linearly from positive values at the bottom of this layer to negatives ones near the ground surface, with the positive and negative values corresponding to the elastic resistance of the cemented sand to the pile rotation. The magnitude of these values was proportional to the degree of pile rotation, with the largest values in the 3x1 pile group and the smallest ones in the 6x2 pile group. Actually, since the rotation of the 6x2 pile group was very small at the beginning, the soil resistance increased linearly with depth, being consistent with a regular lateral soil pressure profile.

Once the gaps developed on the downslope side of the pile groups, the negative lateral resistance was reduced significantly. As the passive failure progressed and the confinement provided by the bottom cemented sand dropped, the lateral resistance decreased.

8.9 Summary and Analyses of Lateral Forces against Pile Groups

The force time history applied by the top cemented layer against a single pile was obtained by integrating the lateral resistance along the top cemented layer for each time instant. Following the approach discussed in sections 7.4.8, 7.5.9. and 7.6.9, the lateral force time histories against the pile groups were obtained and plotted in Fig. 8.8. The forces increased quickly, reaching a maximum value after about 4 sec of shaking. Afterwards, the forces decreased to some extent until the end of shaking. The maximum force against the 3x2 pile group was significantly larger than the one in the 3x1 pile group; however at the end of shaking both lateral forces reached the same residual value.

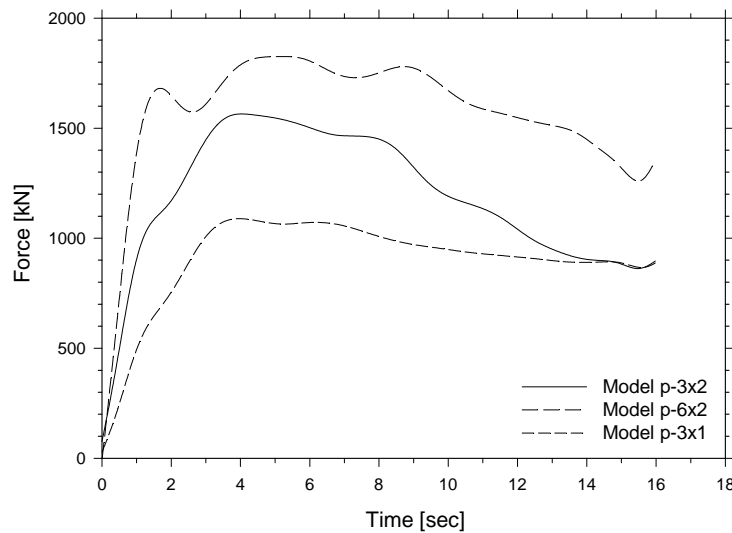


Figure 8.8: Summary of back-calculated lateral force time histories

Figure 8.9 shows the back-calculated lateral force versus the pile cap lateral displacement for the 3 pile groups. These curves exhibit the typical behavior of loading tests. The stiffer the structural system, the larger is the load and the more brittle is the failure, as in the case in Model p-6x2. The 3x1 pile group on the other hand was able to withstand less load, although its behavior was

more ductile. As expected, the response of the 3x2 pile group was in between these two cases. In order to compare these curves (Fig. 8.9) in the linear-elastic range, the forces in the 6x2 and 3x1 pile groups were normalized with respect to the one in the 3x2 pile group. Since at the very beginning of the excitation the passive failure had not yet developed and the top layer was still a rigid block around the piles, the pile caps were not playing any role. For that reason, the force against the pile groups should be proportional only to the number of piles. Therefore, the force against the 6x2 pile group was divided by 2 and the force acting on the 3x1 pile group was multiplied by 2. Figure 8.10 presents these normalized lateral forces versus the pile cap lateral displacements. The normalized stiffness in the linear-elastic range is practically the same in the three cases, validating the hypothesis that at the very beginning of shaking the lateral stiffness was proportional to the number of piles.

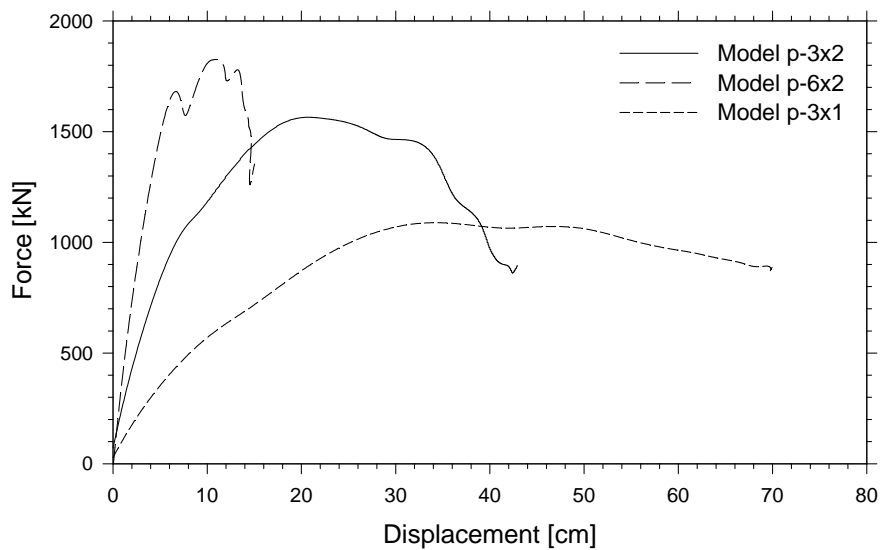


Figure 8.9: Back-calculated lateral force versus pile cap lateral displacement

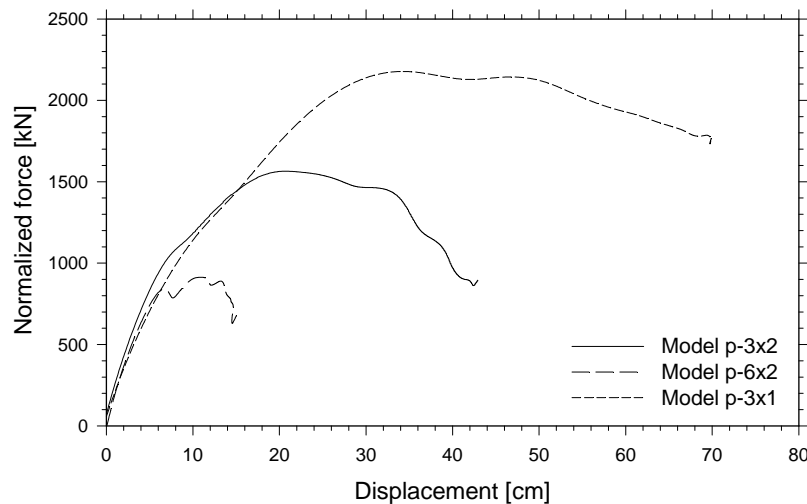


Figure 8.10: Normalized lateral force versus pile cap lateral displacement

Based on Fig. 8.10, it is possible to infer that at the very beginning of shaking the shear strength of the cemented sand was so large that the force was controlled by the pile group stiffness. However, as the confinement of the bottom cemented sand was being reduced and the passive failure started developing in the upper cemented layer, the lateral stiffness of the pile groups started decreasing. At some point during shaking the soil was not able to withstand more stresses and the forces started decreasing as well. As the passive failure kept developing and the corresponding shear strains were increasing, it appears that the cementation along the passive plane started disappearing. Finally, the passive force decreased up to a “residual” value controlled by the residual strength of the soil without cementation and by the effective area corresponding to the passive wedge. In order to support this hypothesis, the “residual” passive force (P) against the 3x1 and 3x2 pile groups was estimated as a first approximation using the Rankine theory, as follows:

$$P = \frac{1}{2} \cdot \gamma' \cdot h^2 \cdot \tan^2(\theta) \cdot w \quad [8.1]$$

where γ' is the buoyant unit weight, h is the height of the top cemented layer, θ is the angle of the failure plane with respect to the vertical, and w is the effective width of the pile group subjected to the passive pressure. The value of θ used in this analysis was 57° , corresponding to the average of the angles measured in the vertical cuts after the tests, as shown in Fig. 7.53 and 7.80 (56° in Model p-3x1 and 58° in Model p-6x2). In order to consider the vertical sides of the passive wedges, an effective width of 1.5 m at each side of the pile group was added to the 5 m width of the pile cap. This approximation gives a passive force of 980 kN, very close to the 900 kN back-calculated in both pile groups at the end of shaking. In the 6x2 pile group each side of the passive wedge was also considered as an additional effective width of 1.5 m, giving a total effective width of 13 m. This dimension is almost 1.6 times the effective width in the 3x1 and 3x2 pile groups, which is very close to the ratio of residual forces $1300/900 = 1.45$ (Fig. 8.8), supporting the analyses.

Figure 8.11 shows the relative displacement between the pile cap and the ground surface, obtained by subtracting the pile cap lateral displacement from the top cemented layer displacement, after filtering out the cyclic component. Figure 8.12 shows the back-calculated force presented in Fig. 8.8 versus the relative displacement between the pile cap and the ground surface. The forces in the 3x2 and 6x2 pile groups increased practically with no relative displacement. However, as soon as the passive failure started developing, the forces started decreasing as well. In Model p-3x1 the negative relative displacement is related to the snapping of the pile group into the cemented sand in the downslope direction, as shown in Fig. 7.77.

8.10 Analysis of Pile Pinning Effect

As previously discussed in chapter 1, the Newmark approach involves a series of assumptions like the magnitude of the shear strength of the liquefied soil, and sliding occurring within a known plane. Besides, in order to implement the pinning effect, the pile shear forces at the location of the failure plane have to be represented as an equivalent shear strength. Trying to implement the Newmark approach for our centrifuge tests proved to be difficult and uncertain. Therefore, it was decided to continue the analyses with the back-calculated forces and lateral displacement measurements.

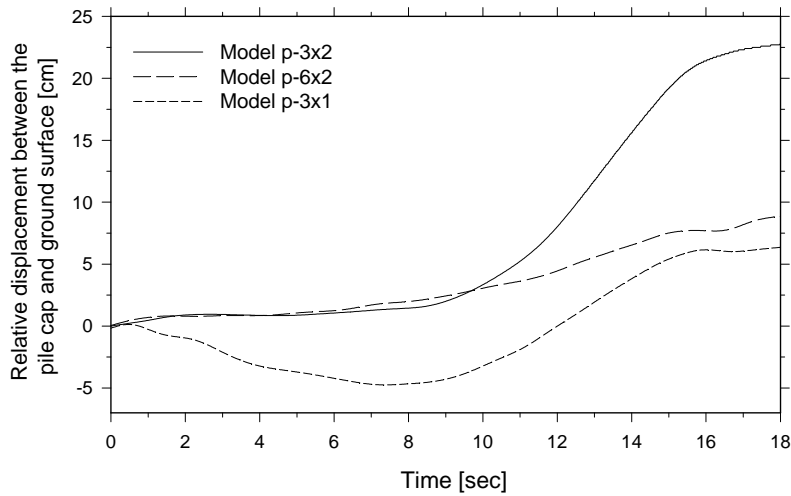


Figure 8.11: Relative displacement between the pile cap and ground surface time histories

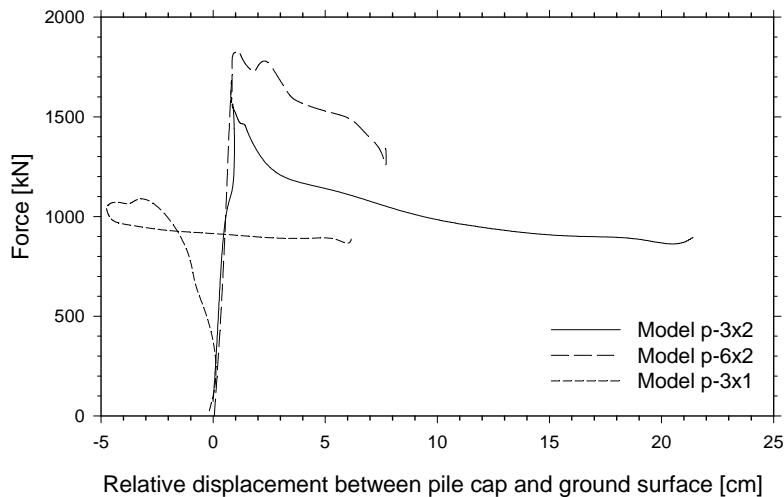


Figure 8.12: Lateral force versus relative displacement between pile cap and ground surface

Figure 8.13 summarizes the reduction of lateral spreading time histories with respect to the free field condition. These curves were obtained by subtracting the ground surface lateral displacement of the models involving piles from the one measured in the free field condition (Model p-0), after filtering out the cyclic component. As expected, the largest reduction was in Model p-6x2 and the smallest one in Model p-3x1. In the first 4 sec the reduction seems to be proportional to the pile group stiffness. However, once the passive failure developed, the additional reduction seems to become proportional to the effective width subjected to the passive pressure.

The response of the centrifuge models is now analyzed using a superposition approach. First, the pile cap is assumed to displace the same amount as in the free field (Model p-0), offering no

restriction to the lateral movement. Then, the back-calculated force time history against the pile group is applied against the top cemented layer, moving the pile group back to its actual position at the end of shaking. This pile cap movement is in other words the reduction of lateral spreading (presented in Fig. 8.13) plus the relative displacement between the pile cap and the ground surface (presented in Fig. 8.11). Figure 8.14 shows this relative displacement between pile cap and ground surface in the free field condition versus time in the three centrifuge models. The amount the pile cap moved back is related to the pile group force applied to the top cemented layer. Moreover, the longer the force is applied, the longer the displacement should be. The pile force applied against the top layer (Fig. 8.8) was hence integrated in time for the three cases and is plotted in Fig. 8.15. Figure 8.16 shows the integrated force in time versus the relative displacement between the pile cap and ground surface in the free field condition (presented in Fig. 8.14) for the three pile groups, showing an excellent linear correlation between these two parameters.

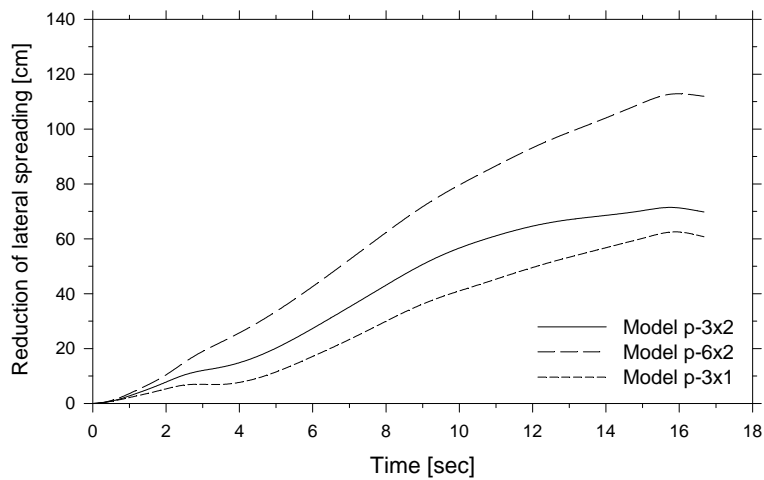


Figure 8.13: Reduction of lateral spreading time histories

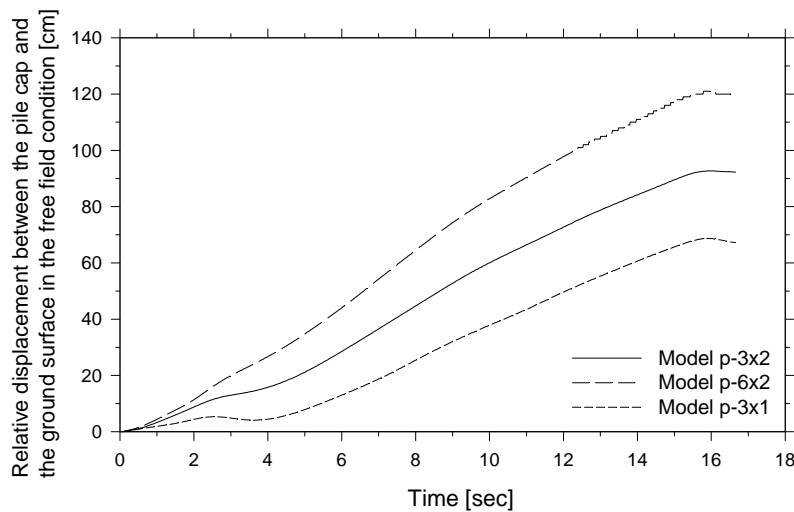


Figure 8.14: Relative displacement between the pile cap and the ground surface in the free field condition (Model p-0) time histories

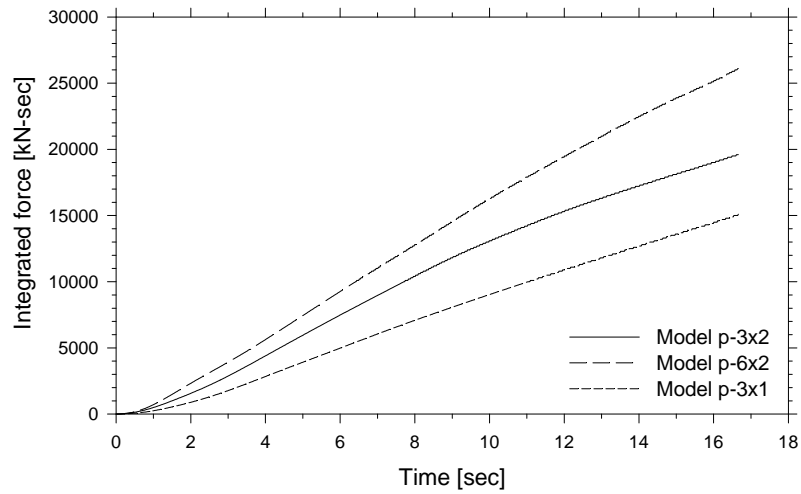


Figure 8.15: Integrated force (over time) time histories

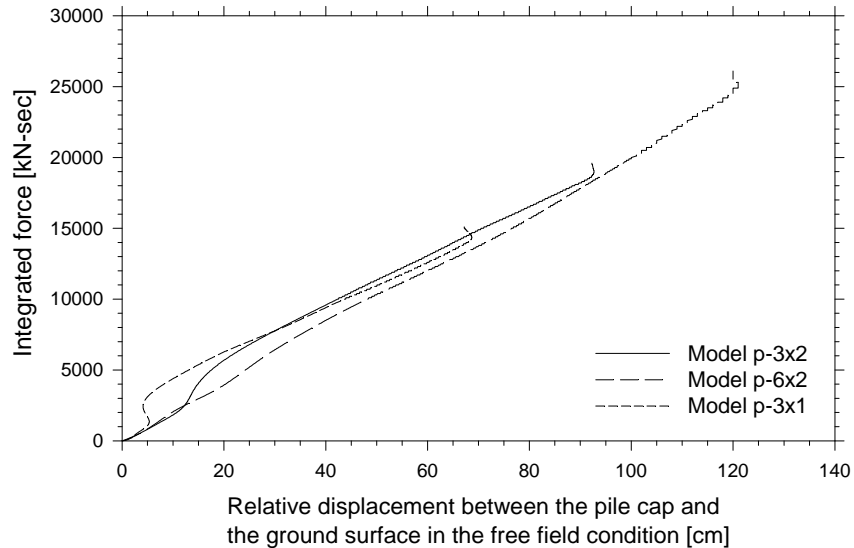


Figure 8.16: Integrated force (Fig. 8.15) versus relative displacement between the pile cap and the ground surface in the free field condition (Fig. 8.14)

Given the fact the ground surface lateral displacement in the free field condition (Model p-0) is known, this correlation could be used to estimate the lateral displacement of other pile group configurations for the same soil setup. Moreover, assuming a small passive failure displacement, it would be possible to estimate the reduction in lateral spreading of the ground surface.

Consequently, in order to estimate the pile group displacement, the force-time history against the pile group is needed. Unfortunately, it is not possible to obtain directly the force time history, unless the pile group is subjected to the lateral spreading induced by the same input shaking. On the other hand, a force versus displacement curve, like the ones of Fig. 8.9, is not easy to obtain. These are not typical push-over curves since the force against the pile group is also controlled by

the cemented sand resistance, explaining the reduction in force during shaking. Even in the case of estimating a force versus displacement curve, the pile cap displacement time history is still needed in order to obtain the force-time history.

To compare the pile cap displacement time histories of the three pile groups, they were normalized with respect to their maximum values at the end of shaking, as shown in Fig. 8.17. Considering the large difference in pile group stiffness between the 3x1 and 6x2 pile groups, the difference in the normalized curves is not that significant.

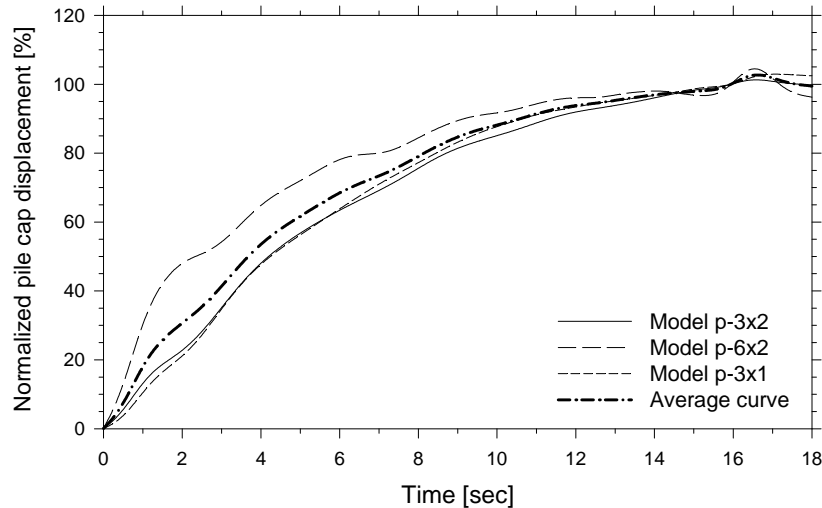


Figure 8.17: Normalized pile cap lateral displacement time histories

As an approximation, it can be assumed that a pile group with a lateral stiffness between the ones of the 3x1 and 6x2 pile groups will have a normalized pile cap lateral displacement similar to the average curve, as shown in Fig. 8.17. Therefore, the only additional curve needed for the analysis is a force versus displacement curve. For the approach presented below, the linear correlation between the integrated force in time and the “relative displacement between the pile cap and ground surface in the free field” was obtained only with the maximum value of the 6x2 pile group curve (25000 kN-sec, 120 cm) of Fig. 8.16, passing through the origin. This approach however is useful only for conditions similar to the ones of the centrifuge tests, like profile, soil properties, ground inclination, and input motion. More than a predictive tool, this can be used as a sensitivity analysis to investigate the reinforcing effect pile groups have on the reduction of lateral spreading. A simplified iterative analysis is described below and is illustrated in Fig. 8.18.

1. The average curve in Fig. 8.17 is assumed as normalized pile cap displacement.
2. Assuming a maximum pile cap displacement at the end of the excitation (trial), the pile cap displacement time history is obtained by multiplying the normalized curve by the trial value.
3. The pile cap displacement for a certain time instant is used in the force versus displacement curve to estimate the force at that time.

4. The force-time history curve against the pile group is obtained by repeating step 3 for the whole duration of the excitation (using a small computer subroutine).
5. The force-time history is integrated in time.
6. Using the integrated force in time at the end of shaking in the linear correlation, the relative displacement between the pile cap and ground surface in the free field (Δp_g) can be estimated.
7. The calculated pile cap displacement is obtained by subtracting the estimated Δp_g from the maximum ground surface lateral displacement in the free field condition (Model p-0).
8. The process is repeated from step 2 increasing the trial with a small increment until the calculated pile cap displacement is equal to the trial value.

In order to verify this approach, the 3x1 pile group displacement was estimated following the approach presented above. Using the force versus displacement curve shown in Fig. 8.9 and the average normalized pile cap displacement curve instead of the measured one (Fig. 8.17), the predicted pile cap displacement is 63 cm, as illustrated in Fig. 8.19, compared to 67 cm measured in Model p-3x1. Considering that the linear correlation was obtained with the value of the 6x2 pile group and that the average curve was used as normalized pile cap displacement, the prediction is very good. Following the same approach, the predicted displacement of the 3x2 pile group is 41 cm, in very good agreement with 43 cm measured in Model p-3x2.

Since the 3x1 pile group proved to be very efficient in reducing lateral spreading, two 3x1 pile groups seems like an interesting configuration, separated long enough to avoid any influence within the cemented sand layers. In this particular case the force versus displacement curve would be the one obtained in the 3x1 pile group, but multiplied by a factor of 2. The estimated pile group displacements using the analytical approach above is 23 cm, much smaller than the 3x2 pile group displacement.

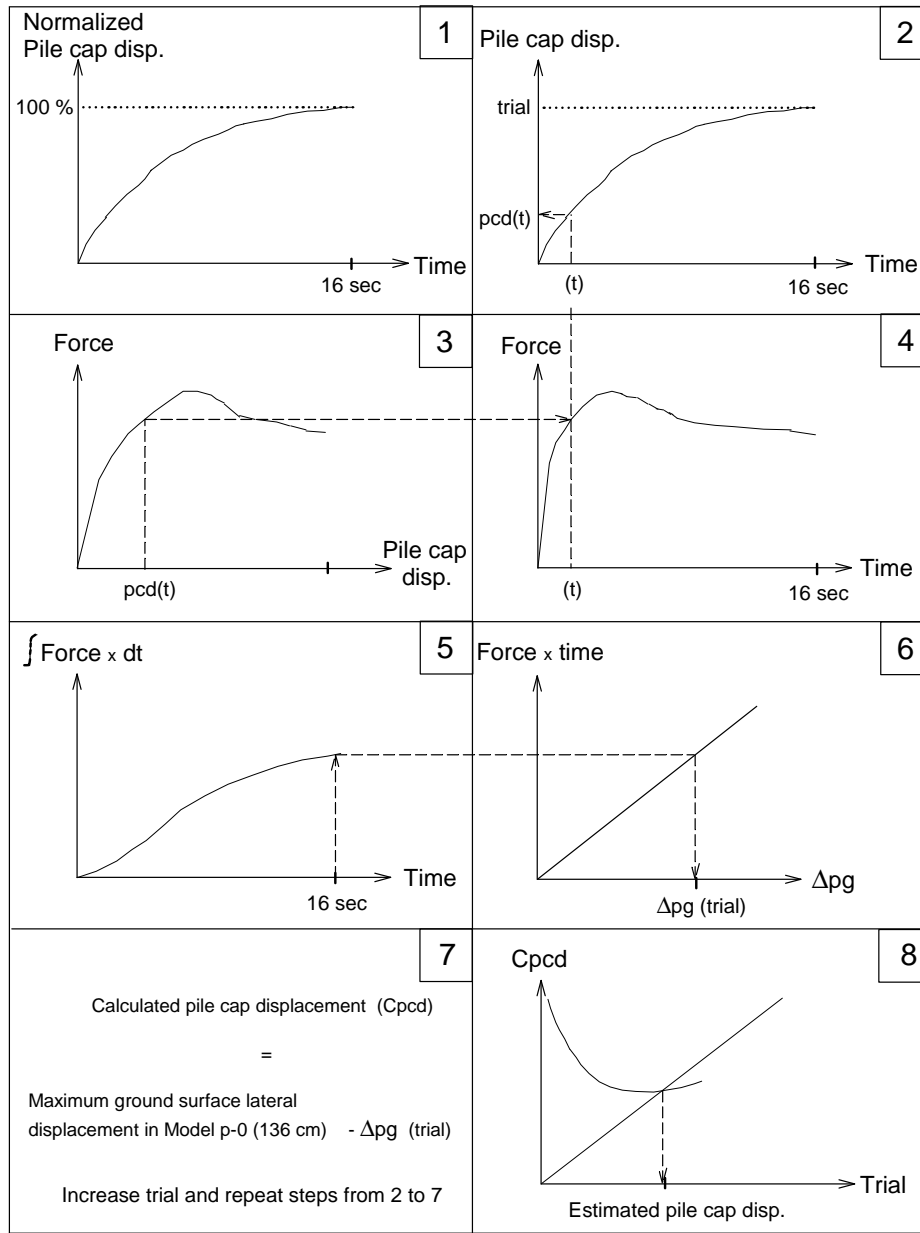


Figure 8.18: Steps to estimate the pile cap displacement, (Δpg corresponds to the relative displacement between the pile cap and the ground surface in the free field)

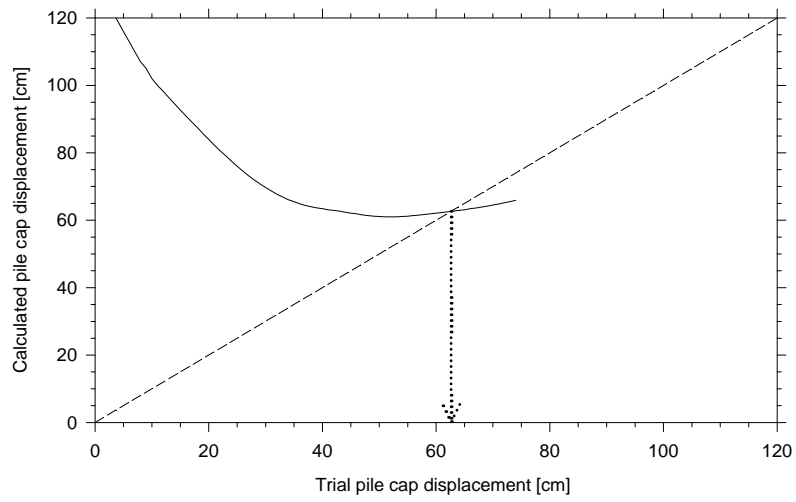


Figure 8.19: Iteration curve to estimate the 3x1 pile group lateral displacement

SECTION 9 CONCLUSIONS AND RECOMMENDATIONS

9.1 Soil Permeability Effect on Pile Response to Lateral Spreading

9.1.1 Conclusions

Liquefaction-induced lateral spreading continues to be a major cause of damage to deep foundations. A series of six centrifuge tests were conducted at the 150 g-ton RPI centrifuge to investigate the effect of soil permeability on the response of single piles and pile groups to lateral spreading. The most relevant conclusions based mainly on the summary and discussions presented in chapter 6 are:

- Even though the free field ground surface deformation was very similar in all six tests, in the models with a higher permeability the shear strains tended to decrease with depth, whereas in the models with a lower permeability the shear strains tended to increase with depth. This phenomenon appears to be related to a reduction in pore pressure near the bottom of the liquefiable layer in the water-saturated models due to the fast dissipation process, as well as to the reduction in pore pressure near the ground surface in the models saturated with viscous fluid due to shear strains developed under low confinement.
- In the high permeability models (water-saturated) the pile lateral displacements and associated bending moments reached a maximum value after a few seconds of shaking, decreasing afterwards. However, in the low permeability models (saturated with viscous fluid), the pile lateral displacements and associated moments increased gradually, reaching at the end of the excitation values as large as 6 times the ones observed in the models saturated with water.
- The reduction in lateral stress on the downslope side of the piles, as well as large shear strains with a dilative response of the liquefied soil close to the foundations, seems to have been responsible for the development of negative increments of pore pressure near the piles. In the water-saturated models the soil permeability was so high that water flowed fast from the free field, dissipating these negative increments. However, in the low permeability models that simulate a fine sand layer the fluid was not able to flow fast enough from the free field to dissipate these negative increments, allowing a stiff zone of high effective stress to develop and expand during shaking, particularly at shallow elevations. The pore pressure records, pattern of colored sand and visual animations indicate that this nonliquefied zone had the approximate shape of an inverted cone, wider near the surface and decreasing with depth.

- In the high permeability models that simulate a coarse sand layer, the liquefied sand moved around the individual piles, affecting the soil pattern close to the piles themselves. On the other hand, in the low permeability models (saturated with viscous fluid), the soil flowed around the whole foundation, affecting the soil pattern up to a considerable distance at both sides. The comparison of soil deformation patterns at different elevations suggests that the affected zone around the foundations also had an inverted conical shape. This observation suggests that as the excess pore pressure was decreasing around the foundation, the soil was becoming stiffer and the liquefied soil in the free field had to move around it.
- The limit equilibrium analyses proved that considering the liquefied soil pressure acting on the foundations and on the nonliquefied zone was a valid assumption, since the estimated bending moments and pile displacements were in very good agreement with the measured ones. The estimated liquefied soil pressures agrees very well with the one obtained by Abdoun (1997). The larger effective area subjected to the liquefied soil pressure in the models with lower permeability would explain the larger pile displacements and bending moments, as well as the lack of rebound of the piles.
- This study suggests that the bending moments and lateral displacements for a pile foundation installed in silty sand in the field could be much higher than those measured in the same foundation installed in clean sand, due to the lower permeability of the silty sand.

9.1.2 Recommendations

Engineering recommendations based directly on the results and trends observed in the centrifuge tests are:

- Centrifuge modeling of soil-pile interaction is very useful for studying the effects of liquefaction hazard on deep foundations, as well as to calibrate analytical models.
- Soil permeability is an important factor that should be considered when estimating the design loads acting on pile foundations subjected to lateral spreading.

The author would like to recommend the following future work:

- Additional centrifuge testing with drains around the foundation to avoid or mitigate the development of a nonliquefied stiff zone, hence reducing the displacement and bending moments of the piles
- Conduct comparisons with 1g full-scale prototype tests to find out the viscosity of the pore fluid that better simulates the pile foundation response to lateral spreading.

- Additional centrifuge testing varying the g-level and pore fluid viscosity to conduct modeling of models, aimed at clarifying the issue of the correct pore fluid viscosity/time scaling law.
- Additional centrifuge testing to investigate the strain rate effect in the increase of pile displacement and bending moments, related to the decrease in excess pore pressure close to the foundations.
- Use of micro-mechanical numerical simulations, developed recently at RPI to analyze the micro-scale pore fluid flow and solid phase deformation of saturated cohesionless soils, to further investigate the complex soil-fluid interaction around the pile foundations.
- Additional centrifuge testing using advance sensors to provide additional information and a higher resolution picture of the system response, such as high speed cameras, fiber-optic/MEMS shape-acceleration sensors, and flexible sheets of tactile pressure sensors.
- Additional centrifuge testing and analyses to further refine the limit equilibrium used in this study.

9.2 Pile Pinning Effect on Lateral Spreading

9.2.1 Conclusions

The vulnerability of highway bridges to earthquake-induced ground failures arising from liquefaction has been clearly demonstrated by the extensive damage observed in past earthquakes. Liquefaction induced lateral spreading may be reduced by the restraining forces provided by pile group foundations. This reduction in lateral displacement in fact reduces the loads and displacement demands that are imposed on the piles. A series of four centrifuge tests were conducted at the 150 g-ton RPI centrifuge facility to study the reinforcing or pinning effect pile groups have on lateral spreading. The most relevant conclusions based mainly on the summary and discussions presented in chapter 8 are:

- This work clearly demonstrates that centrifuge modeling of soil-pile interaction during liquefaction is both realistic and useful. Consistent results were obtained from all four centrifuge tests, which provided detailed information about pile foundation response subjected to lateral spreading with a nonliquefied crust riding on top of the liquefied soil.
- No plastic hinges developed in the piles; in fact, the top cemented sand failed first, as evidenced by the cracks on the ground surface corresponding to the passive failure developed in front of the pile groups. The colored cemented sand was very helpful to visualize the passive failure planes. Even though cracks developed on the downslope side of the pile groups, no apparent active or passive type of failure were observed in the vertical cuts.

- At the very beginning of the excitation, before the cemented sand had failed around the pile groups, the lateral stiffness of the pile groups was directly proportional to the number of piles, with the pile caps playing minimum role. Moreover, the lateral force applied by the top cemented layer was controlled by the pile group stiffness.
- The final passive force against the pile groups was controlled by the residual strength of the soil without cementation in conjunction with the effective area corresponding to the passive wedge.
- As the pile models used were very rigid compared to the cemented sand, most of the pile group deformation was caused by rotation at the base of the piles. The 3x1 pile group was more efficient in the reduction of lateral spreading since the bottom cemented sand around the line of piles provided a much better confinement than the one around the pile groups developing a frame effect (3x2 and 6x2 pile groups).
- As expected, the largest reduction of lateral spreading was caused by the 6x2 pile group and the smallest one by the 3x1 pile group. Before the soil had failed, the reduction seems proportional to the pile group stiffness. However, once the passive failure developed, the additional reduction seems to be more proportional to the effective area subjected to passive pressure.
- The liquefied soil pressure was negligible compared to the one applied by the top cemented sand, as clearly evidenced in the back-calculated lateral resistance along the piles.
- Except for the 3x1 pile group at the end of shaking, the pile groups were subjected to double curvature. The maximum bending moments at the lower part were measured close to the boundary between the liquefied and bottom cemented layer, with this position moving down as the confinement around the piles was lost. The maximum bending moments at the upper part were measured within the top cemented layer, with this position moving up as the passive failure developed.
- In the 3x2 and 6x2 pile groups, the measured bending moments were larger in the downslope piles compared with the upslope piles due to a pseudo $p-\Delta$ effect, which tended to increase the bending moments in the downslope piles and decrease the moments in the upslope piles as the pile group displacement increased.
- The analytical approach presented in this study proved to be very useful in understanding the reinforcement effect pile groups have in liquefaction-induced lateral spreading, as well as to give a good estimation, at least in the centrifuge models considered, of the expected pile group deformations.

9.2.2 Recommendations

Engineering recommendations based directly on the results and trends observed in centrifuge tests are:

- The reduction in lateral spreading due to the pinning effect should be considered in analyses when designing pile foundations.
- The separation between piles should be large enough to ensure that the confinement around the piles does not decrease significantly due to the frame effect.
- If pinning piles are used as remediation technique (passive piles), the capacity of the piles should be just slightly larger than the capacity of the soil so as to optimize the design.
- The liquefied soil pressure can be neglected in the analyses when a nonliquefied crust rides on top of the liquefied soil.
- The end-bearing soil layer should provide enough vertical support for the large axial forces that can be generated during lateral spreading, so that the frame action can act and significantly reduce pile bending moments and lateral displacements. The pile-cap connections should be also carefully design for the large bending moments and axial forces induced by lateral spreading.
- The $P-\Delta$ effect should be considered in the analyses, since it may increase considerably the bending moments in the downslope piles.

The author would like to recommend the following future work:

- Additional centrifuge testing with different pile group configurations to provide a better understanding of the pile pinning effect, and to check the correlation presented in this work (Fig. 8.16).
- Additional centrifuge testing with different pile spacing to find out the optimum distance between piles so the confinement at the base is not affected by the frame effect.
- Additional centrifuge testing with different pile bending stiffnesses to find out the optimum value so that pile deformation by rotation and curvature is minimized.
- Further evaluations of the approach presented in section 8.10 in order to propose engineering recommendations for quantitative evaluation of pile pinning effect in the field.
- Additional centrifuge testing with a different setup so that the Newmark approach can be directly implemented and analyzed.

CHAPTER 10 REFERENCES

- Abdoun T. (1997), "Modeling of seismically induced lateral spreading on multi-layered soil and its effect on pile foundations," Ph.D. Thesis, Rensselaer Polytechnic Institute, Troy, NY, USA.
- Abdoun, T., and Dobry, R. (2002), "Evaluation of pile foundation response to lateral spreading," *Soil Dynamics and Earthquake Engineering*, 22 (9-12), pp. 1051-1058.
- Abdoun, T., Dobry, R., O'Rourke, T. D., and Goh, S. H. (2003), "Pile response to lateral spreads: centrifuge modeling," *Journal of Geotechnical & Geoenvironmental Engineering*, 129 (10), pp. 869-878.
- Adalier, K. (1996), "Mitigation of earthquake induced liquefaction hazards," Ph.D. Thesis, Rensselaer Polytechnic Institute, Troy, NY, USA.
- Arulanandan, K., Thompson, P. Y., Kutter, B. L., Meegoda, N. J., Muraleetharan, K. K., and Yogachandran, C. (1988), "Centrifuge modeling of transport processes for pollutants in soils," *Journal of Geotechnical Engineering*, ASCE, Vol. 114, No. 2, pp. 185-205.
- Arulanandan, K., and Scott, R. F. (eds.) (1993), "Verification of numerical procedures for the analysis of soil liquefaction problems," *International Conference*, Davis, CA, USA, Vol.1, Balkema, Rotterdam.
- Arulmoli, K., Muraleetharan, K. K., Hossain, M. M., and Fruth, L. S. (1992), "Verification of liquefaction analysis by centrifuge studies laboratory testing program soil data," *Technical Report*, The Earth Technology Corporation, Irvine, CA, USA, 404 pages.
- Ashour, M., and Norris, G. (2003), "Lateral loaded pile response in liquefiable soil," *Journal of Geotechnical and Geoenvironmental Engineering* 129(5), pp. 404-414.
- Berrill, J. B., Christensen, S. A., Keenan, R. P., Okada, W., and Pettinga, J. R. (1997), "Lateral-spreading loads on a piled bridge foundation," *Proc. Special Technical Session on Earthquake Geotechnical Engineering*, XIV Intl. Conf. Soil Mechanics and Foundation Engineering, Hamburg, pp. 173-183.
- Berrill, J. B., Christensen, S. A., Keenan, R. P., Okada, W., and Pettinga, J. R. (2001), "Case study of lateral spreading forces on a piled foundation," *Geotechnique* 51, pp. 501-517.
- Berrill, J. B., and Yasuda S. (2002), "Liquefaction and piled foundations: some issues," *Journal of Earthquake Engineering*, Vol.6 Special Issue 1, pp. 1-41.
- Boulanger, R. W., Chang, D., Gulerce, U., Brandenburg, S. J., and Kutter, B. L. (2005), "Evaluating pile pinning effects on abutments over liquefied ground," *Workshop on Pile Foundations in Liquefied and Lateral Spreading Ground*, University of California at Davis, Davis, CA, USA.

- Castro, G. (1987), "On the behavior of soils during earthquakes-liquefaction," *Soil Dynamics and Liquefaction*, Cakmak A. S. (ed.), Elsevier Science Pub., Amsterdam, pp. 169-204.
- De Alba, P., and Ballesterio, T. P. (2004), "Residual strength after liquefaction: a rheological approach," *Proc. of the 11th International Conference on Soil Dynamics and Earthquake Engineering*, Vol. 2, pp. 513-520.
- Dewoolkar, M. M., Ko, H. Y., Stadler, A. T., and Astaneh, S. M. F. (1999), "A substitute pore fluid for seismic centrifuge modeling," *Geotechnical Testing Journal*, Vol. 22, No. 3, pp. 196-210.
- Dobry, R., and Abdoun, T. (2001), "Recent studies on seismic centrifuge modeling of liquefaction and its effect on deep foundation," *State-of-the-Art Paper, Proc. of 4th International Conference on Recent Advances in Geotechnical Earthquake Engineering and Soil Dynamics*, Prakash, S. (ed.), Paper SOAP 3, San Diego, CA, March 26-31, Vol. 2, 30 pages.
- Dobry, R., Abdoun, T., and O'Rourke, T. D. (2002), "Centrifuge-based evaluation of pile foundation response to lateral spreading and mitigation strategies," Report No. MCEER-01-SP01, Multidisciplinary Center for Earthquake Engineering Research, University of Buffalo, Buffalo, NY, USA.
- Dobry, R. (2004), Personal communication.
- Dungca, J. R., Kuwano, J., Saruwatari, T., Izawa, J., Suzuki, H., and Tokimatsu, K. (2004), "Shaking table tests on the lateral response of a pile buried in liquefied sand," *Proc. of the 11th International Conference on Soil Dynamics and Earthquake Engineering*, Vol. 2, pp. 471-477.
- Fukuoka, M. (1966), "Damage to civil engineering structures". *Soils Foundations* Vol.2, pp. 45-52.
- Gonzalez, L. (2002), "Study of effect of high confining stress on the development of soil liquefaction using centrifuge modeling," MSc. Thesis, Rensselaer Polytechnic Institute, Troy, NY, USA.
- Haigh, S. K., and Madabhushi, S. P. G. (2002), "Centrifuge modeling of lateral spreading past foundation," *Proc. Intl. Conf. on Physical Modeling in Geotechnics, Centrifuge '02*, St. John's, Canada, July 10-12, (Phillips, Guo and Popescu, eds.), Balkema, pp. 471-475.
- Hamada, M., Yasuda, S., Isoyama, R., and Emoto, K. (1986), "Study on liquefaction induced permanent ground displacements," *Research Report, Assessment for Development of Earthquake Prediction*, Japan, November, 87 pages.
- Hamada, M., and O'Rourke, T. D. (eds.) (1992), "Case studies of liquefaction and lifeline performance during past earthquakes," Vol. 1: Japanese Case Studies, National Center for Earthquake Engineering Research, (Tech. Report. NCEER-92-0001, February), SUNY-Buffalo, Buffalo, NY, USA.

- Hamada, M., (1992). "Large ground deformations and their effects on lifelines: 1964 Niigata earthquake," in Hamada M., and O'Rourke, T. D. (eds.) (1992), Case studies of liquefaction and lifeline performance during past earthquakes, (Tech. Report NCEER-92-0001) NCEER, Buffalo, NY, USA. pp. 3-i to 3-123.
- Hamada, M. (1998), "A study on ground displacement caused by soil liquefaction," Proc. Japanese Society of Civil Engineers, No. 596, Vol. III-43, pp. 189-208.
- Higuchi, H., and Matsuda, T. (2002), "Effects of liquefaction-induced lateral flow of ground against a pile foundation," Proc. International Conference of Physical Modeling in Geotechnics, St. John's Canada, Balkema, pp.465-470.
- Hwang, J. I., Kim, C. Y., Chung, C. K., and Kim, M. M. (2004), "Behavior of a single pile subjected to flow of liquefied soil of an infinite slope," Proc. of the 11th International Conference on Soil Dynamics and Earthquake Engineering, Vol. 2, pp. 573-580.
- Ishihara, K., Verdugo, R., and Acacio, A. A. (1991), "Characterization of cyclic behavior of sand and post-seismic stability analyses," Proc. 9th Asian Regional Conference on Soil Mechanic and Foundation Engineering, Vol.2, Bangkok, Thailand, December, pp. 45-67.
- Ishihara, K., Yasuda, S., and Nagase, H. (1996), "Soil characteristics and ground damage," Soils and Foundations, 109-118, January.
- Iwasaki, T. (1973), "Earthquake resistant design of bridges in Japan," Bull. Public Works Research Inst., Ministry of Construction, Japan, Vol. 29.
- Japan Road Association (1996), "Specifications for highway bridges," Part V Seismic Design, (in Japanese).
- Kramer, S. L. (1996), "Geotechnical earthquake engineering," International Series in Civil Engineering, Prentice Hall, 653 pages.
- Law, H. (2000), "Lateral spreading on pile at the Oakland Mole SFOBB East Span Seismic Safety Project," Memorandum 09-12-2000, Earth Mechanics, Inc., Fountain Valley, CA, USA.
- Liu, L., and Dobry, R. (1995), "Effect of liquefaction on lateral response of piles by centrifuge model tests," National Center for Earthquake Engineering Research (NCEER) Bulletin Annual, 9(1), pp. 7-11.
- Madabhushi, S. P. G. (1994), "Effect of pore fluid in dynamic centrifuge modeling," Centrifuge 94, Balkema, Rotterdam, pp. 127-132.
- Martin, G. R. (2000), "Foundation design for liquefaction induced lateral displacements (Task E1-2)," Annual Report for Research Year 1, June 1, 1999 to September 30, 2000, MCEER Highway Project 094.

- Martin, G. R., Marsh, M. L., Anderson, D. G., Mayes, R. L., and Power, M. S. (2002), "Recommended design approach for liquefaction induced lateral spreads," Proc. 3rd National Seismic Conference and Workshop on Bridges and Highways, Portland, OR, USA.
- Matlock, H. (1970), "Correlations for design of laterally-loaded piles in soft clay," Proc., 2nd Annual Offshore Technology Conf., Vol. 1, pp. 577– 594.
- McCulloch, D. S., and Bonilla, M. G. (1970), "Effects of the earthquake of March 27, 1964 on the Alaska railroad," Professional Paper 545-D, U.S. Geological Survey.
- MCEER Highway Project 094 (2000), "Seismic vulnerability of the highway system," Annual Report for Research Year 1, June 1, 1999 to September 30, 2000.
- Mizuno, H. (1987), "Pile damage during earthquakes in Japan (1923-1983)," Proc. Session on Dynamic Response of Pile Foundations, T. Nogami (Ed.), ASCE, Atlantic City, NJ, USA, April 27, pp. 53-77.
- National Instruments (2001), "Signal conditioning fundamentals for computer-based measurement systems," Application Note 048, Web page: <http://zone.ni.com>.
- National Research Council (1985), "Liquefaction of soils during earthquakes," Committee on Earthquake Engineering, Report No. CETS-EE-001, National Academy Press, Washington, D.C. USA, 240 pages.
- Okamura, M., Abdoun, T., Dobry, R., Sharp, M. K., and Taboada, V. M. (2001), "Effects of sand permeability and weak aftershocks on earthquake-induced lateral spreading," Soils and Foundations, Vol. 41, No 6. pp. 63-77.
- O'Rourke, T. D., and Hamada, M. (eds.) (1992), "Case studies of liquefaction and lifeline performance during past earthquakes," Vol. 2: United States Case Studies, National Center for Earthquake Engineering Research, (Tech Report NCEER-92-0002, February), SUNY-Buffalo, Buffalo, NY, USA.
- Pamuk, A. (2004), "Modeling of pile group response to lateral spreading and pile retrofitting including soil-pile remediation by passive site remediation," Ph.D. Thesis, Rensselaer Polytechnic Institute, Troy, NY, USA.
- Perez-Cobo, A., and Abghari, A. (1996), "Lateral spreading and settlement potential for Salinas River Bridge (Bridge No. 44-0002)," Memorandum 02-22-1996, Caltrans, Office of Structural Foundations, Sacramento, CA, USA.
- Ramos, R. (1999), "Centrifuge study of bending response of pile foundation to a lateral spread including restraining effects of superstructure," Ph.D. Thesis, Rensselaer Polytechnic Institute, Troy, NY, USA.

- Rauch, A. F. (1997), "EPOLLS: an empirical method for predicting surface displacements due to liquefaction-induced lateral spreading in earthquakes," Ph.D. Thesis, Virginia Tech., Blacksburg, VA, USA.
- Rollins, K. M., Gerber, T. M., Lane, J. D., and Ashford, S. A. (2005), "Lateral resistance of a full-scale pile group in liquefied sand," *Journal of Geotechnical & Geoenvironmental Engineering*, 131 (1), pp. 115-125.
- Sato, M., et al. (2004). In Progress.
- Swan S. W., Flores, P. J., and Hooper, J. D. (1996), "The Manzanillo Mexico earthquake of October 9, 1995," *NCEES Bulletin, The Quarterly Publication of NCEER*, 10 (1), January.
- Seed, H. B., and Lee K. L. (1966), "Liquefaction of saturated sands during cyclic loading," *Journal of the Soil Mechanics and Foundations Division, ASCE*, Vol. 92, No. SM6, pp. 105-134.
- Seed, H. B., Tokimatsu, K., Harder, L. F., and Chung, R.M. (1985), "Influence of SPT procedures in soil liquefaction resistance evaluation," *Journal of Geotechnical Engineering*, Vol. 111, No 12. pp. 1425-1445.
- Seed, R. B., Cetin, K. O., Moss, R. E. S., Kammerer, A. M., Wu, J., Pestana, J. M., Riemer, M. F., Sancio, R. B., Bray, J. D., Kayen, R. E., and Faris, A. (2003), "Recent advances in soil liquefaction engineering: a unified and consistent framework," 26th Annual ASCE Los Angeles Geotechnical Spring Seminar, Keynote Presentation, H.M.S. Queen Mary, Long Beach, CA, USA.
- Sharp, M. K. (1999), "Development of centrifuge based prediction charts for liquefaction and lateral spreading from cone penetration testing," Ph.D. Thesis, Rensselaer Polytechnic Institute, Troy, NY, USA.
- Steedman, R. S., and Ledbetter, R. H. (1994), "Centrifuge modeling of earthquake problems," *International Workshop on Remedial Treatment of Liquefiable Soils, Tsukuba Science City, Japan, July 4-6. Task Committee on Soil Behavior and Stability during Earthquakes, U.S.-Japan.*
- Steedman, R. S., Ledbetter, R. H., and Hynes, M. H. (2000), "The influence of high confining stress on the cyclic behavior of saturated sand," *Proc. Soil Dynamics and Liquefaction 2000*, pp. 35-57, Denver, CO, USA.
- Suzuki, H., and Tokimatsu, K. (2004), "Effects of pore water pressure around pile on p-y relation during liquefaction," *Proc. 11th Intl. Conf. on Soil Dynamics & Earthquake Engineering and 3rd Intl. Conf. on Earthquake Geotechnical Engineering*, Doolin, Kammerer, Nogami, Seed and Towhata, (eds.), Stallion Press, Berkeley, CA, USA, Vol. 2, pp. 567-572.
- Taboada, V. (1995), "Centrifuge modeling of earthquake-induced lateral spreading in sand using a laminar box," Ph.D. Thesis, Rensselaer Polytechnic Institute, Troy, NY, USA.

- Taylor, R. N. (1995), "Geotechnical centrifuge technology," 1st edition, Chapman & Hall, 296 pages.
- Tokimatsu K., Mizuno, H., and Kakurai, M. (1996), "Building damage associated with geotechnical problems," *Soils and Foundations*, January, pp. 219-234.
- Tokimatsu, K. (1999), "Performance of pile foundations in laterally spreading soils," Proc. 2nd International Conference on Earthquake Geotechnical Engineering, Seco e Pinto, P. (ed.), Lisbon, Portugal, June 21-25, Vol.3, pp. 957-964.
- Transportation Research Board (2002), "Comprehensive specification for the seismic design of bridges," National Cooperative Highway Research Program (NCHRP) Report 472, National Research Council, 47 pages.
- Ubilla, J. (2004). In progress.
- Van Laak, P. (1996), "Development of dynamic capability for geotechnical centrifuge model studies," Ph.D. Thesis, Rensselaer Polytechnic Institute, Troy, NY, USA.
- Wang, S.-T., and Reese, L. C. (1998), "Design of pile foundations in liquefied soils," *Geotechnical Earthquake Engineering and Soil Dynamic III*, GSP No. 75, P. Dakoulas and M. Yegian, (eds.), Vol. 2, ASCE, Reston, VA, USA, pp. 1331–1343.
- Wang, Y. (2001), "Evaluation of pile foundation retrofitting against lateral spreading and inertial effects during liquefaction using centrifuge models," MS Thesis, Rensselaer Polytechnic Institute, Troy, NY, USA.
- Whitman, R. V., and Lambe, P. C. (1986), "Effect of boundary conditions upon centrifuge experiments using ground motion simulation," *Geotechnical Testing Journal*, Vol. 9, No. 2.
- Wilson, D. W. (1998), "Soil-pile-superstructure interaction in liquefying sand and soft clay," Ph.D. Thesis, University of California at Davis, Davis, CA, USA.
- Wilson D. W., Boulanger, R. W., and Kutter, B. L. (2000), "Observed seismic lateral resistance of liquefying sand," *ASCE Journal of Geotechnical and Geoenvironmental Engineering*, Vol. 126, No. 10, October, pp. 898-906.
- Yokoyama K., Tamura, K., and Matsuo, O. (1997), "Design methods of bridge foundations against soil liquefaction and liquefaction-induced ground flow," 2nd Italy-Japan Workshop on Seismic Design and Retrofit of Bridges Rome, Italy, February 27-28, pp. 109-131.
- Yoshida, N., and Hamada, M. (1991), "Damage to foundation piles and deformation pattern of ground due to liquefaction-induced permanent ground deformations," Proc. 3rd Japan-US Workshop on Earthquake Resistant Design of Lifeline Facilities and Countermeasures for Soil Liquefaction, Report NCEER-91-0001, pp. 141-161.

- Youd, T. L. (1993), "Liquefaction-induced damage to bridges," Transportation Research Record, Published by the Transportation Research Board and the National Research Council, Washington, D.C., USA, 1411, pp. 35-41.
- Youd, T. L., Idriss, I. M., Andrus, R. D., Arango, I., Castro, G., Christian, J. T., Dobry, R., Finn, W. D. L., Harder, Jr. L. F., Hynes, M. E., Ishihara, K., Koester, J. P., Liao, S. S. C., Marcuson, W. F., Martin, G. R., Mitchell, J.K., Moriwaki, Y., Power, M. S., Robertson, P.K., Seed, R. B., Stokoe, K. H. (2001), "Liquefaction resistance of soils: Summary report from the 1996 NCEER and 1998 NCEER/NSF Workshop on evaluation of liquefaction resistance of soils," Journal of Geotechnical and Geoenvironmental Engineering, ASCE, pp. 817-833.
- Zha, Jin-xing (2004), "Lateral spreading forces on bridge abutment walls/piles," Geotechnical Engineering for Transportation Projects, Geotechnical Special Pub. 126, M. K. Yegian and E. Kavazanjian, (eds.), ASCE, Vol. 2, 1711-1720.
- Zeghal, M., Dobry, R., Abdoun, T., Zimmie, T. F., and Elgamal, A.-W. M. (2000), "NEES earthquake simulation and networking capabilities at RPI Centrifuge," Proc. 7th U.S. National Conference on Earthquake Engineering, 7NCEE, Boston, MA, USA.

MCEER Technical Reports

MCEER publishes technical reports on a variety of subjects written by authors funded through MCEER. These reports are available from both MCEER Publications and the National Technical Information Service (NTIS). Requests for reports should be directed to MCEER Publications, MCEER, University at Buffalo, State University of New York, Red Jacket Quadrangle, Buffalo, New York 14261. Reports can also be requested through NTIS, 5285 Port Royal Road, Springfield, Virginia 22161. NTIS accession numbers are shown in parenthesis, if available.

- NCEER-87-0001 "First-Year Program in Research, Education and Technology Transfer," 3/5/87, (PB88-134275, A04, MF-A01).
- NCEER-87-0002 "Experimental Evaluation of Instantaneous Optimal Algorithms for Structural Control," by R.C. Lin, T.T. Soong and A.M. Reinhorn, 4/20/87, (PB88-134341, A04, MF-A01).
- NCEER-87-0003 "Experimentation Using the Earthquake Simulation Facilities at University at Buffalo," by A.M. Reinhorn and R.L. Ketter, to be published.
- NCEER-87-0004 "The System Characteristics and Performance of a Shaking Table," by J.S. Hwang, K.C. Chang and G.C. Lee, 6/1/87, (PB88-134259, A03, MF-A01). This report is available only through NTIS (see address given above).
- NCEER-87-0005 "A Finite Element Formulation for Nonlinear Viscoplastic Material Using a Q Model," by O. Gyebe and G. Dasgupta, 11/2/87, (PB88-213764, A08, MF-A01).
- NCEER-87-0006 "Symbolic Manipulation Program (SMP) - Algebraic Codes for Two and Three Dimensional Finite Element Formulations," by X. Lee and G. Dasgupta, 11/9/87, (PB88-218522, A05, MF-A01).
- NCEER-87-0007 "Instantaneous Optimal Control Laws for Tall Buildings Under Seismic Excitations," by J.N. Yang, A. Akbarpour and P. Ghaemmaghami, 6/10/87, (PB88-134333, A06, MF-A01). This report is only available through NTIS (see address given above).
- NCEER-87-0008 "IDARC: Inelastic Damage Analysis of Reinforced Concrete Frame - Shear-Wall Structures," by Y.J. Park, A.M. Reinhorn and S.K. Kunnath, 7/20/87, (PB88-134325, A09, MF-A01). This report is only available through NTIS (see address given above).
- NCEER-87-0009 "Liquefaction Potential for New York State: A Preliminary Report on Sites in Manhattan and Buffalo," by M. Budhu, V. Vijayakumar, R.F. Giese and L. Baumgras, 8/31/87, (PB88-163704, A03, MF-A01). This report is available only through NTIS (see address given above).
- NCEER-87-0010 "Vertical and Torsional Vibration of Foundations in Inhomogeneous Media," by A.S. Veletsos and K.W. Dotson, 6/1/87, (PB88-134291, A03, MF-A01). This report is only available through NTIS (see address given above).
- NCEER-87-0011 "Seismic Probabilistic Risk Assessment and Seismic Margins Studies for Nuclear Power Plants," by Howard H.M. Hwang, 6/15/87, (PB88-134267, A03, MF-A01). This report is only available through NTIS (see address given above).
- NCEER-87-0012 "Parametric Studies of Frequency Response of Secondary Systems Under Ground-Acceleration Excitations," by Y. Yong and Y.K. Lin, 6/10/87, (PB88-134309, A03, MF-A01). This report is only available through NTIS (see address given above).
- NCEER-87-0013 "Frequency Response of Secondary Systems Under Seismic Excitation," by J.A. HoLung, J. Cai and Y.K. Lin, 7/31/87, (PB88-134317, A05, MF-A01). This report is only available through NTIS (see address given above).
- NCEER-87-0014 "Modelling Earthquake Ground Motions in Seismically Active Regions Using Parametric Time Series Methods," by G.W. Ellis and A.S. Cakmak, 8/25/87, (PB88-134283, A08, MF-A01). This report is only available through NTIS (see address given above).
- NCEER-87-0015 "Detection and Assessment of Seismic Structural Damage," by E. DiPasquale and A.S. Cakmak, 8/25/87, (PB88-163712, A05, MF-A01). This report is only available through NTIS (see address given above).

- NCEER-87-0016 "Pipeline Experiment at Parkfield, California," by J. Isenberg and E. Richardson, 9/15/87, (PB88-163720, A03, MF-A01). This report is available only through NTIS (see address given above).
- NCEER-87-0017 "Digital Simulation of Seismic Ground Motion," by M. Shinozuka, G. Deodatis and T. Harada, 8/31/87, (PB88-155197, A04, MF-A01). This report is available only through NTIS (see address given above).
- NCEER-87-0018 "Practical Considerations for Structural Control: System Uncertainty, System Time Delay and Truncation of Small Control Forces," J.N. Yang and A. Akbarpour, 8/10/87, (PB88-163738, A08, MF-A01). This report is only available through NTIS (see address given above).
- NCEER-87-0019 "Modal Analysis of Nonclassically Damped Structural Systems Using Canonical Transformation," by J.N. Yang, S. Sarkani and F.X. Long, 9/27/87, (PB88-187851, A04, MF-A01).
- NCEER-87-0020 "A Nonstationary Solution in Random Vibration Theory," by J.R. Red-Horse and P.D. Spanos, 11/3/87, (PB88-163746, A03, MF-A01).
- NCEER-87-0021 "Horizontal Impedances for Radially Inhomogeneous Viscoelastic Soil Layers," by A.S. Veletsos and K.W. Dotson, 10/15/87, (PB88-150859, A04, MF-A01).
- NCEER-87-0022 "Seismic Damage Assessment of Reinforced Concrete Members," by Y.S. Chung, C. Meyer and M. Shinozuka, 10/9/87, (PB88-150867, A05, MF-A01). This report is available only through NTIS (see address given above).
- NCEER-87-0023 "Active Structural Control in Civil Engineering," by T.T. Soong, 11/11/87, (PB88-187778, A03, MF-A01).
- NCEER-87-0024 "Vertical and Torsional Impedances for Radially Inhomogeneous Viscoelastic Soil Layers," by K.W. Dotson and A.S. Veletsos, 12/87, (PB88-187786, A03, MF-A01).
- NCEER-87-0025 "Proceedings from the Symposium on Seismic Hazards, Ground Motions, Soil-Liquefaction and Engineering Practice in Eastern North America," October 20-22, 1987, edited by K.H. Jacob, 12/87, (PB88-188115, A23, MF-A01). This report is available only through NTIS (see address given above).
- NCEER-87-0026 "Report on the Whittier-Narrows, California, Earthquake of October 1, 1987," by J. Pantelic and A. Reinhorn, 11/87, (PB88-187752, A03, MF-A01). This report is available only through NTIS (see address given above).
- NCEER-87-0027 "Design of a Modular Program for Transient Nonlinear Analysis of Large 3-D Building Structures," by S. Srivastav and J.F. Abel, 12/30/87, (PB88-187950, A05, MF-A01). This report is only available through NTIS (see address given above).
- NCEER-87-0028 "Second-Year Program in Research, Education and Technology Transfer," 3/8/88, (PB88-219480, A04, MF-A01).
- NCEER-88-0001 "Workshop on Seismic Computer Analysis and Design of Buildings With Interactive Graphics," by W. McGuire, J.F. Abel and C.H. Conley, 1/18/88, (PB88-187760, A03, MF-A01). This report is only available through NTIS (see address given above).
- NCEER-88-0002 "Optimal Control of Nonlinear Flexible Structures," by J.N. Yang, F.X. Long and D. Wong, 1/22/88, (PB88-213772, A06, MF-A01).
- NCEER-88-0003 "Substructuring Techniques in the Time Domain for Primary-Secondary Structural Systems," by G.D. Manolis and G. Juhn, 2/10/88, (PB88-213780, A04, MF-A01).
- NCEER-88-0004 "Iterative Seismic Analysis of Primary-Secondary Systems," by A. Singhal, L.D. Lutes and P.D. Spanos, 2/23/88, (PB88-213798, A04, MF-A01).
- NCEER-88-0005 "Stochastic Finite Element Expansion for Random Media," by P.D. Spanos and R. Ghanem, 3/14/88, (PB88-213806, A03, MF-A01).

- NCEER-88-0006 "Combining Structural Optimization and Structural Control," by F.Y. Cheng and C.P. Pantelides, 1/10/88, (PB88-213814, A05, MF-A01).
- NCEER-88-0007 "Seismic Performance Assessment of Code-Designed Structures," by H.H-M. Hwang, J-W. Jaw and H-J. Shau, 3/20/88, (PB88-219423, A04, MF-A01). This report is only available through NTIS (see address given above).
- NCEER-88-0008 "Reliability Analysis of Code-Designed Structures Under Natural Hazards," by H.H-M. Hwang, H. Ushiba and M. Shinozuka, 2/29/88, (PB88-229471, A07, MF-A01). This report is only available through NTIS (see address given above).
- NCEER-88-0009 "Seismic Fragility Analysis of Shear Wall Structures," by J-W Jaw and H.H-M. Hwang, 4/30/88, (PB89-102867, A04, MF-A01).
- NCEER-88-0010 "Base Isolation of a Multi-Story Building Under a Harmonic Ground Motion - A Comparison of Performances of Various Systems," by F-G Fan, G. Ahmadi and I.G. Tadjbakhsh, 5/18/88, (PB89-122238, A06, MF-A01). This report is only available through NTIS (see address given above).
- NCEER-88-0011 "Seismic Floor Response Spectra for a Combined System by Green's Functions," by F.M. Lavelle, L.A. Bergman and P.D. Spanos, 5/1/88, (PB89-102875, A03, MF-A01).
- NCEER-88-0012 "A New Solution Technique for Randomly Excited Hysteretic Structures," by G.Q. Cai and Y.K. Lin, 5/16/88, (PB89-102883, A03, MF-A01).
- NCEER-88-0013 "A Study of Radiation Damping and Soil-Structure Interaction Effects in the Centrifuge," by K. Weissman, supervised by J.H. Prevost, 5/24/88, (PB89-144703, A06, MF-A01).
- NCEER-88-0014 "Parameter Identification and Implementation of a Kinematic Plasticity Model for Frictional Soils," by J.H. Prevost and D.V. Griffiths, to be published.
- NCEER-88-0015 "Two- and Three- Dimensional Dynamic Finite Element Analyses of the Long Valley Dam," by D.V. Griffiths and J.H. Prevost, 6/17/88, (PB89-144711, A04, MF-A01).
- NCEER-88-0016 "Damage Assessment of Reinforced Concrete Structures in Eastern United States," by A.M. Reinhorn, M.J. Seidel, S.K. Kunnath and Y.J. Park, 6/15/88, (PB89-122220, A04, MF-A01). This report is only available through NTIS (see address given above).
- NCEER-88-0017 "Dynamic Compliance of Vertically Loaded Strip Foundations in Multilayered Viscoelastic Soils," by S. Ahmad and A.S.M. Israil, 6/17/88, (PB89-102891, A04, MF-A01).
- NCEER-88-0018 "An Experimental Study of Seismic Structural Response With Added Viscoelastic Dampers," by R.C. Lin, Z. Liang, T.T. Soong and R.H. Zhang, 6/30/88, (PB89-122212, A05, MF-A01). This report is available only through NTIS (see address given above).
- NCEER-88-0019 "Experimental Investigation of Primary - Secondary System Interaction," by G.D. Manolis, G. Juhn and A.M. Reinhorn, 5/27/88, (PB89-122204, A04, MF-A01).
- NCEER-88-0020 "A Response Spectrum Approach For Analysis of Nonclassically Damped Structures," by J.N. Yang, S. Sarkani and F.X. Long, 4/22/88, (PB89-102909, A04, MF-A01).
- NCEER-88-0021 "Seismic Interaction of Structures and Soils: Stochastic Approach," by A.S. Veletsos and A.M. Prasad, 7/21/88, (PB89-122196, A04, MF-A01). This report is only available through NTIS (see address given above).
- NCEER-88-0022 "Identification of the Serviceability Limit State and Detection of Seismic Structural Damage," by E. DiPasquale and A.S. Cakmak, 6/15/88, (PB89-122188, A05, MF-A01). This report is available only through NTIS (see address given above).
- NCEER-88-0023 "Multi-Hazard Risk Analysis: Case of a Simple Offshore Structure," by B.K. Bhartia and E.H. Vanmarcke, 7/21/88, (PB89-145213, A05, MF-A01).

- NCEER-88-0024 "Automated Seismic Design of Reinforced Concrete Buildings," by Y.S. Chung, C. Meyer and M. Shinozuka, 7/5/88, (PB89-122170, A06, MF-A01). This report is available only through NTIS (see address given above).
- NCEER-88-0025 "Experimental Study of Active Control of MDOF Structures Under Seismic Excitations," by L.L. Chung, R.C. Lin, T.T. Soong and A.M. Reinhorn, 7/10/88, (PB89-122600, A04, MF-A01).
- NCEER-88-0026 "Earthquake Simulation Tests of a Low-Rise Metal Structure," by J.S. Hwang, K.C. Chang, G.C. Lee and R.L. Ketter, 8/1/88, (PB89-102917, A04, MF-A01).
- NCEER-88-0027 "Systems Study of Urban Response and Reconstruction Due to Catastrophic Earthquakes," by F. Kozin and H.K. Zhou, 9/22/88, (PB90-162348, A04, MF-A01).
- NCEER-88-0028 "Seismic Fragility Analysis of Plane Frame Structures," by H.H-M. Hwang and Y.K. Low, 7/31/88, (PB89-131445, A06, MF-A01).
- NCEER-88-0029 "Response Analysis of Stochastic Structures," by A. Kardara, C. Bucher and M. Shinozuka, 9/22/88, (PB89-174429, A04, MF-A01).
- NCEER-88-0030 "Nonnormal Accelerations Due to Yielding in a Primary Structure," by D.C.K. Chen and L.D. Lutes, 9/19/88, (PB89-131437, A04, MF-A01).
- NCEER-88-0031 "Design Approaches for Soil-Structure Interaction," by A.S. Veletsos, A.M. Prasad and Y. Tang, 12/30/88, (PB89-174437, A03, MF-A01). This report is available only through NTIS (see address given above).
- NCEER-88-0032 "A Re-evaluation of Design Spectra for Seismic Damage Control," by C.J. Turkstra and A.G. Tallin, 11/7/88, (PB89-145221, A05, MF-A01).
- NCEER-88-0033 "The Behavior and Design of Noncontact Lap Splices Subjected to Repeated Inelastic Tensile Loading," by V.E. Sagan, P. Gergely and R.N. White, 12/8/88, (PB89-163737, A08, MF-A01).
- NCEER-88-0034 "Seismic Response of Pile Foundations," by S.M. Mamoon, P.K. Banerjee and S. Ahmad, 11/1/88, (PB89-145239, A04, MF-A01).
- NCEER-88-0035 "Modeling of R/C Building Structures With Flexible Floor Diaphragms (IDARC2)," by A.M. Reinhorn, S.K. Kunnath and N. Panahshahi, 9/7/88, (PB89-207153, A07, MF-A01).
- NCEER-88-0036 "Solution of the Dam-Reservoir Interaction Problem Using a Combination of FEM, BEM with Particular Integrals, Modal Analysis, and Substructuring," by C-S. Tsai, G.C. Lee and R.L. Ketter, 12/31/88, (PB89-207146, A04, MF-A01).
- NCEER-88-0037 "Optimal Placement of Actuators for Structural Control," by F.Y. Cheng and C.P. Pantelides, 8/15/88, (PB89-162846, A05, MF-A01).
- NCEER-88-0038 "Teflon Bearings in Aseismic Base Isolation: Experimental Studies and Mathematical Modeling," by A. Mokha, M.C. Constantinou and A.M. Reinhorn, 12/5/88, (PB89-218457, A10, MF-A01). This report is available only through NTIS (see address given above).
- NCEER-88-0039 "Seismic Behavior of Flat Slab High-Rise Buildings in the New York City Area," by P. Weidlinger and M. Ettouney, 10/15/88, (PB90-145681, A04, MF-A01).
- NCEER-88-0040 "Evaluation of the Earthquake Resistance of Existing Buildings in New York City," by P. Weidlinger and M. Ettouney, 10/15/88, to be published.
- NCEER-88-0041 "Small-Scale Modeling Techniques for Reinforced Concrete Structures Subjected to Seismic Loads," by W. Kim, A. El-Attar and R.N. White, 11/22/88, (PB89-189625, A05, MF-A01).
- NCEER-88-0042 "Modeling Strong Ground Motion from Multiple Event Earthquakes," by G.W. Ellis and A.S. Cakmak, 10/15/88, (PB89-174445, A03, MF-A01).

- NCEER-88-0043 "Nonstationary Models of Seismic Ground Acceleration," by M. Grigoriu, S.E. Ruiz and E. Rosenblueth, 7/15/88, (PB89-189617, A04, MF-A01).
- NCEER-88-0044 "SARCF User's Guide: Seismic Analysis of Reinforced Concrete Frames," by Y.S. Chung, C. Meyer and M. Shinozuka, 11/9/88, (PB89-174452, A08, MF-A01).
- NCEER-88-0045 "First Expert Panel Meeting on Disaster Research and Planning," edited by J. Pantelic and J. Stoyke, 9/15/88, (PB89-174460, A05, MF-A01).
- NCEER-88-0046 "Preliminary Studies of the Effect of Degrading Infill Walls on the Nonlinear Seismic Response of Steel Frames," by C.Z. Chrysostomou, P. Gergely and J.F. Abel, 12/19/88, (PB89-208383, A05, MF-A01).
- NCEER-88-0047 "Reinforced Concrete Frame Component Testing Facility - Design, Construction, Instrumentation and Operation," by S.P. Pessiki, C. Conley, T. Bond, P. Gergely and R.N. White, 12/16/88, (PB89-174478, A04, MF-A01).
- NCEER-89-0001 "Effects of Protective Cushion and Soil Compliancy on the Response of Equipment Within a Seismically Excited Building," by J.A. HoLung, 2/16/89, (PB89-207179, A04, MF-A01).
- NCEER-89-0002 "Statistical Evaluation of Response Modification Factors for Reinforced Concrete Structures," by H.H-M. Hwang and J-W. Jaw, 2/17/89, (PB89-207187, A05, MF-A01).
- NCEER-89-0003 "Hysteretic Columns Under Random Excitation," by G-Q. Cai and Y.K. Lin, 1/9/89, (PB89-196513, A03, MF-A01).
- NCEER-89-0004 "Experimental Study of 'Elephant Foot Bulge' Instability of Thin-Walled Metal Tanks," by Z-H. Jia and R.L. Ketter, 2/22/89, (PB89-207195, A03, MF-A01).
- NCEER-89-0005 "Experiment on Performance of Buried Pipelines Across San Andreas Fault," by J. Isenberg, E. Richardson and T.D. O'Rourke, 3/10/89, (PB89-218440, A04, MF-A01). This report is available only through NTIS (see address given above).
- NCEER-89-0006 "A Knowledge-Based Approach to Structural Design of Earthquake-Resistant Buildings," by M. Subramani, P. Gergely, C.H. Conley, J.F. Abel and A.H. Zaghaw, 1/15/89, (PB89-218465, A06, MF-A01).
- NCEER-89-0007 "Liquefaction Hazards and Their Effects on Buried Pipelines," by T.D. O'Rourke and P.A. Lane, 2/1/89, (PB89-218481, A09, MF-A01).
- NCEER-89-0008 "Fundamentals of System Identification in Structural Dynamics," by H. Imai, C-B. Yun, O. Maruyama and M. Shinozuka, 1/26/89, (PB89-207211, A04, MF-A01).
- NCEER-89-0009 "Effects of the 1985 Michoacan Earthquake on Water Systems and Other Buried Lifelines in Mexico," by A.G. Ayala and M.J. O'Rourke, 3/8/89, (PB89-207229, A06, MF-A01).
- NCEER-89-R010 "NCEER Bibliography of Earthquake Education Materials," by K.E.K. Ross, Second Revision, 9/1/89, (PB90-125352, A05, MF-A01). This report is replaced by NCEER-92-0018.
- NCEER-89-0011 "Inelastic Three-Dimensional Response Analysis of Reinforced Concrete Building Structures (IDARC-3D), Part I - Modeling," by S.K. Kunnath and A.M. Reinhorn, 4/17/89, (PB90-114612, A07, MF-A01). This report is available only through NTIS (see address given above).
- NCEER-89-0012 "Recommended Modifications to ATC-14," by C.D. Poland and J.O. Malley, 4/12/89, (PB90-108648, A15, MF-A01).
- NCEER-89-0013 "Repair and Strengthening of Beam-to-Column Connections Subjected to Earthquake Loading," by M. Corazao and A.J. Durrani, 2/28/89, (PB90-109885, A06, MF-A01).
- NCEER-89-0014 "Program EXKAL2 for Identification of Structural Dynamic Systems," by O. Maruyama, C-B. Yun, M. Hoshiya and M. Shinozuka, 5/19/89, (PB90-109877, A09, MF-A01).

- NCEER-89-0015 "Response of Frames With Bolted Semi-Rigid Connections, Part I - Experimental Study and Analytical Predictions," by P.J. DiCorso, A.M. Reinhorn, J.R. Dickerson, J.B. Radzinski and W.L. Harper, 6/1/89, to be published.
- NCEER-89-0016 "ARMA Monte Carlo Simulation in Probabilistic Structural Analysis," by P.D. Spanos and M.P. Mignolet, 7/10/89, (PB90-109893, A03, MF-A01).
- NCEER-89-P017 "Preliminary Proceedings from the Conference on Disaster Preparedness - The Place of Earthquake Education in Our Schools," Edited by K.E.K. Ross, 6/23/89, (PB90-108606, A03, MF-A01).
- NCEER-89-0017 "Proceedings from the Conference on Disaster Preparedness - The Place of Earthquake Education in Our Schools," Edited by K.E.K. Ross, 12/31/89, (PB90-207895, A012, MF-A02). This report is available only through NTIS (see address given above).
- NCEER-89-0018 "Multidimensional Models of Hysteretic Material Behavior for Vibration Analysis of Shape Memory Energy Absorbing Devices, by E.J. Graesser and F.A. Cozzarelli, 6/7/89, (PB90-164146, A04, MF-A01).
- NCEER-89-0019 "Nonlinear Dynamic Analysis of Three-Dimensional Base Isolated Structures (3D-BASIS)," by S. Nagarajaiah, A.M. Reinhorn and M.C. Constantinou, 8/3/89, (PB90-161936, A06, MF-A01). This report has been replaced by NCEER-93-0011.
- NCEER-89-0020 "Structural Control Considering Time-Rate of Control Forces and Control Rate Constraints," by F.Y. Cheng and C.P. Pantelides, 8/3/89, (PB90-120445, A04, MF-A01).
- NCEER-89-0021 "Subsurface Conditions of Memphis and Shelby County," by K.W. Ng, T-S. Chang and H-H.M. Hwang, 7/26/89, (PB90-120437, A03, MF-A01).
- NCEER-89-0022 "Seismic Wave Propagation Effects on Straight Jointed Buried Pipelines," by K. Elhadi and M.J. O'Rourke, 8/24/89, (PB90-162322, A10, MF-A02).
- NCEER-89-0023 "Workshop on Serviceability Analysis of Water Delivery Systems," edited by M. Grigoriu, 3/6/89, (PB90-127424, A03, MF-A01).
- NCEER-89-0024 "Shaking Table Study of a 1/5 Scale Steel Frame Composed of Tapered Members," by K.C. Chang, J.S. Hwang and G.C. Lee, 9/18/89, (PB90-160169, A04, MF-A01).
- NCEER-89-0025 "DYNA1D: A Computer Program for Nonlinear Seismic Site Response Analysis - Technical Documentation," by Jean H. Prevost, 9/14/89, (PB90-161944, A07, MF-A01). This report is available only through NTIS (see address given above).
- NCEER-89-0026 "1:4 Scale Model Studies of Active Tendon Systems and Active Mass Dampers for Aseismic Protection," by A.M. Reinhorn, T.T. Soong, R.C. Lin, Y.P. Yang, Y. Fukao, H. Abe and M. Nakai, 9/15/89, (PB90-173246, A10, MF-A02). This report is available only through NTIS (see address given above).
- NCEER-89-0027 "Scattering of Waves by Inclusions in a Nonhomogeneous Elastic Half Space Solved by Boundary Element Methods," by P.K. Hadley, A. Askar and A.S. Cakmak, 6/15/89, (PB90-145699, A07, MF-A01).
- NCEER-89-0028 "Statistical Evaluation of Deflection Amplification Factors for Reinforced Concrete Structures," by H.H.M. Hwang, J-W. Jaw and A.L. Ch'ng, 8/31/89, (PB90-164633, A05, MF-A01).
- NCEER-89-0029 "Bedrock Accelerations in Memphis Area Due to Large New Madrid Earthquakes," by H.H.M. Hwang, C.H.S. Chen and G. Yu, 11/7/89, (PB90-162330, A04, MF-A01).
- NCEER-89-0030 "Seismic Behavior and Response Sensitivity of Secondary Structural Systems," by Y.Q. Chen and T.T. Soong, 10/23/89, (PB90-164658, A08, MF-A01).
- NCEER-89-0031 "Random Vibration and Reliability Analysis of Primary-Secondary Structural Systems," by Y. Ibrahim, M. Grigoriu and T.T. Soong, 11/10/89, (PB90-161951, A04, MF-A01).

- NCEER-89-0032 "Proceedings from the Second U.S. - Japan Workshop on Liquefaction, Large Ground Deformation and Their Effects on Lifelines, September 26-29, 1989," Edited by T.D. O'Rourke and M. Hamada, 12/1/89, (PB90-209388, A22, MF-A03).
- NCEER-89-0033 "Deterministic Model for Seismic Damage Evaluation of Reinforced Concrete Structures," by J.M. Bracci, A.M. Reinhorn, J.B. Mander and S.K. Kunnath, 9/27/89, (PB91-108803, A06, MF-A01).
- NCEER-89-0034 "On the Relation Between Local and Global Damage Indices," by E. DiPasquale and A.S. Cakmak, 8/15/89, (PB90-173865, A05, MF-A01).
- NCEER-89-0035 "Cyclic Undrained Behavior of Nonplastic and Low Plasticity Silts," by A.J. Walker and H.E. Stewart, 7/26/89, (PB90-183518, A10, MF-A01).
- NCEER-89-0036 "Liquefaction Potential of Surficial Deposits in the City of Buffalo, New York," by M. Budhu, R. Giese and L. Baumgrass, 1/17/89, (PB90-208455, A04, MF-A01).
- NCEER-89-0037 "A Deterministic Assessment of Effects of Ground Motion Incoherence," by A.S. Veletsos and Y. Tang, 7/15/89, (PB90-164294, A03, MF-A01).
- NCEER-89-0038 "Workshop on Ground Motion Parameters for Seismic Hazard Mapping," July 17-18, 1989, edited by R.V. Whitman, 12/1/89, (PB90-173923, A04, MF-A01).
- NCEER-89-0039 "Seismic Effects on Elevated Transit Lines of the New York City Transit Authority," by C.J. Costantino, C.A. Miller and E. Heymsfield, 12/26/89, (PB90-207887, A06, MF-A01).
- NCEER-89-0040 "Centrifugal Modeling of Dynamic Soil-Structure Interaction," by K. Weissman, Supervised by J.H. Prevost, 5/10/89, (PB90-207879, A07, MF-A01).
- NCEER-89-0041 "Linearized Identification of Buildings With Cores for Seismic Vulnerability Assessment," by I-K. Ho and A.E. Aktan, 11/1/89, (PB90-251943, A07, MF-A01).
- NCEER-90-0001 "Geotechnical and Lifeline Aspects of the October 17, 1989 Loma Prieta Earthquake in San Francisco," by T.D. O'Rourke, H.E. Stewart, F.T. Blackburn and T.S. Dickerman, 1/90, (PB90-208596, A05, MF-A01).
- NCEER-90-0002 "Nonnormal Secondary Response Due to Yielding in a Primary Structure," by D.C.K. Chen and L.D. Lutes, 2/28/90, (PB90-251976, A07, MF-A01).
- NCEER-90-0003 "Earthquake Education Materials for Grades K-12," by K.E.K. Ross, 4/16/90, (PB91-251984, A05, MF-A05). This report has been replaced by NCEER-92-0018.
- NCEER-90-0004 "Catalog of Strong Motion Stations in Eastern North America," by R.W. Busby, 4/3/90, (PB90-251984, A05, MF-A01).
- NCEER-90-0005 "NCEER Strong-Motion Data Base: A User Manual for the GeoBase Release (Version 1.0 for the Sun3)," by P. Friberg and K. Jacob, 3/31/90 (PB90-258062, A04, MF-A01).
- NCEER-90-0006 "Seismic Hazard Along a Crude Oil Pipeline in the Event of an 1811-1812 Type New Madrid Earthquake," by H.H.M. Hwang and C-H.S. Chen, 4/16/90, (PB90-258054, A04, MF-A01).
- NCEER-90-0007 "Site-Specific Response Spectra for Memphis Sheahan Pumping Station," by H.H.M. Hwang and C.S. Lee, 5/15/90, (PB91-108811, A05, MF-A01).
- NCEER-90-0008 "Pilot Study on Seismic Vulnerability of Crude Oil Transmission Systems," by T. Ariman, R. Dobry, M. Grigoriu, F. Kozin, M. O'Rourke, T. O'Rourke and M. Shinozuka, 5/25/90, (PB91-108837, A06, MF-A01).
- NCEER-90-0009 "A Program to Generate Site Dependent Time Histories: EQGEN," by G.W. Ellis, M. Srinivasan and A.S. Cakmak, 1/30/90, (PB91-108829, A04, MF-A01).
- NCEER-90-0010 "Active Isolation for Seismic Protection of Operating Rooms," by M.E. Talbott, Supervised by M. Shinozuka, 6/8/9, (PB91-110205, A05, MF-A01).

- NCEER-90-0011 "Program LINEARID for Identification of Linear Structural Dynamic Systems," by C-B. Yun and M. Shinozuka, 6/25/90, (PB91-110312, A08, MF-A01).
- NCEER-90-0012 "Two-Dimensional Two-Phase Elasto-Plastic Seismic Response of Earth Dams," by A.N. Yiagos, Supervised by J.H. Prevost, 6/20/90, (PB91-110197, A13, MF-A02).
- NCEER-90-0013 "Secondary Systems in Base-Isolated Structures: Experimental Investigation, Stochastic Response and Stochastic Sensitivity," by G.D. Manolis, G. Juhn, M.C. Constantinou and A.M. Reinhorn, 7/1/90, (PB91-110320, A08, MF-A01).
- NCEER-90-0014 "Seismic Behavior of Lightly-Reinforced Concrete Column and Beam-Column Joint Details," by S.P. Pessiki, C.H. Conley, P. Gergely and R.N. White, 8/22/90, (PB91-108795, A11, MF-A02).
- NCEER-90-0015 "Two Hybrid Control Systems for Building Structures Under Strong Earthquakes," by J.N. Yang and A. Daniellians, 6/29/90, (PB91-125393, A04, MF-A01).
- NCEER-90-0016 "Instantaneous Optimal Control with Acceleration and Velocity Feedback," by J.N. Yang and Z. Li, 6/29/90, (PB91-125401, A03, MF-A01).
- NCEER-90-0017 "Reconnaissance Report on the Northern Iran Earthquake of June 21, 1990," by M. Mehrain, 10/4/90, (PB91-125377, A03, MF-A01).
- NCEER-90-0018 "Evaluation of Liquefaction Potential in Memphis and Shelby County," by T.S. Chang, P.S. Tang, C.S. Lee and H. Hwang, 8/10/90, (PB91-125427, A09, MF-A01).
- NCEER-90-0019 "Experimental and Analytical Study of a Combined Sliding Disc Bearing and Helical Steel Spring Isolation System," by M.C. Constantinou, A.S. Mokha and A.M. Reinhorn, 10/4/90, (PB91-125385, A06, MF-A01). This report is available only through NTIS (see address given above).
- NCEER-90-0020 "Experimental Study and Analytical Prediction of Earthquake Response of a Sliding Isolation System with a Spherical Surface," by A.S. Mokha, M.C. Constantinou and A.M. Reinhorn, 10/11/90, (PB91-125419, A05, MF-A01).
- NCEER-90-0021 "Dynamic Interaction Factors for Floating Pile Groups," by G. Gazetas, K. Fan, A. Kaynia and E. Kausel, 9/10/90, (PB91-170381, A05, MF-A01).
- NCEER-90-0022 "Evaluation of Seismic Damage Indices for Reinforced Concrete Structures," by S. Rodriguez-Gomez and A.S. Cakmak, 9/30/90, PB91-171322, A06, MF-A01).
- NCEER-90-0023 "Study of Site Response at a Selected Memphis Site," by H. Desai, S. Ahmad, E.S. Gazetas and M.R. Oh, 10/11/90, (PB91-196857, A03, MF-A01).
- NCEER-90-0024 "A User's Guide to Strongmo: Version 1.0 of NCEER's Strong-Motion Data Access Tool for PCs and Terminals," by P.A. Friberg and C.A.T. Susch, 11/15/90, (PB91-171272, A03, MF-A01).
- NCEER-90-0025 "A Three-Dimensional Analytical Study of Spatial Variability of Seismic Ground Motions," by L-L. Hong and A.H.-S. Ang, 10/30/90, (PB91-170399, A09, MF-A01).
- NCEER-90-0026 "MUMOID User's Guide - A Program for the Identification of Modal Parameters," by S. Rodriguez-Gomez and E. DiPasquale, 9/30/90, (PB91-171298, A04, MF-A01).
- NCEER-90-0027 "SARCF-II User's Guide - Seismic Analysis of Reinforced Concrete Frames," by S. Rodriguez-Gomez, Y.S. Chung and C. Meyer, 9/30/90, (PB91-171280, A05, MF-A01).
- NCEER-90-0028 "Viscous Dampers: Testing, Modeling and Application in Vibration and Seismic Isolation," by N. Makris and M.C. Constantinou, 12/20/90 (PB91-190561, A06, MF-A01).
- NCEER-90-0029 "Soil Effects on Earthquake Ground Motions in the Memphis Area," by H. Hwang, C.S. Lee, K.W. Ng and T.S. Chang, 8/2/90, (PB91-190751, A05, MF-A01).

- NCEER-91-0001 "Proceedings from the Third Japan-U.S. Workshop on Earthquake Resistant Design of Lifeline Facilities and Countermeasures for Soil Liquefaction, December 17-19, 1990," edited by T.D. O'Rourke and M. Hamada, 2/1/91, (PB91-179259, A99, MF-A04).
- NCEER-91-0002 "Physical Space Solutions of Non-Proportionally Damped Systems," by M. Tong, Z. Liang and G.C. Lee, 1/15/91, (PB91-179242, A04, MF-A01).
- NCEER-91-0003 "Seismic Response of Single Piles and Pile Groups," by K. Fan and G. Gazetas, 1/10/91, (PB92-174994, A04, MF-A01).
- NCEER-91-0004 "Damping of Structures: Part 1 - Theory of Complex Damping," by Z. Liang and G. Lee, 10/10/91, (PB92-197235, A12, MF-A03).
- NCEER-91-0005 "3D-BASIS - Nonlinear Dynamic Analysis of Three Dimensional Base Isolated Structures: Part II," by S. Nagarajaiah, A.M. Reinhorn and M.C. Constantinou, 2/28/91, (PB91-190553, A07, MF-A01). This report has been replaced by NCEER-93-0011.
- NCEER-91-0006 "A Multidimensional Hysteretic Model for Plasticity Deforming Metals in Energy Absorbing Devices," by E.J. Graesser and F.A. Cozzarelli, 4/9/91, (PB92-108364, A04, MF-A01).
- NCEER-91-0007 "A Framework for Customizable Knowledge-Based Expert Systems with an Application to a KBES for Evaluating the Seismic Resistance of Existing Buildings," by E.G. Ibarra-Anaya and S.J. Fennes, 4/9/91, (PB91-210930, A08, MF-A01).
- NCEER-91-0008 "Nonlinear Analysis of Steel Frames with Semi-Rigid Connections Using the Capacity Spectrum Method," by G.G. Deierlein, S-H. Hsieh, Y-J. Shen and J.F. Abel, 7/2/91, (PB92-113828, A05, MF-A01).
- NCEER-91-0009 "Earthquake Education Materials for Grades K-12," by K.E.K. Ross, 4/30/91, (PB91-212142, A06, MF-A01). This report has been replaced by NCEER-92-0018.
- NCEER-91-0010 "Phase Wave Velocities and Displacement Phase Differences in a Harmonically Oscillating Pile," by N. Makris and G. Gazetas, 7/8/91, (PB92-108356, A04, MF-A01).
- NCEER-91-0011 "Dynamic Characteristics of a Full-Size Five-Story Steel Structure and a 2/5 Scale Model," by K.C. Chang, G.C. Yao, G.C. Lee, D.S. Hao and Y.C. Yeh, 7/2/91, (PB93-116648, A06, MF-A02).
- NCEER-91-0012 "Seismic Response of a 2/5 Scale Steel Structure with Added Viscoelastic Dampers," by K.C. Chang, T.T. Soong, S-T. Oh and M.L. Lai, 5/17/91, (PB92-110816, A05, MF-A01).
- NCEER-91-0013 "Earthquake Response of Retaining Walls; Full-Scale Testing and Computational Modeling," by S. Alampalli and A-W.M. Elgamal, 6/20/91, to be published.
- NCEER-91-0014 "3D-BASIS-M: Nonlinear Dynamic Analysis of Multiple Building Base Isolated Structures," by P.C. Tsopelas, S. Nagarajaiah, M.C. Constantinou and A.M. Reinhorn, 5/28/91, (PB92-113885, A09, MF-A02).
- NCEER-91-0015 "Evaluation of SEAOC Design Requirements for Sliding Isolated Structures," by D. Theodossiou and M.C. Constantinou, 6/10/91, (PB92-114602, A11, MF-A03).
- NCEER-91-0016 "Closed-Loop Modal Testing of a 27-Story Reinforced Concrete Flat Plate-Core Building," by H.R. Somaprasad, T. Toksoy, H. Yoshiyuki and A.E. Aktan, 7/15/91, (PB92-129980, A07, MF-A02).
- NCEER-91-0017 "Shake Table Test of a 1/6 Scale Two-Story Lightly Reinforced Concrete Building," by A.G. El-Attar, R.N. White and P. Gergely, 2/28/91, (PB92-222447, A06, MF-A02).
- NCEER-91-0018 "Shake Table Test of a 1/8 Scale Three-Story Lightly Reinforced Concrete Building," by A.G. El-Attar, R.N. White and P. Gergely, 2/28/91, (PB93-116630, A08, MF-A02).
- NCEER-91-0019 "Transfer Functions for Rigid Rectangular Foundations," by A.S. Veletsos, A.M. Prasad and W.H. Wu, 7/31/91, to be published.

- NCEER-91-0020 "Hybrid Control of Seismic-Excited Nonlinear and Inelastic Structural Systems," by J.N. Yang, Z. Li and A. Daniellians, 8/1/91, (PB92-143171, A06, MF-A02).
- NCEER-91-0021 "The NCEER-91 Earthquake Catalog: Improved Intensity-Based Magnitudes and Recurrence Relations for U.S. Earthquakes East of New Madrid," by L. Seeber and J.G. Armbruster, 8/28/91, (PB92-176742, A06, MF-A02).
- NCEER-91-0022 "Proceedings from the Implementation of Earthquake Planning and Education in Schools: The Need for Change - The Roles of the Changemakers," by K.E.K. Ross and F. Winslow, 7/23/91, (PB92-129998, A12, MF-A03).
- NCEER-91-0023 "A Study of Reliability-Based Criteria for Seismic Design of Reinforced Concrete Frame Buildings," by H.H.M. Hwang and H-M. Hsu, 8/10/91, (PB92-140235, A09, MF-A02).
- NCEER-91-0024 "Experimental Verification of a Number of Structural System Identification Algorithms," by R.G. Ghanem, H. Gavin and M. Shinozuka, 9/18/91, (PB92-176577, A18, MF-A04).
- NCEER-91-0025 "Probabilistic Evaluation of Liquefaction Potential," by H.H.M. Hwang and C.S. Lee," 11/25/91, (PB92-143429, A05, MF-A01).
- NCEER-91-0026 "Instantaneous Optimal Control for Linear, Nonlinear and Hysteretic Structures - Stable Controllers," by J.N. Yang and Z. Li, 11/15/91, (PB92-163807, A04, MF-A01).
- NCEER-91-0027 "Experimental and Theoretical Study of a Sliding Isolation System for Bridges," by M.C. Constantinou, A. Kartoum, A.M. Reinhorn and P. Bradford, 11/15/91, (PB92-176973, A10, MF-A03).
- NCEER-92-0001 "Case Studies of Liquefaction and Lifeline Performance During Past Earthquakes, Volume 1: Japanese Case Studies," Edited by M. Hamada and T. O'Rourke, 2/17/92, (PB92-197243, A18, MF-A04).
- NCEER-92-0002 "Case Studies of Liquefaction and Lifeline Performance During Past Earthquakes, Volume 2: United States Case Studies," Edited by T. O'Rourke and M. Hamada, 2/17/92, (PB92-197250, A20, MF-A04).
- NCEER-92-0003 "Issues in Earthquake Education," Edited by K. Ross, 2/3/92, (PB92-222389, A07, MF-A02).
- NCEER-92-0004 "Proceedings from the First U.S. - Japan Workshop on Earthquake Protective Systems for Bridges," Edited by I.G. Buckle, 2/4/92, (PB94-142239, A99, MF-A06).
- NCEER-92-0005 "Seismic Ground Motion from a Haskell-Type Source in a Multiple-Layered Half-Space," A.P. Theoharis, G. Deodatis and M. Shinozuka, 1/2/92, to be published.
- NCEER-92-0006 "Proceedings from the Site Effects Workshop," Edited by R. Whitman, 2/29/92, (PB92-197201, A04, MF-A01).
- NCEER-92-0007 "Engineering Evaluation of Permanent Ground Deformations Due to Seismically-Induced Liquefaction," by M.H. Baziar, R. Dobry and A-W.M. Elgamel, 3/24/92, (PB92-222421, A13, MF-A03).
- NCEER-92-0008 "A Procedure for the Seismic Evaluation of Buildings in the Central and Eastern United States," by C.D. Poland and J.O. Malley, 4/2/92, (PB92-222439, A20, MF-A04).
- NCEER-92-0009 "Experimental and Analytical Study of a Hybrid Isolation System Using Friction Controllable Sliding Bearings," by M.Q. Feng, S. Fujii and M. Shinozuka, 5/15/92, (PB93-150282, A06, MF-A02).
- NCEER-92-0010 "Seismic Resistance of Slab-Column Connections in Existing Non-Ductile Flat-Plate Buildings," by A.J. Durrani and Y. Du, 5/18/92, (PB93-116812, A06, MF-A02).
- NCEER-92-0011 "The Hysteretic and Dynamic Behavior of Brick Masonry Walls Upgraded by Ferrocement Coatings Under Cyclic Loading and Strong Simulated Ground Motion," by H. Lee and S.P. Prawl, 5/11/92, to be published.
- NCEER-92-0012 "Study of Wire Rope Systems for Seismic Protection of Equipment in Buildings," by G.F. Demetriades, M.C. Constantinou and A.M. Reinhorn, 5/20/92, (PB93-116655, A08, MF-A02).

- NCEER-92-0013 "Shape Memory Structural Dampers: Material Properties, Design and Seismic Testing," by P.R. Witting and F.A. Cozzarelli, 5/26/92, (PB93-116663, A05, MF-A01).
- NCEER-92-0014 "Longitudinal Permanent Ground Deformation Effects on Buried Continuous Pipelines," by M.J. O'Rourke, and C. Nordberg, 6/15/92, (PB93-116671, A08, MF-A02).
- NCEER-92-0015 "A Simulation Method for Stationary Gaussian Random Functions Based on the Sampling Theorem," by M. Grigoriu and S. Balopoulou, 6/11/92, (PB93-127496, A05, MF-A01).
- NCEER-92-0016 "Gravity-Load-Designed Reinforced Concrete Buildings: Seismic Evaluation of Existing Construction and Detailing Strategies for Improved Seismic Resistance," by G.W. Hoffmann, S.K. Kunnath, A.M. Reinhorn and J.B. Mander, 7/15/92, (PB94-142007, A08, MF-A02).
- NCEER-92-0017 "Observations on Water System and Pipeline Performance in the Limón Area of Costa Rica Due to the April 22, 1991 Earthquake," by M. O'Rourke and D. Ballantyne, 6/30/92, (PB93-126811, A06, MF-A02).
- NCEER-92-0018 "Fourth Edition of Earthquake Education Materials for Grades K-12," Edited by K.E.K. Ross, 8/10/92, (PB93-114023, A07, MF-A02).
- NCEER-92-0019 "Proceedings from the Fourth Japan-U.S. Workshop on Earthquake Resistant Design of Lifeline Facilities and Countermeasures for Soil Liquefaction," Edited by M. Hamada and T.D. O'Rourke, 8/12/92, (PB93-163939, A99, MF-E11).
- NCEER-92-0020 "Active Bracing System: A Full Scale Implementation of Active Control," by A.M. Reinhorn, T.T. Soong, R.C. Lin, M.A. Riley, Y.P. Wang, S. Aizawa and M. Higashino, 8/14/92, (PB93-127512, A06, MF-A02).
- NCEER-92-0021 "Empirical Analysis of Horizontal Ground Displacement Generated by Liquefaction-Induced Lateral Spreads," by S.F. Bartlett and T.L. Youd, 8/17/92, (PB93-188241, A06, MF-A02).
- NCEER-92-0022 "IDARC Version 3.0: Inelastic Damage Analysis of Reinforced Concrete Structures," by S.K. Kunnath, A.M. Reinhorn and R.F. Lobo, 8/31/92, (PB93-227502, A07, MF-A02).
- NCEER-92-0023 "A Semi-Empirical Analysis of Strong-Motion Peaks in Terms of Seismic Source, Propagation Path and Local Site Conditions, by M. Kamiyama, M.J. O'Rourke and R. Flores-Berrones, 9/9/92, (PB93-150266, A08, MF-A02).
- NCEER-92-0024 "Seismic Behavior of Reinforced Concrete Frame Structures with Nonductile Details, Part I: Summary of Experimental Findings of Full Scale Beam-Column Joint Tests," by A. Beres, R.N. White and P. Gergely, 9/30/92, (PB93-227783, A05, MF-A01).
- NCEER-92-0025 "Experimental Results of Repaired and Retrofitted Beam-Column Joint Tests in Lightly Reinforced Concrete Frame Buildings," by A. Beres, S. El-Borgi, R.N. White and P. Gergely, 10/29/92, (PB93-227791, A05, MF-A01).
- NCEER-92-0026 "A Generalization of Optimal Control Theory: Linear and Nonlinear Structures," by J.N. Yang, Z. Li and S. Vongchavalitkul, 11/2/92, (PB93-188621, A05, MF-A01).
- NCEER-92-0027 "Seismic Resistance of Reinforced Concrete Frame Structures Designed Only for Gravity Loads: Part I - Design and Properties of a One-Third Scale Model Structure," by J.M. Bracci, A.M. Reinhorn and J.B. Mander, 12/1/92, (PB94-104502, A08, MF-A02).
- NCEER-92-0028 "Seismic Resistance of Reinforced Concrete Frame Structures Designed Only for Gravity Loads: Part II - Experimental Performance of Subassemblages," by L.E. Aycaardi, J.B. Mander and A.M. Reinhorn, 12/1/92, (PB94-104510, A08, MF-A02).
- NCEER-92-0029 "Seismic Resistance of Reinforced Concrete Frame Structures Designed Only for Gravity Loads: Part III - Experimental Performance and Analytical Study of a Structural Model," by J.M. Bracci, A.M. Reinhorn and J.B. Mander, 12/1/92, (PB93-227528, A09, MF-A01).

- NCEER-92-0030 "Evaluation of Seismic Retrofit of Reinforced Concrete Frame Structures: Part I - Experimental Performance of Retrofitted Subassemblages," by D. Choudhuri, J.B. Mander and A.M. Reinhorn, 12/8/92, (PB93-198307, A07, MF-A02).
- NCEER-92-0031 "Evaluation of Seismic Retrofit of Reinforced Concrete Frame Structures: Part II - Experimental Performance and Analytical Study of a Retrofitted Structural Model," by J.M. Bracci, A.M. Reinhorn and J.B. Mander, 12/8/92, (PB93-198315, A09, MF-A03).
- NCEER-92-0032 "Experimental and Analytical Investigation of Seismic Response of Structures with Supplemental Fluid Viscous Dampers," by M.C. Constantinou and M.D. Symans, 12/21/92, (PB93-191435, A10, MF-A03). This report is available only through NTIS (see address given above).
- NCEER-92-0033 "Reconnaissance Report on the Cairo, Egypt Earthquake of October 12, 1992," by M. Khater, 12/23/92, (PB93-188621, A03, MF-A01).
- NCEER-92-0034 "Low-Level Dynamic Characteristics of Four Tall Flat-Plate Buildings in New York City," by H. Gavin, S. Yuan, J. Grossman, E. Pekelis and K. Jacob, 12/28/92, (PB93-188217, A07, MF-A02).
- NCEER-93-0001 "An Experimental Study on the Seismic Performance of Brick-Infilled Steel Frames With and Without Retrofit," by J.B. Mander, B. Nair, K. Wojtkowski and J. Ma, 1/29/93, (PB93-227510, A07, MF-A02).
- NCEER-93-0002 "Social Accounting for Disaster Preparedness and Recovery Planning," by S. Cole, E. Pantoja and V. Razak, 2/22/93, (PB94-142114, A12, MF-A03).
- NCEER-93-0003 "Assessment of 1991 NEHRP Provisions for Nonstructural Components and Recommended Revisions," by T.T. Soong, G. Chen, Z. Wu, R-H. Zhang and M. Grigoriu, 3/1/93, (PB93-188639, A06, MF-A02).
- NCEER-93-0004 "Evaluation of Static and Response Spectrum Analysis Procedures of SEAOC/UBC for Seismic Isolated Structures," by C.W. Winters and M.C. Constantinou, 3/23/93, (PB93-198299, A10, MF-A03).
- NCEER-93-0005 "Earthquakes in the Northeast - Are We Ignoring the Hazard? A Workshop on Earthquake Science and Safety for Educators," edited by K.E.K. Ross, 4/2/93, (PB94-103066, A09, MF-A02).
- NCEER-93-0006 "Inelastic Response of Reinforced Concrete Structures with Viscoelastic Braces," by R.F. Lobo, J.M. Bracci, K.L. Shen, A.M. Reinhorn and T.T. Soong, 4/5/93, (PB93-227486, A05, MF-A02).
- NCEER-93-0007 "Seismic Testing of Installation Methods for Computers and Data Processing Equipment," by K. Kosar, T.T. Soong, K.L. Shen, J.A. HoLung and Y.K. Lin, 4/12/93, (PB93-198299, A07, MF-A02).
- NCEER-93-0008 "Retrofit of Reinforced Concrete Frames Using Added Dampers," by A. Reinhorn, M. Constantinou and C. Li, to be published.
- NCEER-93-0009 "Seismic Behavior and Design Guidelines for Steel Frame Structures with Added Viscoelastic Dampers," by K.C. Chang, M.L. Lai, T.T. Soong, D.S. Hao and Y.C. Yeh, 5/1/93, (PB94-141959, A07, MF-A02).
- NCEER-93-0010 "Seismic Performance of Shear-Critical Reinforced Concrete Bridge Piers," by J.B. Mander, S.M. Waheed, M.T.A. Chaudhary and S.S. Chen, 5/12/93, (PB93-227494, A08, MF-A02).
- NCEER-93-0011 "3D-BASIS-TABS: Computer Program for Nonlinear Dynamic Analysis of Three Dimensional Base Isolated Structures," by S. Nagarajaiah, C. Li, A.M. Reinhorn and M.C. Constantinou, 8/2/93, (PB94-141819, A09, MF-A02).
- NCEER-93-0012 "Effects of Hydrocarbon Spills from an Oil Pipeline Break on Ground Water," by O.J. Helweg and H.H.M. Hwang, 8/3/93, (PB94-141942, A06, MF-A02).
- NCEER-93-0013 "Simplified Procedures for Seismic Design of Nonstructural Components and Assessment of Current Code Provisions," by M.P. Singh, L.E. Suarez, E.E. Matheu and G.O. Maldonado, 8/4/93, (PB94-141827, A09, MF-A02).
- NCEER-93-0014 "An Energy Approach to Seismic Analysis and Design of Secondary Systems," by G. Chen and T.T. Soong, 8/6/93, (PB94-142767, A11, MF-A03).

- NCEER-93-0015 "Proceedings from School Sites: Becoming Prepared for Earthquakes - Commemorating the Third Anniversary of the Loma Prieta Earthquake," Edited by F.E. Winslow and K.E.K. Ross, 8/16/93, (PB94-154275, A16, MF-A02).
- NCEER-93-0016 "Reconnaissance Report of Damage to Historic Monuments in Cairo, Egypt Following the October 12, 1992 Dahshur Earthquake," by D. Sykora, D. Look, G. Croci, E. Karaesmen and E. Karaesmen, 8/19/93, (PB94-142221, A08, MF-A02).
- NCEER-93-0017 "The Island of Guam Earthquake of August 8, 1993," by S.W. Swan and S.K. Harris, 9/30/93, (PB94-141843, A04, MF-A01).
- NCEER-93-0018 "Engineering Aspects of the October 12, 1992 Egyptian Earthquake," by A.W. Elgamal, M. Amer, K. Adalier and A. Abul-Fadl, 10/7/93, (PB94-141983, A05, MF-A01).
- NCEER-93-0019 "Development of an Earthquake Motion Simulator and its Application in Dynamic Centrifuge Testing," by I. Krstelj, Supervised by J.H. Prevost, 10/23/93, (PB94-181773, A-10, MF-A03).
- NCEER-93-0020 "NCEER-Taisei Corporation Research Program on Sliding Seismic Isolation Systems for Bridges: Experimental and Analytical Study of a Friction Pendulum System (FPS)," by M.C. Constantinou, P. Tsopelas, Y-S. Kim and S. Okamoto, 11/1/93, (PB94-142775, A08, MF-A02).
- NCEER-93-0021 "Finite Element Modeling of Elastomeric Seismic Isolation Bearings," by L.J. Billings, Supervised by R. Shepherd, 11/8/93, to be published.
- NCEER-93-0022 "Seismic Vulnerability of Equipment in Critical Facilities: Life-Safety and Operational Consequences," by K. Porter, G.S. Johnson, M.M. Zadeh, C. Scawthorn and S. Eder, 11/24/93, (PB94-181765, A16, MF-A03).
- NCEER-93-0023 "Hokkaido Nansei-oki, Japan Earthquake of July 12, 1993, by P.I. Yanev and C.R. Scawthorn, 12/23/93, (PB94-181500, A07, MF-A01).
- NCEER-94-0001 "An Evaluation of Seismic Serviceability of Water Supply Networks with Application to the San Francisco Auxiliary Water Supply System," by I. Markov, Supervised by M. Grigoriu and T. O'Rourke, 1/21/94, (PB94-204013, A07, MF-A02).
- NCEER-94-0002 "NCEER-Taisei Corporation Research Program on Sliding Seismic Isolation Systems for Bridges: Experimental and Analytical Study of Systems Consisting of Sliding Bearings, Rubber Restoring Force Devices and Fluid Dampers," Volumes I and II, by P. Tsopelas, S. Okamoto, M.C. Constantinou, D. Ozaki and S. Fujii, 2/4/94, (PB94-181740, A09, MF-A02 and PB94-181757, A12, MF-A03).
- NCEER-94-0003 "A Markov Model for Local and Global Damage Indices in Seismic Analysis," by S. Rahman and M. Grigoriu, 2/18/94, (PB94-206000, A12, MF-A03).
- NCEER-94-0004 "Proceedings from the NCEER Workshop on Seismic Response of Masonry Infills," edited by D.P. Abrams, 3/1/94, (PB94-180783, A07, MF-A02).
- NCEER-94-0005 "The Northridge, California Earthquake of January 17, 1994: General Reconnaissance Report," edited by J.D. Goltz, 3/11/94, (PB94-193943, A10, MF-A03).
- NCEER-94-0006 "Seismic Energy Based Fatigue Damage Analysis of Bridge Columns: Part I - Evaluation of Seismic Capacity," by G.A. Chang and J.B. Mander, 3/14/94, (PB94-219185, A11, MF-A03).
- NCEER-94-0007 "Seismic Isolation of Multi-Story Frame Structures Using Spherical Sliding Isolation Systems," by T.M. Al-Hussaini, V.A. Zayas and M.C. Constantinou, 3/17/94, (PB94-193745, A09, MF-A02).
- NCEER-94-0008 "The Northridge, California Earthquake of January 17, 1994: Performance of Highway Bridges," edited by I.G. Buckle, 3/24/94, (PB94-193851, A06, MF-A02).
- NCEER-94-0009 "Proceedings of the Third U.S.-Japan Workshop on Earthquake Protective Systems for Bridges," edited by I.G. Buckle and I. Friedland, 3/31/94, (PB94-195815, A99, MF-A06).

- NCEER-94-0010 "3D-BASIS-ME: Computer Program for Nonlinear Dynamic Analysis of Seismically Isolated Single and Multiple Structures and Liquid Storage Tanks," by P.C. Tsopelas, M.C. Constantinou and A.M. Reinhorn, 4/12/94, (PB94-204922, A09, MF-A02).
- NCEER-94-0011 "The Northridge, California Earthquake of January 17, 1994: Performance of Gas Transmission Pipelines," by T.D. O'Rourke and M.C. Palmer, 5/16/94, (PB94-204989, A05, MF-A01).
- NCEER-94-0012 "Feasibility Study of Replacement Procedures and Earthquake Performance Related to Gas Transmission Pipelines," by T.D. O'Rourke and M.C. Palmer, 5/25/94, (PB94-206638, A09, MF-A02).
- NCEER-94-0013 "Seismic Energy Based Fatigue Damage Analysis of Bridge Columns: Part II - Evaluation of Seismic Demand," by G.A. Chang and J.B. Mander, 6/1/94, (PB95-18106, A08, MF-A02).
- NCEER-94-0014 "NCEER-Taisei Corporation Research Program on Sliding Seismic Isolation Systems for Bridges: Experimental and Analytical Study of a System Consisting of Sliding Bearings and Fluid Restoring Force/Damping Devices," by P. Tsopelas and M.C. Constantinou, 6/13/94, (PB94-219144, A10, MF-A03).
- NCEER-94-0015 "Generation of Hazard-Consistent Fragility Curves for Seismic Loss Estimation Studies," by H. Hwang and J-R. Huo, 6/14/94, (PB95-181996, A09, MF-A02).
- NCEER-94-0016 "Seismic Study of Building Frames with Added Energy-Absorbing Devices," by W.S. Pong, C.S. Tsai and G.C. Lee, 6/20/94, (PB94-219136, A10, A03).
- NCEER-94-0017 "Sliding Mode Control for Seismic-Excited Linear and Nonlinear Civil Engineering Structures," by J. Yang, J. Wu, A. Agrawal and Z. Li, 6/21/94, (PB95-138483, A06, MF-A02).
- NCEER-94-0018 "3D-BASIS-TABS Version 2.0: Computer Program for Nonlinear Dynamic Analysis of Three Dimensional Base Isolated Structures," by A.M. Reinhorn, S. Nagarajaiah, M.C. Constantinou, P. Tsopelas and R. Li, 6/22/94, (PB95-182176, A08, MF-A02).
- NCEER-94-0019 "Proceedings of the International Workshop on Civil Infrastructure Systems: Application of Intelligent Systems and Advanced Materials on Bridge Systems," Edited by G.C. Lee and K.C. Chang, 7/18/94, (PB95-252474, A20, MF-A04).
- NCEER-94-0020 "Study of Seismic Isolation Systems for Computer Floors," by V. Lambrou and M.C. Constantinou, 7/19/94, (PB95-138533, A10, MF-A03).
- NCEER-94-0021 "Proceedings of the U.S.-Italian Workshop on Guidelines for Seismic Evaluation and Rehabilitation of Unreinforced Masonry Buildings," Edited by D.P. Abrams and G.M. Calvi, 7/20/94, (PB95-138749, A13, MF-A03).
- NCEER-94-0022 "NCEER-Taisei Corporation Research Program on Sliding Seismic Isolation Systems for Bridges: Experimental and Analytical Study of a System Consisting of Lubricated PTFE Sliding Bearings and Mild Steel Dampers," by P. Tsopelas and M.C. Constantinou, 7/22/94, (PB95-182184, A08, MF-A02).
- NCEER-94-0023 "Development of Reliability-Based Design Criteria for Buildings Under Seismic Load," by Y.K. Wen, H. Hwang and M. Shinozuka, 8/1/94, (PB95-211934, A08, MF-A02).
- NCEER-94-0024 "Experimental Verification of Acceleration Feedback Control Strategies for an Active Tendon System," by S.J. Dyke, B.F. Spencer, Jr., P. Quast, M.K. Sain, D.C. Kaspari, Jr. and T.T. Soong, 8/29/94, (PB95-212320, A05, MF-A01).
- NCEER-94-0025 "Seismic Retrofitting Manual for Highway Bridges," Edited by I.G. Buckle and I.F. Friedland, published by the Federal Highway Administration (PB95-212676, A15, MF-A03).
- NCEER-94-0026 "Proceedings from the Fifth U.S.-Japan Workshop on Earthquake Resistant Design of Lifeline Facilities and Countermeasures Against Soil Liquefaction," Edited by T.D. O'Rourke and M. Hamada, 11/7/94, (PB95-220802, A99, MF-E08).

- NCEER-95-0001 “Experimental and Analytical Investigation of Seismic Retrofit of Structures with Supplemental Damping: Part 1 - Fluid Viscous Damping Devices,” by A.M. Reinhorn, C. Li and M.C. Constantinou, 1/3/95, (PB95-266599, A09, MF-A02).
- NCEER-95-0002 “Experimental and Analytical Study of Low-Cycle Fatigue Behavior of Semi-Rigid Top-And-Seat Angle Connections,” by G. Pekcan, J.B. Mander and S.S. Chen, 1/5/95, (PB95-220042, A07, MF-A02).
- NCEER-95-0003 “NCEER-ATC Joint Study on Fragility of Buildings,” by T. Anagnos, C. Rojahn and A.S. Kiremidjian, 1/20/95, (PB95-220026, A06, MF-A02).
- NCEER-95-0004 “Nonlinear Control Algorithms for Peak Response Reduction,” by Z. Wu, T.T. Soong, V. Gattulli and R.C. Lin, 2/16/95, (PB95-220349, A05, MF-A01).
- NCEER-95-0005 “Pipeline Replacement Feasibility Study: A Methodology for Minimizing Seismic and Corrosion Risks to Underground Natural Gas Pipelines,” by R.T. Eguchi, H.A. Seligson and D.G. Honegger, 3/2/95, (PB95-252326, A06, MF-A02).
- NCEER-95-0006 “Evaluation of Seismic Performance of an 11-Story Frame Building During the 1994 Northridge Earthquake,” by F. Naeim, R. DiSulio, K. Benuska, A. Reinhorn and C. Li, to be published.
- NCEER-95-0007 “Prioritization of Bridges for Seismic Retrofitting,” by N. Basöz and A.S. Kiremidjian, 4/24/95, (PB95-252300, A08, MF-A02).
- NCEER-95-0008 “Method for Developing Motion Damage Relationships for Reinforced Concrete Frames,” by A. Singhal and A.S. Kiremidjian, 5/11/95, (PB95-266607, A06, MF-A02).
- NCEER-95-0009 “Experimental and Analytical Investigation of Seismic Retrofit of Structures with Supplemental Damping: Part II - Friction Devices,” by C. Li and A.M. Reinhorn, 7/6/95, (PB96-128087, A11, MF-A03).
- NCEER-95-0010 “Experimental Performance and Analytical Study of a Non-Ductile Reinforced Concrete Frame Structure Retrofitted with Elastomeric Spring Dampers,” by G. Pekcan, J.B. Mander and S.S. Chen, 7/14/95, (PB96-137161, A08, MF-A02).
- NCEER-95-0011 “Development and Experimental Study of Semi-Active Fluid Damping Devices for Seismic Protection of Structures,” by M.D. Symans and M.C. Constantinou, 8/3/95, (PB96-136940, A23, MF-A04).
- NCEER-95-0012 “Real-Time Structural Parameter Modification (RSPM): Development of Innervated Structures,” by Z. Liang, M. Tong and G.C. Lee, 4/11/95, (PB96-137153, A06, MF-A01).
- NCEER-95-0013 “Experimental and Analytical Investigation of Seismic Retrofit of Structures with Supplemental Damping: Part III - Viscous Damping Walls,” by A.M. Reinhorn and C. Li, 10/1/95, (PB96-176409, A11, MF-A03).
- NCEER-95-0014 “Seismic Fragility Analysis of Equipment and Structures in a Memphis Electric Substation,” by J-R. Huo and H.H.M. Hwang, 8/10/95, (PB96-128087, A09, MF-A02).
- NCEER-95-0015 “The Hanshin-Awaji Earthquake of January 17, 1995: Performance of Lifelines,” Edited by M. Shinozuka, 11/3/95, (PB96-176383, A15, MF-A03).
- NCEER-95-0016 “Highway Culvert Performance During Earthquakes,” by T.L. Youd and C.J. Beckman, available as NCEER-96-0015.
- NCEER-95-0017 “The Hanshin-Awaji Earthquake of January 17, 1995: Performance of Highway Bridges,” Edited by I.G. Buckle, 12/1/95, to be published.
- NCEER-95-0018 “Modeling of Masonry Infill Panels for Structural Analysis,” by A.M. Reinhorn, A. Madan, R.E. Valles, Y. Reichmann and J.B. Mander, 12/8/95, (PB97-110886, MF-A01, A06).
- NCEER-95-0019 “Optimal Polynomial Control for Linear and Nonlinear Structures,” by A.K. Agrawal and J.N. Yang, 12/11/95, (PB96-168737, A07, MF-A02).

- NCEER-95-0020 "Retrofit of Non-Ductile Reinforced Concrete Frames Using Friction Dampers," by R.S. Rao, P. Gergely and R.N. White, 12/22/95, (PB97-133508, A10, MF-A02).
- NCEER-95-0021 "Parametric Results for Seismic Response of Pile-Supported Bridge Bents," by G. Mylonakis, A. Nikolaou and G. Gazetas, 12/22/95, (PB97-100242, A12, MF-A03).
- NCEER-95-0022 "Kinematic Bending Moments in Seismically Stressed Piles," by A. Nikolaou, G. Mylonakis and G. Gazetas, 12/23/95, (PB97-113914, MF-A03, A13).
- NCEER-96-0001 "Dynamic Response of Unreinforced Masonry Buildings with Flexible Diaphragms," by A.C. Costley and D.P. Abrams, 10/10/96, (PB97-133573, MF-A03, A15).
- NCEER-96-0002 "State of the Art Review: Foundations and Retaining Structures," by I. Po Lam, to be published.
- NCEER-96-0003 "Ductility of Rectangular Reinforced Concrete Bridge Columns with Moderate Confinement," by N. Wehbe, M. Saiidi, D. Sanders and B. Douglas, 11/7/96, (PB97-133557, A06, MF-A02).
- NCEER-96-0004 "Proceedings of the Long-Span Bridge Seismic Research Workshop," edited by I.G. Buckle and I.M. Friedland, to be published.
- NCEER-96-0005 "Establish Representative Pier Types for Comprehensive Study: Eastern United States," by J. Kulicki and Z. Prucz, 5/28/96, (PB98-119217, A07, MF-A02).
- NCEER-96-0006 "Establish Representative Pier Types for Comprehensive Study: Western United States," by R. Imbsen, R.A. Schamber and T.A. Osterkamp, 5/28/96, (PB98-118607, A07, MF-A02).
- NCEER-96-0007 "Nonlinear Control Techniques for Dynamical Systems with Uncertain Parameters," by R.G. Ghanem and M.I. Bujakov, 5/27/96, (PB97-100259, A17, MF-A03).
- NCEER-96-0008 "Seismic Evaluation of a 30-Year Old Non-Ductile Highway Bridge Pier and Its Retrofit," by J.B. Mander, B. Mahmoodzadegan, S. Bhadra and S.S. Chen, 5/31/96, (PB97-110902, MF-A03, A10).
- NCEER-96-0009 "Seismic Performance of a Model Reinforced Concrete Bridge Pier Before and After Retrofit," by J.B. Mander, J.H. Kim and C.A. Ligozio, 5/31/96, (PB97-110910, MF-A02, A10).
- NCEER-96-0010 "IDARC2D Version 4.0: A Computer Program for the Inelastic Damage Analysis of Buildings," by R.E. Valles, A.M. Reinhorn, S.K. Kunnath, C. Li and A. Madan, 6/3/96, (PB97-100234, A17, MF-A03).
- NCEER-96-0011 "Estimation of the Economic Impact of Multiple Lifeline Disruption: Memphis Light, Gas and Water Division Case Study," by S.E. Chang, H.A. Seligson and R.T. Eguchi, 8/16/96, (PB97-133490, A11, MF-A03).
- NCEER-96-0012 "Proceedings from the Sixth Japan-U.S. Workshop on Earthquake Resistant Design of Lifeline Facilities and Countermeasures Against Soil Liquefaction, Edited by M. Hamada and T. O'Rourke, 9/11/96, (PB97-133581, A99, MF-A06).
- NCEER-96-0013 "Chemical Hazards, Mitigation and Preparedness in Areas of High Seismic Risk: A Methodology for Estimating the Risk of Post-Earthquake Hazardous Materials Release," by H.A. Seligson, R.T. Eguchi, K.J. Tierney and K. Richmond, 11/7/96, (PB97-133565, MF-A02, A08).
- NCEER-96-0014 "Response of Steel Bridge Bearings to Reversed Cyclic Loading," by J.B. Mander, D-K. Kim, S.S. Chen and G.J. Premus, 11/13/96, (PB97-140735, A12, MF-A03).
- NCEER-96-0015 "Highway Culvert Performance During Past Earthquakes," by T.L. Youd and C.J. Beckman, 11/25/96, (PB97-133532, A06, MF-A01).
- NCEER-97-0001 "Evaluation, Prevention and Mitigation of Pounding Effects in Building Structures," by R.E. Valles and A.M. Reinhorn, 2/20/97, (PB97-159552, A14, MF-A03).
- NCEER-97-0002 "Seismic Design Criteria for Bridges and Other Highway Structures," by C. Rojahn, R. Mayes, D.G. Anderson, J. Clark, J.H. Hom, R.V. Nutt and M.J. O'Rourke, 4/30/97, (PB97-194658, A06, MF-A03).

- NCEER-97-0003 "Proceedings of the U.S.-Italian Workshop on Seismic Evaluation and Retrofit," Edited by D.P. Abrams and G.M. Calvi, 3/19/97, (PB97-194666, A13, MF-A03).
- NCEER-97-0004 "Investigation of Seismic Response of Buildings with Linear and Nonlinear Fluid Viscous Dampers," by A.A. Seleemah and M.C. Constantinou, 5/21/97, (PB98-109002, A15, MF-A03).
- NCEER-97-0005 "Proceedings of the Workshop on Earthquake Engineering Frontiers in Transportation Facilities," edited by G.C. Lee and I.M. Friedland, 8/29/97, (PB98-128911, A25, MR-A04).
- NCEER-97-0006 "Cumulative Seismic Damage of Reinforced Concrete Bridge Piers," by S.K. Kunnath, A. El-Bahy, A. Taylor and W. Stone, 9/2/97, (PB98-108814, A11, MF-A03).
- NCEER-97-0007 "Structural Details to Accommodate Seismic Movements of Highway Bridges and Retaining Walls," by R.A. Imbsen, R.A. Schamber, E. Thorkildsen, A. Kartoum, B.T. Martin, T.N. Rosser and J.M. Kulicki, 9/3/97, (PB98-108996, A09, MF-A02).
- NCEER-97-0008 "A Method for Earthquake Motion-Damage Relationships with Application to Reinforced Concrete Frames," by A. Singhal and A.S. Kiremidjian, 9/10/97, (PB98-108988, A13, MF-A03).
- NCEER-97-0009 "Seismic Analysis and Design of Bridge Abutments Considering Sliding and Rotation," by K. Fishman and R. Richards, Jr., 9/15/97, (PB98-108897, A06, MF-A02).
- NCEER-97-0010 "Proceedings of the FHWA/NCEER Workshop on the National Representation of Seismic Ground Motion for New and Existing Highway Facilities," edited by I.M. Friedland, M.S. Power and R.L. Mayes, 9/22/97, (PB98-128903, A21, MF-A04).
- NCEER-97-0011 "Seismic Analysis for Design or Retrofit of Gravity Bridge Abutments," by K.L. Fishman, R. Richards, Jr. and R.C. Divito, 10/2/97, (PB98-128937, A08, MF-A02).
- NCEER-97-0012 "Evaluation of Simplified Methods of Analysis for Yielding Structures," by P. Tsopelas, M.C. Constantinou, C.A. Kircher and A.S. Whittaker, 10/31/97, (PB98-128929, A10, MF-A03).
- NCEER-97-0013 "Seismic Design of Bridge Columns Based on Control and Repairability of Damage," by C-T. Cheng and J.B. Mander, 12/8/97, (PB98-144249, A11, MF-A03).
- NCEER-97-0014 "Seismic Resistance of Bridge Piers Based on Damage Avoidance Design," by J.B. Mander and C-T. Cheng, 12/10/97, (PB98-144223, A09, MF-A02).
- NCEER-97-0015 "Seismic Response of Nominally Symmetric Systems with Strength Uncertainty," by S. Balopoulou and M. Grigoriu, 12/23/97, (PB98-153422, A11, MF-A03).
- NCEER-97-0016 "Evaluation of Seismic Retrofit Methods for Reinforced Concrete Bridge Columns," by T.J. Wipf, F.W. Klaiber and F.M. Russo, 12/28/97, (PB98-144215, A12, MF-A03).
- NCEER-97-0017 "Seismic Fragility of Existing Conventional Reinforced Concrete Highway Bridges," by C.L. Mullen and A.S. Cakmak, 12/30/97, (PB98-153406, A08, MF-A02).
- NCEER-97-0018 "Loss Assessment of Memphis Buildings," edited by D.P. Abrams and M. Shinozuka, 12/31/97, (PB98-144231, A13, MF-A03).
- NCEER-97-0019 "Seismic Evaluation of Frames with Infill Walls Using Quasi-static Experiments," by K.M. Mosalam, R.N. White and P. Gergely, 12/31/97, (PB98-153455, A07, MF-A02).
- NCEER-97-0020 "Seismic Evaluation of Frames with Infill Walls Using Pseudo-dynamic Experiments," by K.M. Mosalam, R.N. White and P. Gergely, 12/31/97, (PB98-153430, A07, MF-A02).
- NCEER-97-0021 "Computational Strategies for Frames with Infill Walls: Discrete and Smeared Crack Analyses and Seismic Fragility," by K.M. Mosalam, R.N. White and P. Gergely, 12/31/97, (PB98-153414, A10, MF-A02).

- NCEER-97-0022 "Proceedings of the NCEER Workshop on Evaluation of Liquefaction Resistance of Soils," edited by T.L. Youd and I.M. Idriss, 12/31/97, (PB98-155617, A15, MF-A03).
- MCEER-98-0001 "Extraction of Nonlinear Hysteretic Properties of Seismically Isolated Bridges from Quick-Release Field Tests," by Q. Chen, B.M. Douglas, E.M. Maragakis and I.G. Buckle, 5/26/98, (PB99-118838, A06, MF-A01).
- MCEER-98-0002 "Methodologies for Evaluating the Importance of Highway Bridges," by A. Thomas, S. Eshenaur and J. Kulicki, 5/29/98, (PB99-118846, A10, MF-A02).
- MCEER-98-0003 "Capacity Design of Bridge Piers and the Analysis of Overstrength," by J.B. Mander, A. Dutta and P. Goel, 6/1/98, (PB99-118853, A09, MF-A02).
- MCEER-98-0004 "Evaluation of Bridge Damage Data from the Loma Prieta and Northridge, California Earthquakes," by N. Basoz and A. Kiremidjian, 6/2/98, (PB99-118861, A15, MF-A03).
- MCEER-98-0005 "Screening Guide for Rapid Assessment of Liquefaction Hazard at Highway Bridge Sites," by T. L. Youd, 6/16/98, (PB99-118879, A06, not available on microfiche).
- MCEER-98-0006 "Structural Steel and Steel/Concrete Interface Details for Bridges," by P. Ritchie, N. Kauh and J. Kulicki, 7/13/98, (PB99-118945, A06, MF-A01).
- MCEER-98-0007 "Capacity Design and Fatigue Analysis of Confined Concrete Columns," by A. Dutta and J.B. Mander, 7/14/98, (PB99-118960, A14, MF-A03).
- MCEER-98-0008 "Proceedings of the Workshop on Performance Criteria for Telecommunication Services Under Earthquake Conditions," edited by A.J. Schiff, 7/15/98, (PB99-118952, A08, MF-A02).
- MCEER-98-0009 "Fatigue Analysis of Unconfined Concrete Columns," by J.B. Mander, A. Dutta and J.H. Kim, 9/12/98, (PB99-123655, A10, MF-A02).
- MCEER-98-0010 "Centrifuge Modeling of Cyclic Lateral Response of Pile-Cap Systems and Seat-Type Abutments in Dry Sands," by A.D. Gadre and R. Dobry, 10/2/98, (PB99-123606, A13, MF-A03).
- MCEER-98-0011 "IDARC-BRIDGE: A Computational Platform for Seismic Damage Assessment of Bridge Structures," by A.M. Reinhorn, V. Simeonov, G. Mylonakis and Y. Reichman, 10/2/98, (PB99-162919, A15, MF-A03).
- MCEER-98-0012 "Experimental Investigation of the Dynamic Response of Two Bridges Before and After Retrofitting with Elastomeric Bearings," by D.A. Wendichansky, S.S. Chen and J.B. Mander, 10/2/98, (PB99-162927, A15, MF-A03).
- MCEER-98-0013 "Design Procedures for Hinge Restrainers and Hinge Sear Width for Multiple-Frame Bridges," by R. Des Roches and G.L. Fenves, 11/3/98, (PB99-140477, A13, MF-A03).
- MCEER-98-0014 "Response Modification Factors for Seismically Isolated Bridges," by M.C. Constantinou and J.K. Quarshie, 11/3/98, (PB99-140485, A14, MF-A03).
- MCEER-98-0015 "Proceedings of the U.S.-Italy Workshop on Seismic Protective Systems for Bridges," edited by I.M. Friedland and M.C. Constantinou, 11/3/98, (PB2000-101711, A22, MF-A04).
- MCEER-98-0016 "Appropriate Seismic Reliability for Critical Equipment Systems: Recommendations Based on Regional Analysis of Financial and Life Loss," by K. Porter, C. Scawthorn, C. Taylor and N. Blais, 11/10/98, (PB99-157265, A08, MF-A02).
- MCEER-98-0017 "Proceedings of the U.S. Japan Joint Seminar on Civil Infrastructure Systems Research," edited by M. Shinozuka and A. Rose, 11/12/98, (PB99-156713, A16, MF-A03).
- MCEER-98-0018 "Modeling of Pile Footings and Drilled Shafts for Seismic Design," by I. PoLam, M. Kapuskar and D. Chaudhuri, 12/21/98, (PB99-157257, A09, MF-A02).

- MCEER-99-0001 "Seismic Evaluation of a Masonry Infilled Reinforced Concrete Frame by Pseudodynamic Testing," by S.G. Buonopane and R.N. White, 2/16/99, (PB99-162851, A09, MF-A02).
- MCEER-99-0002 "Response History Analysis of Structures with Seismic Isolation and Energy Dissipation Systems: Verification Examples for Program SAP2000," by J. Scheller and M.C. Constantinou, 2/22/99, (PB99-162869, A08, MF-A02).
- MCEER-99-0003 "Experimental Study on the Seismic Design and Retrofit of Bridge Columns Including Axial Load Effects," by A. Dutta, T. Kokorina and J.B. Mander, 2/22/99, (PB99-162877, A09, MF-A02).
- MCEER-99-0004 "Experimental Study of Bridge Elastomeric and Other Isolation and Energy Dissipation Systems with Emphasis on Uplift Prevention and High Velocity Near-source Seismic Excitation," by A. Kasalanati and M. C. Constantinou, 2/26/99, (PB99-162885, A12, MF-A03).
- MCEER-99-0005 "Truss Modeling of Reinforced Concrete Shear-flexure Behavior," by J.H. Kim and J.B. Mander, 3/8/99, (PB99-163693, A12, MF-A03).
- MCEER-99-0006 "Experimental Investigation and Computational Modeling of Seismic Response of a 1:4 Scale Model Steel Structure with a Load Balancing Supplemental Damping System," by G. Pekcan, J.B. Mander and S.S. Chen, 4/2/99, (PB99-162893, A11, MF-A03).
- MCEER-99-0007 "Effect of Vertical Ground Motions on the Structural Response of Highway Bridges," by M.R. Button, C.J. Cronin and R.L. Mayes, 4/10/99, (PB2000-101411, A10, MF-A03).
- MCEER-99-0008 "Seismic Reliability Assessment of Critical Facilities: A Handbook, Supporting Documentation, and Model Code Provisions," by G.S. Johnson, R.E. Sheppard, M.D. Quilici, S.J. Eder and C.R. Scawthorn, 4/12/99, (PB2000-101701, A18, MF-A04).
- MCEER-99-0009 "Impact Assessment of Selected MCEER Highway Project Research on the Seismic Design of Highway Structures," by C. Rojahn, R. Mayes, D.G. Anderson, J.H. Clark, D'Appolonia Engineering, S. Gloyd and R.V. Nutt, 4/14/99, (PB99-162901, A10, MF-A02).
- MCEER-99-0010 "Site Factors and Site Categories in Seismic Codes," by R. Dobry, R. Ramos and M.S. Power, 7/19/99, (PB2000-101705, A08, MF-A02).
- MCEER-99-0011 "Restrainer Design Procedures for Multi-Span Simply-Supported Bridges," by M.J. Randall, M. Saiidi, E. Maragakis and T. Isakovic, 7/20/99, (PB2000-101702, A10, MF-A02).
- MCEER-99-0012 "Property Modification Factors for Seismic Isolation Bearings," by M.C. Constantinou, P. Tsopelas, A. Kasalanati and E. Wolff, 7/20/99, (PB2000-103387, A11, MF-A03).
- MCEER-99-0013 "Critical Seismic Issues for Existing Steel Bridges," by P. Ritchie, N. Kauh and J. Kulicki, 7/20/99, (PB2000-101697, A09, MF-A02).
- MCEER-99-0014 "Nonstructural Damage Database," by A. Kao, T.T. Soong and A. Vender, 7/24/99, (PB2000-101407, A06, MF-A01).
- MCEER-99-0015 "Guide to Remedial Measures for Liquefaction Mitigation at Existing Highway Bridge Sites," by H.G. Cooke and J. K. Mitchell, 7/26/99, (PB2000-101703, A11, MF-A03).
- MCEER-99-0016 "Proceedings of the MCEER Workshop on Ground Motion Methodologies for the Eastern United States," edited by N. Abrahamson and A. Becker, 8/11/99, (PB2000-103385, A07, MF-A02).
- MCEER-99-0017 "Quindío, Colombia Earthquake of January 25, 1999: Reconnaissance Report," by A.P. Asfura and P.J. Flores, 10/4/99, (PB2000-106893, A06, MF-A01).
- MCEER-99-0018 "Hysteretic Models for Cyclic Behavior of Deteriorating Inelastic Structures," by M.V. Sivaselvan and A.M. Reinhorn, 11/5/99, (PB2000-103386, A08, MF-A02).


- MCEER-99-0019 "Proceedings of the 7th U.S.- Japan Workshop on Earthquake Resistant Design of Lifeline Facilities and Countermeasures Against Soil Liquefaction," edited by T.D. O'Rourke, J.P. Bardet and M. Hamada, 11/19/99, (PB2000-103354, A99, MF-A06).
- MCEER-99-0020 "Development of Measurement Capability for Micro-Vibration Evaluations with Application to Chip Fabrication Facilities," by G.C. Lee, Z. Liang, J.W. Song, J.D. Shen and W.C. Liu, 12/1/99, (PB2000-105993, A08, MF-A02).
- MCEER-99-0021 "Design and Retrofit Methodology for Building Structures with Supplemental Energy Dissipating Systems," by G. Pekcan, J.B. Mander and S.S. Chen, 12/31/99, (PB2000-105994, A11, MF-A03).
- MCEER-00-0001 "The Marmara, Turkey Earthquake of August 17, 1999: Reconnaissance Report," edited by C. Scawthorn; with major contributions by M. Bruneau, R. Eguchi, T. Holzer, G. Johnson, J. Mander, J. Mitchell, W. Mitchell, A. Papageorgiou, C. Scaethorn, and G. Webb, 3/23/00, (PB2000-106200, A11, MF-A03).
- MCEER-00-0002 "Proceedings of the MCEER Workshop for Seismic Hazard Mitigation of Health Care Facilities," edited by G.C. Lee, M. Ettouney, M. Grigoriu, J. Hauer and J. Nigg, 3/29/00, (PB2000-106892, A08, MF-A02).
- MCEER-00-0003 "The Chi-Chi, Taiwan Earthquake of September 21, 1999: Reconnaissance Report," edited by G.C. Lee and C.H. Loh, with major contributions by G.C. Lee, M. Bruneau, I.G. Buckle, S.E. Chang, P.J. Flores, T.D. O'Rourke, M. Shinozuka, T.T. Soong, C-H. Loh, K-C. Chang, Z-J. Chen, J-S. Hwang, M-L. Lin, G-Y. Liu, K-C. Tsai, G.C. Yao and C-L. Yen, 4/30/00, (PB2001-100980, A10, MF-A02).
- MCEER-00-0004 "Seismic Retrofit of End-Sway Frames of Steel Deck-Truss Bridges with a Supplemental Tendon System: Experimental and Analytical Investigation," by G. Pekcan, J.B. Mander and S.S. Chen, 7/1/00, (PB2001-100982, A10, MF-A02).
- MCEER-00-0005 "Sliding Fragility of Unrestrained Equipment in Critical Facilities," by W.H. Chong and T.T. Soong, 7/5/00, (PB2001-100983, A08, MF-A02).
- MCEER-00-0006 "Seismic Response of Reinforced Concrete Bridge Pier Walls in the Weak Direction," by N. Abo-Shadi, M. Saiidi and D. Sanders, 7/17/00, (PB2001-100981, A17, MF-A03).
- MCEER-00-0007 "Low-Cycle Fatigue Behavior of Longitudinal Reinforcement in Reinforced Concrete Bridge Columns," by J. Brown and S.K. Kunnath, 7/23/00, (PB2001-104392, A08, MF-A02).
- MCEER-00-0008 "Soil Structure Interaction of Bridges for Seismic Analysis," I. PoLam and H. Law, 9/25/00, (PB2001-105397, A08, MF-A02).
- MCEER-00-0009 "Proceedings of the First MCEER Workshop on Mitigation of Earthquake Disaster by Advanced Technologies (MEDAT-1), edited by M. Shinozuka, D.J. Inman and T.D. O'Rourke, 11/10/00, (PB2001-105399, A14, MF-A03).
- MCEER-00-0010 "Development and Evaluation of Simplified Procedures for Analysis and Design of Buildings with Passive Energy Dissipation Systems, Revision 01," by O.M. Ramirez, M.C. Constantinou, C.A. Kircher, A.S. Whittaker, M.W. Johnson, J.D. Gomez and C. Chrysostomou, 11/16/01, (PB2001-105523, A23, MF-A04).
- MCEER-00-0011 "Dynamic Soil-Foundation-Structure Interaction Analyses of Large Caissons," by C-Y. Chang, C-M. Mok, Z-L. Wang, R. Settgast, F. Waggoner, M.A. Ketchum, H.M. Gonnermann and C-C. Chin, 12/30/00, (PB2001-104373, A07, MF-A02).
- MCEER-00-0012 "Experimental Evaluation of Seismic Performance of Bridge Restrainers," by A.G. Vlassis, E.M. Maragakis and M. Saiid Saiidi, 12/30/00, (PB2001-104354, A09, MF-A02).
- MCEER-00-0013 "Effect of Spatial Variation of Ground Motion on Highway Structures," by M. Shinozuka, V. Saxena and G. Deodatis, 12/31/00, (PB2001-108755, A13, MF-A03).
- MCEER-00-0014 "A Risk-Based Methodology for Assessing the Seismic Performance of Highway Systems," by S.D. Werner, C.E. Taylor, J.E. Moore, II, J.S. Walton and S. Cho, 12/31/00, (PB2001-108756, A14, MF-A03).

- MCEER-01-0001 "Experimental Investigation of P-Delta Effects to Collapse During Earthquakes," by D. Vian and M. Bruneau, 6/25/01, (PB2002-100534, A17, MF-A03).
- MCEER-01-0002 "Proceedings of the Second MCEER Workshop on Mitigation of Earthquake Disaster by Advanced Technologies (MEDAT-2)," edited by M. Bruneau and D.J. Inman, 7/23/01, (PB2002-100434, A16, MF-A03).
- MCEER-01-0003 "Sensitivity Analysis of Dynamic Systems Subjected to Seismic Loads," by C. Roth and M. Grigoriu, 9/18/01, (PB2003-100884, A12, MF-A03).
- MCEER-01-0004 "Overcoming Obstacles to Implementing Earthquake Hazard Mitigation Policies: Stage 1 Report," by D.J. Alesch and W.J. Petak, 12/17/01, (PB2002-107949, A07, MF-A02).
- MCEER-01-0005 "Updating Real-Time Earthquake Loss Estimates: Methods, Problems and Insights," by C.E. Taylor, S.E. Chang and R.T. Eguchi, 12/17/01, (PB2002-107948, A05, MF-A01).
- MCEER-01-0006 "Experimental Investigation and Retrofit of Steel Pile Foundations and Pile Bents Under Cyclic Lateral Loadings," by A. Shama, J. Mander, B. Blabac and S. Chen, 12/31/01, (PB2002-107950, A13, MF-A03).
- MCEER-02-0001 "Assessment of Performance of Bolu Viaduct in the 1999 Duzce Earthquake in Turkey" by P.C. Roussis, M.C. Constantinou, M. Erdik, E. Durukal and M. Dicleli, 5/8/02, (PB2003-100883, A08, MF-A02).
- MCEER-02-0002 "Seismic Behavior of Rail Counterweight Systems of Elevators in Buildings," by M.P. Singh, Rildova and L.E. Suarez, 5/27/02. (PB2003-100882, A11, MF-A03).
- MCEER-02-0003 "Development of Analysis and Design Procedures for Spread Footings," by G. Mylonakis, G. Gazetas, S. Nikolaou and A. Chauncey, 10/02/02, (PB2004-101636, A13, MF-A03, CD-A13).
- MCEER-02-0004 "Bare-Earth Algorithms for Use with SAR and LIDAR Digital Elevation Models," by C.K. Huyck, R.T. Eguchi and B. Houshmand, 10/16/02, (PB2004-101637, A07, CD-A07).
- MCEER-02-0005 "Review of Energy Dissipation of Compression Members in Concentrically Braced Frames," by K.Lee and M. Bruneau, 10/18/02, (PB2004-101638, A10, CD-A10).
- MCEER-03-0001 "Experimental Investigation of Light-Gauge Steel Plate Shear Walls for the Seismic Retrofit of Buildings" by J. Berman and M. Bruneau, 5/2/03, (PB2004-101622, A10, MF-A03, CD-A10).
- MCEER-03-0002 "Statistical Analysis of Fragility Curves," by M. Shinozuka, M.Q. Feng, H. Kim, T. Uzawa and T. Ueda, 6/16/03, (PB2004-101849, A09, CD-A09).
- MCEER-03-0003 "Proceedings of the Eighth U.S.-Japan Workshop on Earthquake Resistant Design of Lifeline Facilities and Countermeasures Against Liquefaction," edited by M. Hamada, J.P. Bardet and T.D. O'Rourke, 6/30/03, (PB2004-104386, A99, CD-A99).
- MCEER-03-0004 "Proceedings of the PRC-US Workshop on Seismic Analysis and Design of Special Bridges," edited by L.C. Fan and G.C. Lee, 7/15/03, (PB2004-104387, A14, CD-A14).
- MCEER-03-0005 "Urban Disaster Recovery: A Framework and Simulation Model," by S.B. Miles and S.E. Chang, 7/25/03, (PB2004-104388, A07, CD-A07).
- MCEER-03-0006 "Behavior of Underground Piping Joints Due to Static and Dynamic Loading," by R.D. Meis, M. Maragakis and R. Siddharthan, 11/17/03, (PB2005-102194, A13, MF-A03, CD-A00).
- MCEER-03-0007 "Seismic Vulnerability of Timber Bridges and Timber Substructures," by A.A. Shama, J.B. Mander, I.M. Friedland and D.R. Allicock, 12/15/03.
- MCEER-04-0001 "Experimental Study of Seismic Isolation Systems with Emphasis on Secondary System Response and Verification of Accuracy of Dynamic Response History Analysis Methods," by E. Wolff and M. Constantinou, 1/16/04 (PB2005-102195, A99, MF-E08, CD-A00).

- MCEER-04-0002 "Tension, Compression and Cyclic Testing of Engineered Cementitious Composite Materials," by K. Kesner and S.L. Billington, 3/1/04, (PB2005-102196, A08, CD-A08).
- MCEER-04-0003 "Cyclic Testing of Braces Laterally Restrained by Steel Studs to Enhance Performance During Earthquakes," by O.C. Celik, J.W. Berman and M. Bruneau, 3/16/04, (PB2005-102197, A13, MF-A03, CD-A00).
- MCEER-04-0004 "Methodologies for Post Earthquake Building Damage Detection Using SAR and Optical Remote Sensing: Application to the August 17, 1999 Marmara, Turkey Earthquake," by C.K. Huyck, B.J. Adams, S. Cho, R.T. Eguchi, B. Mansouri and B. Houshmand, 6/15/04, (PB2005-104888, A10, CD-A00).
- MCEER-04-0005 "Nonlinear Structural Analysis Towards Collapse Simulation: A Dynamical Systems Approach," by M.V. Sivaselvan and A.M. Reinhorn, 6/16/04, (PB2005-104889, A11, MF-A03, CD-A00).
- MCEER-04-0006 "Proceedings of the Second PRC-US Workshop on Seismic Analysis and Design of Special Bridges," edited by G.C. Lee and L.C. Fan, 6/25/04, (PB2005-104890, A16, CD-A00).
- MCEER-04-0007 "Seismic Vulnerability Evaluation of Axially Loaded Steel Built-up Laced Members," by K. Lee and M. Bruneau, 6/30/04, (PB2005-104891, A16, CD-A00).
- MCEER-04-0008 "Evaluation of Accuracy of Simplified Methods of Analysis and Design of Buildings with Damping Systems for Near-Fault and for Soft-Soil Seismic Motions," by E.A. Pavlou and M.C. Constantinou, 8/16/04, (PB2005-104892, A08, MF-A02, CD-A00).
- MCEER-04-0009 "Assessment of Geotechnical Issues in Acute Care Facilities in California," by M. Lew, T.D. O'Rourke, R. Dobry and M. Koch, 9/15/04, (PB2005-104893, A08, CD-A00).
- MCEER-04-0010 "Scissor-Jack-Damper Energy Dissipation System," by A.N. Sigaher-Boyle and M.C. Constantinou, 12/1/04 (PB2005-108221).
- MCEER-04-0011 "Seismic Retrofit of Bridge Steel Truss Piers Using a Controlled Rocking Approach," by M. Pollino and M. Bruneau, 12/20/04 (PB2006-105795).
- MCEER-05-0001 "Experimental and Analytical Studies of Structures Seismically Isolated with an Uplift-Restraint Isolation System," by P.C. Roussis and M.C. Constantinou, 1/10/05 (PB2005-108222).
- MCEER-05-0002 "A Versatile Experimentation Model for Study of Structures Near Collapse Applied to Seismic Evaluation of Irregular Structures," by D. Kusumastuti, A.M. Reinhorn and A. Rutenberg, 3/31/05 (PB2006-101523).
- MCEER-05-0003 "Proceedings of the Third PRC-US Workshop on Seismic Analysis and Design of Special Bridges," edited by L.C. Fan and G.C. Lee, 4/20/05, (PB2006-105796).
- MCEER-05-0004 "Approaches for the Seismic Retrofit of Braced Steel Bridge Piers and Proof-of-Concept Testing of an Eccentrically Braced Frame with Tubular Link," by J.W. Berman and M. Bruneau, 4/21/05 (PB2006-101524).
- MCEER-05-0005 "Simulation of Strong Ground Motions for Seismic Fragility Evaluation of Nonstructural Components in Hospitals," by A. Wanitkorkul and A. Filiatrault, 5/26/05 (PB2006-500027).
- MCEER-05-0006 "Seismic Safety in California Hospitals: Assessing an Attempt to Accelerate the Replacement or Seismic Retrofit of Older Hospital Facilities," by D.J. Alesch, L.A. Arendt and W.J. Petak, 6/6/05 (PB2006-105794).
- MCEER-05-0007 "Development of Seismic Strengthening and Retrofit Strategies for Critical Facilities Using Engineered Cementitious Composite Materials," by K. Kesner and S.L. Billington, 8/29/05 (PB2006-111701).
- MCEER-05-0008 "Experimental and Analytical Studies of Base Isolation Systems for Seismic Protection of Power Transformers," by N. Murota, M.Q. Feng and G-Y. Liu, 9/30/05 (PB2006-111702).
- MCEER-05-0009 "3D-BASIS-ME-MB: Computer Program for Nonlinear Dynamic Analysis of Seismically Isolated Structures," by P.C. Tsopelas, P.C. Roussis, M.C. Constantinou, R. Buchanan and A.M. Reinhorn, 10/3/05 (PB2006-111703).


- MCEER-05-0010 "Steel Plate Shear Walls for Seismic Design and Retrofit of Building Structures," by D. Vian and M. Bruneau, 12/15/05 (PB2006-111704).
- MCEER-05-0011 "The Performance-Based Design Paradigm," by M.J. Astrella and A. Whittaker, 12/15/05 (PB2006-111705).
- MCEER-06-0001 "Seismic Fragility of Suspended Ceiling Systems," H. Badillo-Almaraz, A.S. Whittaker, A.M. Reinhorn and G.P. Cimellaro, 2/4/06 (PB2006-111706).
- MCEER-06-0002 "Multi-Dimensional Fragility of Structures," by G.P. Cimellaro, A.M. Reinhorn and M. Bruneau, 3/1/06 (PB2007-106974, A09, MF-A02, CD A00).
- MCEER-06-0003 "Built-Up Shear Links as Energy Dissipators for Seismic Protection of Bridges," by P. Dusicka, A.M. Itani and I.G. Buckle, 3/15/06 (PB2006-111708).
- MCEER-06-0004 "Analytical Investigation of the Structural Fuse Concept," by R.E. Vargas and M. Bruneau, 3/16/06 (PB2006-111709).
- MCEER-06-0005 "Experimental Investigation of the Structural Fuse Concept," by R.E. Vargas and M. Bruneau, 3/17/06 (PB2006-111710).
- MCEER-06-0006 "Further Development of Tubular Eccentrically Braced Frame Links for the Seismic Retrofit of Braced Steel Truss Bridge Piers," by J.W. Berman and M. Bruneau, 3/27/06 (PB2007-105147).
- MCEER-06-0007 "REDARS Validation Report," by S. Cho, C.K. Huyck, S. Ghosh and R.T. Eguchi, 8/8/06 (PB2007-106983).
- MCEER-06-0008 "Review of Current NDE Technologies for Post-Earthquake Assessment of Retrofitted Bridge Columns," by J.W. Song, Z. Liang and G.C. Lee, 8/21/06 06 (PB2007-106984).
- MCEER-06-0009 "Liquefaction Remediation in Silty Soils Using Dynamic Compaction and Stone Columns," by S. Thevanayagam, G.R. Martin, R. Nashed, T. Shenthan, T. Kanagalingam and N. Ecemis, 8/28/06 06 (PB2007-106985).
- MCEER-06-0010 "Conceptual Design and Experimental Investigation of Polymer Matrix Composite Infill Panels for Seismic Retrofitting," by W. Jung, M. Chiewanichakorn and A.J. Aref, 9/21/06 (PB2007-106986).
- MCEER-06-0011 "A Study of the Coupled Horizontal-Vertical Behavior of Elastomeric and Lead-Rubber Seismic Isolation Bearings," by G.P. Warn and A.S. Whittaker, 9/22/06 (PB2007-108679).
- MCEER-06-0012 "Proceedings of the Fourth PRC-US Workshop on Seismic Analysis and Design of Special Bridges: Advancing Bridge Technologies in Research, Design, Construction and Preservation," Edited by L.C. Fan, G.C. Lee and L. Ziang, 10/12/06 (PB2007-109042).
- MCEER-06-0013 "Cyclic Response and Low Cycle Fatigue Characteristics of Plate Steels," by P. Dusicka, A.M. Itani and I.G. Buckle, 11/1/06 06 (PB2007-106987).
- MCEER-06-0014 "Proceedings of the Second US-Taiwan Bridge Engineering Workshop," edited by W.P. Yen, J. Shen, J-Y. Chen and M. Wang, 11/15/06.
- MCEER-06-0015 "User Manual and Technical Documentation for the REDARSTM Import Wizard," by S. Cho, S. Ghosh, C.K. Huyck and S.D. Werner, 11/30/06 (PB2007-114766).
- MCEER-06-0016 "Hazard Mitigation Strategy and Monitoring Technologies for Urban and Infrastructure Public Buildings: Proceedings of the China-US Workshops," edited by X.Y. Zhou, A.L. Zhang, G.C. Lee and M. Tong, 12/12/06 (PB2008-500018).
- MCEER-07-0001 "Static and Kinetic Coefficients of Friction for Rigid Blocks," by C. Kafali, S. Fathali, M. Grigoriu and A.S. Whittaker, 3/20/07 (PB2007-114767).
- MCEER-07-0002 "Hazard Mitigation Investment Decision Making: Organizational Response to Legislative Mandate," by L.A. Arendt, D.J. Alesch and W.J. Petak, 4/9/07 (PB2007-114768).

- MCEER-07-0003 “Seismic Behavior of Bidirectional-Resistant Ductile End Diaphragms with Unbonded Braces in Straight or Skewed Steel Bridges,” by O. Celik and M. Bruneau, 4/11/07 (PB2008-105141).
- MCEER-07-0004 “Modeling Pile Behavior in Large Pile Groups Under Lateral Loading,” by A.M. Dodds and G.R. Martin, 4/16/07(PB2008-105142).
- MCEER-07-0005 “Experimental Investigation of Blast Performance of Seismically Resistant Concrete-Filled Steel Tube Bridge Piers,” by S. Fujikura, M. Bruneau and D. Lopez-Garcia, 4/20/07 (PB2008-105143).
- MCEER-07-0006 “Seismic Analysis of Conventional and Isolated Liquefied Natural Gas Tanks Using Mechanical Analogs,” by I.P. Christovasilis and A.S. Whittaker, 5/1/07.
- MCEER-07-0007 “Experimental Seismic Performance Evaluation of Isolation/Restraint Systems for Mechanical Equipment – Part 1: Heavy Equipment Study,” by S. Fathali and A. Filiatrault, 6/6/07 (PB2008-105144).
- MCEER-07-0008 “Seismic Vulnerability of Timber Bridges and Timber Substructures,” by A.A. Sharma, J.B. Mander, I.M. Friedland and D.R. Allicock, 6/7/07 (PB2008-105145).
- MCEER-07-0009 “Experimental and Analytical Study of the XY-Friction Pendulum (XY-FP) Bearing for Bridge Applications,” by C.C. Marin-Artieda, A.S. Whittaker and M.C. Constantinou, 6/7/07.
- MCEER-07-0010 “Proceedings of the PRC-US Earthquake Engineering Forum for Young Researchers,” Edited by G.C. Lee and X.Z. Qi, 6/8/07.
- MCEER-07-0011 “Design Recommendations for Perforated Steel Plate Shear Walls,” by R. Purba and M. Bruneau, 6/18/07.
- MCEER-07-0012 “Performance of Seismic Isolation Hardware Under Service and Seismic Loading,” by M.C. Constantinou, A.S. Whittaker, Y. Kalpakidis, D.M. Fenz and G.P. Warn, 8/27/07.
- MCEER-07-0013 “Experimental Evaluation of the Seismic Performance of Hospital Piping Subassemblies,” by E.R. Goodwin, E. Maragakis and A.M. Itani, 9/4/07.
- MCEER-07-0014 “A Simulation Model of Urban Disaster Recovery and Resilience: Implementation for the 1994 Northridge Earthquake,” by S. Miles and S.E. Chang, 9/7/07.
- MCEER-07-0015 “Statistical and Mechanistic Fragility Analysis of Concrete Bridges,” by M. Shinozuka, S. Banerjee and S-H. Kim, 9/10/07.
- MCEER-07-0016 “Three-Dimensional Modeling of Inelastic Buckling in Frame Structures,” by M. Schachter and AM. Reinhorn, 9/13/07.
- MCEER-07-0017 “Modeling of Seismic Wave Scattering on Pile Groups and Caissons,” by I. Po Lam, H. Law and C.T. Yang, 9/17/07.
- MCEER-07-0018 “Bridge Foundations: Modeling Large Pile Groups and Caissons for Seismic Design,” by I. Po Lam, H. Law and G.R. Martin (Coordinating Author), 12/1/07.
- MCEER-07-0019 “Principles and Performance of Roller Seismic Isolation Bearings for Highway Bridges,” by G.C. Lee, Y.C. Ou, Z. Liang, T.C. Niu and J. Song, 12/10/07.
- MCEER-07-0020 “Centrifuge Modeling of Permeability and Pinning Reinforcement Effects on Pile Response to Lateral Spreading,” by L.L. Gonzalez-Lagos, T. Abdoun and R. Dobry, 12/10/07.



EARTHQUAKE ENGINEERING TO EXTREME EVENTS

University at Buffalo, The State University of New York
Red Jacket Quadrangle ▪ Buffalo, New York 14261
Phone: (716) 645-3391 ▪ Fax: (716) 645-3399
E-mail: mceer@buffalo.edu ▪ WWW Site <http://mceer.buffalo.edu>



University at Buffalo *The State University of New York*

ISSN 1520-295X